NSEL Report Series
Report No. NSEL-045
September 2015

Targeted Energy Transfer using Nonlinear Energy Sinks for the Attenuation of Transient Loads on Building Structures

Nicholas E. Wierschem

and

Billie F. Spencer, Jr.

Department of Civil and Environmental Engineering
University of Illinois at Urbana-Champaign

UILU-ENG-2015-1811

ISSN: 1940-9826

The Newmark Structural Engineering Laboratory (NSEL) of the Department of Civil and Environmental Engineering at the University of Illinois at Urbana-Champaign has a long history of excellence in research and education that has contributed greatly to the state-of-the-art in civil engineering. Completed in 1967 and extended in 1971, the structural testing area of the laboratory has a versatile strong-floor/wall and a three-story clear height that can be used to carry out a wide range of tests of building materials, models, and structural systems. The laboratory is named for Dr. Nathan M. Newmark, an internationally known educator and engineer, who was the Head of the Department of Civil Engineering at the University of Illinois [1956-73] and the Chair of the Digital Computing Laboratory [1947-57]. He developed simple, yet powerful and widely used, methods for analyzing complex structures and assemblages subjected to a variety of static, dynamic, blast, and earthquake loadings. Dr. Newmark received numerous honors and awards for his achievements, including the prestigious National Medal of Science awarded in 1968 by President Lyndon B. Johnson. He was also one of the founding members of the National Academy of Engineering.

Contact:
Prof. B.F. Spencer, Jr.
Director, Newmark Structural Engineering Laboratory
2213 NCEL, MC-250
205 North Mathews Ave.
Urbana, IL 61801
Telephone (217) 333-8630
E-mail: bfs@illinois.edu

This technical report is based on the first author's doctoral dissertation of the same title, which was completed in May 2014. The second author served as the dissertation advisor for this work.

This research program was sponsored by the Defense Advanced Research Projects Agency through grant HR0011–10–1–0077; Dr. Aaron Lazarus was the program manager. The content of this report does not necessarily reflect the position or the policy of the U. S. Government, and no official endorsement should be inferred.

The authors would like to thank the numerous collaborators on this work, including Lawrence Bergman, Alexander Vakakis, Larry Fahnestock, Michael McFarland, Dane Quinn, Mohammad Al Shudeifat, Jie Luo, Sean Hubbard, and Richard Ott. Additionally, the authors would like to acknowledge the support of collaborators at the US Army Corps of Engineers, including Jim Wilcoski, Jonathan Trovillion, and Matt Holmer.

The cover photographs are used with permission. The Trans-Alaska Pipeline photograph was provided by Terra Galleria Photography (http://www.terragalleria.com/).

ABSTRACT

Nonlinear energy sinks (NESs) have been proposed as a practical and robust means of passively protecting buildings structures subjected to extreme transient loads. NESs are a type of passive attachment that differentiate themselves from tradition linear attachments through the exploitation of essentially nonlinear stiffness elements. The essentially nonlinear restoring force provided by these elements allows the NES to interact with any mode of the primary structure to which the NES is attached and participate in targeted energy transfer (TET), the broadband transfer of energy from the primary structure to the NES where it can be rapidly dissipated. Additionally, this nonlinear restoring force allows the linear modes of the primary structure to become coupled and energy to be transferred from the lower modes of vibration to the higher modes where it is dissipated at a faster rate. Previous experimental investigations of the effectiveness of NESs have used table-top sized specimens; however, little, if any, work has been done using larger-scale models that allow practical implementation issues to be considered. In addition, the existing body of work with NESs is far from complete, with limited work presented on the use of systems of multiple NESs, the experimental realization of several different NES types, or their response to realistic loads.

The primary objective of this research is to explore the potential for nonlinear energy sinks to be a practical and robust means of passively protecting buildings structures subjected to extreme transient loads. In this research, experimental testing and numerical simulations will be used to perform this investigation. The two types of transient loads focused on are impulsive loads, such as blasts, and broadband random loads, such as seismic ground motions. As a part of this investigation, small-, medium-, and large-scale primary structures and several types of NESs were designed and fabricated. With these structures and NESs, the experimental investigation of the performance of these different types of NESs was carried out using impulse-like shake-table-produced ground motion. Additionally, large-scale investigation of a non-parasitic (no net added mass) system NESs was performed with explosive blast loading and seismic loading. Furthermore, numerical simulations were performed to validate experimentally identified NES models and to investigate the robustness of NES systems. The results of this research show that NESs can significantly attenuate the response of building structures subjected to a variety of different transient load types, as well as reduce the peak demand on a structure. Furthermore, the synergistic effects realized by the simultaneous use of the different types of NESs allows for consistent performance to be maintained across a broad range of load amplitudes.

CONTENTS

INTRODUCTION

1.1 Problem definition

Civil infrastructure is the one of the foundations of modern life. We rely on highways, railroads, and bridges to get from one place to another. Electricity, water, and waste are processed or produced in facilities and transported via complex networks. Perhaps most importantly, we spend the majority of the day living, working, and studying in buildings, both large and small. All these vital pieces of civil infrastructure are, however, vulnerable to the ever-present threat of natural and man-made hazards. These hazards put civil infrastructure in danger of both damage and destruction, as well as threaten the lives and livelihoods of the people who occupy and rely on this infrastructure. Most extreme hazards that critically effect civil infrastructure can be classified as transient loading events. These transient loading events include loads of an impulsive nature and broadband random loadings, such as seismic ground motion.

Hazards of an impulsive nature that critically effect build structures come from both natural and man-made sources. These hazards include wind gusts, impacts or collisions, and, perhaps most importantly, blasts. In recent years, due to concerns of foreign and domestic terrorism, a great deal of attention has been placed on mitigating the effects of blast loading on structures. While the likelihood of a structure being subjected to a blast event is arguably quite small compared to chances of the structure being subjected other critical hazards, the high profile nature of these events has made counteracting their results a high priority. Moreover, design with these impulsive events in mind is becoming increasingly required in design codes, especially for critical structures (ASCE 2011).

The increased interest in blast loading on structures had led to a large amount of research, with most focused on the local effects of blasts and progressive collapse in structures resulting from local failures. Despite recent efforts, structures remain vulnerable to failure mechanisms related to their global response (Ngo et al. 2007). The global response of structures is particularly important when considering blasts at moderate standoff distances. Furthermore, as the local protection of structures subjected to blast improves and failure mechanisms change, controlling a structure's global blast response is becoming increasingly important for blasts with short standoff distances, too. In addition to the focus on the local effects of blast, the complex logistics involved with blast testing and limited facilities make blast testing difficult for experimental research to be done investigating the global effects and response of structures subjected to blast loading.

Aside from impulsive loads, another category of transient loading that can critically affect structures is broadband random loads, such as seismic ground motion. Earthquakes, which also can sometimes have impulsive features, are an important natural hazards facing civil infrastructure. From 2000 to 2009 earthquakes and their aftereffects led to an estimated 470,000 deaths globally, which is an estimated 60% of the total number of deaths from all natural disasters during this period (UNISDR 2012). Additionally, from 2000 to 2009, geophysical natural disasters, which consist primarily of earthquakes, led to an estimated average yearly global economic losses of 18.7 billion USD, which account for an estimated 19% of the total losses due to natural disasters (Guha-Sapir et al. 2011). While the risk of destruction from

earthquakes is not found uniformly in all parts of the world, moderate and high risk areas are present on all continents. The widespread global nature of the problem is demonstrated by the fact that 11 of the world's 20 largest metropolitan areas are located within moderate to very high seismic hazard zones.

In contrast to blast loading, research on mitigating the effects of seismic loading on building structures has been active for many decades. Additionally, a large amount experimental work on this subject has been conducted with realistic loading, in part, due to the relatively widespread availability of shake table testing. Nonetheless, as has been demonstrated time and time again, earthquakes can still be very deadly and destructive events, even in the developed world.

The reason for the destructive nature of earthquakes is, in part, the high amplitude of the ground acceleration that of some earthquakes present; however, the earthquake's amplitude is not the complete story. Another reason why earthquakes can be so deadly and destructive is that the characteristics of the loading posed by earthquakes are highly variable. In addition to the amplitude, the frequency content, direction, and duration of the ground motion experienced by a structure can vary tremendously and is a function of local conditions, such as soil type, as well as the type of fault rupture and distance to the earthquake epicenter (Chen and Scawthorn 2003). Consequently, the limited resources of building owners still challenges engineers and, in some cases, prevents them from economically being able to adequately protect building from these highly variable events.

1.2 Structural control systems

Structural control systems have been studied and implemented to mitigate the threat to building structures posed by extreme transient load and other hazards. The advantage of these systems is that they offer protection for a structure without the need to dramatically increase the size or complexity of the underlying structural system. The three main families of structural control systems are passive, semi-active, and active systems. In general, semi-active and active control systems, which both utilize feedback from sensors, have shown great promise at achieving structural control goals. However, due to factors such as the complexity of the systems, high costs, a reliance on a constant power source, and a conservative construction industry, semi-active and active structural control systems have only been utilized in only a limited number of real-world structures, especially in the United States.

Passive control devices and systems, which are commonly less complex and do not rely on a constant source of power, have enjoyed widespread use. One of the most popular types of passive control devices are tuned mass dampers (TMDs). In their simplest form, TMDs consist of a supplemental mass that is coupled linearly to a structure. These devices are referred to as tuned because, with informed selection of their mass and linear coupling, the devices are tuned to reduce the response of a particular mode of vibration of the primary structure to which they are attached. This reduction in response primarily occurs because the TMD changes the dynamic response of the structure near the vibration mode it is tuned to and these changes allow energy to be transferred to the TMD.

The ability of the TMD to utilize linear dynamics to reduce the response of a structure has made them particularly popular in high rise structures. In this type of structure, the critical design lateral loading is generally a wind loading, where the structure is design to remain elastic. Where the TMDs have shown weakness, and thus are not as popular for, are situations where extreme transient loads, such as earthquakes and blasts, dominate the design of a structure. In these cases, many times the structure is designed to response inelastically, thus the natural

frequencies of the structure can shift. This shift in natural frequency detunes the TMD (its frequency no longer corresponds with the structure's) and thus this detuning is detrimental to the TMD's effectiveness. Another concern in extreme events is the possibility of multiple modes being critically excited; because the TMD is tuned to a particular mode of a structure, the TMD is incapable of effectively reducing the response of multiple modes. Perhaps most importantly, concern has been placed in the use of the TMD, and other traditional passive system, during extreme transient events because the effectiveness of these systems at reducing the peak of the response can be limited.

1.3 Nonlinear energy sinks (NESs)

Nonlinear energy sinks (NESs) are a relatively new class of passive control devices with significant potential for mitigating dynamic loads on structures. In general, NESs are composed of a mass (or set of masses) which is coupled to a structure with elements that produce an essentially nonlinear (non-linearizable) restoring force. Superficially, the NES schematically appears similar to traditional linear TMD, except, as mentioned above, TMDs are coupled to structures with a linear restoring force. However, this small change introduces dramatic changes to the dynamics of the system. With this essentially nonlinear restoring force, the response of an NES is not dominated by a single natural frequency and has the ability engage in resonant vibration with the primary structure across a broad frequency range. Thus, the NES can interact with any mode of an underlying structure and participate in Targeted Energy Transfer (TET) (Vakakis et al. 2008), the broadband transfer of energy from the primary structure to the NES where the energy can be rapidly dissipated due to the relative motion of the device. In addition to transferring energy to the NES, the nonlinearity in the NES allows the modes of the underlying structure to be coupled and energy to be transfer from the lower modes of vibration to higher ones where it is can be dissipated more quickly.

The essentially nonlinear restoring force, which is necessary to obtain the unique properties of NESs, exists in two basic forms. The first form is a smooth nonlinear restoring force in which no linear component is present. As a result of the lack of a linear component in this smooth restoring force, the NES does not have a particular natural frequency, and the device can resonate with and participate in the transfer of energy from any mode of the primary structure to which it is attached (Vakakis et al. 2008). The second form of essentially nonlinear restoring force is a restoring force with a discontinuity. This discontinuity in restoring force, which is commonly the result of an impact, is a broadband event and, because of it, energy is scattered throughout the underlying structure, particularly to its higher modes (Al-Shudeifat et al. 2013). The transfer of energy to higher modes that occurs as a result of both types of NESs is beneficial because, at these higher frequencies, the energy can be naturally dissipated faster due to the reduced time scale.

In recent years, the ability of nonlinear energy sinks (NESs) to quickly mitigate the global response of structures subjected to impulsive loads has been extensively studied (Quinn et al. 2011; Sapsis et al. 2012; Schmidt and Lamarque 2010; Vaurigaud et al. 2011). However, key gaps in knowledge clearly exist in this work, including experimental investigations of the performance of NESs using larger than table-top-sized specimens. Additionally, most of the research on NESs has focused on basic versions of NESs, with relatively little work, especially experimentally, done on multi-degree-of-freedom NESs and NESs that utilize discontinuities in restoring force. Finally, while the performance of NESs in mitigating idealized impulsive loads

has been studied extensively, little attention has been paid to investigating the performance of systems with NESs subjected to realistic transient loads, such as blasts and earthquakes.

1.4 Report Overview

The primary objective of this research is to explore the potential for nonlinear energy sinks to be a practical and robust means of passively protecting buildings structures subjected to extreme transient loads. The two types of transient loads focused on in this research are impulsive loads, such as blasts, and broadband random loads, such as seismic ground motions. As a part of this investigation, small, medium, and large-scale test structures and several types of nonlinear energy sinks will be designed and fabricated. With these structures and NESs, the experimental exploration of the performance of these different types of NESs will be performed using an impulse-like shake-table-produced ground motion. Additionally, large-scale investigations will be performed with explosive blast loading and seismic loading.

A secondary objective of this research is the development of a methodology for the creation of ground motions for the simulation of the global effects on structures due to blasts. This objective is motivated by the difficulties involved with performing experimental work related to global blast effects on structures due to the inherent logistical concerns involved in explosive blast testing and the limited number of suitable facilities for these tests.

A brief description of the content of each the subsequent chapters in this report is provided below.

Chapter 2 lays the foundation for the investigation presented in this report by reviewing related literature. Included in this review is work related to NESs, traditional structural control devices, and experimental blast simulation methods.

In Chapter 3, background information related to several numerical and mathematical tools used in this report will be discussed. The topics and methods discussed in this chapter include nonlinear system identification using the restoring force method, the quantitative evaluation of the response of nonlinear systems using a measure known as effective damping, and wavelet transforms.

In Chapter 4, a new methodology for using shake-table-produced ground motion for the experimental simulation of global blast response in building structures is proposed. First, the feasibility of this type of simulation and the practical constraints on it are discussed, followed by an introduction of the methodology. Then, the proposed approach is validated using numerical simulation and experimental testing. For this validation, comparisons of a structure's blast response will be made with its response to a ground motion produced using the proposed methodology.

The experimental investigation of the effectiveness of NESs at rapidly reducing the response of building structures subjected to idealized impulsive loads has been previously considered using table-top sized specimens. Because little, if any, work has been done using larger-size models, the feasibility of effectively scaling up these devices for implementation in civil structures was not clear. Thus, in Chapter 5, the development and experimental investigation of larger small- and medium-scale NESs for the protection of build structures against extreme transient loads is presented. The types of NESs that will be studied at this stage of the research are the small-scale Type I and Type III NESs and medium-scale a Type III NES; these types of NESs are shown conceptually in Figure 1-1. The experimental investigation of these different NESs will be performed using shake-table-produced impulsive ground motion.

Building on the small- and medium-scale success discussed in the previous chapter, Chapter 6 presents the development of a large-scale base structure and system of NESs. This system features a combination of Type I NESs, which employ a smooth essential nonlinearity, and single-sided vibro-impact (SSVI) NESs, which employ a sharp essential nonlinearity; conceptual models of these types of NESs are shown in Figure 1-1. This system of NESs is designed to be non-parasitic; thus, its presence results in no net added mass in the structure. As part of this development, an experimental modal analysis is performed on the large-scale base structure to determine the modal properties of the built large-scale structure.

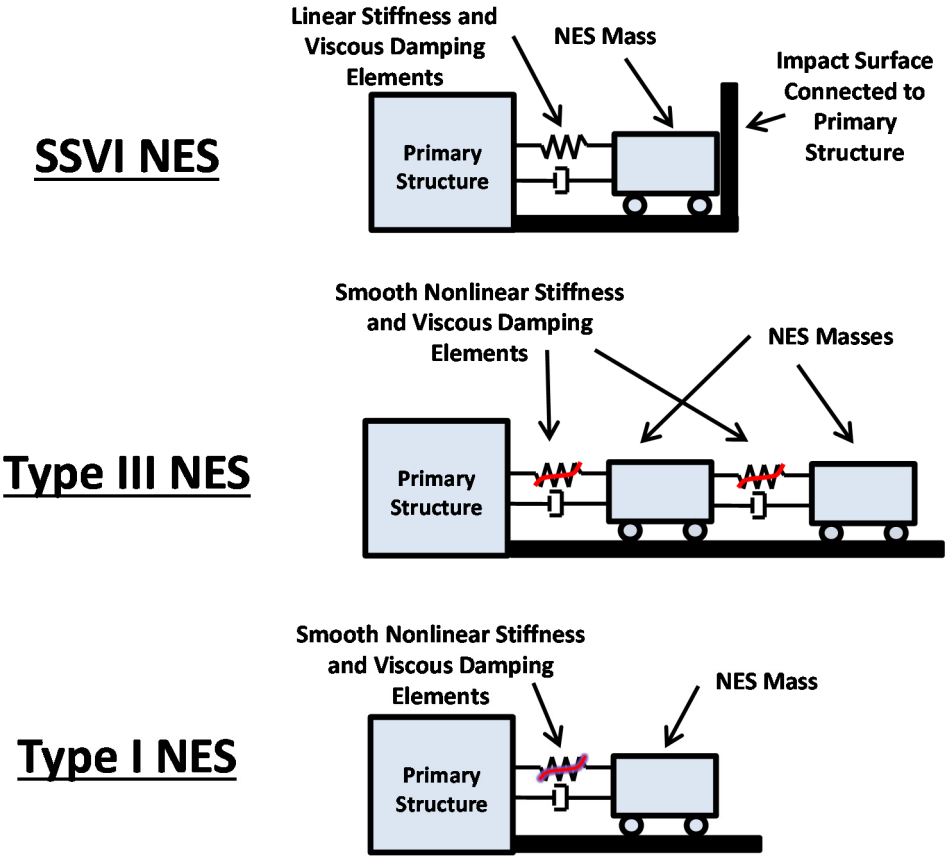

Figure 1-1. Conceptual models of the different types of nonlinear energy sinks considered in this work

No large-scale experimental investigation of the performance of NESs has been performed; consequently, in Chapter 7 the experimental investigation of the performance of the system of NESs featured in the large-scale structure developed in the previous chapter is presented. For this experimental investigation, the structure will be tested using explosive blast loading, shake-table-produced impulse-like ground motion, and sine-sweep ground motion. Of the impulse-like ground motions that will be used to load the structure during the shake table tests, one will be specially designed to simulate the structure's global response to an explosive blast test. Furthermore, this large-scale system of NESs will be used to investigate the synergistic effects of multiple types of NESs acting in combination.

In Chapters 5, 6, and 7, the effectiveness of NESs at rapidly reducing the response of structures subjected to transient loads primarily of an impulsive nature is examined. While this type of loading is important, other forms of transient loading, such as seismic ground motions can critically effect structures. Accordingly, the goal of Chapter 8 is to investigate the potential effectiveness of NESs at mitigating the response of building structures subjected to seismic ground motion using several case studies. As a part of this study, both numerical simulations and experimental testing will be utilized.

In Chapter 9, a summary of the contributions found in this report are presented, major conclusions from this work are reiterated, and directions for future work on this subject are outlined and discussed.

LITERATURE REVIEW

The literature related to the work presented in this report is divided into three main sections: a review of literature related to structural control, a review related to nonlinear energy sinks, and a review related to experimental blast simulation. In the review of the structural control literature, active, semi-active, and passive control systems will be discussed. While other control systems are discussed in limited detail, particular attention in this section will be paid to passive mass damper systems. In the review of work related to NESs, a brief overview of the history of NES research will be presented. Additionally, specific topics such as the different types of NESs and studies featuring systems of multiple NESs will be examined. Finally, techniques currently used for blast simulation are examined.

2.1 Control of civil structures

Civil structures are generally designed to remain elastic under normal loading conditions; however, extremely uneconomical designs would result if structures were required to remain elastic during extreme loading event. The design of structures to remain elastic under extreme seismic loading would be particularly uneconomical, as the greatly increased weight of an elastic design would serve to attract even larger loads that would subsequently also need to be resisted elastically. As a consequence of uneconomical elastic design for extreme loads, modern structural codes allow structures to respond inelastically when subjected to extreme loads (ACI 2011; AISC 2011; ASCE 2011). By allowing inelastic behavior in structures, the amplitude of the loads used in designing structures can be dramatically reduced; in the design codes used in the US, this reduction factor is referred to as the Response Modification Factor (ASCE 2011).

In most structures, inelastic behavior under extreme loads is designed to be introduced into the structure via the ductile response of the structure's members. This ductile response includes yielding of the member which dissipates some of the energy introduced into the structure, but is a form of damage and results in inelastic deformation. At the system level, these inelastic deformations combine to produce residual drifts in the structural system. While the occurrence of residual drifts in the structure has been deemed acceptable to ensure the life safety of the structure's occupants, these residual drifts compromise the serviceability of the structure after the extreme event has taken place. In many cases, this damage requires replacement of the structure or expense repairs (Wilkinson et al. 2013).

In response to the desire of engineers and building owners to protect structures from extreme loads using methods that delayed the reliance on the inelastic deformations of the structural system, the field of structural control has gradually evolved (Soong and Dargush 1997). With structural control, the goal is not simply to make a structure stronger or stiffer, but to change the dynamic properties of a structure to improve its performance during a dynamic event. These changes can include modifying the natural frequencies of the structure, damping, frequency response, or a multitude of other properties, all designed to create a more ideal response of the structure. The different types of structure control systems used to modify these dynamic properties can be classified as passive, semi-active, and active.

2.1.1 Active control systems

Active control systems are closed-loop systems in which a controller is used to a control a plant (in the case of structural control the plant is the structure). Information regarding the response of the plant and the control system is gathered by sensors and is used in a feedback loop to direct the actions of the controller. An example of active control in an everyday system is cruise control in a car; in this system, once a goal speed is set, the throttle is adjusted to achieve this speed with the help of information from the speedometer. An example of active control in a structural system is a structure equipped with a controllable mass, also known as an active mass driver. In this system, measurements of the response of the underlying structure and the control mass are taken with accelerometers and displacement sensors. With these measurements, a control algorithm produces a command for the control mass in an attempt to attenuate any disruption in the underling structure and the control mass moves to achieve this command.

Examples of full-scale implementations of active control systems in civil structures are shown in Figure 2-1. In this figure, two structures with active mass drivers, which are described above, are shown. One of the structures is the 11-story Kyobashi Seiwa Building in Tokyo (Kobori et al. 1991). The other structure is the Rainbow Bridge in Tokyo, which has active control systems implemented in the bridge pylons (Spencer and Nagarajaiah 2003).

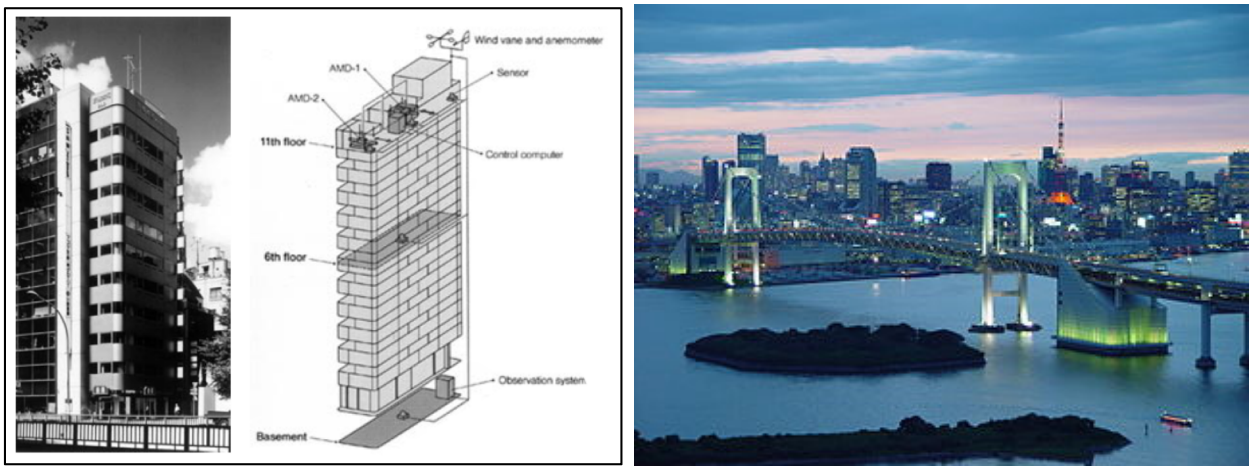

Figure 2-1. Example structures with active control systems: left – Kyobashi Seiwa Building (Spencer Jr and Sain 1997), right – Rainbow Bridge (Photo Credit: Cors)

Recent advances in the active control of civil structures are summarized in (Casciati et al. 2012; Housner et al. 1997; Korkmaz 2011; Soong 1988). As these review articles show, active control systems have been demonstrated to be, in general, effective in controlling civil structures; however, they have some distinct disadvantages. Included in these disadvantages are the facts that active systems require a constant source of power, their complex nature can make them prohibitively expensive, and the inherent possibility that, because energy is being introduced into the system, the controller can cause the system to go unstable if incorrectly designed. While there has been great research interest in these systems, the disadvantages listed above have led to the limited practical application of active control systems for civil structures (Casciati et al. 2012). This limited set of applications is particularly true in United State where the construction industry tends to be conservative.

2.1.2 Semi-active control systems

Another type of structural control methodology studied is semi-active control. A review of semi-active devices is presented by (Spencer and Nagarajaiah 2003; Symans and Constantinou 1999). Semi-active control devices can be thought of as controllable passive devices. In these devices, sensors measure the response of a structure and, via an algorithm running on a control computer, this data is used to change the properties of an otherwise passive control device. As a result of this configuration, semi-active control devices are BIBO stable; thus, their addition into a system cannot lead to an instability (Dyke et al. 1996; Hespanha 2009).

An example of a semi-active control device is a hydraulic damper with variable orifice value (Feng and Shinozuka 1990). With a controller and a sensor system, this semi-active device can change its properties, the orifice of the damper, and thus its flow resistivity can be altered in real time to best control the structure it is incorporated in.

One disadvantage of semi-active control schemes is that most semi-active control systems require a constant source of power or a battery backup. However, these systems do provide some protection in a total power outage; without power, in most cases, the control system ceases to be semi-active, but the passive component of the system remains functional. Another disadvantage of semi-active control devices is that, despite the increased expense and complexity, they are generally capable of only modest improvements in performance over passive systems. Like active control, these disadvantages have led to a limited number of real-world examples of deployed semi-active structural control system in use for civil structures, especially in the United States.

2.1.3 Passive control systems

While most of the advancements in active and semi-active control of civil structures have occurred within the last few decades, the field of passive control has been studied, in one form or another, for much longer. With passive control, the control of a structure is achieved with no feedback; thus, passive control systems are inherently stable. Additionally, due to the lack of feedback in passive control devices, these devices do not require sensors, actuators, control computers, or a constant energy source. Passive structural control devices, such as friction dampers, viscous dampers, base isolation, tuned mass dampers, and tuned liquid dampers, are reviewed in (Soong and Spencer 2002; Soong 1988). As the nonlinear energy sinks studied in this research are a type of passive mass damper, a more in-depth review of tuned mass dampers is presented below. Furthermore, given its nonlinear characteristics, a review of a particular pseudo-negative stiffness device that has recently been proposed for the control of civil structures is presented.

2.1.3.1 Tuned mass dampers

Tuned mass dampers (TMDs) have long been explored as a means of reducing the dynamic response of civil structures. A recent review of their theoretical background, related research, and implementations is presented in (Gutierrez Soto and Adeli 2013). These devices have been implemented in structures worldwide and are primarily used in tall buildings and towers to attenuate the response of the building's first mode due to wind loading (Soong and Dargush 1997). In its simplest form, a TMD consists of a relatively small mass, generally less than 5% of the total mass of the structure (De Angelis et al. 2011), coupled to a building with linear spring and damping elements. When the spring element and mass are adjusted such that the natural period of the TMD is tuned close to a natural period of the building structure, the response of

that mode of the building is reduced (see Figure 2-2a for an example transfer function representation of this phenomenon for a single degree-of-freedom (SDOF) structure). This reduction occurs due to the energy of this mode being directed to the TMD (Soong and Dargush 1997).

One of the shortcomings of these devices is that, due to their narrowband mode of operation, they must be tuned to a specific structural natural frequency; thus, their effectiveness lacks robustness to uncertainties due to errors in the initial estimate of the natural frequency and to changes in the natural frequency, known as detuning. An example of this phenomenon is illustrated in Figure 2-2b, which shows the transfer function for a SDOF structure where the structure's natural frequency has decreased since the initial tuning of the TMD. Because changes in the natural frequency of a structure are expected due to common processes such as settlement, creep, and temperature effects, detuning is a concern in any structure employing a TMD. Moreover, the lack of robustness of TMDs to detuning is one contributing factor that has prevented their widespread use for mitigating the effects of extreme seismic events (Soto-Brito and Ruiz 1999); significant changes in natural frequency are expected during a major event due to the designed inelastic deformations of the structure. Several methods have been examined to help reduce the sensitivity of TMDs to detuning. Most of these methods include using two or more TMDs together to increase the effective bandwidth (Casciati and Giuliano 2009; Marano et al. 2008) or using an active tuned mass system (Lin et al. 2010); however, little progress has been made to counteract the effects of detuning in simple systems employing only one completely passive TMD.

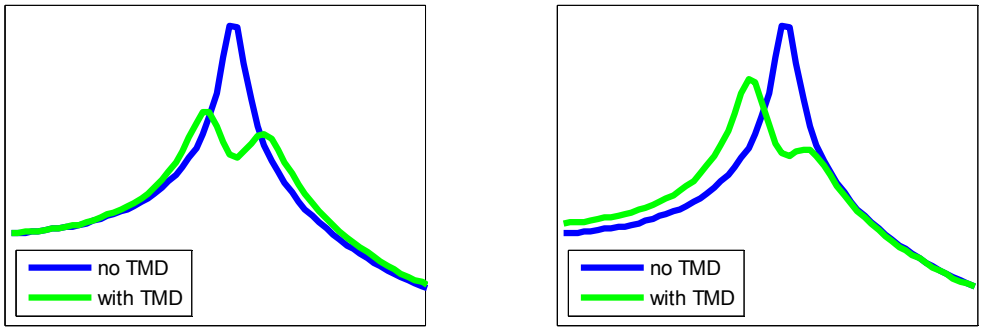

Figure 2-2: Example frequency response (a) tuned TMD (b) detuned TMD

2.1.3.1.1 Types of tuned mass dampers

Multiple types of tuned mass dampers have been proposed and implemented. The types of tuned mass dampers include the traditional tuned mass dampers, pendulum tuned mass damper, and tuned liquid column dampers (TLCDs) (Gutierrez Soto and Adeli 2013). Figure 2-3 shows diagrams illustrating these types of TMDs.

As discussed above, traditional TMDs are composed of a mass attached to a primary structure with a linear spring with or without an additional damping element. These TMDs are the most prevalent kind of TMD installed in building structures.

Pendulum TMDs are composed of a mass attached to a structure with a cable or link, which allows the mass to move as a pendulum. When considering small-angles, the EOM of a pendulum TMD simplifies down to a mass-spring system. The resulting natural frequency of the pendulum is the square root of the ratio of the acceleration due to gravity and the length of the

pendulum (Gutierrez Soto and Adeli 2013). As a consequence of this relationship, the natural frequency of the pendulum can be tuned by adjusting its length. Supplemental damping devices can also be attached to the mass to tune the damping of the TMD. Additionally, the pendulum TMD can be easily designed to work bi-directionally to control a structure.

As shown in Figure 2-3, TLCDs consist of a two columns of water that are connected by a horizontal passage. When the structure the TLCD is attached to begins to move, the water in the TLCD moves between the two columns. Damping is added to this system by adding an orifice into the horizontal portion of the device. In order to tune the device, the properties of the setup can be configured to give the motion of the water a particular natural frequency. An advantage of this type of damper is that the moving mass of the damper, the water, can serve dual purposes; for example, the water in the damper might be used for the sprinkler system in an emergency (Gutierrez Soto and Adeli 2013).

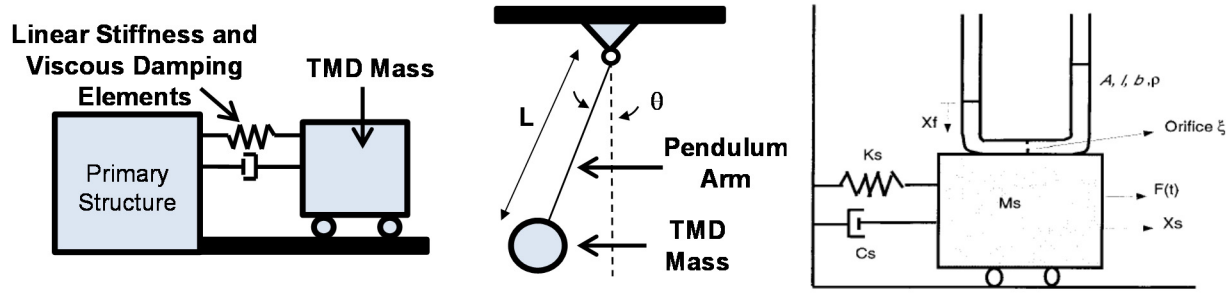

Figure 2-3. Types of TMDs: traditional TMD (left), pendulum TMD (center), and tuned liquid column damper (Yalla and Kareem 2000) (right)

2.1.3.1.2 Implementation in building structures

TMDs have been commercially implemented in building structures since the 1970s, with one of the first major implementations occurring in 1977 in Boston's John Hancock Tower (ENR 1977). Since then, TMDs have been incorporated into many important structures throughout the world. Incomplete lists of major structures with TMDs can be found in (Gutierrez Soto and Adeli 2013; Holmes 1995).

From the information on the lists referenced above, one can see that the majority of TMDs implemented in these structures are traditional TMDs. One of the world's largest traditional TMDs is 600 tons and installed in the 600 m tall Canton Tower in Guangzhou, China, which was completed in 2009. The mass ratio of this device is approximately 0.35%. The largest PTMD is 730 tons and installed in the 449 m tall Taipei 101 in Taipei Taiwan and was completed in 2004. The mass ratio of this device is also approximately 0.35%. The largest TLCD is 1300 tons and installed in the 297 m tall Comcast Center in Philadelphia Pennsylvania and was completed in 2008. The mass ratio of this device is not published, but as this structure is much shorter and smaller square footage than the previous examples, it is expected the mass ratio is much larger.

In addition to dampers for the main tower, TMDs for the spires or masts have been installed in multiple structures, including the Al Mas Tower, Al Rostamani Tower, and Taipei 101 (Gutierrez Soto and Adeli 2013). It is expected that the mass ratio for these dampers is higher than the main tower TMD.

2.1.3.2 Psuedo-negative stiffness devices

Recent advances in passive structural control include the development of an adaptive pseudo-negative stiffness device (Pasala et al. 2012; Sarlis et al. 2013). This device combines a negative stiffness element with a linear element to create a device that exhibits "apparent weakening". This apparent weakening, which is an elastic phenomenon, mimics the behavior exhibited by a yielding structures and limits the force in the structural system, but is not associated with any permanent damage. The experimental realization of the negative stiffness device presented in (Pasala et al. 2012; Sarlis et al. 2013) is accomplished primarily through the incorporation of a precompressed spring into a specially designed frame which is attached to a structural. This spring is initially orientated vertically; consequently, when the frame deflects laterally, the geometry of the system is changed and the precompression force in the spring gains a lateral component. This lateral component is directed such that it wants to push the frame further laterally. The negative stiffness from the precompressed spring is stabilized by the inherent stiffness of the frame the spring is incorporated into. The result of this combination of forces is an apparently softening response. Gaps are built into this system to control when the negative stiffness component is initiated. Additionally, supplemental damping is added into this system with the inclusion of a viscous damping device.

Results of experimental component testing of this system verify the "apparent weaken" that this system is designed to exhibit (Sarlis et al. 2013). Additionally, numerical simulations were performed with this system incorporated into a model structural frame which is subjected to periodic and seismic ground motions. (Pasala et al. 2012). The results of this numerical analysis show that the adaptive pseudo-negative stiffness device is capable of greatly improving the performance of the frame when compared to a structure utilizing only supplemental damping. Additionally, the results of this study showed that this device is capable of sustainably reducing the base shear, column forces, and frame accelerations in the structural frame.

2.2 Nonlinear energy sinks (NESs)

In this section, work related to nonlinear energy sinks is reviewed. Particular focus is placed on the history of nonlinear energy sinks, the different types of NESs that have been studied, the study of systems of multiple NESs, and the experimental investigation of NES for the protection of civil structures.

2.2.1 History of nonlinear energy sinks

NESs were first introduced in a series of papers by Gendelmen and Vakakis in 2001 (Gendelman 2001; Vakakis and Gendelman 2001; Vakakis 2001) and the name "nonlinear energy sink" was coined in (Vakakis 2001). In these papers, the analytical methods were primarily used to investigate two-DOF systems composed of one linear DOF and one essentially nonlinear DOF. With these systems, the ability of passive NESs to engage in nonlinear energy pumping, also known as Targeted Energy Transfer (TET) (Vakakis et al. 2008) the broadband transfer of energy from the linear system to the NES, was studied. These papers also explored the energy dependent nature of the NES and its broadband properties. Future papers extended these ideas to MODF linear system where investigations were performed on topics such as the NES's ability to vibrate with any mode of the linear structure and participate in TET. Additionally, these papers showed that the nonlinear nature of the NES allows the modes of the primary structure to be

coupled and energy to be transferred from the primary structure's lower modes to its higher modes where it can be dissipated at a faster rate (Vakakis et al. 2008).

Following their introduction, these devices have been investigated by numerous researchers, primarily in the fields of mechanical and aerospace engineering. This research has led to many noteworthy milestones in the development NESs. These milestones include first reported study of a two-DOF NES (Panagopoulos et al. 2004; Tsakirtzis et al. 2005), the first experimental investigation of NES effectiveness (McFarland et al. 2005), and the first experimental study of the performance of a system of multiple NES (Nucera et al. 2007). These milestones and several others are summarized in Table 2-1.

Table 2-1. Selected NES research milestones

Year	Authors	Contribution
2001	Gendelman; Vakakis; Vakakis and Gendelman	NESs first reported
2004	Panagopoulos et al.	First reported MDOF NES
2005	McFarland et al.	First reported experimental investigation of NES performance
2005	Gourdon and Lamarque	First study of NESs involving seismic ground motion
2008	Nucera et al.	First experimental study of a system of multiple NESs
2012	Gendelman et al.	First reported rotational NES
2012	Sapsis et al.	Effective damping measure used to evaluate NES performance introduced

2.2.2 NES types

A variety of different types of NESs have been studied in literature. In this section, the Type I, Type II, Type III, and vibro-impact NES will be briefly reviewed. While other types of NESs exist, particular attention is paid towards these devices due to their relevance to the NESs studied in this research. These types of NESs are all used as passive mass energy dissipation devices that are attached to a primary structure; however, these various types of NESs are differentiated by the form of restoring force that is used to couple the NES mass to the primary structure.

2.2.2.1 Type I NES

The most studied type of NES is known as the Type I NES (Gendelman and Starosvetsky 2007; Vakakis et al. 2008). A conceptual model of the Type I NES is shown in Figure 2-4. This NES is coupled to a primary structure with a linear viscous damping element and a cubic stiffness

element. An expression for the nonlinear restoring force provided by this NES is shown in Eq. (0.1).

$$F_{NES} = c_{NES}\left(\dot{x}_{NES} - \dot{x}_p\right) + k_{NES}\left(x_{NES} - x_p\right)^3 \tag{0.1}$$

In this expression, x_{NES} is the displacement of the NES, x_p is the displacement of the primary structure at the point the NES is attached, c_{NES} is coefficient on the linear damping term, and k_{NES} is coefficient on the nonlinear stiffness term. The cubic stiffness term in this restoring force forms this type of NES's essential nonlinearity. With this essential nonlinearity, the NES has no linear stiffness component, thus no preferred vibration frequency. This type of NES can also be viewed as a Duffing oscillator with the linear stiffness coefficient set to zero.

In addition to extensive numerical and analytical studies of this NES, experimental studies with this type of NES have been performed. In these studies, the base structure to which the NES is attached varies and has included general dynamic models (McFarland et al. 2005), models of shear buildings (Nucera et al. 2008; Vaurigaud, Savadkoohi, et al. 2011), and models of aerospace structures (Hubbard et al. 2010). While multiple experimental studies have been performed on the Type I NES, all of these studies have used very small scale setups.

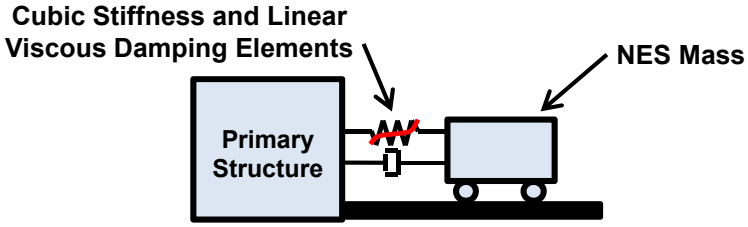

Figure 2-4. Conceptual model of the Type I NES

2.2.2.2 Type II NES

Another type of NES that has been studied is referred to as a Type II NES (Andersen et al. 2012, 2011; Sapsis et al. 2012). The Type II NES is basically a modified version of the Type I NES in which the linear damping element is exchanged for a quadratic element. A conceptual model of the Type II NES is shown in Figure 2-5. An expression for the nonlinear restoring force provided by this type of NES is shown in Eq. (0.2).

$$F_{NES} = c_{NES}\left(x_{NES} - x_p\right)^2\left(\dot{x}_{NES} - \dot{x}_p\right) + k_{NES}\left(x_{NES} - x_p\right)^3 \tag{0.2}$$

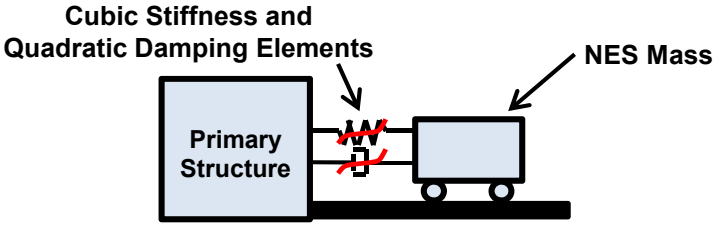

Figure 2-5. Conceptual model of the Type II NES

2.2.2.3 Type III NES

NESs composed of multiple discrete masses have also been studied (Lee et al. 2008; Sapsis et al. 2012). One type of NES that is composed of two masses is known as a Type III NES. A conceptual model of the Type III NES is shown in Figure 2-6. As shown by this figure, the Type III NES is essentially a combination of two Type I NESs in series. Due to its increased number of parameters, the dynamic properties of this type of NES can be varied tremendously. The large variability in the dynamic characteristics of this type of NES is demonstrated by increased complexities in its resulting frequency-energy plots (Quinn et al. 2012).

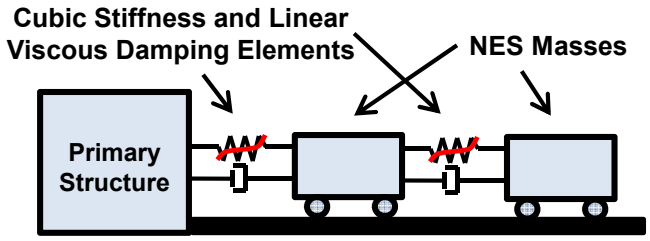

Figure 2-6. Conceptual model of the Type III NES

2.2.2.4 Vibro-impact NES

Passive mass dampers utilizing impacts, also known as impact NESs, have also been studied (Duncan et al. 2005; Karayannis et al. 2008; Lee et al. 2009; Nucera et al. 2007; Al-Shudeifat et al. 2013). Conceptual models of two types of impact NESs known as single-sided and double-sided vibro-impact (VI) NESs are shown in Figure 2-7. In these types of NESs, the relative displacement of the mass is limited on one, or two, side(s) due to an impact surface that is connected to the primary structure. Due to the discontinuity in restoring force, these impacts are broadband event and because of them energy is scatter throughout the structure, including to its higher modes (Nucera et al. 2007; Al-Shudeifat et al. 2013). As with other types of NESs, the transfer of energy to higher modes that occurs due to the presence of the NES is beneficial because at these higher frequencies the energy can be naturally dissipated faster due to the reduced time scale. Furthermore, this type of NES also helps to quickly attenuate the response of the structure it is attached to due to the energy dissipated by their relative motion.

Direct comparison of single-sided and double-sided VI NESs has been done in a study which utilized numerical and experimental analyses (Al-Shudeifat et al. 2013). From this study, it was found that both single-sided and double-sided VI NES require a minimum input energy before they are effective at controlling a structure's response. At higher input energy levels both single-sided and double-sided VI NES quickly reach their peak in terms effectiveness at attenuating the response of the base structure they are attached to. At input energy levels beyond this peak point, the effectiveness of the double-sided VI NES is quickly diminished; however, the effectiveness of the single-sided VI NES is maintained over a broad range of higher input energies. This study surmised that the increase in effectiveness of the single-sided NES is due to the stronger impacts that were allowed at higher energy levels due to the lack of an impact surface on one side.

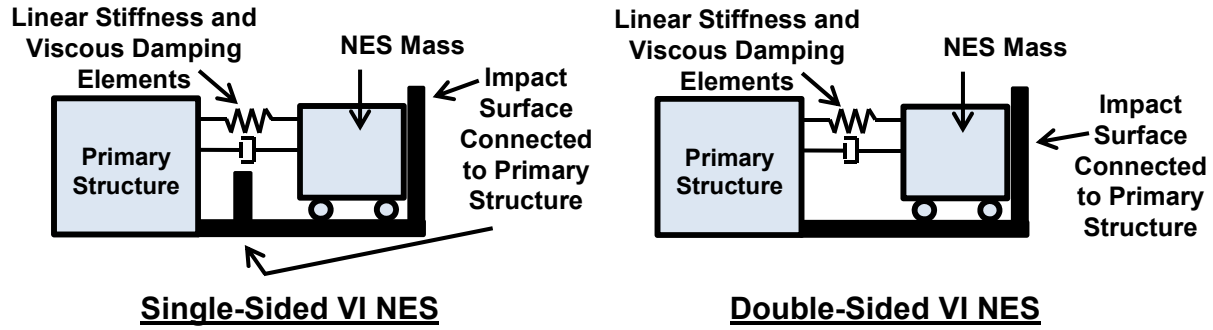

Figure 2-7. Conceptual models of single-sided and double-sided vibro-impact NESs

2.2.3 Systems of Multiple NES

One of the tasks in this report is the development and experimental exploration of a system of multiple NESs designed to control the response of a large-scale experimental test structure. While previous investigations of the behavior of NESs have predominantly focused on systems where only one NES is utilized, some research has been done on systems utilizing multiple NESs.

One example of a system of multiple NESs being studied is shown in work by Vaurigaud and colleagues (Savadkoohi et al. 2012; Vaurigaud, Savadkoohi, et al. 2011; Vaurigaud, Ture Savadkoohi, et al. 2011). The system studied by this group with theoretical analysis was a general multi degree-of-freedom primary structure with the possibility to have multiple Type 1 NESs attached to each degree-of-freedom. The system studied with numerical simulations and experiments testing was more limited and consisted of four degree-of-freedom primary structure with two parallel Type I NESs attached to the top floor. Through this work multiple NESs were shown to be effective at control the primary structure when subjected to impulsive and harmonic loading; however, only a limited comparison of these results were made to the single NES case. Additionally, the complexity of the system evaluated was restricted as the properties of the two NESs were not allowed to be independently varied.

Systems of multiple NESs were also studied by Nucera and colleagues (Nucera et al. 2007, 2008, 2010). The systems this group considered with numerical and experimental studies were two- and three-story shear buildings with a Type I NES and a vibro-impact NES attached. This group found that this system was effective at controlling the structures' response to seismic group motion. It was also demonstrated that, for the systems considered, individually the vibro-impact NES has superior performance when subjected to large intensity ground motion, while the Type I NES had superior performance when subjected to medium level ground motion. When utilized together, it was found that synergies between the two NESs types allowed for greater overall control of the primary structures.

2.2.4 Nonlinear energy sinks designed for civil structures

To date, experiments investigating the effectiveness of NESs have been performed at very small scales; this point is particularly true for experiments exploring NESs for civil applications. In Figure 2-8, a diagram is presented which shows the primary structures that have been previously used in literature (Manevitch et al. 2007; Nucera et al. 2008; Vaurigaud, Savadkoohi, et al. 2011). This diagram is drawn to scale; thus, the diagram can be used to compare the dimensions

of these primary structures. As this diagram shows, all of the previous experiments involving NES for civil structures have involved very small-scale table-top size models. The largest primary structure used in this previous work had a height of approximately 0.6 m (Nucera et al. 2008) and the biggest had a mass of 3.3 kg (Manevitch et al. 2007). While studies at these small-scales are valuable, it is unclear if the NESs studied, or the mechanisms used to create their nonlinear restoring forces, can be scaled up for use at larger-scales and in more modal complex structures.

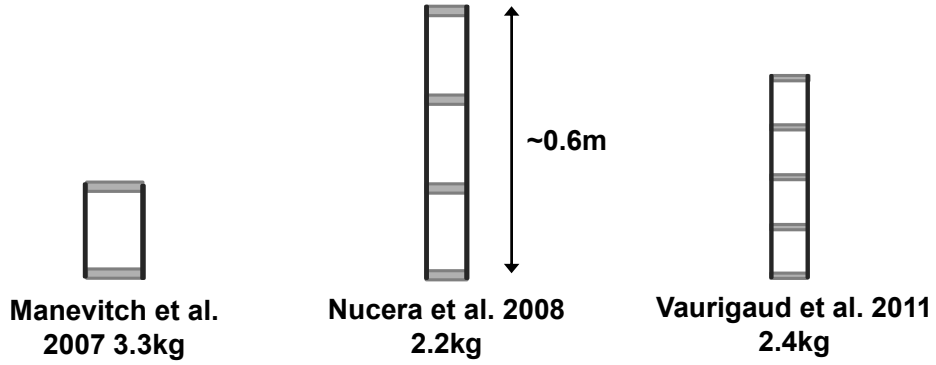

Figure 2-8. Base structures previously used in literature for the study of the application of NESs for in civil structures

2.3 Experimental blast simulation

Due to the inherent safety and security concerns regarding blast testing, locating suitable facilities to legally perform tests with explosives can prove to be difficult. Additionally, when suitable facilities do exist, potential restrictions imposed on the facility by local statutes, noise concerns, and a multitude of other sources can greatly impede the scope and progress of a project. Furthermore, the remote sites these facilities often occupy, combined with the large setbacks which are required due to safety concerns, result in additional challenges for sensor deployment and data acquisition. As a consequence of the logistical difficulties involved with explosive blast testing, a number of simulated blast testing methods have been developed. Available blast simulation methods, which include methods using shock tubes, impacts, and shake table motion, are reviewed below.

2.3.1 Blast simulation using shock tubes

One of the most common blast simulation methods is to use a shock tubes to create pressure waves which mimic the pressure waves that occur in an actual blast. In its basic configuration, a shock tube consists of a long tube that is divided into two sections: a driver section and a driven section (Bertrand and Matthews 1965; Martin 1958). In the driver section air or another gas is compressed to form a high pressure zone. The driven section is evacuated or kept at atmospheric pressure and forms the low pressure zone of the shock tube. The specimen being tested is secured at the end of the driven section. Separating the driver and driven section is a diaphragm. When this diaphragm is ruptured, the pressures in the two sections of the shock tube attempt to equalize. This equalization process creates a pressure wave that travels down the driven section of the pressure tube where it intersects with the specimen being tested. The characteristics of the

pressure wave created by the shock tube can be modified as desired by changes in the diameter of the shock tube, the length of the driven section, the pressure ratio between the driven and driver sections, and the type of gas used.

In addition to the basic shock tube, which utilizes compressed gas and a single diaphragm, other types of shock tubes, which use different configurations and different mechanisms for creating a pressure wave, have been developed. These other types of shock tubes include compressed gas shock tubes that utilize multiple diaphragms (Colombo et al. 2011) and shock tubes that use small explosives or the combustion of fuel-air mixtures to create the desired pressure wave (Courtney et al. 2012).

While large shock tubes exist in specialized facilities, including one which is 6.1 m in diameter (EMRTC 2013), the majority of shock tubes have a much smaller diameter. Additionally, the geometric limitations of even the largest shock tubes severely limit the size of the specimen to be tested. Consequently, while shock tubes are a valuable tool for simulated blast testing at the component level, the geometric limitations of available shock tube testing facilities make them unsuitable for large-scale testing of structural systems.

2.3.2 Blast simulation using impact

Non-explosive blast simulation techniques using impact has been implemented in several forms. One impact blast simulation implementation is the UCSD blast simulator (Rodriguez-Nikl et al. 2011). This device is attached to a strong wall and uses high speed hydraulic actuators to launch specially designed impactors at a specimen. These impactors consist of a mass and pad of viscoelastic material which comes in contact with the specimen. The geometry of the pad, as well as the properties of the viscoelastic material used, can be altered to tailor the imparted impulse (Freidenberg et al. 2013). Comparisons with explosive blast tests have confirmed the ability of this system to accurately deliver a realistic blast-like impulse. This device has been used successfully in number of tests of full-scale structural members (Oesterle et al. 2009; Stewart 2012); however, the limited size of the device precludes the use of it for testing complete large-scale structural systems.

Another non-explosive blast simulation technique which uses impacts is a testing method that utilizes a projectile which is fired from a gas gun (Chen et al. 2011). The projectile used in this method consists of aluminum mass with fins attached for stabilization during flight and a crushable foam front section which is used to make contact with the specimen being tested. The pressure impulse imparted by this projectile is controlled based on the density of the foam used in the projectile and its velocity. This method was used with 79 mm diameter projectiles to test small-scale composite beams (Chen et al. 2011). While useful for component testing, the applicability of this method for testing complete large-scale structural systems is doubtful given the expense and technical challenges involved with dramatically scaling up the necessary hardware.

2.3.3 Blast simulation with shake table

As discussed in detail in Chapter 4, one of the goals of the research presented in this report is the development of a blast simulation technique in which a shake-table-produced ground motion is used to experimentally simulate the global effects of a blast on a building structure. Previously, similar ideas have been briefly mentioned (Eskew and Jang 2012); however, little evidence is found in literature that these ideas have been thoroughly investigated or implemented.

Existing methods of blast simulation using shake tables that have been implemented generally have a much more refined focus and do not seek to directly simulate the effects of blasts on a structure. Rather, these implemented methods using shake tables are predominantly designed to test the limitations of critical pieces of hardware that would be inside structures or shelters subjected to a general shock loading (Gaberson and Eubanks 1982).

An example of a shake table used to deliver this shock loading is the Triaxial Earthquake and Shock Simulator (TESS) (U.S. Army Engineer Research and Development Center 2008), formally known as the Biaxial Shock Test Machine before its upgrade (Hayes et al. 1991). This device, which is basically a six degree-of-freedom shake table, is located at the US Army Corps of Engineering Construction Engineering Research Laboratory in Champaign, IL. In its original form, this device was designed to test the shock tolerance of equipment as part of a cold war era program intended to harden ballistic missile sites against nuclear attack. The shock loading provided by the shake table consisted primarily of a very short duration acceleration pulse. Due to the special requirements of this type of testing, the TESS shake table is capable of producing high acceleration over a large range of frequencies.

BACKGROUND

In this chapter, background information is given on some methods and topics that were not developed by the author, but will be discussed or used in the subsequent chapters of this report. The topics or methods discussed in this chapter include nonlinear system identification using the restoring force method, the quantitative evaluation of the response of nonlinear systems with a measure known as effective damping, and wavelet transforms.

3.1 Restoring force surface method

In this report, experimental work with multiple types of NESs will be presented. In order to determine an estimate of the actual parameters of the built NESs, system identification on the NESs must be done. Because the NES is a nonlinear device, the system identification technique used must be able to handle and identify nonlinear systems. For the work presented in this report, the nonlinear system identification technique chosen is the restoring force method (Masri and Caughey 1979; Worden 1990).

3.1.1 Method summary

The restoring force surface method is based on the equation of motion (EOM) of a system. As an example, the equation of motion of a generalized single degree of freedom (SDOF) EOM is

$$m\ddot{x} + f\left(x,\dot{x}\right) = G\left(t\right) \tag{0.1}$$

In this EOM, $f\left(x,\dot{x}\right)$ is the generalized internal restoring force in the system, which is assumed to be a function of the states of the system x and $\dot{x}$. Additionally, in this EOM, $G\left(t\right)$ is the generalized input force, m is the mass of the DOF, and $\ddot{x}$ is acceleration. For this method, an assumption is made that m, $G\left(t\right)$, x, $\dot{x}$, and $\ddot{x}$ are all known. The practicality of this assumption will be discussed in a subsequent subsection.

The unknown internal restoring force of the system can then be solved for given that the rest of the EOM in this SDOF example is known:

$$f\left(x,\dot{x}\right) = G\left(t\right) - m\ddot{x} \tag{0.2}$$

This restoring force can be thought of as a surface of possible values of the restoring force of the system that is being identified. Based on this surface, the value of the restoring force at a particular point in time is a function of the states of the system. In Figure 3-1, an illustration is shown of a possible restoring force surface which is dependent on system displacement and velocity for the SDOF example. For more complex systems, the restoring force surface can extend beyond the three dimensional example shown.

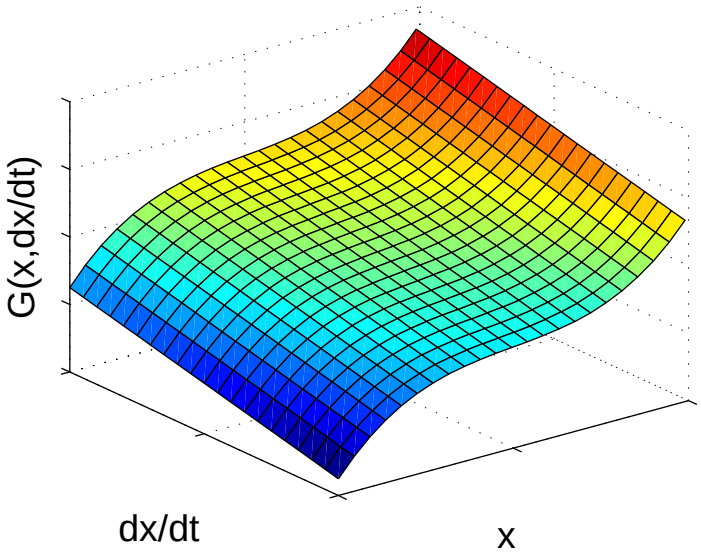

Figure 3-1: Example restoring force surface for SDOF system

Once the internal restoring force for the system being identified has been calculated, the next step in the method is to assume a form for the restoring force, which previously had been generalized. An example of a typical restoring force for a SDOF system that might be assumed is

$$f\left(x,\dot{x}\right)=c_1\left(\dot{x}\right)+c_2 sign\left(\dot{x}\right)\left|\dot{x}\right|^{\alpha_1}+k_1\left(x\right)+k_2 sign\left(x\right)\left|x\right|^{\alpha_2} \tag{0.3}$$

In this example the restoring force is assumed to be composed of linear and nonlinear damping and stiffness terms with parameters c_1, c_2, k_1, k_2, α_1, and α_2.

When performing a system identification with the restoring force surface method, care should be placed in choosing the assumed form of the restoring force as this decision will greatly affect the outcome of the identification. If possible, assuming a form of this restoring force based on the physical system being evaluated is suggested. With the assumed form of the restoring force and the estimated restoring force time history, the parameters that make up the assumed form can be solved for. This solution is done by performing a minimization, such as least squares, to determine the parameters which result in the minimum error between the experimentally determined restoring force time history and the restoring force time history using the identified parameters. Alternatively, one could also minimize the error between the experimentally determined restoring force surface and the restoring force surface with the identified parameters.

3.1.2 Practical considerations

As mentioned above, the restoring force surface method assumes that some parameters of the system are known, such as $_m$, $G\left(t\right)$, $_x$, $\dot{x}$, and $\ddot{x}$ for the SDOF example. Consequently, to use this method, one must determine these quantities directly or through estimation. Of these quantities, perhaps the most straight-forward to determine is the mass of the system being identified. For the work presented in this report, the masses used in the identification are generally directly measured, as they are relatively small and compact.

Determining the motion of the system being identified is a more complicated task. The displacement, velocity, and acceleration records (x, $\dot{x}$, and $\ddot{x}$ for the SDOF example) related to the DOF examined in the system identification can all be directly measured with accelerometers, velocity transducers, and displacement transducers; however, in most cases, obtaining a complete set of measurements is impractical due to the limitations on resources available for testing. Due to these limitations, the usual method for obtaining these records is to measure one and then use integration and/or differentiation to estimate the other records. Both integrating and differentiating experimentally obtained records present challenges. Some of the most prevalent challenges are the presence of artificial drift that tends to occur when integrating records and the sensitivity of differentiation to small errors, which tend to substantially affect the reliability of the results (Worden 1990). In the work presented in this report, the system identification the acceleration records are experimentally recorded then velocity and displacement records are determined using numerical integration with low pass filtering used to suppress any resulting artificial drift. Using this method, errors due to differentiation are avoided and artificial drift from integration is controlled.

The last quantity that the restoring force method requires is the external load, $G(t)$. In this research, the nonlinear energy sink is tested for the identification in one of two ways. The first way is to remove the NES from its base structure and to test the NES independently using an impulsive load. In this case, the external load can be ignored as the identification can be done on the system with no external loading by using data for the identification only after the impulse has been applied to the system. The second way the NES is tested for identification in this research is by subjecting the NES to a ground motion (either independently or when the NES is connected to the primary structure). In this case the equation of motion can be rewritten so that the external loading can be stated as a function of the displacement and velocity of the level the NES is attached to, which can be measured or estimated.

3.2 Effective damping measure

To evaluate the ability of the NES to affect the response a primary structure, a set of performance measures is needed. In this report, traditional structural engineering measures such as strain, interstory drift, and top floor displacement will be used as measures to evaluate the effect of the NES; however, in addition to this, insight from performance measures related to the dynamics of the response are needed. Because of the nonlinear behavior of the primary structure-NES system, typical linear measures of dynamic behavior, such as viscous damping ratio and loss factor, do not directly apply. As a result of the nonlinear behavior, a damping measure, referred to as effective damping, was developed to take into account both the energy dissipation and energy transfer effects provided by the NES (Sapsis et al. 2012). In short, what the measure does is evaluate the response of the base structure in a particular mode, which can include energy going in and out of the mode due to the nonlinearity and normal energy dissipation, and calculates the corresponding most representative damping value for this modal behavior.

In this section, the original method for calculating the effective damping measure is described in detail along with an alternate method. Additionally, an extension of this effective damping measure is discussed which can be used to evaluate the forced response of a system, such as the response of a structure with an NES during an earthquake.

3.2.1 Calculation of effective damping

The initial development of the effective damping measure was designed to evaluate the free vibration response of a system that was subjected to external load that had concluded or a set of initial conditions (Sapsis et al. 2012). Additionally, this initial development considered the response of a SDOF system; however, this work stated that the derivation of the measure could easily be extended to determine the modal effective damping in multiple-DOF (MDOF) structures. Consequently, when introducing the effective damping measure in this section, the free response of one mode of a MDOF structure is considered. The EOM for the mode considered is

$$m_i\ddot{q}_i + b_{eff,i}(t)\dot{q}_i + k_{eff,i}(t)q_i = 0 \tag{0.4}$$

In this equation, m_i, $b_{eff,i}(t)$, and $k_{eff,i}(t)$ are the modal mass, instantaneous effective linear damping coefficient, and instantaneous effective linear stiffness coefficient for the ith mode. Note that the effect of the attachment of the NES to the linear base structure is accounted for with the time dependency of both $b_{eff,i}(t)$ and $k_{eff,i}(t)$. Additionally, in this equation, the modal displacement, velocity, and acceleration of the ith mode are represented by $\ddot{q}_i$, $\dot{q}_i$, and q_i, respectively. The total energy in this mode can be represented by the sum of the kinetic and potential energies.

$$E_i(t) = KE_i(t) + PE_i(t) \tag{0.5}$$

$$E_i(t) = \frac{1}{2}m\dot{q}_i^2 + \frac{1}{2}k_{eff,i}(t)q_i^2 \tag{0.6}$$

In the presence of the assumed linear and time dependent viscous damping, the rate of decrease of the energy in the mode considered is

$$\dot{E}_i(t) = -b_{eff,i}(t)\dot{q}_i^2(t) \tag{0.7}$$

Given the following equivalences, the expression for the total energy in the mode considered and the rate of change in energy can be mass normalized

$$\lambda_{eff,i}(t) = \frac{b_{eff,i}(t)}{m} \tag{0.8}$$

$$\omega_{eff,i}^2(t) = \frac{k_{eff,i}(t)}{m} \tag{0.9}$$

$$\varepsilon_i(t) = \frac{E_i(t)}{m_i} = \frac{1}{2}\dot{q}_i^2 + \frac{1}{2}\omega_{eff,i}^2(t)q_i^2 \tag{0.10}$$

$$\dot{\varepsilon}_i(t) = \frac{\dot{E}_i(t)}{m_i} = -\lambda_{eff,i}(t)\dot{q}_i^2 \tag{0.11}$$

As with SDOF systems, the energy contained in the mode under consideration will oscillate between fully kinetic and fully potential. Consequently, when considering a system with low damping, one can approximate the total energy in the mode with the envelope of either the kinetic energy or the potential energy, which are approximately equal.

$$\varepsilon_i(t) \approx \left\langle \frac{1}{2}\dot{q}_i^2(t) \right\rangle \tag{0.12}$$

$$\left\langle \frac{1}{2}\dot{q}_i^2(t)\right\rangle \approx \left\langle \frac{1}{2}\omega_{eff,i}^2(t)q_i^2(t)\right\rangle \tag{0.13}$$

In the above expressions, the envelope of a function $F(t)$ is denoted by $\langle F(t)\rangle$. In practice, an estimation of this envelope can easily be done by spline fitting the local maximum of the function of interest. As a consequence of these approximation, an expression for $\lambda_{eff,i}(t)$ can be solved for.

$$\dot{\varepsilon}_i(t) = \frac{d}{dt}\left(\left\langle \dot{q}_i^2(t)\right\rangle\right) = -\lambda_{eff,i}(t)\left\langle \dot{q}_i^2(t)\right\rangle \tag{0.14}$$

$$\lambda_{eff,i}(t) = -\frac{\frac{d}{dt}\left(\left\langle \dot{q}_i^2(t)\right\rangle\right)}{\left\langle \dot{q}_i^2(t)\right\rangle} \tag{0.15}$$

The instantaneous effective damping measure shown in equation (0.15) calculates the effective damping at time t; however, this value constantly changes throughout the time history of the response of a system. For this measure to be useful in producing a single effective damping measure given the response of a particular mode of a structure, averaging needs to be done. Equation (0.16) shows an expression for the weighted-average effective damping. In this equation the effective damping at each time has been weighted by the energy in the ith mode at that time. As a consequence of this weighting, the weighted-average effective damping expression is affected more by the effective damping when the system's energy is large, which allows this measure to be more reflective of behavior of the system rather than simple mean of instantaneous effective damping.

$$\overline{\lambda}_{eff,i} = -\frac{\int_0^\infty \lambda_{eff,i}(s)\left\langle \dot{q}_i^2(s)\right\rangle ds}{\int_0^\infty \left\langle \dot{q}_i^2(s)\right\rangle ds} = -\frac{\int_0^\infty \frac{d}{dt}\left(\left\langle \dot{q}_i^2(s)\right\rangle\right) ds}{\int_0^\infty \left\langle \dot{q}_i^2(s)\right\rangle ds} \tag{0.16}$$

3.2.2 Alternative effective damping calculation

The method of effective damping calculation shown in the previous subsection relies on an approximation of the total energy in a mode using a spline fit of the peaks of the kinetic energy. For cases when the effective damping in a system is high, the validity of this approximation is diminished due to the reduced number of peaks available with which to make the spline fit. Accordingly an alternative calculation of the effective damping measure was developed that does not rely on this spline approximation of total energy.

The effective damping measure used in this report is primarily a modal quantity; thus, once again, given the free response of a system with an NES, the first step in calculating the effective damping is to convert this free response of the linear primary structure into modal coordinates. The mass normalized single-degree-of-freedom (SDOF) equation of motion (EOM) for the free vibration response of the i^{th} mode of a structure is

$$\ddot{q}_i + \lambda_{eff,i}(t)\dot{q}_i + \omega_{eff,i}^2(t)q_i = 0 \tag{0.17}$$

Once again, in this equation, q_i is the displacement of the i^{th} mode, $\lambda_{eff,i}(t)$ its instantaneous effective damping, and $\omega_{eff,i}^2(t)$ its instantaneous effective modal stiffness. The average

effective damping, $\overline{\lambda}_{eff,i}$, can then be derived by multiplying (0.17) by $\dot{q}_i$ and integrating over the length of the record, from T_0 to T_{end},

$$\int_{T_0}^{T_{end}} \dot{q}_i \ddot{q}_i dt + \int_{T_0}^{T_{end}} \dot{q}_i \lambda_{eff,i}(t) \dot{q}_i dt + \int_{T_0}^{T_{end}} \dot{q}_i \omega_{eff,i}^2(t) q_i dt = 0 \tag{0.18}$$

Assuming that the change in effective stiffness is small, this equation can be simplified by replacing $\omega_{eff,i}^2(t)$ with ω_i^2, where ω_i is the natural frequency of the i^{th} mode. The result of this integration is

$$\frac{1}{2}\dot{q}_i^2(T_{end}) - \frac{1}{2}\dot{q}_i^2(T_0) + \overline{\lambda}_{eff,i}\int_{T_0}^{T_{end}} \dot{q}_i^2 dt + \frac{1}{2}\omega_i^2 q_i^2(T_{end}) - \frac{1}{2}\omega_i^2 q_i^2(T_0) = 0 \tag{0.19}$$

This expression can be solved for $\overline{\lambda}_{eff,i}$ as

$$\overline{\lambda}_{eff,i} = \frac{\frac{1}{2}\dot{q}_i^2(T_0) - \frac{1}{2}\dot{q}_i^2(T_{end}) + \frac{1}{2}\omega_i^2 q_i^2(T_0) - \frac{1}{2}\omega_i^2 q_i^2(T_{end})}{\int_{T_0}^{T_{end}} \dot{q}_i^2 dt} \tag{0.20}$$

The numerator of (0.20) can also be written in terms of $E_i(t)$, the energy in the i^{th} mode of the structure at time *t,*

$$\overline{\lambda}_{eff,i} = \frac{E_i(T_0) - E_i(T_{end})}{\int_{T_0}^{T_{end}} \dot{q}_i^2 dt} \tag{0.21}$$

Finally, this effective damping measure can be expressed as the effective viscous damping ratio via the expression

$$\overline{\zeta}_{eff,i} = \overline{\lambda}_{eff,i} \Big/ 2\omega_i \tag{0.22}$$

3.2.3 Forced vibration effective damping measure

The previously presented effective damping measures were designed to evaluate the free vibration response of a system; however, there are many instances when evaluating the response of the system during a forced vibration event is of interest. The response of a system to seismic ground motion is an example of when the forced vibration response is of interest. In this example, the most interesting behavior in the structure, as well as its peak response, is likely to occur in the middle of the force vibration. As a consequence of this limitation, the effective damping measure developed by (Sapsis et al. 2012) was extended by (Ott, R. J. 2012) to be used to examine the forced vibration response of structures.

Once again, this effective damping measure evaluates a SDOF response, thus the derivation of this measure will be done in modal coordinates. The linear mass normalized equation of motion for a particular mode, i, is

$$\ddot{u}_i + 2\zeta_i \omega_{n,i} \dot{u}_i + \omega_{n,i}^2 u_i = f_i(t) \big/ m_i \tag{0.23}$$

Where u_i, m_i, ζ_i, and $\omega_{n,i}$ are the i^{th} mode displacement, mass, damping coefficient, and natural frequency, respectively. Additionally, $f_i(t)$ is the i^{th} mode's modal forcing function. The mass normalized energy in this system can be defined as the normalized combination of the kinetic and potential energy.

$$\frac{E_i}{m_i} = \frac{1}{2}\dot{u}_i^2 + \frac{1}{2}\omega_{2,i}^2 u_i^2 \tag{0.24}$$

The time rate of change of the energy in this mode is defined as

$$\frac{\dot{E}_i}{m_i} = \dot{u}_i\left(\ddot{u}_i + \omega_{2,i}^2 u_i\right) \tag{0.25}$$

This equation can be rewritten to include the forcing function on the system by substituting in an expression for $\ddot{u}_i$, as defined by Eq. (0.23).

$$\frac{\dot{E}_i}{m_i} = \frac{f_i(t)}{m_i}\dot{u}_i - 2\zeta_i\omega_{n,i}\dot{u}_i^2 \tag{0.26}$$

The coefficients on $\dot{u}_i^2$ in Eq. (0.26) can be replaced by $\lambda_{eff,i}(t)$, which is defined to be the instantaneous effective damping.

$$\frac{\dot{E}_i}{m_i} = \frac{f_i(t)}{m_i}\dot{u}_i - \lambda_{eff,i}(t)\dot{u}_i^2 \tag{0.27}$$

Eq. (0.27) then can be rearranged to solve for $\lambda_{eff,i}(t)$

$$\lambda_{eff,i}(t) = \frac{\frac{f_i(t)}{m_i}\dot{u}_i - \frac{\dot{E}_i}{m_i}}{\dot{u}_i^2} \tag{0.28}$$

In a nonlinear system, such as one with a NES attached, $\lambda_{eff,i}(t)$ is a time varying quantity; therefore, it is once again advantageous to define an effective damping measure that evaluates the complete time history of a response. Consequently, the global, or averaged, effective damping of the i^{th} mode response of a system is defined as

$$\overline{\lambda}_{eff,i} = \frac{\int_0^{T_{end}}\left(\frac{f_i(\tau)}{m_i}\dot{u}_i - \frac{\dot{E}_i}{m_i}\right)d\tau}{\int_0^{T_{end}}\dot{u}_i^2 d\tau} \tag{0.29}$$

To facilitate the practical calculation of the effective damping presented in this method, the fast dynamics and noise in the response of the mode considered can be reduced by low pass filter the response. After this filtering, the slow dynamics of the system, which are primarily responsible for the system's damping, remain. Eq. (0.30) and (0.31) contain the expression for the instantaneous and global effective damping using this filtering. In these equations $\{\ \}$ denotes a low pass filtered quantity. For the calculation of the effective damping presented in this report, the low pass filter cut-off frequency was selected as 0.75 Hz. This cut-off frequency is low enough to eliminate most of the noise in the system response as well as the fast dynamics of the mode considered in the calculation, but high enough to capture relatively quick changes in the energy profile of the response.

$$\lambda_{eff,i}(t) = \frac{\left\{\frac{f_i(t)}{m_i}\dot{u}_i\right\} - \left\{\frac{\dot{E}_i}{m_i}\right\}}{\left\{\dot{u}_i^2\right\}} \tag{0.30}$$

$$\overline{\lambda}_{eff,i}(t) = \frac{\int_0^{T_{end}} \left(\left\{ \frac{f_i(\tau)}{m_i} \dot{u}_i \right\} - \left\{ \frac{\dot{E}_i}{m_i} \right\} \right) d\tau}{\int_0^{T_{end}} \left\{ \dot{u}_i^2 \right\} d\tau} \tag{0.31}$$

3.3 Wavelet transformation

One of the typical tools used for studying the dynamics of structures is the Fourier transform. With Fourier transforms the behavior of a system can be examine in the frequency domain with autospectral densities, coherence functions, transfer functions, and other frequency domain representations. The basis of many of these frequency domain tools is that system being examined is assumed to be both linear and time-invariant. Unfortunately, the NESs being studied in this research have strongly nonlinearity behavior; consequently, this assumption is violated. As a result of this violation, even though these frequency domain techniques can and are used to *qualitatively* examine the response of the systems studied in this research, their potential for use is limited. Additionally, when transforming a signal into the frequency domain with a Fourier transform, all data regarding the temporal variability of the frequency content is lost. Because the NESs examined in this research are designed to transfer of energy throughout the modes of the base structure, the ability to track the timing of this transfer and the related frequency content is highly desirable. As a consequence of the desire for information on the time-dependent frequency content of the signal, the standard Fourier transform does not provide an ideal general-purpose tool for examining the response of a system with an NES.

There are several widely used signal analysis tools that are capable of examining the time dependent frequency content of a signal; these tools include the short-time Fourier transform, chirplet transform, wavelet transform, and the fractional Fourier transform. In this report, wavelet transformations are frequently used.

An example of a wavelet spectrum is shown in Figure 3-2. In this figure, the time history of a signal with time dependent frequency content is shown along with the corresponding wavelet spectrum and FFT of the signal. As previously mentioned and demonstrated in this figure, the wavelet spectrum is able to track the time dependent changes in both the frequency and the relative amplitude of the signal; however, the FFT of the signal is only able to track general information regarding the frequencies of the signal and their relative amplitude, but not information regarding the timing of the signals.

Wavelet spectra, like the one shown in Figure 3-2, are produced by computing the continuous time wavelet transformation. The continuous time wavelet transformation of a signal $x(t)$ is defined as

$$X(a,t') = \frac{1}{\sqrt{|a|}} \int_{-\infty}^{\infty} x(t) \psi^* \left(\frac{t-t'}{a} \right) dt \tag{0.32}$$

where ψ is a normalized mother wavelet, t' is the localized time index, and a is the wavelet scale; additionally, in this equation * denotes the complex conjugate. This equation can be solved for each wavelet scale and time point t' of interest. Evaluating this transformation across a range of a and t' results in a wavelet spectrum. Depending on the mother wavelet, a relationship between the wavelet scaling factor and the frequency of vibration may exist. If this relationship does exists, a wavelet spectrum produced with this mother wavelet can be used as a tool to directly evaluate the time-dependent frequency content of a signal.

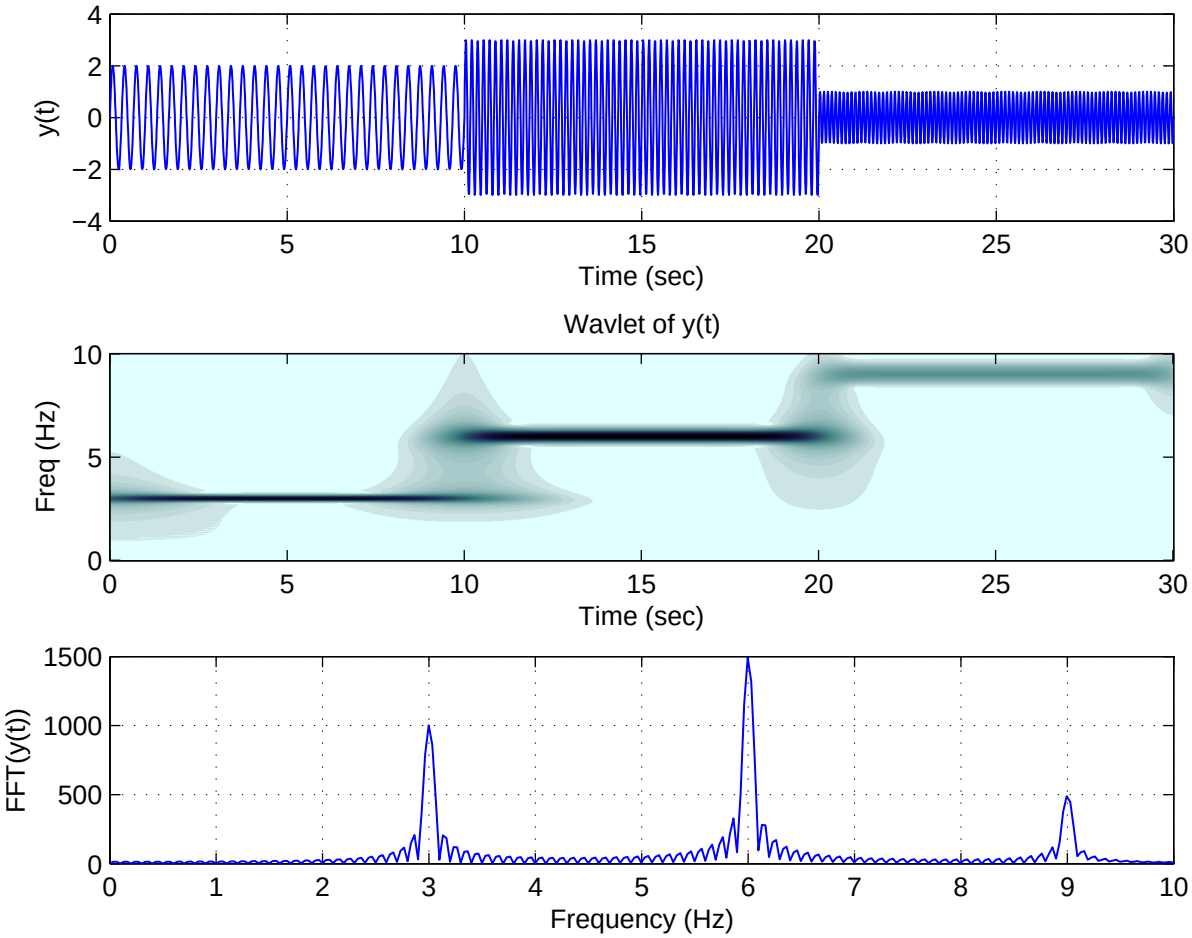

Figure 3-2. The time history, wavelet spectrum, and Fourier transform of an example signal with time dependent frequency content

3.3.1 Mother wavelet

One important decision in producing a wavelet spectrum is the choice of the mother wavelet. Examples of commonly used mother wavelets are presented in Figure 3-3, which shows the Morlet, Mexican Hat, and Shannon wavelets. While the appearance of these mother wavelets vary, they all share several common characteristics. One of these characteristics is that all of the energy of each of these wavelets is concentrated in a finite amount of time; this concentration is an important property that allows the wavelets to be used for time localization. Another characteristic these mother wavelets share is that they all satisfy the admissibility condition defined by Eq. (0.33) (Xing et al. 2012).

$$C_{\psi} = \int_{\square} \frac{\left|\Psi(\omega)\right|^2}{\left|\omega\right|} d\omega < \infty \tag{0.33}$$

In this admissibility condition, $\Psi(\omega)$ is the Fourier transform of the mother wavelet $\psi(t)$. As a consequence of this condition,

$$0 = \Psi(0) = \int \psi(t)\, dt \tag{0.34}$$

The result of this admissibility condition is that another shared characteristic of the mother wavelets is that they are zero mean signals.

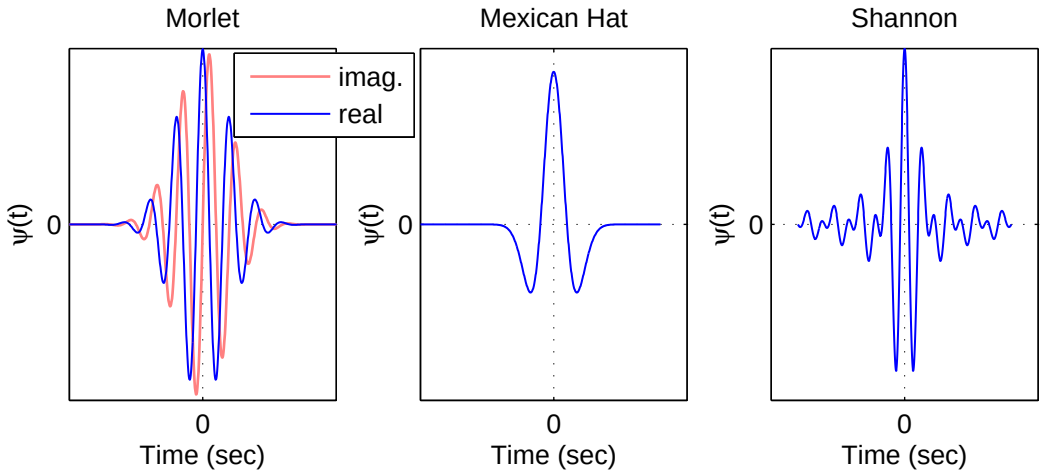

Figure 3-3. Commonly used mother wavelets

3.3.2 Morlet wavelet

For the wavelet spectra presented in this report, the Morlet wavelet is used as the mother wavelet. One advantage obtained from using the Morlet wavelet is that the Morlet wavelet is a Gaussian. This property is advantageous because, as a Gausian, the Morlet wavelet has simple analytical forms for both its time-domain and frequency-domain representations. Additionally, the parameters of the Morlet wavelet give the user the advantage of extra flexibility in fine-tuning the wavelet to provide good time-frequency resolution. The expression for the Morlet wavelet in the time domain is

$$\psi_0(t) = \pi^{-1/4} e^{i\omega_0 t} e^{-t^2/2} \tag{0.35}$$

In this expression, ω_0 is a parameter which sets the center frequency of the unscaled mother wavelet. The corresponding Fourier transformation of this mother wavelet is

$$\Psi_0(s\omega) = \pi^{-1/4} H(\omega) e^{-(s\omega-\omega_0)^2/2} \tag{0.36}$$

In this expression, s is a scaling factor applied to the mother wavelet and $H(\omega)$ is the Heaviside step function, which is equal to 1 when $\omega > 0$ and otherwise equal to 0. The effect of changes in ω_0 on the time history and frequency response of the Morlet wavelet is investigated in Figure 3-4. This figure shows that changing ω_0 corresponds to a shift in frequency response with little change in the shape; however, in the time domain this modification corresponds to a change in the apparent frequency and number of cycles present in the wavelet. Figure 3-5 shows the effect of changes in the scaling factor, s, to the time history and frequency response of the wavelet. As this figure indicates, changes in the scaling correspond to a shift in the frequency response of the wavelet coupled with a decrease in the bandwidth when s is increased. Additionally, the time histories in this figure show that the number of cycles in the wavelet is unaffected by changes in s, but that decreases in s results in a constricting of the wavelet.

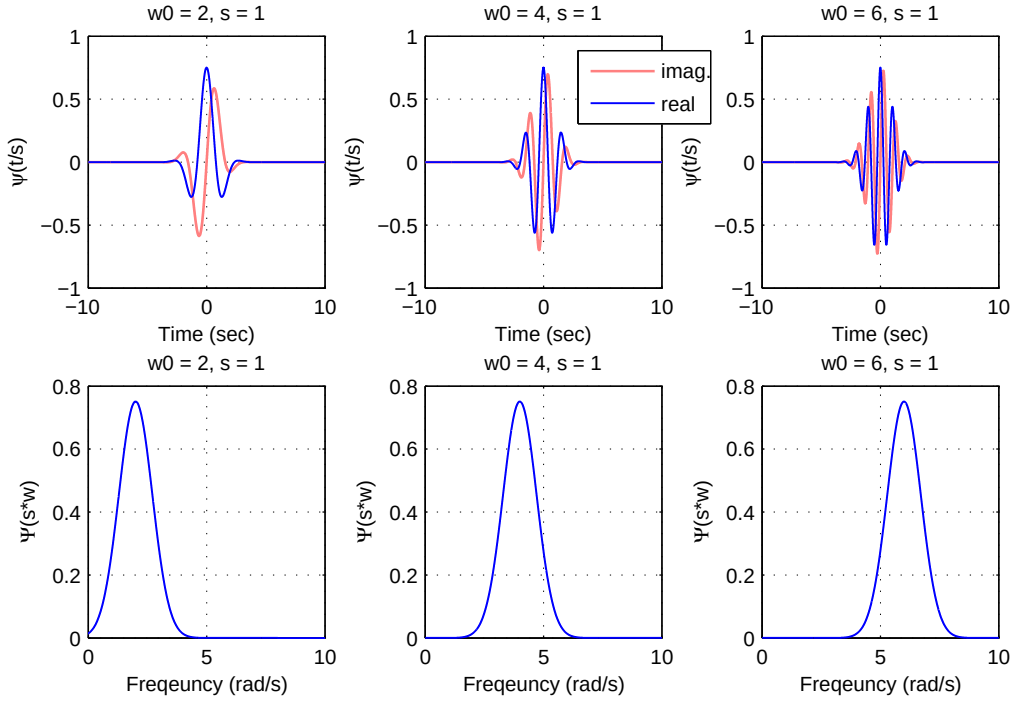

Figure 3-4. Effect of parameter ω_0 on the time history and frequency response of the Morlet wavelet

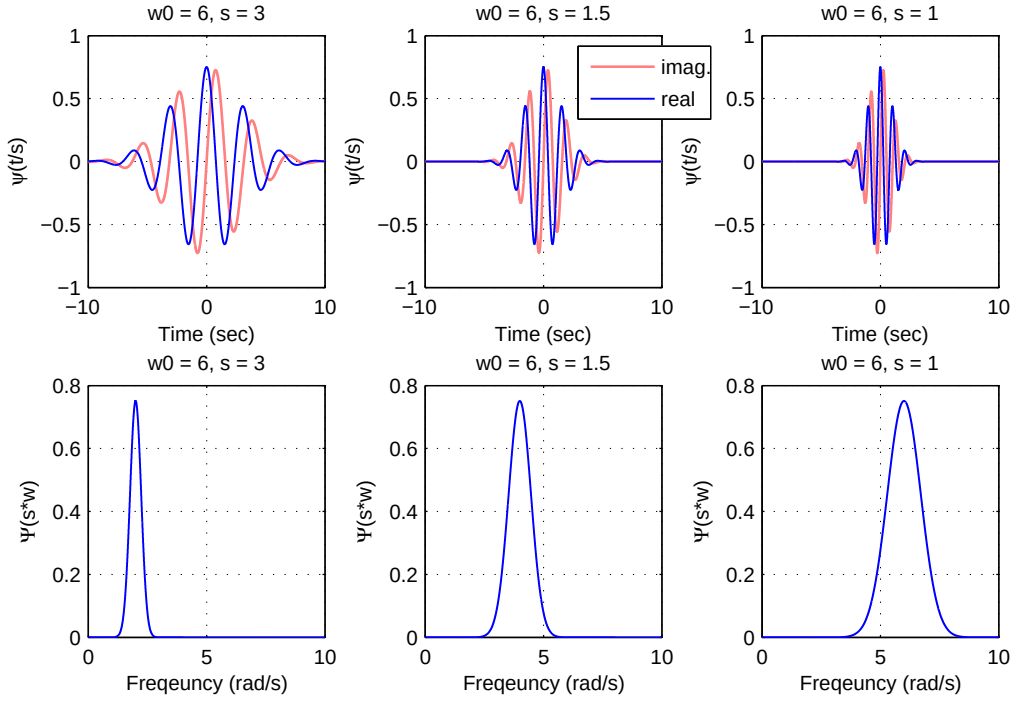

Figure 3-5. Effect of parameter s on the time history and frequency response of the Morlet wavelet

3.3.3 Wavelet spectrum calculation

Calculation of wavelet spectra can be done by performing the convolution integral shown in the definition of the continuous time wavelet transformation in Equation (0.32) at each pair t' and s that is desired to be evaluated. Unfortunately, when experimental collected signals are being analyzed a continuous form of the signal, as assumed in Equation (0.32), is rarely available. Consequently, a discrete form of the continuous wavelet transform is widely used when processing experimentally collected data. The continuous wavelet transform of a discretely sampled signal $x[n]$ can be produced using (Torrence, C. and Compo, G. P. 1998)

$$W(n,s) = \sum_{n'=0}^{N-1} x_{n'} \psi^* \left[\frac{(n'-n)\delta t}{s} \right] \tag{0.37}$$

where $\psi[\ ]$ is the discretely sampled normalized continuous mother wavelet and δt is the sampling time step. Calculation of the wavelet transformation with this discrete convolution can be computationally demanding given the large amount points (n,s) needed to produce a high resolution wavelet spectrum. To reduce the computational burden for this calculation, the discrete Fourier transformation of this convolution summation is exploited. With this simplification, the Fourier transformation of $W_n(s)$, the wavelet transformation across all n for a given s, is defined as the product of the Fourier transformation of the normalized and scaled wavelet and signal being evaluated.

$$F(W_n(s)) = F(x[n])\Psi^*(s\omega) \tag{0.38}$$

The normalized version of the Fourier transformation of the wavelet is defined as

$$\Psi(s\omega) = \left(\frac{2\pi s}{\delta t} \right)^{\frac{1}{2}} \Psi_0(s\omega) \tag{0.39}$$

This normalization ensures that even at different scaling levels the energy of the wavelet will remain unity. $W_n(s)$, the wavelet transformation across all n for a given s, can then be calculated by taking the inverse discrete Fourier transformation on this product.

$$W_n(s) = F^{-1}\left(F(x[n])\Psi^*(s\omega)\right) \tag{0.40}$$

This calculation can be performed efficiently using FFTs. Additionally, gains in efficiency can also be made when an analytical representation of the Fourier transformation of the wavelet is available. With this analytical representation, $\Psi(s\omega)$ in Equation (0.40) can be produced directly without the need for the Fourier transformation of $\psi(t)$ calculated repeatedly.

DEVELOPMENT OF EXPERIMENTAL BLAST SIMULATION TECHNIQUE USING SHAKE-TABLE-PRODUCED GROUND MOTION

Physical testing of structures can be used to experimentally investigate the effectiveness of devices designed to mitigate a structure's response due to an explosion; however, due to logistical and legal concerns with explosive testing, alternative methods of experimental blast simulation are required to increase the accessibility to this type of research. Given the relatively widespread availability of shake tables in universities, government facilities, and commercial research institutions, the goal of this chapter is the development of a technique to allow the shake tables to be used to simulate the global response of structures due to blast. Despite the very short time scale of a blast event, the simulation of the global effects of a blast is thought to be possible with a shake table due to the global response's dependence on the structure's fundamental periods of vibration, which are, in general, considerably longer.

The development of the experimental blast simulation technique using shake-table-produced ground motion presented in this chapter is separated into six sections. In the first section, starting from a basic level, a comparison is made between the external loading on a structure due to blast and the demand on a structure that results from a ground motion. Included in this section is an examination of the physical constraints that exist on any potential blast simulation ground motion. In the second section, a case study is performed to investigate the how the change in load application affects a structure with an internal mass damper system. In the third section, a generalized prototype ground motion for blast simulation is proposed. Once this prototype ground motion is established, a methodology is presented for modifying the prototype ground motion for the global response blast simulation of particular structure subjected to a particular blast event. In the fourth section, using numerical simulations, an example of how this methodology can be used to create a blast simulation ground motion is presented. Additionally, in this section a comparison using numerical simulations is made of the resulting global response from the design blast and blast simulation. In the fifth section, the blast simulation technique developed in this chapter is experimentally validated. For this validation, a comparison of the experimentally measured response of the large-scale base structure, which is introduced in Chapter 6, when subjected to a blast loading and a ground motion designed using the proposed technique is presented. In the last section, a review of the limitations of this experimental blast simulation technique is made and areas for future improvement are identified.

4.1 Feasibility of blast simulation using shake-table-produced ground motion

Before undertaking the development of specific ground motions that can be used for simulated blast testing, the feasibility of doing blast simulation with shake-table-produced ground motion must be assessed. As first step in this assessment, the loading on a structure during a blast event is compared to the loading on a structure due to a ground motion. With this comparison, the similarities in the loadings that might make this type of simulation possible can be distinguished.

The next step in assessing the feasibility of using ground motion for experimental blast simulation is identifying the fundamental restrictions that exist on these grounds motions due to the physical constraints of the loading.

4.1.1 Comparison of load application to structure

The nature of the loading on a structure during a blast event and a ground motion are fundamentally quite different. Figure 4-1 shows a basic comparison of these two types of loadings on an example structure. As illustrated by this figure, in an external blast, the loading on a building originates as a pressure loading on the building's exterior elements, such as the cladding. This load is then transferred from the exterior elements to the building's structural system. As a consequence of this load transfer from the cladding, the effective loading introduced by a blast to each portion of a building's structural system is dependent on the associated tributary area that is affected by the blast pressure. Furthermore, the complexity of this load is increased by the fact that the pressure resulting from a blast is generally not uniform across the exterior of a structure. Alternatively, as illustrated in Figure 4-1, during a ground motion the loading on a structure is a result of inertial effects created by the ground acceleration. As the loading is from inertia effects, the distribution of this loading on the structural system is dependent on the distribution of mass in the structure.

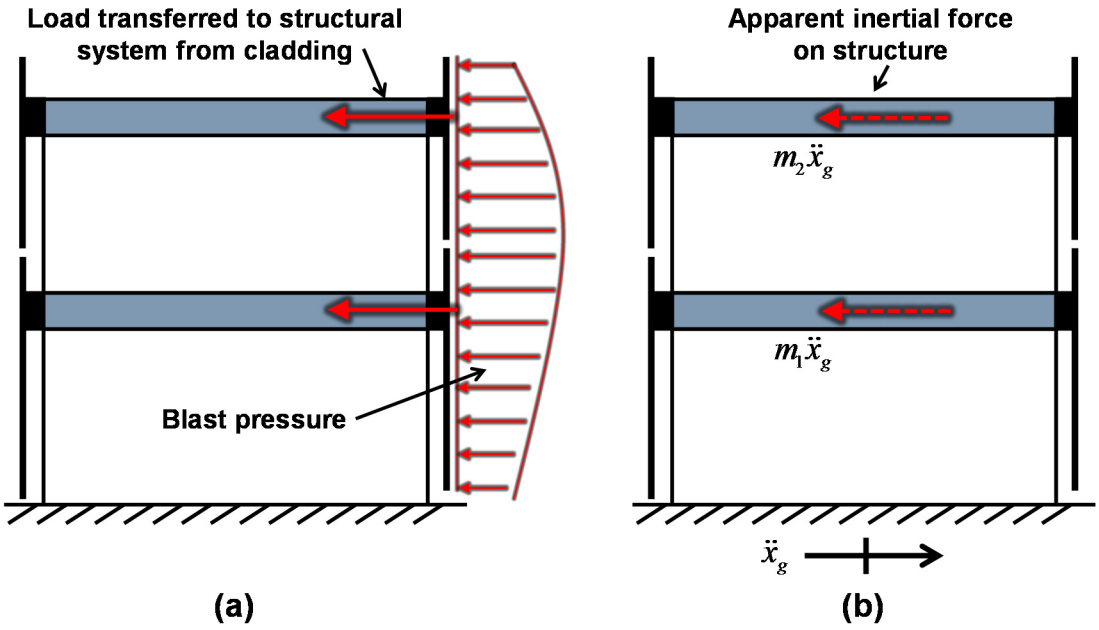

Figure 4-1. Basic comparison of the loading on an example structure during (a) blast event and (b) ground motion

The resulting fundamental differences in these loads is that, for a given structure, during a blast the characteristics of the global response of the structure are a function of the pressure time history which can vary across the face of the structure; however, during a ground motion the characteristics of the global response of the same structure are a function of ground acceleration, which, unlike the pressure time history, does not vary with position in the structure. In this situation, where a blast simulation technique using ground motion is being developed, the practical effect of this difference is that an over-constrained problem exists as a ground acceleration, which can only vary

with time, is being used to simulate the effect of a blast pressure, which can vary in time and position. One alternative which would allow some control over the load distribution during a blast simulation would be to arrange supplemental mass or the mass of the structure being tested in way that the loads resulting from a ground motion can better replicate the distribution of the load during a blast. Unfortunately, this solution is not ideal as changes to the mass of the structure will also have a large effect on the dynamics of the structure.

Instead of attempting to alter the structure being tested in an attempt to better realize a load distribution that may occurs in a blast, in this work, the goal is to develop a blast simulation technique which relies only on a designed ground motion. While this technique may fail to replicate the load distribution on a structure during a particular blast, as the proceeding sections will show, the global response can still be reasonably simulated.

4.1.2 Fundamental restrictions on ground motion used for blast simulation

Some common simplified blast pressure models consist of a triangular pressure time history in which the pressure starts at a peak pressure and linearly drops to zero after a specified duration. When this duration is small compared to the dynamics of the structure being loaded, this pressure time history model can be further simplified to a pressure impulse. As discussed in the previous subsection, the load on a structure during a ground motion is a function of the ground acceleration; consequently, one might assume that a ground acceleration impulse might be a good first guess for an appropriate ground motion to approximate a structure's global response from this simplified blast loading. Unfortunately, this type of loading is not possible due to basic physical restrictions. As shown in Figure 4-2, an impulse in ground acceleration corresponds with a constant ground velocity and a linearly increasing ground displacement; thus, because it is not a realistic for a shake table to provide an unbound ground displacement during a test, it is not possible to load a structure with a ground acceleration impulse.

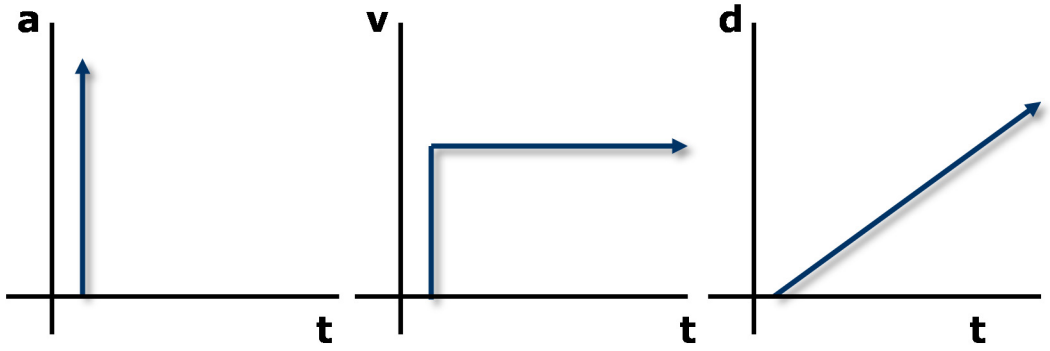

Figure 4-2. Corresponding ground velocity and displacement time histories for ground acceleration impulse

To avoid unrealistic shake table behavior, the ground acceleration used for blast simulation must have corresponding realistic ground velocities and displacement. While specific shake tables will be capable of achieving different ranges of acceleration, velocity, and displacement, the fundamental restriction on the ground acceleration is that its corresponding displacement must be bounded.

4.2 Effect of load application differences on structure with internal mass damper

In this section a case study is performed on a structure with an internal mass damper to examine the differences that result from an explosive blast, where an internal damper would not be directly loaded, compared to a blast simulation using ground motion, where an internal mass damper is directly loaded due to inertial effects. In the following subsections, the structure and input considered for this case study are introduced, the response is examined, and conclusions are drawn.

4.2.1 System examined

The system investigated in this case study is comprised of a two story linear base structure (modeled as 2 DOF) with a Type I NES attached to the second story, see Figure 4-3. The mass, stiffness, and damping matrix for the linear base structure are shown below.

$$\mathbf{M} = \begin{bmatrix} 26.178 & 0 \\ 0 & 26.178 \end{bmatrix} \text{ kg} \qquad \mathbf{K} = \begin{bmatrix} 15276 & -8400 \\ -8400 & 8400 \end{bmatrix} \text{ N/m} \tag{4.1}$$

$$\mathbf{C} = \begin{bmatrix} 5.936 & -2.180 \\ -2.180 & 4.152 \end{bmatrix} \frac{\text{N}(\text{sec})}{\text{m}}$$

These matrices are based on the degrees of freedom for the linear system which are the displacement of the first and second floor relative to the base of the structure. The first and second natural frequencies of this structure are 1.63 and 4.50 Hz. The properties of the Type I NES attached to the second floor are listed below.

$$m_{NES} = 1.3 \text{ kg}, \quad k_{NES} = 6.15 \times 10^5 \text{ N/m}^3, \quad c_{NES} = 10.72 \text{ N-s/m} \tag{4.2}$$

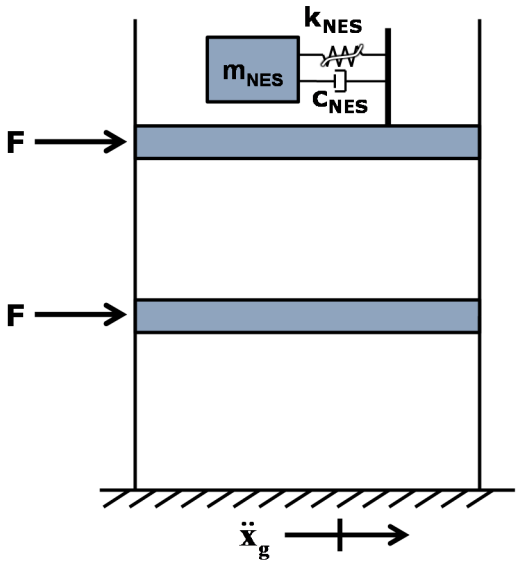

Figure 4-3. Diagram of system considered in case study

4.2.2 Input considered

As mentioned above, the goal of this case study is to compare the response of the system considered when the input is a ground motion and when the input is blast loading. For the ground motion, the input into the structure is applied as a ground acceleration; for the blast, the input is applied as a set of equal forces on the first and second floors of the base structure. The scope of this case study does not include a comparison of response due to shape of the loading. Consequently, in both cases, the same triangular load profile shown in Figure 4-4 is used. As discussed in Section 4.1.2, due to the physical constraints of the ground motion, this triangular profile is not a realistic loading profile; however, this profile is still useful for the simplified loading considered in this case study.

In each loading case, the load profile shown in Figure 4-4 can be scaled to input the desired amount of energy into the building. Due to the nature of the different types of loadings considered, different scaling is required to input the same amount of energy for the blast and ground motion. For both loading types, the period of this loading is short enough, relative to the period of the building, such that the loading can be consider to be impulse. Accordingly, the impulse, in terms of N-s, of the blast loading will be used to distinguish the load level on the structure. For a comparison at each blast level considered, the ground motion has been scaled to produce an equal peak displacement of the base structure.

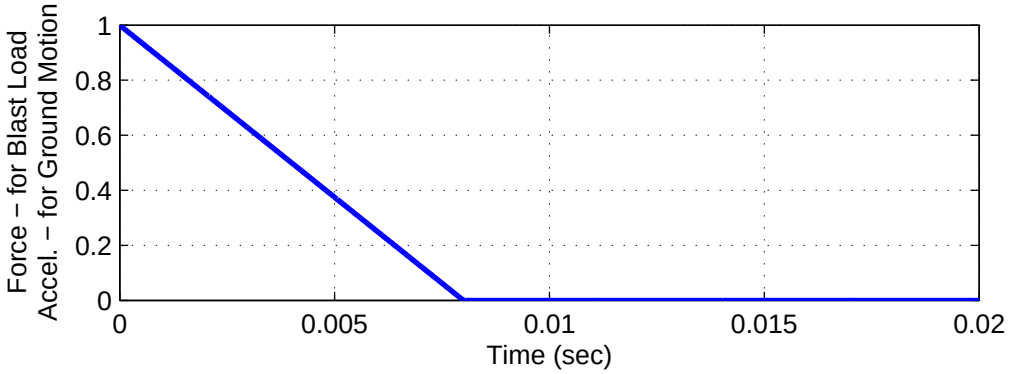

Figure 4-4: Shape of impulsive load used

4.2.3 System response

In Figure 4-5 the response of the base structure to a blast impulse of 13.2 N-s and the equivalent ground motion are shown. In this figure, the response of the floors to the two different loading types are almost identical. Figure 4-6 shows the response of the NES, including restoring force hysteresis, displacement relative to the host floor versus time, and the restoring force versus time. Figure 4-7 shows a zoom in of the beginning part of the time history of the NES displacement relative to the host floor and the restoring force. As one can see from Figure 4-7, even though the response of the NES is different in the first half cycle of the time history, the records closely converge to an almost identical state and are practically indistinguishable in the time histories shown in Figure 4-6. One effect of the differences in the beginning of the NES time history is that maximum restoring force in the NES is not the same in both loading cases.

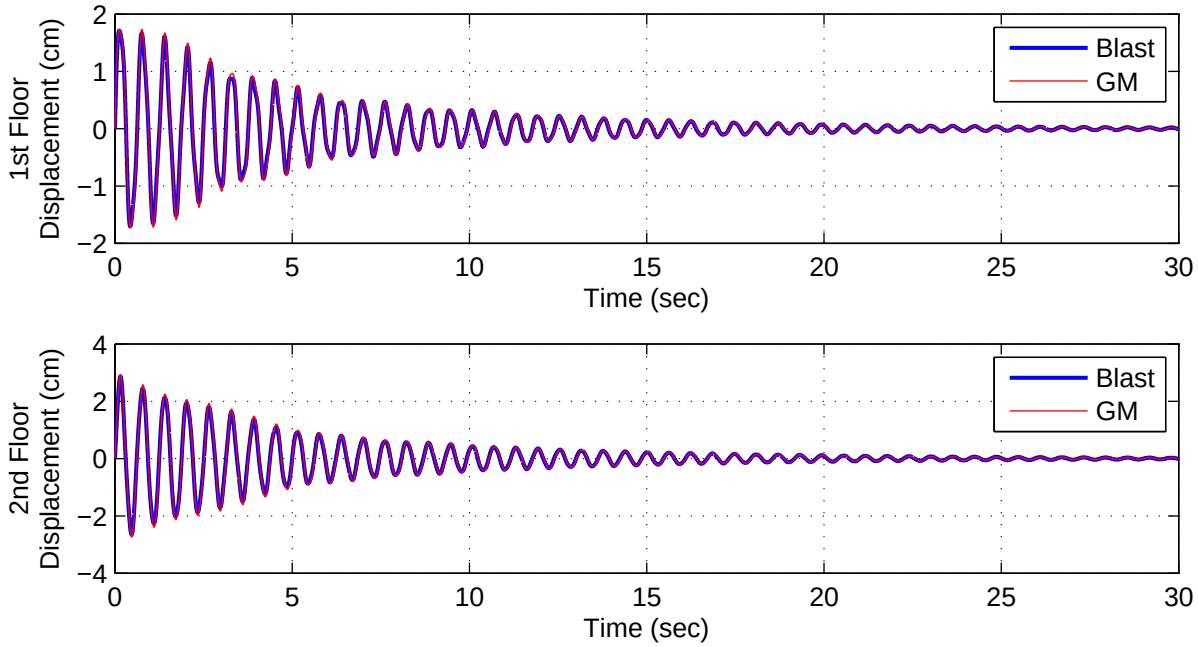

Figure 4-5: Response of base structure to loading

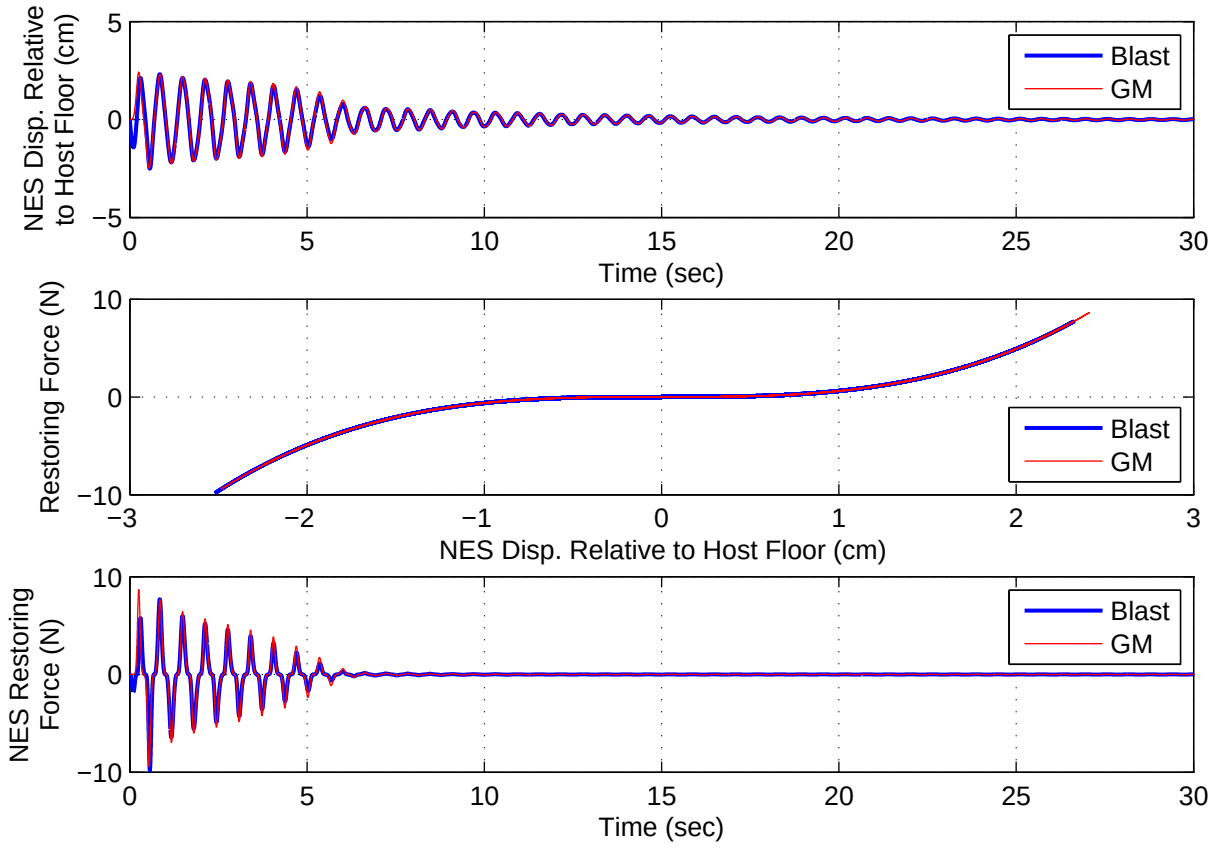

Figure 4-6: Response of NES to loading

In addition to looking at comparisons of the response to the different loading types at one level, comparisons can be made at varying energy levels. To make this comparison, two metrics will be used. The first is the energy in the system at 15 seconds from the start of the impulse. This measure provide a good tool to compare the effect of the load level on the overall response of the structure. The second metric used to evaluate the response to different loading levels is the maximum absolute value of the restoring force. This measure is useful is showing the difference in the NES behavior at the beginning part of the time history that result at different load levels.

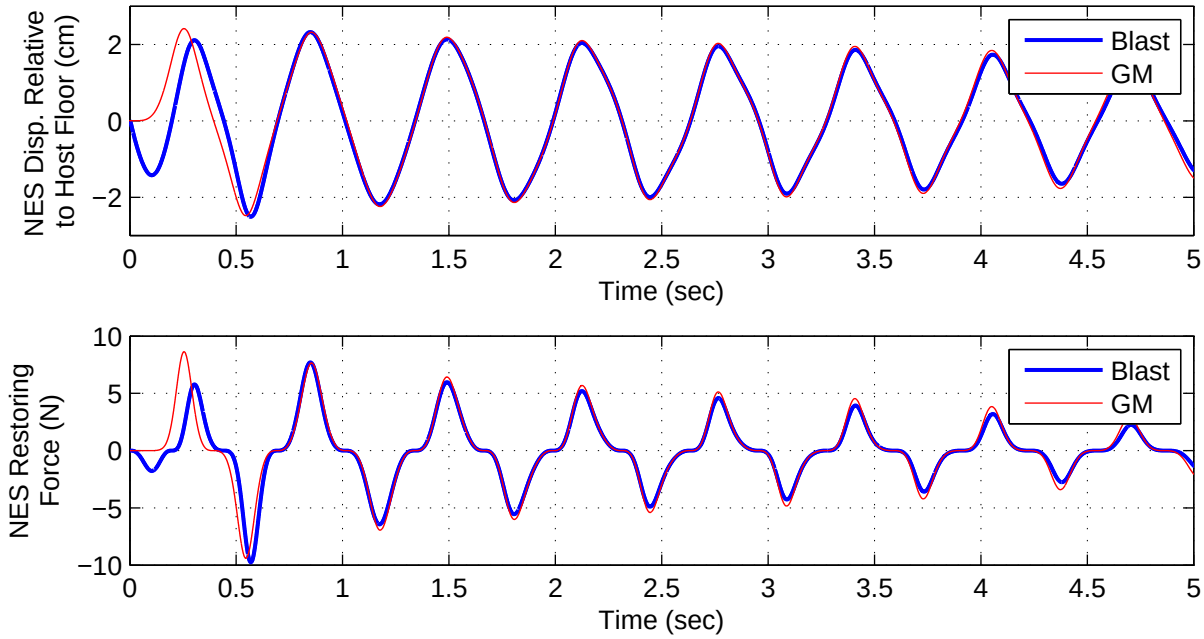

Figure 4-7: Response of NES to loading (zoomed in)

In Figure 4-8 the total energy after 15 seconds is shown for the system in response to the two loading types across a range of input levels. This figure shows that at most impulse levels the energy in the system at 15 seconds is close for the two different input cases. This result is indicative of the fact that the effect of the input type has a negligible effect on the global response of the system for most of the impulse levels. To investigate the discrepancies in energy seen at low impulse levels Figure 4-10 shows the response of the NES at the lowest impulse level. In this figure one can see a dramatic difference in the behavior of the NES. This difference is due to the fact that at in the impulse is so small that the discrepancies in the beginning of the NES time history have a large effect on the complete time history of the NES. In this case the ground motion loading was large enough to move the NES, but after that the restoring forces were not large enough to overcome the damping forces and recenter the NES.

In Figure 4-9 the maximum NES restoring force is shown for the system in response to the two loading types across a range of input levels. This figure shows that the maximum restoring force is generally different for the two types of loading. In this figure one can see that the trend in this difference is predictable and dependent on the impulse level. Despite these differences, a good comparison in global response of the system is obtained at most load levels.

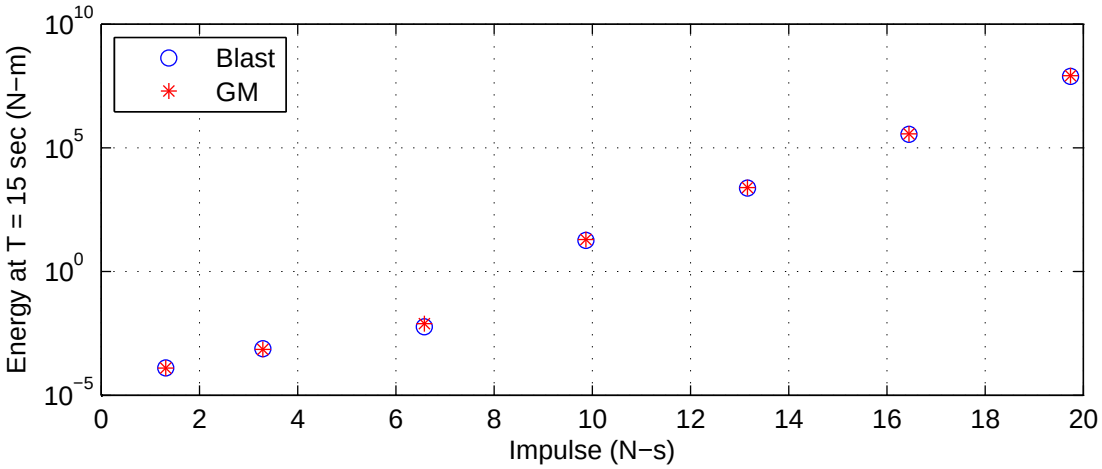

Figure 4-8: Total energy in system at T = 15 sec vs. impulse level

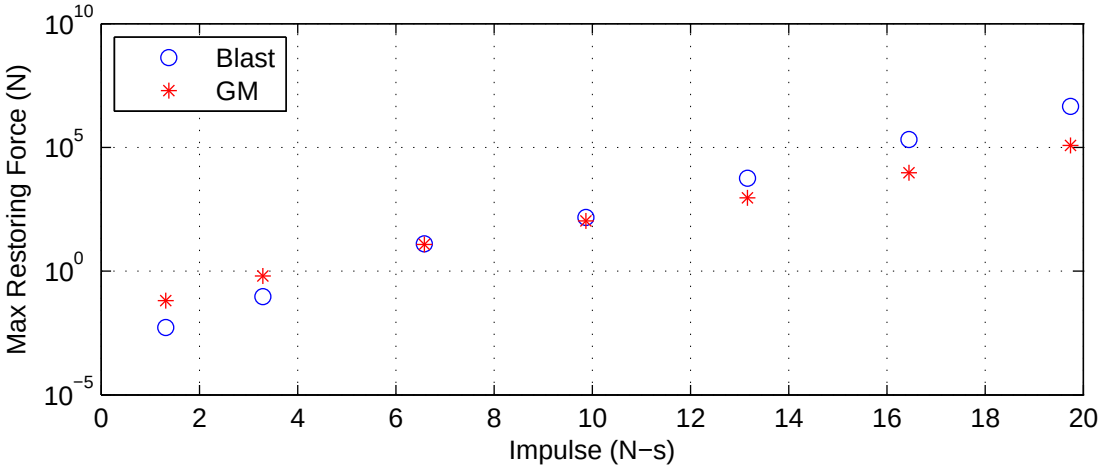

Figure 4-9: Max NES restoring force vs. impulse level

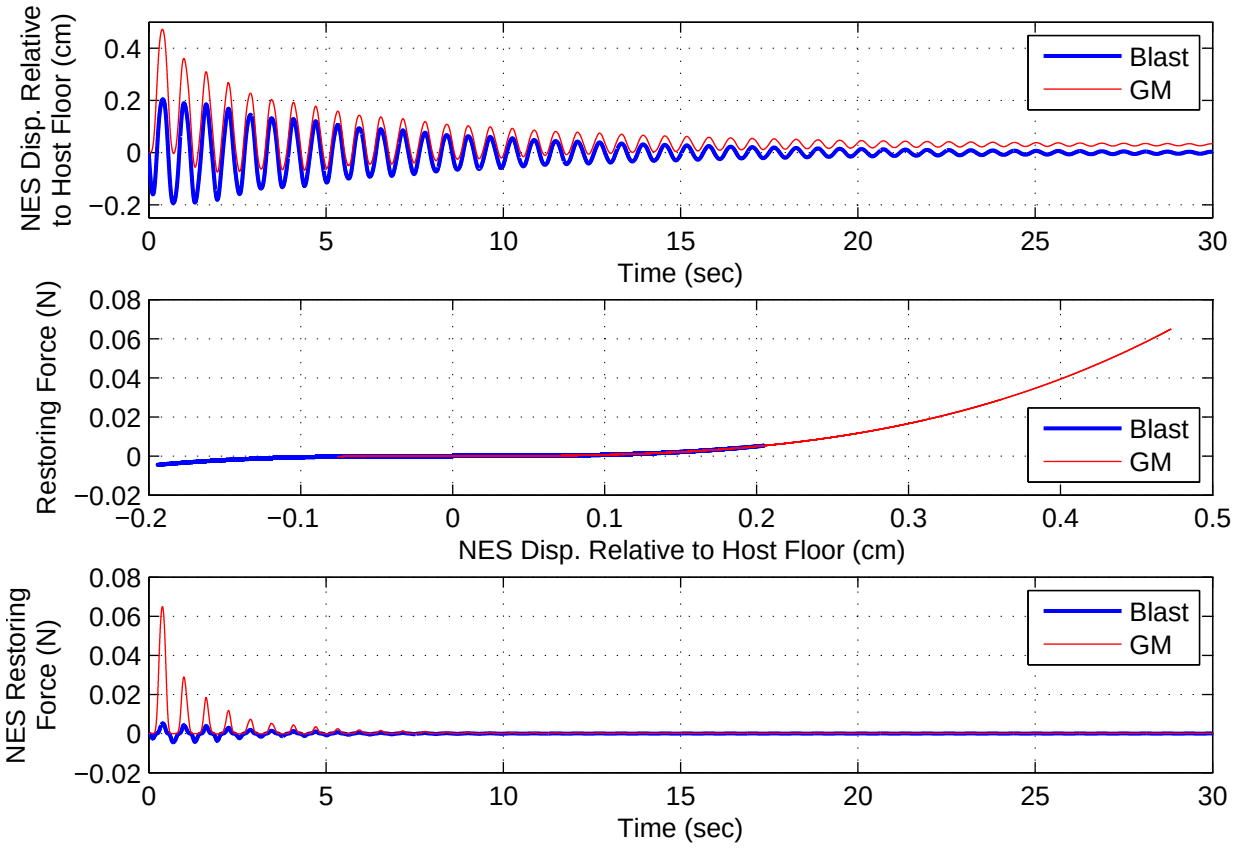

Figure 4-10: Response of the NES at the lowest impulse level studied

4.2.4 Conclusions drawn from case study

This case study has investigated the response of a 2DOF base structure with an attached Type I NES to different loading types. These loading types are both approximately impulsive, but one is a ground motion and the other consists of forces applied directly to the base structure's DOFs (blast). From this investigation, it was shown that, for at all but the lowest impulse level investigated, the global behavior of the base structure was similar, regardless of loading type. Additionally this investigation has shown that despite good global agreement in the response of the base structure, large differences in the response of the NES (most notably in the maximum restoring force applied to the NES) are possible, especially at the very beginning of the response.

4.3 Ground motion design for blast simulation

In this section, a prototype ground motion is introduced for blast simulation. The specific shape of this ground motion is a function of several different parameters which serve to alter the shape of the ground motion as desired. After this prototype ground motion is established, a methodology is presented for choosing its parameters of this ground motion for a specific blast simulation test.

4.3.1 Prototype ground motion

In developing this technique for blast simulation, it is desirable that a single prototype ground motion is established which can serve as a straightforward starting point for all applications of the technique. However, as it is also desirable that this blast simulation technique is applicable for a wide range of structures and blasts, it is necessary that this prototype ground motion has the flexibility to be refined for a particular test. Additionally, flexibility in this prototype ground motion is necessary as different shake tables will have unique stoke and velocity limitations.

The acceleration time-history of the prototype ground motion for blast simulation that is proposed in this work is shown in Figure 4-11. As shown in this figure, several parameters define the shape of this ground acceleration. This ground acceleration starts at zero then linearly increases at rate E_{acc} to a maximum acceleration level, $a^{+}_{\max}$, which is held for time t^{+}_{hold}. After this hold, the acceleration decreases at rate $-E_{acc}$ until a maximum negative acceleration of $a^{-}_{\max}$ is achieved. After holding this acceleration for time t^{-}_{hold} the acceleration again increases at rate E_{acc} until it is zero again. The ratio of the absolute values of the peak negative ground acceleration $a^{-}_{\max}$ to the peak positive ground acceleration $a^{+}_{\max}$ is defined as α.

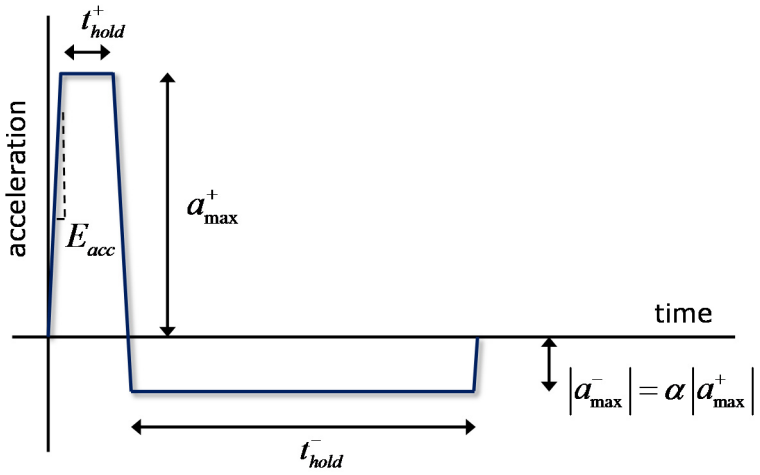

Figure 4-11. Prototype blast simulation ground motion – acceleration time history

In order to ensure this prototype acceleration is zero mean, t^{-}_{hold} is defined as a function of $a^{+}_{\max}$, α, t^{+}_{hold}, and E_{acc}.

$$t^{-}_{hold} = \frac{1}{\alpha E_{acc}}\left(E_{acc}t^{+}_{hold} + a^{+}_{\max} - a^{+}_{\max}\alpha^{2}\right) \tag{4.3}$$

This function is designed to ensure the negative portion of the acceleration balances out the positive portion. As a consequence of the zero mean ground acceleration time history, the corresponding ground displacement is bounded, assuming no initial velocity. Additionally, the corresponding ground velocity is a smooth function which is greater than or equal to zero throughout the entire ground motion. An example of this ground acceleration and the resulting velocity and displacement time histories are shown in Figure 4-12. While the specific shapes of these example time histories are a function of particular ground acceleration variables, the general

form of the time histories is representative of the motions derived from the prototype ground acceleration.

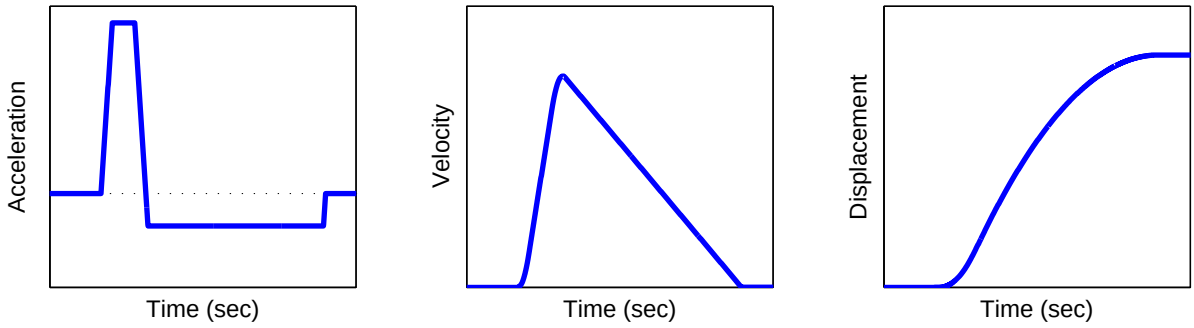

Figure 4-12. Example realization of prototype ground acceleration and resulting velocity and displacement time histories

4.3.2 Ground motion design methodology for blast simulation

When loading a structure with a ground motion derived from the prototype ground motion introduced in subsection 4.3.1, the response of the structure will be highly dependent on the variables that control the shape of the ground motion. As previously discussed and shown in Figure 4-11 these variables are the prototype ground motion's acceleration rate of change $\left(E_{acc}\right)$, the maximum acceleration $\left(a_{\max}^{+}\right)$, the length of time this maximum acceleration is maintained $\left(t_{hold}^{+}\right)$, and the ratio of peak negative acceleration to peak positive acceleration $\left(\alpha\right)$. As a consequence of this dependency, when using this prototype ground motion for blast simulation, it is important that these variables are chosen in an intelligent manner.

The methodology for determining the parameters of the prototype ground motion used in a blast simulation that is proposed in this work is illustrated in the flow chart shown in Figure 4-13. As this figure shows, in order to determine a finalize ground motion, models of the structure being tested and of the blast are needed in addition to the prototype ground motion. With these models a numerical simulation of the structure during the blast event is computed and the resulting modal energy profile of the structure's global response can be produced. Likewise with the prototype ground motion, using the model of the structure, a numerical simulation of the structures response to the ground motion can be computed and the resulting modal energy profile can be obtained. However, as the parameters of the ground motion have not been determined, this numerical analysis must be done multiple times over a range of the parameters that define the prototype ground motion. Once the modal energy profiles from blast and the multiple ground motions are obtained, a comparison can be made and the parameters of the ground motion that best simulate the blast, in terms of modal energy distribution, can be identified. With these optimal parameters identified, the acceleration, velocity, and displacement time histories of the candidate ground motion can be produced. In order to ensure that the shake table that will be used for this experimental blast simulation is capable of delivering this ground motion, the ground motion time histories must be compared to the shake table's limitations. If this candidate ground motion violates the shake table's limitations, it is necessary to return to the modal energy profile

comparison step to choose a new candidate ground motion. If the shake table's limitations are not violated, the ground motion is ready for experimental blast simulation testing.

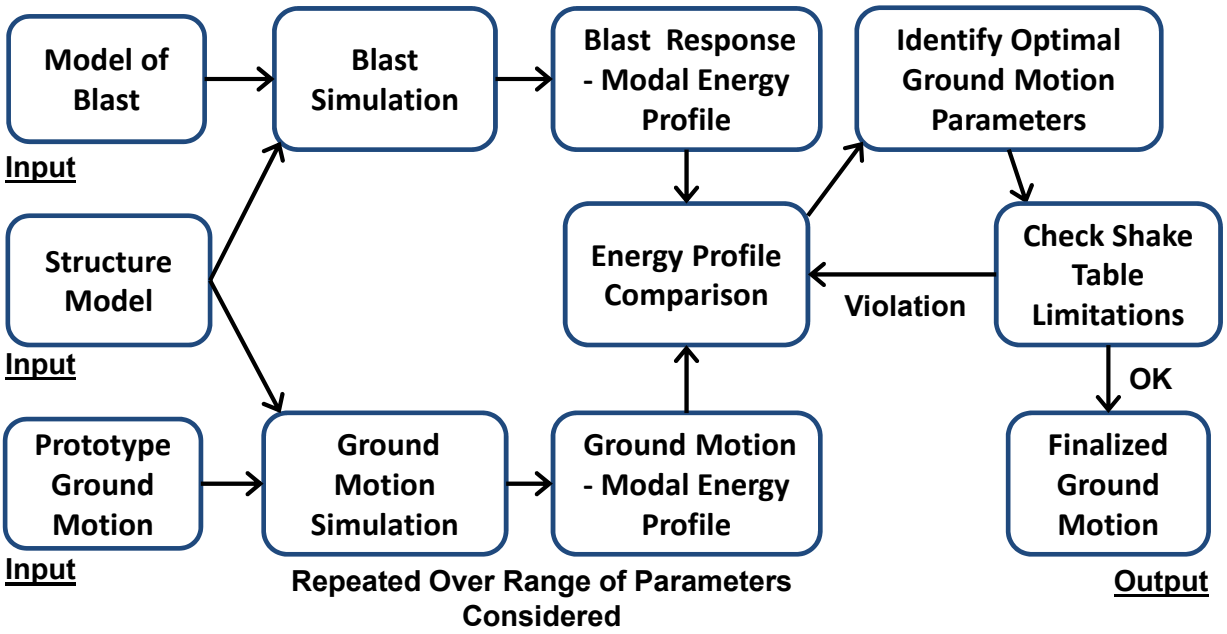

Figure 4-13: Flow chart of ground motion design methodology for blast simulation

4.4 Example blast simulation ground motion design

In Section 4.3 the prototype ground motion for experimental blast simulation that is proposed in this work was presented along with a proposed methodology for determining the parameters of this ground motion for the testing of a particular structure subjected to a specific blast. In this section an example application of this technique is shown. The structure used for this example is the large-scale structure which is discussed in detail in Chapter 6. The model of this structure, which is used in the necessary numerical simulations of its response, is nine degrees-of-freedom and considers only the linear motion of the structure in its weak translational direction. The blast model for this example is a uniform pressure that is triangular in time with a total duration of 0.01 seconds. The typical floor force time history that results on the structure from this model blast is shown in Figure 4-14.

As the structure in this example is assumed to be linear, some parameters of the prototype ground motion do not need to be tested in simulation. The parameters that do not need to be considered include the maximum positive acceleration of the motion, $a^{+}_{\max}$, which will only affect the amplitude of the energy distributed to the structure, not its modal distribution. Additionally, for the purpose of simplifying this example, the parameters α and E_{acc} will be considered when investigating modal energy profile of the ground motion. While α and E_{acc} do have some effect on the modal energy profile of the structure's response, it is small compared to the parameter that will be investigated, t^{+}_{hold}. Also, with all the other parameters held constant and t^{+}_{hold} varied, it may be more beneficial to think of the parameter being varied as the total length of the ground acceleration pulse, T_{pulse}.

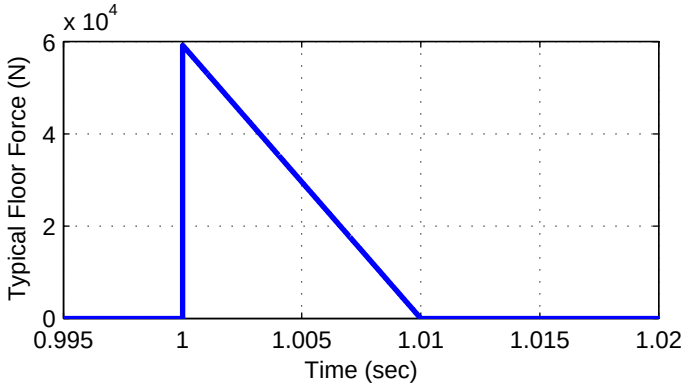

Figure 4-14. Blast time history considered in example ground motion design

With T_{pulse} varied, the ground motion numerical simulation was performed then the results post-processed to determine the modal profile of the resulting energy in the structure being loaded. In Figure 4-15 the resulting modal profile from the ground motion numerical simulations are shown in comparison to the modal profile that resulted from the blast numerical simulation. As this figure shows, the blast and all the ground motions provide modal energy profiles that contain most of the energy in the lower modes; however, there is still a good deal of variability in energy profile of the different ground motions. From this figure, it was noted that the 0.18 sec ground motion provides the best fit of the blast modal energy profile. To obtain the necessary scaling of this ground motion so that it provides the desired level of response, the ground motion was scaled such that the peak displacement of the structure that results from the blast and the ground motion is the same.

The resulting acceleration, velocity, and displacement of this ground motion are shown in Figure 4-16. If this ground motion was going to be used experimentally, the data from these time histories, such as necessary stroke, maximum velocity, and maximum acceleration, would be used to evaluate if the intended shake table was capable of providing the desired ground motion. If it was found that the shake was unable to produce the desired ground motion, Figure 4-15 would again be consulted to choose another candidate ground motion.

In Figure 4-17 the response of the structure to the blast and to the ground motion shown in Figure 4-16 is compared. As this figure shows the blast simulation with the ground motion results in a top floor displacement response that matches up well with the blast response. Additionally, while reasonable agreement is found in the acceleration records, the match is not as good as the displacement record. The reason for this superior acceleration match is that the acceleration is more heavily influenced by the higher mode behavior, which is not as well matched in the case of the ground motion.

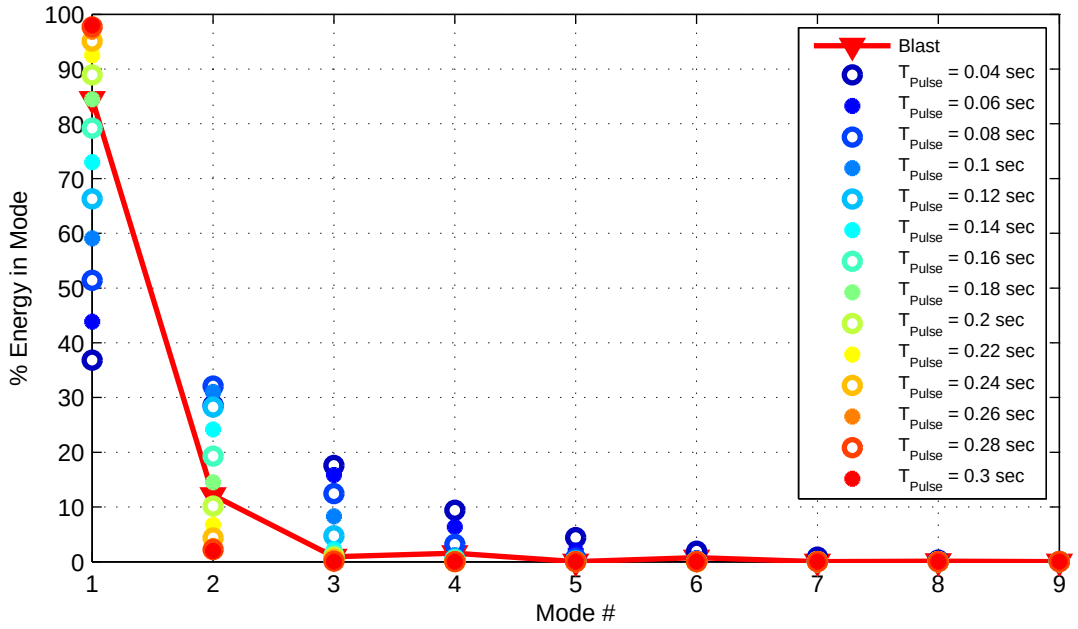

Figure 4-15. Modal energy profile of blast response and multiple realizations of blast simulation ground motion

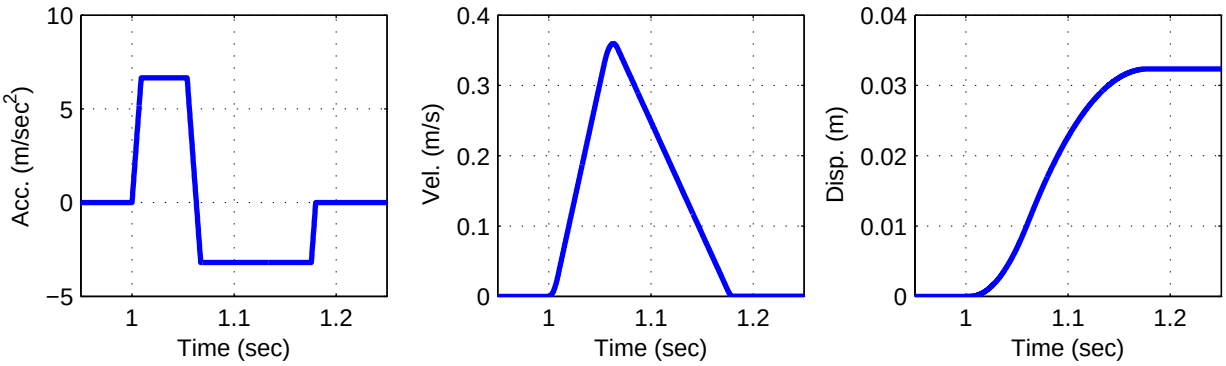

Figure 4-16. Resulting ground motion from example blast simulation ground motion design

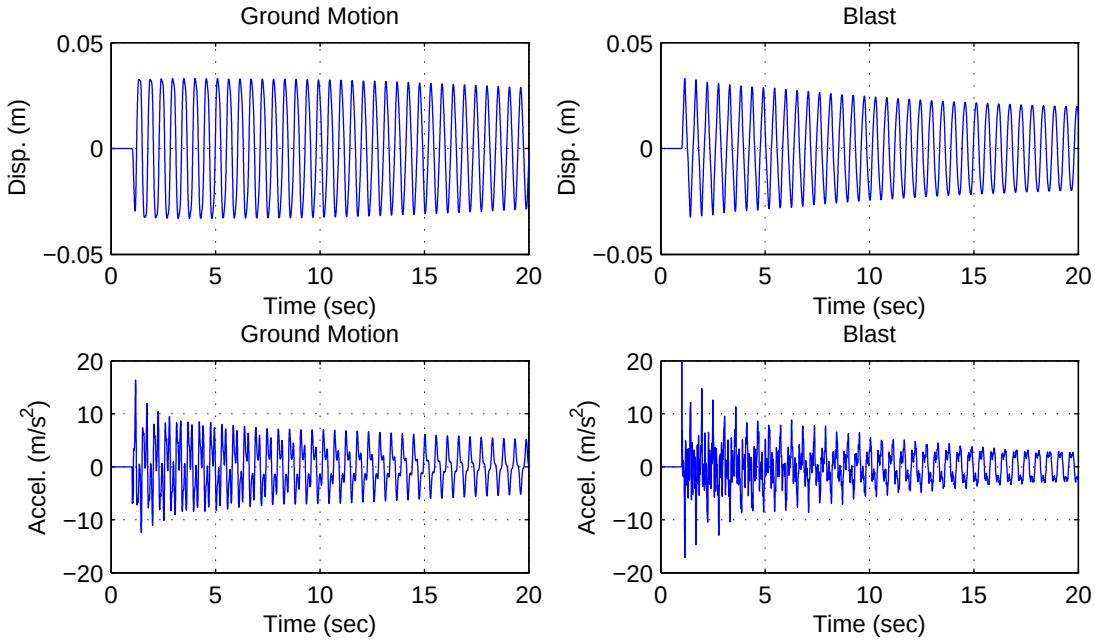

Figure 4-17. Comparison of blast and simulated blast response of the top floor of the nine story structure

4.5 Experimental validation

As presented in Chapter 7, experimental blast and shake table testing was performed on the large-scale base structure developed in Chapter 6. This combination of testing provided the unique opportunity for an experimental validation of the blast simulation technique using ground motion that was developed in the previous sections of this chapter.

4.5.1 Blast loading

As detailed in Chapter 7, the large-scale base structure was tested with three different blast loadings. These loads are identified as the 106 kPa-msec, 209 kPa-msec, and 620 kPa-msec blasts; this designation refers to the design average pressure impulse on the cladding from each blast. For the validation efforts presented in this section, the 209 kPa-msec blast will be focused on. The cladding pressure measured during this blast is shown in Figure 4-18. As this figure shows, this measured pressure time history is more complicated than the pressure used in the example of Section 4.4, which was assumed to be spatially uniform and purely triangular in time. The corresponding displacement response of the third and seventh floors of the base structure with the system of NESs locked to this blast loading is shown in Figure 4-19.

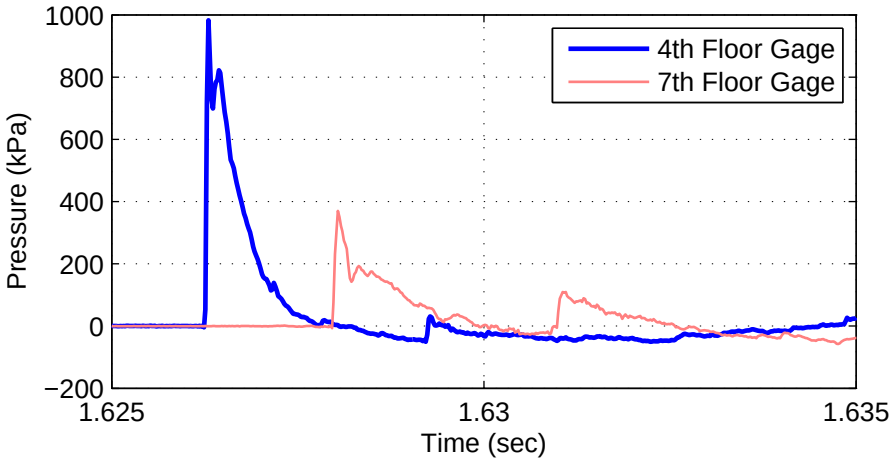

Figure 4-18. Cladding pressure measured during 209 kpa-msec blast test

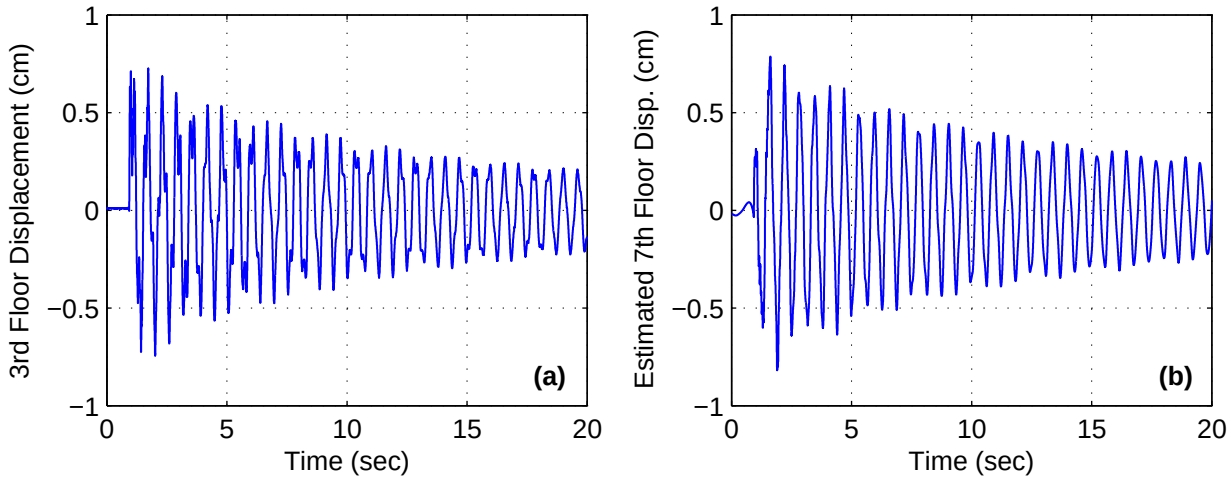

Figure 4-19. Displacement time history response of the base structure with NESs locked to 209 kpa-msec blast loading (a) third floor and (b) seventh floor

4.5.2 Determination of desired blast simulation ground motion

To design the ground motion that will be used in the experimental blast simulation, the prototype ground motion introduced in Section 4.3.1 was modified using the methodology introduced in Section 4.3.2. Thus, the first step in this design was to determine the modal energy distribution in the structure that resulted from the blast loading. To determine this distribution, the measured response of the structure to this load was transformed into modal coordinates, then the energy in each mode of the structure was calculated after the blast pressure has dissipated. The resulting modal energy distribution of the blast loading is shown in Figure 4-20.

After determining the modal energy distribution of the blast response, the next step in the ground motion design is to optimize the parameters of the prototype ground motion to deliver, as closely as possible, the desired energy distribution. For this optimization, a parametric study was performed to determine the optimal ground motion parameters to deliver the correct modal energy

distribution, in terms of percentage. The parameters considered in this study are the total duration of the ground motion and the percentage of ground motion that has positive acceleration. This parametric study was performed by running numerical simulation to determine the response of the structure to the ground motion. After optimizing the ground motion to best match the percentage of energy in each mode, the ground motion was then scaled to match the total energy in the structure due to the blast. The resulting optimized ground motion is shown in Figure 4-21.

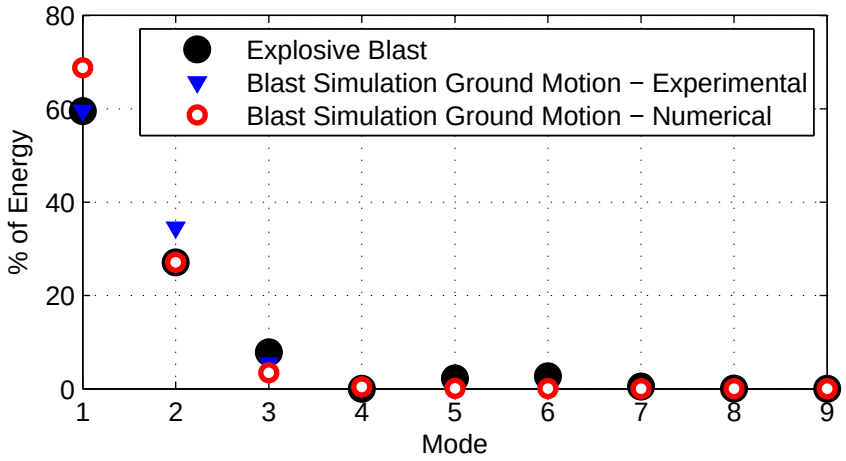

Figure 4-20. Estimated modal energy distribution in structure resulting from 209 kpa-msec blast, experimental blast simulation, and numerical blast simulation

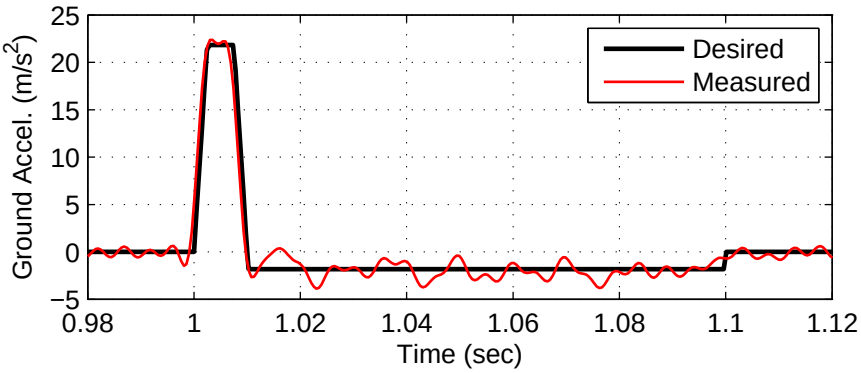

Figure 4-21. Desired and measured shake-table-produced ground acceleration during experimental simulation of 209 kpa-msec blast

4.5.3 Experimental blast simulation results and comparison to blast testing results

The blast simulation ground motion that was designed in the previous section was used to load the large-scale structure with the Triaxial Earthquake and Shock Simulator (TESS) shake table at the US Army Corps of Engineers Construction Engineering Research Laboratory in Champaign, IL. More information on the shake table testing of this structure can be found in Chapter 7. The resulting ground motion produced by this table is shown in Figure 4-21. As this figure shows, the measured acceleration of the shake table closely matches the desired ground motion. The main

difference between the measured and desired accelerations is the addition of a small amount of high-frequency vibration in the measured record.

The third floor displacement response of the structure with the NESs locked and unlocked to the blast simulation ground motion is shown in Figure 4-22. In this figure, the third floor displacement response measured in this testing is compared with the blast test results. The comparison presented in this figure shows that, with the NESs unlocked, there is a small difference in peak response, but an overall good agreement between the blast and blast simulation results. With the NESs locked, the same small difference in peak responses exists; however, there are additionally differences shown in the subsequent response. These differences are primarily caused by small changes in natural frequency that make a beat phenomenon more prevalent in the blast test as well as an increase in damping due to some changes in the blast testing set up.

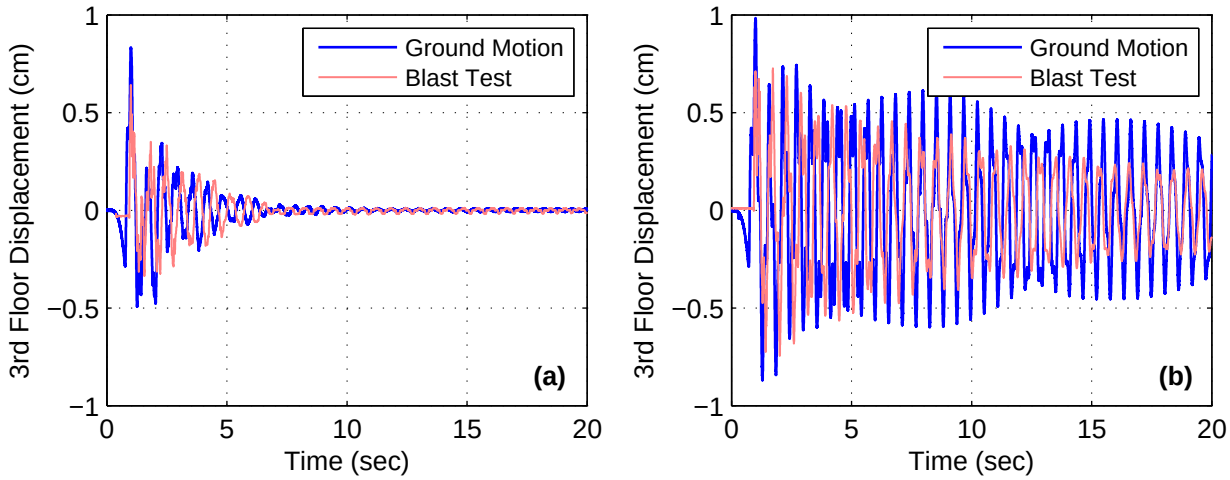

Figure 4-22. Third floor displacement time history of the base structure in response to the 209 kpa-msec blast loading and the corresponding blast simulation ground motion (a) NESs unlocked and (b) NESs locked

In Figure 4-23 the strain in the first floor columns with the NESs locked and unlocked are compared for the 209 kpa-msec blast and blast simulation test. This figure shows similar agreement to what was seen from the third floor displacement response; however, in these results, the larger prevalence of high-frequency vibrations during the blast tests are observed.

In Figure 4-20 the modal energy distribution that results from this experimental blast simulation is compared to the blast results and a numerical analysis performed with the blast simulation ground motion. From this figure, one can see that percentage of energy distribution is roughly in line when comparing the blast and experimental blast simulation. The exception to this trend is the second mode which show a modestly higher experimental blast simulation energy content. Furthermore, as demonstrated by the strain results, the allocation to the higher modes (mainly mode five) is higher in the blast loading. Additionally, this figure shows the numerical and experimental simulation results have a comparable modal energy distribution, with some relatively small discrepancies in the first two modes.

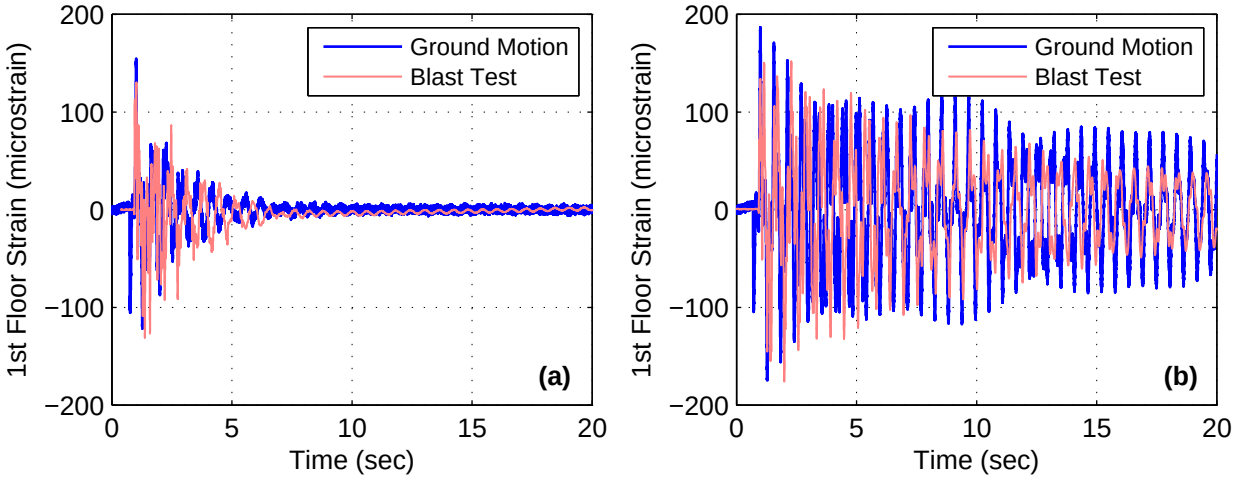

Figure 4-23. First floor column strain time history of the base structure in response to the 209 kpa-msec blast loading and the corresponding blast simulation ground motion (a) NESs unlocked and (b) NESs locked

A blast simulation using shake-table-produced ground motion was also performed for the 620 kpa-msec blast. Although the pressure distribution on the structure, and thus resulting modal energy varied somewhat from the 209 kpa-msec test, a scaled version of the ground motion shown in Figure 4-21 was initially desired. Unfortunately, limitations of the shake table required that this scaled ground motion by filtered to remove some of the sharp changes in desired acceleration. The resulting desired and measured shake-table-produced ground motion for this blast simulation test is shown in Figure 4-24. Once again, this figure shows good agreement between the desired and measured ground motion.

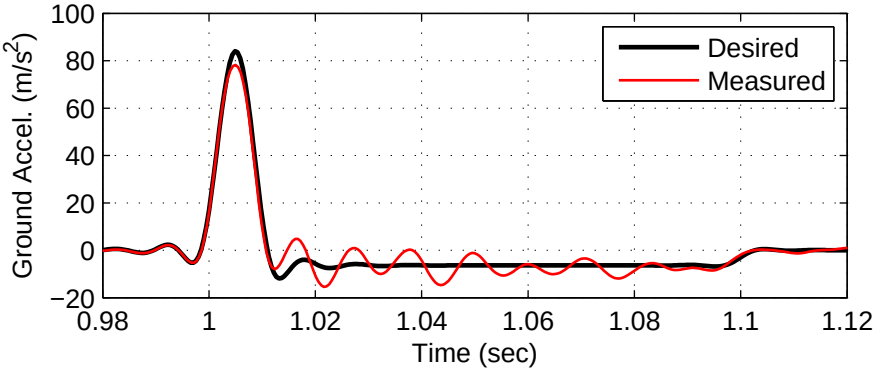

Figure 4-24. Desired and measured shake-table-produced ground acceleration during experimental simulation of 620 kpa-msec blast

In Figure 4-25 the third floor displacement response that resulted from the 620 kpa-msec blast and blast simulation are shown. In Figure 4-26 the resulting first floor strain response during blast and blast simulation tests are shown. In both , a 620 kpa-msec blast test with the NESs locked is not shown. This portion is missing because time constraints at the blast test site prevented a test with the NESs locked at this load level. These figures show the same trends identified in the results from the 209 kpa-msec blast; a good comparison is shown for the blast and simulated blast results

with the NESs unlocked, with some high-frequency response missing in the simulated blast response.

The modal energy that results from this experimental blast simulation is compared with the results of a numerical simulation. As with the results from the 209 kpa-msec blast simulation, the numerical and experimental simulation results have a comparable modal energy distribution, with some relatively small discrepancies in the first two modes.

The reasonable agreement in both time history and in modal energy distribution between the blast and blast simulations serve to validate the potential of this proposed blast simulation technique. Suggestions to help further improve this technique are discussed in the next section.

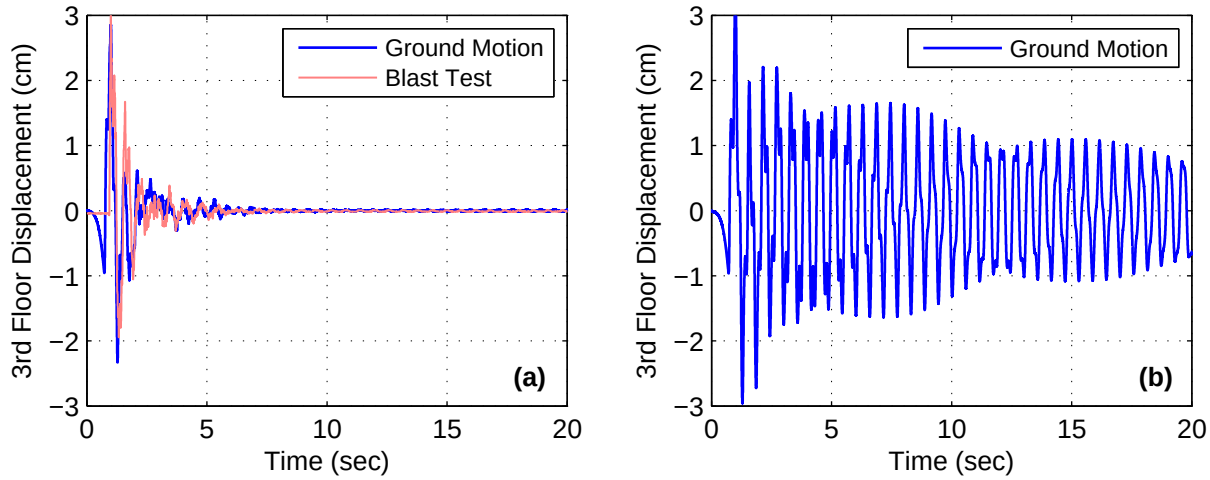

Figure 4-25. Third floor displacement time history of the base structure in response to the 620 kpa-msec blast loading and the corresponding blast simulation ground motion (a) NESs unlocked and (b) NESs locked

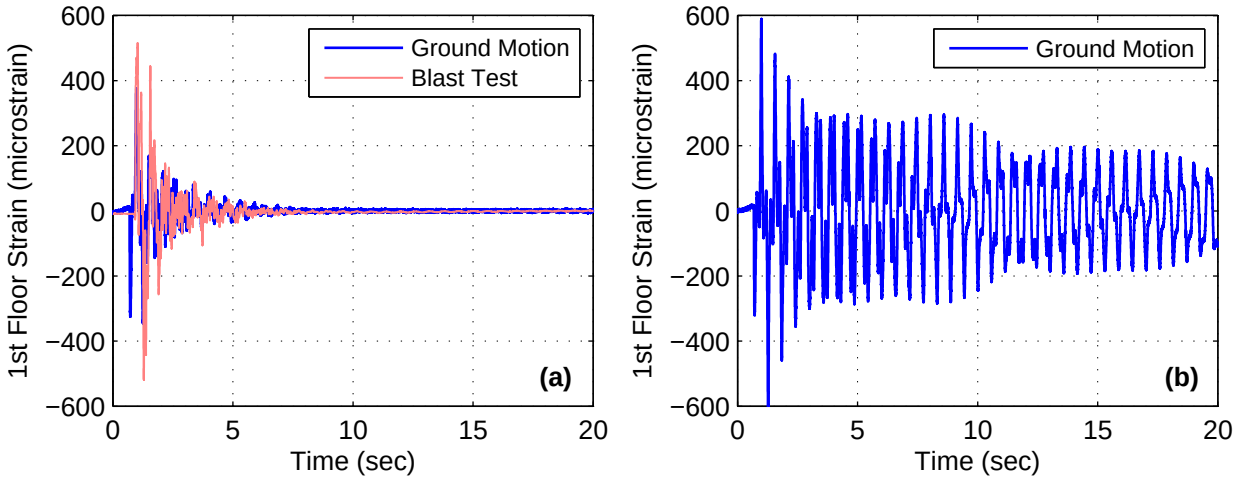

Figure 4-26. First floor column strain time history of the base structure in response to the 620 kpa-msec blast loading and the corresponding blast simulation ground motion (a) NESs unlocked and (b) NESs locked

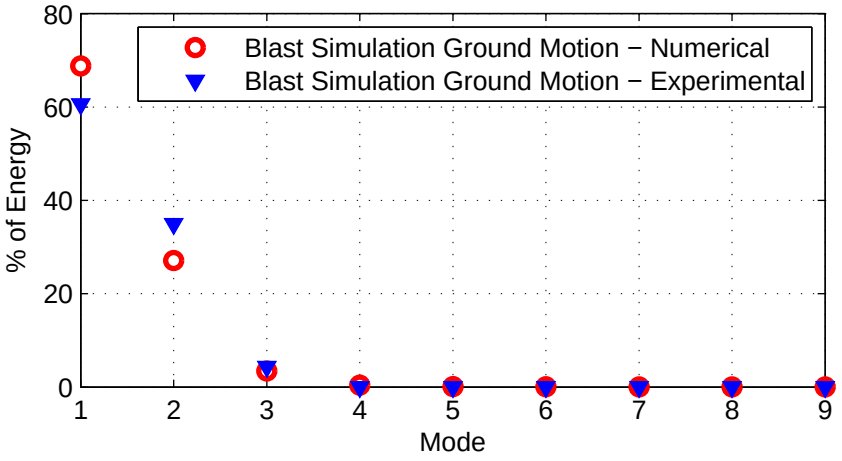

Figure 4-27. Experimentally estimated modal energy distribution in structure resulting from 620 kpa-msec blast and blast simulation test

4.6 Review of technique limitations and areas of future improvement

The main limitation on the experimental blast simulation technique proposed in this chapter is the inability of this technique to be used to simulate local blast effects on a structure. This issue is important as the local effects of blasts on structures are often the most important. The importance of local effects is especially true in cases where the blast is located close to a structure or when high-quality structural detailing has not been implemented in order to reduce the probability that local failure modes will dominate.

Despite this fundamental limitation, the proposed experimental blast simulation technique does have promising applications. These applications include situations where the global effect of a blast dominate the response of a structure or situations where researchers are most interested in the global effects, irrespective of the probability that they will dominate the structural response. Situations when the global effects of blasts are more likely to dominate the response of a structure are large blasts occurring at a distance (Li et al. 2009), structures which are designed with blast detailing in mind, and in structures types that are particularly susceptible to global failure mechanisms (Ngo et al. 2007).

In addition to the major fundamental limitation mention above, other limitation on the effectiveness of this blast simulation technique exist. These limitation include that the load distribution on the structure is tied to the mass distribution instead of the surface area of the cladding and pressure distribution of the blast. Additionally, as demonstrated in Section 4.4 and Section 4.5, the effectiveness of the technique is limited by the utilized prototype ground motion, which has difficulty in both matching the desired energy distribution across multiple modes and putting energy into higher frequency modes.

Future areas of research designed to improve this experimental blast simulation technique would benefit by focusing on overcoming the limitations listed above. Included in these future areas of research is an investigation of different prototype ground motions. More advanced prototype ground motions may be able to better deliver the desired energy distribution to the structure across more modes than the prototype ground motion featured in this research.

Additionally, more advance prototype ground motions may show more success in delivering energy to high frequency modes of vibration. Another area for future research would be work examining improving the load distribution in the experimental blast simulation by using movable masses in the structure being tested. As part of this research, the gains in load distribution from the reallocation of mass would have to be weighed against the resulting changes in the dynamic properties of the system studied.

4.7 Summary

In this chapter, the development of a technique to experimentally simulate, using shake-table-produced ground motion, the global response of a structure due to blast has been presented. As a part of this development, the feasibility of the technique was assessed along with the effect this changed load type has on an internally housed NES. This assessment showed that the type of experimental simulation proposed in this chapter was feasible, but some fundamental limitations and restriction existed on the ground motion that could be used. Additionally, a case study demonstrated only minor differences in the response are likely due to the inertial loading of an internally housed NES. Once the feasibility of this technique was established, a generalized prototype ground motion was proposed along with a methodology for determining the optimum parameters to customize this motion for a particular blast simulation. An example of the use of this methodology was presented with numerical simulations. To validate this technique, the results of experimental testing of a large-scale structure were compared. The results of this validation study showed the technique is capable of producing good overall agreement between the global response measured during an explosive blast and a ground motion design with the methodology presented. Areas identified from these results where room for improvement exist include the high frequency response in the simulated response and improving the modal energy distribution. Finally, the limitations of this technique were discussed along with suggestions on how to further improve the technique.

DEVELOPMENT AND EXPERIMENTAL INVESTIGATION OF SMALL- AND MEDIUM-SCALE NESS

The experimental investigation of the effectiveness of NESs at rapidly reducing the response of building structures subjected to idealized impulsive loads has been previously conducted using table-top sized specimens; however, little, if any, work has been done using more moderately sized small-scale or medium-scale models. Therefore, the ability of these devices to be effectively scaled up for use in civil structures is unclear. In addition to this, the existing experimental body of work with NESs is far from complete with limited work on NESs that utilize components other than offset wires to realize the needed nonlinear restoring force and no experimental work done on several different NES types.

The goal of this chapter is to fill in some of those gaps in knowledge with the development and experimental investigation of several different types of NESs at small and medium-scales. Accordingly, this chapter is divided into three sections. The first section discusses the development of the small and medium-scale NESs and the associated scaled base structures that they are incorporated in. Included in this development are a small-scale Type I NES, a small-scale Type III NES (the world's first known realization of this two mass NES), and a medium-scale Type III NES. The small-scale NESs developed use offset wires to produce a nonlinear restoring force, while the medium-scale Type III NES utilize specially shaped elastomeric bumpers. In the second section of this chapter, the experimental investigation of the effectiveness of the small and medium-scale NESs at rapidly reducing the response of the base structures is discussed. For this investigation, the primary loading considered is an impulse-like ground motion. Additionally, in this section, a robustness study utilizing the medium-scale Type III NES is presented. In the final section of this chapter, the result of this work are summarized.

5.1 Development of small and medium-scale base structures and NESs

In this section, the development of small- and medium-scale NESs are discussed. The types of NES developed are a small-scale Type I NES, a small-sca1e Type III NES, and a medium-scale Type III NES. For these small-scale NESs, the necessary essentially nonlinear restoring force was provided by offset wires which were arranged to produce a geometric nonlinearity. For the medium-scale NES, specially shaped elastomeric bumpers were used to produce the necessary nonlinear restoring force.

In addition to the development of NESs, in this section, the small- and medium-scale base structures that these NESs were designed to be attached to are discuss. The small-scale base structure was designed specifically for NES testing, while the medium-scale base structure was repurposed from a previous experiment.

5.1.1 Small-scale base structure

The experimental small-scale investigations of NESs presented in this report focus on exploring the ability of the NESs to rapidly reduce the response of an underlying base structure. For each of

the small-scale NES investigations, the two story steel base structure shown in Figure 5-1 was used as the underlying base structure. This structure, located in the Smart Structures Technology Laboratory at the University of Illinois, was designed and built specifically to be used for the small-scale investigation of NESs. Detailed design drawings for this base structure can be found in Appendix A.

The small-scale base structure used for experimental investigation consists of two floor plates and a base plate connected by four spring steel columns. The total height of this structure is 444.5 mm. The base structure's floor masses and the base plate are 457.2 × 457.2 × 12.7 mm steel plates. These plates have been appropriately detailed to attach to the floor plates to multiple types NESs and attach the base plate to a shake table. The masses of first and second floors are 24.3 kg and 24.2 kg, respectively. The cross-section of each column connecting these plates is 50.8 × 1.27 mm, and there is a 203.2 mm clear span distance between each of the floors plates. These columns are made from high yield strength spring steel to ensure high displacement capacity without yielding. Additionally, the columns are oriented such that their weak axis is in the direction of loading. With this orientation, the stiffness and the natural frequencies of the building perpendicular to the direction of loading are much higher than stiffness and the natural frequencies in the direction parallel to loading. As a consequence, the response of the building is predominantly composed of the superposition of the responses of the two translational global modes in the direction of loading.

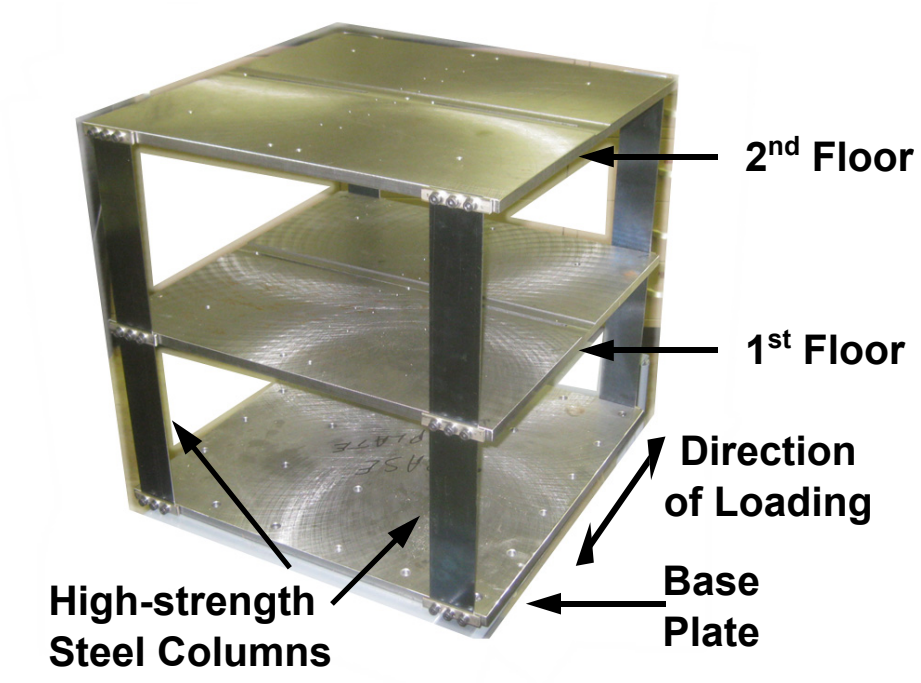

Figure 5-1. Base structure used for small-scale NES studies

An experimental modal analysis was performed to determine precise modal properties of the small-scale base structure in the as-built condition. To perform this analysis the linear system without the NES attached was excited using a displacement step function produced by a shake

table. The response of the base structure to this step function was collected using accelerometers placed on the base and two floors. With averaging, data from multiple trials were used to calculate the transfer functions from the base excitation to the floor responses; see Figure 5-2. Additionally, exponential windowing of the time response data used to calculate the transfer functions was utilized to reduce spectral leakage and help suppress any noise in the system (Fladung, W. and Rost R. 1997). As one can see from Figure 5-2, the resulting transfer functions clearly show a primarily two degree of freedom system.

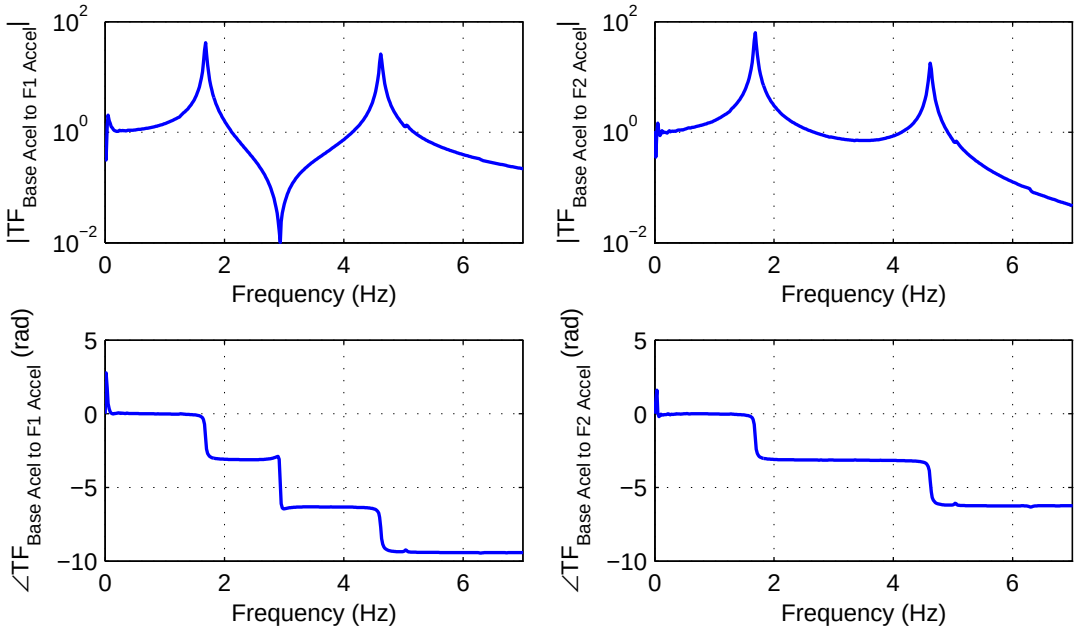

Figure 5-2. Experimental base acceleration to floor acceleration transfer functions of small-scale base structure

To precisely complete the modal identification of the system, the MATLAB-based software MFDID (Kim et al. 2005) was used to curve-fit the experimental transfer functions and produce a mathematical model of the system. From this identified model, the natural frequencies of the system were determined to be 1.68 and 4.62 Hz. The resulting identified mode shapes of the system are shown in Figure 5-3. In addition to determining experimental mode shapes and natural frequencies, the identification of this structure determined modal damping ratios of 0.01 and 0.003 for the structure's first and second modes, respectively.

Because the different types of NESs tested with this structure have both moving and non-moving components with different masses, the natural frequencies of the small-scale base structure shift depending on the NES tested; nevertheless, because the NES masses are relatively light compared to the weight of the structure, the change in natural frequencies and mode shapes of the base structure are small.

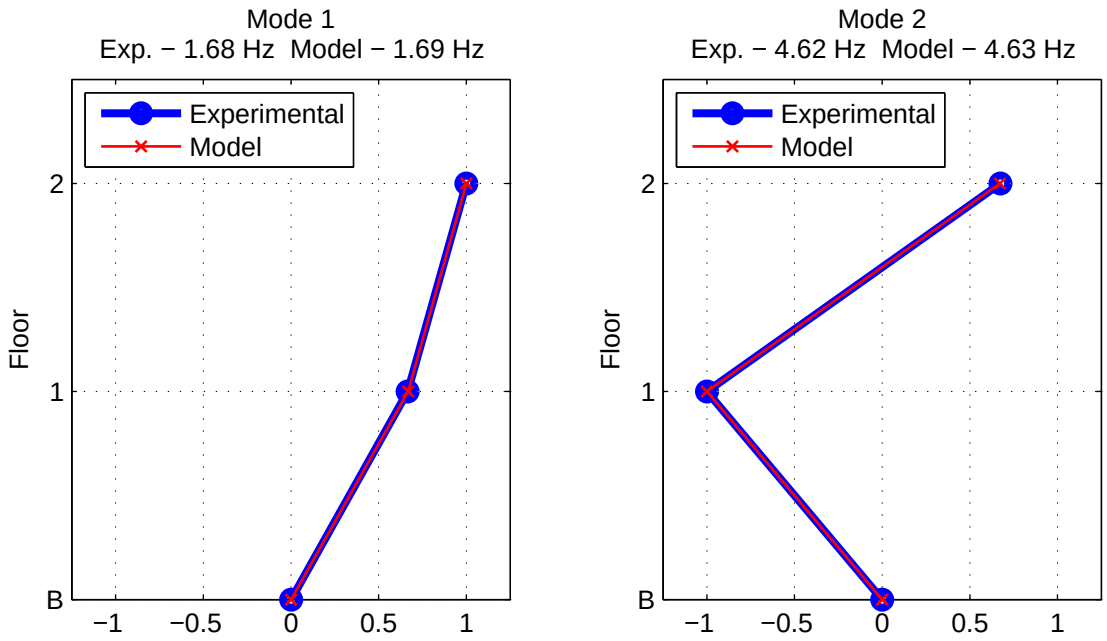

Figure 5-3. Mode shapes and natural frequencies of small-scale base structure from experimental identification and numerical model

Based on the modal identification, a two-degree of freedom numerical model of the structure was created. The equation of motion for this model is shown in Eq. (0.1). In this equation, $\mathbf{M}$, $\mathbf{K}$, and $\mathbf{C}$ are the structure's mass, stiffness, and damping matrices. Additionally, $\mathbf{x}$ is a vector containing the first and second floor displacement, measured relative to the structure's base. Numerical values for $\mathbf{M}$, $\mathbf{K}$, and $\mathbf{C}$ are shown in Eq. (0.2). The mode shapes and natural frequencies resulting from this numerical model of the structure are shown in Figure 5-3 where they are compared to the experimentally identified results. As this figure shows, the identified mode shapes and natural frequencies of the as-built small-scale base structure correspond quite well with the numerical model of the system.

$$\mathbf{M}\ddot{\mathbf{x}} + \mathbf{C}\dot{\mathbf{x}} + \mathbf{K}\mathbf{x} = \mathbf{0} \tag{0.1}$$

$$\mathbf{M} = \begin{bmatrix} 24.3 & 0 \\ 0 & 24.2 \end{bmatrix} \text{kg} \qquad \mathbf{K} = 10^4 \begin{bmatrix} 1.504 & -0.822 \\ -0.822 & 0.822 \end{bmatrix} \text{N/m} \tag{0.2}$$

$$\mathbf{C} = \begin{bmatrix} 10.239 & -5.807 \\ -5.807 & 5.422 \end{bmatrix} \frac{\text{N}(\text{sec})}{\text{m}}$$

5.1.2 Small-scale Type I NES development

In this subsection, the development of the small-scale Type I NES and the experimental identification of this NES's parameters is presented. Detailed design drawings for this NES can be found in Appendix A.

5.1.2.1 Description of Type I NES realization

The small-scale Type I NES used in this experimental investigation is shown installed on the top floor of the small-scale base structure in Figure 5-5. The main mass of this NES is built around a pair of XA-81420 Thomson Extra Precision steel ball bushing bearings. Using this pair of bearings, alignment of the mass on the rail it moves along is maintained, which is necessary to prevent excessive friction in the system. The rail that the mass moves unidirectionally along is mounted to the top floor of the base structure and oriented parallel with the direction the base structure is loaded in. The mass of the NES can be adjustable by adding or removing mass plates; however, for the tests outlined in this report, the NES mass was fixed at 2.04 kg. This mass is equivalent to 4.2% of the moving mass of the linear structure; i.e., the mass of the base structure excluding the base plate. Additionally, for tests without the NES, the NES mass can be secured to the top floor of the base structure

The restoring force applied to the NES is provided by a steel wire that is fed into the NES where it is internally clamped. The ends of this wire are fixed to rigid metal blocks on each side of the NES. These blocks are positioned such that the NES exhibits the geometrically nonlinear stiffness characteristic of a Type 1 NES. A diagram of showing this wire configuration is shown in Figure 5-4.

The theoretical nonlinear stiffness of this system is (McFarland et al. 2005)

$$F_r = \frac{EA}{L} x\left[1 - L\left(L^2 + x^2\right)^{-1/2}\right] \tag{0.3}$$

In this expression, F_r is the restoring force and x is the relative displacement of the NES. Additionally, E, A, and L are the modus of elasticity, cross-sectional area, and original length of the wire. This expression can be simplified by taking the Taylor series expansion. The result of this expansion is

$$F_r = \frac{EA}{L^3} x^3 + O\left(x^5\right) \tag{0.4}$$

As Eq. (0.4) shows, the results this expansion are a restoring force expression with a third order term and fifth and greater higher order terms. The higher order terms in this expression are often neglected in the analysis of NES systems utilizing wires.

This expression for the nonlinear restoring force shown in Eq. (0.3) and (0.4) assumes that the wires have been installed without any tension force. With tensile force in the wires while the NES mass is in its undeformed position, a linear term becomes present in the restoring force expression. Consequently, tensile force in the wires is avoided when configuring the NES. Nevertheless, in practice, a small amount of tension is applied to the wire so that the unmodeled sag in the wire is overcome.

The nonlinear stiffness of this Type I NES is adjustable and can be set within a large range of values by changing the diameter of the steel wire used and adjusting the distance between the NES and the blocks used to fix the wire. As shown in Figure 5-5, when the desired distance between the NES and the blocks used to fix the wire is greater than the width of the top floor, these blocks can be extended beyond the floor using a metal extender platform.

The inherent damping of the NES is quite low; consequently, the damping of the NES is increased by attaching rubber seals to the ends of the bearing and filling the internal compartment where the ball bearings contact the rail with 5W20 motor oil. Because the seals contained the oil within the bearing with minimal losses, the NES can be used many times without substantial changes in the damping provided by the oil-filled bearings.

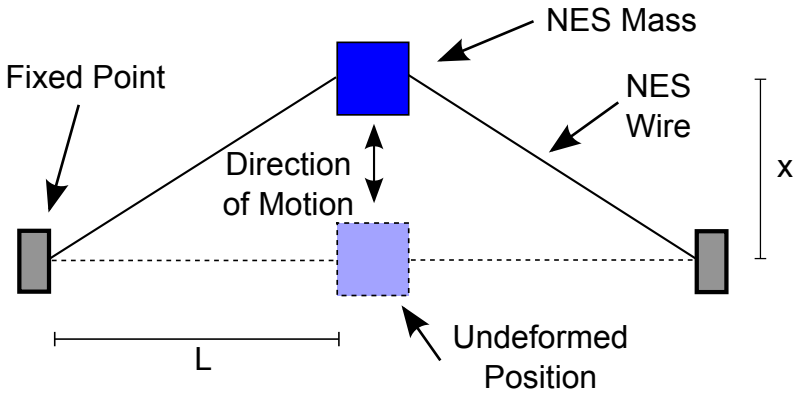

Figure 5-4. Wire configuration used to produce nonlinear restoring force in small-scale Type I NES

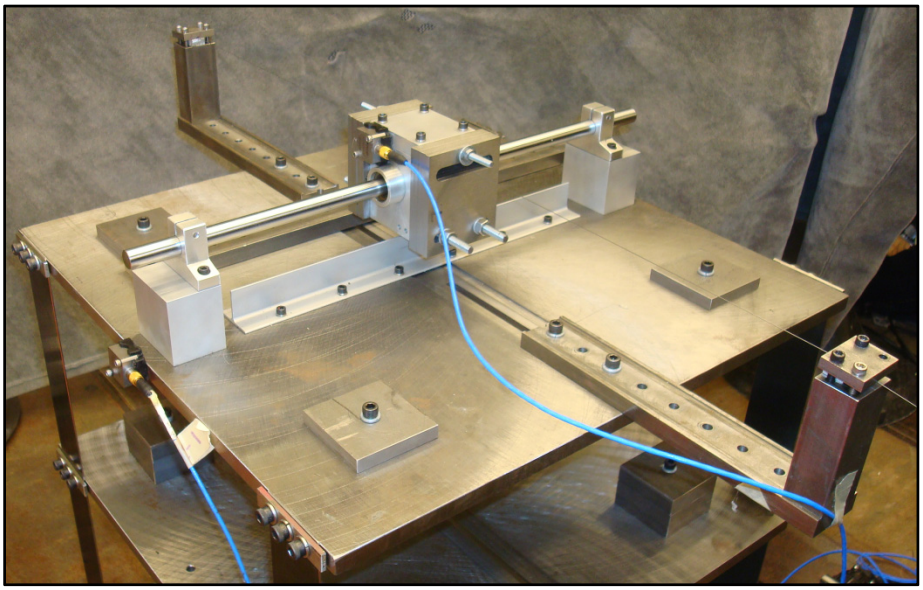

Figure 5-5. Small-scale Type I NES

5.1.2.2 Identification of Type I NES parameters

In order to calibrate models used to compare the analytical and experimental results, an identified model of the NES was required. To perform this identification, the restoring force surface method was utilized (Masri and Caughey 1979; Worden 1990). This method is discussed in detail in Chapter 3. To collect measurements of the NES response needed for this method, the top floor of the base structure with the NES mounted on it was removed from the rest of the structure. The top floor and NES were secured to a strong floor, as shown in Figure 5-6. To excite the system, the NES mass was hit sharply by hand in the direction of the NES rail. The measurement of the NES motion after this strike was used to implement the restoring force surface method.

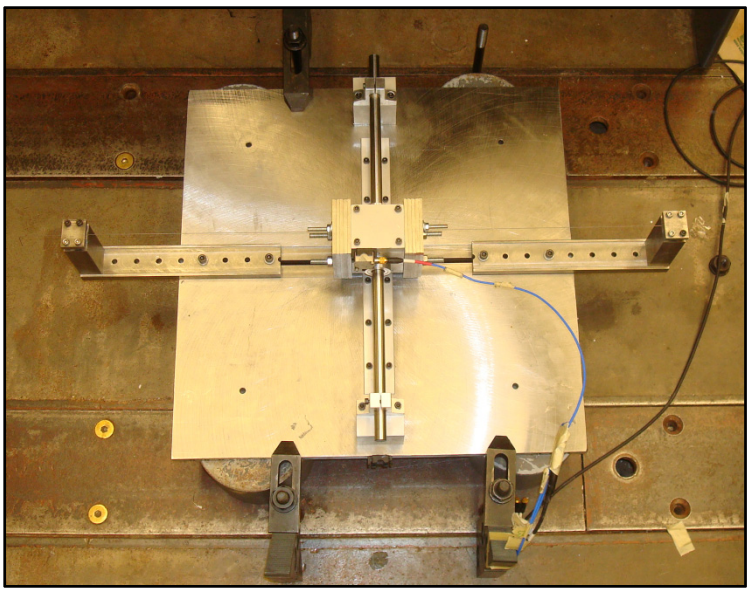

Figure 5-6. Small-scale Type I NES and base structure top floor removed for identification of NES parameters

The assumed equation of motion of the free vibration of the NES after being struck is

$$m_{NES}\ddot{x} + F_r\left(\dot{x}, x\right) = 0 \tag{0.5}$$

where x is the displacement of the NES, m_{NES} is the mass of the NES, and $F_r\left(\dot{x}, x\right)$ is a general expression for the restoring force applied to the NES, assumed to be a function of the NES displacement and velocity. To identify the parameters of the NES with the restoring force surface method, a form for the restoring force must be assumed. The form assumed for this identification is shown in Eq. (0.6) and consists of viscous damping term and a generic one-term polynomial nonlinear stiffness term.

$$F_{\text{Restoring}}\left(\dot{x}, x\right) = c\dot{x} + k_{NL}\, sign\left(x\right) x^{\alpha} \tag{0.6}$$

The assumed form has three parameters: the coefficient of the viscous damping component $\left(c\right)$, the coefficient of the nonlinear stiffness component $\left(k_{NL}\right)$, and the exponent of the nonlinear stiffness component $\left(\alpha\right)$. With the restoring force surface method, these unknown parameters can be estimated. The results of the estimation procedure, produced considering multiple measurements of NES response, are shown in Table 5-1. Additionally, a comparison of the time history of the restoring force estimated from the acceleration response and from the fit model is shown in Figure 5-7. As indicated, this method can be used to produce a reasonably accurate model of the NES.

As shown in Table 5-1, the identified model of the small-scale Type I NES diverges from the cubic nonlinearity that theoretically should result from this offset wires configuration. This divergence could result from a number of sources including the tension in the wire designed to overcome sag and the boundary condition changes due to the wires being clamped at the ends instead of pinned. Due to the small nature of the divergence of nonlinear stiffness term's exponent, 2.7 instead of 3, only a negligible effect on the system's dynamics is expected.

Table 5-1. Estimated parameters of small-scale Type I NES

Viscous Damping Coefficient, (c)	2.00 N-s/m
Nonlinear Stiffness Coefficient, (k_{NL})	21.9x10^4 N/m$^\alpha$
Nonlinear Stiffness Exponent, (α)	2.7

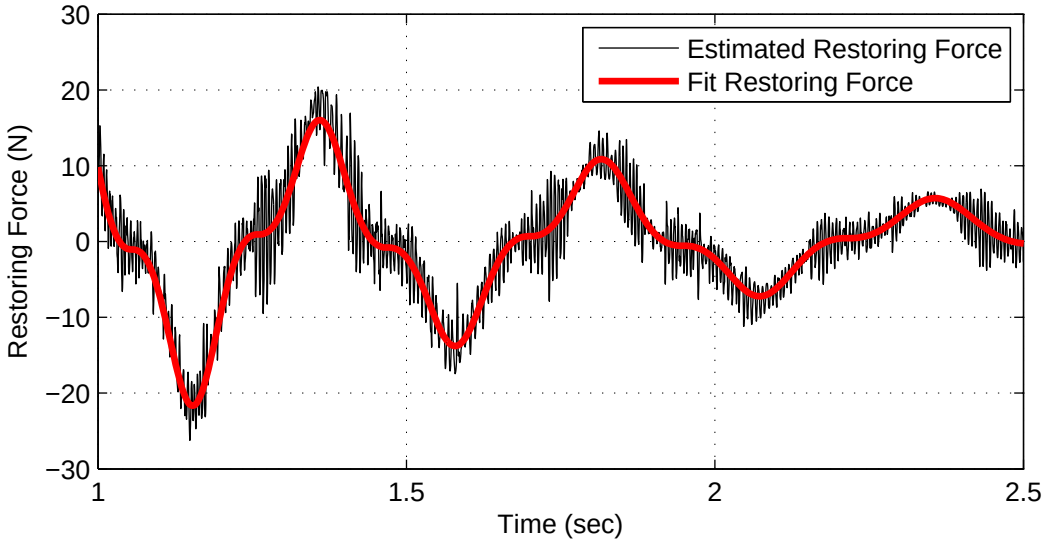

Figure 5-7. Example of estimated nonlinear restoring force for experimental results and fitted model

5.1.3 Small-scale Type III NES development

In this subsection, the development of the small-scale Type III NES and the experimental identification of this NES's parameters is presented. Detailed design drawings for this NES can be found in Appendix A.

5.1.3.1 Description of Type III NES realization

The 2-DOF NES designed and manufactured for this study can be seen in Figure 5-8. This NES consists of a bottom NES stage, painted primarily orange, and a top NES stage, painted primarily blue. The bottom mass of the NES moves uniaxially in the direction of loading on a Thompson 2DA Dual Shaft RoundRail carriage, which has a matching rail system that is attached to the top floor of the base structure. The top mass of the NES is nested on top of the bottom mass. This mass moves uniaxially in the direction of loading on a linear bearing that moves along a rail that is attached to the bottom mass. The bottom and top NES masses are 2.15 kg and 0.51 kg, which represent 4.6% and 1.1% of the total mass of the structure, respectively.

The bottom NES mass is attached to the top floor of the base structure through a 0.38 mm diameter spring steel wire. This wire is anchored on each side of the bottom mass, perpendicular

to the direction of motion. As with the small-scale Type I NES, presented in Section 5.1.2, this configuration of wires creates a geometrically nonlinear spring. The top NES mass is connected to the bottom NES mass through a 0.5 mm diameter nylon wire. Similar to the lower mass, this wire is attached on both sides of the mass, perpendicular to the direction of motion, in order to create a geometric nonlinearity. The wires connecting the bottom NES mass to the base structure and the top NES mass to the bottom NES mass have a small amount of tensile force in them to overcome sag in the wire; however, this tensile force is very small in order to prevent unintended linearity in the restoring force provided by the wires.

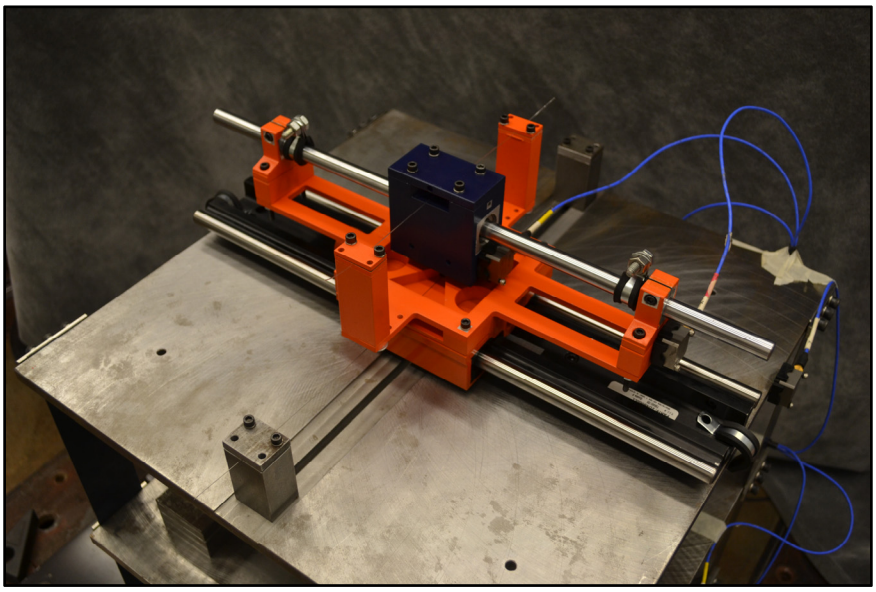

Figure 5-8. Small-scale Type III NES

Both NES masses are designed with locks to prevent their relative motion when desired. The bottom NES lock is built directly into the Thompson 2DA Dual Shaft RoundRail carriage the NES is built on. The locking mechanism for the top NES mass is a pair of rubber cushioned loop clamps. When the loop clamps are attached to the rail with the NES mass securely in between them, the top NES mass is unable to move. These locking mechanisms are shown in Figure 5-9. With both locks engaged, the behavior of the building, with the same total mass but no functional NES, can be investigated. As expected with the NES locked, the building behaves predominantly linear. Additionally, the dynamics of the structure with locked NES can be compared to the structure with a functional, or unlocked, NES in order to study the nonlinear effects of the NES with no added mass effects.

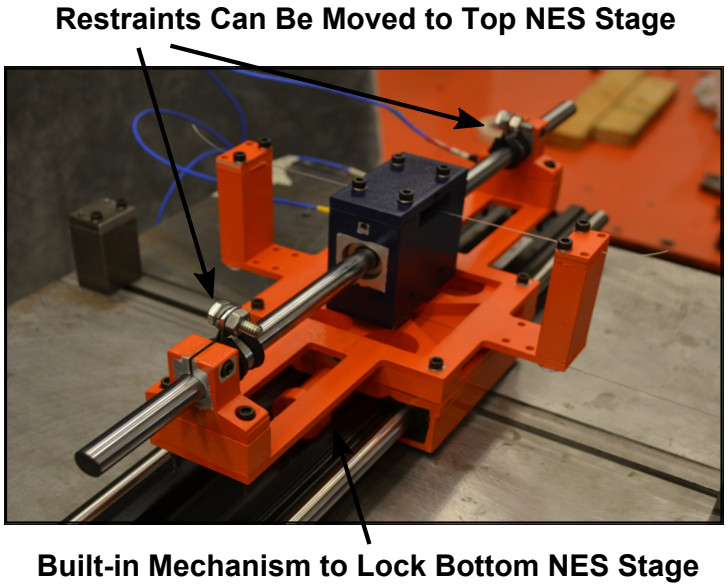

Figure 5-9. Small-scale Type III NES locking mechanism

5.1.3.2 Type III NES parameter optimization

The parameters of the wires in bottom and top NES stages are designed to allow these NES stages to achieve a pair of nonlinear stiffness profiles. These desired restoring force profiles are the result of a numerical optimization analysis performed on this system by a colleague (Wierschem et al. 2012). In this optimization, numerical analyses of the base structure with an attached and unlocked Type III NES are performed. For these analyses, the system is subjected to an initial velocity, the amplitude of which corresponds to a realistic level of response in the experimental structure. Using these simulations, a constrained optimization with the fmincon command in MATLAB ®, is performed to determine the optimal Type III NES parameters. For this optimization, the objective function is to maximize the first mode effective damping in the base structure. The results of this optimization analysis are shown in Table 5-2. More information regarding this optimization analysis can be found in (Wierschem et al. 2012).

Table 5-2. Optimized properties of small-scale Type III NES

	Mass (kg)	Damping Coefficient (N-s/m)	Nonlinear Stiffness Coefficient $\left(N/m^3\right)$
Top NES Stage	1.30	5.59	3.76×10^5
Bottom NES Stage	2.15	0	14.1×10^5

5.1.3.3 Identification of small-scale Type III NES parameters

While the parameters listed in Table 5-2 guided the physical design of this small-scale Type III NES, the parameters of the NES in the as-built condition must be established in order to accurately

simulate the response of the actual physical system. To determine these parameters, the restoring force surface method was once again used (Masri and Caughey 1979; Worden 1990). A detailed description of this technique can be found in Chapter 3. To implement this method, the top floor of the base structure with the Type-III NES attached was detached from rest of the base structure and secured directly to a shake table. The NES was then excited with a sinusoidal ground motion using the shake table, and the resulting accelerations of the NES and the shake table were measured. Additionally, in order to simplify the identification, data was collected this way twice, once when the top stage of the NES was locked and once when the bottom stage of the NES was locked. From the acceleration data, the velocities and displacements of the NES and the shake table were calculated.

With the acceleration, velocity, and displacement of the shake table and the NES stages, the restoring force method can then be separately implemented to estimate the parameters of each stage of the NES. To proceed with this method, the assumed equation of motion for the top and bottom NES stages are

$$m_T \ddot{u}_T = -c_T\left(\dot{u}_T - \dot{u}_B\right) - k_T \operatorname{sgn}\left(u_T - u_B\right)\left|u_T - u_B\right|^{\alpha_T} \tag{0.7}$$

and

$$\left(m_T + m_B\right)\ddot{u}_B = -c_B\left(\dot{u}_B - \dot{x}_{table}\right) - k_B \operatorname{sgn}\left(u_B - x_{table}\right)\left|u_B - x_{table}\right|^{\alpha_B} \tag{0.8}$$

In these equation u_T is the motion of the NES top stage, u_B is the motion of the NES bottom stage, x_{table} is the motion of the table, m_T and m_B are the masses of the top and bottom NES stages, c_T and c_B are the damping terms of the top and bottom NES stages, k_T and k_B are the coefficients of the top and bottom NES stage nonlinear stiffness terms, and α_T and α_B are the exponents of the top and bottom NES nonlinear stiffness terms. In Eq. (0.8) the mass of the top and bottom stages of the NES appear because, when performing the identification of the bottom NES stage separately, the top NES stage is locked and thus serves as extra mass for the bottom NES stage. Using this equation, the unknown system parameters $\left(c_T,\ k_T,\ \alpha_T,\ c_B,\ k_B,\ \alpha_B\right)$ can be estimated by determining the parameters that best satisfy the equations of motion, given the measured values for m_T, m_B, and the system response.

The parameters of the 2-DOF NES that were identified with the method discussed above are listed in Table 5-3. This table shows that the identified exponent of the nonlinear restoring force deviates from the cubic exponent predicted by the dominant term in a simple mathematical model of the system. The reason for this divergence is that a weak linear component perturbs the nonlinear restoring force and results in an identified exponent with of lower order. This small linear component, which is more significant in the top NES stage due to its shorter wire length, is the result of a difficult-to-avoid small amount pretension in the wire (Gourdon et al. 2007) and the unmodeled stiffness of the wire due to rotations at the wire ends being fixed. Even though the order of the nonlinearity is different than that studied in the optimization analysis previously discussed, the results from the optimization are still qualitatively valid for the system because the nature of the nonlinearity was not changed substantially. Quantitatively, the optimization results will also be similar, the only significant change being the magnitude of the coefficient of the nonlinear restoring force term.

Table 5-3. Identified properties of small-scale Type III NES

	Mass (kg)	Damping Coefficient (N-s/m)
Top NES Stage	0.51	1.55
Bottom NES Stage	2.15	7.50

	Nonlinear Stiffness Coefficient $\left(N/m^{\alpha}\right)$	Nonlinear Stiffness Exponent (α)
Top NES Stage	6.0×10^{4}	2.25
Bottom NES Stage	1.3×10^{6}	2.70

5.1.4 Medium-scale base structure

The medium-scale experimental investigation of NES performance utilized six-story base structure, which the NES is designed to be attached to. This structure, which is shown in Figure 5-10, has been used in previous research efforts to study active base isolation (Chang and Spencer 2010; Chang et al. 2013). This 970 kg structure is 1.97 m tall and consists of six 711 mm ×1143 mm × 25 mm steel floor plates and one steel base plate. At each level, these plates are supported by six high-strength steel columns. The use of high-strength steel in the columns allows the structure to undergo substantial deformation without yielding, as desired. For further details on the layout of this structure, the original design drawings can be found in Appendix A.

In the experiments conducted for this study in the Smart Structures Technology Laboratory at the University of Illinois, the structure was loaded unidirectionally along its weak axis with shake-table-produced ground motion. To increase the flexibility of the structure for these tests, exterior braces that can be attached to the structure have been removed. With these braces removed, in the direction loading, the natural frequencies of the translational modes of the base structure, not including the mass of the NES, are 1.62, 4.51, 7.46, 9.78, 11.65, and 14.43 Hz. With this frequency range, the structure is modally similar to a full-scale midrise steel frame building. Additionally, although the center of mass and stiffness of the structure are nearly collinear with the direction of loading, small deviations allow the torsional modes of the structure to be excited. The relevant torsional natural frequencies of the structure are 2.93, 12.77, 17.27, and 20.63 Hz.

Figure 5-10. Six-story base structure

5.1.5 Medium-scale Type III NES development

In this subsection, the development of the medium-scale Type III NES and the experimental identification of this NES's parameters is presented.

5.1.5.1 Description of Type III NES realization

The NES employed in this study was attached to the top floor of the primarily linear base structure. This NES is shown in a rendering attached to the top floor plate of the structure in Figure 5-11. The medium-scale NES studied is a Type III NES, a two-mass attachment in which the masses are connected to each other and to the top floor of the structure by essentially nonlinear spring elements. In this implementation, the second (top) mass is nested within the first (bottom) mass. The masses of the top and bottom NES stages are 21 and 28 kg, which correspond to 2.2% and 2.9% of the total mass of the structure, respectively. The NES bottom stage mass is mounted on a set of bushing bearings and translates on round shafts that are connected to the linear base structure. The NES top stage mass is mounted on a cart that translates on a rail connected to the NES bottom stage mass. Additionally, both stages of the NES can be locked so that the response of the base structure in the absence of NES dynamics can be examined while holding the total mass of the system constant.

The nonlinear restoring forces that couple the top floor of the base structure to the NES bottom stage mass and the NES bottom stage mass to the NES top stage mass are generated by elastomeric bumpers that act in compression only. The bumpers are interchangeable and can be shaped to utilize geometric nonlinearities in combination with material properties to provide a target nonlinear restoring force. Additionally, the nonlinear restoring force provided by these bumpers is elastic and highly repeatable (Luo et al. 2014). The bumpers primarily used in the testing of the medium-scale Type III NES presented in this report are shown in Figure 5-12. The pair of bumpers used between the NES top and bottom stage masses are pyramid-shaped with a base of 17.8 cm ×

17.8 cm and height of 3.2 cm. The pair of bumpers between the NES bottom stage mass and the top floor of the base structure are tapered wedge-shaped with a base of 20.3 cm × 20.3 cm, a height of 10.2 cm, and a top width of 5.1 cm. Further information on the development of these bumpers as nonlinear restoring force elements can be found in (Luo et al. 2014).

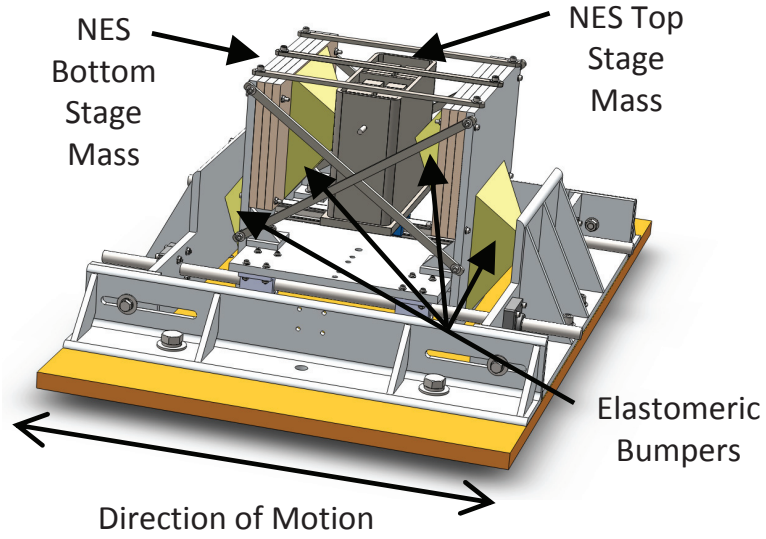

Figure 5-11. Rendering of medium-scale Type III NES attached to the top floor of the base structure

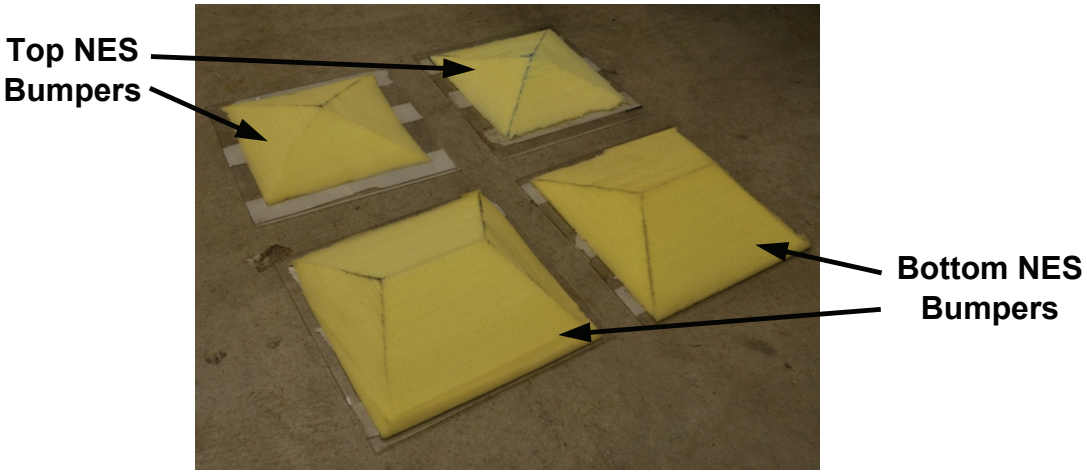

Figure 5-12. Elastomeric bumpers installed in the medium-scale Type III NES

5.1.5.2 Identification of medium-scale Type III NES parameters

As mentioned previously, the elastomeric bumpers used to provide the nonlinear NES restoring forces can be shaped to obtain desired restoring force profiles. With a pair of optimized restoring force profiles as targets for the top and bottom NES stages, the elastomeric bumpers shown in Figure 5-12 were manufactured to replicate the identified optimal parameters. As this figure shows, these resulting bumpers are shaped differently for the top and bottom stages. To

experimentally confirm the dynamic properties of the NES incorporating these elastomeric bumpers, nonlinear system identification was performed using the acquired acceleration time history of the NES when attached to the top of the base structure and subjected to a shock-like ground motion. The technique used for this experimental identification is the restoring force surface method (Masri and Caughey 1979; Worden 1990). This method, which is discussed in detail in Chapter 3 presumes an equation of motion of the system, including an assumed form for the nonlinear restoring force with unknown parameters, and performs a least squares fit of the experimental measurements to the model response.

For this system the equation of motion for the top NES stage immediately after the completion of the ground motion is given by

$$m_{TopNES}\ddot{x}_{TopNES} + f_{RTop}\left(\dot{x}_{TopNES}, x_{TopNES}, \dot{x}_{BotNES}, x_{BotNES}\right) = 0 \tag{0.9}$$

where m_{TopNES} is the known mass of the NES top stage, x_{TopNES} the displacement of the NES's top stage mass, x_{BotNES} the displacement of the NES's bottom stage mass, and f_{RTop} a generic restoring force term. For the NES top stage mass, the restoring force is a function of $\dot{x}_{TopNES}$, x_{TopNES}, $\dot{x}_{BotNES}$, and x_{BotNES}, where the velocity and displacement of the NES top and bottom stage masses can be estimated from experimentally measured accelerations. In the case of the NES top stage mass, the assumed form of the restoring force consists of a viscous damping term, a linear stiffness term, and a nonlinear stiffness term. The assumed form of the top NES stage restoring force is

$$\begin{aligned} f_{RTop} = {} & c_{Top}\left(\dot{x}_{TopNES} - \dot{x}_{BotNES}\right) + k_{Top}\left(x_{TopNES} - x_{BotNES}\right) \\ & + k_{nlTop}\,\mathrm{sgn}\left(x_{TopNES} - x_{BotNES}\right)\left|x_{TopNES} - x_{BotNES}\right|^{\alpha_{Top}} \end{aligned} \tag{0.10}$$

where c_{Top} is the viscous damping coefficient, k_{Top} the linear stiffness coefficient, k_{nlTop} the nonlinear stiffness coefficient, and α_{Top} the exponent of the nonlinear stiffness term, all of the top NES stage. Using the restoring force surface method, these unknown parameters can be determined. Note that, while the nonlinear stiffness was assumed to be cubic in the initial design optimization, the exponent of this stiffness term was also included in the identification. This added flexibility in the exponent of the nonlinear stiffness term allows for improved fidelity of the resulting system model.

After the unknown parameters of the top NES stage have been identified, these results can be used to help identify the parameters of the bottom NES stage, again with the restoring force surface method. The equation of motion of the bottom NES stage directly after completion of the ground motion is

$$\begin{aligned} & m_{BotNES}\ddot{x}_{BotNES} + f_{RBot}\left(\dot{x}_{BotNES}, x_{BotNES}, \dot{x}_{6Floor}, x_{6Floor}\right) \\ & \quad - f_{RTop}\left(\dot{x}_{TopNES}, x_{TopNES}, \dot{x}_{BotNES}, x_{BotNES}\right) \end{aligned} = 0 \tag{0.11}$$

where m_{BotNES} is the known mass of the NES bottom stage and f_{RBot} is a generic restoring force term for the forces coupling the bottom NES stage to the sixth floor of the base structure. For the NES bottom stage mass, this restoring force is a function of $\dot{x}_{BotNES}$, x_{BotNES}, $\dot{x}_{6Floor}$, and x_{6Floor}; the velocity and displacement of the NES bottom stage mass and the sixth floor of the base structure can be estimated from experimentally measured accelerations. In the case of the NES bottom stage mass, the following assumed form of this restoring force consists of a viscous damping term, a linear stiffness term, and a nonlinear stiffness term,

$$f_{RBot} = \begin{matrix} c_{Bot}\left(\dot{x}_{BotNES} - \dot{x}_{6Floor}\right) + k_{Bot}\left(x_{BotNES} - x_{6Floor}\right) \\ +k_{nlBot}\,\mathrm{sgn}\left(x_{BotNES} - x_{6Floor}\right)\left|x_{BotNES} - x_{6Floor}\right|^{\alpha_{Bot}} \end{matrix} \tag{0.12}$$

In this equation, c_{Bot} is the viscous damping coefficient, k_{Bot} the linear stiffness coefficient, $k_{nl\,Bot}$ the nonlinear stiffness coefficient, and α_{Bot} the exponent of the nonlinear stiffness term, all of the bottom NES stage.

Using the restoring force surface method with experimental data along with the equations of motion and assumed form of the nonlinear restoring forces shown above, the parameters of the medium-scale Type III NES were estimated. The results of the identification are summarized in Table 5-4. The restoring force surface for the top NES stage defined by these parameters is compared in Figure 5-13 to the restoring force from the top stage NES measured indirectly during the experimental identification process. Based on the coinciding nature of the measured restoring force and the surface defined by the identified parameters, this figure helps to verify the effectiveness, over the range of interest, of the NES identification. In Figure 5-14 and Figure 5-15 the identified models of the restoring forces from the stiffness components of the top and bottom NES stages are compared to the NES stiffness models from the optimization study over the range of relative displacements measured. These results show that the experimentally identified model provides a reasonable fit to the calculated optimal stiffness values for each stage. The small error in the fit is likely due to imprecise manufacturing; thus, the utilization of more advanced bumper manufacturing techniques would likely further improve this fit.

Table 5-4. Identified medium-scale Type III NES parameters

	NES Top Stage	NES Bottom Stage
c $\left(N\text{-}s/m\right)$	132	96.3
k $\left(N/m\right)$	3302	1647
k_{nl} $\left(N/m^{\alpha}\right)$	3.50E+11	1.07E+12
α	6.03	6.13

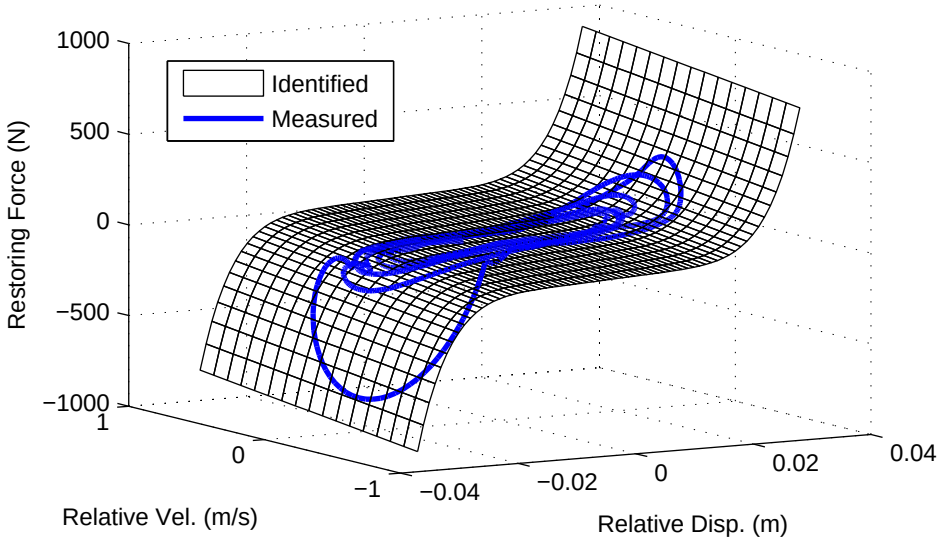

Figure 5-13. Comparison of top stage NES restoring force experimentally measure and surface defined by identified parameters

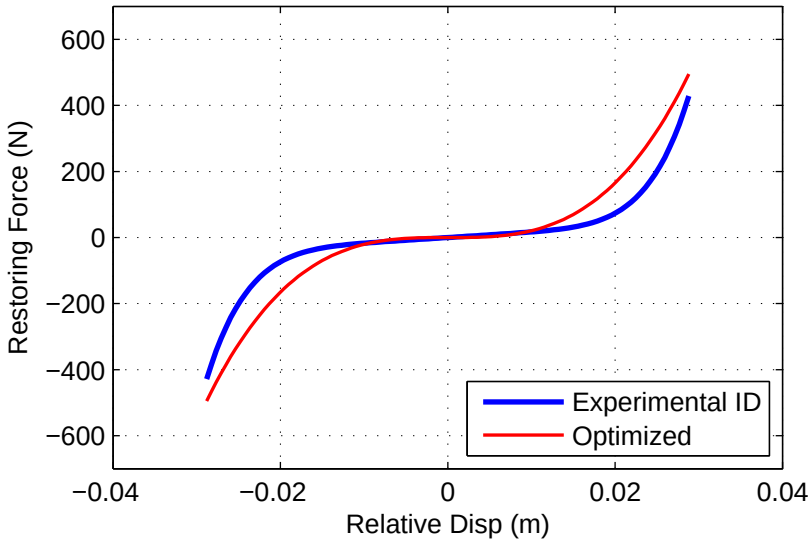

Figure 5-14. Comparison between restoring force from the optimized stiffness profile and identified stiffness model for the NES top stage

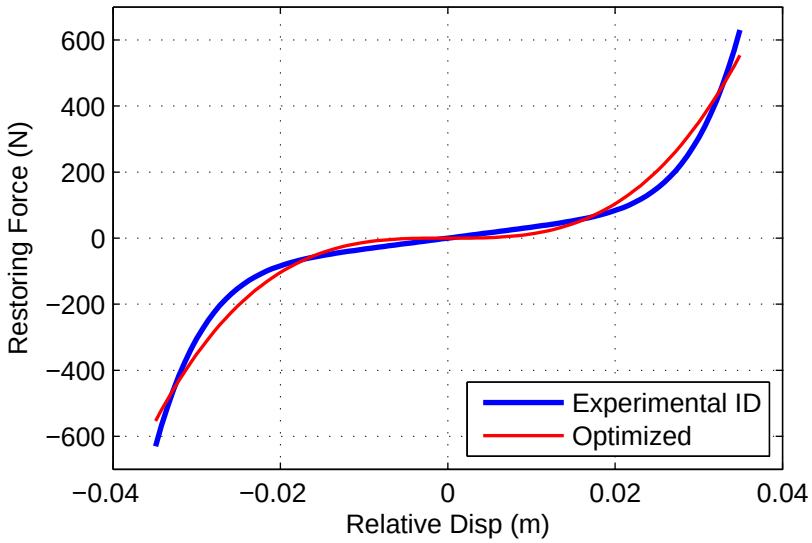

Figure 5-15. Comparison between restoring force from the optimized stiffness profile and identified stiffness model for the NES bottom stage

5.2 Experimental investigation of small and medium-scale systems

In this section the experimental investigation of the ability of the small-scale Type I NES and the small- and medium-scale Type III to rapidly reduce the response of an underlying base structure is presented. For the experiments with these NESs, the primary loading considered is an impulse-like ground acceleration. In all cases, this loading is experimentally produced by a step-like displacement function delivered by a shake table. Using these experimental results, the validation of numerical models of the NESs is also provided.

5.2.1 Small-scale Type I NES

In this subsection the experimental investigation of the performance of the small-scale Type I NES is presented. The development of this NES was presented in Section 5.1.2. This NES is connected to the top floor of the small-scale base structure, presented in Section 5.1.1.

5.2.1.1 Experimental setup

Testing of this structure was performed at the Smart Structures Technology Laboratory at the University of Illinois, where a uniaxial shake table with a 457 mm × 457 mm connector plate was used to excite the structure. This custom built shake table was manufactured by SMI Technology and is powered by a servo-motor which has a stroke of ±5 cm. Displacement of the table is measured using an encoder built into the table. Displacement control of the shake table is performed with a PD controller that is realized using a Quanser Consulting MultiQ-3 Board and host PC along with feedback from the displacement encoder. This shake table, without any structure attached, is shown in Figure 5-16.

Using the shake table described above, the primary excitation provided to the small-scale base structure and Type I NES was a commanded step function. This commanded step to the shake table results in a displacement step function with small overshoot and correction, due to a displacement feedback loop used to control the table. An example of the acceleration of the table,

as measured from the base plate of the attached base structure, that results from this step function is shown in Figure 5-17.

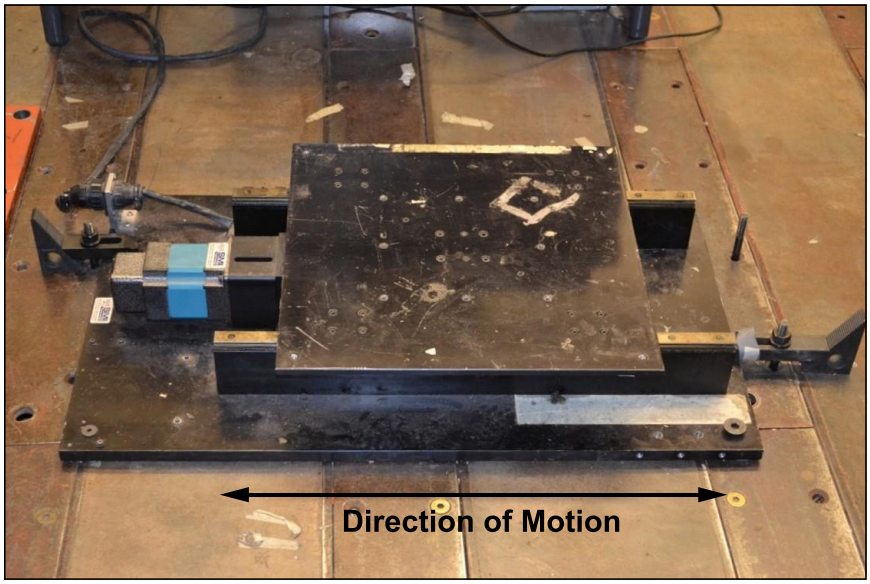

Figure 5-16. Shake table used for small-scale testing

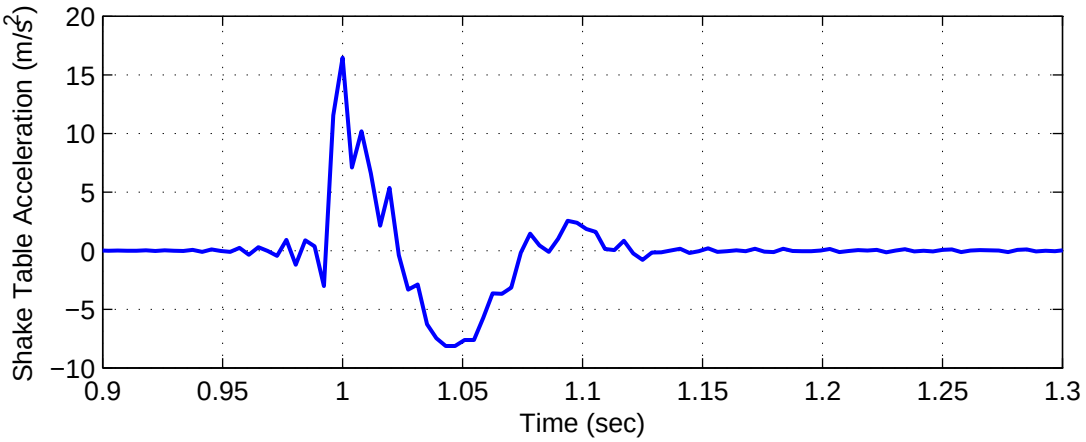

Figure 5-17. Example input ground acceleration used for small-scale testing

To measure the response of the base structure and NES during testing, the test setup was instrumented with PCB 3701G3FA3G capacitive accelerometers placed on the base structure's base plate, first floor, and second floor, as well as the NES mass. This accelerometer layout is shown in Figure 5-18. The small mass of the accelerometers, 20 g, and careful placement of the associated cables allowed these sensors to measure the response of the base structure with insignificant change to the system itself.

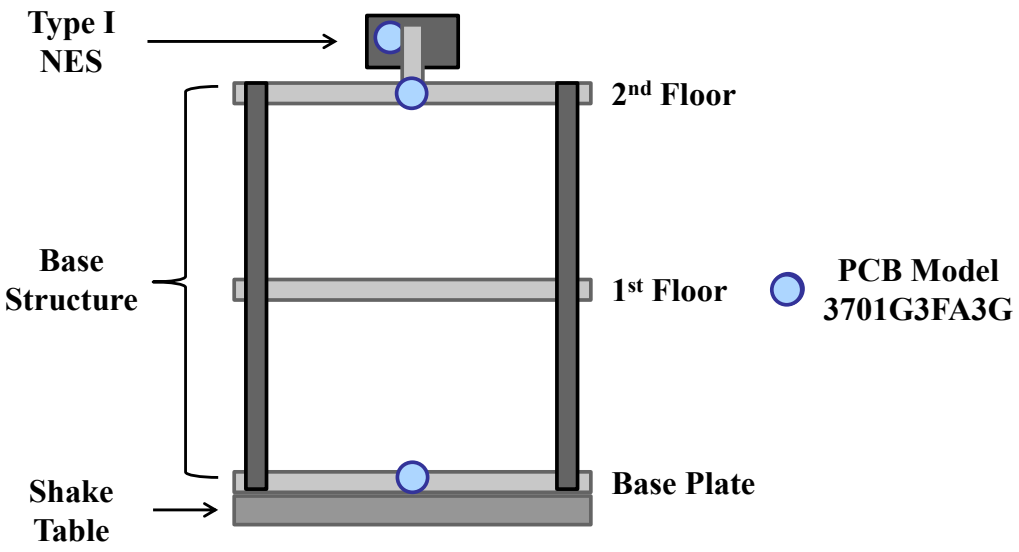

Figure 5-18. Diagram showing layout of accelerometers on the base structure and NES for the small-scale Type I NES experiments

The acquisition system used to collect data with these accelerometers was the VibPilot system by m+p international. High-quality, anti-aliased data was acquired at a sampling rate of 1024 Hz. This high sampling rate, relative to the natural frequencies of the structure, was employed to aid in the direct comparison of the experimental data with simulations results.

5.2.1.2 Experimental results

Using the shake table described in the previous section, the small-scale base structure equipped with the Type I NES was loaded with an impulse-like ground motion with the NES locked and unlocked. An example of the ground motion used for these tests is shown in Figure 5-17. This short duration impulse-like ground acceleration results in a displacement step with an overshoot and correction.

The acceleration time history of the second floor of the small-scale base structure in response to the ground motion displayed Figure 5-17 is shown in Figure 5-19 with the Type I NES locked and unlocked. When the NES is locked, the response of the second floor persists at a high level throughout the time window observed; however, with the NES unlocked, there is a clear increase in the rate of attenuation of the response of the base structure. This accelerated attenuation results in an 80% reduction in the acceleration response of the base structure within about ten seconds; in the same amount of time, with the NES locked the reduction in acceleration response is only about 20%.

In addition to the acceleration time histories, Figure 5-19 shows the wavelet spectra of the second floor acceleration with the NES locked and unlocked. With the NES locked, the sustained response of the base structure results in an acceleration wavelet spectrum that includes two dense and persistent bars, which correspond to the natural frequencies of the base structure. With the NES unlocked, the portion of the wavelet spectrum corresponding to the first mode of the base structure is rapidly eliminated and, after a brief delay, smaller reductions are observed in the portion of the wavelet spectrum corresponding to the second mode.

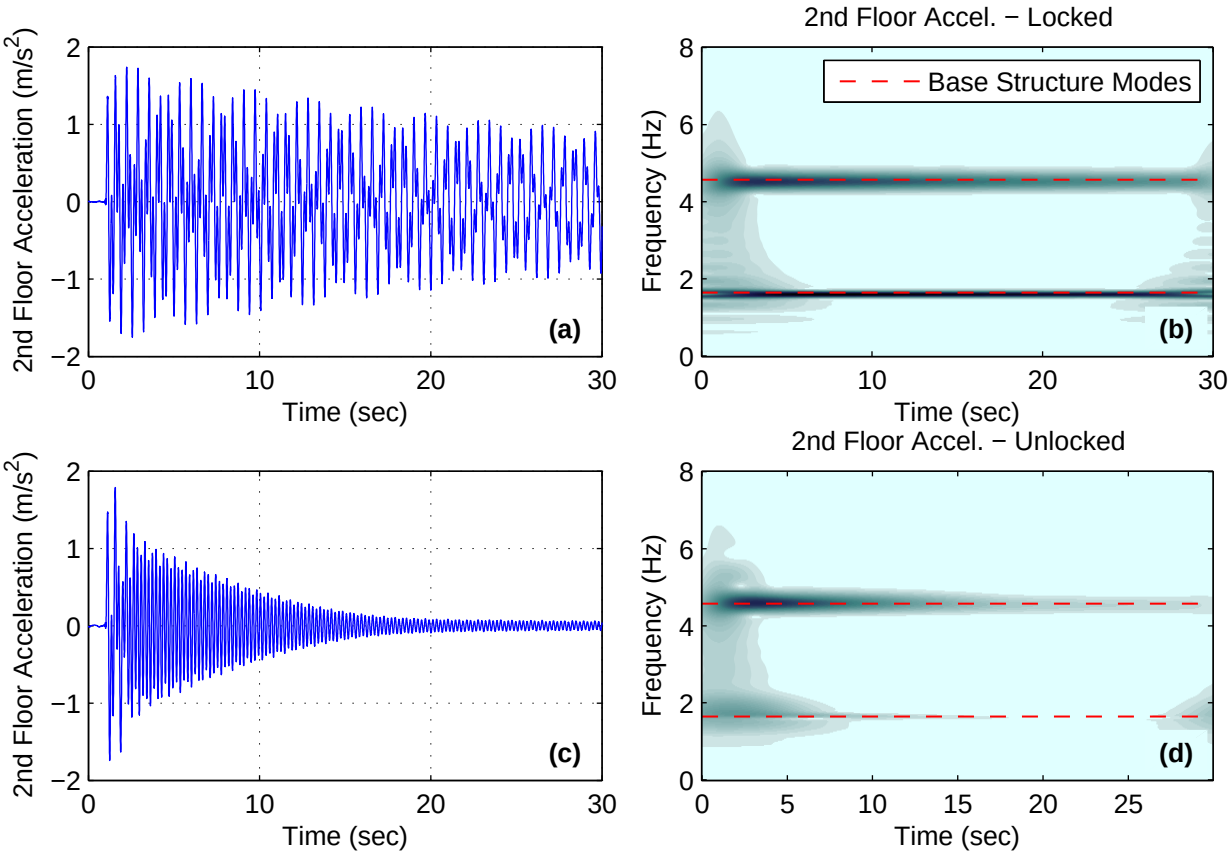

Figure 5-19. Top floor acceleration from small-scale Type I NES test a) NES locked time history, b) NES locked wavelet spectra, c) NES unlocked time history, and d) NES unlocked wavelet spectra

The acceleration response of the base structure can be converted into modal coordinates, as shown in Figure 5-20. The conversion to modal coordinates presented in this figure is not perfect, as some multi-frequency behavior can be observed in the response. This, in part, is caused by the same model of the structure, which includes the NES mass, being used in the modal conversion with the NES locked and unlocked. Additionally, error in the modal conversion for the unlocked response is present due to the nonlinear nature of the NES. Nevertheless, this figure can still be used to gain insight into the modal response of the structure. As Figure 5-20 shows, the trends displayed in the wavelet spectra of Figure 5-19 are again present. This includes that the first mode acceleration is sustained with the NES locked, but is rapidly attenuated with the NES locked. Additionally, with the NES unlocked, after a brief delay, the second mode acceleration is attenuated at a less dramatic, but still quicker pace compared to the response with the NES locked. One feature that is more obvious in this figure is the small increase in second mode amplitude that occurs with the NES unlocked about one second after the ground motion initiates. This increase in second mode amplitude demonstrates the modal coupling and transfer of energy that is facilitated by the NES.

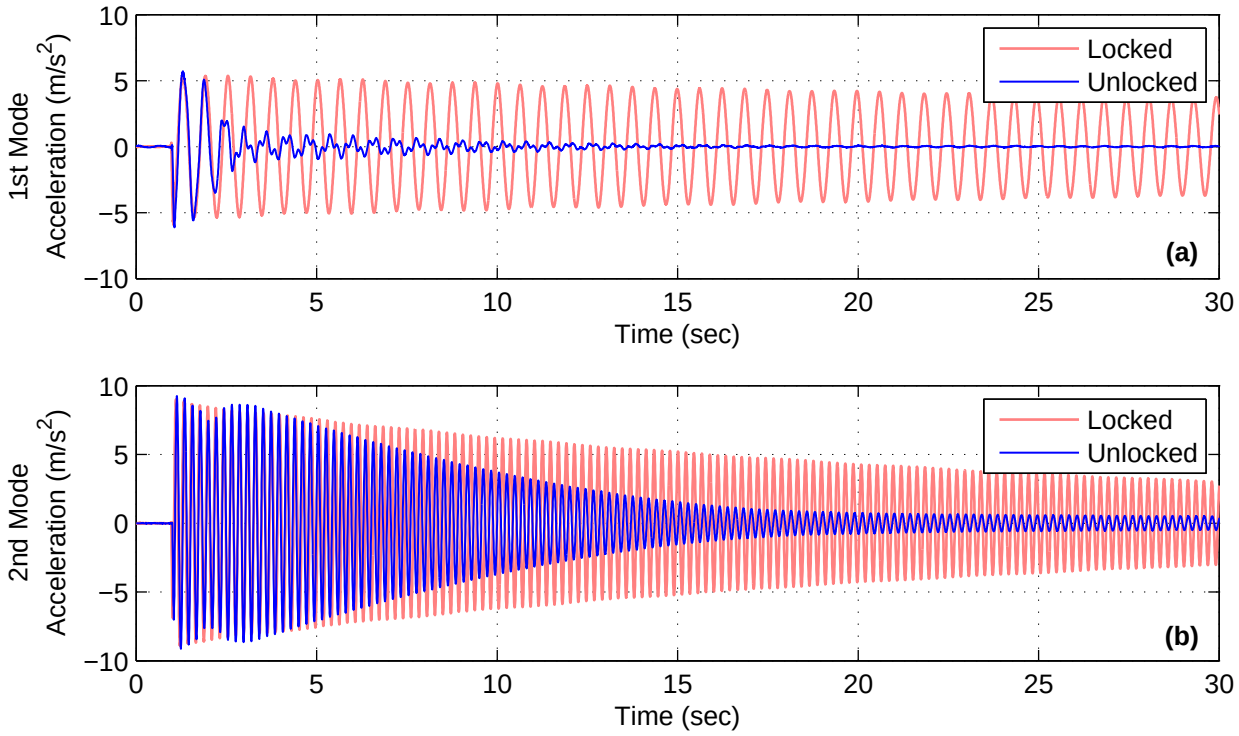

Figure 5-20. Acceleration response of the base structure in modal coordinates from small-scale Type I NES test with NES locked and unlocked (a) first mode and (b) second mode

Figure 5-21 shows the calculated top floor displacement response of the base structure subjected to the ground motion shown in Figure 5-17. This figure shows that, with the Type I NES unlocked, the response of the top floor is predominantly attenuated within two cycles of the building. The attenuation is much faster than what was observed in the acceleration response of the structure. This fast attenuation of displacement response is due to the quick elimination of the low frequency and large displacement modes of the base structure, as observed in Figure 5-20. As the displacement of the structure, and related interstory drifts, correspond to the demands on the structural system, this result shows one of the benefits of quickly eliminating low frequency vibration and shifting energy to the higher frequency modes of the base structure.

The time history and wavelet spectrum of the acceleration response of the NES to the loading considered is shown in Figure 5-22. As this figure shows, the NES response to the loading primarily last only a short time, about two seconds; during which the acceleration of the NES reaches a level much higher than the acceleration of the base structure. Additionally, as seen in Figure 5-22b, during this time the response of the NES is broadband in frequency. This broadband behavior allow to NES to couple the modes of the base structure and participate in TET, the broadband transfer of energy to the NES where it is dissipated.

To examine the response of the system at multiple scaling levels of the ground motion shown in Figure 5-17, the first mode effective damping measure is used. This effective damping measure was introduced in Chapter 3 and the alternative calculation method is utilized in this section. The first mode effective damping is shown in Figure 5-23 and is plotted as a function of peak energy in the base structure during the test considered. With the NES locked, the effective damping remains low across the entire energy range consider; however, some increase at the high end of

the energy range is observed. This increased effective damping in the locked structure at high loads is likely due larger control-structure interaction at higher energy levels. Furthermore, as this figure shows, with the NES unlocked the effective damping in the system starts out low, but quickly reaches a peak point. The response of the system at this peak point is shown in Figure 5-19 to Figure 5-22. After the effective damping peaks, with increased energy in the system the effective damping reduces dramatically. This figure demonstrates that, if one understands the design amplitude well, the NES can be designed to be quite effective at increasing the effective damping of the system.

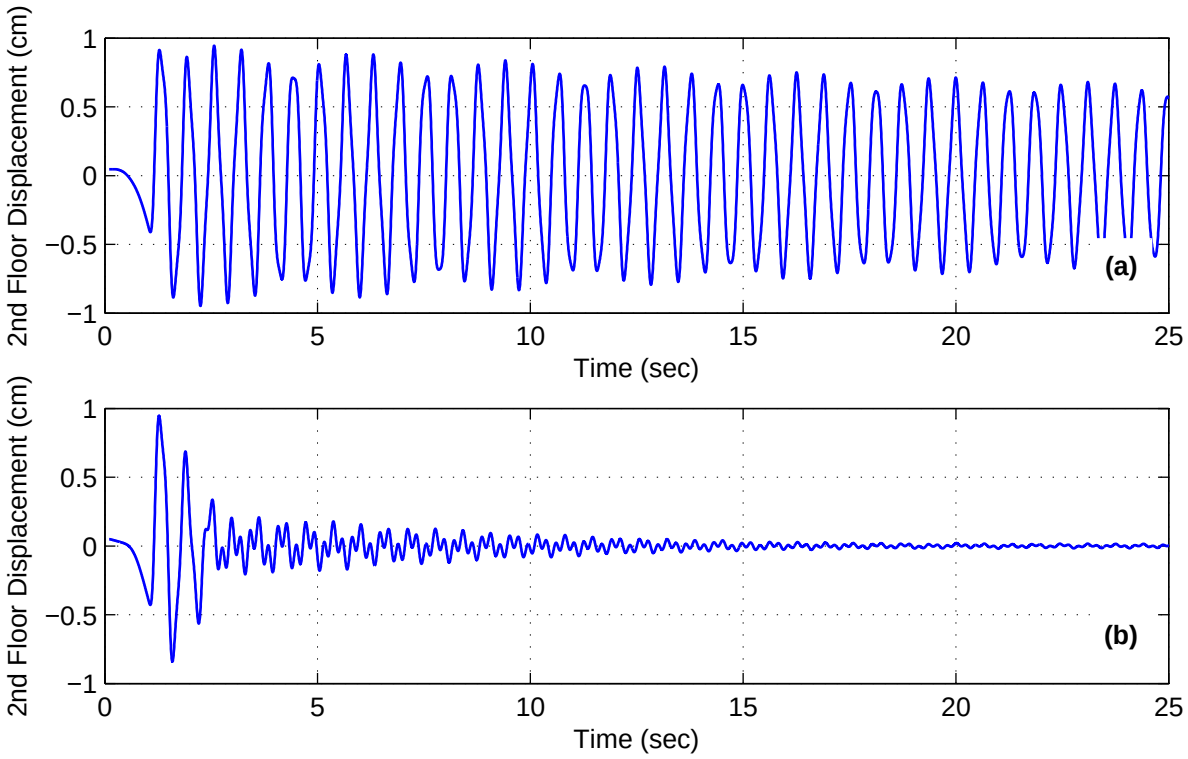

Figure 5-21. Top floor displacement from small-scale Type I NES test with NES (a) locked and (b) unlocked

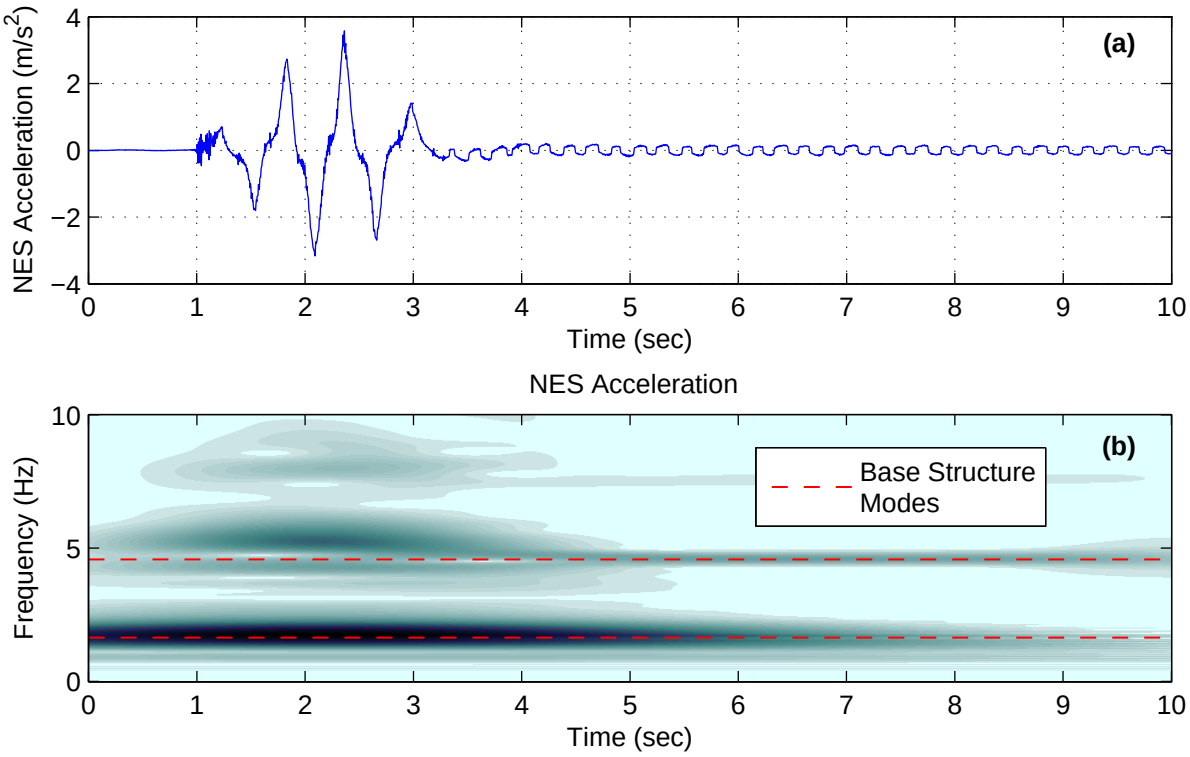

Figure 5-22. NES acceleration from small-scale Type I NES test (a) NES time history and (b) NES wavelet spectra

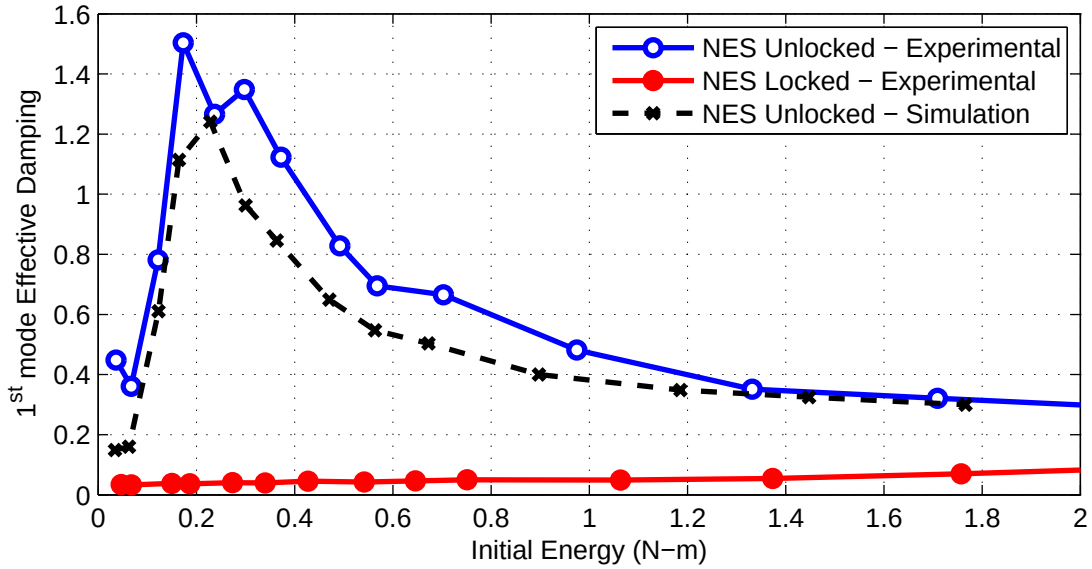

Figure 5-23. Effective damping vs. input energy for experimental Type I NES tests with NES locked and unlocked and numerical results

5.2.1.3 Additional Plots

Additional plots showing the response of the structure and Type I NES to different scaling levels ground motion considered in this section can be found in Appendix B.

5.2.1.4 Comparison with numerical results

Using the model of the structure introduced in Section 5.1.1 and the model of the small-scale Type I NES identified in Section 5.1.2.2, the response of the system can be simulated. Figure 5-24 shows a comparison between the experimental and numerical simulation displacement response of the second floor of the structure with the NES unlocked in response to the loading in Figure 5-17. As this figure shows, the simulated response largely agrees with the displacement response calculated from the experimentally measured response. The largest difference in these results occur after the amplitude of the system response has been brought down to a relatively low level. At this low level, the difference in the response is likely due to the fact that the identified model of the NES does not include phenomenon that become more dominant at lower amplitudes, such friction and stiction in the NES.

Using the effective damping measure, the simulated response is compared to the experimental response in across a wide range of energy levels of the system response in Figure 5-23. Like the time history response, the effective damping results diverge some at the lower levels. Additionally, the peak level of the effective damping is somewhat underestimated. Nevertheless, the overall shape of the experimentally calculated and simulation calculated effective damping curves match well. These curves both show similar levels of effective damping and peak at nearly the same level of energy in the system.

Although not perfect, there is a general agreement between the simulated response of the system with the experimental response in the time history presented in Figure 5-24 and in the effective damping results across a range of energy levels presented in Figure 5-23. This agreement serves to validate the fidelity of identified model of the small-scale Type I NES examined in this section.

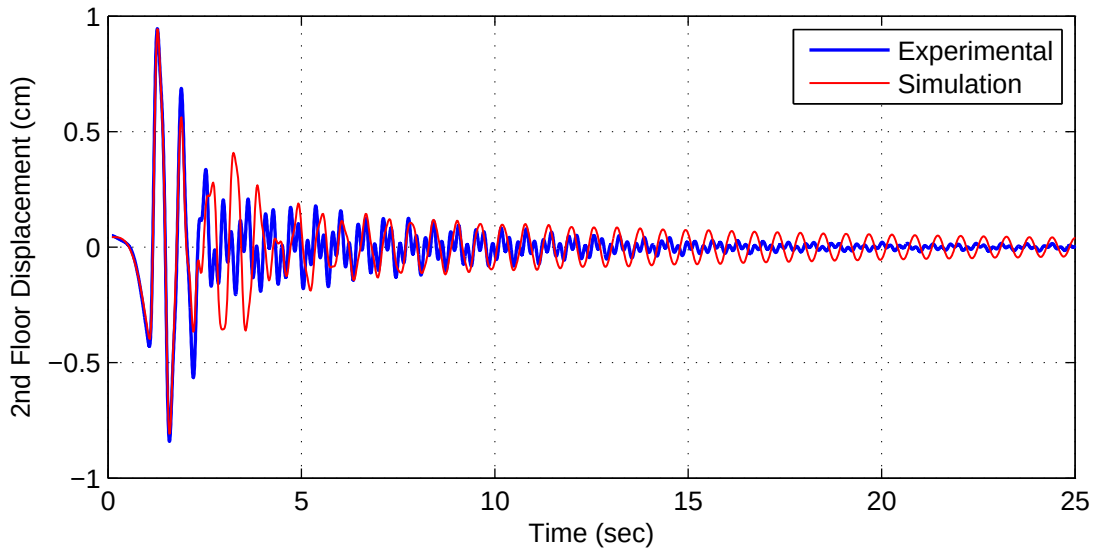

Figure 5-24. Comparison of experimental and simulated small-scale base structure response at optimum input level with Type I NES

5.2.2 Small-scale Type III NES

In this subsection the experimental investigation of the performance of the small-scale Type III NES is presented. The development of this NES was presented in Section 5.1.3. This NES is connected to the top floor of the small-scale base structure, presented in Section 5.1.1.

5.2.2.1 Experimental setup

The experimental setup for the small-scale investigation of the Type III NES was nearly identical to the setup used for the small-scale investigation of the Type I NES, which is discussed in section 5.2.1.1. For this setup, the same shake table, base structure and data acquisition system were used. The main difference in this set of tests is that the Type III NES introduced in section 5.1.3 is added to the top of the base structure, and the Type I NES previously studied is removed. The accelerometer layout used for this testing is also virtually the same as for the small-scale investigation of the Type I NES; however, for this experiment two PCB model 3701G3FA3G accelerometers were used to measure the response of the NES, one for each stage of the NES. This accelerometer layout is shown in Figure 5-25.

Similar to the small-scale Type I NES tests, for the investigation of the Type III NES, the shake table was commanded with a displacement step to load the structure. An example of the resulting ground acceleration input delivered to the structure by the shake table is shown in Figure 5-26. As before, to investigate the behavior of the NES at different load levels, the amplitude of the commanded displacement step function was varied.

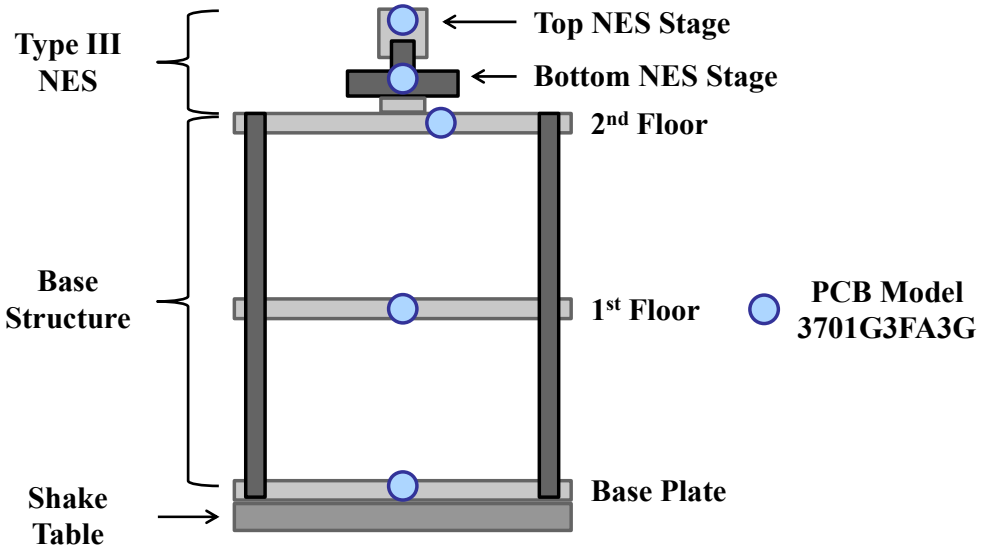

Figure 5-25. Diagram showing layout of accelerometers on the base structure and NES for the small-scale Type III NES experiments

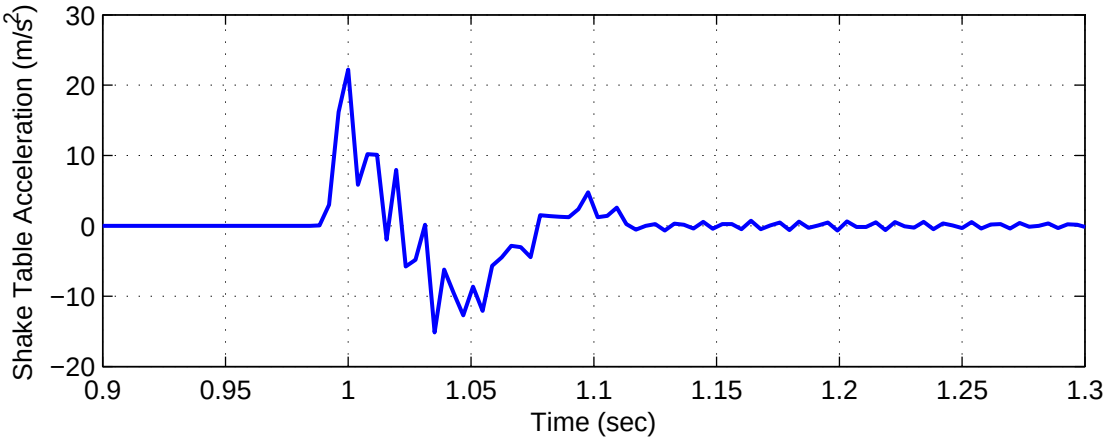

Figure 5-26. Example input ground acceleration used for small-scale Type III NES testing

5.2.2.2 Experimental results

Using the ground motion shown in Figure 5-26 the structure was excited with the shake table. By performing this experiment with the NES locked and then unlocked, the effect of the NES on the response of the system becomes clear. The resulting acceleration time histories of the top floor of the structure are shown in Figure 5-27a,b. As seen in the figure, when the NES is unlocked the response amplitude is rapidly dissipated, as compared with the locked response of the structure. In fact, with the NES unlocked, the amplitudes of the accelerations of the two floors of the base structure are nearly zero in under 15 seconds, but with the NES locked these accelerations are still significant at the end of the 30 second window.

In addition to rapidly reducing the amplitude of the building's response, the predominant frequencies of the response quickly transition to higher values in the presence of the unlocked NES. This effect is seen more clearly in Figure 5-27c,d, which depicts the wavelet transforms of the top floor acceleration for the locked and unlocked cases. For the locked case, the frequency components of the acceleration slowly decay in time and are dominated by the components at the natural frequencies of the base structure. For the unlocked case, the frequency component of the acceleration at the first natural frequency rapidly decays, and is soon followed by the component at the second natural frequency, which faster than previously observed as well. Both the time history and wavelet spectra results demonstrate the capacity of the 2-DOF NES to rapidly absorb and dissipate energy from both structural modes of the structure. Moreover, judging from the wavelet spectra of the responses of the two masses of the NES, shown below, it is clear that broadband TET takes place in this passive system.

As the previous figures show, the effect of the NES on the base structure can be substantial; consequently, it is important to examine the behavior of the NES in addition to the behavior of the base structure. In Figure 5-28a,b the absolute accelerations of the top and bottom masses of the NES are shown. In the test presented here, both masses of the NES undergo substantial oscillations in the initial five seconds of the motion, but after that they show little movement. Nevertheless, during this initial interval enough energy has been redistributed and dissipated so that there is no longer sufficient energy in the system to allow for large relative movement of the NES masses. This response is typical of the dynamic behavior associated with the essentially nonlinear restoring force; there are sharp peaks in the higher amplitude acceleration cycles, and the period of the NES motion increases as the amplitude decreases. In addition to the time history of the acceleration

response, Figure 5-28c,d shows the wavelet transforms of the top and bottom masses of the NES. While the NES masses are in motion, the frequency content of their responses appears to be broadband in nature. This behavior is indicative of the NES's ability to absorb and transfer energy across a broad range of frequencies.

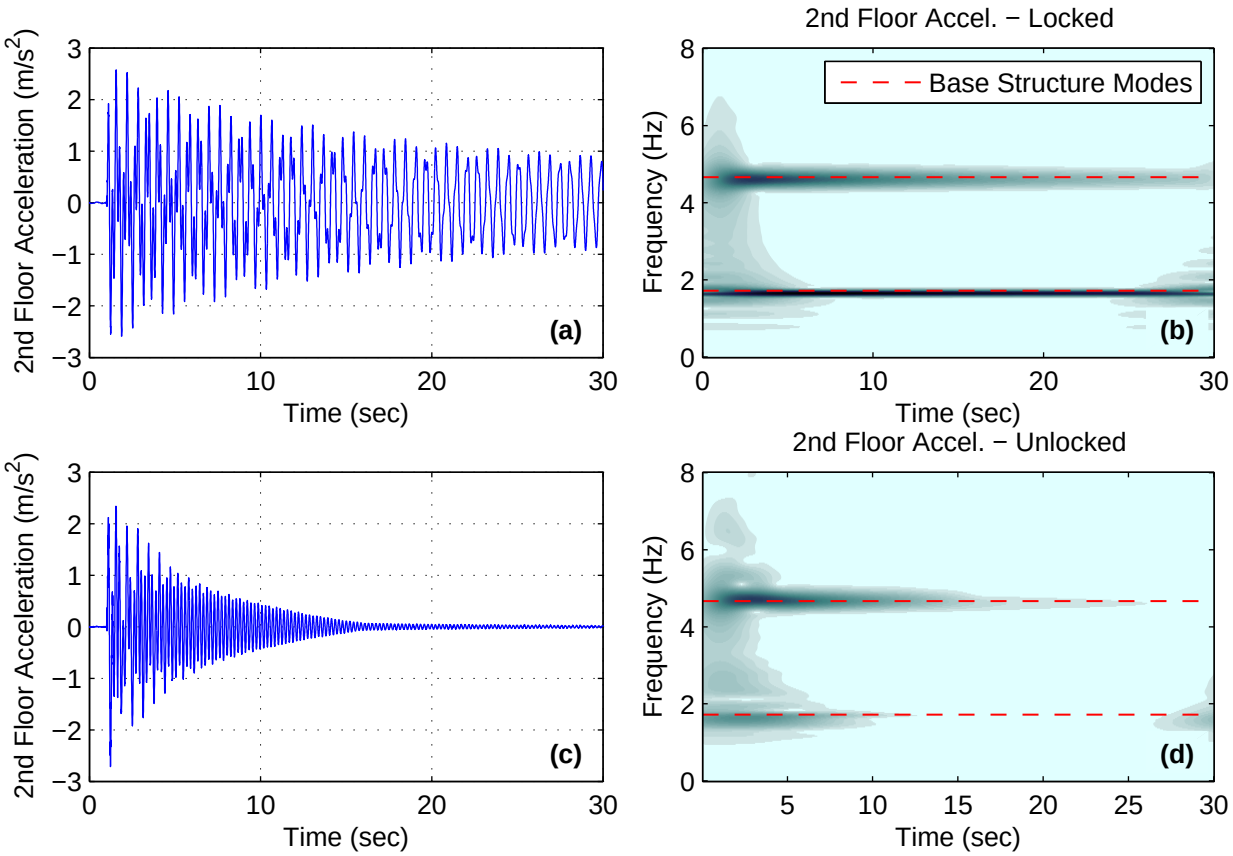

Figure 5-27. Top floor acceleration from small-scale Type III NES test a) NES locked time history, b) NES locked wavelet spectra, c) NES unlocked time history, and d) NES unlocked wavelet spectra

In summary, the action of the two-DOF NES is very effective in the initial phase of the response, which is highly energetic. After this strongly nonlinear phase, which only last a few seconds, the amplitude of the NES motion is greatly reduced. This behavior is one more indication of the efficacy of the strongly nonlinear NES to passively absorb and rapidly dissipate vibration energy in a broadband fashion, thus drastically enhancing the effective damping properties of the integrated base structure-NES system. Furthermore, this broadband TET is much more effective than that achieved with previously the considered Type I NES designs.

The response of the structure can also be examined in modal coordinates, as seen in Figure 5-29, showing the acceleration response of the two modes of the linear structure with NES locked and unlocked. When represented in modal coordinates, the locked version acts as a linear structure; indeed, the response for each mode independently decreases according to the damping in that mode. However, for the unlocked case the effect of the NES is quite significant. This effect most prominently includes a rapid reduction in the response of the first mode, well above what is

expected based on the inherent structural damping in that mode. Additionally, one can see that near the beginning of the response in the second mode, the amplitude decreases slightly, then increases before decreasing for the rest of the response. This nonlinear beat phenomenon is indicative of the strong coupling of the modes and energy exchange due to the NES (Vakakis et al. 2008).

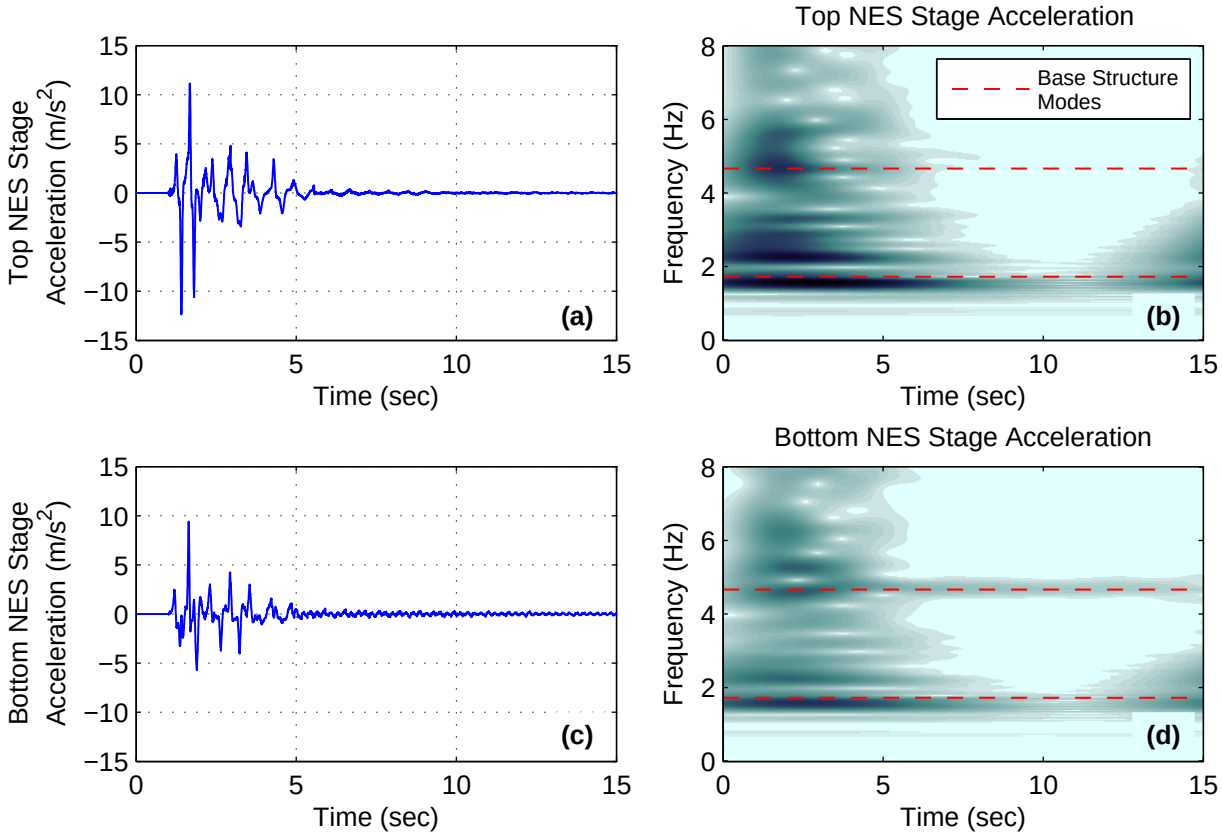

Figure 5-28. NES relative acceleration from small-scale Type III NES test a) top NES stage time history, b) top NES stage wavelet spectra, c) bottom NES stage time history, and d) bottom NES stage wavelet spectra

While for a given load the effect of the NES can be studied in detail, the nonlinear nature of the NES results in different behaviors when the amplitude, or energy, of the input is changed. Consequently, the behavior of the NES needs to be examined across a large range of input energies. This behavior is best evaluated through the effective damping measure that was introduced in Chapter 3. Using the parameters from the identification of the NES and the previously discussed model of the base structure, a model of the base structure with the NES attached can be produced. In determining the overall effectiveness of the model in simulating the response of the system across all energy levels investigated, a comparison of the effective damping calculated from both the experimental and simulation data is shown in Figure 5-30. The model of the system quite accurately produces an effective damping curve that tracks the general shape and amplitude of the experimentally developed curve. In this figure, the experimentally determined effective damping is shown across a range of energies and can be compared to the corresponding theoretically

predicted results for the same system parameters and under the same loading conditions. For the results depicted here, the initial energy was calculated by determining the sum of the kinetic and potential energies in the system immediately after the input ground motion is applied. We conclude that the effective damping is indeed sensitive to the initial energy, increasing as energy increases until it reaches an optimal region at about $0.10\ N \cdot m$ with $\lambda_* \approx 1.4$. Beyond this optimal region, the effective damping decreases with increasing initial energy until it reaches a stable value of approximately $\lambda_* = 0.4$ at the higher initial energies studied.

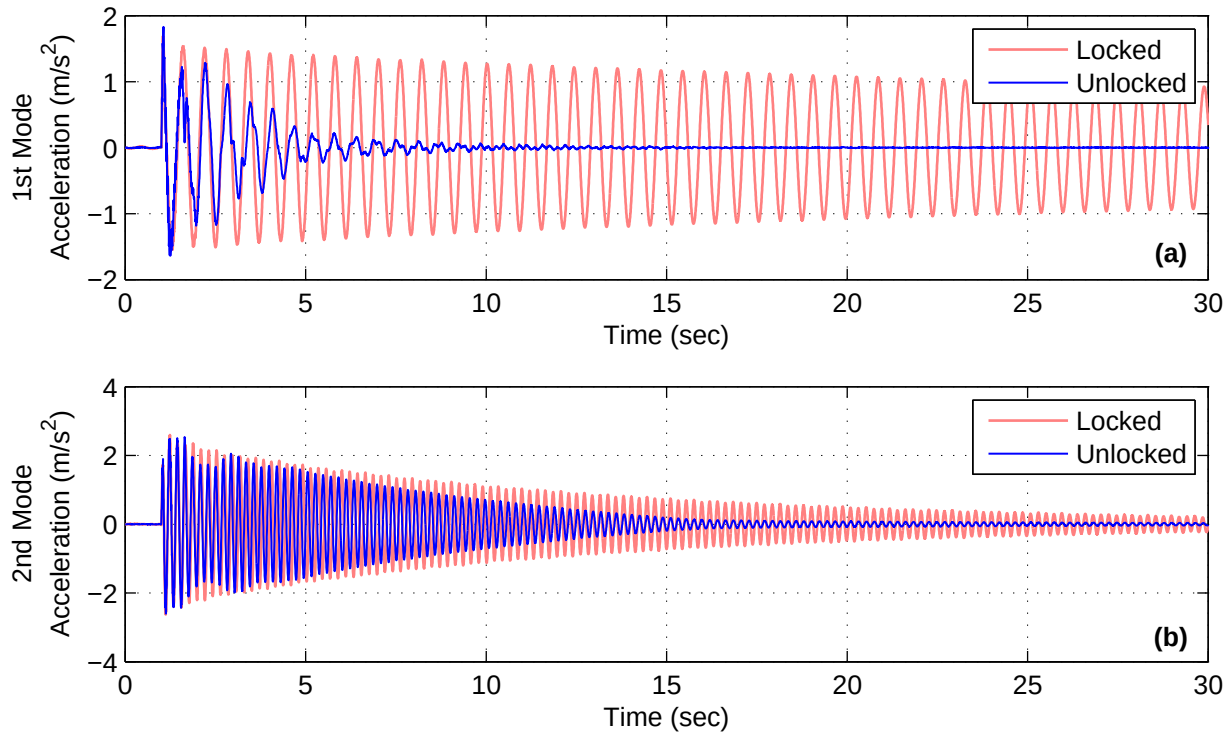

Figure 5-29. Acceleration response of base structure in modal coordinates from small-scale Type III NES test with NES locked and unlocked (a) first mode and (b) second mode

In addition to evaluating the ability of the model to accurately predict global measures, it is important to determine the ability of the model to simulate the time history response of the system. Accordingly, Figure 5-31 shows a comparison of the acceleration and displacement responses of the second floor of the structure subjected to ground motion, corresponding to the optimal effective damping. As seen from this figure, the envelope of the acceleration and displacement time histories are accurately tracked by the model, except at low response levels where the experimental response dies out faster. The reason for this discrepancy may be inaccuracies in determining the structural damping or the small amplitude behavior of the NES; however, because the small amplitude segment of the response is primarily affected, this model is considered to be predictive.

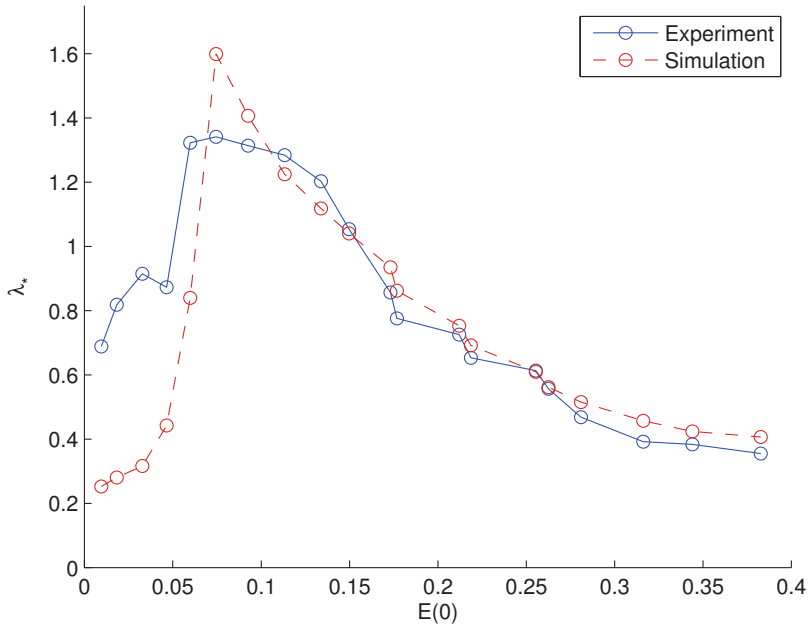

Figure 5-30. Effective damping over range of input energies from the measured experimental response and numerical simulations

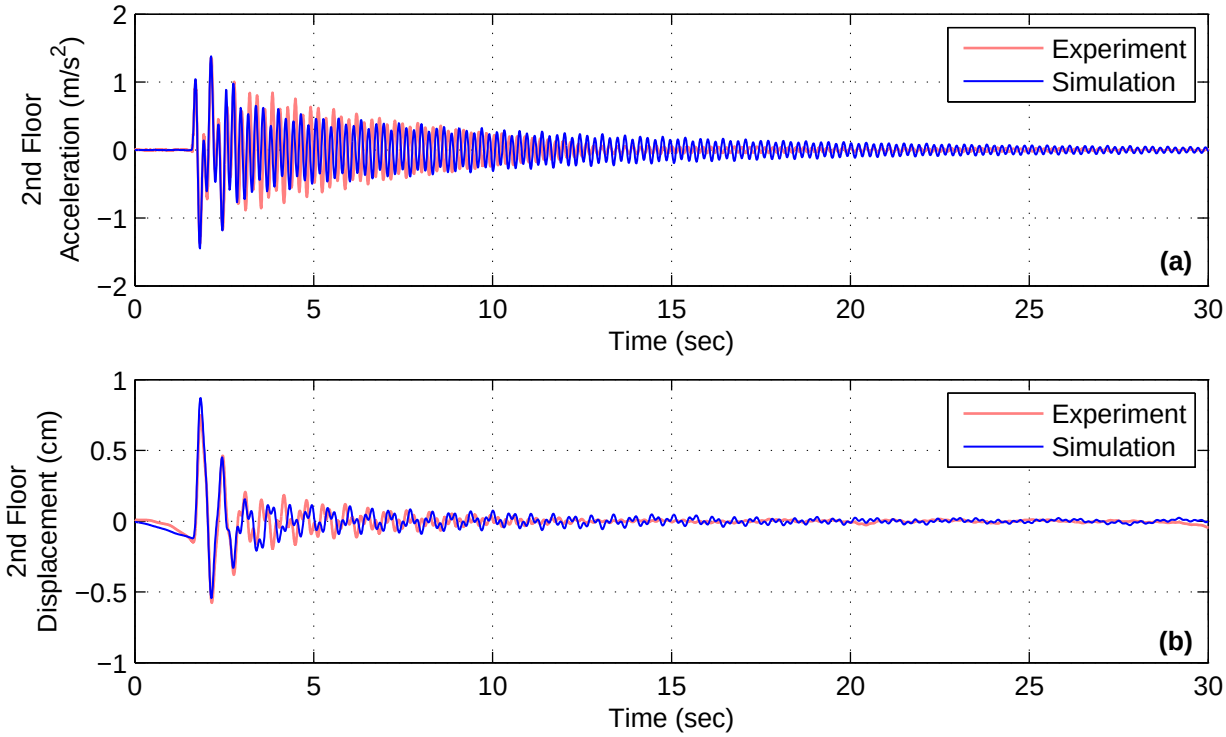

Figure 5-31. Comparison of experimental and simulated small-scale base structure response at optimum input level with Type III NES

5.2.2.3 Additional Plots

Additional plots showing the response of the structure and Type III NES to different scaling levels ground motion considered in this section can be found in Appendix C.

5.2.3 Medium-scale Type III NES

In this subsection the experimental investigation of the performance of the medium-scale Type III NES is presented. The development of this NES was presented in Section 5.1.5. This NES is connected to the top floor of the medium-scale base structure, presented in Section 5.1.4.

5.2.3.1 Experimental setup

For the testing presented in this section, the medium-scale base structure was bolted to a hydraulic shake table, which was used to excite the structure along its weak axis with a step-function-like ground motion designed to simulate a uniform shock load on its face. The 2.13 m × 2.13 m shake table used for this testing is shown in Figure 5-32. To measure the response of the system to this excitation, PCB® model 3701G3FA3G uniaxial capacitive accelerometers were installed at each floor of the base structure and on each mass of the NES. Additionally, PCB® model 353B33 uniaxial piezoelectric accelerometers were installed on each of the NES masses to provide redundancy in the NES response measurement. These acceleration measurements were collected and anti-aliased with a VibPilot® data acquisition system manufactured by m+p International. Data was collected at 1024 Hz and low pass filtered to 50 Hz unless otherwise noted.

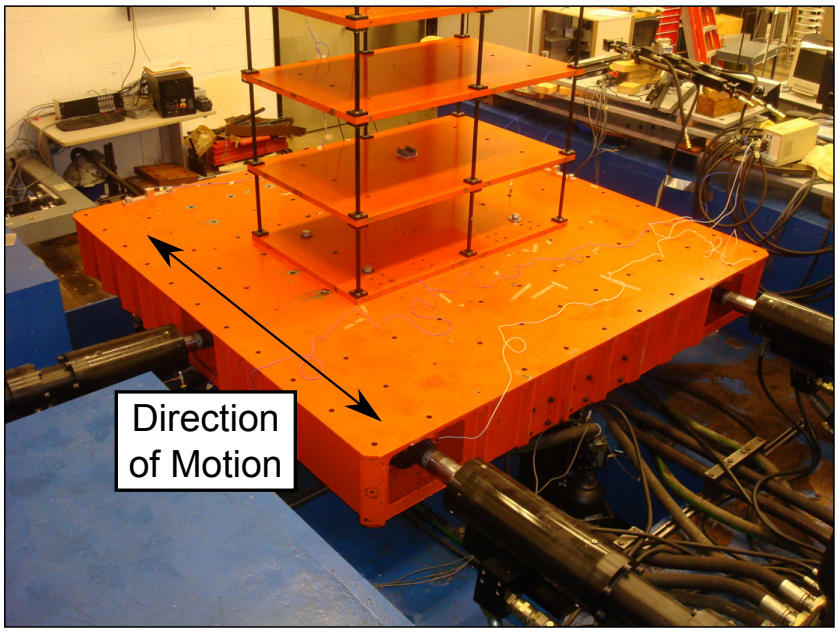

Figure 5-32. Shake table used to excite medium-scale base structure with Type III NES attached

5.2.3.2 Experimental results

In the experiments presented in this study, the base structure is excited by a shake table with a short impulse-like ground motion of varying amplitude. An example of this type of ground motion is shown in Figure 5-33. This differs from the loading used in the simulation studies utilized for the design optimization of the NES parameters, which assumed an initial velocity and zero initial

displacement for each story. However, the short shock-like ground motion replicates well the initial energy distribution among the modes used in the optimization studies; consequently, the design parameters resulting from the optimization are still expected to lead to an NES design that effectively dissipates energy from the structural system in this set of experiments.

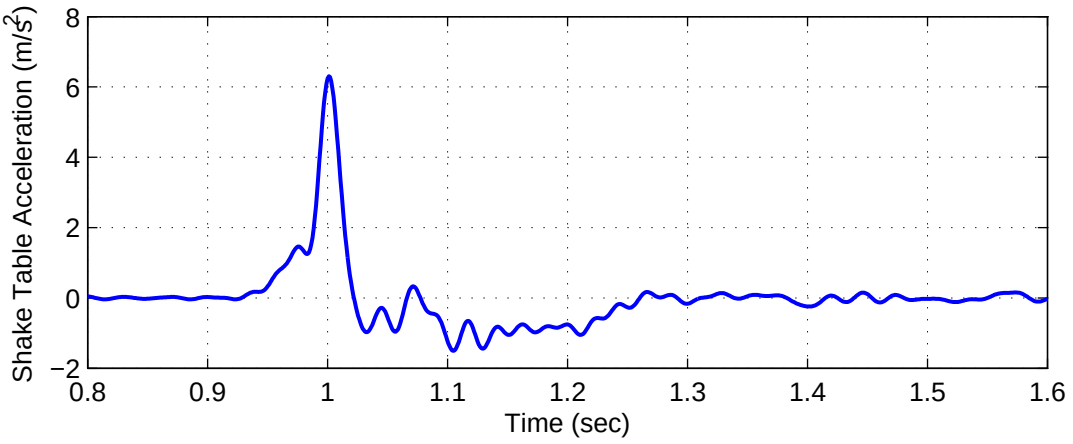

Figure 5-33. Example input ground acceleration used for medium-scale Type III NES testing

For the specific ground motion seen in Figure 5-33, the top floor accelerations of the base structure with the NES locked and unlocked are shown in Figure 5-34a,c. These plots show that when the NES is unlocked, the response of the structure decreases substantially in the first five seconds after the loading ceases. In addition to showing a decrease in the amplitude of the acceleration response, they also show that, for the unlocked case, the response appears to be composed predominantly of high frequency accelerations, as opposed to the low frequency accelerations seen in the locked case. This behavior is examined in more depth by studying the Morlet wavelet transforms of the top floor accelerations, shown in Figure 5-34b,d. These wavelet spectra do indeed confirm the phenomenon observed in the time histories of the acceleration; i.e., when the NES is unlocked the first mode response of the structure is very quickly attenuated, and energy is rapidly transferred to the higher modes of the structure.

Insight into the behavior of the base structure with NES unlocked can be gained by observing the behavior of the NES. Figure 5-35 shows the time histories and wavelet spectra of the NES relative accelerations (i.e., NES top stage mass relative to the NES bottom stage mass and the NES bottom stage mass relative to the top floor of the base structure). It demonstrates that the NES engages only for a few seconds immediately after the ground motion initiates. During that time, both NES masses experience high levels of acceleration, compared with the top floor of the base structure (see Figure 5-34); however, it can also be seen that the acceleration of the NES top stage mass is higher than that of the NES bottom stage mass, which is expected as the NES bottom stage is used as a vehicle to further excite the top stage mass. Additionally, the wavelet spectra in Figure 5-35 show the broadband behavior of both NES masses, necessary for broadband passive TET responsible for reducing the response of the base structure.

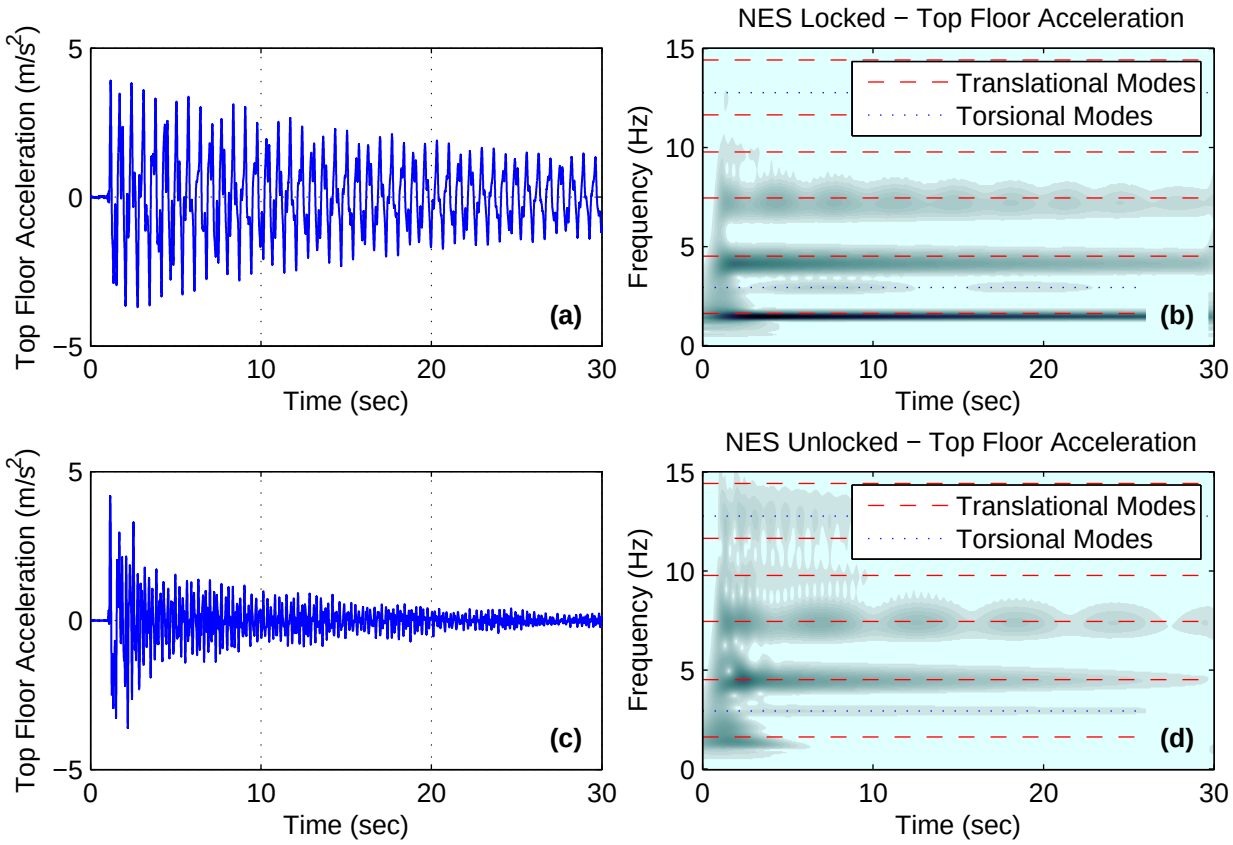

Figure 5-34. Top floor acceleration from medium-scale Type III NES test a) NES locked time history, b) NES locked wavelet spectra, c) NES unlocked time history, and d) NES unlocked wavelet spectra

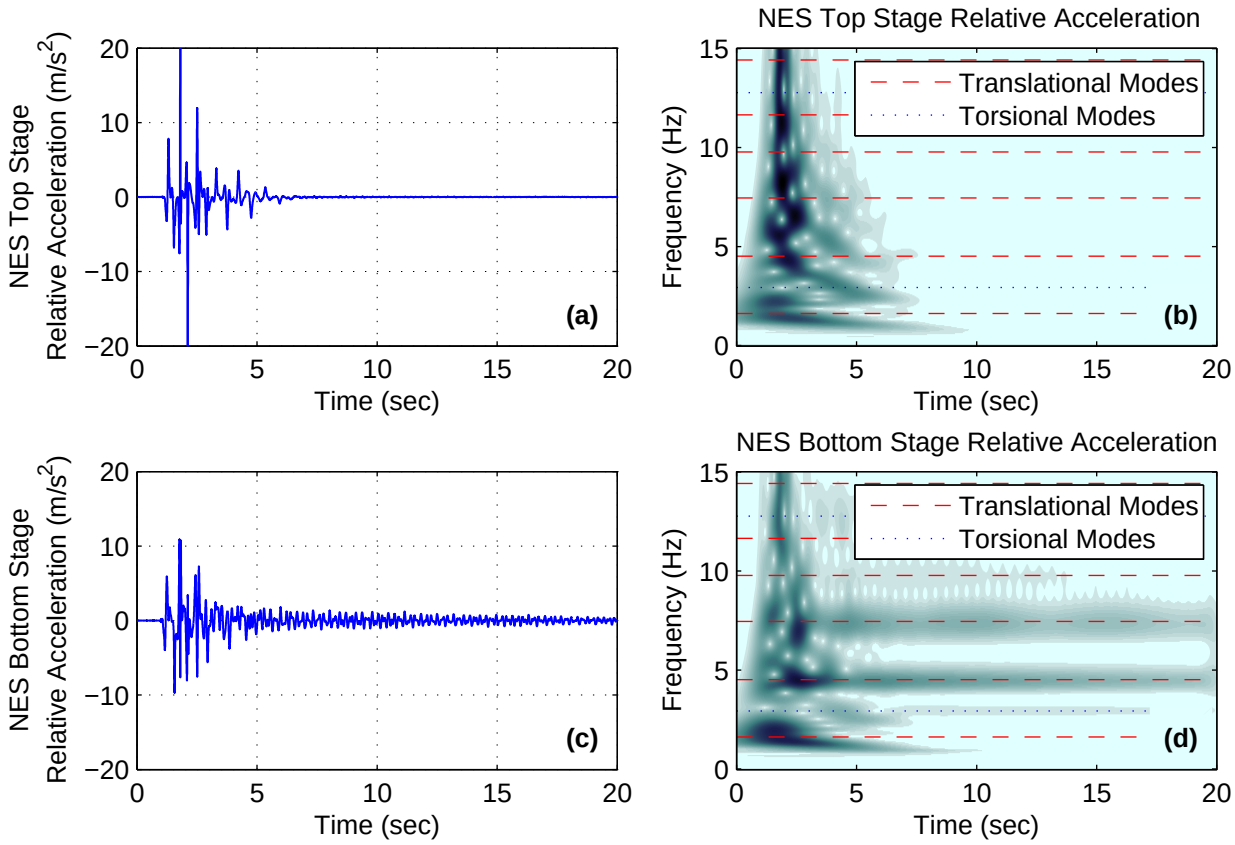

Figure 5-35. NES relative acceleration from medium-scale Type III NES test a) top NES stage time history, b) top NES stage wavelet spectra, c) bottom NES stage time history, and d) bottom NES stage wavelet spectra

Figure 5-36 shows the displacement response of the top floor of the structure (calculated from the measured acceleration record) with the NES both locked and unlocked. This figure better serves to highlight the effect of the NES, as it shows that the NES quickly and drastically reduces the displacement of the structure. Additionally, after this initial reduction in the response, most of the remaining energy is in the higher modes of the structure, leading to even greater attenuation. Moreover, as discussed later, this mitigation performance is robust to changes in the amplitude content of the shock excitation.

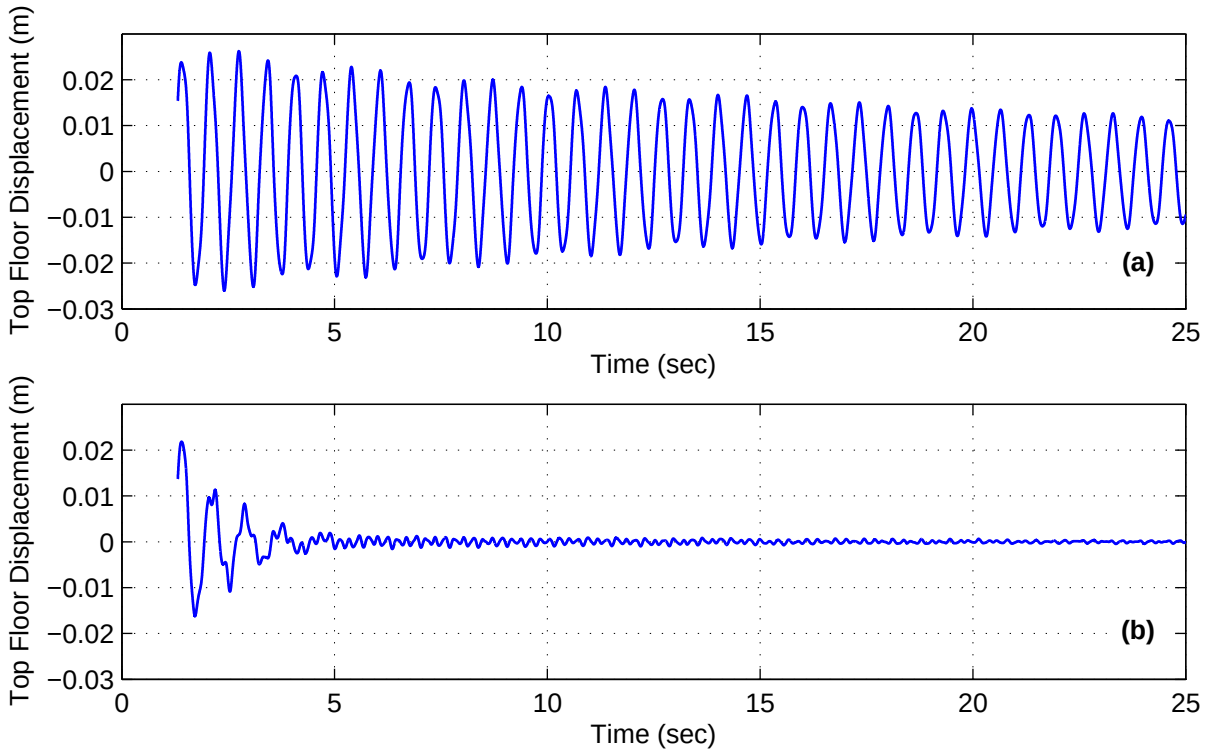

Figure 5-36. Top floor displacement from medium-scale Type III NES test with NES a) locked and b) unlocked

Aside from assessing the effectiveness of the NES by comparing time histories and corresponding wavelet spectra, the effective damping measure that was introduced earlier proves to be quite insightful. In this section, the alternate method for calculating the effective damping, as discussed in Chapter 3, is utilized. Figure 5-37 shows the resulting effective damping in the first mode of the structure across the range of ground motions studied. In this figure, each ground motion is identified by the total amount of calculated input energy it imparts to the system. For reference, the results shown in Figure 5-33 through Figure 5-36 correspond to the 21.4 N-m point on the input energy vs. effective damping plot shown in Figure 5-37. This figure shows that the effective damping in the first mode is much higher when the NES is unlocked versus locked. Additionally, the effective damping varies with input energy, and peaks near the energy level used to determine the optimal NES parameters. Although the ability of the NES to increase the effective damping of the base structure varies with the input energy level, the NES provides appreciable robustness because it increases the effective damping over a wide range of input energy levels. Furthermore, the system can be configured based on a particular input design energy level through optimization, followed by tailoring the elastomeric bumpers in the NES to achieve the required nonlinear stiffness values.

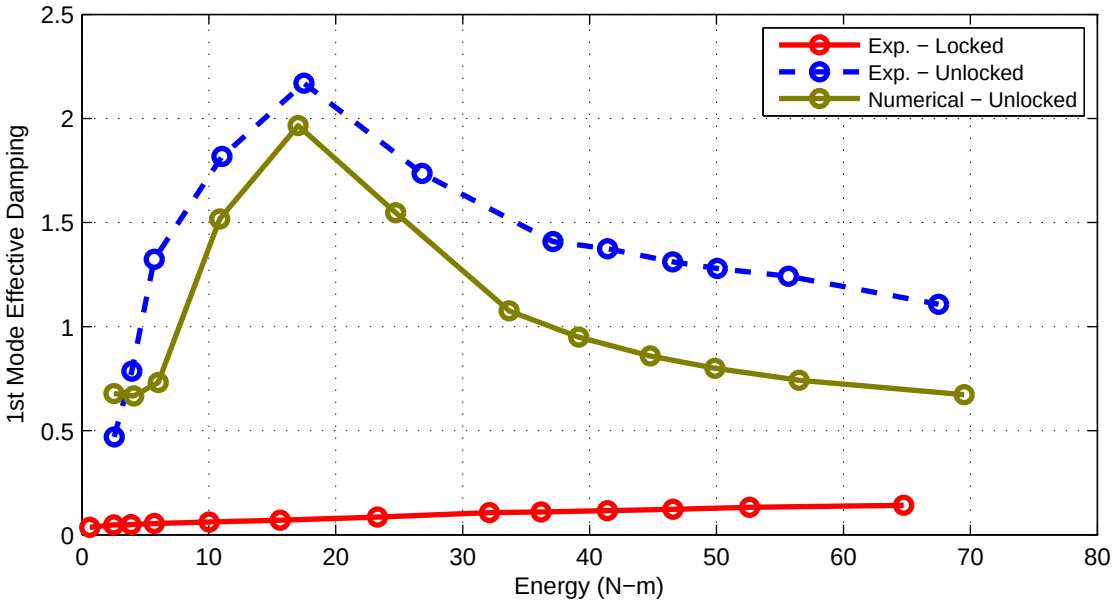

Figure 5-37. Effective damping vs. input energy for experimental results with NES locked and unlocked and numerical results

The addition of the NES to the linear base structure makes the system strongly nonlinear; however, determining the experimental transfer function of the system, which is a based on an underlying assumption of linearity, can be used to approximately evaluate the response of the system. Figure 5-38 shows the magnitude of the ground acceleration to top floor acceleration transfer functions of the system. In this figure, one transfer function is shown for the case when the NES is locked and the system is linear, and multiple transfer functions at several different input energy levels are shown when the NES is unlocked and the system response is amplitude dependent. These transfer functions are shown from 1 to 6 Hz so that the first and second translational modes are emphasized. In calculating these transfer functions, exponential windowing of the response is used to suppress noise in the signal and ensure the signal is minimized at the end of the record in preparation for the discrete Fourier transform. The number of points used in the discrete Fourier transform is equal to the number of points in the entire 30 second response record. The magnitude of the transfer function for the locked case clearly shows two peaks corresponding to the first two translational natural frequencies, at 1.5 and 4.2 Hz. When comparing this transfer function to the transfer function for the unlocked case at the lowest input energy level, the natural frequencies for the locked case are lower. This result is expected because locking the NES adds more fixed mass to the system. The effects of the NES are apparent when examining the transfer functions as the input energy level increases. In particular, as the energy level increases, the peak corresponding to the first mode reduces until the transfer function is nearly flat at the 21.4 N-m input energy level, which corresponds to the peak in the effective damping curve shown in Figure 5-37. After this point, the peak of the transfer function again emerges, but shifted to a lower frequency. This behavior is consistent with that shown on the frequency energy plot for other systems with Type III NESs (Wierschem et al. 2012). Another effect of the NES is seen when examining the transfer function near the second mode and beyond. This part of the

transfer function is elevated, compared with the locked case, which may be due to TET, whereby energy from the first mode is transferred to modes at higher frequencies.

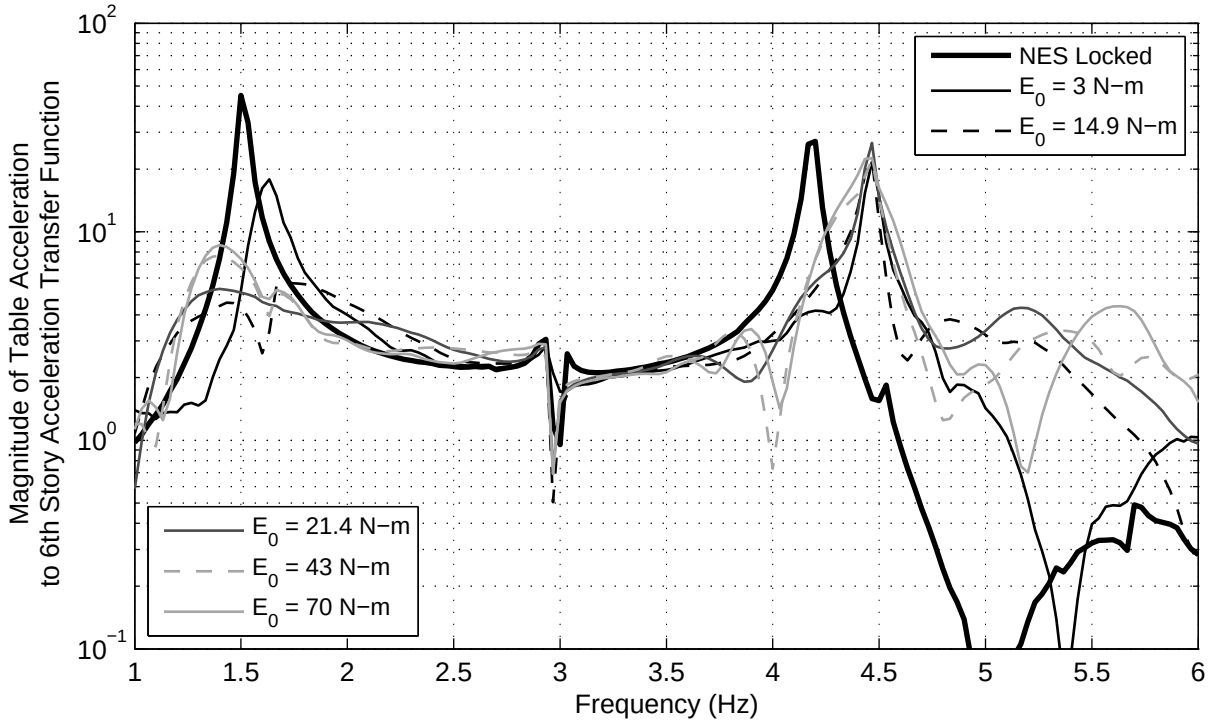

Figure 5-38. Transfer function of ground acceleration to top floor acceleration for base structure with NES locked and with NES unlocked at multiple energy levels

5.2.3.3 Comparison with numerical results

Using the model developed previously for the optimization study but employing the experimentally determined coefficient and exponent for the nonlinear stiffness term, numerical simulations of the system were performed employing the experimental acceleration time histories recorded at the base of the linear base structure. The time history and wavelet spectra of the top floor displacement obtained from this numerical model when subjected to the loading in Figure 5-33 is shown in Figure 5-39, where it is compared with the experimentally determined displacement. Here, the simulated and experimental results show good agreement, with noticeable differences appearing only after the displacement has been rapidly reduced to a low level, and in the higher frequency responses.

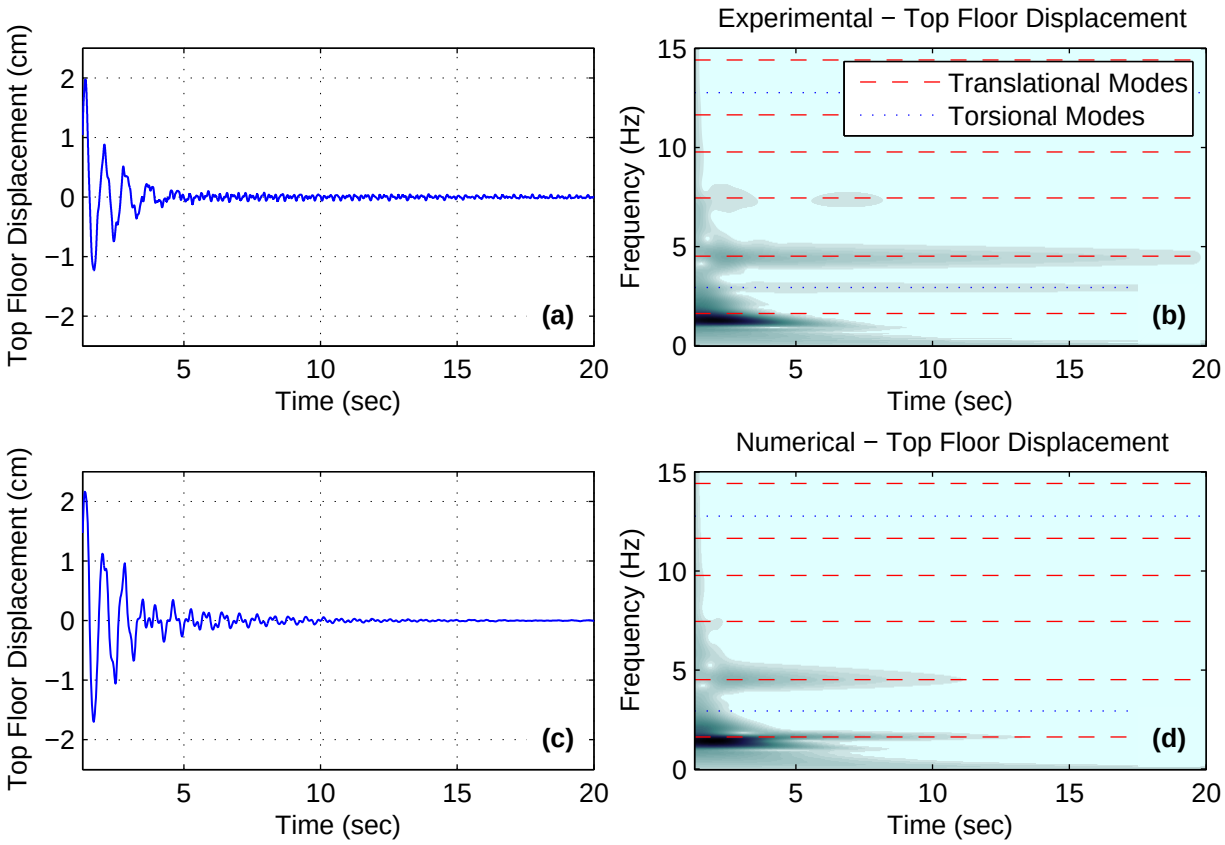

Figure 5-39. Top floor displacement a) experimental time history, b) experimental wavelet spectra, c) numerical simulation time history, and d) numerical simulation wavelet spectra

The effective damping for the first mode of the structure, over the range of simulations is shown in Figure 5-37, where it is compared with the experimentally determined effective damping. As shown, the effective damping curve predicted from numerical simulation is in qualitative agreement with the experimentally determined curve; the effective damping peaks at a particular energy level, similar for both the experimental and numerical cases, while below that energy there is a sharp decrease, and above that energy there is a more gradual decrease. Although the general shape matches well, the numerical model modestly underestimates the magnitude of the effective damping, especially at high loads. Potential explanations for this behavior include that unmodeled dynamics in the NES at higher loads, nonlinear damping in the bumpers, and the assumption of constant first mode stiffness used in the effective damping calculation. Additionally, the numerical model does not include the torsional modes of the structure, which are excited more at higher loads due to actuator imperfections; thus, the total energy in the structure is lower for the numerical simulations. Nevertheless, the reasonable agreement in both time history results and global effective measures, especially at the peak, serves to verify the fidelity of the numerical model and its use for the design of the NES.

5.2.3.4 Robustness studies

As discussed in literature (Lee et al. 2008), and explored at different points in this report, the broadband behavior of NESs has the potential to make the effectiveness of the NES robust to frequency changes in primary structure the NES is designed to control. This type of change in the

primary structure can occur due to settlement of the structure, thermal effects, or damage from to a prior extreme event. While the robustness of the NES to changes in the primary structure are important, changes to the NES itself can also occur. In this section, the robustness of the Type III NES to changes to the NES restoring force and failure of individual stages of the NES is examined. The robustness study presented in this section was done experimentally using the medium-scale primary structure and Type III NES previously introduced. As in the prior study involving this medium-scale Type III NES, scaled versions of the ground motion shown in Figure 5-33 are used to load the structure during this study.

5.2.3.4.1 Robustness study – NES stiffness

In practice, a nonlinear energy sink installed in a building structure would remain in place for decades. During this time, the properties of the NES restoring force mechanism might deviate from the design values due to improper maintenance, material degradation, corrosion in the system, or errors in the initial installation. Consequently, it is important assess the robustness of the NES change in the restoring force. In this study, the robustness of the NES to changes in the stiffness of the Type III NES restoring force mechanism is investigated.

Bumpers sets consider

To investigate the robustness of the performance of the NES to changes in the NES's nonlinear stiffness, tests were performed with the medium-scale Type III NES using four sets of different elastomeric bumpers. Included in these sets of bumpers are the bumpers shown in Figure 5-12; this set of bumpers was used for the tests presented in Section 5.2.3.2 and in this current section is referred to as the original bumpers. The other sets of bumpers used in this study are shown in Figure 5-40, Figure 5-41, and Figure 5-42. These bumpers are referred to as moderately soft, soft, and stiff. This naming scheme refers to the bumper sets' relative stiffness compared to the original bumper set.

The differences in the stiffnesses achieved by these four sets of bumpers is a result of the variations in the material used to make the bumpers as well as the bumper dimensions, which are shown in Table 5-5. As shown in this table, for all of the bumper sets considered, pyramid-shaped bumpers were used in the top stage of the NES and wedge-shaped bumpers were used in the bottom stage of the NES. The original, moderately soft, and soft bumper sets were all made from high reliance foam; however, various stiffnesses of this foam were used. Alternatively, the stiff bumper set was made out of rebound foam.

The bumpers used for this Type III NES were shaped by cutting blocks of the foam material. Due to the soft nature of the low stiffness high resilience foam used for the soft bumper set and the non-homogeneous nature of the rebound foam used for the stiff bumper set, some manufacturing irregularities can be seen in these bumpers, as shown in Figure 5-41, and Figure 5-42. Although visible, these irregularities are relatively minor and are not anticipated to have a large effect on the restoring force, nor reduce its repeatability. If implemented in a real building structure, the utilization of higher quality manufacturing and standardization would likely prevent these kinds of irregularities from occurring.

Figure 5-40. Moderately soft bumper set for the medium-scale Type III NES top stage (pyramid-shaped) and bottom stage (wedge-shaped)

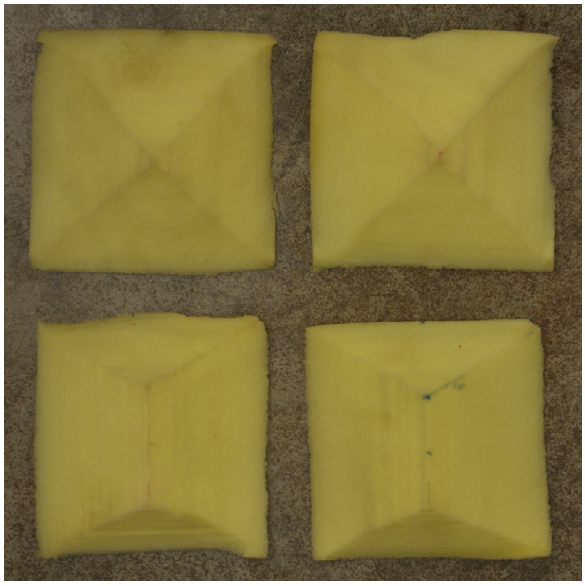

Figure 5-41. Soft bumper set for the medium-scale Type III NES top stage (pyramid-shaped) and bottom stage (wedge-shaped)

Figure 5-42. Stiff bumper set for the medium-scale Type III NES top stage (pyramid-shaped) and bottom stage (wedge-shaped)

Table 5-5. Dimensions of bumpers considered in robustness study

Bumper Set	Material	NES Stage	Width (mm)	Length (mm)	Top Width (mm)	Height (mm)
Original	High Stiffness High Resilience Foam	Top	178	178	0	32
		Bottom	203	203	102	51
Moderately Soft	Moderate Stiffness High Resilience Foam	Top	178	178	0	44
		Bottom	178	178	89	51
Soft	Low Stiffness High Resilience Foam	Top	178	178	0	51
		Bottom	178	178	86	51
Stiff	Rebound Foam	Top	178	178	0	51
		Bottom	178	178	89	51

System identification

System identification was performed to determine the properties of the Type III NES when the various bumper sets outlined above are installed. The system identification technique used to determine these properties was the restoring force surface method, which is discussed in Section 5.1.5.2. The assumed model of the NES's restoring force needed for this method included a linear stiffness term, a generic nonlinear stiffness term, and a viscous damping term for each stage of the NES. With this assumed model, the outputs of the restoring force surface method are the viscous damping coefficient, linear stiffness coefficient, nonlinear stiffness coefficient, and the nonlinear stiffness exponent.

Plots of the stiffness contribution to the identified restoring force for the top and bottom stages of the NES is shown in Figure 5-43 for the various bumper sets considered. In this figure, the restoring force curves are plotted over the range of relative displacement estimated during each

system identification. As shown by this figure, the intended stiffness levels of the soft, moderately soft, and stiff bumpers, relative to the original set of bumpers, was achieved by both the top and bottom bumpers sets. Additionally, this figure shows that the basic shape of all of the restoring force curves are quite similar. This similarity indicates that the differences in the identified stiffnesses models can primarily be described as a scaling of the restoring force relationships rather than meaningful differences in the exponent of the nonlinearity stiffness terms of the system.

The identified viscous damping coefficients for the top and bottom NES stages with the various bumper sets considered are shown in Figure 5-44. This figure indicates that the identified damping in the NES is consistently larger for the bottom stage, compared to the top stage. Additionally, while the use of different bumpers was intended to affect the stiffness properties of the NES, this figure shows that the damping is unintentionally modified as well. This modification to the damping is a result of the fact that the specific damping level in the NES was not purposefully part of the NES physical realization. Instead, the damping in the NES is a function of the various inherent effects in the system, including damping in the rails, aerodynamic drag on the system, and damping that results from the deformation of the bumpers. While the different levels of identified damping is not ideal for this stiffness related robustness study, this variability is not expected to have a large effect on the results.

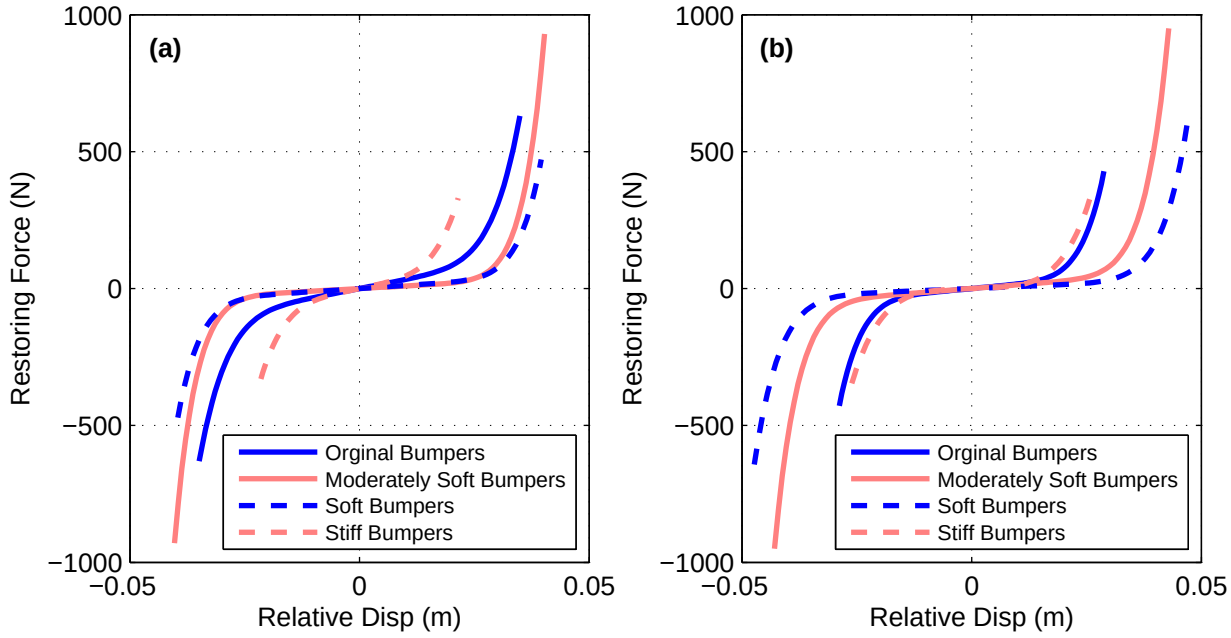

Figure 5-43. Comparison of experimentally identified stiffness contribution to the restoring force-displacement relationships from bumper sets considered (a) bottom NES stage bumpers and (b) top NES stage bumpers

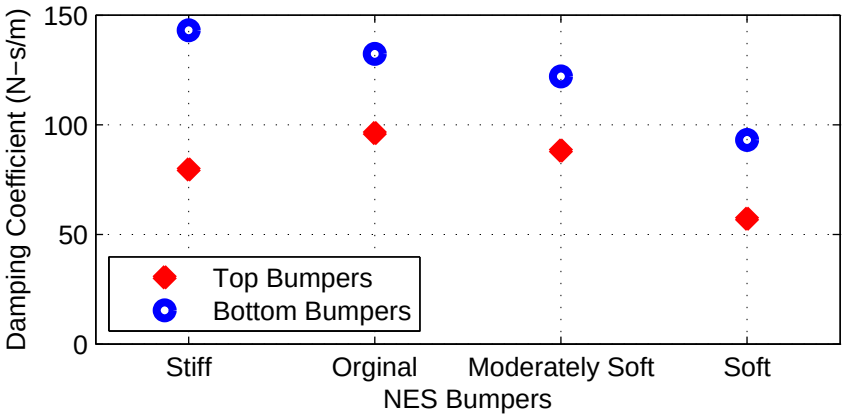

Figure 5-44. Comparison of experimentally identified viscous damping coefficients from bumper sets considered

Results

The first mode effective damping of the primary structure calculated from the response of the medium-scale base structure to a range of scaling levels of the impulse-like ground motion considered in this section is shown in Figure 5-45. Included in this figure are the calculated effective damping curves for when the NES is locked and when it is unlocked with the soft, moderately soft, original, and stiff bumpers are installed. This figure shows that the biggest change in the effective damping that occurs with the use of the different bumper sets is a shift in the energy level at which the peak effective damping occurs. With an increase in stiffness of the NES restoring force mechanism, the peak effective damping is shifted to a lower energy level; in contrast, with a decrease in stiffness, the peak effective damping occurs at a higher energy level. Another difference seen in these effective damping curves is that, with the soft and moderately soft bumpers, the range of energy levels that the NES performs near its peak effectiveness is increased. It remains unclear if this behavior is related to the change in stiffness of the NES, change in damping, or some other unmodeled dynamics effect.

In Figure 5-46, the top floor displacement when the NES is locked is plotted against the displacement when the NES is unlocked with the soft, moderately soft, original, and stiff bumper sets. In each case, the ground motion used to produce these plots corresponds to the motion at which the peak first mode effective damping is observed (see Figure 5-45). So that a comparison of the peak performance of the system can be made, in each case, the top floor displacement has been normalized such the maximum displacement of the structure with the NES locked is unity. Based on the normalized displacement plots shown in Figure 5-46, a rapid attenuation of the motions at the peak performance level is achieve by all the bumper sets considered in this robustness study. Additionally, the performance of all the bumper sets shown in this figure is quite similar, with the only exception being slightly slower attenuation and higher residual vibration for the case when the soft bumpers are utilized.

The results shown in this robustness study demonstrate that, even with large changes in the stiffness of the NES restoring force mechanism utilized in the Type III NES, similar peak performance of the NES can be maintained. One drawback that does occur with stiffness changes is that the energy level that this peak performance is achieved at can shift significantly; increased stiffness in the restoring force relationship shifts the peak performance to lower energy levels. As a consequence of this, in a realistic Type III NES implementation, the possible stiffness changes

(softening or stiffening) of the restoring force mechanism used should be evaluated. With the likely direction of stiffness change identified, the NES could then be designed such that the effects of this anticipated stiffness change could be minimized.

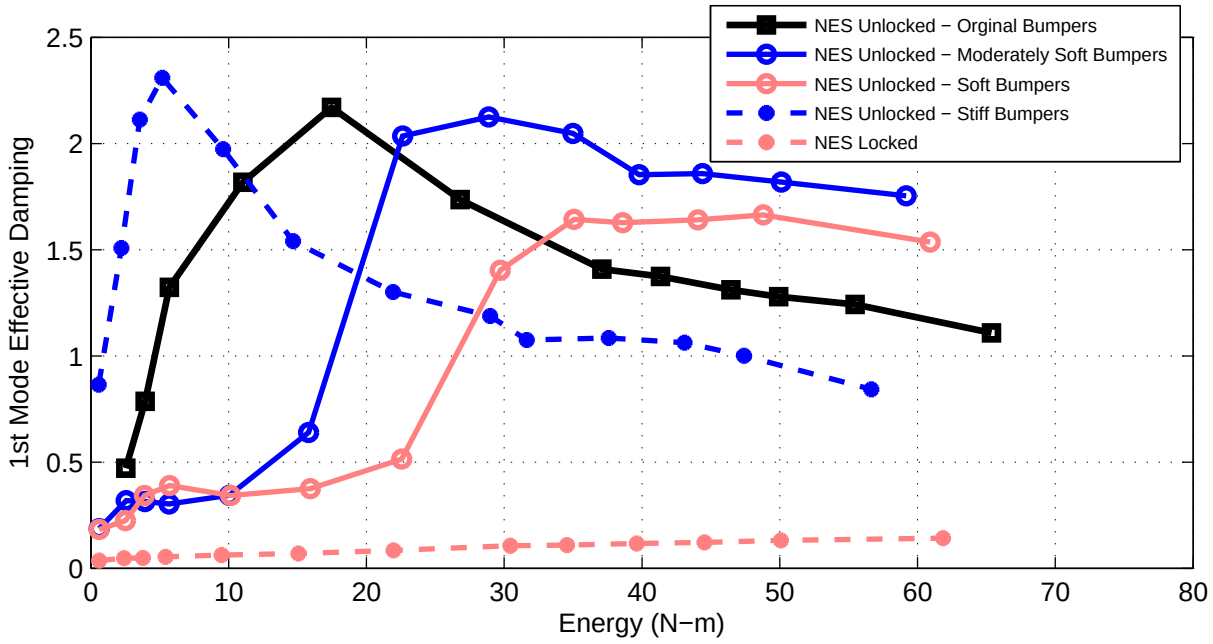

Figure 5-45. Effective damping vs. input energy for experimental results from the stiffness robustness study

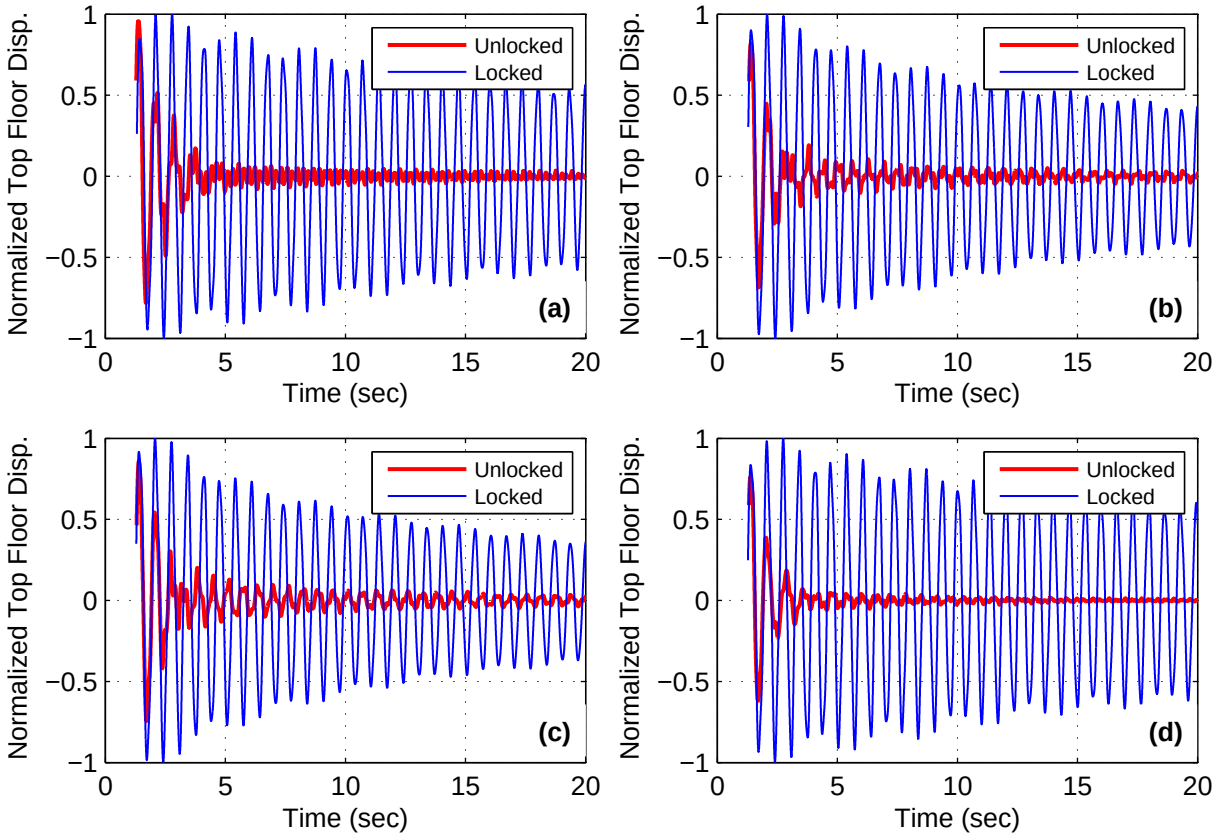

Figure 5-46. Normalized top floor displacement, unlocked vs. locked, at load level corresponding to peak effective damping for (a) original bumpers, (b) moderately soft bumpers, (c) soft bumpers, and (d) stiff bumpers

5.2.3.4.2 Robustness study – NES stage failure

In this study, the robustness of the medium-scale Type III NES to failure of one of its stages is investigated. This study is motivated by a desired to understand if the failure of one stage of the two-stage Type III NES would critically affect the effectiveness of the NES. While intermediate levels of functionality are possible in a damaged NES, as a simplification, in this study only complete stage failure is considered. To simulate this failure, locks used to prohibit the relative motion of the individual stages of the NES. These locks are the same mechanisms that have previously been used to investigate the behavior of the primary structure without the functional NES.

For this robustness study, the elastomeric bumpers used to produce the nonlinear restoring force in the medium-scale Type III NES are shown in Figure 5-12. This set of bumpers was used in the investigation study presented in Section 5.2.3.2.

The first mode effective damping of the primary structure calculated from the response of this structure to a range of scaling levels of the impulse-like ground motion considered in this section is shown in Figure 5-47. In this figure, the effective damping relationship is shown for four cases: both stages of the NES unlocked, a simulated failure of the top stage of the NES, a simulated failure of the bottom stage of the NES, and both stages of the NES locked. This figure shows that the failure of the top stage of the NES leads to an NES that is still very effective at mitigating the

response of the structure, but a significant shift in the energy level where optimal performance is observe. In contrast, in the event of the failure of the NES's bottom stage, a large reduction in peak effective damping is observed, in addition to a shift in the energy level of the peak effective damping point. The results observed here are likely due in large part to the differences in mass distribution that occur when the two stages fail When the top NES stage fails, the mass becomes incorporated into the bottom NES stage; however, when the bottom NES stage fails, the mass of that stage is no longer part of the NES.

In Figure 5-48, the top floor displacement when the NES is locked is plotted against the displacement when the NES is unlocked, when the failure of the top stage is simulated, and when the failure of the bottom stage is simulated. In each case, the ground motion used to produce these plots corresponds to the motion at which the peak first mode effective damping is observed (see Figure 5-47). So that a comparison of the peak performance of the system can be made, in each case the top floor displacement has been normalized such the maximum displacement of the structure with the NES locked is unity. With this normalization, it can be observed from Figure 5-48 that similar peak performance is achieve when the NES is unlocked and when the failure of the top stage is simulated; however, the peak attenuation provided in the case of bottom NES stage failure is much lower.

The results shown in this section highlight the particular importance of the functionality of the bottom stage of the Type III NES. Without the bottom stage functional, the NES becomes not only a non-optimal Type I NES, but also loses a significant portion of its mass. Consequently, in a realistic Type III NES implementation, a higher level of reliability would be desirable for the bottom stage of the NES.

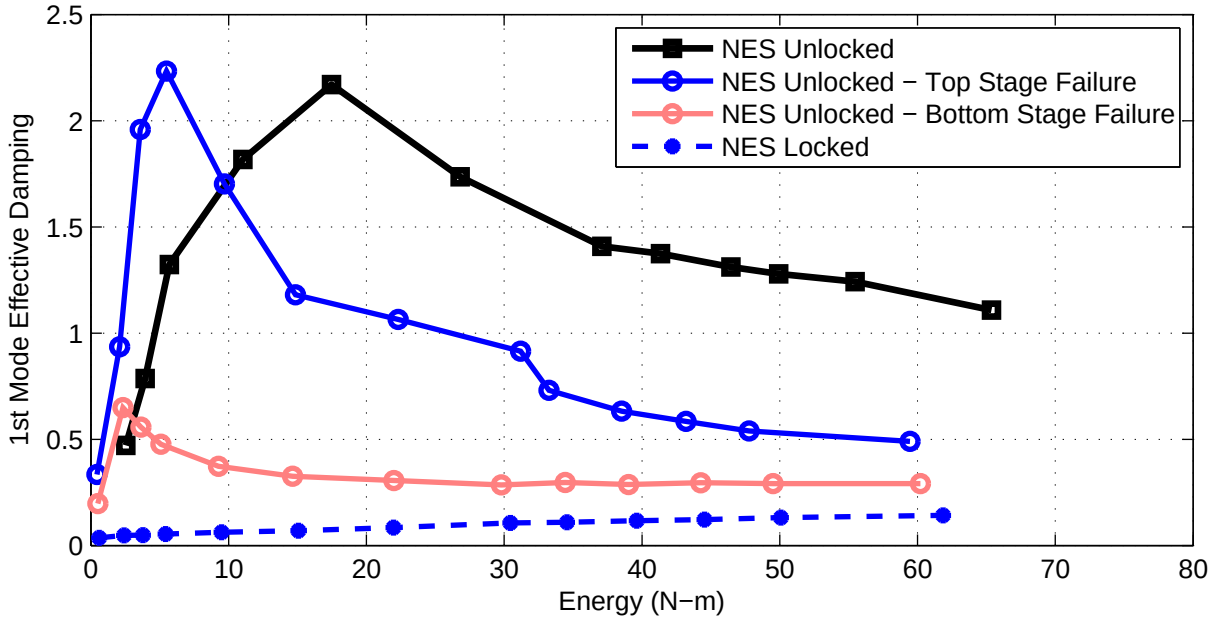

Figure 5-47. Effective damping vs. input energy for experimental results from the stage failure robustness study

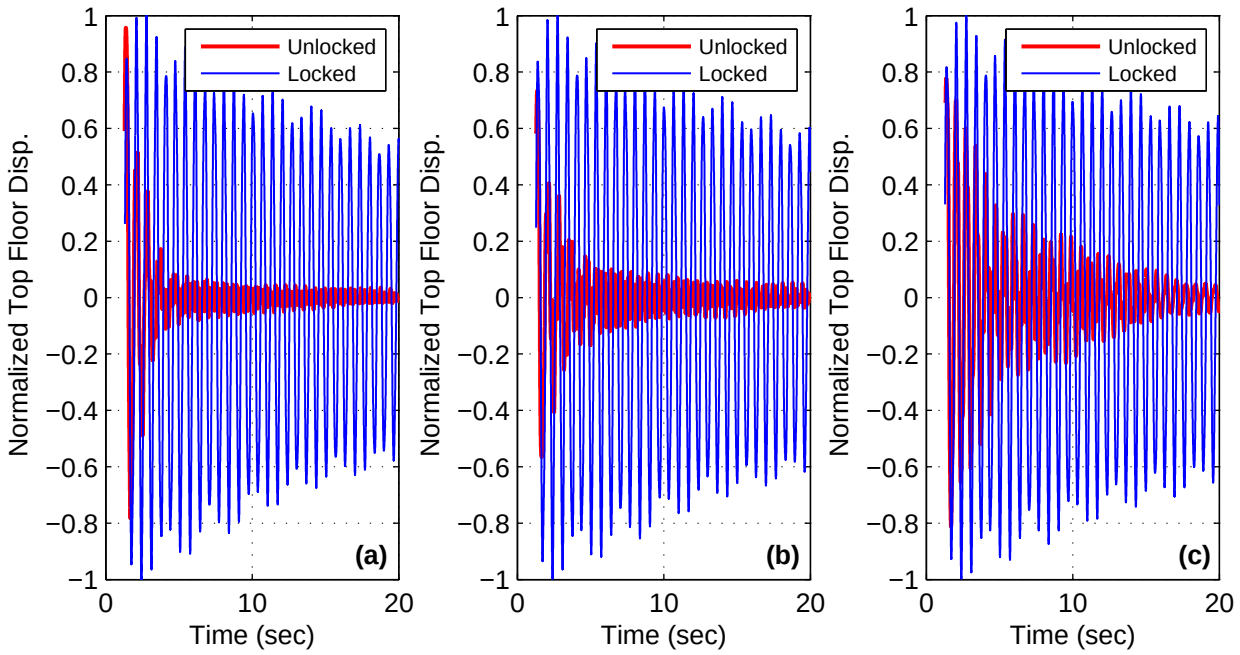

Figure 5-48. Normalized top floor displacement, unlocked vs. locked, at load level corresponding to peak effective damping for (a) no stage failure, (b) top stage failure, and (c) bottom stage failure

5.3 Summary

In this chapter the development and experimental investigation of several different types of NESs at small and medium-scales is presented. In the first section of this chapter, the development of small and medium-scale base structures is presented along with the development of a small-scale Type I NES, a small-scale Type III NES, and a medium-scale Type III NES. This development includes the world's first known realization of a Type III NES and the first realization of an NES utilizing elastomeric bumpers to produce its nonlinear restoring force. In the second section of this chapter, the experimental investigation of the performance of the small and medium- scale NESs is discussed. The results of these studies show that the NESs examined were capable of quickly attenuating the response of the base structures when subjected to shock-like ground motions. This rapid attenuation in response was shown to be largely due to targeted energy transfer, where input energy is transferred in nearly one way fashion to the NES where it is dissipated and by the NES facilitating energy transfer from low to high frequency modes in the primary structure, where dissipation occurs over shorter time scales. While the effectiveness of the NESs were shown to be load amplitude dependent, the NESs dramatically increased the first mode effective damping of the system over a reasonably wide range of amplitudes. For all of the NESs studied, reasonable agreement was found between the experimental results and numerical simulations using experimentally identified NES parameters.

DEVELOPMENT OF LARGE-SCALE BASE STRUCTURE AND SYSTEM OF NESs

No large-scale experimental investigation of the performance of NESs has been previously attempted; additionally, only a limited number of tests have been performed on structures employing multiple types of NESs. In this chapter, the development of a large-scale base structure which is specifically designed to serve as a platform to experimentally investigate the effectiveness of a system of nonlinear energy sinks is discussed. Additionally, in this chapter, the development of the associated system of NESs is presented, including their theoretical background and their physical realization. This system of NESs features a combination of Type I NESs, which employ a smooth essential nonlinearity, and single-sided vibro-impact (SSVI) NESs, which employ a sharp essential nonlinearity. This system of NESs was designed to be nonparasitic; thus, demonstrating the concept that the NESs can be incorporated into the floors of a structure in a manner such that there is no appreciable change in total structural mass due to the addition of the NESs.

The work in this chapter related to the development of this large-scale base structure and system of NESs is presented in six sections. In the first and second sections, the large-scale base structure developed and system of NESs are introduced. In the next section, the long-term instrumentation incorporated into the base structure will be discussed. In the fourth section, the modifications that were made to this structure during the blast testing, which is presented in Chapter 7, is discussed. The fifth section presents a review of the modal analysis done to determine the as-built modal properties of the large-scale base structure developed in this chapter. In the last section, a summary of the large-scale system development featured in this chapter is presented.

6.1 Nine-story large-scale base structure

The base structure used in this experimental study is shown in Figure 6-1. This structure, which was specifically developed for the large-scale investigation of a system of NESs, is 5.13 m tall and has a mass of approximately 11,000 kg. Currently, these dimensions make the structure the world's largest test bed for NES technology. Moreover, this structure is substantially larger in both height and mass than the previous largest test bed (Wierschem et al. 2012), which is the medium-scale test structure used in the investigation presented in Chapter 5. This large-scale structure consists of nine 2.74 m by 1.22 m steel plate floors and one 2.90 m by 1.22 steel base plate. The bottom seven floors are solid 3.81 cm thick plate, while the base plate and the top two floors are 4.44 cm thick. Additionally, the two top floor plates have cutouts in them to accommodate the NESs within the floors, thus alleviating the parasitic mass associated with earlier NES designs. A complete set of design drawings for this structure can be found in Appendix A.

An identical column layout is used for each floor of the base structure. As shown in Figure 6-1, this layout consists of eight columns arranged such that there is one bay in the short direction of the plates and three bays in the long direction. The columns are manufactured using high-strength steel to allow the building to elastically accommodate relatively large

deformations. All the columns in the structure are rectangular with the columns on the bottom floor being 66.04 cm tall with a 19.05 cm by 1.43 cm cross-section. The columns used on every other floor are 50.80 cm tall and have a 13.97 cm by 1.43 cm cross-section. Because of their shapes, the bending stiffness of the columns in one direction is much larger than in the other. The columns are oriented so that their weak direction is along the short length of the plates and in the direction of the blast.

Figure 6-1. Large-scale base structure equipped with system of NESs

Covering one of the long sides of the base structure is the cladding. During the blast testing, the structure is positioned such that the cladded side is nearest to the blast. When the blast occurs, the pressure load that builds up on the cladding is transferred to the structure. The cladding is also present for the shake table tests; however, the configuration of the cladding is different for the blast and shake table tests. These different cladding configurations are shown in Figure 6-2.

For the blast testing, the cladding is comprised of a series of overlapping 0.13 cm thick steel plates. The majority of these plates are 274 cm by 107 cm, which is long enough for the cladding sections to span the distance between two floors. Two overlapped sections of cladding are connected to the structure via a row of 21 bolts into the side of the floor slab at floor levels one through eight. At these levels the overlapping cladding plates are also connected to each other via two rows of bolts above and below the floor plate connection. At the top of the structure, the ninth floor, one section of cladding is connected to the floor plate with a row bolts. Additionally, this top plate is also folded over and connected vertically to the plate with bolts. At the bottom of the structure one section of cladding is also attached to the structure via a row of bolts. This bottom section of cladding is folded such that the cladding is directly connected to the foundation via a row of anchors embedded into the concrete.

The cladding configuration for shake table testing was less complicated. For this testing only one layer of cladding was used. This cladding was secured by bolts to the structure's floor plates and only overlap occasionally at the floor plate connections. For this cladding configuration, no bent over parts were used at the top or base of the structure.

Figure 6-2. Cladding on large-scale base structure during (left) blast testing and (right) shake table testing

In all cases, due to the relatively small mass of the cladding and its flexibility in the weak translational direction of the structure, the cladding's effect on the weak direction translational natural frequencies is minor. However, larger stiffness in torsion and strong translation mean that this cladding serves to increase, as compared with the structure without cladding, the torsional and strong direction translational natural frequencies.

During the blast testing, some failures of the connection between the cladding and the structure occurred. As described in Section 6.4, for the subsequent tests, the connection of the cladding was reinforced so that the cladding could still effectively transfer the pressure from the blast to the structure. No major effect on the modal properties of the structure resulted from this reinforcement.

6.2 System of nonlinear energy sinks

As mentioned in the previous section, the NESs in the base structure are positioned within cutouts built into the floor plates of the eighth and ninth floors. These cutouts and NES masses, which are nearly identical for both floors, are shown in Figure 6-3. As this figure shows, three NESs are built into each of the top floors; the side two NESs are Type I NESs and the center is a single-sided vibro-impact NES (SSVI NES). Conceptual models of these two types of NESs are shown in Figure 6-4. The idealized representations of both types of NESs are quite simple and consist of masses, springs, and dampers. The SSVI NES consists of a mass attached to a base structure through a viscous damping element and a weak linear spring element; for this type of NES the relative displacement of the mass is limited on one side by an impact surface that is connected to the base structure. The result of these impacts is discontinuity in the restoring force. These discontinuities are broadband events and, because of them, energy is scattered

throughout the structure, particularly to its higher modes (Al-Shudeifat et al. 2013). Additionally, as shown in Figure 6-4, the Type I NES is composed of a mass connected to a base structure through a viscous damping element and a smooth (no discontinuities in the restoring force) essentially nonlinear spring element. As a result of the smooth essential nonlinearity of this spring, the response of the NES is not dominated by a natural frequency, and the device can resonate with and participate in the transfer of energy from any mode of the base structure (Vakakis et al. 2008). The damping elements in the NESs help to quickly reduce the response of the base structure by dissipating the energy transferred to the NES when an NES moves relative to the floor to which it is attached. Furthermore, the transfer of energy to higher modes that occurs as a result of both types of NESs is beneficial because, at these higher frequencies, the energy in the structure can be naturally dissipated faster due to the reduced time scale.

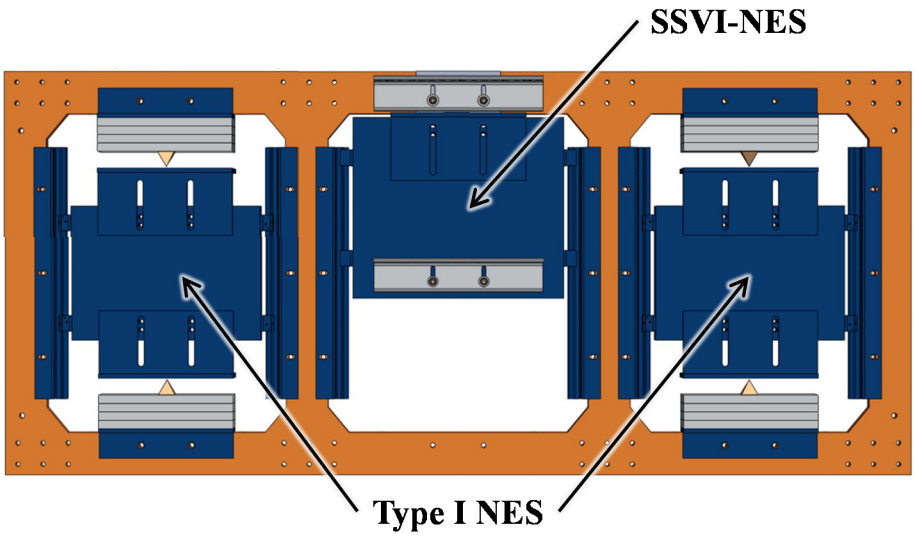

Figure 6-3. Eighth and ninth Floors with built in NESs

The physical realization of these NESs, shown in Figure 6-3, Figure 6-5, and Figure 6-6, all consist of solid steel masses that have Thomson SSUPB012 pillow blocks containing linear bearings mounted on their sides. These linear bearings allow the masses to move on sets of 1.91 cm round rails that are attached to the floor plate inside each cutout. The rails are positioned such that the masses move parallel to the short direction of the floor plate in the direction of the blast. In the center of the eighth and ninth floors are SSVI NESs. Each SSVI NES is coupled to the floor plate with a set of elastic cords. These elastic cords are positioned such that, at rest, the NES mass is in contact with one side of the floor plate. While unintended, there is a small amount of pretension in the elastic cords; the result of this pretension is that the NES mass is secured against the side of the floor plate under very low loading conditions. When the motion of the floor is large enough to exceed this small pretensioning force the SSVI NES moves relative to the floor. When this relative motion occurs, the elastic cords connecting the NES to the floor plate stretch and produce a restoring force that results in the NES mass being forced to collide with the floor with significant velocity. The result of this steel on steel collision is energy dissipation (the amount of which is related to the coefficient of restitution) and high frequency scattering of the remaining energy. The two NESs on each side of the floors shown in Figure 6-3

and Figure 6-6 are the Type I NESs. These NESs are coupled to the structure using specially shaped elastomeric bumpers that are mounted on each side of the NES and are placed in compression when the NES moves. The special shape of these bumpers provides an essentially nonlinear, and approximately cubic, restoring force to the NES masses. Each Type I NES on the eighth floor uses the same set of bumpers, but the Type I NESs on the ninth floor use a different set. Each of the NESs in this system has its own locking mechanism; consequently, tests can be performed with the NESs locked (prevented from moving relative to the floor) or unlocked (free to move).

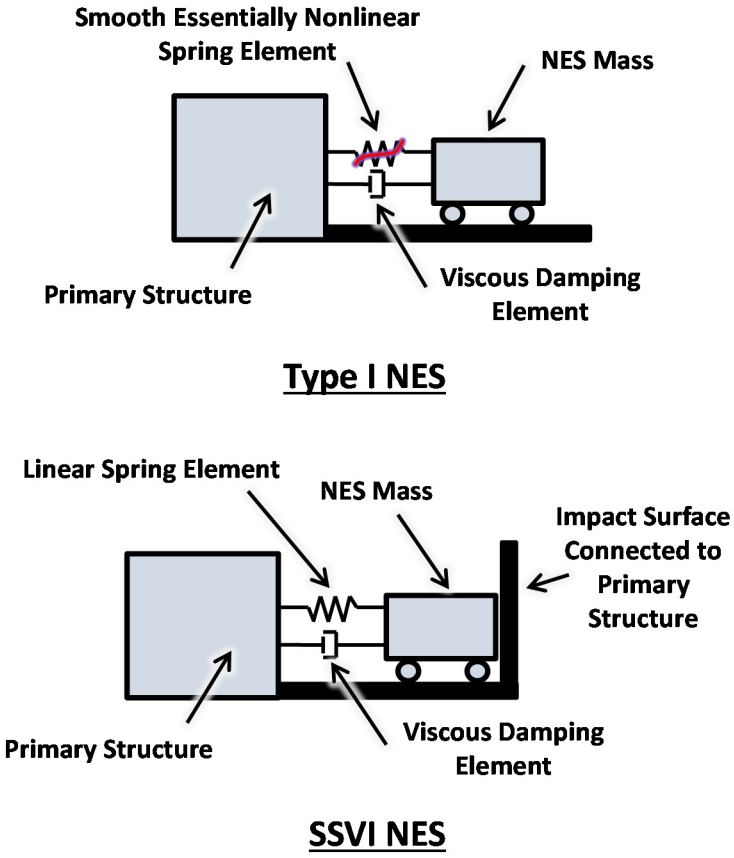

Figure 6-4. Conceptual models of the Type I and SSVI NESs

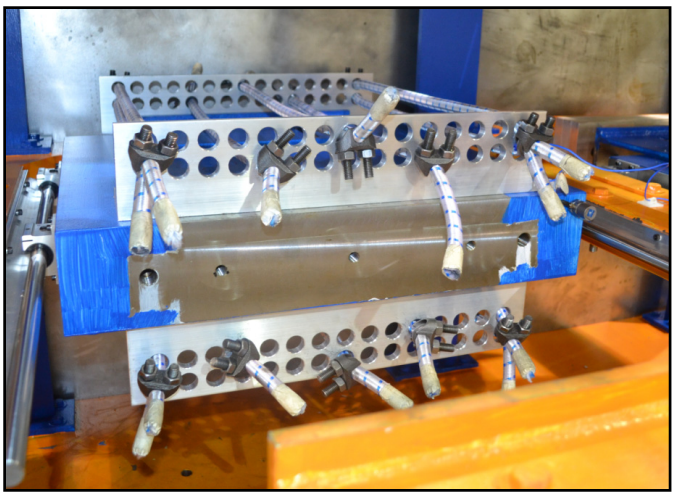

Figure 6-5. Physical realization of SSVI NES in large-scale base structure

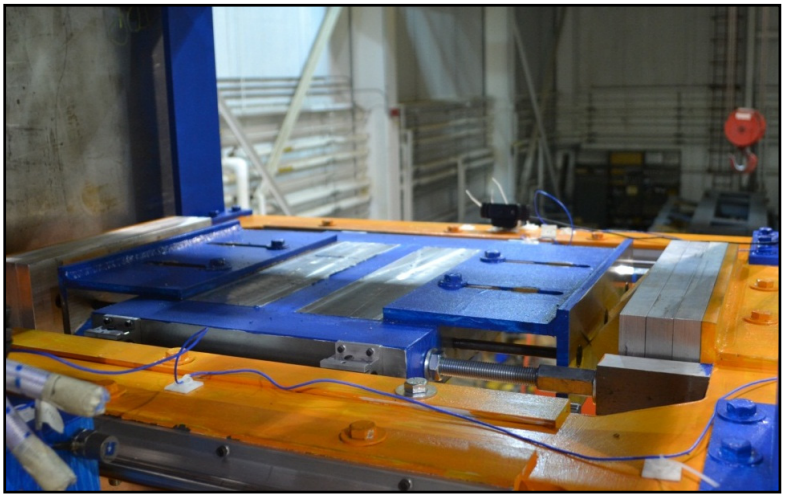

Figure 6-6. Physical realization of Type I NES in large-scale base structure

Using an estimate of the energy imparted to the structure from an idealized blast as the loading, the parameters of the NESs were determined through an optimization procedure. Here, the goal of the objective function was to maximize a measure of the apparent damping in the first mode; i.e., the effective damping (Sapsis et al. 2012). The stiffness parameters for the NESs that resulted from this analysis, as well as the mass percentage of each NES, can be found in Table 6-1. These stiffness parameters were used to design the elastomeric bumpers for the Type I NESs and elastic cords for the SSVI NESs.

Table 6-1. Design values of mass and stiffness for NESs

	Mass (% of Structure Total Mass)	Design Stiffness Coefficient (N/m)	Design Stiffness Exponent
Eight Floor Type I NES	1.5	7.56×10^8	3
Ninth Floor Type I NES	1.5	1.07×10^8	3
Eight Floor SSVI NES	3.5	14546	1
Ninth Floor SSVI NES	3.5	12219	1

6.3 Long term instrumentation

Much of the instrumentation used in the testing of this structure is changed based on the facility the tests are being performed at and the requirements of each test; however, the one group of permanently installed instrumentation on the structure are strain gages on the first story columns. These strain gages are YEFLA-5-5LT gages manufactured by the Tokyo Sokki Kenkyujo Co. These unidirectional strain gages were placed on each of the eight first floor columns. As shown in Figure 6-7, these gages are located approximately 7.6 cm from the end of the column and at the column's mid-width. At these locations the surface of the columns has been thoroughly prepared with a combination of grinding, sanding, and acid/base washing. Figure 6-8 shows the first floor columns after strain gage application, but before installation in the structure and painting. The large number of strain gages installed on these columns are not intended to all be measure in every test, but were all installed to give flexibility in the columns chosen for strain measurements and to provide redundancy against failure of gages. With strain measurements from just a few gages positioned at different locations, the strain due to both translational and torsional motion can be measured. Furthermore, with these strain measurements the real structural demand on the first floor, which in many cases is the critical point in a structure, can be measured and compared.

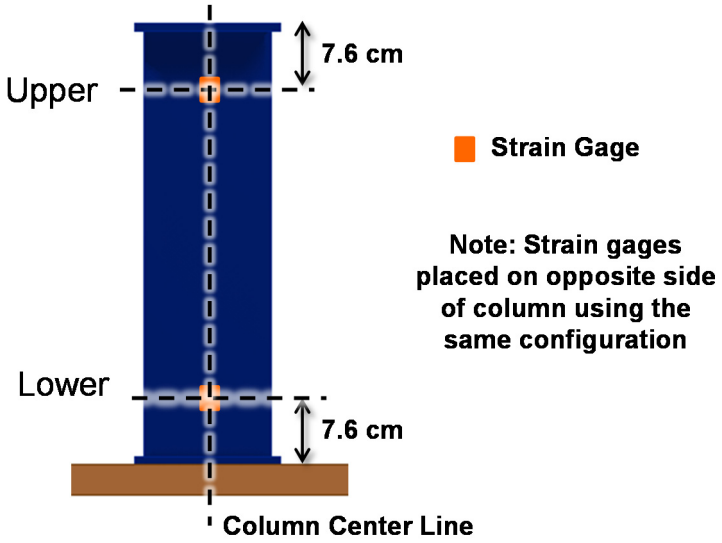

Figure 6-7. Location of strain gages on first floor columns of large-scale base structure

Figure 6-8. First floor columns with strain gages attached

6.4 Modifications to structure during blast testing

During the blast testing of this structure, which is discussed in detail in Chapter 7, damage to the cladding was observed after all of the tests; however, after some tests, this damage was more severe. The main source of damage to the cladding was the failure of the connection of the cladding to the floors of the structure. An example of this damage is shown in Figure 6-9. The cladding is used to accumulate the blast pressure on the structure; thus, the connection of the cladding to the floor plate is required to adequately transmit the resulting load to the structure. Consequently, severe damage to the cladding connection to floors needed to be addressed before resuming testing.

Figure 6-9. Example of failed cladding to floor plate connection observed during blast testing

To address severe damage to the cladding connection, two on-site modifications to the structure were implemented in between blast tests. The first modification was to repurpose the plates that the orifice of the cladding pressure gages were mounted to. These plates overlapped with the cladding and were connected to a bracket holding the remainder of the pressure gage. Furthermore, this bracket was attached to the structure's floor plate. To allow these plates to better participate in connecting the cladding to the structure, larger high-strength bolts were substituted in the connection of the mounting plates to their brackets, with the cladding sandwich in between. Additionally, the top and bottom of the mounting plates were removed to prevent dislodging of the mounting plate due to flexure of the cladding. An example of the original and modified pressure gage mounting plates are shown in Figure 6-10. This modification was applied to the pressure mounts on the first, fifth, and seventh floors.

The second modification was to sandwich the cladding in between the floor plate and a supplemental piece of long horizontal tube steel. Rods coming off of this tube were connected in the back of the floor plate. These rods were put into tension to secure the tube into place. An example of this modification, which was applied to the second and third floors, is shown in Figure 6-11.

With the modifications presented above, the cladding on the structure performed as an effective loading surface for the five blasts that the available resources allowed; however, after the last and largest blast, there were multiple additional failure points of the cladding.

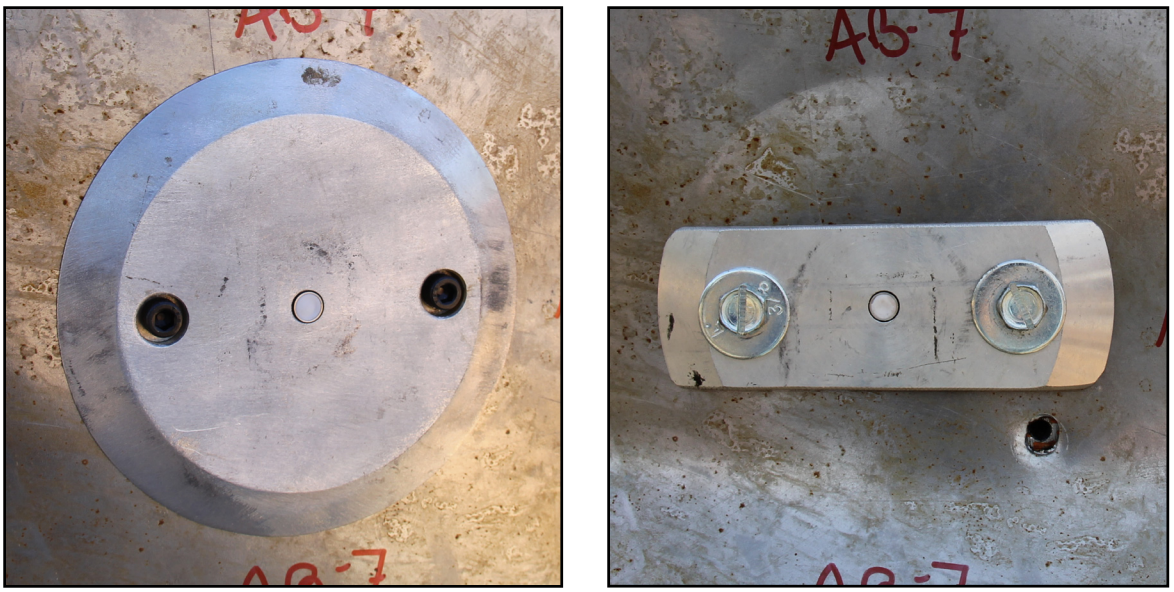

Figure 6-10. Pressure tap mounting (left) original configuration and (right) modified to reinforce connection of cladding to floor plate

Figure 6-11. Tied back tube used to reinforce cladding to floor plate connection

6.5 Identification of linear system

To determine the as-constructed modal parameters of the structure, instrumented hammer testing and sine-sweeps, via shake table excitation, were performed. For this testing the NESs were locked and the structure can be considered to be linear. As a result of this testing, the natural frequencies of the structure in the weak direction were determined to be 1.74, 5.37, 9.10, 12.72, 15.96, 18.95, 21.63, 23.92, 25.48 Hz. Additionally, the torsional natural frequencies of the structure less than 30 Hz were determined to be 5.81, 18.16, and 29.36 Hz. A transfer function of the translation response of the structure developed from one of the sine-sweep tests is shown

in Figure 6-12. The experimentally identified mode shapes determined from this transfer function are shown in Figure 6-13.

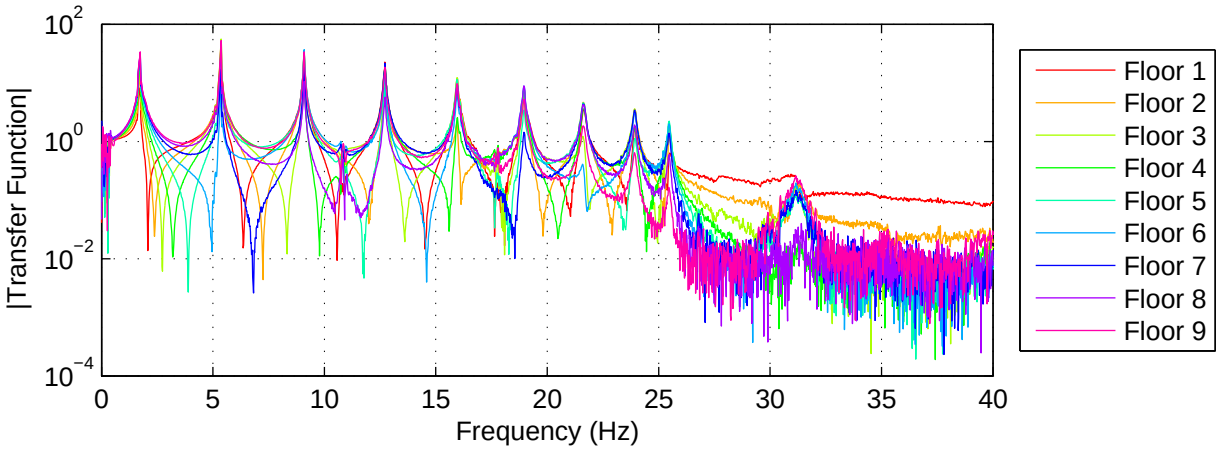

Figure 6-12. Magnitude of ground acceleration to floor acceleration transfer function developed from sine-sweep test results

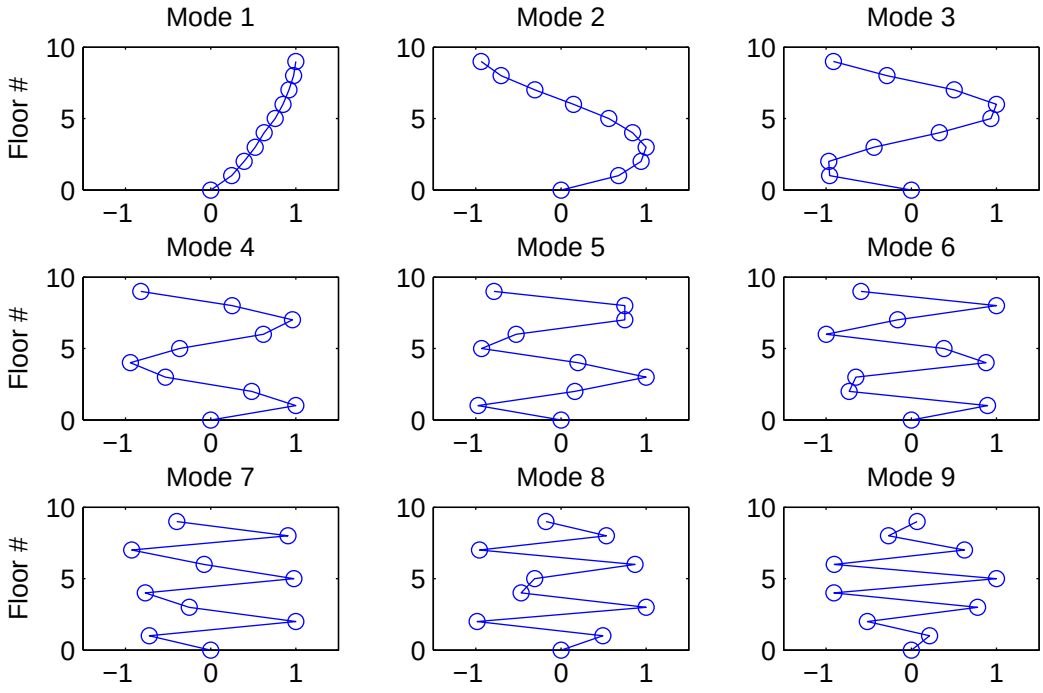

Figure 6-13. Experimentally obtained translational mode shapes of the large-scale structure

6.6 Summary

In this chapter, the development of a large-scale base structure which is specifically designed to serve as a platform to experimentally investigate the effectiveness of a system of nonlinear energy sinks is discussed. Additionally, in this chapter, the development of the associated system of NESs is discussed, including their theoretical background and their physical realization. This system of NESs features a combination of Type I NESs, which employ a smooth essential nonlinearity, and single-sided vibro-impact (SSVI) NESs, which employ a sharp essential nonlinearity. Currently, this structure and NESs represent the world's largest test bed for NES technology. After the introduction of the system of NESs, the long-term instrumentation incorporated into the base structure and the modifications that were made to the structure in response to blast damage were discussed, as well as, a review of the modal analysis performed on the structure.

EXPERIMENTAL INVESTIGATION OF NES PERFORMANCE USING LARGE-SCALE BASE STRUCTURE SUBJECTED TO REAL AND SIMULATED BLAST LOADING

This chapter investigates experimentally the performance of the system of NESs featured in the large-scale structure developed in Chapter 6. For this experimental investigation, the structure will tested using blast loading, impulse-like shake-table-produced ground motion, and sine-sweep ground motion. Additionally, as the base structure will be designed to remain elastic and the ground motion is readily repeatable, shake table testing of the structure will provide the opportunity for a large number of experiments; consequently, investigation of the performance will be done across a wide range of load scales. This data will enable an in-depth investigation of how the performance of the system of NESs varies with the level energy imparted into the system from the ground motion. Furthermore, with tests utilizing the complete system of NESs, alongside tests where only part of the system of NESs is utilized, the synergistic effects of the multiple types of NESs acting in combination will be investigated.

7.1 Simulated blast testing

Simulated blast testing of the structure outlined in Chapter 6 was performed using the Triaxial Earthquake and Shock Simulator (TESS) shake table at the US Army Corps of Engineers Construction Engineering Research Laboratory in Champaign, IL (U.S. Army Engineer Research and Development Center 2008). This shake table was chosen for this work due to its proximity to the University of Illinois and its large size; the table is 3.66 m by 3.66 and can support payloads in excess of 50000 kg. Additionally, due to its design with shock loading in mind, TESS has large force capabilities and frequency range, which make this shake table more than capable of delivering the ground motions desired for this testing.

Before the experimental results obtained with this table are discussed, the prototype ground motion used for the blast simulation is introduced, and the instrumentation on the structure is discussed.

7.1.1 Prototype ground motion

As the purpose of this study is to investigate the effectiveness of the system of NESs at mitigating the effects of impulsive loads on the base structure, a suitable ground motion for this task was required. To develop this ground motion, a numerical model of the structure, updated based on the linear experimental parameter identification discussed in a Chapter 6, was used. With this model, the response of the structure when subjected to a uniform impulsive load in the weak direction of the structure was simulated. From this response and further simulations, a ground motion was developed to match the impulsive load response in both amplitude and modal energy distribution. Additional information on the development of the ground motion for this simulated blast testing can be found in Chapter 4. The resulting basis ground motion used as an input for the experiments in this study can be seen in Figure 7-1 along with the corresponding

experimentally measure ground acceleration using the TESS shake table. To investigate the response of the structure at different load levels, this desired basis ground motion can be scaled accordingly.

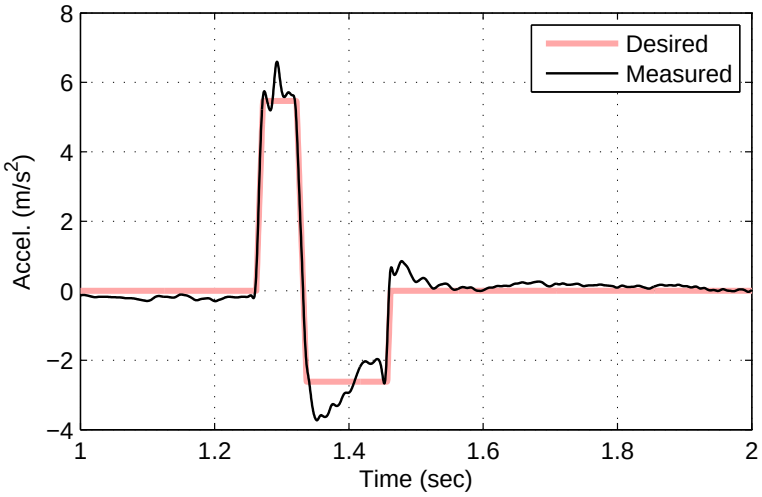

Figure 7-1. Basis ground motion

Before beginning testing, a routine developed by the manufacturer of the TESS shake table control system, designed to improve the tracking of the shake table, was performed. In this routine, measurements of the shake table response were acquired for individual sine-sweeps performed in each of the shake table's six degree-of-freedom. From these measurements, a compensation matrix that was developed is automatically applied to each desired ground motion input into the system. The effectiveness of the compensation routine can be seen in Figure 7-1; the desired and achieved motions match reasonably well.

7.1.2 Instrumentation

In order to measure the response of the system due to the ground motion, the structure and NESs were instrumented with accelerometers. The accelerometer layout used for this testing is shown in Figure 7-2. Accelerometers oriented in the direction of the shale-table-produced ground motion were placed on each NES, and two were placed at each floor. With the two acceleration measurements on each floor at different locations, the torsional response of each floor can be calculated. Moreover, with this information and the mode shapes of the structure, the acceleration data is sufficient to calculate the translational and torsional responses of the structure in modal coordinates. As shown in Figure 7-2, different accelerometers were used for this testing, including PCB models 353B33, 353B01, 353B03, 353A, and 3701G3FA3G as well as Endevco models 7290A and 7490E. This wide array of accelerometers was necessary due to the large number needed and the diverse set of demands anticipated at different locations on the structure. To best capture the response of the structure, higher capacity models were positioned where the highest accelerations where anticipated, which include the SSVI NESs and the floors with NESs.

In addition to acceleration measurements, the strain in the first floor columns was also measured. General information regarding these strain gages and their application can be found

in Chapter 6. With these strain measurements the real structural demand on the first floor, which in many cases is the critical point in the structure, can be measured and compared.

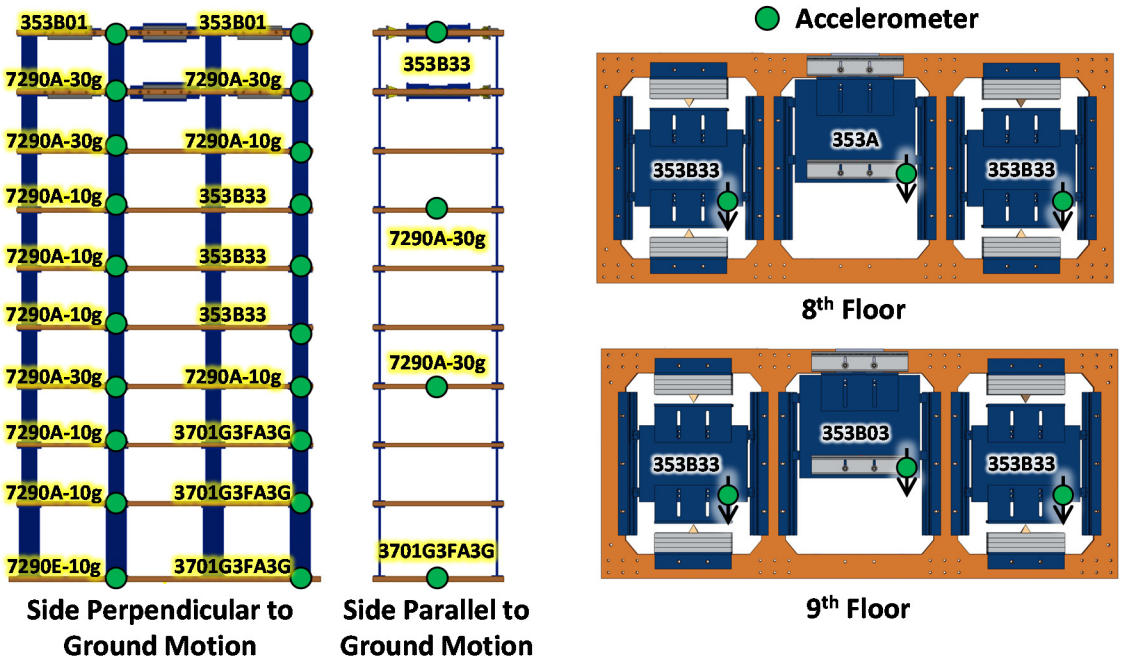

Figure 7-2. Accelerometer layout used for simulated blast testing

7.1.3 Experimental results

Using the TESS table, the structure was subjected to the ground motion shown in Figure 7-1. To investigate the effectiveness of the system of NESs, tests using this ground motion were performed with the NESs both unlocked (free to move) and locked. The calculated displacement response of the seventh floor relative to the shake table is shown in Figure 7-3a and c. The displacement records shown in this figure were calculated from the acceleration response using a combination of numerical integration and low and high pass filtering to suppress noise in the data and prevent unrealistic drift in the signal (Boore and Bommer 2005). Figure 7-3a and c shows that, when the NESs are unlocked, the response of the structure is quickly attenuated, with the response reduced to a small fraction of the locked system response after only a few seconds. Careful inspection of the unlocked response shows that after several cycles the structure is nearly completely quiescent with only the higher frequency content remaining. This phenomenon can also be seen in the wavelet spectrum of the acceleration response of the seventh floor, which is shown in Figure 7-3b and d. The wavelet spectrum is an advantageous way of examining a non-stationary signal as this tool shows how the frequency content varies with time (Labat 2005). These figures show that, in the case when the NESs are locked, the acceleration response is dominated by the first mode and contains little additional higher mode behavior; however, when the NESs are unlocked the response contains some quickly diminished first mode content that is dominated by higher mode behavior.

Figure 7-4 presents the time histories and wavelet spectra of the acceleration response of the ninth floor NESs when the structure is subject to the basis ground motion. This figure shows that

the NESs can experience high accelerations during the test. Particularly high asymmetric accelerations are observed in the response of the SSVI NES due to the impacts that occur in one direction only. Examining the wavelet spectra reveals the broadband nature of the NESs which allows them to interact with multiple widely spaced modes of the structure. In the case of the SSVI NES, the broadband frequency response of the NES occurs in bands that correspond to the impacts in the acceleration time history. For the Type I NESs, the broadband frequency response is more continuous due to their smooth nonlinearity. Both the high accelerations and broadband behavior of the NESs last just for a few seconds in this test after which the response of the structure is attenuated enough that the NESs are no longer excited.

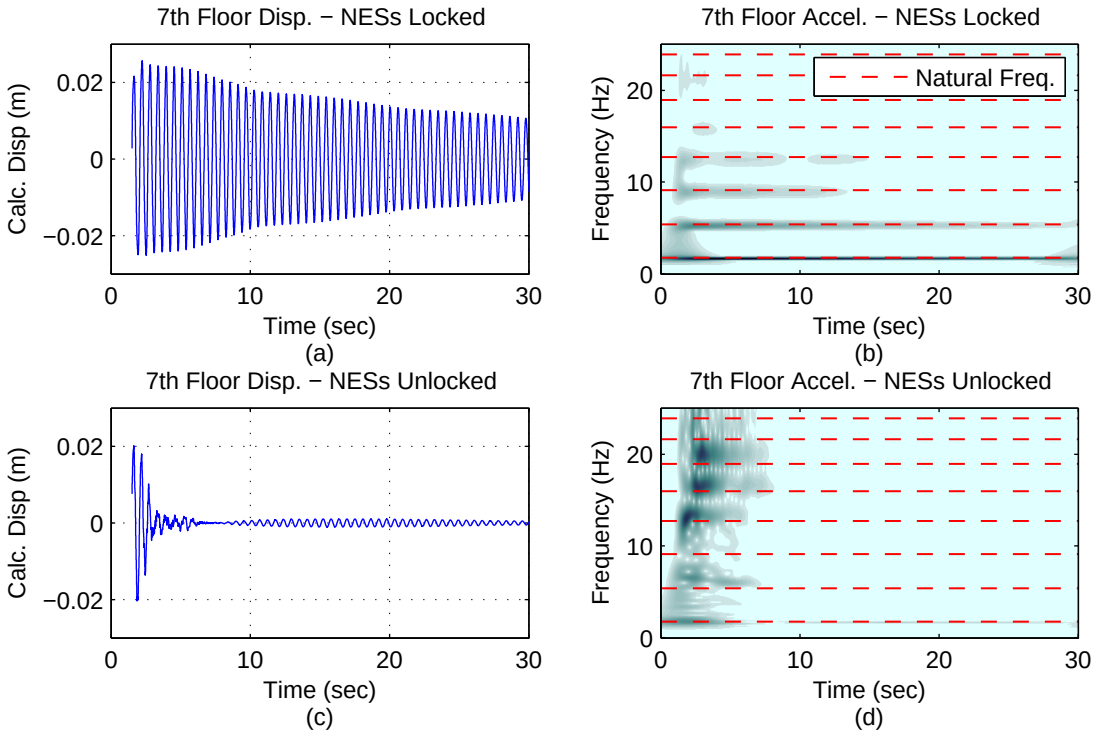

Figure 7-3. Response of the seventh floor of the base structure a) Locked case, calculated displacement, b) Locked case, acceleration wavelet spectra, c) Unlocked case, calculated displacement, and d) Unlocked case, acceleration wavelet spectra

Examining the acceleration and displacement time histories can give meaningful insight into the response of the structure; however, these measures do not directly correspond to the structural demand on the system. Unlike other response measures, examining the strain in the first floor columns does give insight into the demand due to the proportionality of this strain with the column moment demand. Accordingly, the measured strain of one of the interior first floor columns during tests with the NESs locked and unlocked is shown in Figure 7-5. Like the displacement and acceleration responses, when the NESs are unlocked the strain in the first floor column is rapidly reduced compared to the case with the NESs locked. Furthermore, this figure also shows the transition with the NESs unlocked of the structure's response from first mode dominated to predominately higher mode behavior. Perhaps most importantly, Figure 7-5 also shows that with the NESs unlocked a substantial reduction in maximum strain occurs.

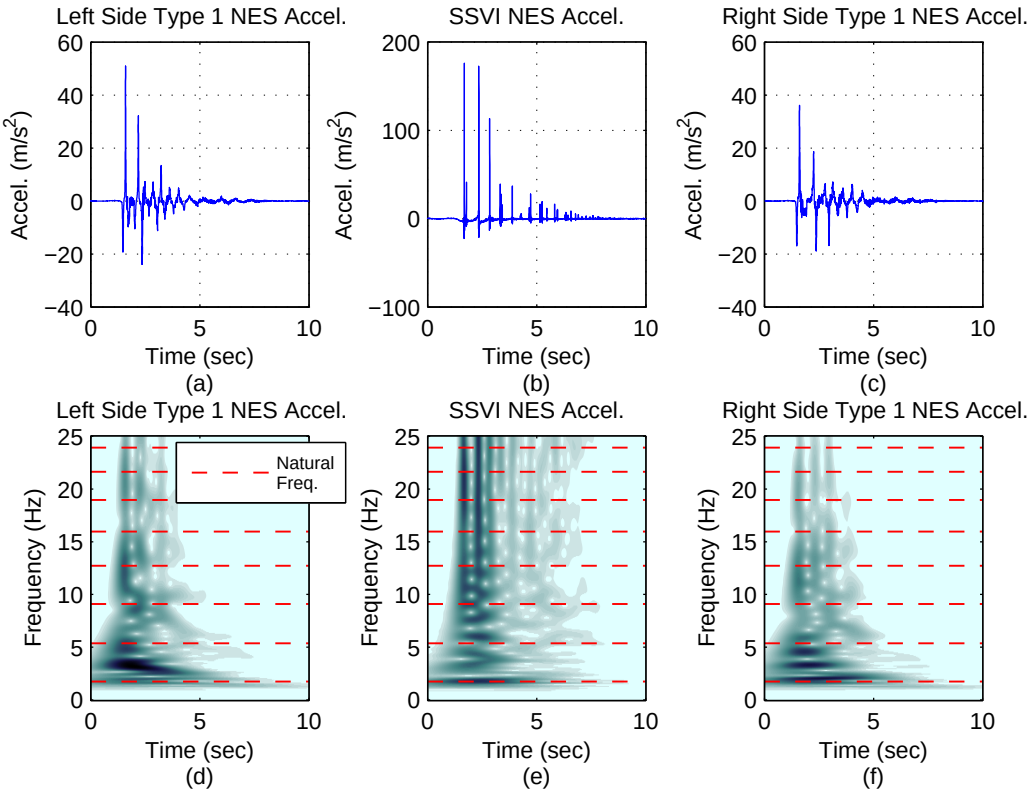

Figure 7-4. Acceleration response of the ninth floor NESs (a) Left side Type I NES time history, (b) SSVI NES time history, (c) Right side Type I NES time history, (d) Left side Type I NES wavelet spectra, (e) SSVI NES wavelet spectra, and (f) Right side Type I NES wavelet spectra

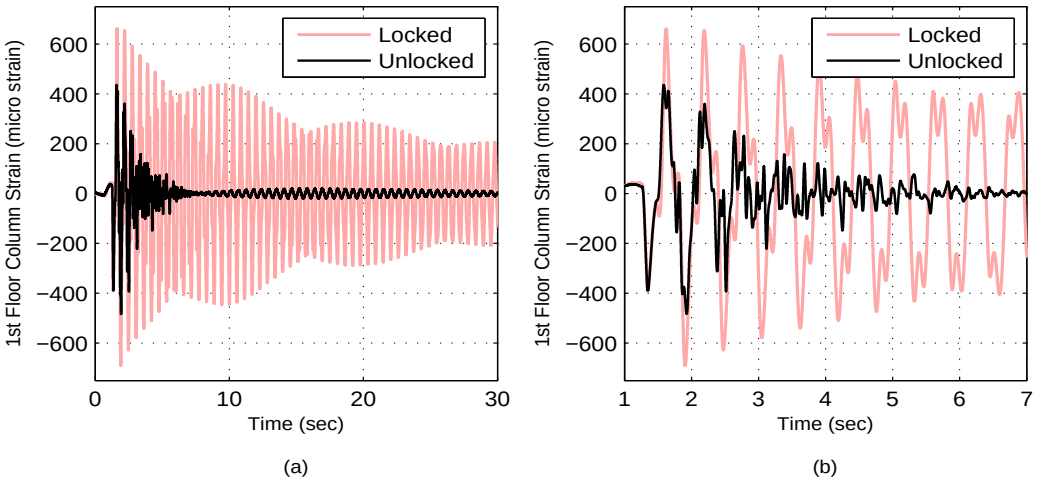

Figure 7-5. First floor column strain (a) Full view (b) Zoomed view

Figure 7-3 through Figure 7-5 show the capability of the system of NESs to quickly reduce the response of structure at the particular load level specified by the basis ground motion. In order to shows the NESs are robust to changes in load, additional tests were performed across a range of load levels. These levels correspond to a scaling of the basis ground motion, shown in Figure 7-1, and vary from 50% to 200% of the basis. Using the strain response to these ground motions, two performance measures were calculated comparing the cases when the NESs are unlocked and locked. The first measure is the reduction in peak first floor column strain; the second is the reduction in the RMS of the strain time history calculated using thirty seconds of data. The resulting measures over the range of ground motions tested are shown in Figure 7-6. As shown, a large reduction in peak and RMS strains is observed over the entire range of ground motions. Additionally, this figure shows that the maximum reduction in both of these measures occurs at the 100% ground motion level, which is the load level the system was designed at. At this level, with the NESs unlocked, the peak and RMS first floor column strains are reduced by 30.0% and 74.8%, respectively.

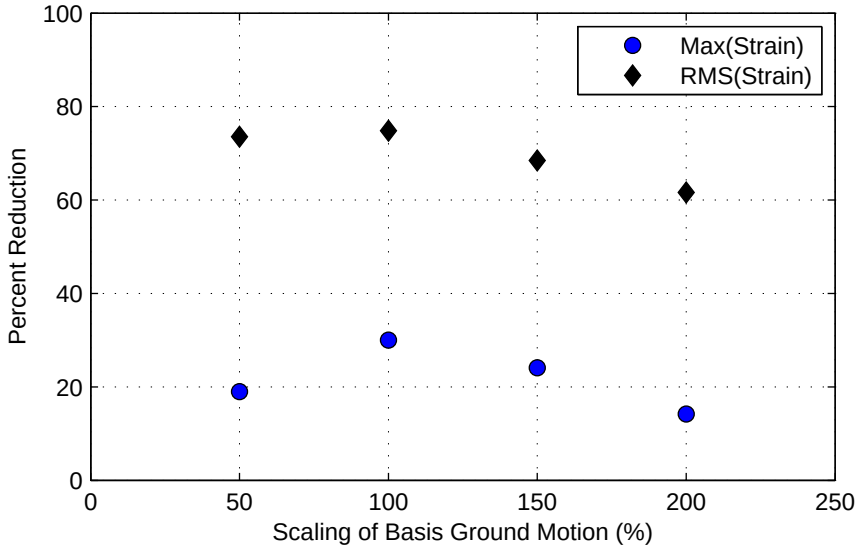

Figure 7-6. Percent reduction in maximum and RMS first floor column strains across a range of scaled bases motion for NESs unlocked and locked

7.1.4 Additional Plots

Additional plots showing the response of the structure and system of NESs to different scaling levels of the prototype blast simulation ground motion can be found in Appendix D. Additionally, in this appendix, the response of the structure is also shown for all four of the different configurations of the system of NESs (all NESs locked, Type I NESs unlocked, SSVI NESs unlocked, and all NESs unlocked).

7.2 Blast testing

In addition to simulated blast loading, the large scale 9-story structure equipped with the system of NESs introduced in Chapter 6 was tested using live explosives. The objective of this testing was to experimentally investigate the ability of the system of NESs to quickly eliminate the response of the structure when subjected to an actual blast loading. These tests were performed

at the US Army Corps of Engineers Big Black Test Site. This test site is affiliated with and located near the US Army Corps of Engineers Engineer Research and Development Center in Vicksburg, Mississippi. At the site, the structure is connected, via the base plate, to a concrete pad for testing. The mass and dimensions of this pad are sufficient to ensure that during the blast the base of the structure remains secured against movement. In this section, the testing is discussed, including the design of the explosive charge, the instrumentation utilized, and the experimental results.

7.2.1 Charge design

Blast testing of the nine-story structure was performed using air bursts of the high explosive C-4. For these tests the structure was oriented such that its cladding faced toward the blast. With this orientation, the energy introduced into the structure from the blast resulted in motion of the structure in its weak direction, as intended.

The objective of this testing was to investigate the ability of the system of NESs to quickly attenuate the response of the structure due to a general blast loading. Consequently, the goal of the charge design was to provide a nearly uniform pressure impulse to the face of the cladding. When designing the charges, the variables considered were the standoff distance (the horizontal distance of the charge from the structure), the height of the charge, and the weight of the charge. In general, when the standoff distance is increased, the uniformity of the pressure load on the structure also increases; however, with increased standoff distance, the pressure and resulting impulse on the structure is reduced. Consequently, if the standoff distance of a blast is increased, the charge weight must also be increased to maintain the same total average impulse on the structure.

Taking into account the variables associated with the charge configuration, the constraints on charge size due to the timing and location of the test program, and the geometry of the base structure, the software UrbanFx, an extension of the BlastX software published by the US Army Corps of Engineers (Britt et al. 2001), was used to simulate the effects of the blast on the structure. With these simulations and a set of desired levels of average pressure impulse, the charge configurations shown in Table 7-1 were designed. As seen from this table, the standoff distance of the blast is quite small in all cases, because of the limitation on charge size at the test site. Additionally, Table 7-1 also shows that the first two designs feature one explosive charge positioned at roughly the mid-height of the structure; however, the last, which produces the largest average impulse on the structure, is designed using three separate charges. The reason for dispersing the charge along the height of the structure is the large charge weight required to achieve the desired average pressure impulse; without distribution of the charge, the local effects closest to the blast would be unacceptably high.

In addition to calculating the average pressure impulse on the structure, BlastFx provides the pressure impulse and maximum pressure at points along the cladding face. Contour plots of the pressure impulse and maximum pressure on the structure for the configurations listed in Table 7-1 are shown in Figure 7-7, Figure 7-8, and Figure 7-9. These contour plots show that, while the design goal of the blasts was to provide a uniform pressure impulse on the face of the structure, the resulting charge configurations deviate significantly from uniformity. Additionally, by comparing Figure 7-9 with Figure 7-7 and Figure 7-8, we see the increase in complexity that results from the three charges in the 620 kPa-msec blast configuration; however, the multi-charge configuration results in a relative increase in uniformity of the loading. Despite the non-uniformity in loading for all the configurations, these blasts are adequate because, while

not perfectly uniform, they result in a large pressure impulse spread across a significant portion of the cladding.

Table 7-1. Charge configurations

Charge #	Average Pressure Impulse (kPa-msec)	Standoff (cm)	Height of Burst (cm)	C-4 Charge Weight (kg)
1	106	213	295	0.54
2	209	213	295	1.40
3	620	173	76, 295, 404	1.27, 1.27, 1.27

To produce the standoff distances and heights for the charges shown in Table 7-1, a system of rigging towers and cords was used to suspend the charges. Adjustable lengths of cord were attached to the charge and strung between two of the rigging towers to control the height of burst, while an additional cord attached to the charge and a third tower was used to control the standoff distance. The rigging towers, which are shown in Figure 7-10, were constructed of steel tubing, had a heavy base and a small profile, which allowed them to survive the blast undamaged. The final component of the charge configuration, the weight of the charge, was simple to produce as the pliability of the C-4 made shaping into a sphere of exact weight straightforward.

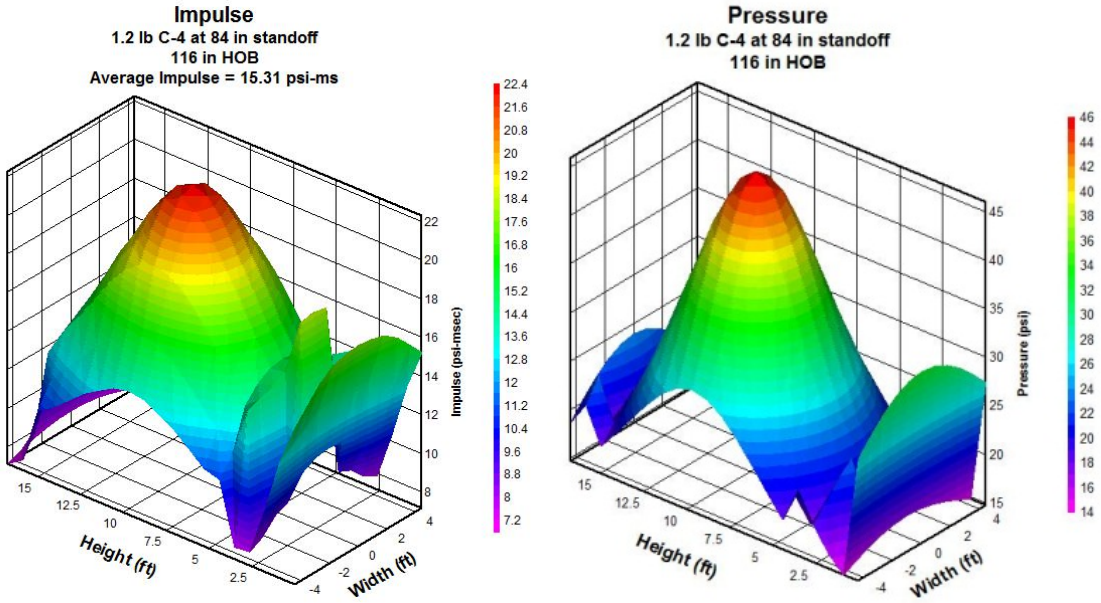

Figure 7-7. Charge # 1 - cladding pressure impulse and maximum cladding pressure contour plots

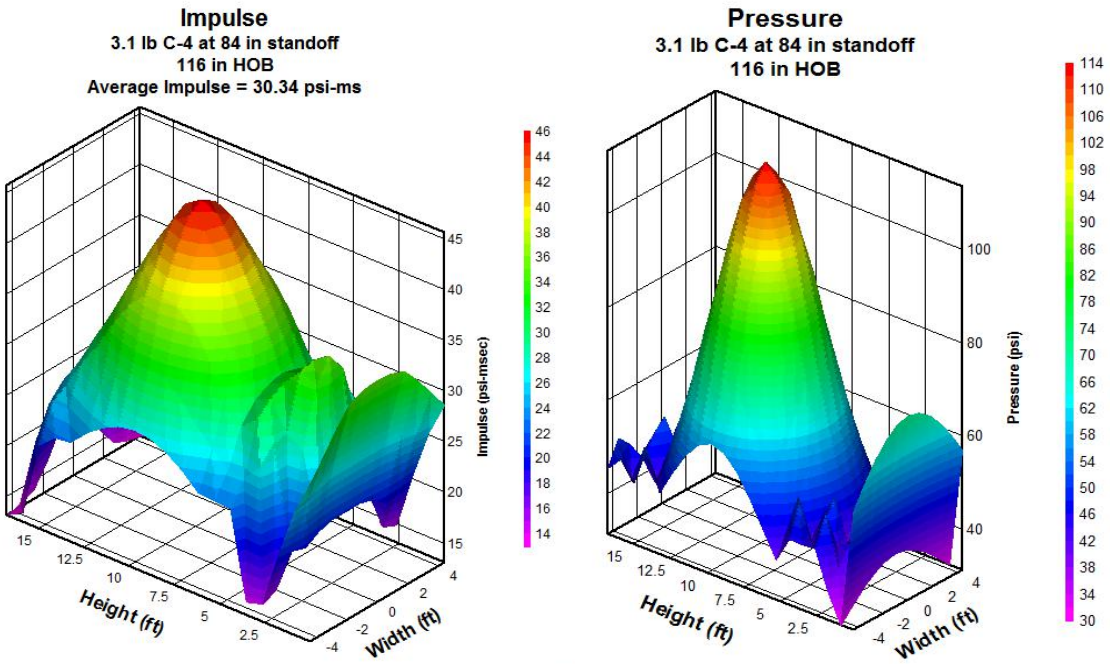

Figure 7-8. Charge # 2 - cladding pressure impulse and maximum cladding pressure contour plots

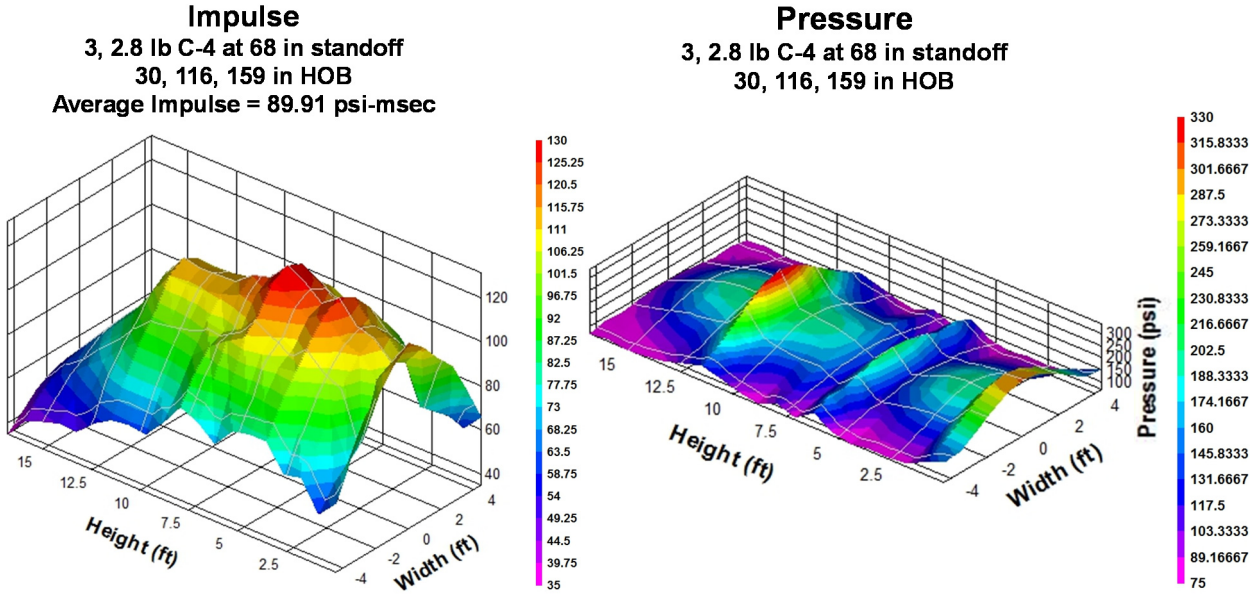

Figure 7-9. Charge # 3 - cladding pressure impulse and maximum cladding pressure contour plots

Figure 7-10. Base Structure and rigging towers set up for 620 kPa-msec charge

7.2.2 Instrumentation

Various sensors were utilized to record the loading and response of the structure during the blast testing, including accelerometers, pressure gages, strain gages, and displacement transducers. The accelerometers were PCB model 353B33, Endevco model 7264-200, and Endevco model 7264-2000. The layout of the accelerometers is shown in Figure 7-11. Most of the accelerometers were oriented to measure the response of the structure in the direction of the blast. Accordingly, accelerometers were placed on every floor of the structure and on each of the NESs. At locations of anticipated high acceleration, such as the SSVI NESs and the floors with NESs, the accelerometer models with higher maximum acceleration capacity were utilized. In addition to acceleration, direct measurements of the motions of the first and third floors were obtained with displacement transducers.

As in the previous blast simulation tests, the strain in the first floor columns was measured. With these strain measurements the actual structural demand on the first story, which is often a critical point in the structure, can be determined and compared.

To measure the loading on the cladding from the blast, the structure was instrumented with multiple pressure gages. These gages were attached to mounts directly connected to floor plates of the structure. To allow the gage to measure the pressure on the face of the cladding, the head of the gage extended through a small hole in the cladding.

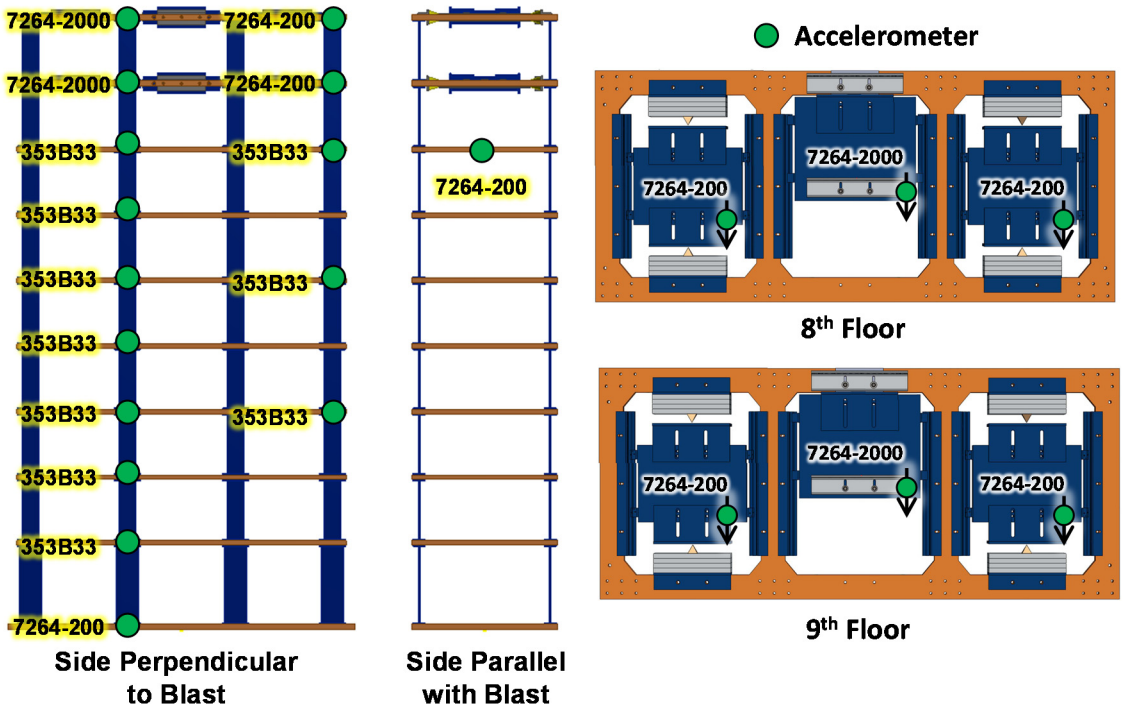

Figure 7-11. Accelerometer layout used for blast testing

7.2.3 Experimental results

In this subsection the results for this experimental blast testing are discussed. The presentation and discussion of these results is separated by the charge configuration used for the testing. As mentioned previously, the charges configurations produce an average blast face pressure impulse of 106, 209, and 620 kPa-msec, which correspond to the low, medium, and high blast loads, respectively.

7.2.3.1 106 kPa-msec charge configuration (low blast load)

Using the 106 kPa-msec charge configuration outlined in Table 7-1 the structure was tested twice: first with the NESs unlocked (free to move) and then with NESs locked (prevented from moving).

Pressure measurements taken from gages on the cladding during the locked and unlocked tests are shown in Figure 7-12. The pressure gages used to obtain this data are mounted on the fourth and seventh floors. As shown, the gages on the fourth floor indicate a much higher peak pressure than the gages on the seventh floor. Qualitatively, this result agrees with the simulation results found in Figure 7-8 and is logical as the gages on the seventh floor are further from the center of the blast than the fourth floor gages. Aside from differences in peak pressure, the figure also indicates a time lag in the pressure measurements between the fourth and seventh floors. Once again, this result is logical due to the proximity of the respective gages from the blast center. In addition to the characteristics of the blast pressure at different points along the cladding, Figure 7-12 demonstrates that the pressure loading on the structure for both unlocked and locked tests is nearly equivalent. This equivalency is important as it implies that the response of the structure from the two blasts can be accurately compared.

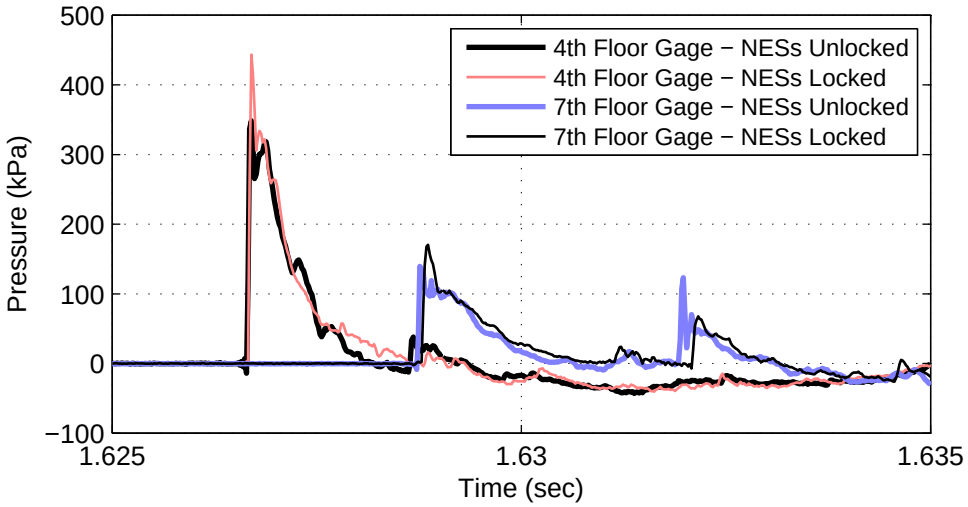

Figure 7-12. Pressure time history from various gages mounted in the center of the structure's width during the 106 kPa-msec blast

In Figure 7-13 the third floor displacements measured during the two tests are shown. As indicated, when the NESs are unlocked, the response of the structure rapidly decays; however, when the NESs are locked, the motion of the structure continues for a significantly longer time. Additionally, this figure shows that along with rapidly attenuating the motion, the peak displacement is reduced with the NESs unlocked. The reduction observed in the negative direction is relatively small (4%), but the reduction in the positive direction is substantial (24%). Due to the relatively low displacements shown in this figure, an irregularity is noticeable in the unlocked case a few seconds after the blast when the displacement is substantially reduced. This irregularity, which appears as a square wave in the displacement data, occurs because the resolution of the displacement sensor has been reached, which prevents the sensor from accurately measuring the small residual motion that persists.

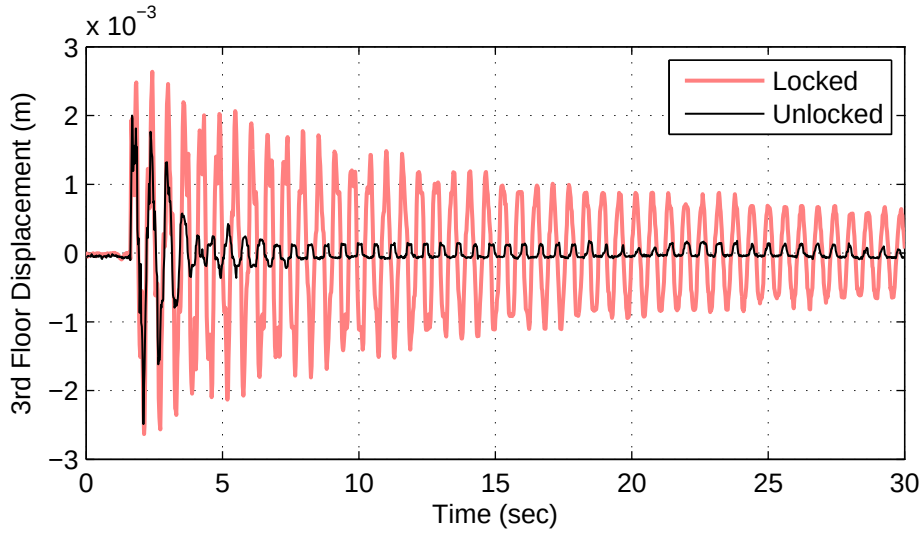

Figure 7-13. Third floor displacement response to the 106 kPa-msec blast

Figure 7-14 shows the wavelet spectra of the acceleration response of the seventh floor to the blast tests when the NESs are locked and unlocked. When the NESs are locked, the seventh floor acceleration response of the structure due to the blast is spread over most of the modes of the structure in the weak translational direction; however, the most prolonged motion is observed in the lowest three modes. When the NESs are unlocked, the motion in nearly all the modes of the structure decay faster; this observation is especially true for the lowest modes of the structure, which attenuate very rapidly. Furthermore, as the input was comparable for the two tests, the increase in the spectrum at higher frequencies shown in this figure substantiates the transfer of vibrational energy to the higher modes of the structure as a result of the NESs.

To better understand the behavior observed in Figure 7-14, Figure 7-15 shows the time histories and wavelet spectra of the acceleration response of the unlocked eighth floor NESs during the 106 kPa-msec blast test. The plots show that the Type 1 NESs are only in motion for several seconds after the blast. During this time, the frequency content of the Type 1 NES responses are broadband, as expected due to the essential nonlinearities in the restoring forces. This broadband behavior allows the NESs to couple the modes of the structure and promote targeted energy transfer. As the accelerometers on the SSVI NESs were designed to measure the much larger accelerations anticipated during the higher blast levels, the measured acceleration of the SSVI NES is noisy. Nevertheless, peaks corresponding to the impacts of the SSVI NES still appear in the acceleration time history. These peaks also correspond to broadband behavior observed in the SSVI acceleration wavelet, as shown by the dark bands in the spectrum.

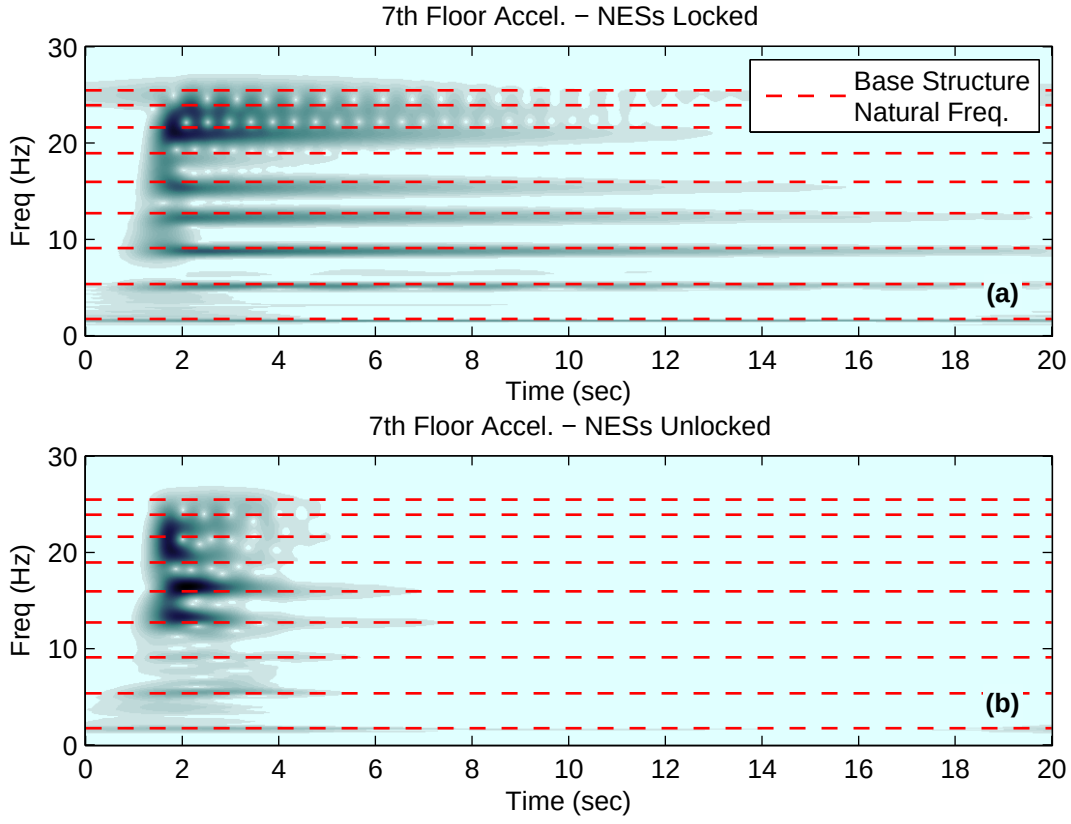

Figure 7-14. Wavelet spectra of the seventh floor acceleration during the 106 kPa-msec blast with (a) NES locked (b) NESs unlocked

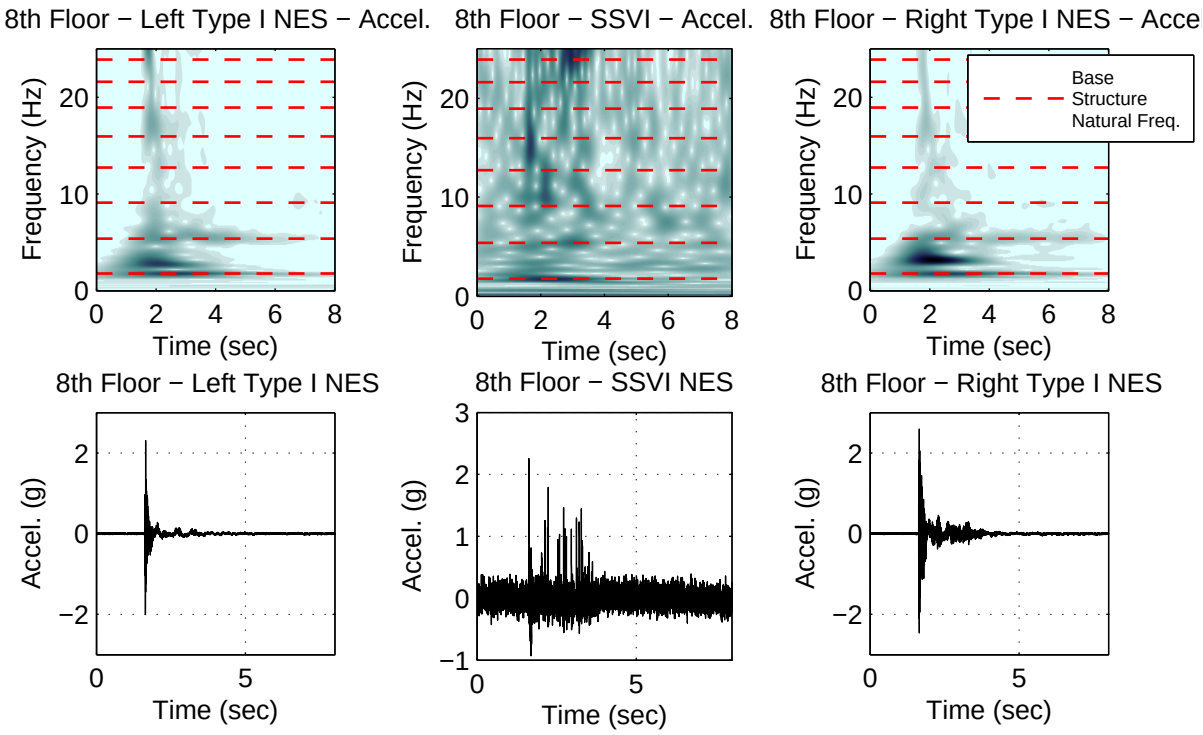

Figure 7-15. Eighth floor NESs acceleration response during the 106 kPa-msec blast – time history and wavelet spectra

Displacements and accelerations due to the blast loading are useful to assess the behavior of the structure; however, these measures do not directly correspond to the actual demand on the structure. To examine the actual demand, the strain measured at one of the interior first story columns is useful and is shown in Figure 7-16. This strain is proportional to the column bending moment which results from the blast loading; thus, the measurement can be used examine the structural demand on the first story, often the most critical part of a structure. Figure 7-16 shows that, like the displacement and acceleration responses previously examined, the strain in the first floor columns decays quickly when the NESs are unlocked. Additionally, with a reduction of 21.9% in measured peak strain compared to the locked case, we show that the passive system of NESs is able to substantially reduce the maximum demand on the first story due to blast.

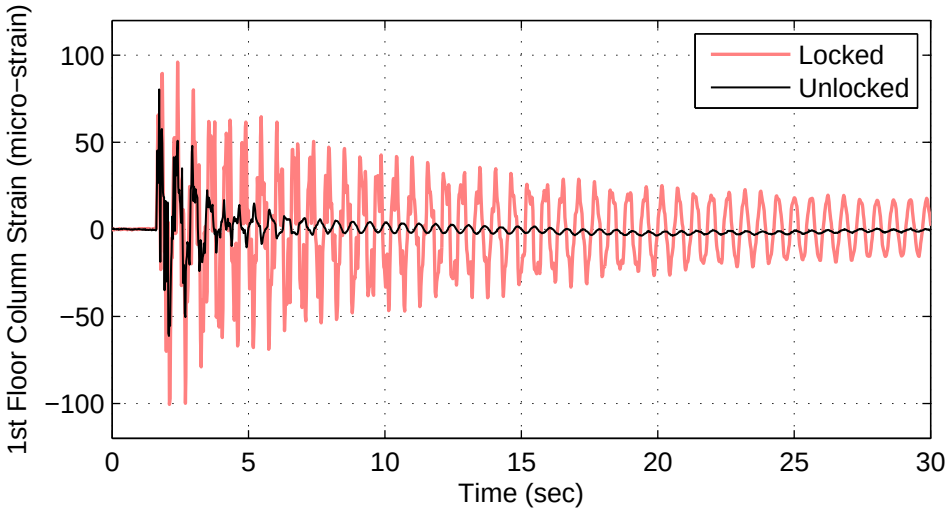

Figure 7-16. First floor column strain response to 106 kPa-msec

7.2.3.2 209 kPa-msec charge configuration (medium blast load)

Using the 209 kPa-msec charge configuration outlined in Table 7-1 the structure was tested twice: first with the system of NESs unlocked and then with the system of NESs locked. In Figure 7-17 a frame from a high speed video of the blast during the first test is shown. As this frame was taken only milliseconds after the blast was initiated, NESs, which are installed in the top two floors of the structure, have not yet had time to displace significantly. However, the frame shows that the pressure wave resulting from the blast causes significant deformation in the cladding. Despite this deformation the cladding remained intact and, after minor repair, was able to transfer the load of the next blast to the structure.

Pressure measurements taken from gages on the cladding during the locked and unlocked tests are shown in Figure 7-18. The pressure gages used to obtain this data are mounted on the fourth and seventh floors. As observed during the 106 kPa-msec blasts, the gages on the fourth floor indicate a much higher peak pressure than the gages on the seventh floor. Qualitatively, this result agrees with the simulation results found in Figure 7-8. Aside from differences in peak pressure, the figure also indicates a time lag in the pressure measurements between the fourth and seventh floors. Once again, this result is logical due to the proximity of the respective gages from the blast center. Due to the similarity in these pressures, Figure 7-18 suggests that the pressure loading on the structure for both unlocked and locked tests for this load level are nearly equivalent. Consequentially, this implies that the response of the structure from the two blasts at this load level can be accurately compared.

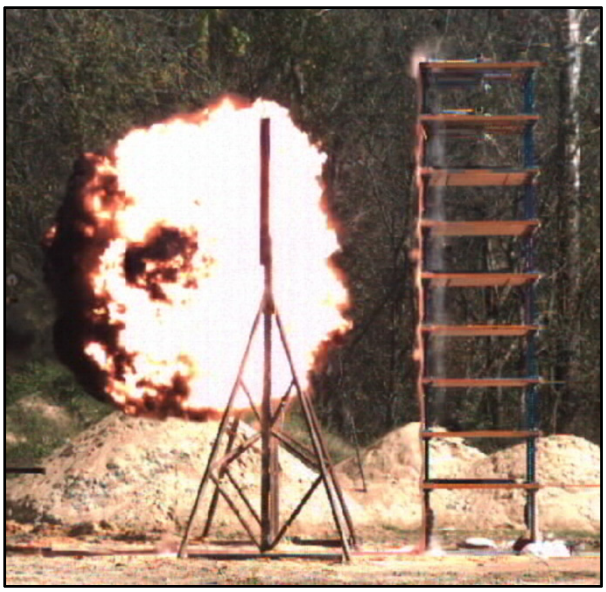

Figure 7-17. Structure during the 209 kPa-msec blast

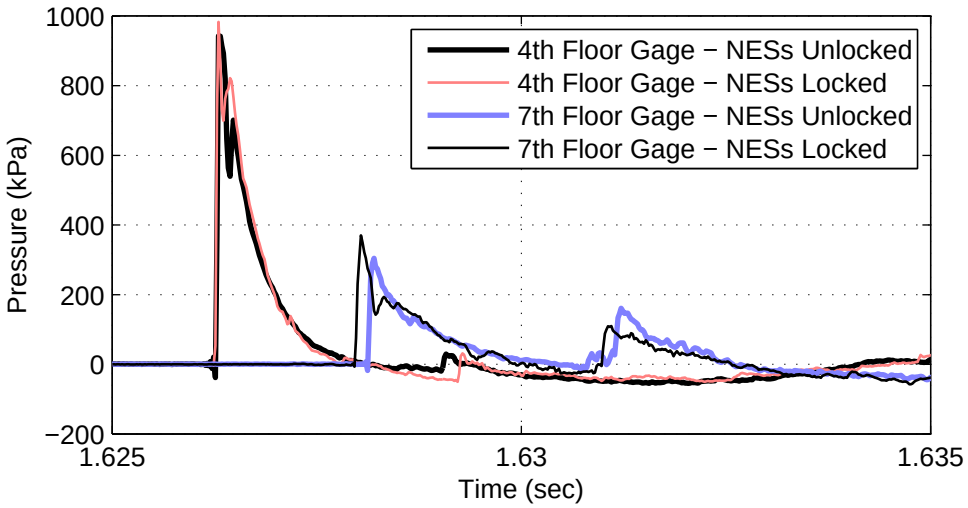

Figure 7-18. Pressure time history from various gages mounted in the center of the structure's width during the 209 kPa-msec blast

In Figure 7-19 the third floor displacements measured during the two tests are shown. As indicated, when the NESs are unlocked, the response of the structure rapidly decays; however, when the NESs are locked, the motion of the structure continues for a significantly longer time. Additionally, this figure shows that along with rapidly attenuating the motion, the peak displacement is reduced with the NESs unlocked. The reduction observed in the positive direction is relatively small, but the reduction in the negative direction is substantial.

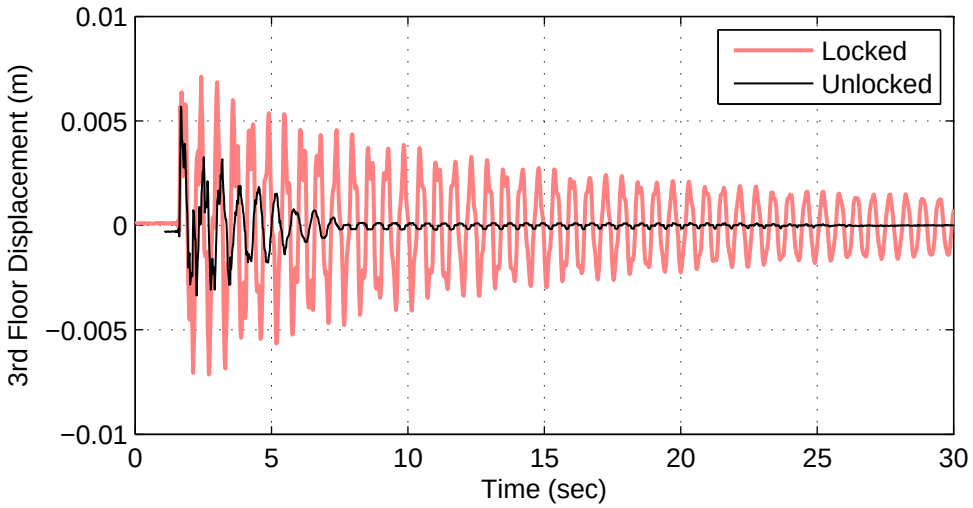

Figure 7-19. Third floor displacement response to the 209 kPa-msec blast

Figure 7-20 shows the wavelet spectra of the acceleration response of the seventh floor to the blast tests when the NESs are locked and unlocked. When the NESs are locked, the seventh floor acceleration response of the structure due to the blast is spread over most of the modes of the structure in the weak translational direction with the most significant and prolonged motion observed in the lowest three modes. As previously shown with the 106 kPa-msec blast, when the NESs are unlocked, the motion in nearly all the modes of the structure decay faster than when the NES are locked; this observation is especially true for the lowest modes of the structure which decay very rapidly. Furthermore, as the input was comparable for the two tests, this figure once again substantiates the transfer of vibrational energy to the higher modes of the structure as a result of the NESs.

To better understand the behavior shown in Figure 7-20, Figure 7-21 shows the time histories and wavelet spectra of the acceleration response of the unlocked eighth floor NESs during the blast test. The plots show that the NESs undergo large accelerations, but are only in motion for several seconds after the blast. During this time, the frequency content of the NES responses are broadband as expected due to the essential nonlinearities in the restoring forces. This broadband behavior is especially apparent during the impacts of the SSVI NES, which correspond to the peaks in the time history of the SSVI NES acceleration and the matching dark bands in the wavelet spectrum. The broadband behavior of the NESs allows them to couple the modes of the structure and promote targeted energy transfer.

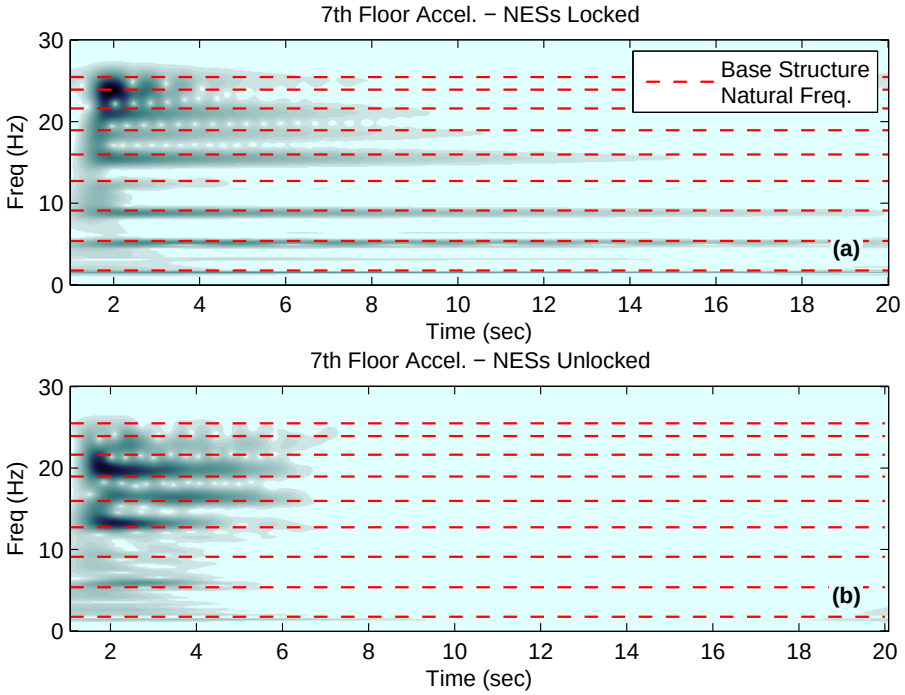

Figure 7-20. Wavelet spectra of the seventh floor acceleration during the 209 kPa-msec blast with (a) NES locked (b) NESs unlocked

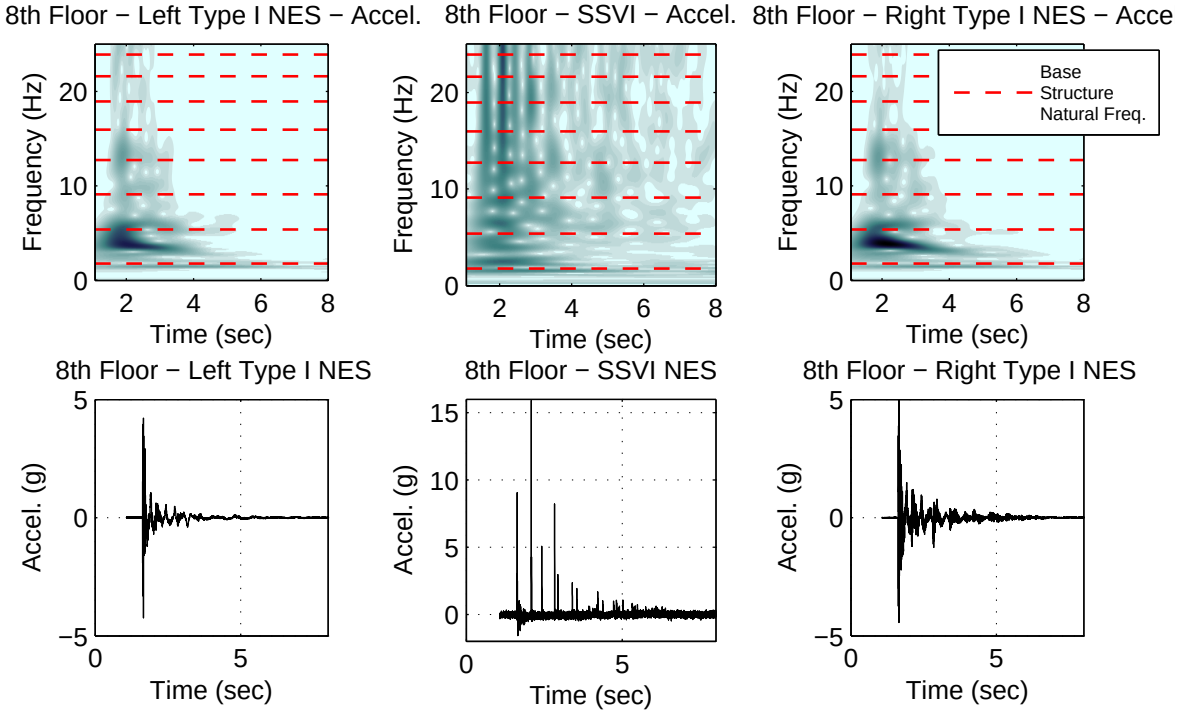

Figure 7-21. Eighth floor NESs acceleration response during the 209 kPa-msec blast – time history and wavelet spectra

To examine the actual demand on the structure during these tests, the strain measured at one of the interior first story columns is shown in Figure 7-22. This figure shows that, like the displacement and acceleration responses previously examined, the strain in the first floor columns decays quickly when the NESs are unlocked. Additionally, with a reduction of 21.9% in measured peak strain compared to the locked case, we show that the passive system of NESs is able to substantially reduce the maximum demand on the first story due to blast. Furthermore, these results demonstrate robustness to changes in load level, as substantial strain reduction when the NESs were unlocked was observed in the response of the structure to both the 106 and 209 kPa-msec blasts.

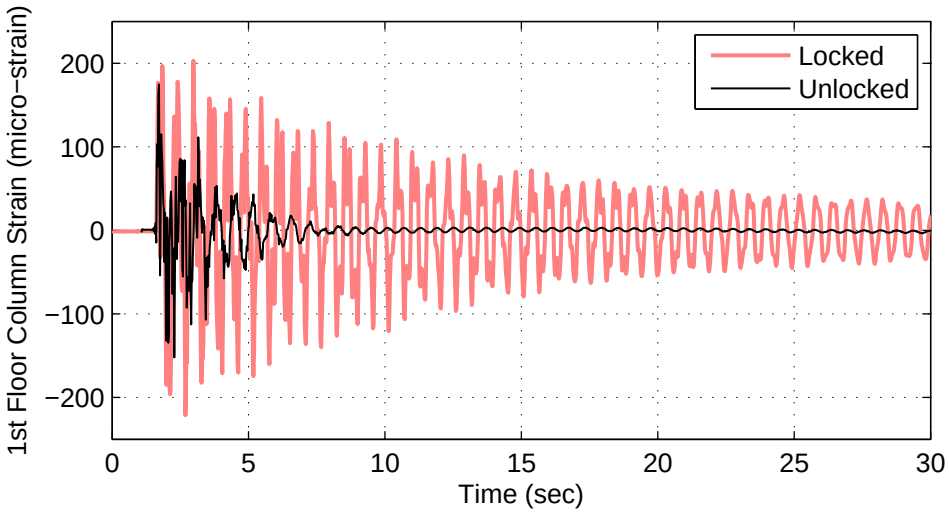

Figure 7-22. First floor column strain response to 209 kPa-msec

7.2.3.3 620 kPa-msec charge configuration (high blast load)

Using the 620 kPa-msec charge configuration outlined in Table 7-1 the structure was tested only one, with the system of NESs unlocked. While a second test would ideally have been performed on the structure with the system of NESs locked, this test was not possible due to time limitations at the test site and damage to the cladding sustained during the blast with this charge configurations. Figure 7-23 shows views of the damaged cladding after this blast. As this figure shows, the damage to the cladding include failure of the bolts connecting the cladding to the structure as well as failure in the fasteners that connecting overlapping sheets of cladding material. Without both corresponding tests with the NESs locked and unlocked, direct comparisons cannot be made to quantitatively determine the effectiveness of the system of NESs; however, the unlocked test that was performed can be used in a qualitative manner to explore the performance of the system.

Pressure measurements taken from gages on the cladding during test are shown in Figure 7-24. As in the previous tests, the pressure gages used to obtain this data are mounted on the fourth and seventh floors. Similarly to previous tests, the fourth floor gages indicate a much higher peak pressure than the gages on the seventh floor; however, unlike previous tests, the pressure readings from the gages on the separate floors show only a very small time lag between the pressure time histories. Qualitatively, this pressure distribution agrees with the simulation results found in Figure 7-9. The near synchronization of pressure measurements observed in this

test can be attributed to the distribution of the charge in this configuration, which allows the pressure wave to arrive at the different gages nearly simultaneously.

Figure 7-23. Damage to cladding caused by 620 kPa-msec blast

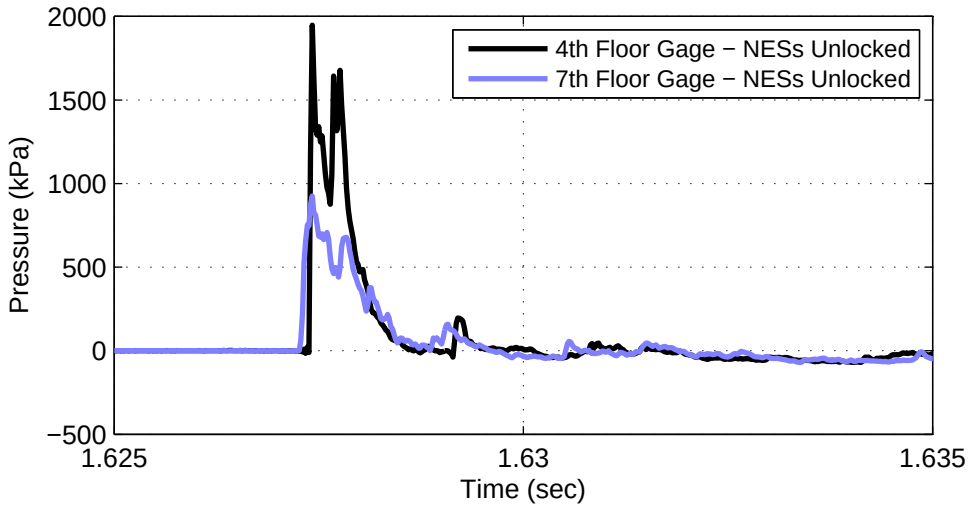

Figure 7-24. Pressure time history from various gages mounted in the center of the structure's width during the 620 kPa-msec blast

In Figure 7-25 the third floor displacements measured during the test is shown. As this figure shows, with the system of NESs unlocked, the response of the structure decays very rapidly. This rapid reduction is demonstrated by the fact that in about two cycles the amplitude of the displacements decreased by more than 80%; in the 106 and 209 kPa-msec tests about three and five cycles, respectively, were necessary for that level of reduction to occur.

Figure 7-26 shows the wavelet spectra of the acceleration response of the seventh floor to the blast test with the 620 kPa-msec charge configuration. As similarly observed in the previously examined tests with the system of NESs unlocked, all the translational modes of vibration of the structure are attenuated a few seconds after the blast; however, the lower modes are attenuated especially quickly. Additionally, this figure shows that the response of the structure includes a large amount of activity in its higher modes. With no locked test to compare with, the possibility that this abundance of higher mode energy is solely a result of the blast cannot be precluded; however, previous results with the system of NESs locked and unlocked suggest that the abundance of higher mode energy is a consequence of the system of NESs.

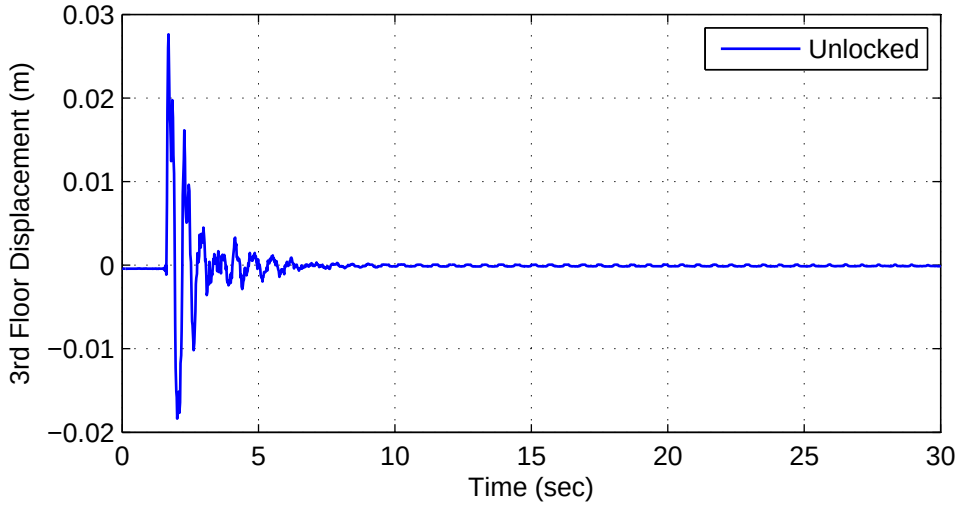

Figure 7-25. Third floor displacement response to the 620 kPa-msec blast

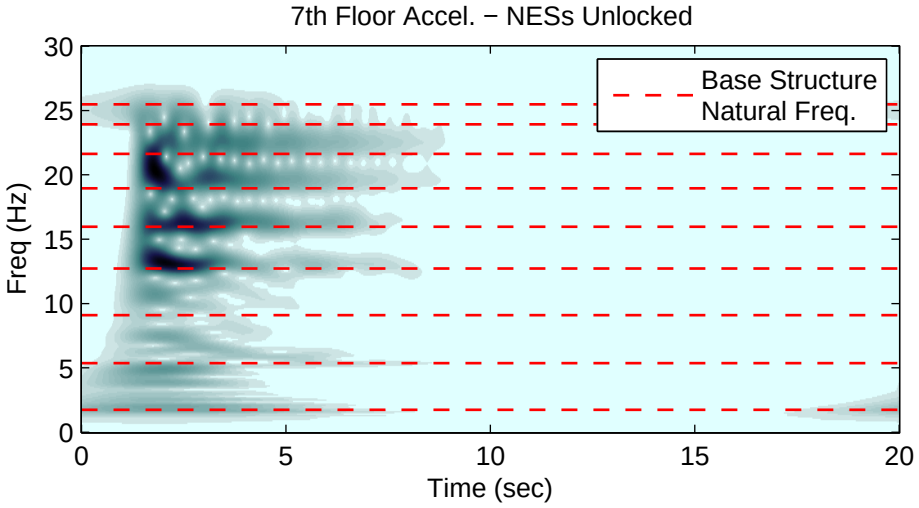

Figure 7-26. Wavelet spectra of the seventh floor acceleration during the 620 kPa-msec blast with NESs unlocked

Figure 7-27 examines the motion of the NESs on the eighth floor of the structure with time histories and wavelet spectra of the acceleration responses to the 620 kPa-msec blast. Once again, these plots show that the Type I NESs undergo large accelerations, but are only in motion for several seconds after the blast. While in motion the frequency content of the Type I NESs is quite broadband, as intended. Another noteworthy feature that can be observed from the wavelet spectrum of the Type I NESs are clearly defined diagonal marks which are occur as the NESs exit their period of large accelerations. When viewed in the frequency-energy plane, these diagonal marks would translate to the NES following the backbone curve defined by the dynamics of the undamped Hamtonian NES-structure system (Quinn et al. 2012). In Figure 7-27 the motion and wavelet spectrum of the SSVI NES on the eighth floor is shown as well. As shown in this figure, after the blast the SSVI NES experiences four major impacts within two seconds, then a series of minor impacts. During the major impacts, the signal to noise ratio of the accelerometer on the SSVI NES is excellent and distinct dark bands, corresponding to broadband behavior of the SSVI NES, can be observed in the wavelet spectrum.

The strain measured at one of the interior first story columns during this test is shown in Figure 7-28. This figure shows that the strain in the first floor columns attenuates quickly when the NESs are unlocked with an 80% reduction in amplitude achieved in less than 1.5 seconds. Like the displacement measurement for this test shown in Figure 7-25, the attenuation in strain is faster than that observed in the lower level blast tests. The good performance of the system of NESs in response to the 620 kPa-msec blast, combined with the good performance observed at the other load levels, further demonstrates that the system of NESs examined is capable of providing good performance and quick attenuation of the response of the structure across a large range of load levels.

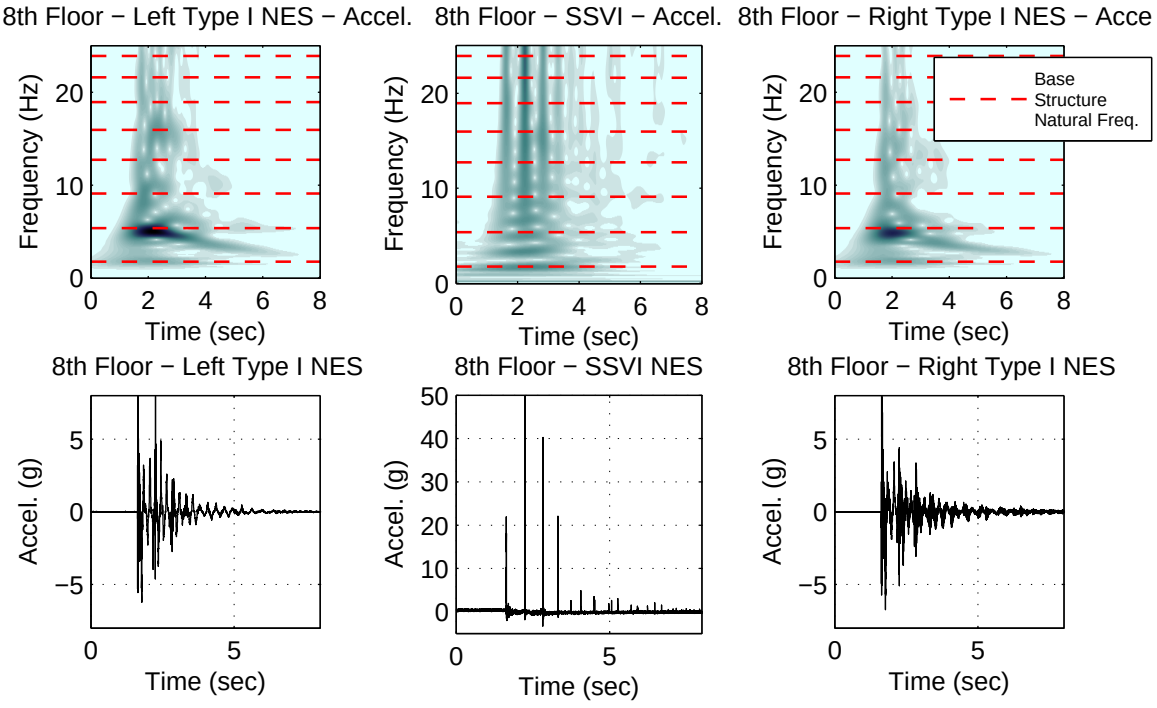

Figure 7-27. Eighth floor NESs acceleration response during the 620 kPa-msec blast – time history and wavelet spectra

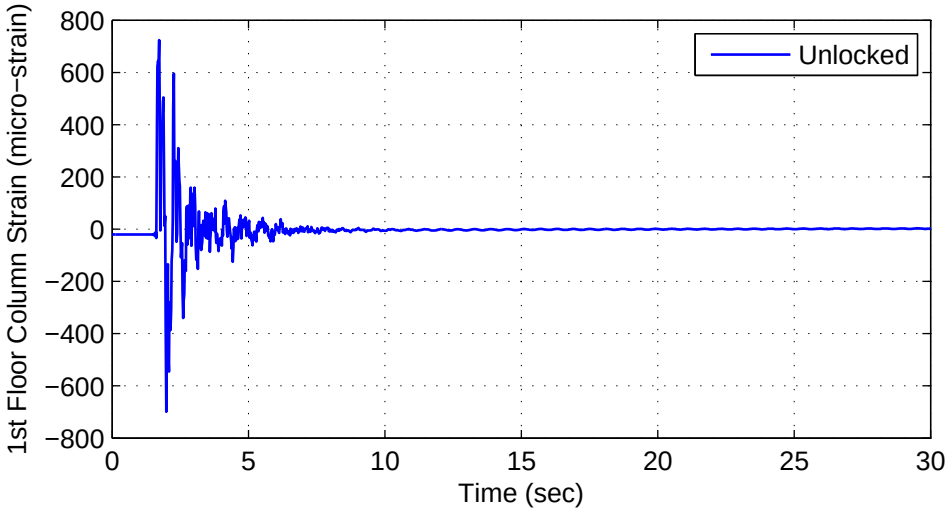

Figure 7-28. First floor column strain response to 620 kPa-msec

7.3 Sine-sweep testing

In addition to tests using the simulated blast ground motions, sine-sweep testing of the structure was done using the shake table at the US Army Corps of Engineers Construction Engineering Research Laboratory in Champaign, IL (U.S. Army Engineer Research and Development Center 2008). As this work was done in concert with the simulated blast testing, the instrumentation layout used for this testing was same as the layout presented for the simulated blast testing. In this section, the shake-table-produced ground motion used for this testing is introduced and then the results of the testing are presented.

7.3.1 Table motion used for sine-sweep testing

The desired sine-sweep ground motion maintains a constant acceleration amplitude, has a starting frequency of 0.5 Hz, and sweeps linearly to an ending frequency of 12 Hz. As the NESs being tested are nonlinear devices and thus exhibit load dependent behavior, the response of the system to this sine-sweep will be examined with desired sweep acceleration amplitudes of 0.0075, 0.015, 0.0225, and 0.030 g. An example of the desired sine-sweep table acceleration is shown in Figure 7-29 where the desired table acceleration is compared to the experimentally measured table acceleration. The measured data shown in this figure was collected during a 0.015 g sine-sweep with the structure attached to the table and with the system of NESs locked. While the measured acceleration shown in this figure does not maintain the constant acceleration that is desired, the measured acceleration does follow the desired acceleration closely. The change in dynamics caused by the interaction between the table control and the structure is partially responsible for the lack of complete agreement between the desired and measure acceleration time histories. This interaction will change depending on the amplitude of the sine-sweep being tested and the configuration of the system of NESs; however, all the measured acceleration record follows the desired acceleration fairly well.

To better understand the measured acceleration, Figure 7-30 shows the wavelet spectrum of the measured acceleration displayed in Figure 7-29. The main feature of the wavelet spectrum is

the intended sine-sweep which takes the form of a band that transitions from around 0.5 Hz to 12 Hz over the entirety of the record. Other features of the spectrum are resonances at the first and second translational natural frequencies due to control-structure interaction and higher harmonics of the chirp. As the shading this figure suggests, these unintended features are small in comparison with the sine-sweep.

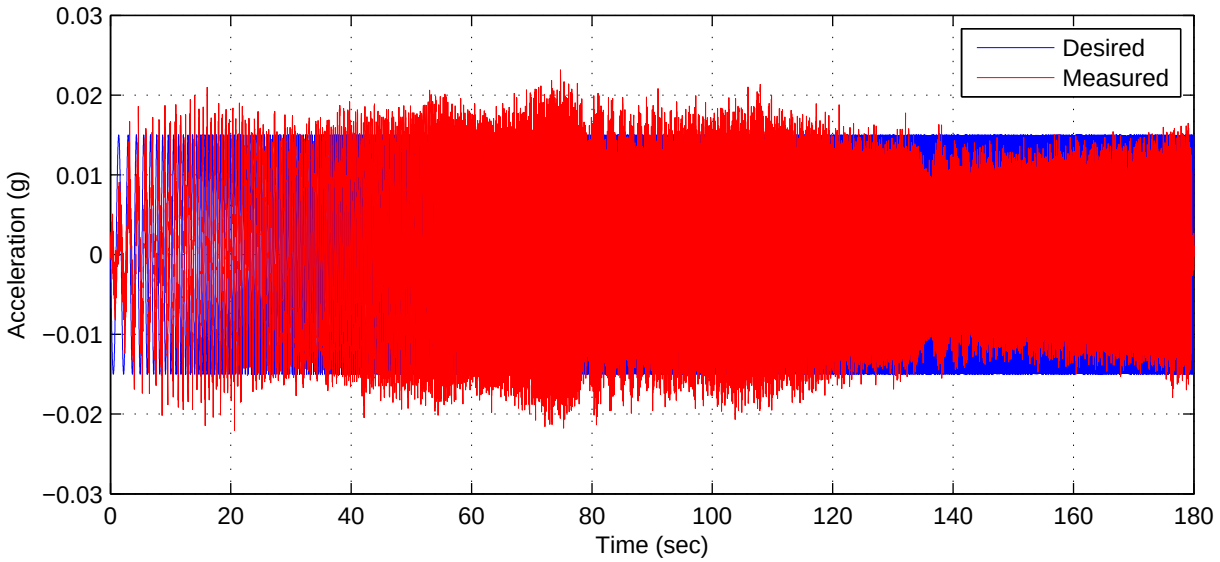

Figure 7-29. Comparison of desired sine-sweep table acceleration and example measured acceleration

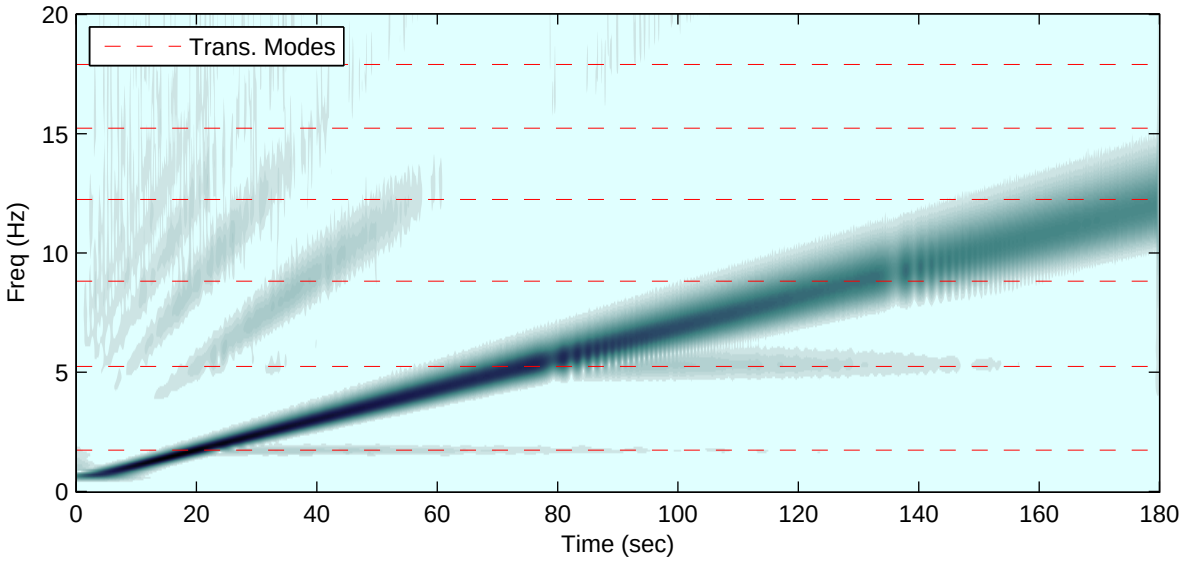

Figure 7-30. Wavelet spectra of example measured table acceleration during sine-sweep

7.3.2 Sine-sweep results

Using the sine-sweep ground motion introduced in the previous section, the structure was tested with the system of NESs in four different configurations (all NESs locked, Type I NESs unlocked, SSVI NESs unlocked, and all NESs unlocked) and with four different sine-sweep amplitudes (0.0075, 0.015, 0.0225, and 0.030 g).

The resulting estimated seventh floor displacements calculated from accelerometer measurements in response to the 0.03 g sine-sweep is shown in Figure 7-31 for all the configurations tested. This figure also shows the corresponding wavelet spectra of the seventh floor acceleration for the configurations. From this figure, it is shown that with the NESs locked, the seventh floor displacement response of structure largely consists of a very slowly attenuating first mode motion. The wavelet spectrum of the seventh floor acceleration during this test shows that the motion also consists of second and third mode motion that is initiated as the sine-sweep progresses. As expected from the structure in this linear configuration, no substantial acceleration exists in the structure's response at frequencies until they have been reached by the sine-sweep.

With the Type I NESs unlocked the peak displacement response of the structure at the seventh floor is reduced slightly and first mode response is attenuated much faster. Examination of the wavelet spectrum for this test shows that with the Type I NESs unlocked the first, second, and third mode responses to the sine-sweep are also attenuated much faster than in the all locked case. Additionally, the wavelet spectrum for this case shows that, due to the action of the Type I NESs, energy is transferred and multiple higher modes become excited when the sine-sweep reaches the first mode of the structure.

Figure 7-31 shows that with SSVI NESs unlocked, the peak displacement response of the structure at the seventh floor is significantly reduced by more than 60%. Additionally, after reaching the peak displacement, the response of structure is very rapidly attenuated. Examination of the wavelet spectrum for this test shows that with the SSVI NESs unlocked, the first, second, and third mode responses to the sine-sweep are attenuated much faster than in the all locked case and also faster than in the case of the Type I NESs unlocked. Additionally, the wavelet spectrum for this case shows distinct high bandwidth streaks that coincide with the impacts of the SSVI NESs. This high bandwidth behavior demonstrates the TET that takes place due to the SSVI NES.

The seventh floor displacement and seventh floor acceleration wavelet spectrum shown in Figure 7-31 with all the NESs unlocked is similar to respond with the only SSVI NESs unlocked; a large reduction in peak displacement is observed along with a rapid attenuation in response after the peak, and high bandwidth behavior corresponding to the SSVI NESs impacts. The largest difference between the response in the all unlocked and the SSVI unlocked cases is that with all the NESs unlocked the second and third mode resonances in the system are further suppressed.

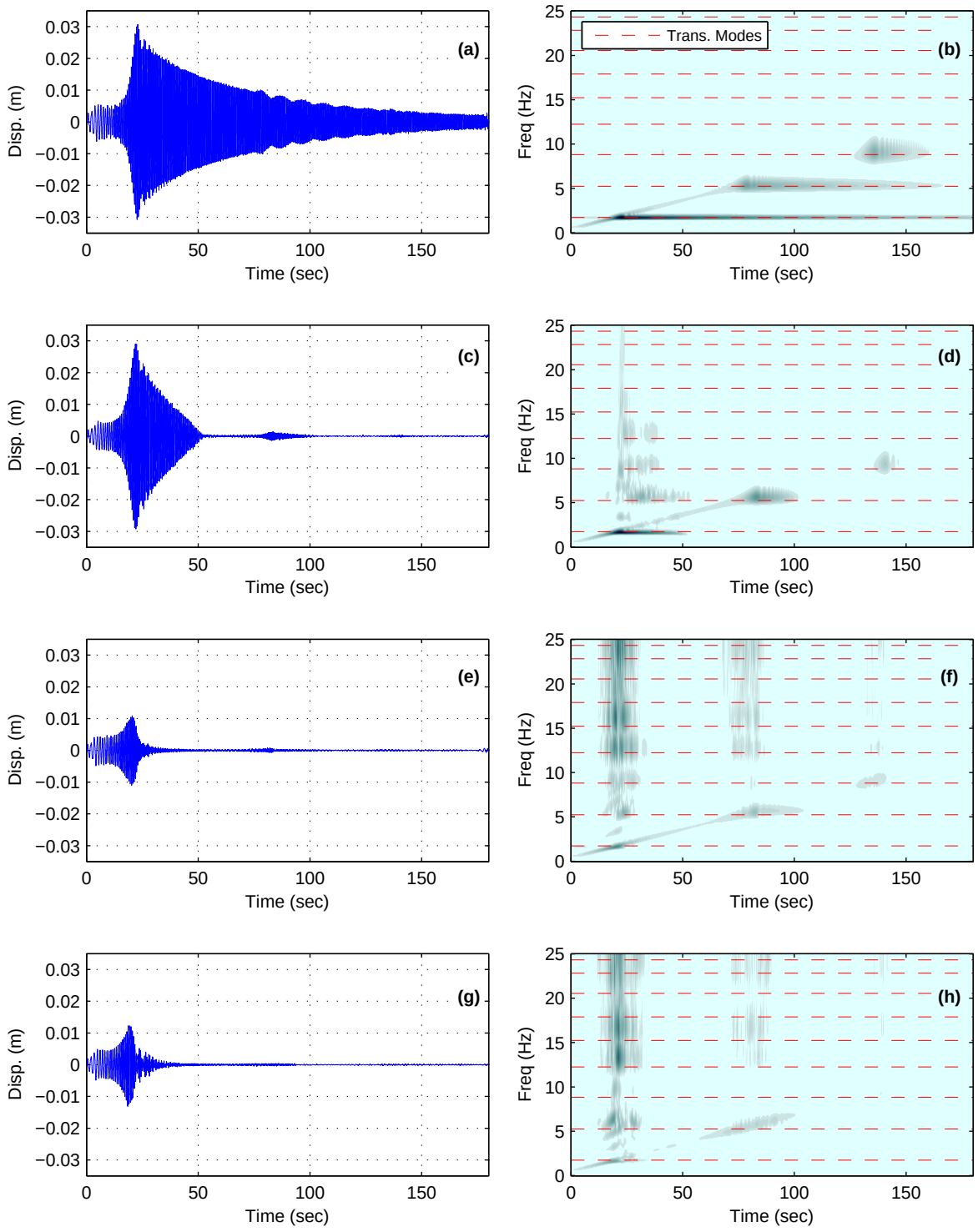

Figure 7-31. Time history of seventh floor displacement and seventh floor acceleration wavelet spectrum for (a, b) all locked configuration, (c, d) Type I NES unlocked configuration, (e, f) SSVI NES unlocked configuration, and (g, h) all unlocked configuration

The effect of the system of NESs on the demands on the structure during the sine-sweeps can be investigated by examining the measured first floor strain. Figure 7-32 and Figure 7-33 show the first floor strain measured with all NESs locked, Type I NESs unlocked, SSVI NESs unlocked, and all NESs unlocked for the 0.015 g and 0.0225g sine-sweeps, respectively. These figures show the same trends identified from the displacement results. With the Type I NESs unlocked, the peak strain is reduced slightly (about 5%); with the SSVI NESs unlocked and all NESs unlocked, the peak strain is reduced substantially (about 60%). Additionally, with the Type I NESs unlocked the response of the structure is quickly attenuated compared to the case with all the NESs locked; however, with the SSVI NESs unlocked or all the NESs unlocked this attenuation is more rapid. Furthermore, the response of the system to the two levels of sine-sweep are very similar. The only substantial difference noticeable in the strain time histories at the different load levels is the decreased effectiveness of, presumably the Type I NESs, at attenuating the first and second modes observed in the Type I NESs unlocked case and partially in the all NESs unlocked case.

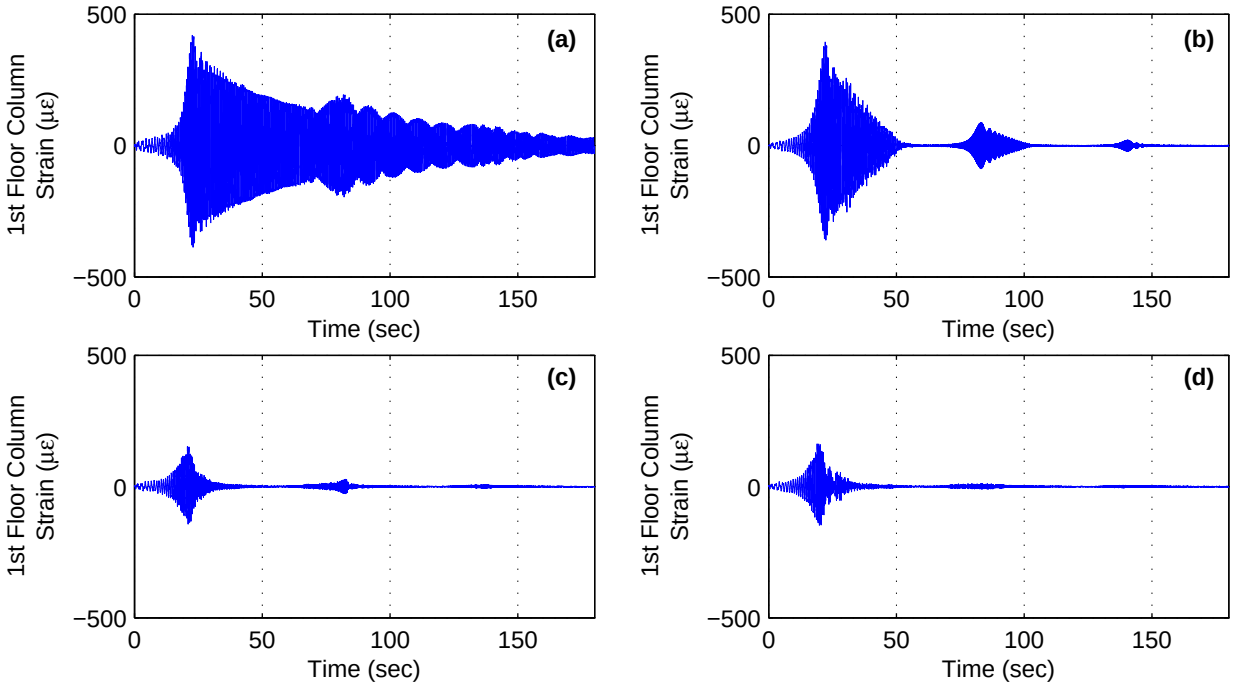

Figure 7-32. First floor column strain response to 0.015 g sine-sweep (a) all NESs locked, (b) type I NES unlocked, (c) SSVI NESs unlocked, and (d) all NESs unlocked

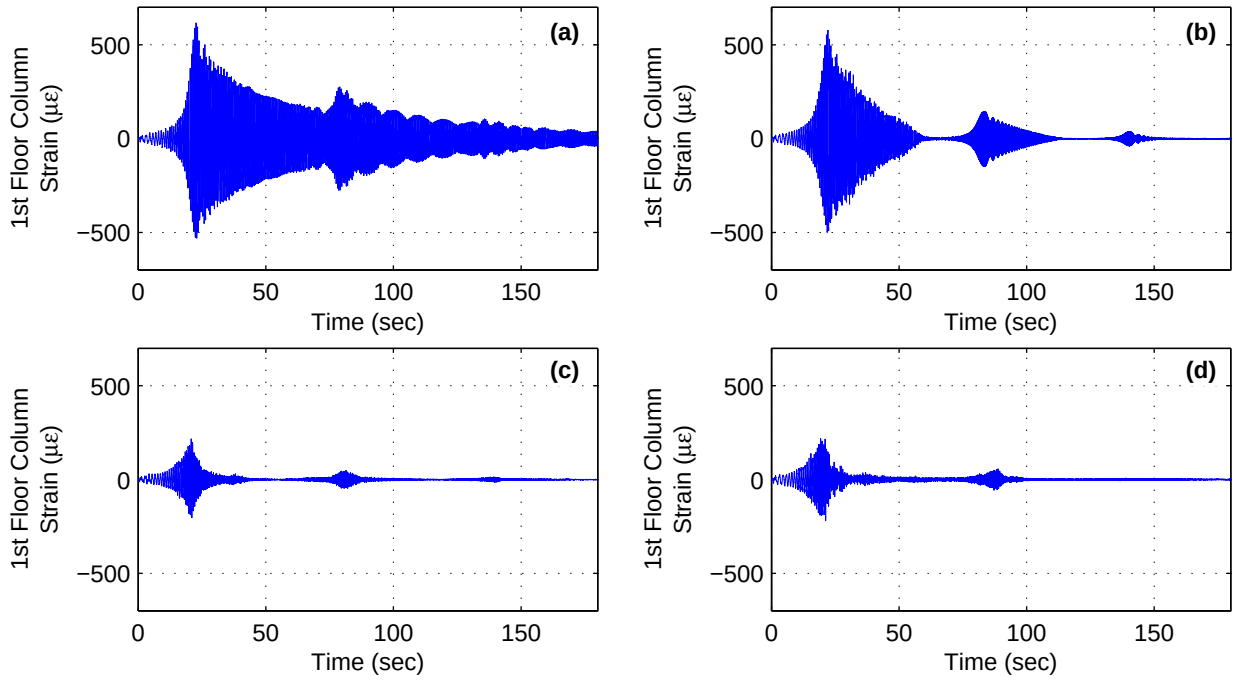

Figure 7-33. First floor column strain response to 0.0225 g sine-sweep (a) all NESs locked, (b) type I NES unlocked, (c) SSVI NESs unlocked, and (d) all NESs unlocked

To further examine the response of the structure in the frequency domain, transfer functions from the ground acceleration to the seventh floor acceleration can be calculated. The transfer function is based on linear theory, which is violated by the NESs being investigated; nevertheless, transfer function can still be used to qualitatively compare the resulting responses. To calculate these transfer function, the 180 seconds of sine-sweep acceleration response data have been separated into five windows. To limit the spectral leakage in the resulting transfer functions, the Hanning window was applied to the data. To increase the averages available for this calculation 50% overlap has been utilized in the transfer function calculation, which has the effect of increasing the number of windows.

In Figure 7-34 and Figure 7-35 the ground motion to seventh floor acceleration transfer functions for the four NES configurations tested are shown plotted together for each of the four sine-sweep amplitudes tested. An alternate view of this data is given in Figure 7-36 and Figure 7-37 which shows the same transfer functions plotted with four different amplitude sine-sweeps together for each of the four NES configurations.

As these transfer function figures show, with the NESs locked, the structure has a predictable and largely stable transfer function that would be expected for a linear structure. In all cases with the NESs locked, the low damping in the system makes the peaks of the transfer functions well defined. A small deviation from linear behavior is observed with a small decrease in the peaks of the transfer function observed at the higher sine-sweep levels. This behavior is not unexpected, as control-structure interaction plays a larger role at higher amplitudes.

With the Type I NESs unlocked, the largest change in the transfer functions is a shift in the peaks to higher frequencies. This shift occurs due to the change in linear dynamics in the system

with the mass of the Type I dampers no longer rigidly connected with the structure. Aside from shifting the frequency of the peaks, the amplitude of all the transfer functions peaks included in the sine-sweep are modestly reduced. A small additional decrease in amplitude of the second mode is observed for the highest amplitude test. This reduction in second mode amplitude occurs because the energy level in the structure has increased enough that the NES and the second mode are beginning to become in resonance. The lack of dramatic reduction in the transfer functions' first mode peak that fails to occur as a result of unlocked Type I NESs is due to the nature of the design of the Type I NESs. The Type I NES implemented in this structure were designed work with the SSVI NES and to mitigate the small residual vibrations that occur in the structure after the motion of the SSVI NES has finished; consequently, it is likely that the all of these sine-sweeps have amplitudes too high to see near optimal performance from the Type I NESs when they are unlocked by themselves.

Similar performance in the transfer functions is observed when the SSVI NES are unlocked and when all the NES are unlocked. This performance includes a large reduction in all modal peaks plotted; however, partially large reduction in the first mode transfer function peaks. With larger amplitude sine-sweeps, the first mode peak is further reduced in both cases too. This effectiveness over a large range of load levels shown in these cases highlights one of the key features desired in the full system of NESs: robustness to load changes. The biggest difference between the case when the SSVI NES are unlocked and when all the NES are unlocked is that with all the NES unlocked larger reduction in the second and third modes can be observed. This behavior is due, in part, to the synergistic effect of combining the Type I NESs and the SSVI NESs.

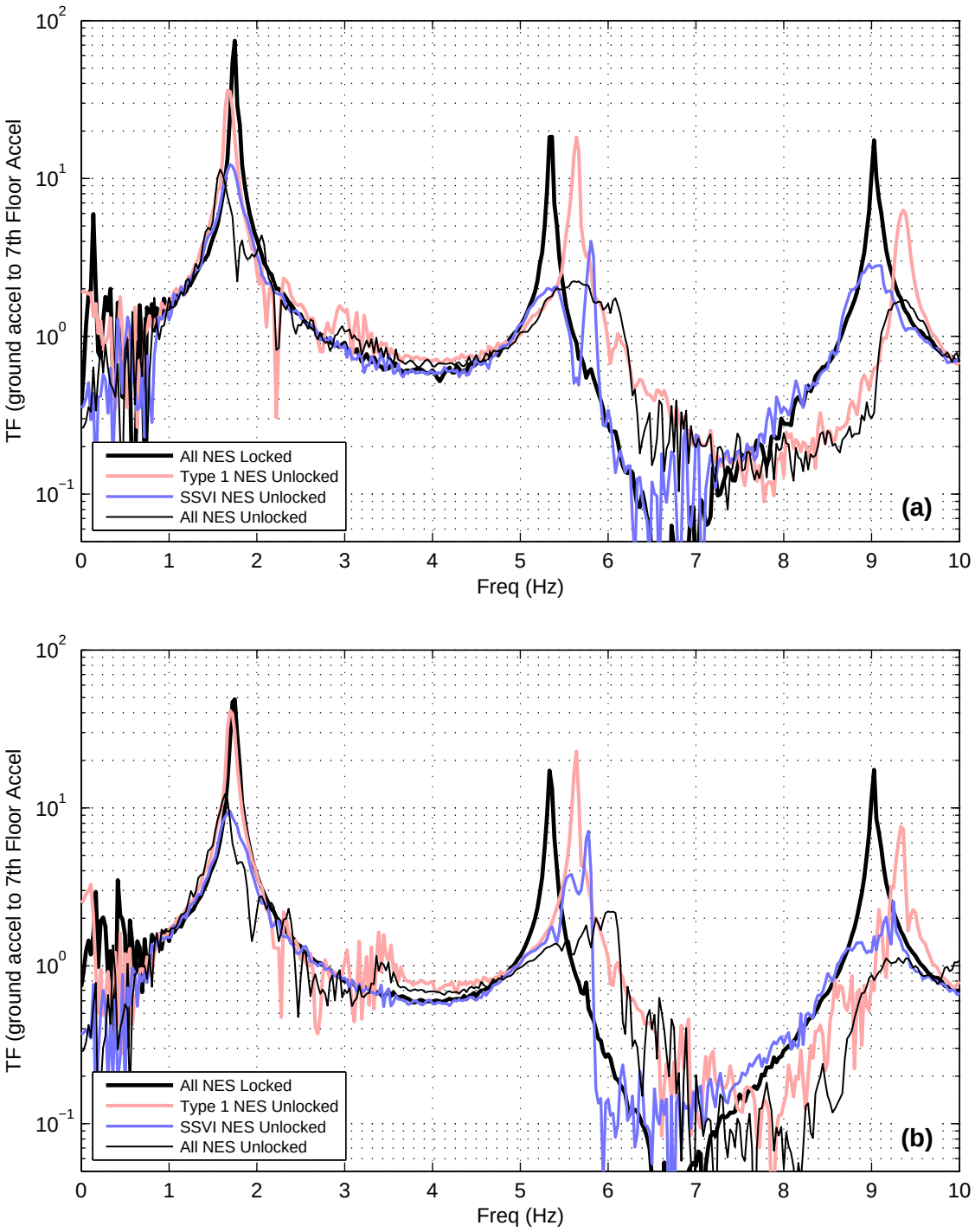

Figure 7-34. Ground acceleration to seventh floor acceleration transfer functions computed for all tested configuration of the system of NESs using (a) 0.0075 g sine-sweep and (b) 0.015 g sine-sweep

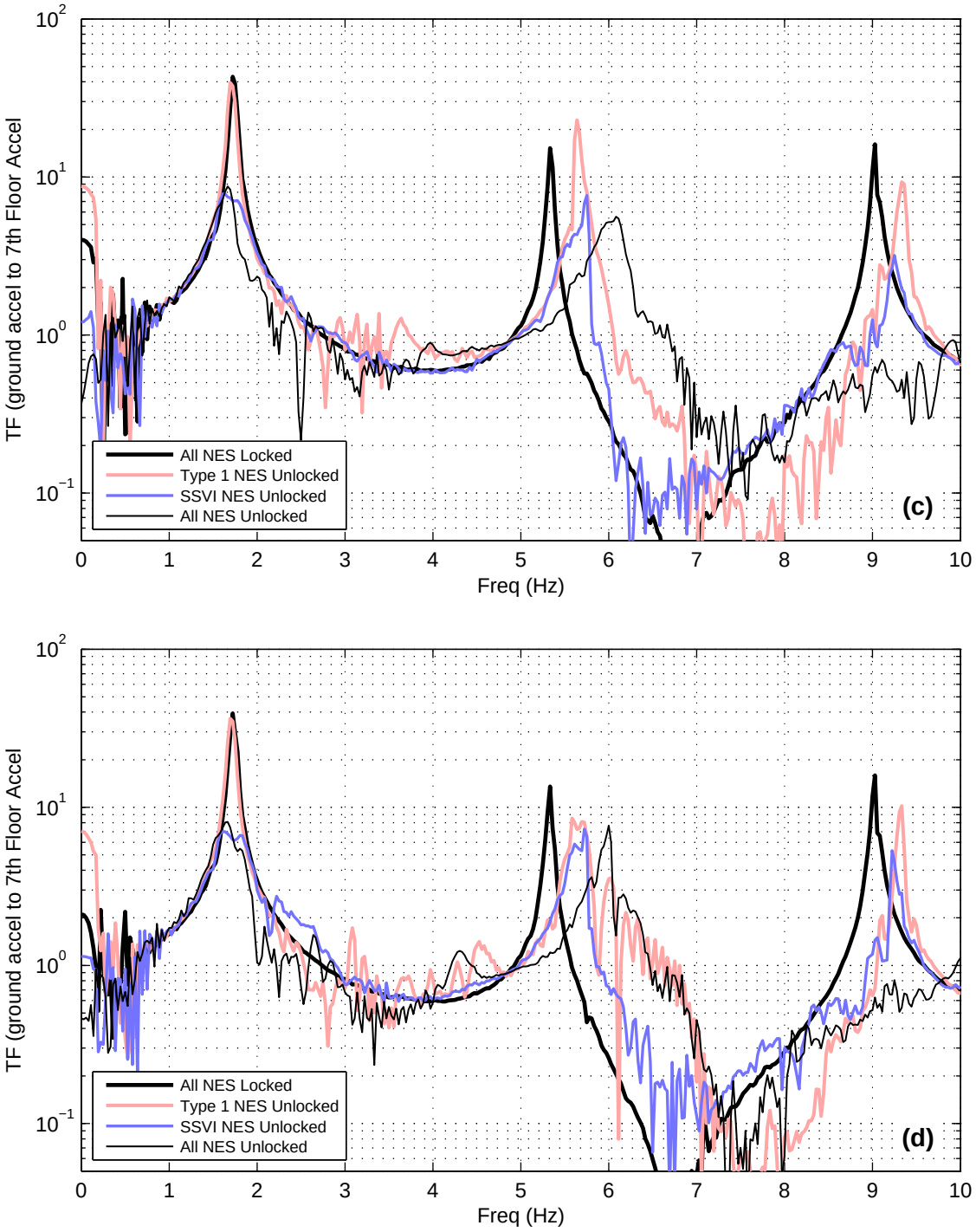

Figure 7-35. Ground acceleration to seventh floor acceleration transfer functions computed for all tested configuration of the system of NESs using (c) 0.0225 g sine-sweep and (d) 0.03 g sine-sweep

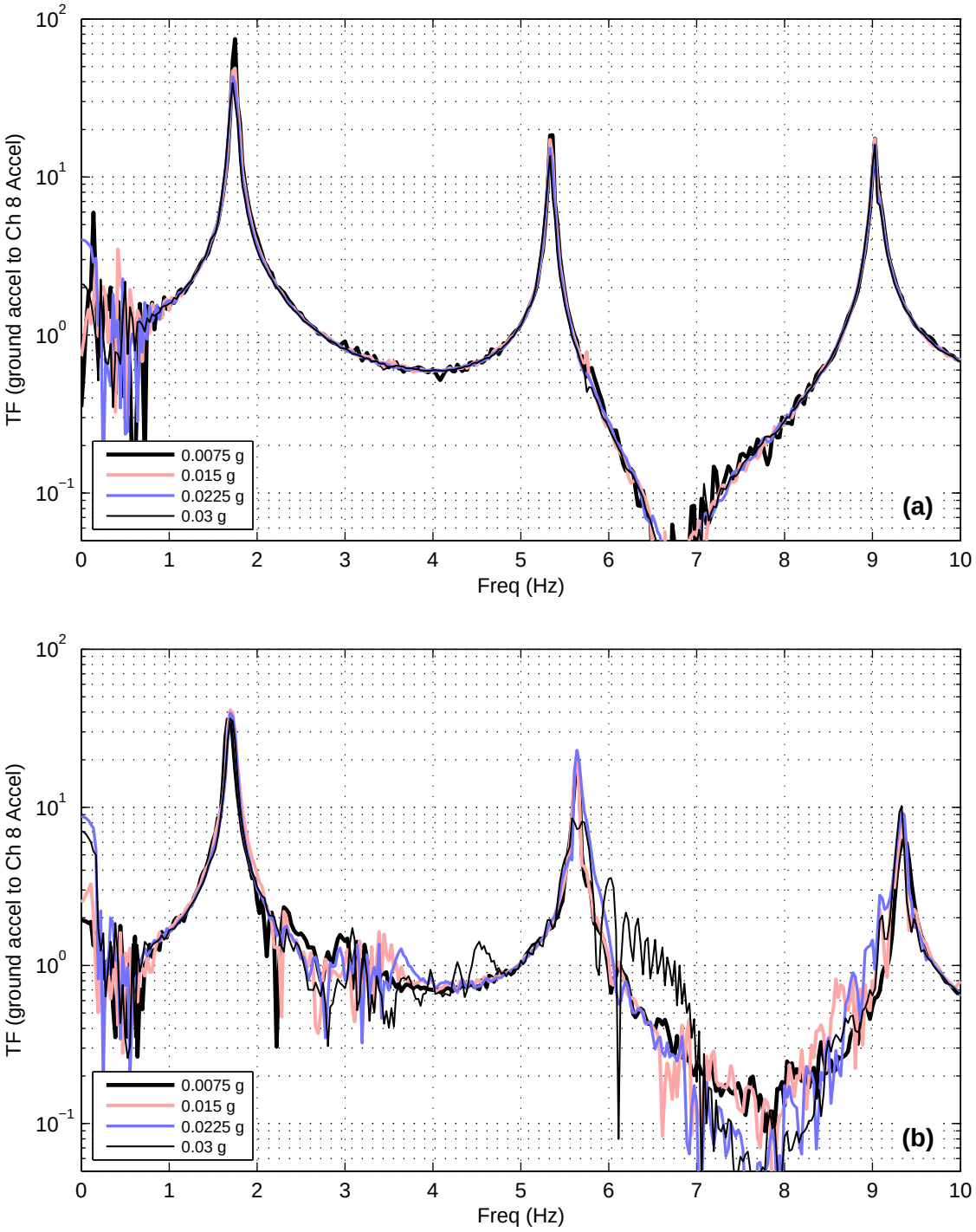

Figure 7-36. Ground acceleration to seventh floor acceleration transfer functions computed for all sine-sweep amplitudes tests for (a) all locked configuration (b) Type I NESs unlocked configuration

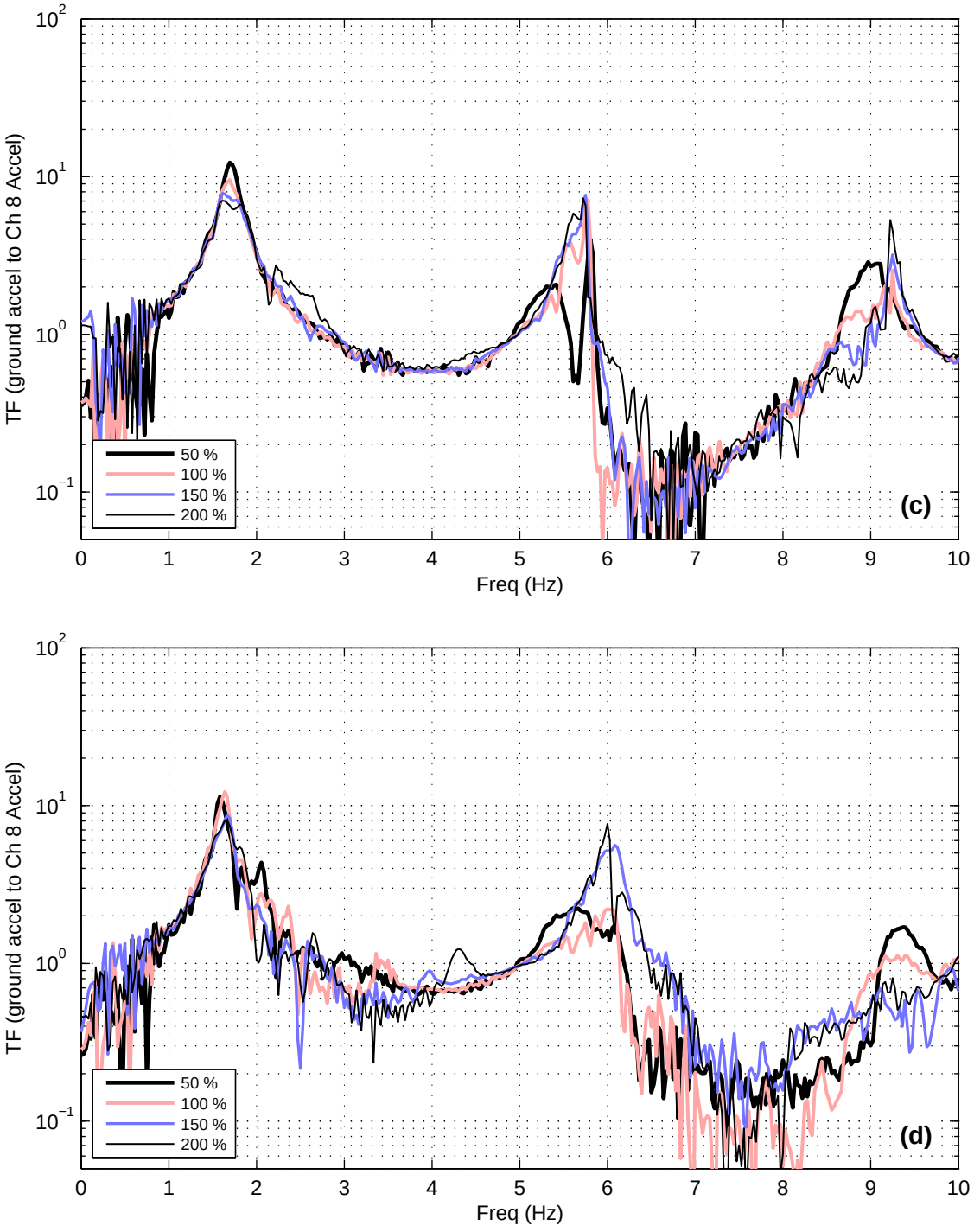

Figure 7-37. Ground acceleration to seventh floor acceleration transfer functions computed for all sine-sweep amplitudes tests for (c) SSVI NESs unlocked configuration (d) all unlocked configuration

7.4 Summary

This chapter presents the experimental investigation of the performance of the system of NESs featured in the large-scale structure developed in Chapter 6. For this experimental investigation, the structure was subjected to explosive blast loading, impulse-like shake table ground motion, and sine-sweep ground motion. The results of these studies shows that this system of NESs is capable of quickly eliminating the response of the structure to all the different loads considered. By examining the response of the NESs and the wavelet spectra of the structure's response, it was shown that this quick response elimination corresponds with the large broad-band response of the NESs and the transfer of energy to the higher modes of the structure. Additionally, the mitigation of the base structure's response by these passive devices includes a significant reduction in the peak demand on the structure, as measured by the strain in the first floor columns, even when subjected to impulse dominated loads. The results from tests at various amplitude levels demonstrated that the system of NESs is capable of reducing and quickly eliminating the response of the structure across a wide range of demands. Furthermore, with sine-sweep tests utilizing the complete system of NESs, alongside tests where only part of the system of NESs is utilized, the synergistic effects of the multiple types of NESs acting in combination were highlighted.

NUMERICAL AND EXPERIMENTAL STUDIES OF THE EFFECTIVENESS OF NESS AT MITIGATING SEISMIC RESPONSE

In Chapters 5 and 7 the effectiveness of NESs for rapidly reducing the response of structures subjected to transient loads, primarily of an impulsive nature, is examined. While this type of loading is important, other forms of transient loading, such as seismic ground motions can critically effect structures. Accordingly, in this chapter, studies are performed to investigate the potential effectiveness of NESs at mitigating the response of building structures subjected to seismic ground motion. Both numerical simulations and experimental testing will be utilized.

For the numerical study presented in the first section, the system considered is a Type I NES attached to a two-degree-of-freedom structure. Using numerical simulations, optimization of the NESs parameters is performed when the system is subjected to a seismic ground motion. Using the resulting system, the effectiveness of the Type I NES will be examined when considering uncertainty in the loading level along with changes in the nature frequency of the base structure. Additionally, as a part of this work, comparisons of the NES's performance are made with a TMD system of equal mass.

For the experimental study presented in the second section, the large-scale structure and system of NESs developed in Chapter 6 are used. In this study, the effectiveness of the system of NESs is investigated when the structure is subjected to several historical ground motions. Additionally, in this study the dependency of the performance of the system of NESs on the amplitude level of the ground motion is investigated by subjected the system to different scaling levels of the ground motions considered. Synergy between the different parts of the system of NESs is investigated with results when the whole system of NESs is unlocked and results when only a portion of the system of NESs is unlocked.

8.1 Numerical investigation of the effectiveness of NESs at mitigating seismic response

8.1.1 Model building structure and supplemental damping devices

In this work, a two-degree-of-freedom linear model of a shear building is evaluated (see Figure 8-1). This model is based on the small-scale test structure introduced in Chapter 5, which was designed to have natural frequencies similar to the natural frequencies of a typical midrise steel structure (American Society of Civil Engineers. 2010). The mass and stiffness matrices for this model in relative coordinates are shown given by

$$\mathbf{M}=\begin{bmatrix} m_1 & 0 \\ 0 & m_2 \end{bmatrix}=\begin{bmatrix} 24.3 & 0 \\ 0 & 24.2 \end{bmatrix}\ \text{kg} \qquad \mathbf{K}=\begin{bmatrix} k_1+k_2 & -k_2 \\ -k_2 & k_2 \end{bmatrix}=\begin{bmatrix} 15040 & -8220 \\ -8220 & 8220 \end{bmatrix}\ \text{N/m} \quad (0.1)$$

With these mass and stiffness matrices, the resulting first and second natural frequencies of the structure are 1.63 and 4.56 Hz, respectively. The damping in the model is set at 2% in each mode, which is again similar to that of a typical midrise steel structure (Tamura 2006).

Figure 8-1 also shows representations of the model structure with TMD and NES attachments. For both the TMD and the NES, the mass ratio, μ, has been set to 5% of the total mass of the building structure, $m_{tot} = m_1 + m_2$. The stiffness and damping parameters of the TMD, k_{TMD} and c_{TMD}, that were considered in the analysis in this study were chosen based on literature. The optimal values of k_{TMD} and c_{TMD} for reducing the displacement response of a structure undergoing random base acceleration was studied using numerical analysis in (Warburton 1982), and a set of empirical equations for the optimized parameters were developed. These optimized parameters and the equations used to calculate them are given by

$$\alpha_{opt} = \frac{(1-\mu/2)^{1/2}}{1+\mu} = 0.94$$

$$\zeta_{opt} = \sqrt{\frac{\mu(1-\mu/4)}{4(1+\mu)(1-\mu/2)}} = 0.110$$

$$\omega_{TMD} = \alpha_{opt}\omega_1 = 0.94(1.63)2\pi = 9.63\,{}^{rad}/_{\sec} \tag{0.2}$$

$$k_{TMD} = \omega_{TMD}^2 \mu m_{tot} = (9.63)^2 (0.05)(24.3+24.2) = 224.89\,{}^{N}/_{m}$$

$$c_{TMD} = 2\zeta_{opt}\sqrt{\mu m_{tot} k_{TMD}} = 5.14\,{}^{Ns}/_{m}$$

where ω_{TMD} is the natural frequency of the TMD, ω_1 is the first natural frequency of the structure, ζ_{opt} is the optimal damping ratio of the TMD, α_{opt} is the optimal ratio of the natural frequency of ω_{TMD} to ω_1, k_{TMD} is the optimal linear stiffness coefficient of the TMD, and c_{TMD} is the optimal linear damping coefficient of the TMD.

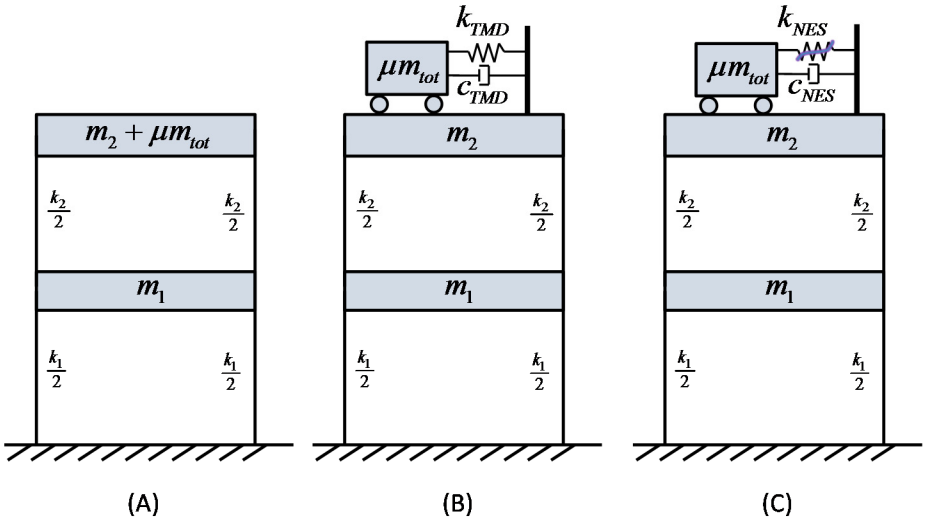

Figure 8-1. Structure model (a) building structure, (b) structure with TMD, and (c) structure with NES

Similar to the TMD in this study, the NES is connected to the top floor of the building structure with nonlinear stiffness and linear damping elements; the stiffness element has a purely cubic nonlinearity

$$F_{NES-spring} = k_{NES} x^3 \tag{0.3}$$

This type of nonlinearity can be implemented in many ways; however, one of the most common has been to use elastic elements and geometric nonlinearities to do so (Andersen et al. 2011). Given the complex nature and amplitude sensitivity of structures with elements containing essential nonlinearities, no simple equations exist to calculate the optimized parameters for the NES. In a subsequent section, a study is performed to determine optimized values of k_{NES} and c_{NES} for the particular loading considered in this study.

8.1.2 Design ground motion

The ground acceleration record that was used as the design input for this study is shown in Figure 8-2. This record is a band-limited white noise that has been passed through an eight-pole elliptical filter with a cutoff frequency at 40 Hz. Additionally, this record was scaled such that the maximum displacement response of the building structure in the time range considered was 0.02 m (see Figure 8-3).

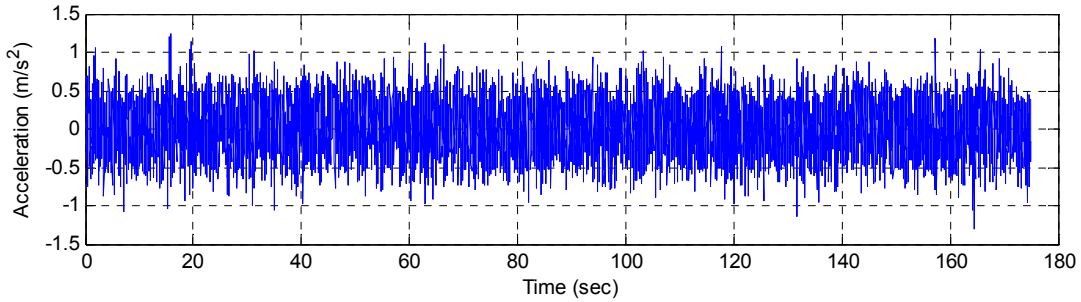

Figure 8-2. Design Input Ground Acceleration Record

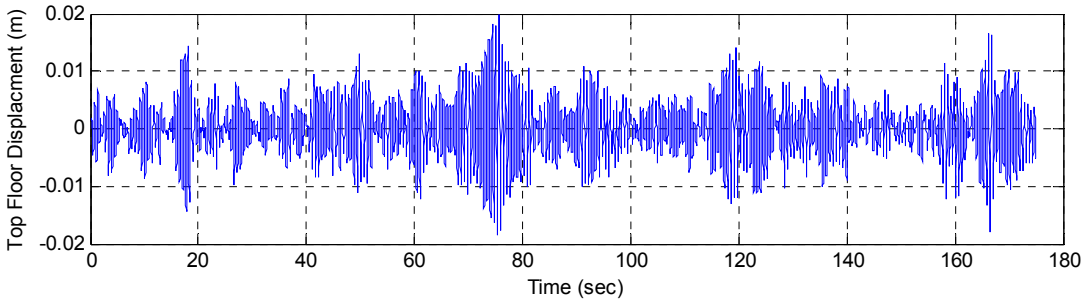

Figure 8-3. Response of model building with locked TMD/NES to the design input ground motion

8.1.3 Response measures

To investigate the performance of the NES and TMD, a set of measures that assess the performance of the structure in the time domain was chosen. Because the NES and TMD are both intended to protect the primary structure by controlling its response, these measures

consider only the response of the building structure, not the response of the NES or TMD. The first measure of interest is the maximum displacement of the building structure. This measure was chosen because the amount of damage a structure sustains in a seismic event has been found to correlate well with the maximum displacement of the building (Elnashai 2008). The second response measure used in this analysis is the RMS displacement of the top floor of the building. Like the first measure, this measure was chosen because of the relationship between damage in the building and the displacement that the building undergoes; however, because this measure accounts for the complete time history response of the building, it is a more general measure of the displacement demand on the structure.

8.1.4 NES optimization

To determine the optimized NES parameters when the model structure is subjected to the design ground motion, a parametric study is performed by varying the values of k_{NES} and c_{NES}. The numerical simulations for this study are run for 175 seconds; however, to avoid the effects of transients in the signal due to the initial conditions, the response measures are calculated using only the last 150 seconds of the signal. The range of k_{NES} considered in this study is 10 to 10^{10} N/m^3 and the range of c_{NES} considered is 1 to 20 Ns/m. The response measures are then used in conjunction with the response measures of the structure without the attachment to create a ratio comparing the response measures with and without the NES. The ratio of the maximum displacement with and without the NES across the range of NES parameters studied is shown in Figure 8-4. The optimal set of parameters for the NES, in terms of reducing the maximum displacement of the top floor of the structure to this particular loading, are $k_{NES} = 10^{6.1}$ N/m^3 and $c_{NES} = 11$ Ns/m, and the resulting reduction in maximum response is 48.5%. Figure 8-4 also shows that the effectiveness of the NES in reducing the top displacement of the structure is sensitive to changes in the nonlinear stiffness coefficient but is relatively insensitive to the value of the damping coefficient near the optimal value.

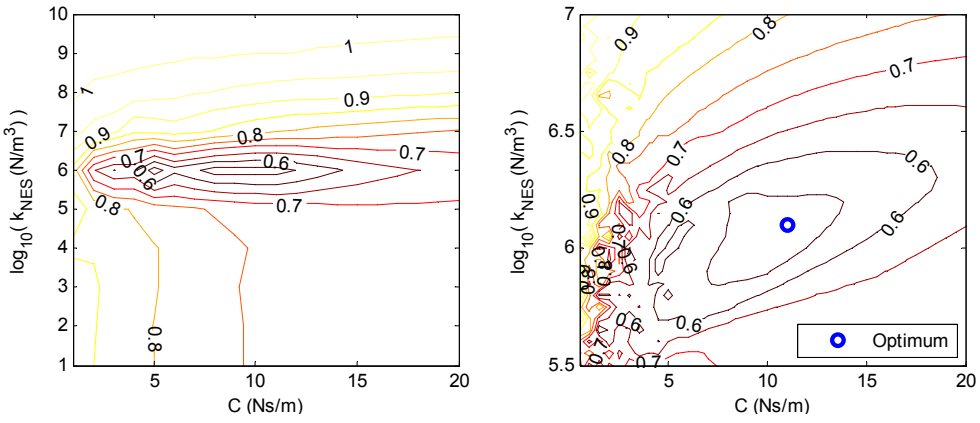

Figure 8-4. Contour plot showing the ratio with and without the NES for reducing the maximum top displacement of the structure versus k_{NES} and c_{NES} (a) full view (b) refined view of area near optimum

Figure 8-5 shows a similar plot with respect to the RMS displacement of the top floor of the structure. From this plot we see that the optimal values of the NES parameters are $k_{NES} = 10^{6.15}\ N/m^3$ and $c_{NES} = 7.5\ Ns/m$, resulting in an RMS response reduction of 38.3%. Although not identical, this point is quite near the optimum with respect to the maximum displacement of the top floor of the structure. This figure also demonstrates that the sensitivity with respect to changes in the NES parameters is similar to that found in the previous case.

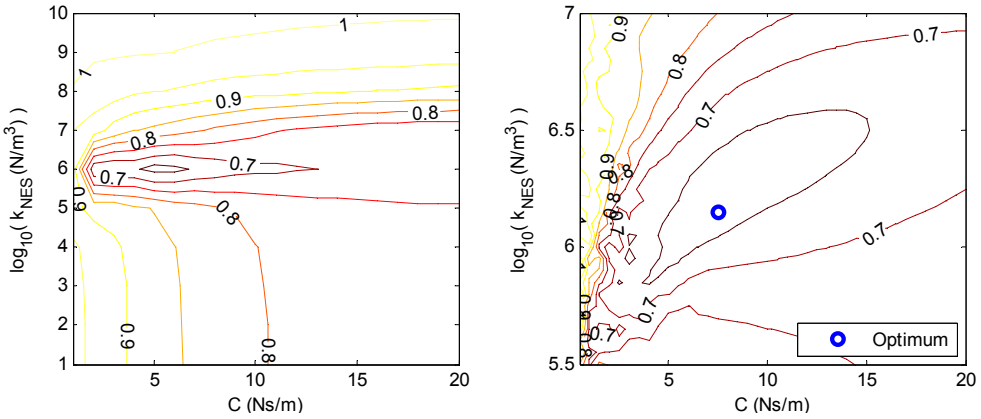

Figure 8-5. Contour plot showing the ratio with and without the NES for reducing the top RMS displacement of the structure versus k_{NES} and c_{NES} (a) full view (b) refined view of area near optimum

Due to the strong nonlinearity of the NES, the optimum NES parameters are dependent on the amplitude of the loading as well as natural frequency changes in the building. In Figure 8-6 contour plots show the response ratio for the top floor displacement of the structure with NES when the load is reduced by 50%, when the first natural frequency of the structure is decreased by 15%, and when both the load is reduced by 50% and the first natural frequency is reduced by 15%. The contour plots have a similar shape in all cases presented. Here, decreasing the amplitude of the load results in an increase in the optimal nonlinear stiffness. The primary reason for this increase is due to the fact that with lower displacements, a higher stiffness is needed to engage the moving mass. Additionally, as shown in the figure, for the cases presented decreasing the natural frequency of the building had the effect of decreasing the performance and generally shifting the most effective region further to the right, into areas of higher damping.

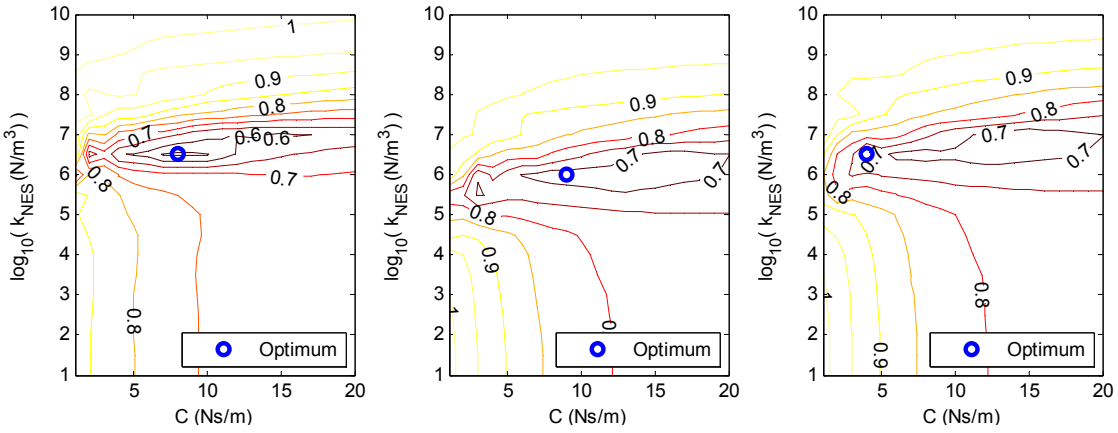

Figure 8-6. Contour plot showing the ratio with and without the NES for reducing the maximum top floor displacement of the structure versus k_{NES} and c_{NES} (a) load reduced by 50% (b) first natural frequency of building reduced by 15% (c) load reduced by 50% and first natural frequency of building reduced by 15%

8.1.5 Detuned response

The sensitivity of the response of the structure with the TMD and with the NES to changes in the load amplitude and the natural frequency of the building structure was also investigated. Numerical simulations of the model structure subjected to the design ground motion were performed for three configurations: (i) with the NES, (ii) with the TMD, and (iii) with no attachment. The amplitude of the load and the story stiffness were varied in the building structure. The range of amplitudes that were investigated was 10% to 120% of the design ground motion and the range of change to the first natural frequency was -35% to +15%. For this analysis, the NES parameters optimized to reduce the maximum top floor displacement of the structure and the optimized TMD parameters proposed by Warburton (Warburton 1982) were utilized.

Contour plots showing the ratio of the maximum top floor displacement of the system with NES and the system with TMD to the system with no attachment across the range of values simulated is shown in Figure 8-7. Here, the effectiveness of the NES varies with changes in the amplitude of loading, and with changes due to the natural frequency of the building structure, while the effectiveness of the TMD only changes with changes due to the natural frequency of the building structure. This figure also shows that when the change in natural frequency is low, the TMD generally outperforms the NES; however, as the change in natural frequency increases, the NES outperforms the TMD. Additionally, Figure 8-7 shows that unlike the TMD, which is completely ineffective at reducing the top floor maximum displacement at high changes to the natural frequency, the NES reduces the response of the building across the entire range of frequencies examined. This behavior is also seen in Figure 8-8, which shows a similar plot, except that the change in top floor RMS displacement is evaluated.

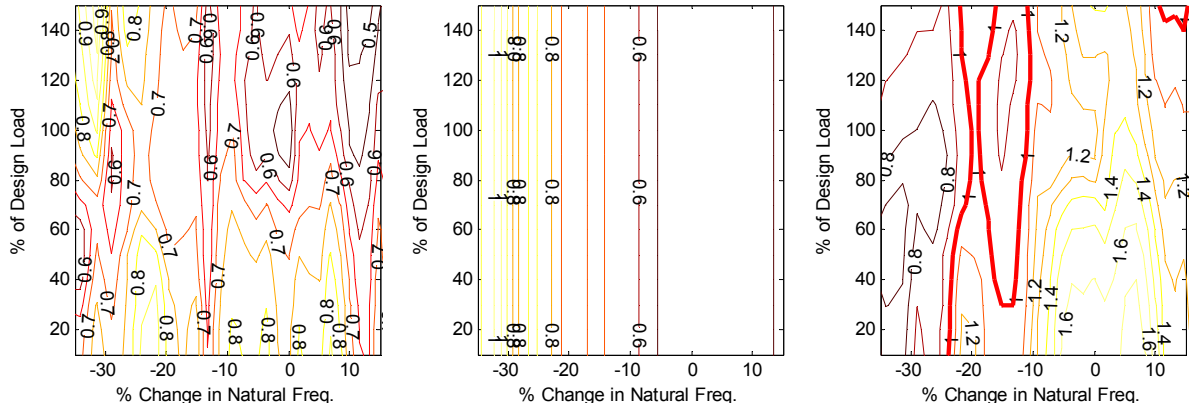

Figure 8-7. Contour plot of the maximum top floor displacement across range of amplitudes and natural frequencies of (a) the system with NES compared to the system with no attachment, (b) the system with TMD compared to the system with no attachment, and (c) the system with NES compared to the system with TMD

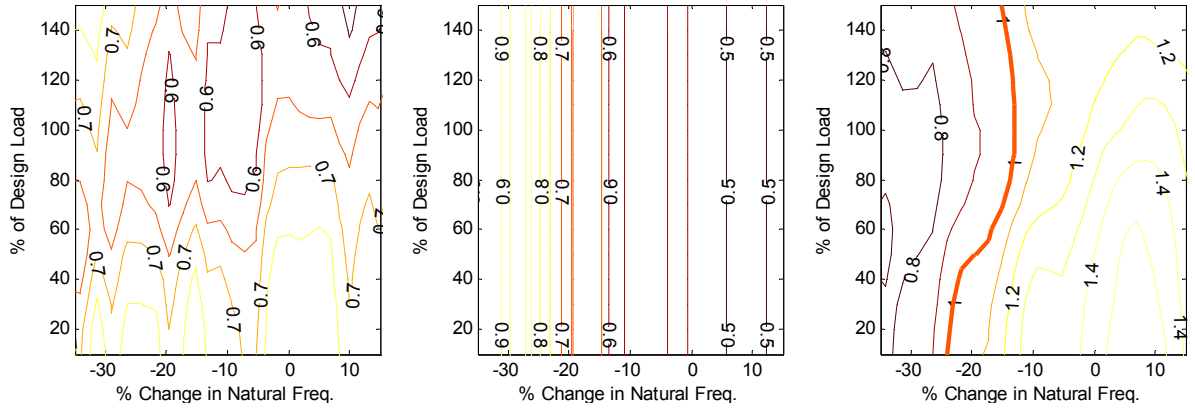

Figure 8-8. Contour plot of the top floor displacement across range of amplitudes and natural frequencies of (a) the system with NES compared to the system with no attachment, (b) the system with TMD compared to the system with no attachment, and (c) the system with NES compared to the system

8.2 Experimental investigation of large-scale system of NESs to seismic loading

In this section, an experimental investigation is presented on the effectiveness of the system of NESs introduced in Chapter 6 at mitigating the seismic response of a large-scale base structure. This section is separated into three subsections. In the first subsection, the base structure and system of NES used in this investigation will be briefly reintroduced. In the second subsection,

the ground motions considered are presented. In the third subsection, the experimental results are presented and discussed.

8.2.1 Base structure and system of NESs

The large-scale base structure and system of NESs introduced in Chapter 6 is utilized for this experimental study. This base structure and system of NESs is shown in Figure 8-9. The system of NESs examined consists of matching set of two Type I NES and one SSVI NES, incorporated into both the eight floor and the ninth floor. For additional details of this large-scale base structure and system of NESs, refer to Chapter 6.

As a system of NESs is used in this investigation, the synergistic effects of utilizing multiple types of NESs can be studied. Consequently, several different cases of the condition of the system of NESs will be examined in this study. These cases include only the Type I NESs unlocked and able to move relative to the structure, only the SSVI NESs unlocked, the whole system of NESs unlocked, and with the whole system of NESs locked.

Figure 8-9. Base structure containing system of NESs used for experimental seismic effectiveness study

8.2.2 Ground motions

Shake table testing of the large-scale base structure and system of NESs introduced in the previous section was performed using the Triaxial Earthquake and Shock Simulator (TESS) shake table at the US Army Corps of Engineers Construction Engineering Research Laboratory in Champaign, IL. Historic ground motions measured from the 1995 Kobe earthquake, 1994 Northridge earthquake, and 1940 El Centro earthquake were used for this study. In Table 8-1, the specific station and component utilized for the ground motions considered are listed.

Additionally, this table contains the record's original PGA, the distance of the station from the fault, and the magnitude of the event. Scaled versions of each of the ground acceleration records considered in this testing are shown in Figure 8-10. Testing with these records was performed at multiple different scaling levels to investigate the amplitude dependency of the performance of the system of NESs.

Table 8-1. Ground motions considered

Earthquake	Magnitude	Component / Station	Original PGA (g)	Distance to Fault (km)
1995 Kobe (Japan)	6.9	KJM000 / 0 KJMA	0.821	0.6
1994 Northridge (USA)	6.7	RRS228 / 77 Rinaldi	0.838	7.1
1940 El Centro (USA)	7.0	North-South Component (Pecknold Version)	0.313	8.3

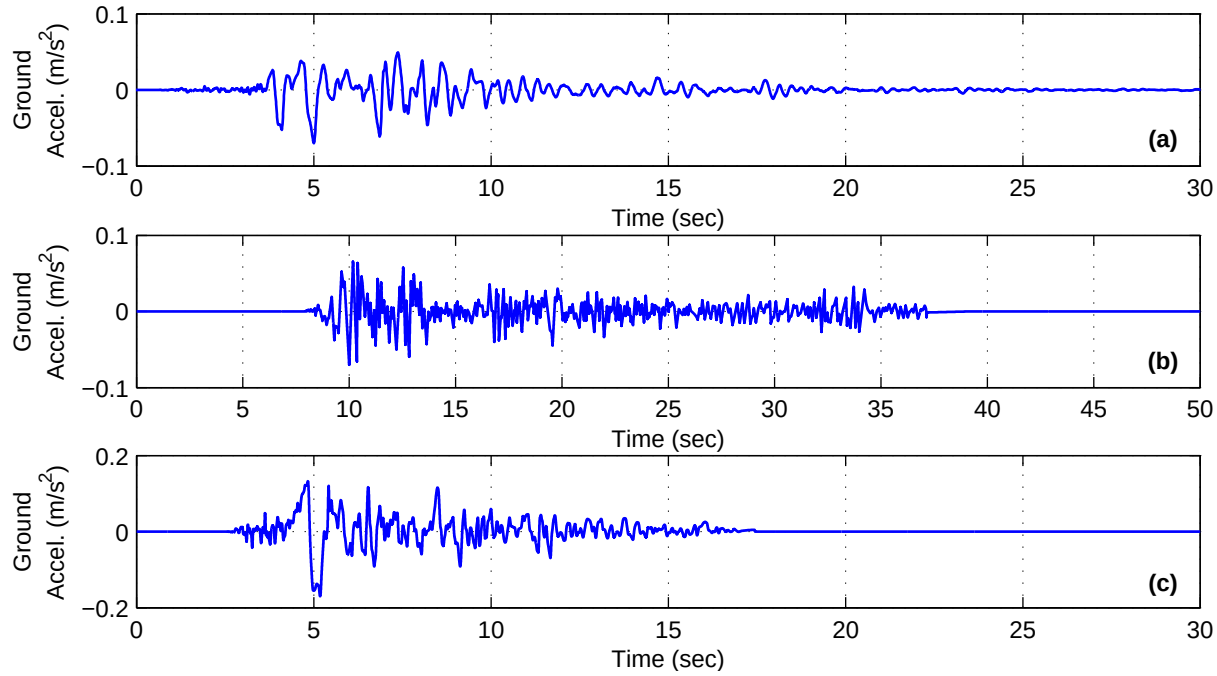

Figure 8-10. Scaled ground motions considered (a) Kobe earthquake, (b) El Centro earthquake, and (c) Northridge earthquake

8.2.3 Experimental results

8.2.3.1 Kobe earthquake

The resulting seventh floor displacement response to the Kobe earthquake ground motion scaled to a PGA of 0.07 g is shown in Figure 8-11a, c, e, and g for each condition of the system of

NESs considered. As this figure shows, during cases when a portion or the entire system of NESs was unlocked, the response of the system was dramatically reduced, including a substantial reduction in peak displacement, compared to the locked case. While response reduction is seen in all cases with NESs unlocked, in some cases better performance is observed. An example of this superior performance, in terms of peak displacement reduction, is the structure's response with the SSVI NES unlocked compared to the case with the Type I NESs unlocked. Another example is the improved attenuation of the low level residual motion that remains after the structure's high amplitude response, which is seen in the case with the Type I NESs unlocked compared to the case with the SSVI NES unlocked. However, with the whole system of NESs unlocked, the individual aspects of the response that the Type I and SSVI NES excel at mitigating are combined to create a system that shows the best overall performance.

Wavelet spectra are used to examine the time dependent frequency content of the structure's response. The wavelet spectra corresponding to the acceleration response of the structure's seventh floor when subjected to the 0.07 PGA Kobe ground motion are shown Figure 8-11b, d, f, and h. This figure shows that the frequency content of the structure's response is concentrated around the first couple structural modes when all the NESs were locked; however, when the NESs were unlocked there is a dramatic shift in frequency content of the response to the higher modes and a rapid attenuation of the lower mode response. This shift in frequency content is evident when the Type I NESs were unlocked, but it is far more evident when the SSVI NESs and the whole system of NESs were unlocked due to the strong impacts of the SSVI NESs.

The acceleration response of the seventh floor of the structure to the 0.07 PGA scaled Kobe earthquake is shown in Figure 8-12 for the four NES configuration considered. This figure shows that there is a reduction in acceleration response, compared to the response with all the NESs locked, only in the case with the Type I NESs unlocked. With the SSVI NES unlocked and with all NESs unlocked, there is a large magnification in the acceleration response observed. The reason for this drastically increased acceleration response is the steel to steel impacts that are used to produce the essential nonlinearity in the restoring force of the SSVI NES. These impacts cause high accelerations for the SSVI NES's host floor, as well as the entire structure. The high acceleration in the structure outside the SSVI NES's host floors is due to the SSVI NES's highly effective ability to shift low frequency vibration to higher frequencies. As shown in Figure 8-11 and Figure 8-12, the result of this transfer of energy to higher modes is lower displacements, but higher accelerations. This resulting high acceleration should be considered when implementing a SSVI NES in a structure that contains non-structural elements particularly vulnerable to high accelerations.

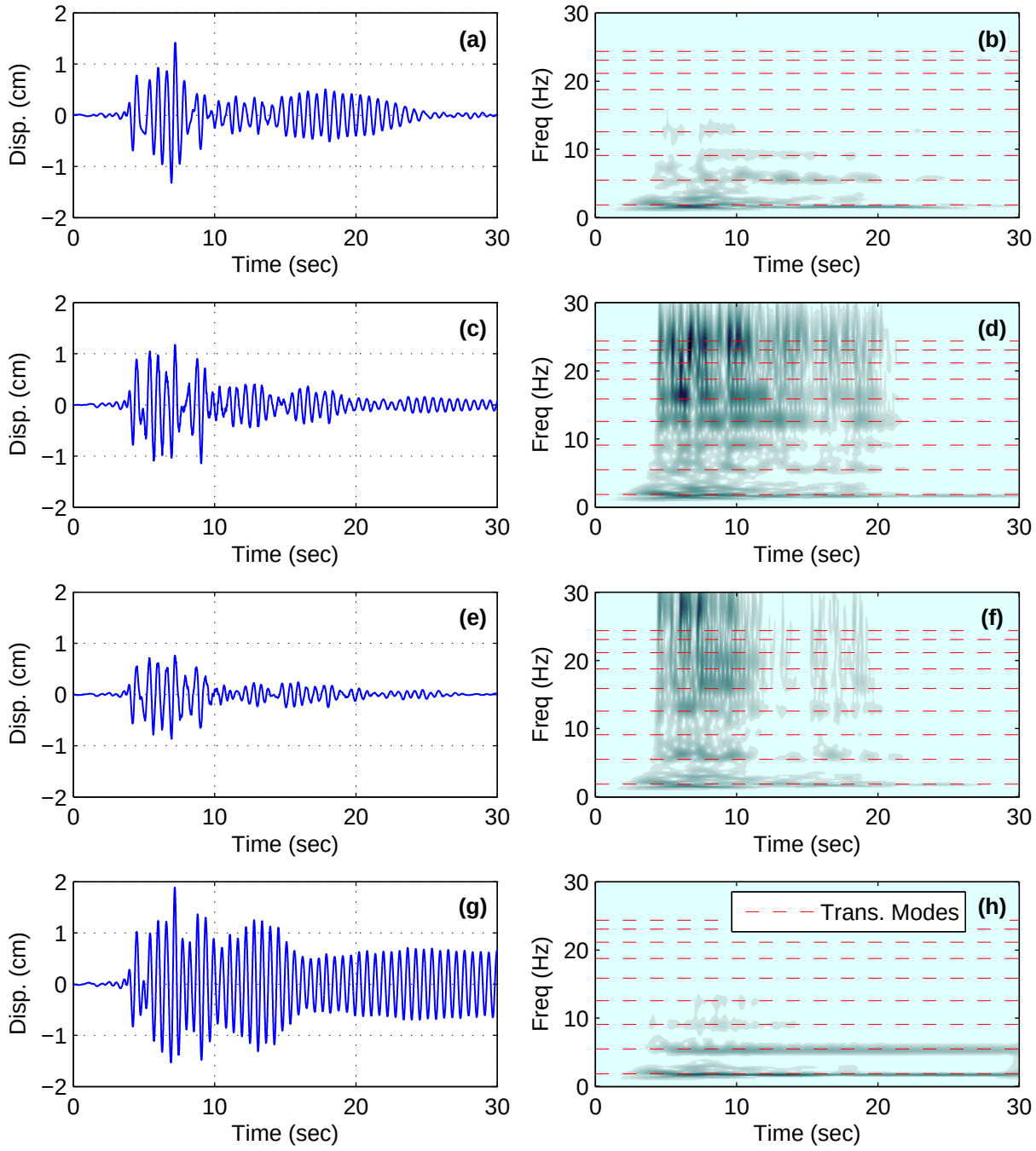

Figure 8-11. Response to 0.07 PGA Kobe earthquake - seventh floor displacement (a) Type I NESs unlocked, (c) SSVI NESs unlocked, (e) All NES unlocked, and (g) All NES locked; seven floor acceleration wavelet spectra (b) Type I NESs unlocked, (d) SSVI NESs unlocked, (f) All NES unlocked, and (h) All NES locked

The accelerations and displacements that have been examined give insight into the behavior of the structure, but they do not directly correlate with the demand on the structure. The first floor columns of a structure are often times where the peak demand on a structure occurs;

consequently, to examine the demand on the structure, strain in the first floor columns was measured. Figure 8-13 shows the time history of the strain in the columns when subject to the Kobe earthquake scaled to a PGA of 0.07 g for the cases when the Type I NESs are unlocked, the SSVI NESs are unlocked, all the NESs are unlocked, and all the NESs are locked. This figure shows that, in all of the cases when the NESs are unlocked, significant attenuation of the response occurs compared to the locked case. This attenuation includes a reduction in peak strain, which is observed to be most significant in the cases when the SSVI NESs are unlocked or all the NESs are unlocked.

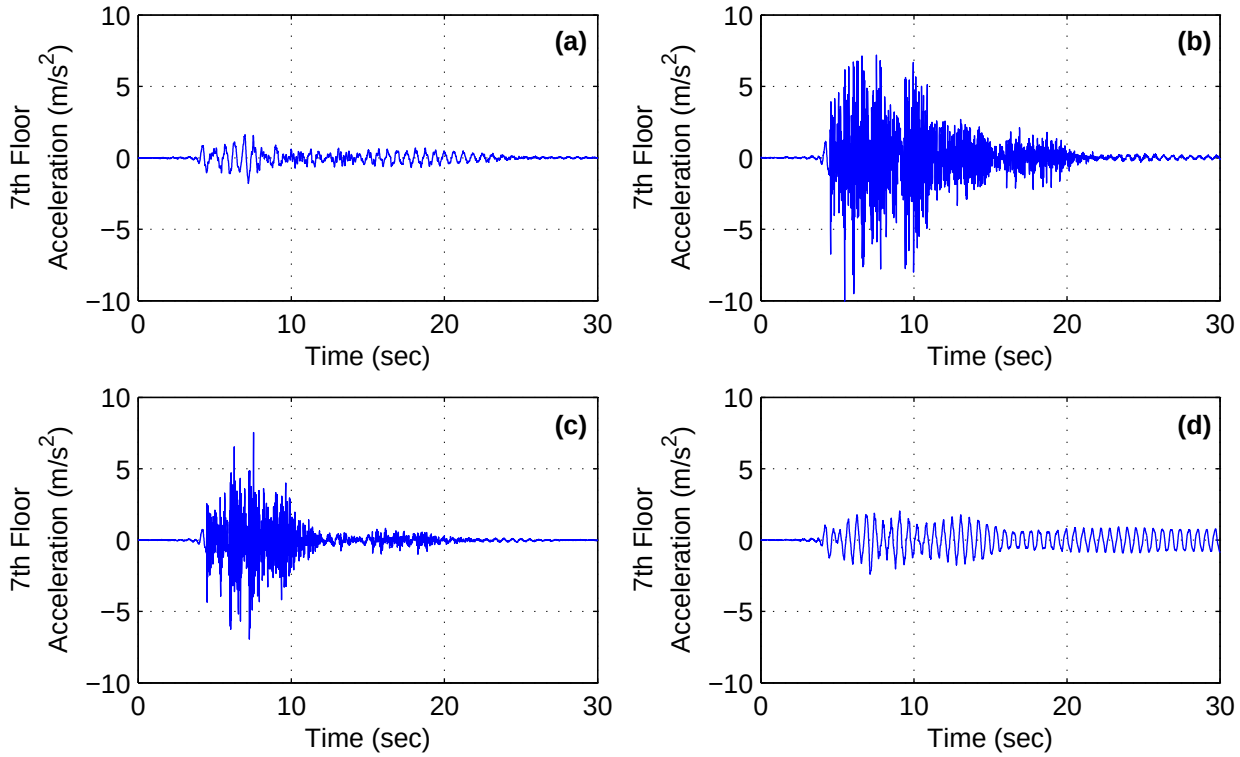

Figure 8-12. Response to 0.07 PGA Kobe earthquake - seventh floor acceleration (a) Type I NESs unlocked, (b) SSVI NESs unlocked, (c) All NES unlocked, and (d) All NES locked

To examine how the amplitude of the ground motion affects the performance of the system of NESs, shake table tests were performed with multiple different scaling levels of the Kobe earthquake ground motion. As discussed in Chapter 3, the apparent damping in the response of the structure can be quantitatively examined through calculation of the effective damping; consequentially, the amplitude dependency of the system's performance will be investigated through the examination of the effective damping. Figure 8-14 shows the change in first mode effective damping across a range ground motion amplitudes for each of the NES cases. As expected, this figure shows that, with the NESs locked, a very low first mode effective damping is consistently measured. Additionally, this figure shows that the peak effective damping of the case with the Type I NESs unlocked and the case where the SSVI NESs are unlocked occurred at different ground motion amplitudes; as intended, the peak of the Type I NES occurs at a lower amplitude and the peak of SSVI NES case occurs at a high amplitude. Furthermore, the synergy between the types of NESs is demonstrated in the case with all NESs unlocked as this case

shows a high level of first most effective damping that is relatively consistent across all ground motion amplitudes considered.

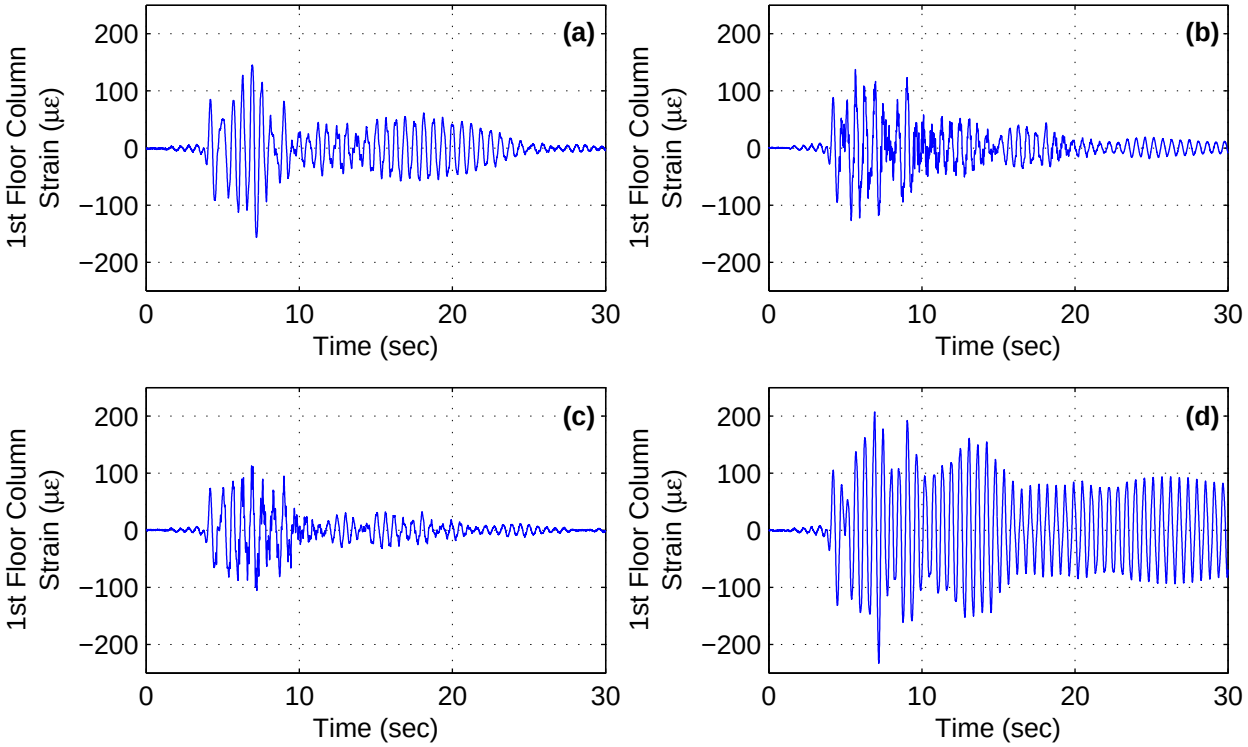

Figure 8-13. Response to 0.07 PGA Kobe earthquake - first floor column strain (a) Type I NESs unlocked, (b) SSVI NESs unlocked, (c) All NES unlocked, and (d) All NES locked

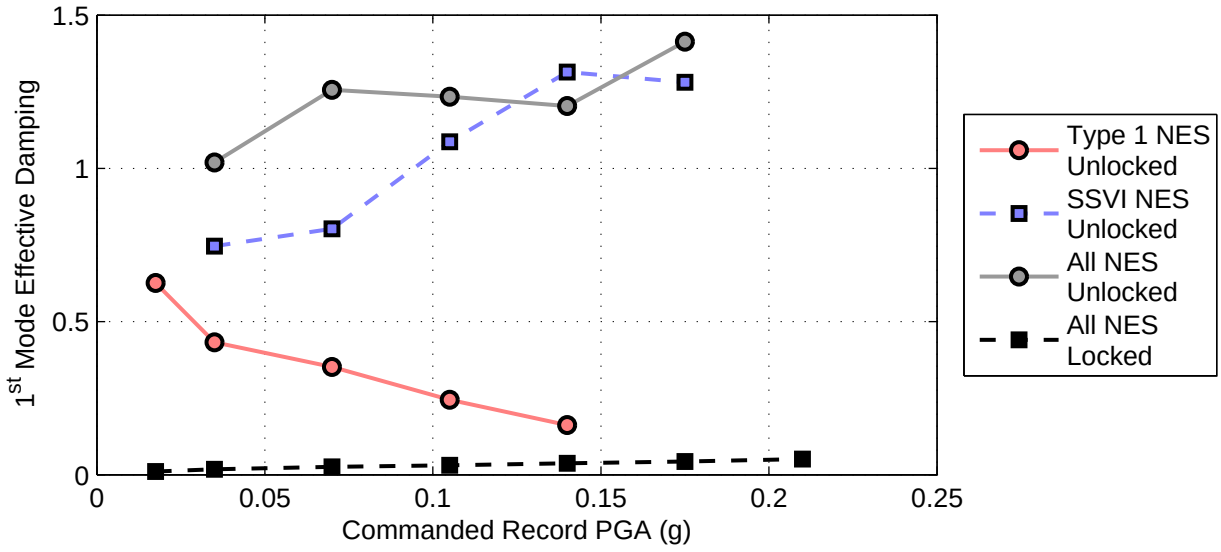

Figure 8-14. Response to Kobe earthquake - first mode effective damping

8.2.3.2 Northridge and El Centro earthquake

Time histories for the seventh floor displacement response and the seventh floor acceleration wavelet spectra are shown in Figure 8-15 and Figure 8-16 for the 0.17 PGA Northridge and the 0.07 PGA El Centro earthquakes, respectively. These figures show similar trends as those which were identified in the response of the structure to the Kobe earthquake. These trends include that during cases when a portion or the entire system of NESs was unlocked, the response of the system, in most cases, was dramatically reduced, including a substantial reduction in peak displacement, compared to the locked case. Additionally, superior performance is usually seen in the case when the SSVI NESs or the whole system of NESs are unlocked. Additionally, another similar trend is that there is an increase in the higher modes content and a rapid attenuation of the lower mode response. This increase in higher mode content is particularly evident during cases when the SSVI NESs are unlocked.

Time histories for the first floor column strain are shown in Figure 8-17 and Figure 8-18 for the 0.17 PGA Northridge and the 0.07 PGA El Centro earthquakes, respectively. These figures show that, in all cases, the NESs are able to reduce the peak strain demand on the structure. This reduction is particularly high in the case of the SSVI NESs unlocked and all the NESs unlocked. Furthermore, the reduction in strain is more dramatic in the response to the El Centro earthquake compared to the Northridge earthquake. The reason for this behavior is that the Northridge earthquake is dominated by an impulse component, which is a more difficult loading for achieving large reductions in peak demand.

The first mode effective damping calculated from the response of the structure to a range of PGA values of the Northridge and the El Centro earthquakes is shown in Figure 8-19 and Figure 8-20, respectively. In these figures, the effective damping results are shown for the four NES configurations considered. Like previously observed, these figures show that the peak effective damping of the case with the Type I NESs unlocked and the case where the SSVI NESs are unlocked occurred at different ground motion amplitudes. For the Type I NES, the peak effective damping occurs at a lower amplitude and for the SSVI NES the peak occurs at a higher amplitude. Furthermore, both figures shown that the synergy between the types of NESs leads to the case with all NESs unlocked showing a high level of first most effective damping that is relatively consistent across a large range of the ground motion amplitudes.

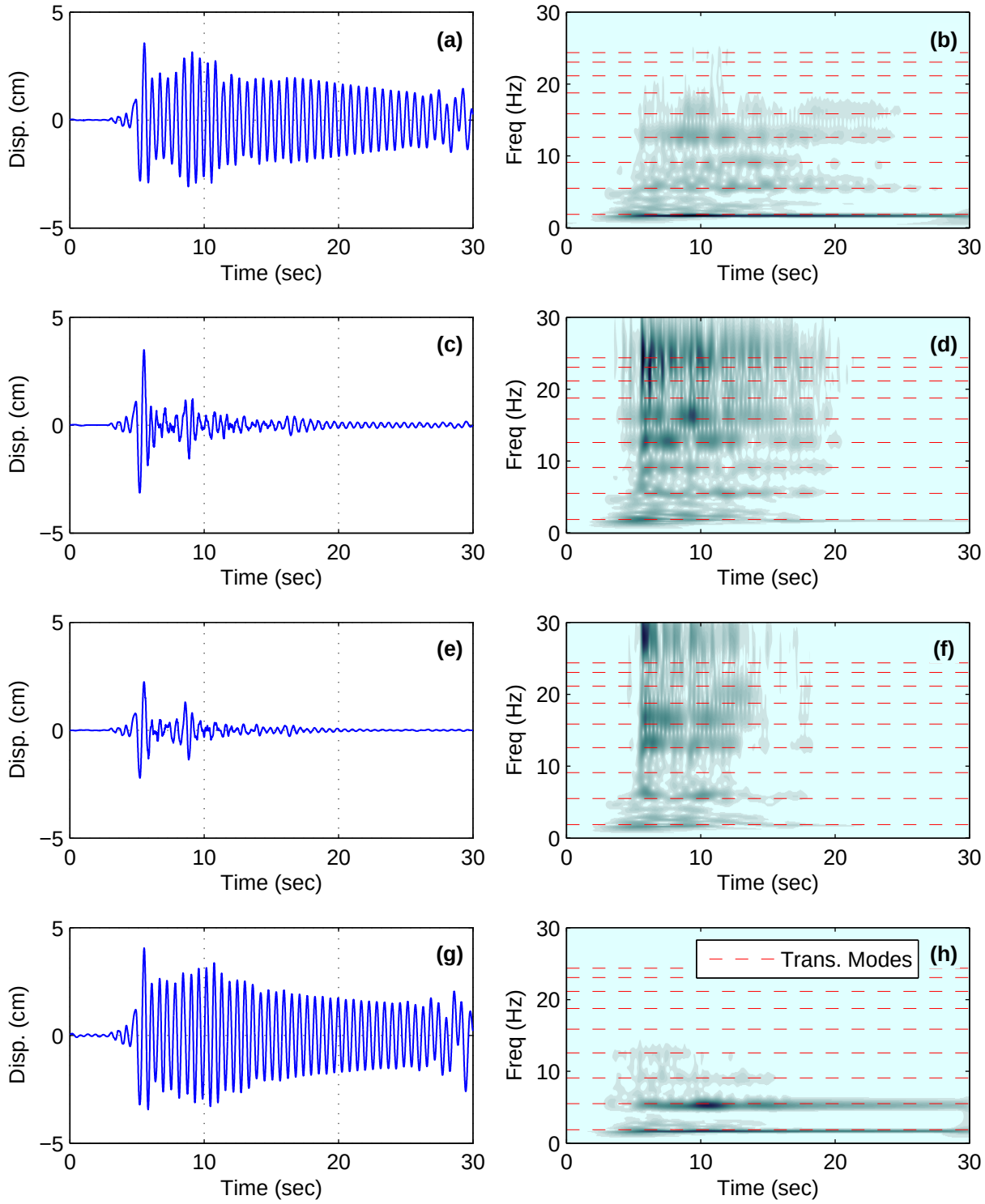

Figure 8-15. Response to 0.17 PGA Northridge earthquake - seventh floor displacement (a) Type I NESs unlocked, (c) SSVI NESs unlocked, (e) All NES unlocked, and (g) All NES locked; seven floor acceleration wavelet spectra (b) Type I NESs unlocked, (d) SSVI NESs unlocked, (f) All NES unlocked, and (h) All NES locked

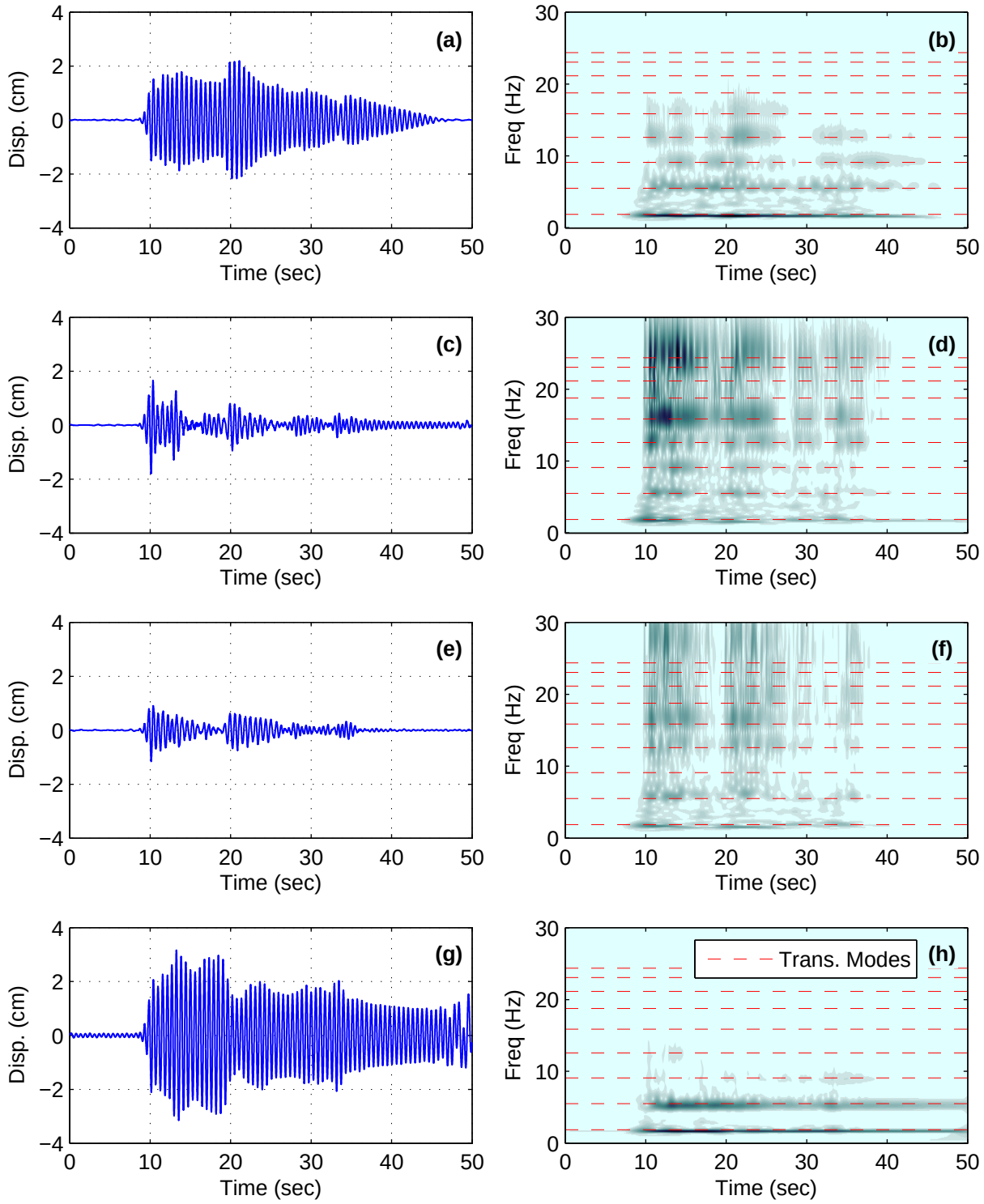

Figure 8-16. Response to 0.07 PGA El Centro earthquake - seventh floor displacement (a) Type I NESs unlocked, (c) SSVI NESs unlocked, (e) All NES unlocked, and (g) All NES locked; seven floor acceleration wavelet spectra (b) Type I NESs unlocked, (d) SSVI NESs unlocked, (f) All NES unlocked, and (h) All NES locked

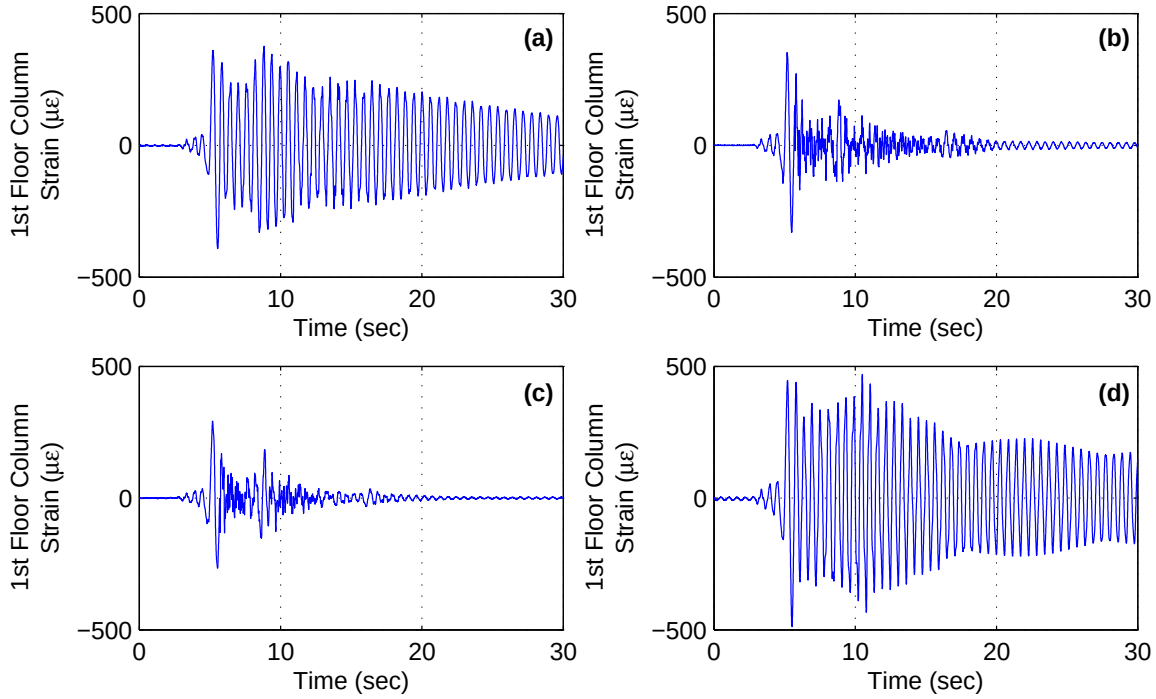

Figure 8-17. Response to 0.17 PGA Northridge earthquake - first floor column strain (a) Type I NESs unlocked, (b) SSVI NESs unlocked, (c) All NES unlocked, and (d) All NES locked

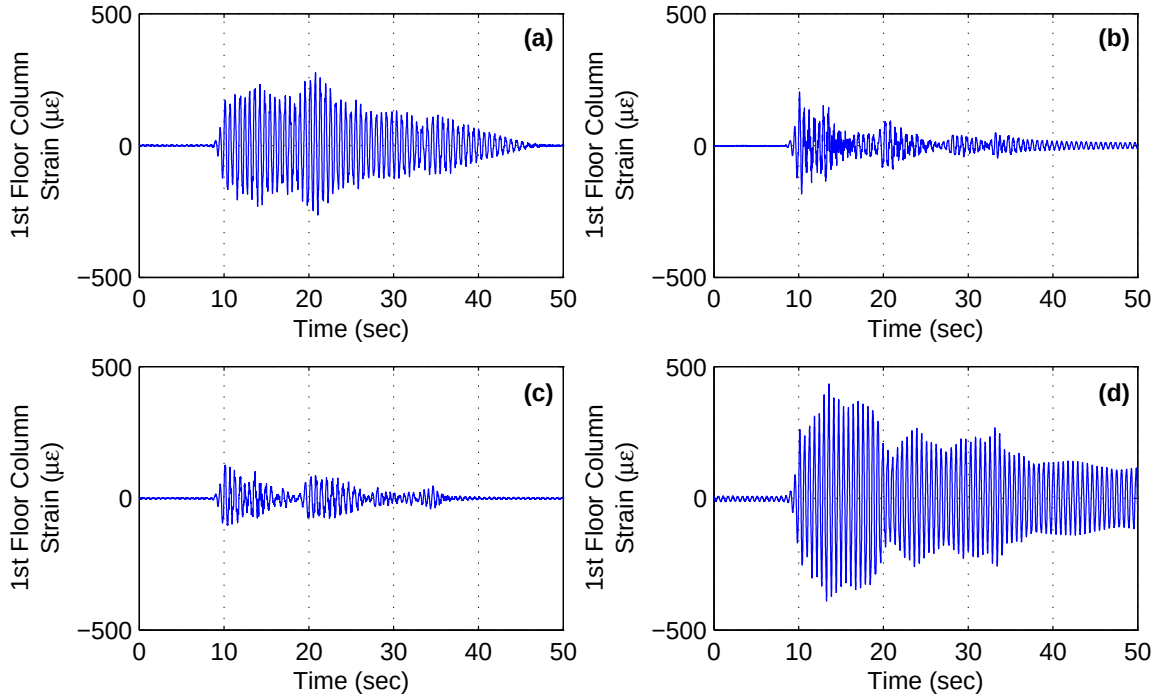

Figure 8-18. Response to 0.07 PGA El Centro earthquake - first floor column strain (a) Type I NESs unlocked, (b) SSVI NESs unlocked, (c) All NES unlocked, and (d) All NES locked

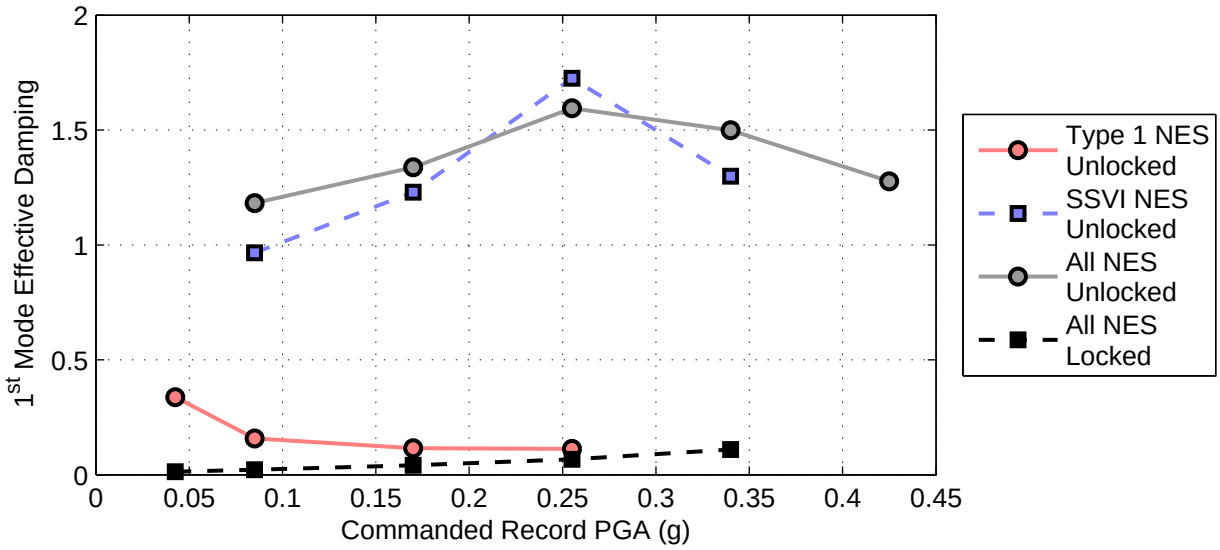

Figure 8-19. Response to Northridge earthquake - first mode effective damping

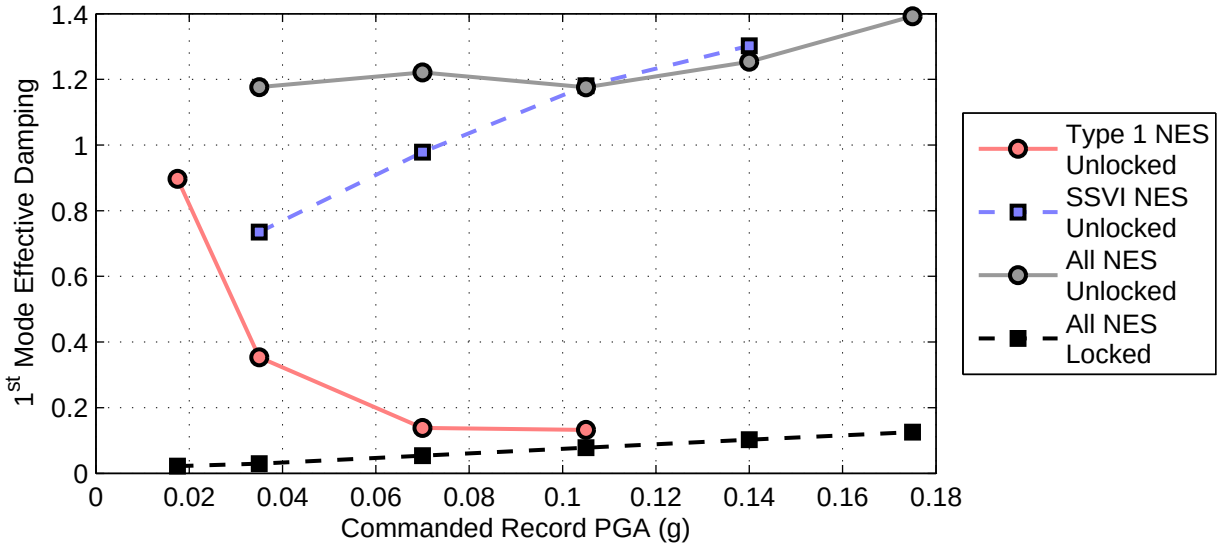

Figure 8-20. Response to El Centro earthquake - first mode effective damping

8.3 Summary

This chapter investigate the potential effectiveness of NESs at mitigating the response of building structures subjected to seismic ground motion. For this investigation, both numerical simulations and experimental testing was utilized. In the numerical study presented, the use of a Type I NES to control the seismic response of a two-degree-of-freedom structure is considered. An optimization using a general ground motion was performed to determine the NESs

parameters, then response of the system was investigated when the amplitude of the ground motion is changed and when the stiffness of the base structure was modified. Comparison with the TMD showed that the performance of the NES was less vulnerable to changes in structural stiffness, but more vulnerable to changes in load amplitude. In the experimental study presented, the effectiveness of a system of nonlinear energy sinks (NESs) at controlling the response of a large-scale base structure subjected to seismic ground motion was experimentally investigated. The system of NESs examined in this work consists of a combination of SSVI NESs, which utilize a non-smooth essential nonlinearity, and Type I NES, which utilize a smooth essential nonlinearity. Examination of the response of the structure to scaled versions of historic ground motions showed that improvements to the attenuation of the structure's response, including a reduction in peak demand, can be observed when the entire system of NESs is unlocked as well as when only the Type I or SSVI NESs are unlocked. Furthermore, tests across a range of ground motion scaling factors indicated that the peak effectiveness of the Type I NESs and the SSVI NESs occurred at different ground motion amplitudes; however, due to the synergy between the types of NESs, superior and more constant performance was observed across a large range of ground motion amplitudes when the entire system of NESs was unlocked.

CONCLUSIONS AND FUTURE STUDIES

9.1 Conclusions

Extreme transient loads introduce a tremendous amount of energy into building structures. This energy must be somehow dissipated or transferred to preserve the integrity of the structure. Semi-active and active control devices have shown promise in protecting structures; however, they have only seen limited usage due to their cost, complexity, and dependence on a reliable power source. Additionally, traditional linear passive devices, such as tuned mass dampers, have only seen limited application for mitigating extreme loads due to their inability to reduce the peak response of structures subjected to loads with a large impulsive component and the limited frequency range for which they are effective. As a consequence of these limitations, this research sought to explore the potential for nonlinear energy sinks (NESs) to be a practical and robust means of passively protecting buildings structures subjected to extreme transient loads. The two types of transient loads focused on this research were impulsive loads, such as blasts, and broadband random loads, such as seismic ground motions.

As discussed in the following paragraphs, the investigation of NESs presented in this report involved both explosive blast testing and shake table testing. Consequently, a secondary objective of this research was the development of a blast simulation technique in which specially designed ground motions are used to simulate the global response of structures subjected to blasts. This objective was motivated by the large cost of blast testing and the inherent logistical constraints that make this type of test unsuitable for many research projects.

In the previous presented chapters of this report, literature related to NESs, traditional passive energy dissipation methods, and simulated blast testing methods was reviewed, then background information related to several numerical tools used in this research were presented. Finally, the contributions of this research are presented in several chapters.

Included in these contributions was the development of a technique to experimentally simulate, using shake-table-produced ground motion, the global response of a structure due to blast and an assessment of the feasibility of this type of experimental simulation. This assessment was done conceptually and for the specific case of a structure with an internally housed NES. This assessment showed that the type of experimental simulation proposed was feasible; however, some challenges existed. These challenges included that the load distribution was coupled to the mass distribution, the need for the desired ground acceleration to result in a bounded displacement, and the inability of this technique to simulate local effects. Additionally, this assessment demonstrated only minor differences in the response are likely due to the inertial loading of an internally housed NES. Once the feasibility of this technique was established, a generalized prototype ground motion was proposed along with a methodology for determining the optimum parameters to customize this motion for a particular blast simulation. An example of the use of this methodology was presented with numerical simulations. To validate this technique, the results of experimental testing of a large-scale structure were compared. The results of this validation study showed that the technique is capable of producing good overall agreement between the global responses measured during an explosive blast and a ground motion design with the methodology proposed.

The investigation of the potential for nonlinear energy sinks to be a practical and robust means of passively protecting buildings structures subjected to extreme transient loads was performed in stages. The first stage of this investigation included the development and experimental investigation of several different types of NESs at small and medium-scales. For this stage, the design and construction of the following NESs was undertaken: a small-scale Type I NES (a one-DOF NES which utilizes a smooth essential nonlinearity), a small-scale Type III NES (a two-DOF NES which utilizes a smooth essential nonlinearity), and a medium-scale Type III NES. This development includes the world's first known realization of a Type III NES and the first realization of an NES utilizing elastomeric bumpers to produce its nonlinear restoring force. The experimental investigation of the performance of the small and medium-scale NESs to reduce the response of base structures to impulse-like ground motion was performed. The results of these investigations show that the NESs examined were capable of rapidly attenuating the response of the base structures when subjected to shock-like ground motions. This quick attenuation in response was shown to be largely due to targeted energy transfer, where input energy is transferred in broadband fashion to the NES where it is dissipated and by the NES facilitating energy transfer from low to high frequency modes in the primary structure, where dissipation occurs over shorter time scales. While the effectiveness of the Type I and Type III NESs were shown to be load amplitude dependent, the NESs dramatically increased the first mode effective damping of the system over a reasonably wide range of amplitudes. For all of the small- and medium-scale NESs studied, good agreement was found between the experimental results and numerical simulations using experimentally identified NES parameters.

The next stage in the investigation of NESs was the development of a large-scale base structure which was specifically designed to serve as a platform to experimentally explore the effectiveness of a large-scale system of nonlinear energy sinks. The system of NESs developed features a combination of Type I NESs and single-sided vibro-impact (SSVI) NESs (a one DOF NES which employ a sharp essential nonlinearity). This structure and system of NESs represents the world's largest test bed for NES technology.

After this large-scale development effort, the investigation of NESs focused on the experimental investigation of the performance of the system of NESs featured in the large-scale structure. For this experimental investigation, the structure was subjected to explosive blast loading, impulse-like shake-table-produced ground motion, and sine-sweep ground motion. The results of these studies shows that this system of NESs is capable of quickly eliminating the response of the structure to all the different loads considered. By examining the response of the NESs and the wavelet spectra of the structure's response, it was shown that this quick response elimination corresponds with the large broad-band response of the NESs and the transfer of energy to the higher modes of the structure. Additionally, the mitigation of the base structure's response by these passive devices included a significant reduction in the peak demand on the structure, even when subjected to impulse dominated loads. The results from tests at various amplitude levels demonstrated that the system of NESs is capable of reducing and quickly eliminating the response of the structure across a wide range of demands. Furthermore, with sine-sweep tests utilizing the complete system of NESs, alongside tests where only part of the system of NESs is utilized, the synergistic effects of the multiple types of NESs acting in combination were highlighted.

The last stage in the investigation of NESs focused on their effectiveness at mitigating the response of building structures subjected to seismic ground motion. For this investigation, both numerical simulations and experimental testing were utilized. In the numerical study presented,

the use of a Type I NES to control the seismic response of a two-degree-of-freedom structure is considered. Comparison with the TMD showed that the performance of the NES was less robust to changes in structural stiffness, but more robust to changes in load amplitude. In the experimental study presented for this stage, the effectiveness of a large-scale system of NESs at controlling the response of a large-scale base structure subjected to seismic ground motion was investigated. The large-scale base structure and system of NESs which was developed and presented previously in this report was used for this investigation. Examination of the response of the structure to scaled versions of historic ground motions showed that improvements to the attenuation of the structure's response, including a reduction in peak demand, can be observed when the entire system of NESs is unlocked as well as when only the Type I or SSVI NESs are unlocked. Furthermore, tests across a range of ground motion scaling factors indicated that the peak effectiveness of the Type I NESs and the SSVI NESs occurred at different ground motion amplitudes; however, due to the synergy between the types of NESs, superior and more constant performance was observed across a large range of ground motion amplitudes when the entire system of NESs was unlocked.

The results of this research have demonstrated the potential for NESs to be used to passively protecting buildings structures subjected to extreme transient loads. Due to these promising results, further investigation of the use of NESs for protecting building structures is highly recommended.

9.2 Future studies

This report has presented a new experimental blast simulation technique and has demonstrated the potential for NESs to be effective devices for attenuating the response of building structures subjected the extreme transient loading. Recommendations for future studies related to this work are summarized below.

9.2.1 Blast simulation ground motion

Advances to the experimental blast simulation technique presented could potentially be made by improving the prototype ground motion. The prototype ground motion used in this work had difficulty matching the desired energy distribution across multiple modes. This problem is likely to be further exacerbated when considering blasts that create more complex modal energy distributions. Furthermore, there is room to improve the ability of the prototype ground motion to deliver a more accurate energy profile to the higher modes of the structure considered. More advanced prototype ground motions may be able to address both of these concerns.

Another area for future research would be work examining the potential for improvements to be made in the load distribution provided by this experimental blast simulation technique. When using a ground motion, the load distribution on a structure is related to the mass distribution; thus, improvements to the load distribution might be possible by modifying the mass distribution with the use of movable masses in a structure. As part of this research, the gains in load distribution from the reallocation of mass would have to be weighed against the resulting changes in the dynamic properties of the system studied.

9.2.2 Nonlinear energy sinks

A valuable area for future research related to NESs is work that brings these devices closer to implementation. In the proceeding paragraphs, a few topics of research which would aid future implementation are listed.

So far, the vast majority of work with NES has considered base structures and NES that move one dimensionally; however, in most structures, the control of lateral motion in two directions is important. Consequently, research needs to be done to develop NESs or systems of NESs that can respond multi-dimensionally.

The work presented in this report, and the work by others that have investigated using NESs in civil structures, has focused on NESs for building structures. There are many challenging vibration problems for bridges; thus, research focused on implementing NESs in bridge structures would be valuable.

Full-scale implementation of NESs will likely require the modification of existing or development of new mechanisms for creating the desired nonlinear restoring force. Thus, research related to the development of these full-scale mechanisms would be valuable. Techniques such as real-time hybrid simulation may be able to aid the economical investigation of these full-scale mechanisms.

The vast majority of research involving NESs has considered linear base structures; thus, studies investigating the effectiveness of NESs at controlling the response of structures that can inelastically respond is necessary. Simple nonlinear models may be useful in initial efforts; however, studies using high-fidelity models of realistic base structures equipped with NESs would be most valuable for assessing the effectiveness of these devices in real structures.

REFERENCES

ACI, 2011. *ACI Committee 318: Building Code Requirements for Reinforced Concrete*, Farmington Hills, Michigan: American Concrete Institute.

AISC, 2011. *Manual of Steel Construction, Load and Resistance Factor Design, 14th Ed.*, Chicago, IL: American Institute of Steel Construction.

Andersen, D. et al., 2012. Dynamic instabilities in coupled oscillators induced by geometrically nonlinear damping. *Nonlinear Dynamics*, 67(1), pp.807–827.

Andersen, D.K., Vakakis, A.F. & Bergman, L.A., 2011. Dynamics of a System of Coupled Oscillators with Geometrically Nonlinear Damping. *Nonlinear Modeling and Applications, Volume 2*, pp.1–7.

De Angelis, M., Perno, S. & Reggio, A., 2011. Dynamic response and optimal design of structures with large mass ratio TMD. *Earthquake Engineering & Structural Dynamics*.

ASCE, 2011. *Blast Protection of Buildings: ASCE/SEI 59-11*, ASCE Publications.

ASCE, 2010. *Minimum design loads for buildings and other structures.*, Reston, Va.: American Society of Civil Engineers; Structural Engineering Institute.

Bertrand, B.P. & Matthews, W.T., 1965. *Overpressures and durations of shock waves emerging from open-ended shock tubes*, Army Ballistic Research Lab Aberdeen Proving Ground.

Boore, D.M. & Bommer, J.J., 2005. Processing of strong-motion accelerograms: needs, options and consequences. *Soil Dynamics and Earthquake Engineering*, 25(2), pp.93–115.

Britt, J.R., Ranta, D.E. & Joachim, C.E., 2001. *BlastX code, version 4.2, user's manual*, Vicksburg, MS: U.S. Army Engineering Research and Development Center.

Casciati, F. & Giuliano, F., 2009. Performance of multi-TMD in the towers of suspension bridges. *Journal of Vibration and Control*, 15(6), p.821.

Casciati, F., Rodellar, J. & Yildirim, U., 2012. Active and semi-active control of structures – theory and applications: A review of recent advances. *Journal of Intelligent Material Systems and Structures*, 23(11), pp.1181–1195.

Chang, C.-M. & Spencer, B.F., 2010. Active base isolation of buildings subjected to seismic excitations. *Earthquake Engineering & Structural Dynamics*, 39(13), pp.1493–1512.

Chang, C.-M., Spencer, B.F. & Shi, P., 2013. Multiaxial active isolation for seismic protection of buildings. *Structural Control and Health Monitoring*, 21(4), pp.484–502.

Chen, A. et al., 2011. Non-explosive simulated blast loading of balsa core sandwich composite beams. *Composite Structures*, 93(11), pp.2768–2784.

Chen, W.-F. & Scawthorn, C., 2003. *Earthquake Engineering Handbook*, CRC Press.

Colombo, M., Prisco, M. di & Martinelli, P., 2011. A New Shock Tube Facility for Tunnel Safety. *Experimental Mechanics*, 51(7), pp.1143–1154.

Courtney, A., Andrusiv, L. & Courtney, M., 2012. Oxy-acetylene driven laboratory scale shock tubes for studying blast wave effects. *Rev. Sci. Instrum.*, 83(4).

Duncan, M.R., Wassgren, C.R. & Krousgrill, C.M., 2005. The damping performance of a single particle impact damper. *Journal of sound and vibration*, 286(1-2), pp.123–144.

Dyke, S.J. et al., 1996. Modeling and control of magnetorheological dampers for seismic response reduction. *Smart Materials and Structures*, 5(5), p.565.

Elnashai, A., 2008. *Fundamentals of earthquake engineering*, Chichester, U.K.: Wiley.

EMRTC, 2013. EMRTC Shock Tube. *Energetic Materials Research and Testing Center*. Available at: http://www.emrtc.nmt.edu/services/shocktube.php [Accessed May 19, 2013].

ENR, 1977. Tuned mass dampers steady sway of skyscrapers in wind. *Eng News-Rec*, (18), pp.28–29.

Eskew, E. & Jang, S., 2012. Impacts and Analysis for Buildings under Terrorist Attacks. *University of Connecticut Digital Commons*.

Feng, Q. & Shinozuka, M., 1990. *Use of a variable damper for hybrid control of bridge response under earthquake*,

Fladung, W. & Rost R., 1997. Application and correction of the exponential window for frequency response functions. *Mechanical Systems and Signal Processing*, 11(1), pp.23–36.

Freidenberg, A. et al., 2013. Characterization of the Blast Simulator Elastomer Material Using a Pseudo-Elastic Rubber Model. *International Journal of Impact Engineering*.

Gaberson, H.A. & Eubanks, R.A., 1982. *Simplified Shock Design for Installation of Equipment*, DTIC Document.

Gendelman, O.V., 2001. Transition of energy to a nonlinear localized mode in a highly asymmetric system of two oscillators. *Nonlinear dynamics*, 25(1-3), pp.237–253.

Gendelman, O.V. & Starosvetsky, Y., 2007. Quasi-Periodic Response Regimes of Linear Oscillator Coupled to Nonlinear Energy Sink Under Periodic Forcing. *Journal of Applied Mechanics*, 74(2), pp.325–331.

Gourdon, E. et al., 2007. Nonlinear energy pumping under transient forcing with strongly nonlinear coupling: Theoretical and experimental results. *Journal of sound and vibration*, 300(3-5), pp.522–551.

Guha-Sapir, D. et al., 2011. *Annual Disaster Statistical Review 2010 The numbers and trends*, Universite catholique de Louvain.

Gutierrez Soto, M. & Adeli, H., 2013. Tuned Mass Dampers. *Archives of Computational Methods in Engineering*, 20(4), pp.419–431.

Hayes, J.R. et al., 1991. *Use and Upgrade of the USACERL Biaxial Shock Test Machine: Workshop Summary*, DTIC Document.

Hespanha, J.P., 2009. *Linear Systems Theory*, Princeton, NJ: Princeton University Press.

Holmes, J.D., 1995. Listing of installations. *Engineering Structures*, 17(9), pp.676–678.

Housner, G.W. et al., 1997. Structural Control: Past, Present, and Future. *ASCE Journal of Engineering Mechanics*, 123(9), pp.897–971.

Hubbard, S.A. et al., 2010. Targeted Energy Transfer Between a Model Flexible Wing and Nonlinear Energy Sink. *Journal of Aircraft*, 47(6), pp.1918–1931.

Karayannis, I., Vakakis, A.F. & Georgiades, F., 2008. Vibro-impact attachments as shock absorbers. *Proceedings of the Institution of Mechanical Engineers, Part C: Journal of Mechanical Engineering Science*, 222(10), pp.1899–1908.

Kim, S.B., Spencer, B.F. & Yun, C.-B., 2005. Frequency domain identification of multi-input, multi-output systems considering physical relationships between measured variables. *Journal of engineering mechanics*, 131(5), pp.461–472.

Kobori, T. et al., 1991. Seismic-response-controlled structure with active mass driver system. Part 1: Design. *Earthquake Engineering & Structural Dynamics*, 20(2), pp.133–149.

Korkmaz, S., 2011. A review of active structural control: challenges for engineering informatics. *Computers and Structures*, 89, pp.2113–2132.

Labat, D., 2005. Recent advances in wavelet analyses: Part 1. A review of concepts. *Journal of Hydrology*, 314(1-4), pp.275–288.

Lee, Y.S. et al., 2008. Enhancing the Robustness of Aeroelastic Instability Suppression Using Multi-Degree-of-Freedom Nonlinear Energy Sinks. *AIAA Journal*, 46(6), pp.1371–1394.

Lee, Y.S. et al., 2008. Passive non-linear targeted energy transfer and its applications to vibration absorption: a review. *Proceedings of the Institution of Mechanical Engineers, Part K: Journal of Multi-body Dynamics*, 222(2), pp.77–134.

Lee, Y.S. et al., 2009. Periodic orbits, damped transitions and targeted energy transfers in oscillators with vibro-impact attachments. *Physica D: Nonlinear Phenomena*, 238(18), pp.1868–1896.

Li, B., Pan, T.-C. & Nair, A., 2009. A case study of the effect of cladding panels on the response of reinforced concrete frames subjected to distant blast loadings. *Nuclear Engineering and Design*, 239(3), pp.455–469.

Lin, C.C. et al., 2010. Vibration control of seismic structures using semi-active friction multiple tuned mass dampers. *Engineering Structures*, 32, p.3404_–3417.

Luo, J. et al., 2014. Realization of a Strongly Nonlinear Shock Mitigation Device using Elastomeric Bumpers. *ASCE Journal of Engineering Mechanics*, 140(5), p.04014009.

Manevitch, L.I., Gourdon, E. & Lamarque, C.H., 2007. Parameters optimization for energy pumping in strongly nonhomogeneous 2 dof system. *Chaos, Solitons & Fractals*, 31(4), pp.900–911.

Marano, G.C. et al., 2008. Robust optimum design of tuned mass dampers devices in random vibrations mitigation. *Journal of Sound and Vibration*, 313(3-5), pp.472–492.

Martin, W.A., 1958. *A review of shock tubes and shock tunnels*, General Dynamics.

Masri, S.F. & Caughey, T.K., 1979. A Nonparametric Identification Technique for Nonlinear Dynamic Problems. *Journal of Applied Mechanics*, 46(2), pp.433–447.

McFarland, D.M., Bergman, L.A. & Vakakis, A.F., 2005. Experimental study of non-linear energy pumping occurring at a single fast frequency. *International Journal of Non-Linear Mechanics*, 40(6), pp.891–899.

Ngo, T. et al., 2007. Blast loading and blast effects on structures–An overview. *Electronic Journal of Structural Engineering*, 7, pp.76–91.

Nucera, F. et al., 2010. Application of broadband nonlinear targeted energy transfers for seismic mitigation of a shear frame: Computational results. *Journal of Sound and Vibration*, 329(15), pp.2973–2994.

Nucera, F. et al., 2008. Application of broadband nonlinear targeted energy transfers for seismic mitigation of a shear frame: experimental results. *Journal of Sound and Vibration*, 313(1-2), pp.57–76.

Nucera, F. et al., 2007. Targeted energy transfers in vibro-impact oscillators for seismic mitigation. *Nonlinear Dynamics*, 50(3), pp.651–677.

Oesterle, M.G., Hegemier, G.A. & Morrill, K.B., 2009. Response of concrete masonry walls to simulated blast loads. In *Proc., Structures Congress, Austin, TX*. pp. 140–140.

Ott, R. J., 2012. *An Effective Damping Measure: Examples Using a Nonlinear Energy Sink*. Akron, OH: University of Akron.

Panagopoulos, P.N., Vakakis, A.F. & Tsakirtzis, S., 2004. Transient resonant interactions of finite linear chains with essentially nonlinear end attachments leading to passive energy pumping. *International Journal of Solids and Structures*, 41(22-23), pp.6505–6528.

Pasala, D. et al., 2012. Adaptive Negative Stiffness: A New Structural Modification Approach for Seismic Protection. *Journal of Structural Engineering*, 139, pp.1112–1123.

Quinn, D.D. et al., 2011. Energy Harvesting From Impulsive Loads Using Intentional Essential Nonlinearities. *Journal of Vibration and Acoustics*, 133, p.011004.

Quinn, D.D. et al., 2012. Equivalent modal damping, stiffening and energy exchanges in multi-degree-of-freedom systems with strongly nonlinear attachments. *Proceedings of the Institution of Mechanical Engineers, Part K: Journal of Multi-body Dynamics*, 226(2), pp.122–146.

Rodriguez-Nikl, T., Hegemier, G.A. & Seible, F., 2011. Blast simulator testing of structures: Methodology and validation. *Shock and Vibration*, 18(4), pp.579–592.

Sapsis, T.P. et al., 2012. Effective Stiffening and Damping Enhancement of Structures With Strongly Nonlinear Local Attachments. *Journal of Vibration and Acoustics*, 134(1), pp.011016–12.

Sarlis, A. et al., 2013. Negative Stiffness Device for Seismic Protection of Structures. *Journal of Structural Engineering*, 139, pp.1124–1133.

Savadkoohi, A.T. et al., 2012. Targeted energy transfer with parallel nonlinear energy sinks, part II: theory and experiments. *Nonlinear Dynamics*, 67(1), pp.37–46.

Schmidt, F. & Lamarque, C.H., 2010. Energy pumping for mechanical systems involving non-smooth Saint-Venant terms. *International Journal of Non-Linear Mechanics*, 45(9), pp.866–875.

Al-Shudeifat, M.A. et al., 2013. Numerical and Experimental Investigation of a Highly Effective Single-Sided Vibro-Impact Nonlinear Energy Sink for Shock Mitigation. *International Journal of Non-Linear Mechanics*, 52, pp.96–109.

Soong, T. & Dargush, G.F., 1997. *Passive energy dissipation systems in structural engineering*, Chichester, New York: Wiley.

Soong, T.T., 1988. State-of-the-art review: Active structural control in civil engineering. *Engineering Structures*, 10(2), pp.74–84.

Soong, T.T. & Spencer, B.F., 2002. Supplemental energy dissipation: state-of-the-art and state-of-the-practice. *Engineering Structures*, 24(3), pp.243–259.

Soto-Brito, R. & Ruiz, S.E., 1999. Influence of ground motion intensity on the effectiveness of tuned mass dampers. *Earthquake Engineering & Structural Dynamics*, 28(11), pp.1255–1271.

Spencer, B.F. & Nagarajaiah, S., 2003. State of the Art of Structural Control. *Journal of Structural Engineering*, 129(7), pp.845–856.

Spencer Jr, B.F. & Sain, M.K., 1997. Controlling buildings: a new frontier in feedback. *Control Systems, IEEE*, 17(6), pp.19–35.

Stewart, L.K., 2012. Experimental and computational methods for steel columns subjected to blast loading. In Structures Under Shock and Impact XII.

Symans, M.D. & Constantinou, M.C., 1999. Semi-active control systems for seismic protection of structures: a state-of-the-art review. *Engineering Structures*, 21(6), pp.469–487.

Tamura, Y., 2006. *Damping in Buildings*, Japan: Tokyo Polytechnic University.

Torrence, C. & Compo, G. P., 1998. A Practical Guide to Wavelet Analysis. *Bulletin of the American Meteorological Society*, 79(1), pp.61–78.

Tsakirtzis, S. et al., 2005. Multi-frequency nonlinear energy transfer from linear oscillators to mdof essentially nonlinear attachments. *Journal of Sound and Vibration*, 285(1-2), pp.483–490.

U.S. Army Engineer Research and Development Center, 2008. Triaxial Earthquake and Shock Simulator (TESS). Available at: http://134.164.46.151/pls/erdcpub/docs/erdc/docs/ERDCFactSheet_Facility_TESS.pdf [Accessed January 8, 2013].

UNISDR, 2012. Earthquakes caused the deadliest disasters in the past decade. *The United Nations Office for Disaster Risk Reduction*. Available at: http://www.unisdr.org/archive/12470 [Accessed July 31, 2012].

Vakakis, A.F., 2001. Inducing Passive Nonlinear Energy Sinks in Vibrating Systems. *Journal of Vibration and Acoustics*, 123(3), pp.324–332.

Vakakis, A.F. et al., 2008. *Nonlinear Targeted Energy Transfer in Mechanical and Structural Systems*, Springer.

Vakakis, A.F. & Gendelman, O., 2001. Energy Pumping in Nonlinear Mechanical Oscillators: Part II—Resonance Capture. *Journal of Applied Mechanics*, 68(1), pp.42–48.

Vaurigaud, B., Savadkoohi, A.T. & Lamarque, C.-H., 2011. Efficient Targeted Energy Transfer With Parallel Nonlinear Energy Sinks: Theory and Experiments. *Journal of Computational and Nonlinear Dynamics*, 6(4), p.041005.

Vaurigaud, B., Ture Savadkoohi, A. & Lamarque, C.-H., 2011. Targeted energy transfer with parallel nonlinear energy sinks. Part I: Design theory and numerical results. *Nonlinear Dynamics*, 66(4), pp.763–780.

Warburton, G.B., 1982. Optimum absorber parameters for various combinations of response and excitation parameters. *Earthquake Engineering & Structural Dynamics*, 10(3), pp.381–401.

Wierschem, N.E., Quinn, D.D., et al., 2012. Passive Damping Enhancement of a Two-degree-of-freedom System Through a Strongly Nonlinear Two-degree-of-freedom Attachment. *Journal of Sound and Vibration*, 331, pp.5393–5407.

Wierschem, N.E., Luo, J., et al., 2012. Simulation and Testing of a 6-Story Structure Incorporating a coupled two Mass Nonlinear Energy Sink. In *Proceedings of the ASME 2012 International Design Engineering Technical Conferences & Computers and Information in Engineering Conference*. Chicago, USA.

Wilkinson, S. et al., 2013. Observations and implications of damage from the magnitude Mw 6.3 Christchurch, New Zealand earthquake of 22 February 2011. *Bulletin of Earthquake Engineering*, 11(1), pp.107–140.

Worden, K., 1990. Data processing and experiment design for the restoring force surface method, part I: integration and differentiation of measured time data. *Mechanical Systems and Signal Processing*, 4(4), pp.295–319.

Xing, S., Halling, M.W. & Meng, Q., 2012. Structural Pounding Detection by Using Wavelet Scalogram. *Advances in Acoustics and Vibration*, 2012, pp.1–10.

Yalla, S.K. & Kareem, A., 2000. Optimum absorber parameters for tuned liquid column dampers. *Journal of Structural Engineering*, 126(8), pp.906–915.

APPENDIX A: DESIGN DRAWINGS FOR BASE STRUCTURES AND NONLINEAR ENERGY SINKS

In this appendix, design drawings are presented related to the small-, medium-, and large-scale base structures and nonlinear energy sinks (NESs) which were developed and used for experimental investigations in Chapters 5, 6, 7, and 8. All of the base structures and NESs outlined in these drawings, with the exception of the medium-base structure, were prepared as part of the work presented in this report. The design drawings for the medium-scale base structure were produced by another researcher as part of a previous study. As these drawings are unpublished elsewhere, this set of drawings is included in this appendix for referencing purposes.

The drawing sets included in this appendix are:

A.1 Small-scale base structure and Type I NES

A.2 Small-scale Type III NES

A.3 Medium-scale base structure

A.4 Large-scale base structure and system of NESs

A.1 Small-scale Base Structure and Type I NES

Design Drawing

Originally Produced - 1/19/2011

Project Contact:
Nick Wierschem
NSEL B119
nwiersc2@illinois.edu
(520) 245-3837

Project:	Sheet Description: Units: Inches	Date:	Sheet #
DARPA – 2 Story Experimental Structure and NES Design	Cover Page	1/19/2011	1

Project Contact: Nick Wierschem, B119, nwiersc2@illlinois.edu, (520) 245 3837

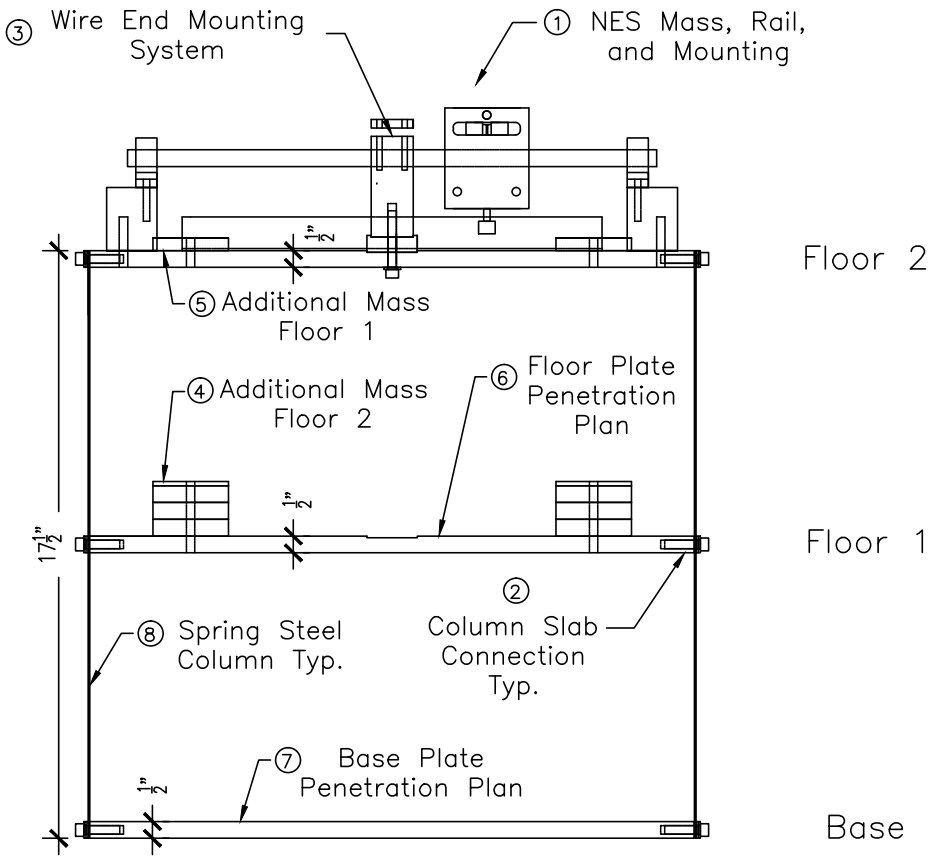

Elevation

Project:	Sheet Description: Units: Inches	Date:	Sheet #
DARPA – 2 Story Experimental Structure and NES Design	Elevation	1/19/2011	2

Project Contact: Nick Wierschem, B119, nwiersc2@illlinois.edu, (520) 245 3837

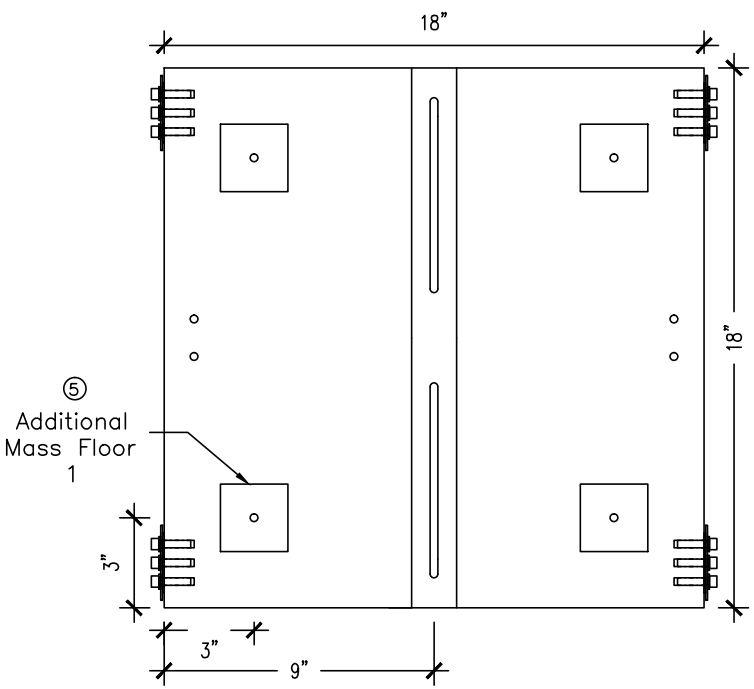

Floor 1

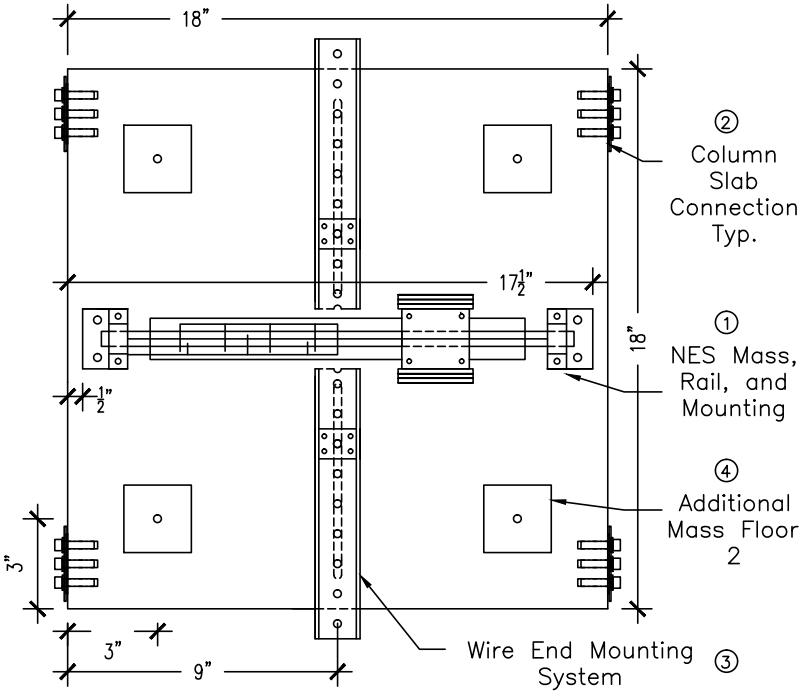

Floor 2

Project:	Sheet Description: Units: Inches	Date:	Sheet #
DARPA – 2 Story Experimental Structure and NES Design	Floor Plans	1/19/2011	3

Project Contact: Nick Wierschem, B119, nwiersc2@illlinois.edu, (520) 245 3837

Plan

Elevation

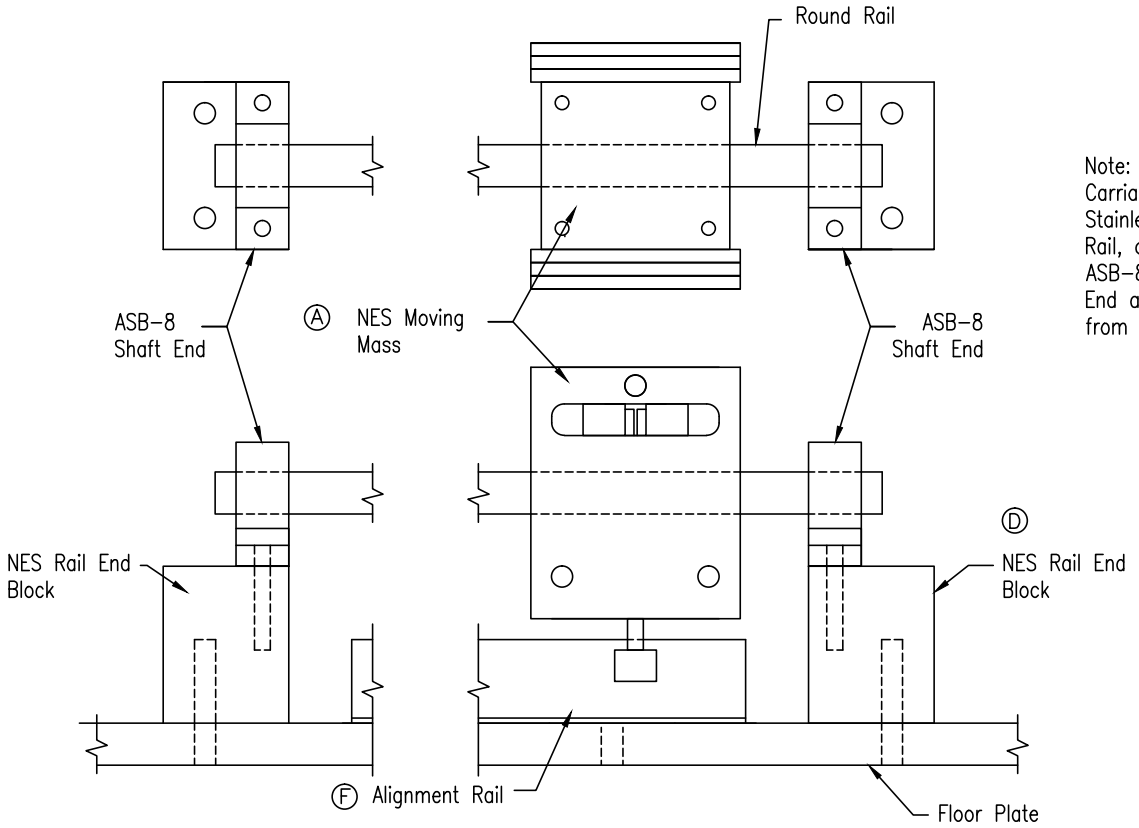

Note: SPB-8 Carriage, Stainless Steel Rail, and ASB-8 Shaft End are Stock from Thomson

① NES, Rail, and Mounting

Project:	Sheet Description: Units: Inches	Date:	Sheet #
DARPA – 2 Story Experimental Structure and NES Design	NES Overview	1/19/2011	4

Project Contact: Nick Wierschem, B119, nwiersc2@illlinois.edu, (520) 245 3837

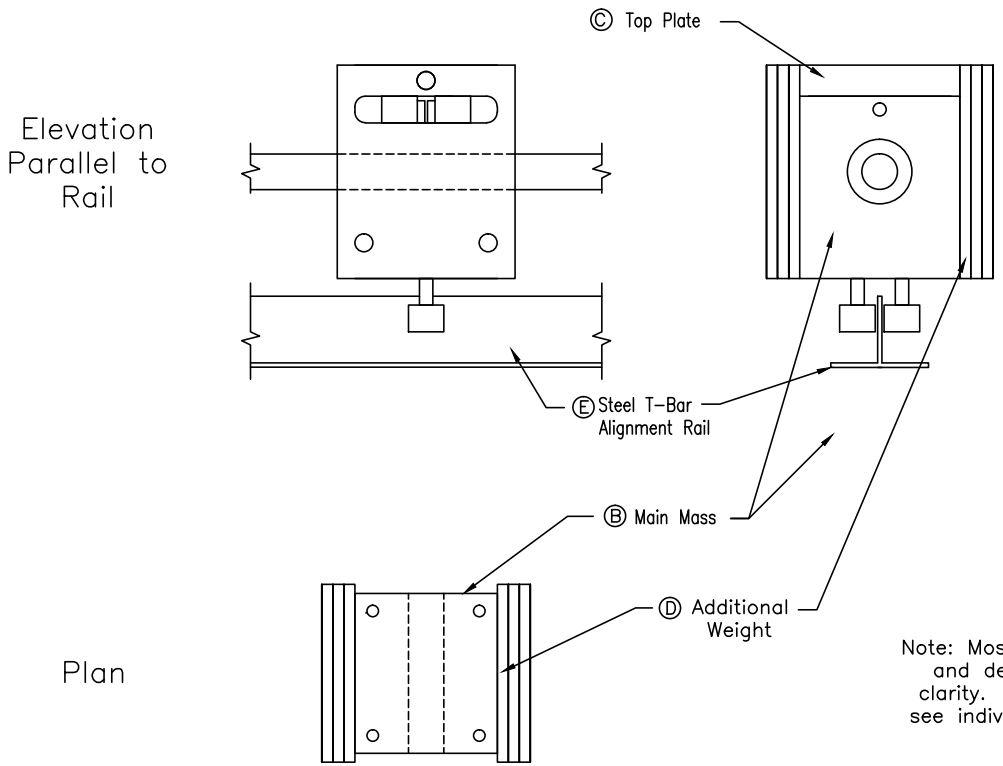

Ⓐ NES Moving Mass

Project:	Sheet Description: Units: Inches	Date:	Sheet #
DARPA – 2 Story Experimental Structure and NES Design	NES Moving Mass	1/19/2011	5

Project Contact: Nick Wierschem, B119, nwiersc2@illlinois.edu, (520) 245 3837

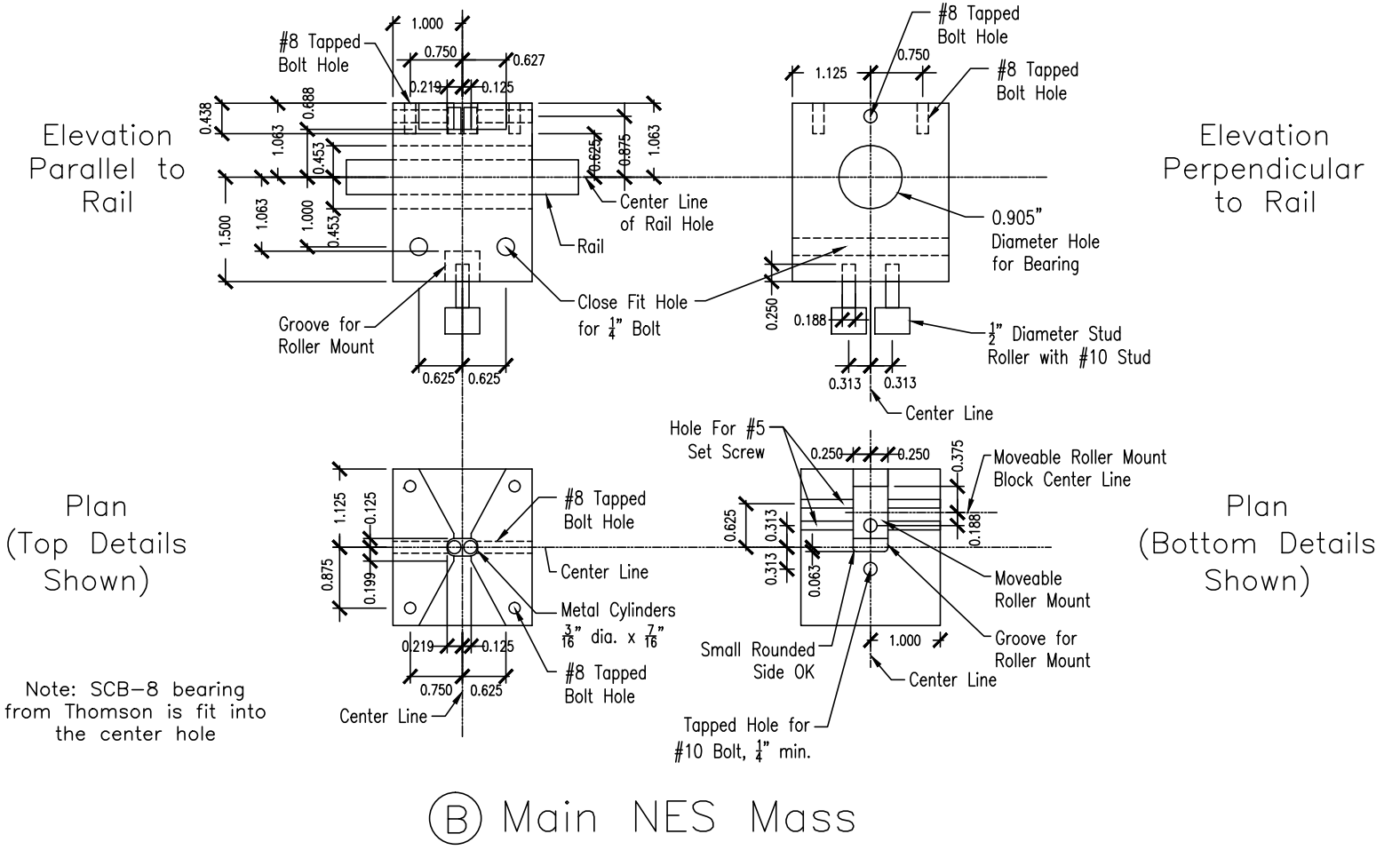

Project:	Sheet Description: Units: Inches	Date:	Sheet #
DARPA – 2 Story Experimental Structure and NES Design	NES Main Mass	1/19/2011	6

Project Contact: Nick Wierschem, B119, nwiersc2@illlinois.edu, (520) 245 3837

Plan
(Top Details
Shown)

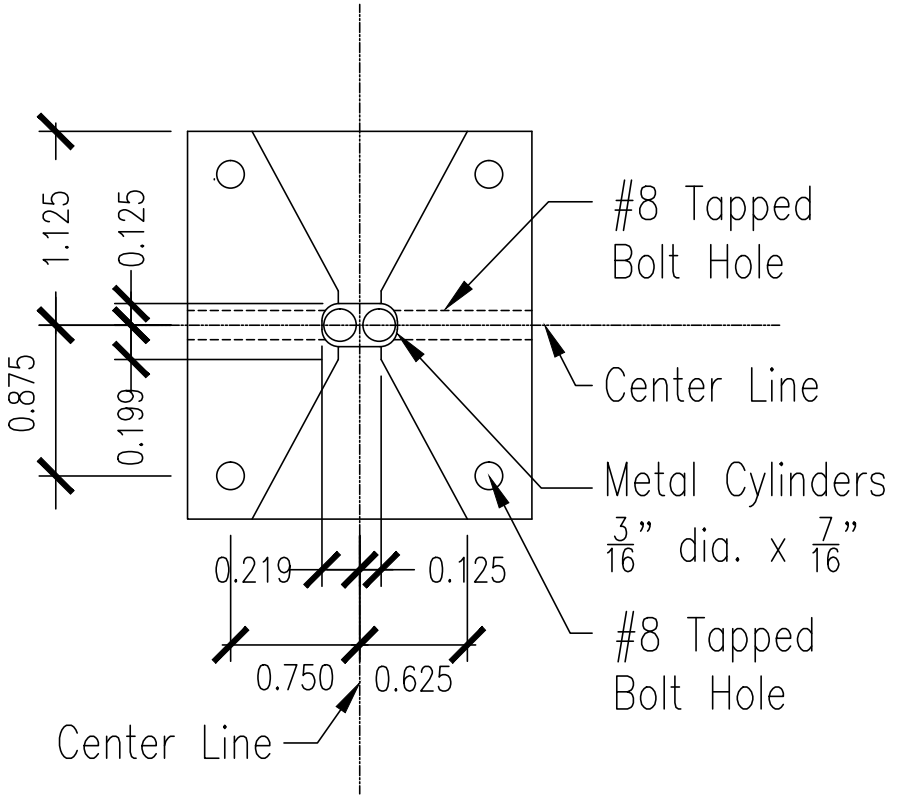

Project:	Sheet Description: Units: Inches	Date:	Sheet #
DARPA – 2 Story Experimental Structure and NES Design	NES Main Mass – Zoom 1/4	1/19/2011	7

Project Contact: Nick Wierschem, B119, nwiersc2@illlinois.edu, (520) 245 3837

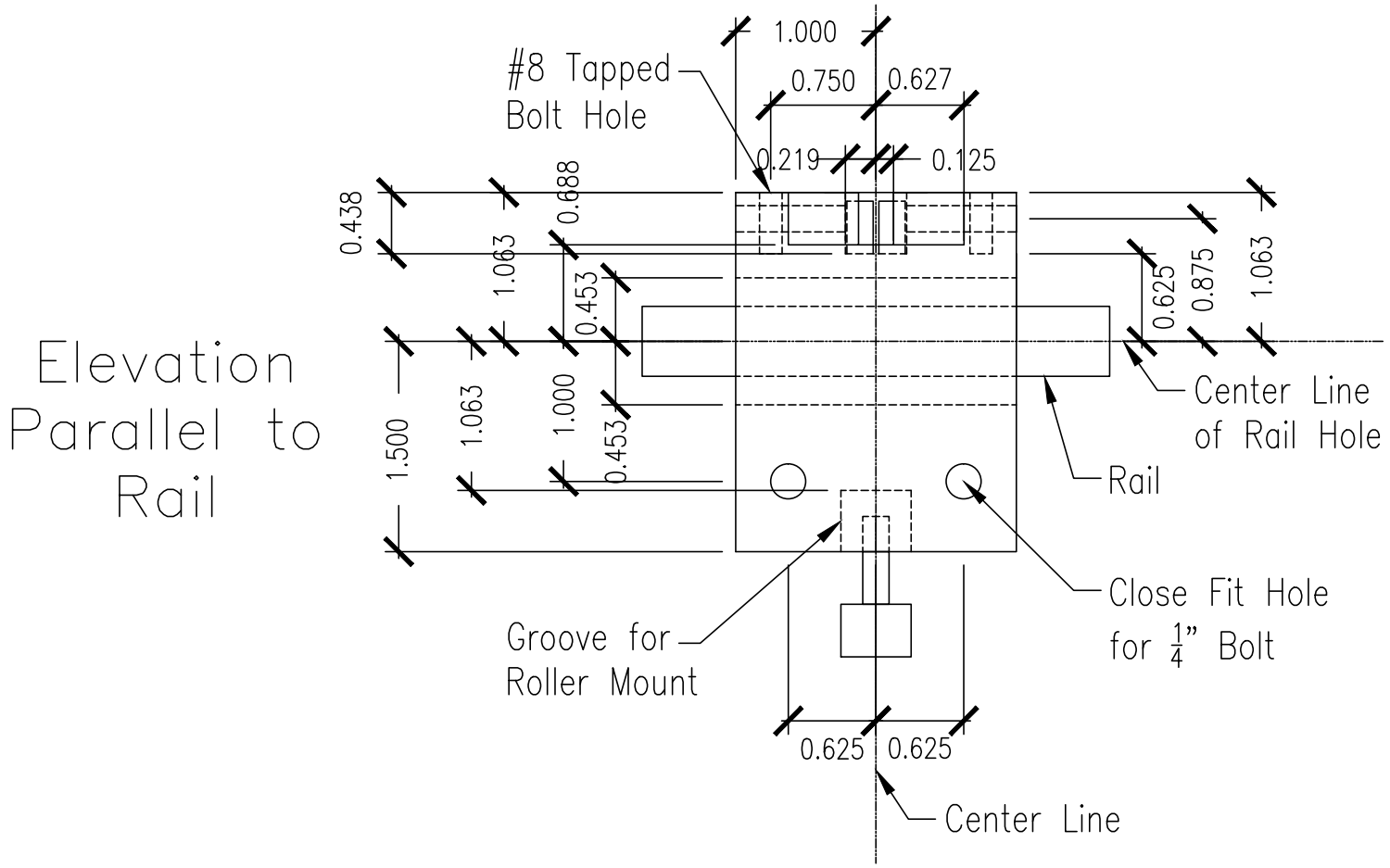

Project:	Sheet Description: Units: Inches	Date:	Sheet #
DARPA – 2 Story Experimental Structure and NES Design	NES Main Mass – Zoom 2/4	1/19/2011	8

Project Contact: Nick Wierschem, B119, nwiersc2@illlinois.edu, (520) 245 3837

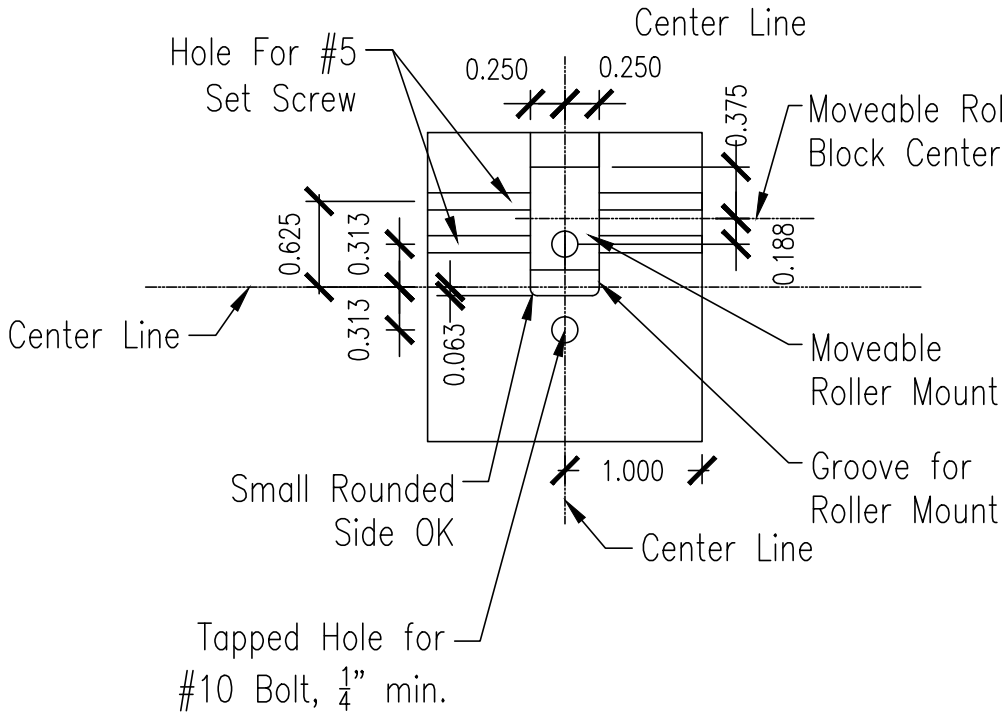

Plan (Bottom Details Shown)

Project:	Sheet Description: Units: Inches	Date:	Sheet #
DARPA – 2 Story Experimental Structure and NES Design	NES Main Mass – Zoom 3/4	1/19/2011	9

Project Contact: Nick Wierschem, B119, nwiersc2@illlinois.edu, (520) 245 3837

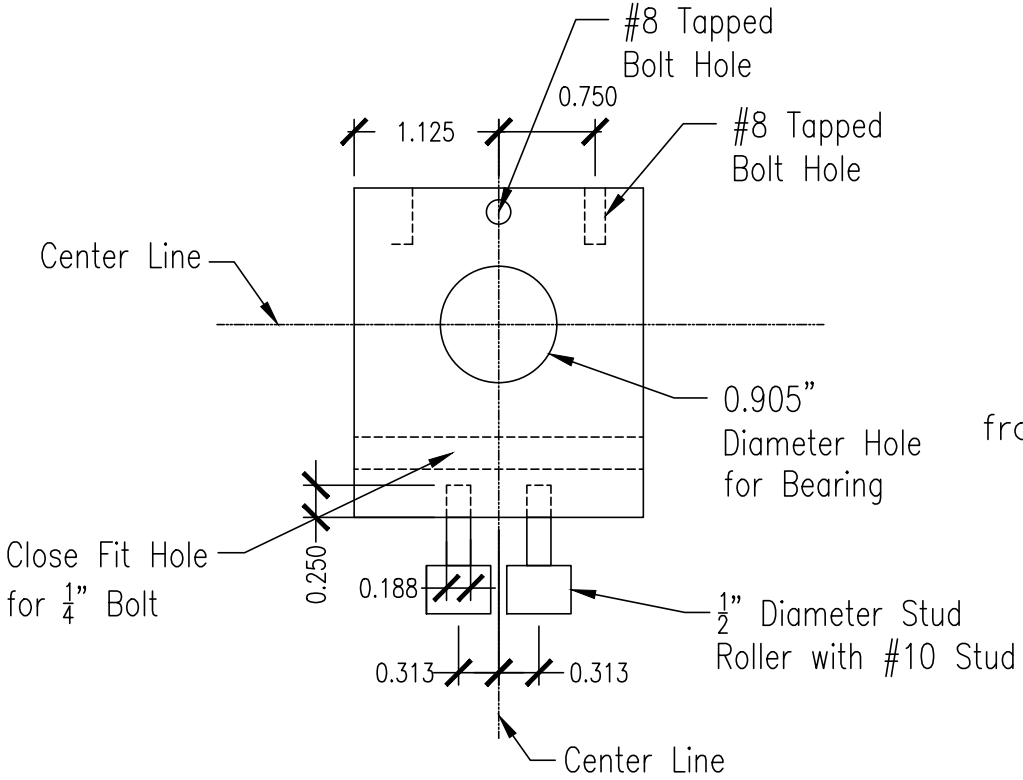

Elevation Perpendicular to Rail

Note: SCB–8 bearing from Thomson is fit into the center hole

Project:	Sheet Description: Units: Inches	Date:	Sheet #
DARPA – 2 Story Experimental Structure and NES Design	NES Main Mass – Zoom 4/4	1/19/2011	10

Project Contact: Nick Wierschem, B119, nwiersc2@illlinois.edu, (520) 245 3837

Plan

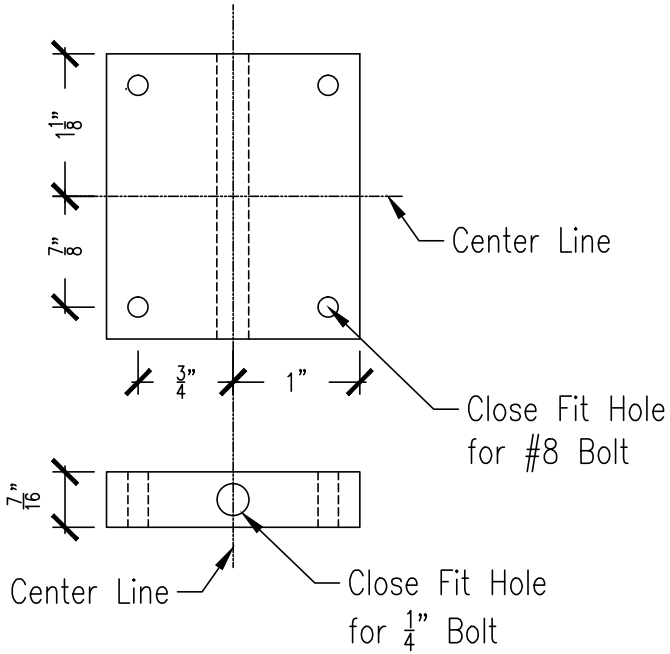

Elevation

© Main Mass Top Plate

Project:	Sheet Description: Units: Inches	Date:	Sheet #
DARPA – 2 Story Experimental Structure and NES Design	NES top Plate	1/19/2011	11

Project Contact: Nick Wierschem, B119, nwiersc2@illlinois.edu, (520) 245 3837

Elevation

Plan

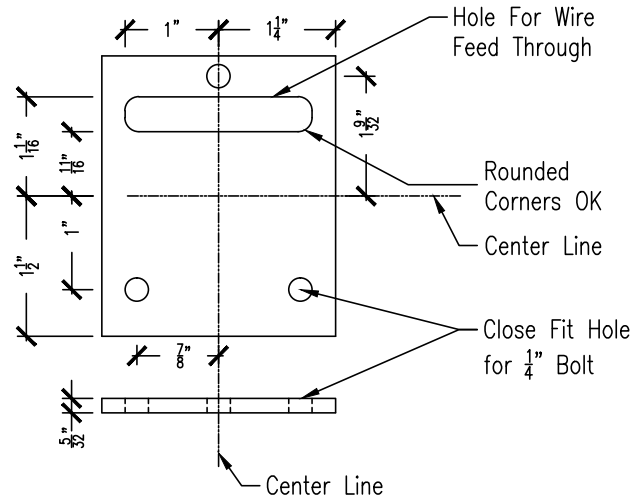

(D) Additional Weight

Project:	Sheet Description: Units: Inches	Date:	Sheet #
DARPA – 2 Story Experimental Structure and NES Design	Additional NES Mass	1/19/2011	12

Project Contact: Nick Wierschem, B119, nwiersc2@illlinois.edu, (520) 245 3837

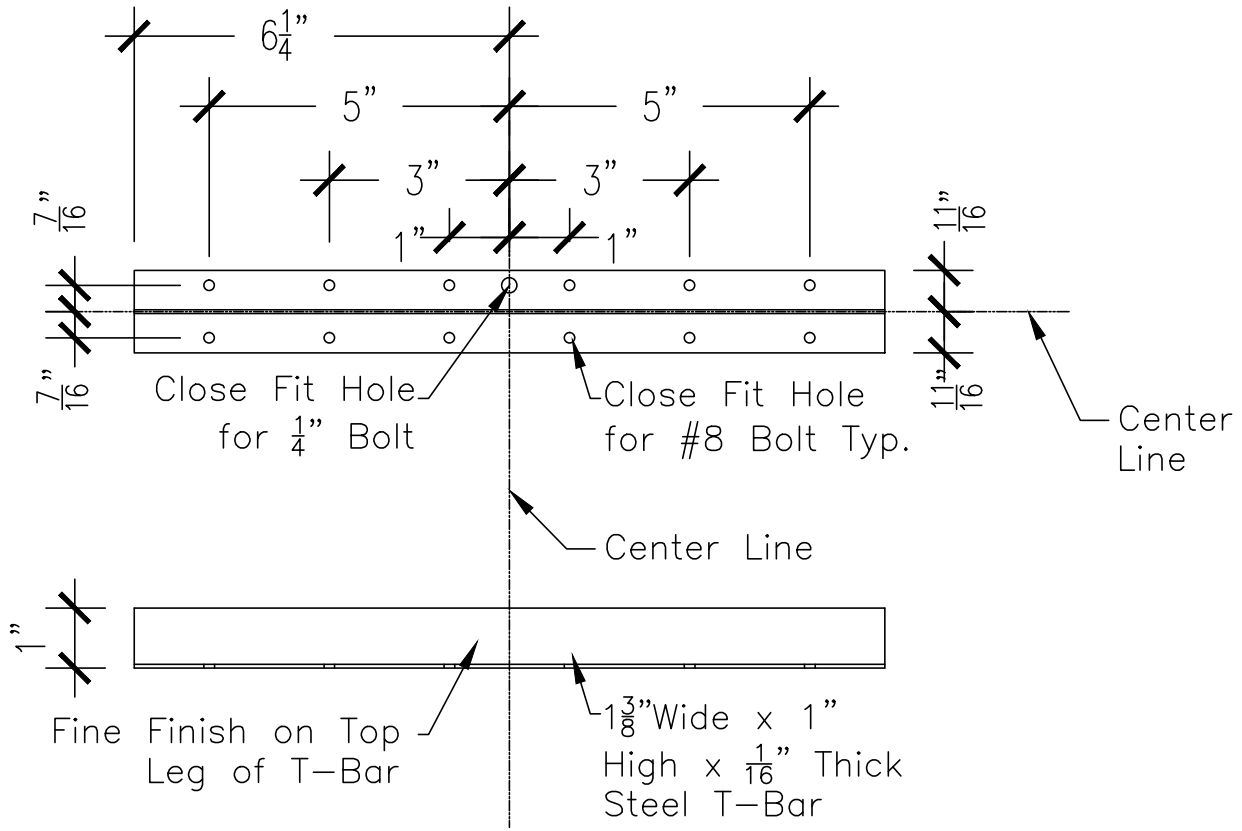

E Alignment Track

Project:	Sheet Description: Units: Inches	Date:	Sheet #
DARPA – 2 Story Experimental Structure and NES Design	Alignment Track	1/19/2011	13

Project Contact: Nick Wierschem, B119, nwiersc2@illlinois.edu, (520) 245 3837

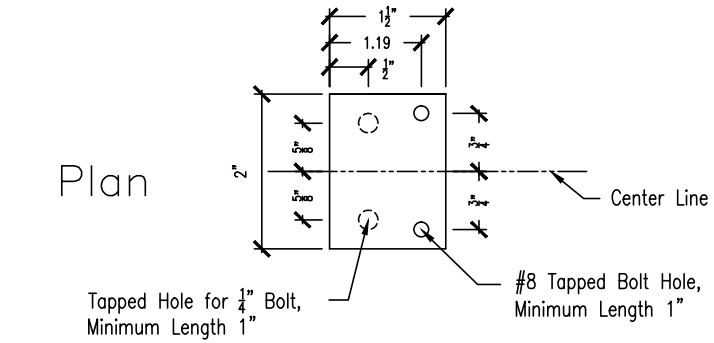

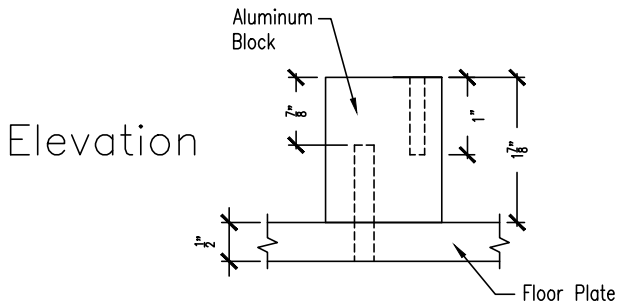

Ⓕ NES Rail End Block

Project:	Sheet Description: Units: Inches	Date:	Sheet #
DARPA – 2 Story Experimental Structure and NES Design	Rail End Block	1/19/2011	14

Project Contact: Nick Wierschem, B119, nwiersc2@illlinois.edu, (520) 245 3837

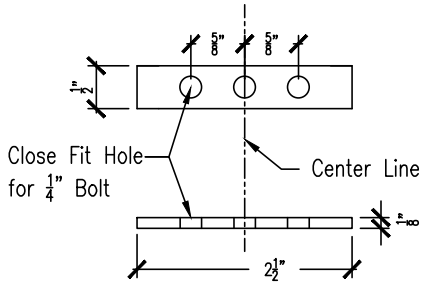

Elevation

Plan

Ⓜ Column Cover Plate

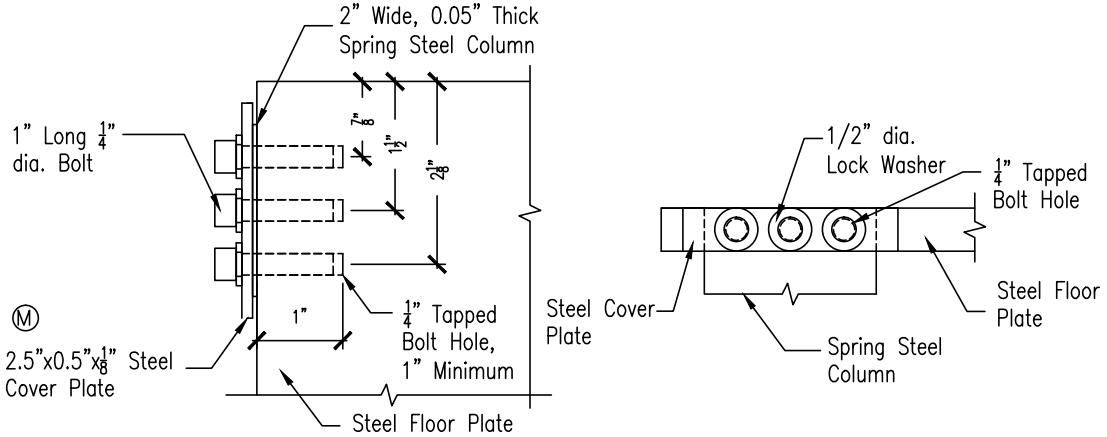

② Column Slab Connection Typ.

Project:	Sheet Description: Units: Inches	Date:	Sheet #
DARPA – 2 Story Experimental Structure and NES Design	Column Slab Connection	1/19/2011	15

Project Contact: Nick Wierschem, B119, nwiersc2@illlinois.edu, (520) 245 3837

* Note:
All details except wire end mount system removed for clarity

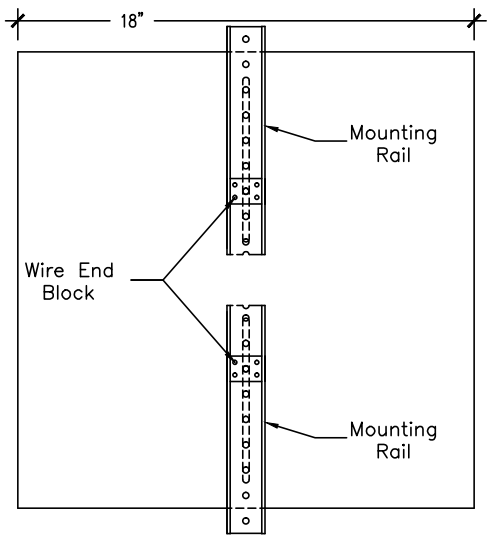

Plan

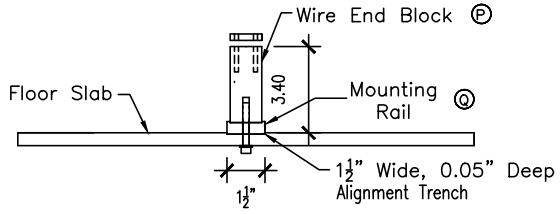

Elevation

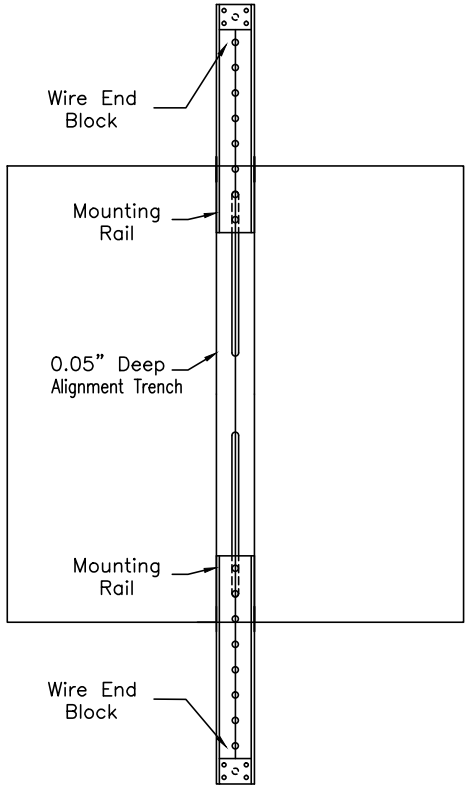

Plan – Mounting Extended

③ Wire End Mounting System

Project:	Sheet Description: Units: Inches	Date:	Sheet #
DARPA – 2 Story Experimental Structure and NES Design	Wire End Support Mounting	1/19/2011	16

Project Contact: Nick Wierschem, B119, nwiersc2@illlinois.edu, (520) 245 3837

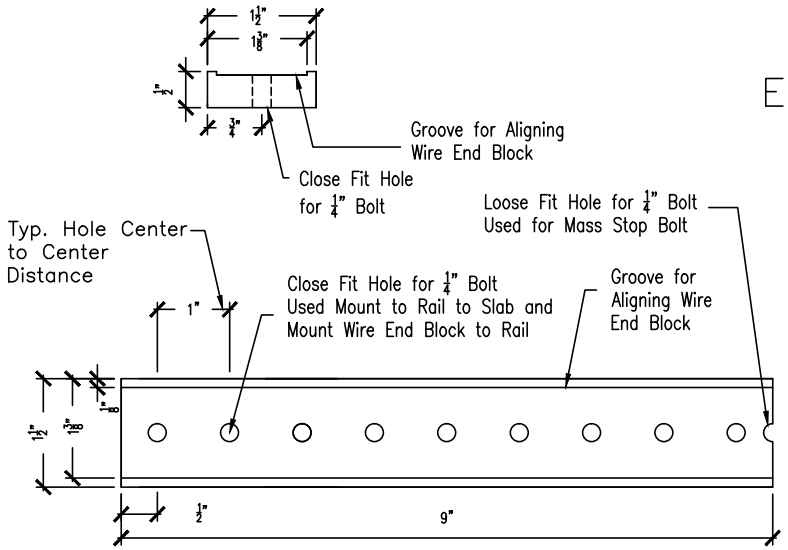

Ⓟ Mounting Rail

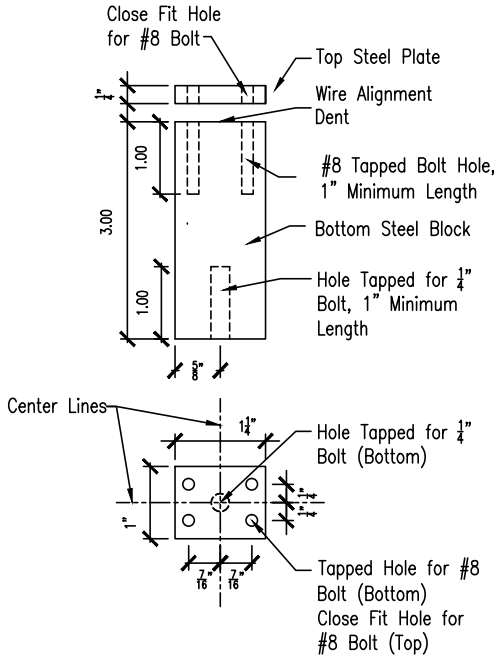

Ⓠ Wire End Block

Project:	Sheet Description:	Units: Inches	Date:	Sheet #
DARPA – 2 Story Experimental Structure and NES Design	Wire Mounting Details		1/19/2011	17

Project Contact: Nick Wierschem, B119, nwiersc2@illlinois.edu, (520) 245 3837

Elevation

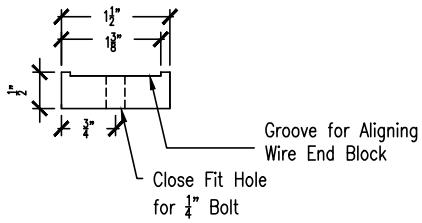

Notes:
1) Rail is steel
2) Quantity 2

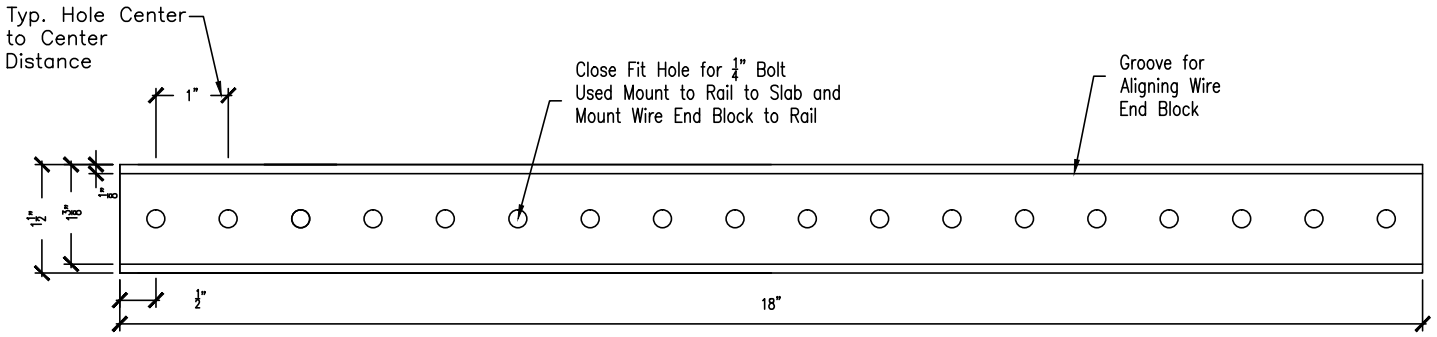

Plan

(P.2) Mounting Rail – Long

Project:	Sheet Description: Units: Inches	Date:	Sheet #
DARPA – 2 Story Experimental Structure and NES Design	Long Mounting Rail	1/19/2011	18

Project Contact: Nick Wierschem, B119, nwiersc2@illlinois.edu, (520) 245 3837

Plan

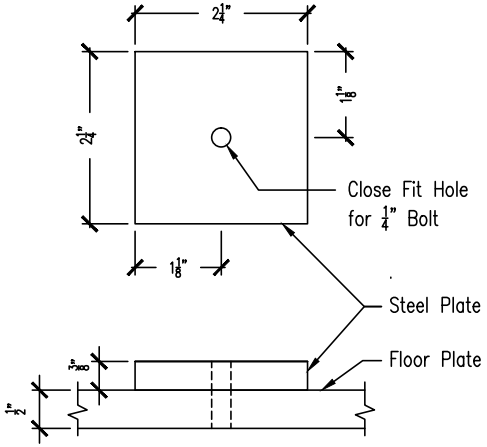

Elevation

④ Additional Mass Floor 2

Plan

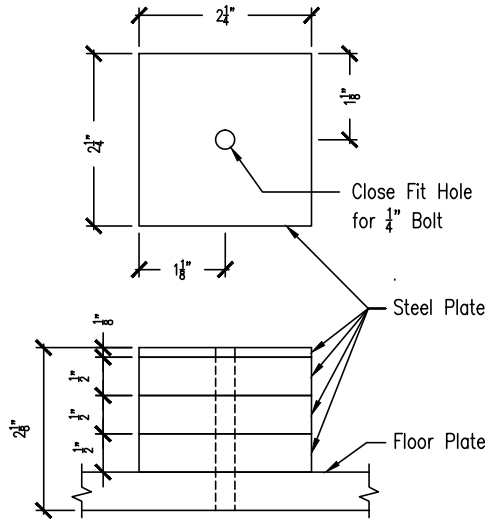

Elevation

⑤ Additional Mass Floor 1

Project:	Sheet Description:	Units: Inches	Date:	Sheet #
DARPA – 2 Story Experimental Structure and NES Design	Additional Masses		1/19/2011	19

Project Contact: Nick Wierschem, B119, nwiersc2@illlinois.edu, (520) 245 3837

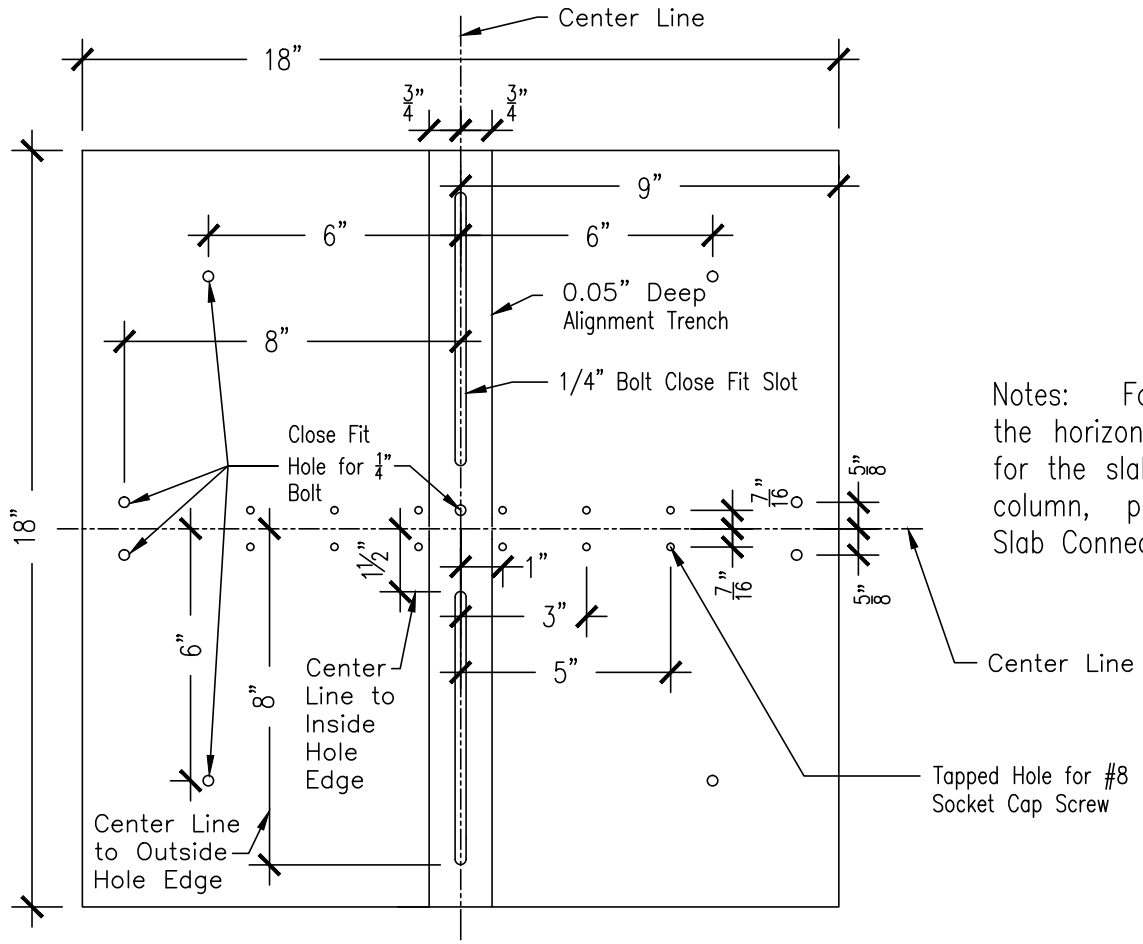

Notes: For details regarding the horizonal slab penetrations for the slab connection to the column, please see Column Slab Connection drawing.

6 Vertical Floor Plate Penetration Plan

Project:	Sheet Description: Units: Inches	Date:	Sheet #
DARPA – 2 Story Experimental Structure and NES Design	Floor Penetration Layout	1/19/2011	20

Project Contact: Nick Wierschem, B119, nwiersc2@illlinois.edu, (520) 245 3837

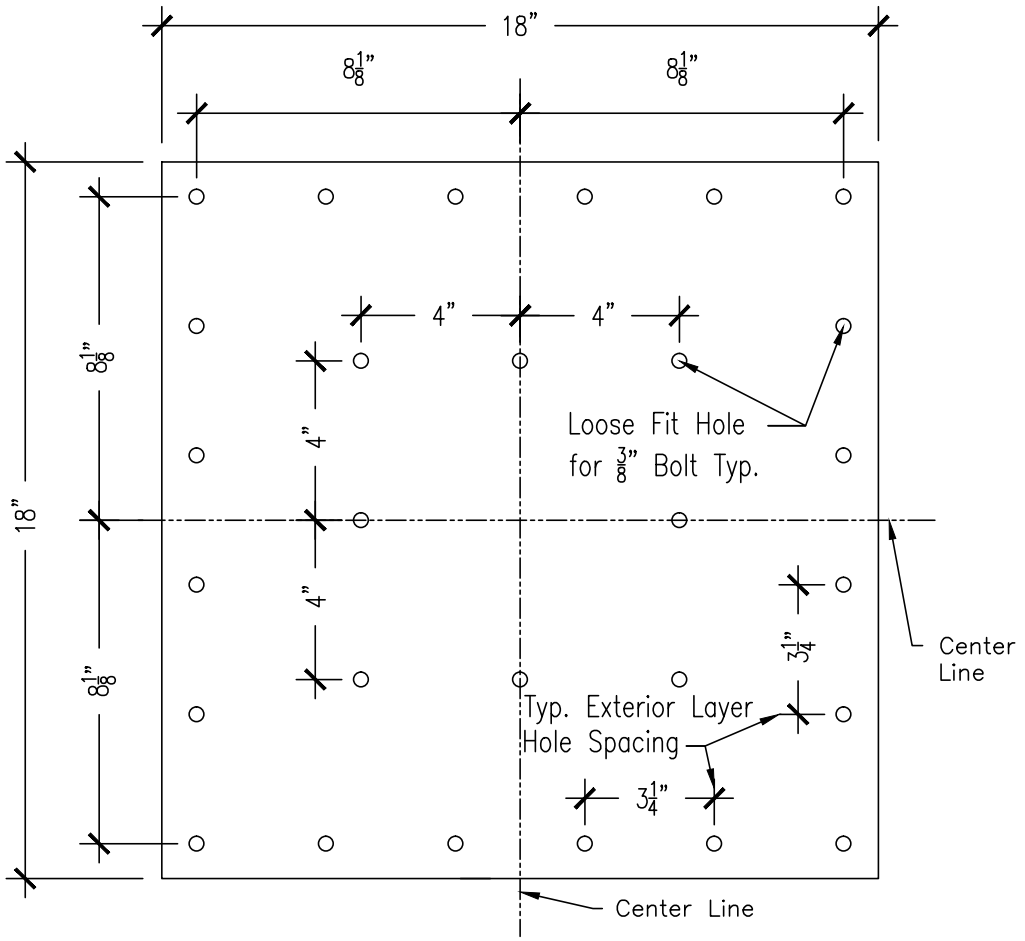

⑦ Base Plate Penetration Plan

Notes:

1) At each corner of the base plate the vertical penetration is known to conflict with a horizontal tapped hole for the connection of the column. To resolve this, both holes can be drilled as shown and a shorter bolt will be used in the horizontal tapped hole.

2) For details regarding the horizonal slab penetrations for the slab connection to the column, please see Column Slab Connection drawing.

Project:	Sheet Description: Units: Inches	Date:	Sheet #
DARPA – 2 Story Experimental Structure and NES Design	Base Plate Penetration Plan	1/19/2011	21

Project Contact: Nick Wierschem, B119, nwiersc2@illlinois.edu, (520) 245 3837

Notes: 1) Column Thickness is 0.05"
2) Column made of spring steel

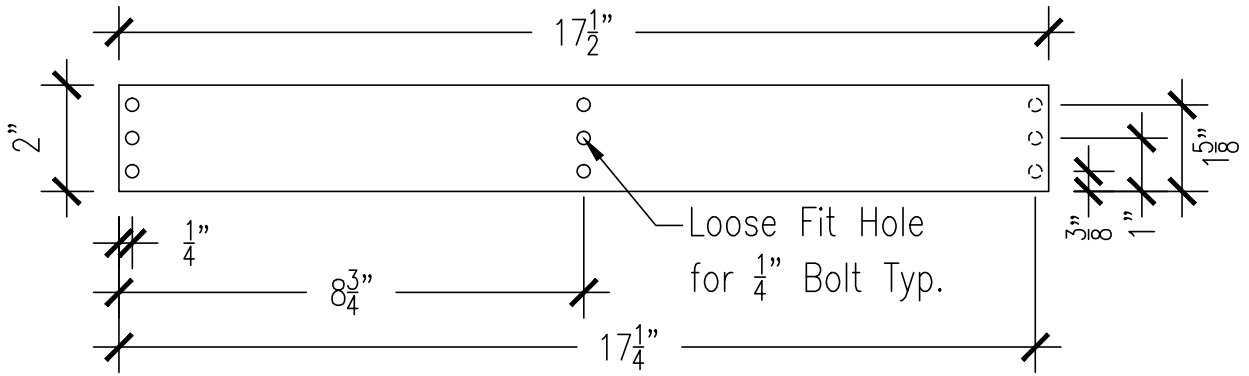

⑧ Column Penetration Plan

Project:	Sheet Description: Units: Inches	Date:	Sheet #
DARPA – 2 Story Experimental Structure and NES Design	Column Penetration Plan	1/19/2011	22

Project Contact: Nick Wierschem, B119, nwiersc2@illlinois.edu, (520) 245 3837

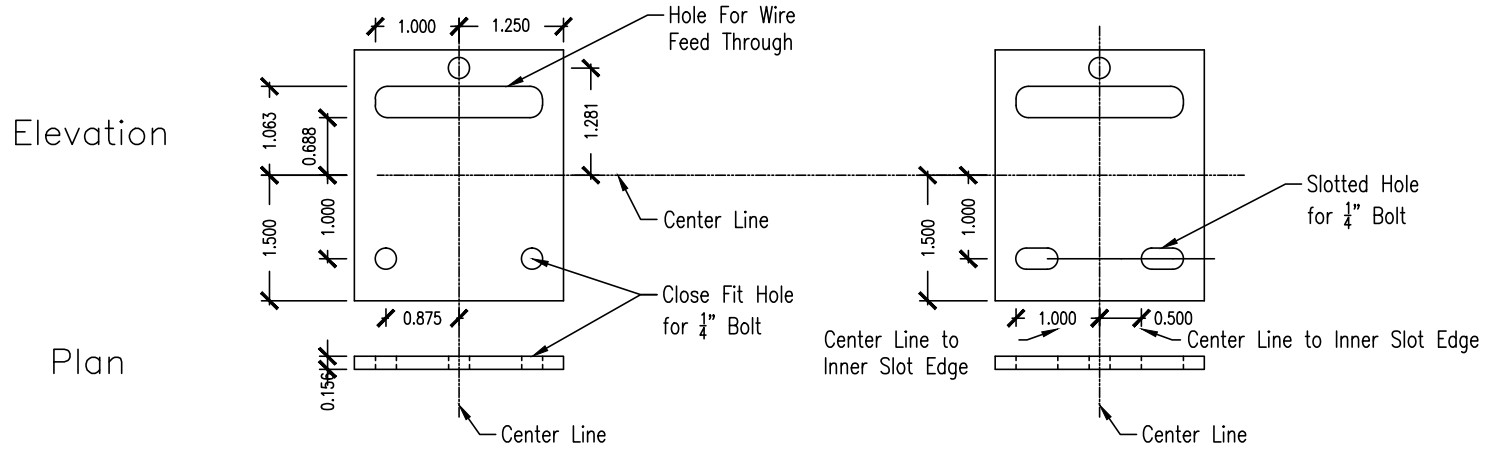

(D) Additional Weight

Project:	Sheet Description: Units: Inches	Date:	Sheet #
DARPA – 2 Story Experimental Structure and NES Design	Changes to NES Additional Mass	1/19/2011	23

Project Contact: Nick Wierschem, B119, nwiersc2@illlinois.edu, (520) 245 3837

Part	Material	Quantity
Base Plate	Steel	1
Floor Plate	Steel	2
Column	1095 Spring Steel	4
Column Cover Plate	Steel	12
Additional NES Mass	Steel	10
NES Main Mass	Aluminum	1
NES Main Mass Top	Aluminum	1
Rail Mounting Block	Aluminum	2
Mounting Rail	Steel	2
Long Mounting Rail	Steel	2
Wire End Block	Steel	2
Alignment Track	Steel	1
$\frac{1}{2}$" Thick Additional Floor Mass	Steel	12
$\frac{3}{8}$" Thick Additional Floor Mass	Steel	4
$\frac{1}{8}$" Thick Additional Floor Mass	Steel	4

Parts From Thomson		
Part	Material	Quantity
SCB-8 Bearing	N/A	1
ASB-8 Shaft End	Aluminum	2
60 Case LinearRace 18" Long $\frac{1}{2}$" Diameter Rail	Chrome Plated Steel	1

Project:	Sheet Description: Units: Inches	Date:	Sheet #
DARPA – 2 Story Experimental Structure and NES Design	Parts List	1/19/2011	24

Project Contact: Nick Wierschem, B119, nwiersc2@illlinois.edu, (520) 245 3837

A.2 Small-scale Type III NES

July 6th, 2011

Contact Person:

Nick Wierschem

NCEL - B119

(520) 245-3837

nwiersc2@illinois.edu

DRAWN	Nick	7/3/2011			
CHECKED			TITLE		
QA					
MFG					
APPROVED					
			SIZE	DWG NO	REV
			C	NES Type 3 for 2 Story	
			SCALE	SHEET 1 OF 18	

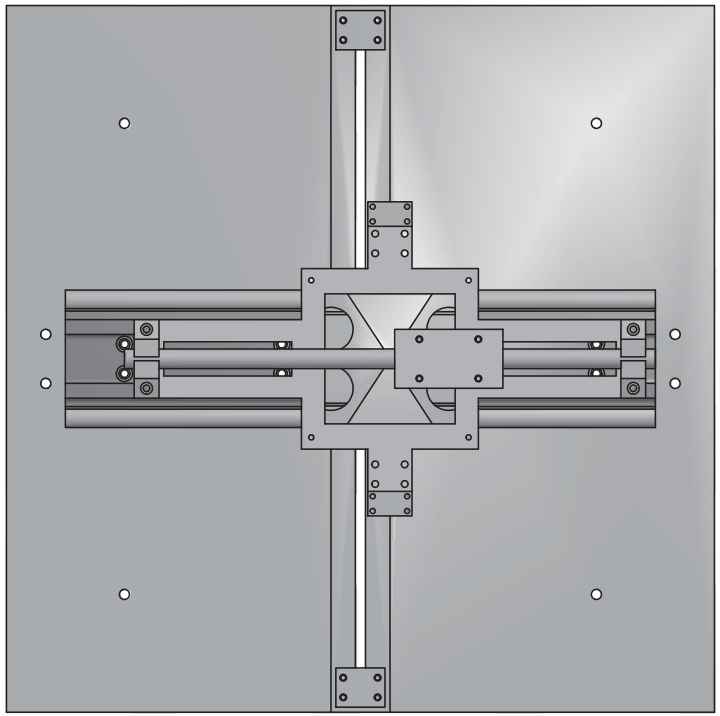

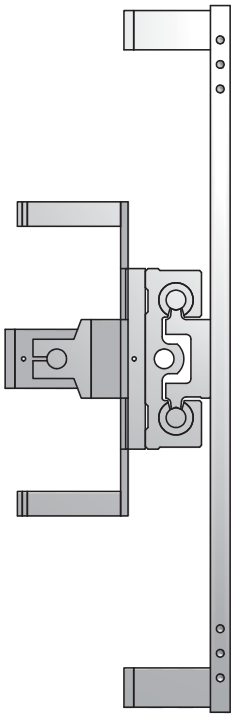

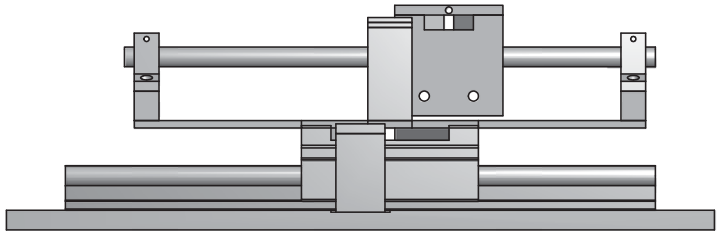

DRAWN Nick	7/3/2011		
CHECKED		TITLE NES Type 3 - Overview	
QA			
MFG			
APPROVED		SIZE C	DWG NO NES Type 3 for 2 Story
		SCALE	SHEET 2 OF 18

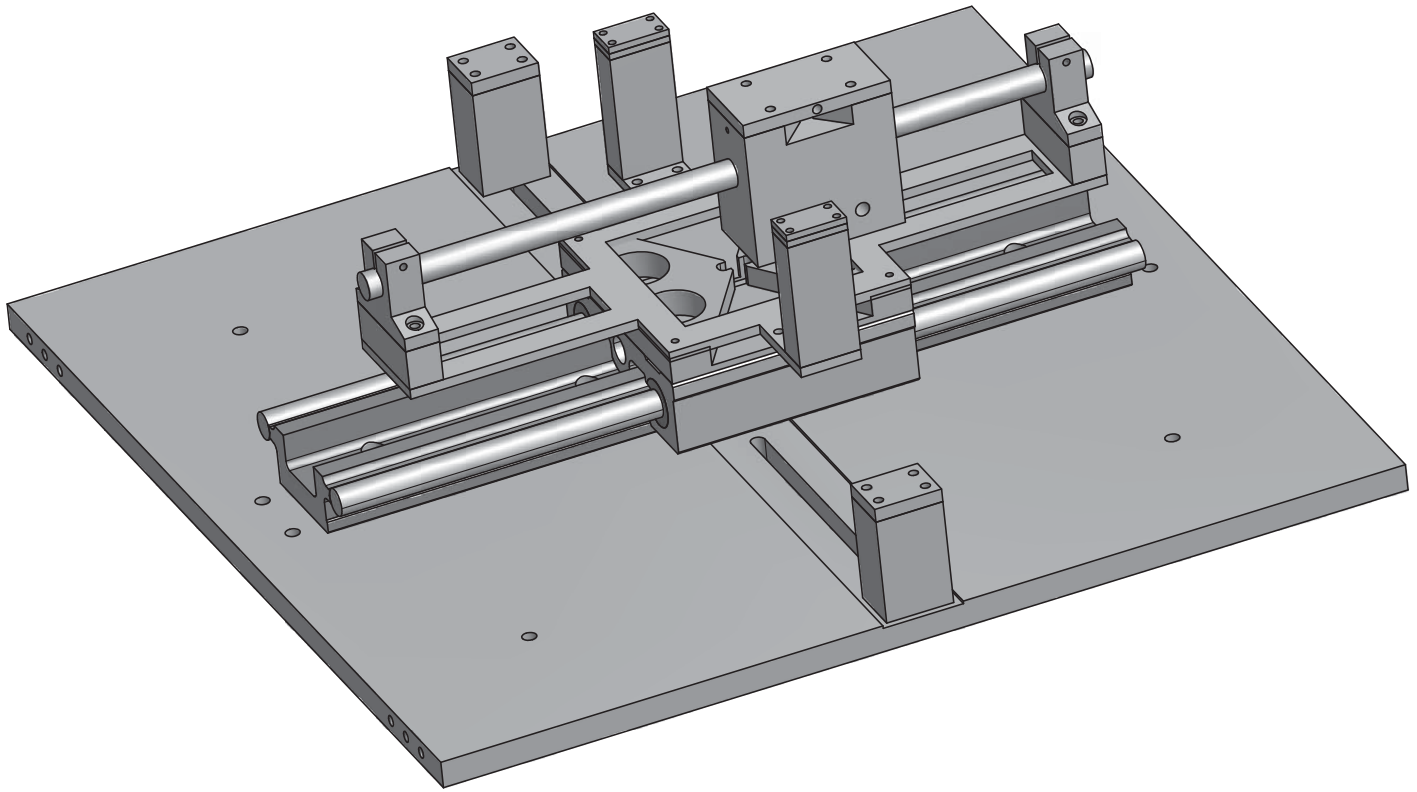

DRAWN Nick	7/3/2011		
CHECKED		TITLE NES Type 3 - Overview	
QA			
MFG			
APPROVED		SIZE C	DWG NO NES Type 3 for 2 Story
		SCALE	SHEET 3 OF 18

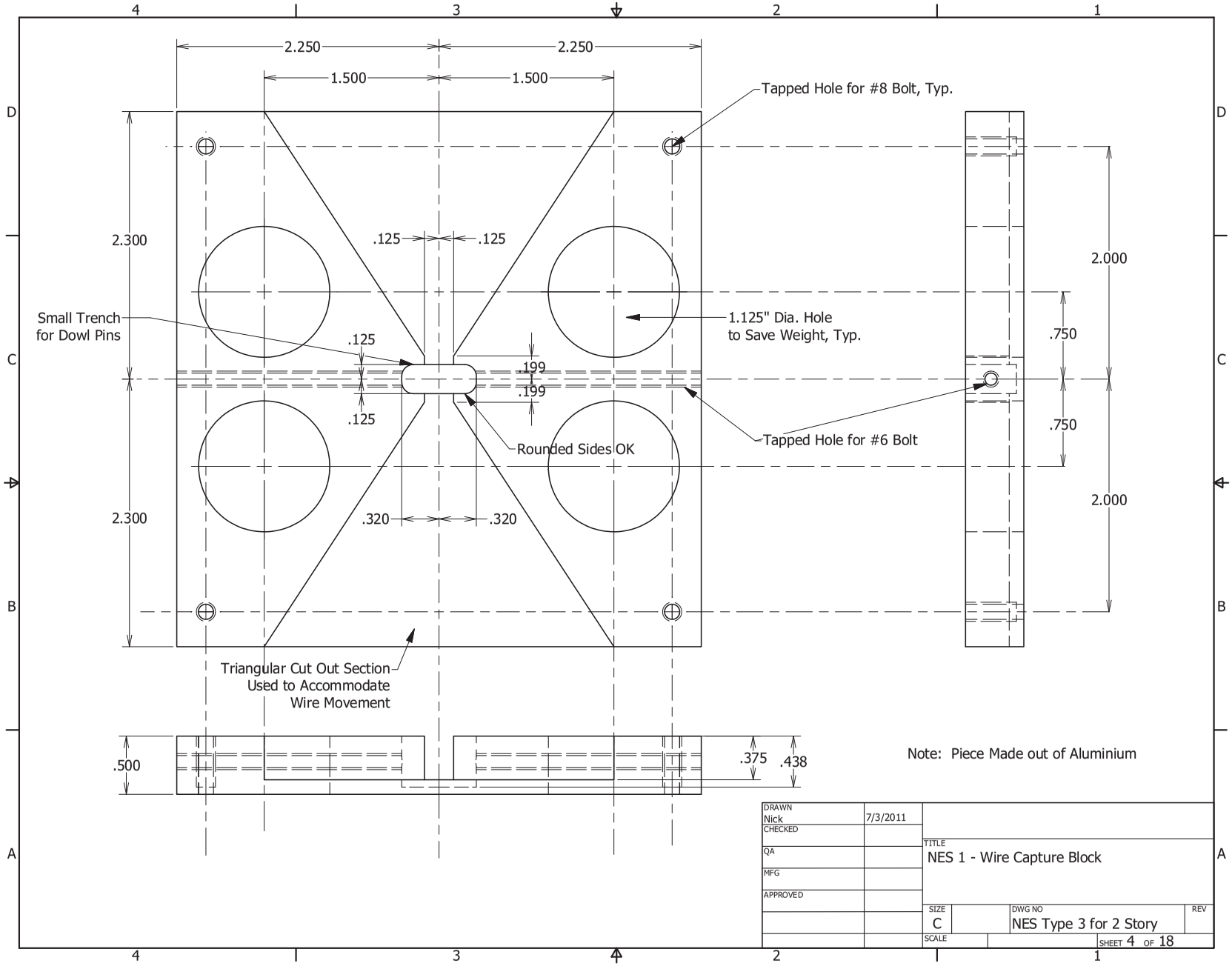
2.250
2.250
1.500
1.500
Tapped Hole for #8 Bolt, Typ.
2.300
.125
.125
2.000
Small Trench
for Dowl Pins
1.125" Dia. Hole
to Save Weight, Typ.
.750
.125
.199
.199
.125
.750
Rounded Sides OK
Tapped Hole for #6 Bolt
2.300
.320
.320
2.000
Triangular Cut Out Section
Used to Accommodate
Wire Movement
.500
.375
.438
Note: Piece Made out of Aluminium
DRAWN
Nick
7/3/2011
CHECKED
QA
MFG
APPROVED
TITLE
NES 1 - Wire Capture Block
SIZE
C
DWG NO
NES Type 3 for 2 Story
REV
SCALE
SHEET 4 OF 18

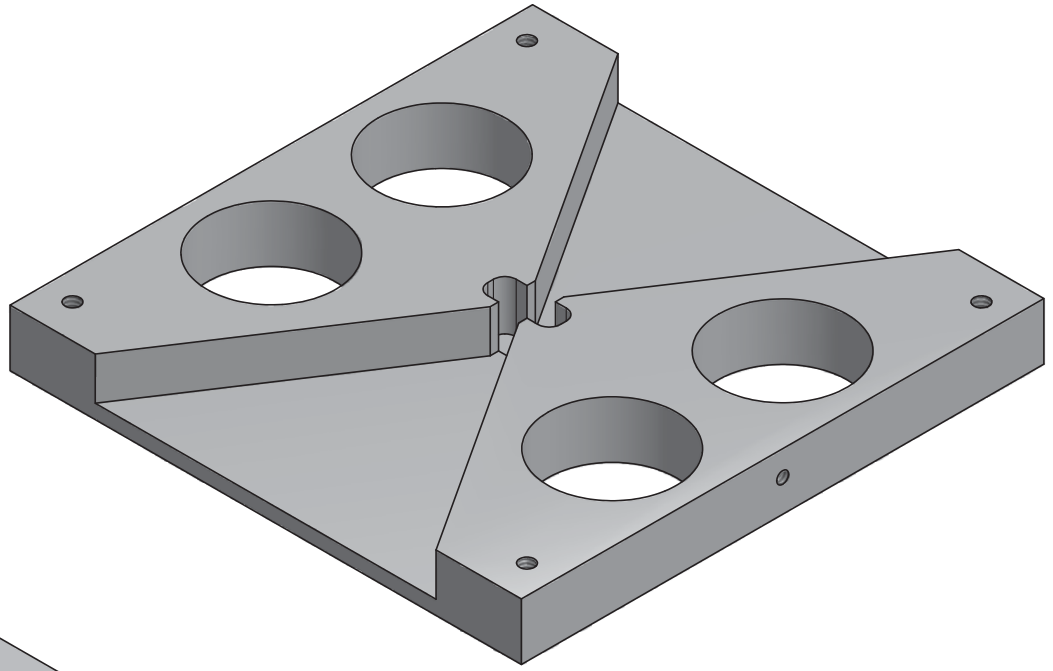

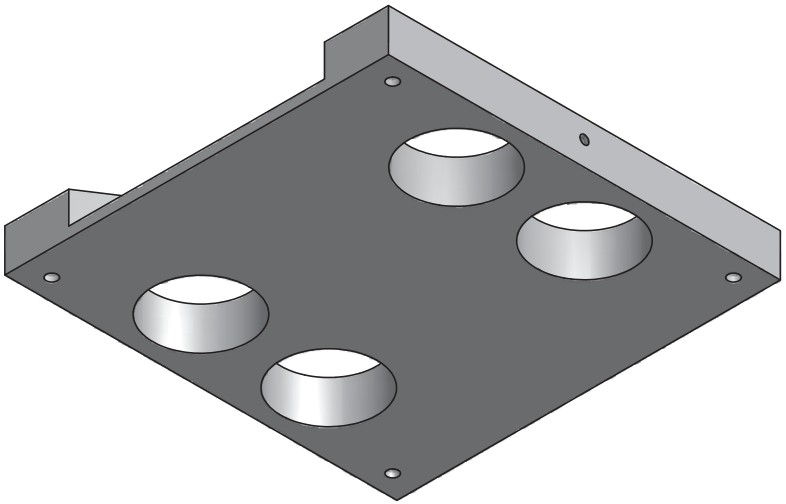

DRAWN Nick	7/3/2011	
CHECKED		TITLE Isometric View NES 1 - Wire Capture Block
QA		
MFG		
APPROVED		SIZE C | DWG NO NES Type 3 for 2 Story | REV
		SCALE | SHEET 5 OF 18

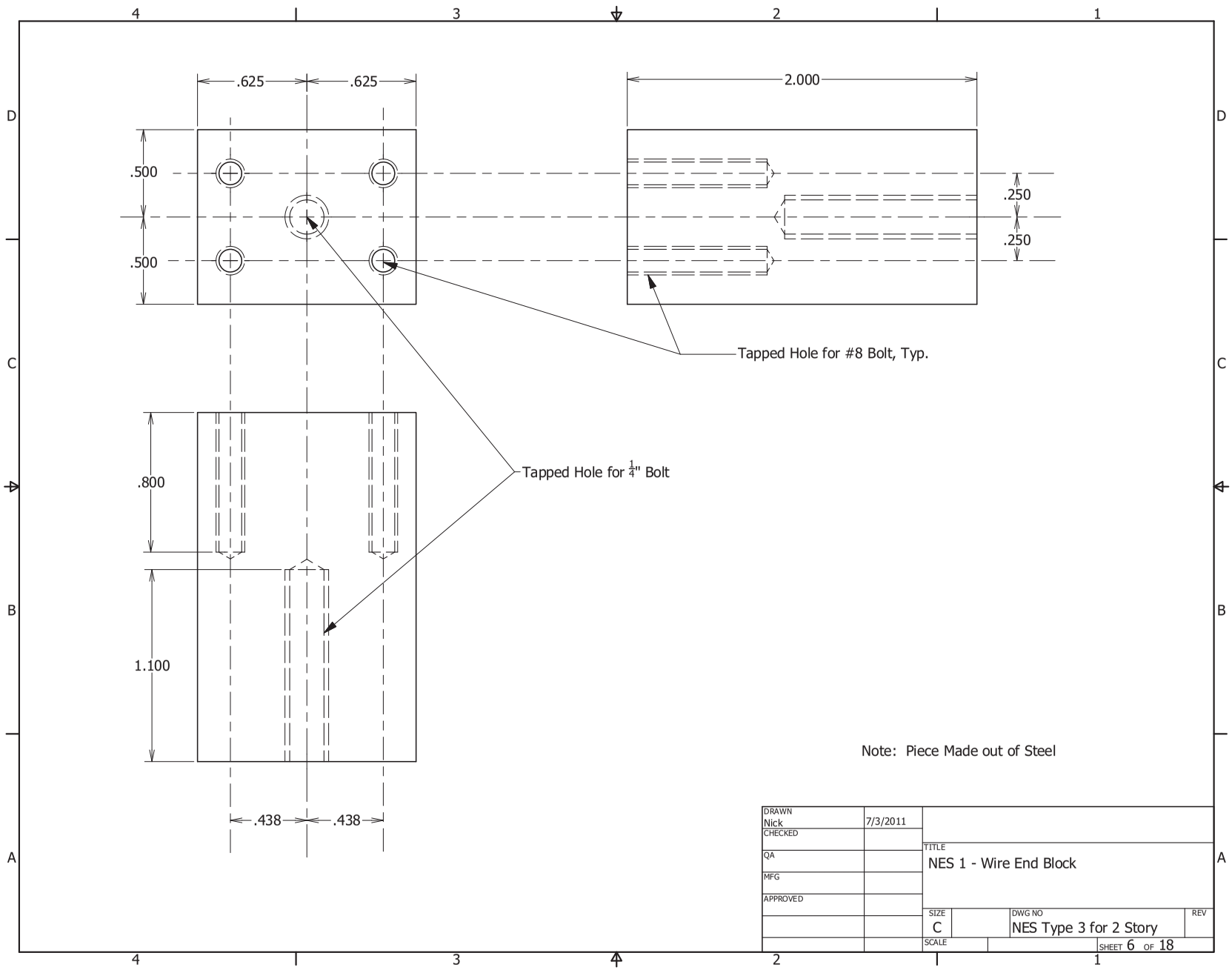
.625
.625
2.000
.500
.500
.250
.250
Tapped Hole for #8 Bolt, Typ.
Tapped Hole for 1/4" Bolt
.800
1.100
.438
.438
Note: Piece Made out of Steel
DRAWN
Nick
7/3/2011
CHECKED
QA
MFG
APPROVED
TITLE
NES 1 - Wire End Block
SIZE
C
DWG NO
NES Type 3 for 2 Story
REV
SCALE
SHEET 6 OF 18

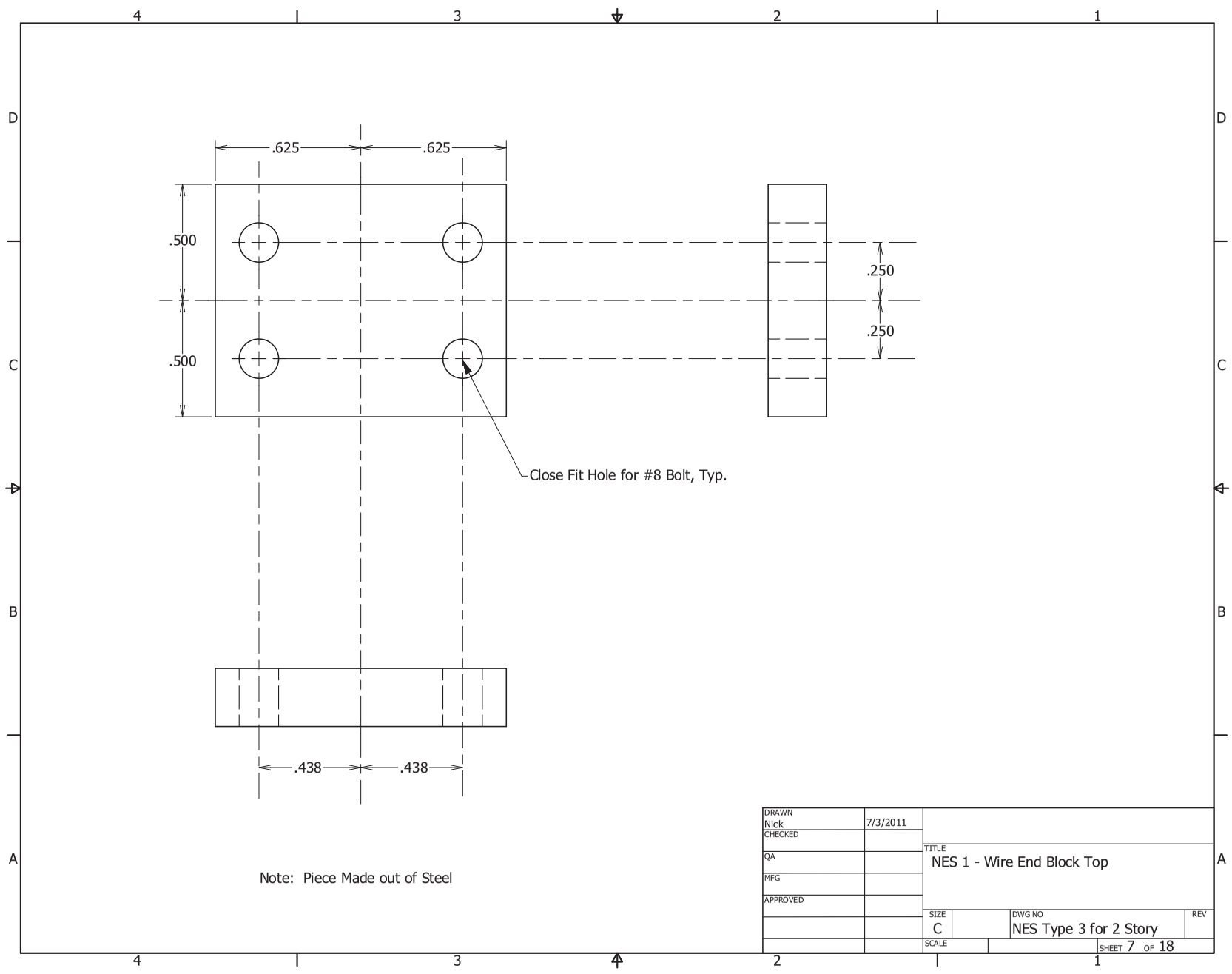
4
3
2
1
D
C
B
A
.625
.625
.500
.500
.250
.250
Close Fit Hole for #8 Bolt, Typ.
.438
.438
Note: Piece Made out of Steel
DRAWN
Nick
7/3/2011
CHECKED
QA
MFG
APPROVED
TITLE
NES 1 - Wire End Block Top
SIZE
C
DWG NO
NES Type 3 for 2 Story
REV
SCALE
SHEET 7 OF 18

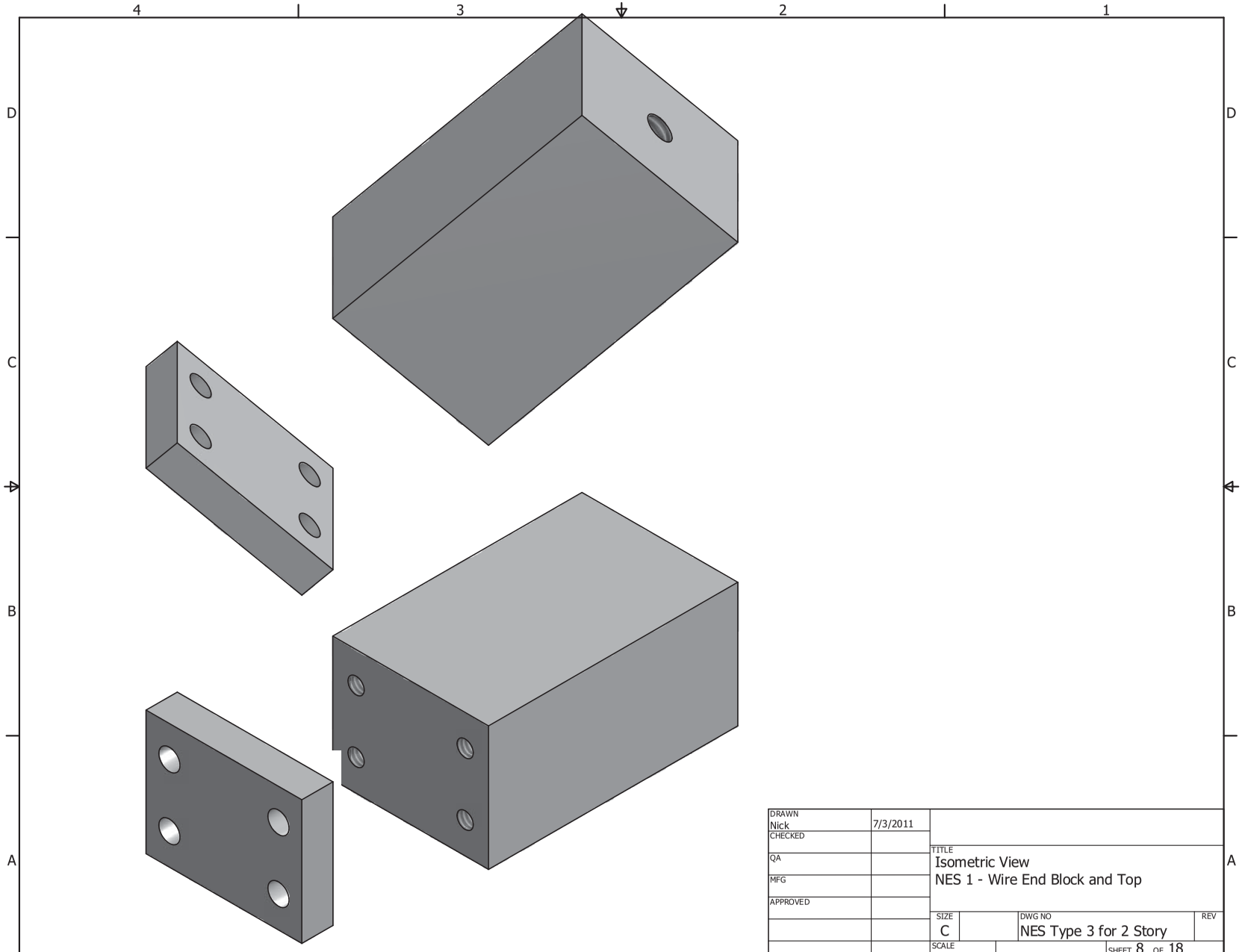

DRAWN Nick	7/3/2011	
CHECKED		
QA		TITLE Isometric View NES 1 - Wire End Block and Top
MFG		
APPROVED		SIZE C | DWG NO NES Type 3 for 2 Story | REV
		SCALE | SHEET 8 OF 18

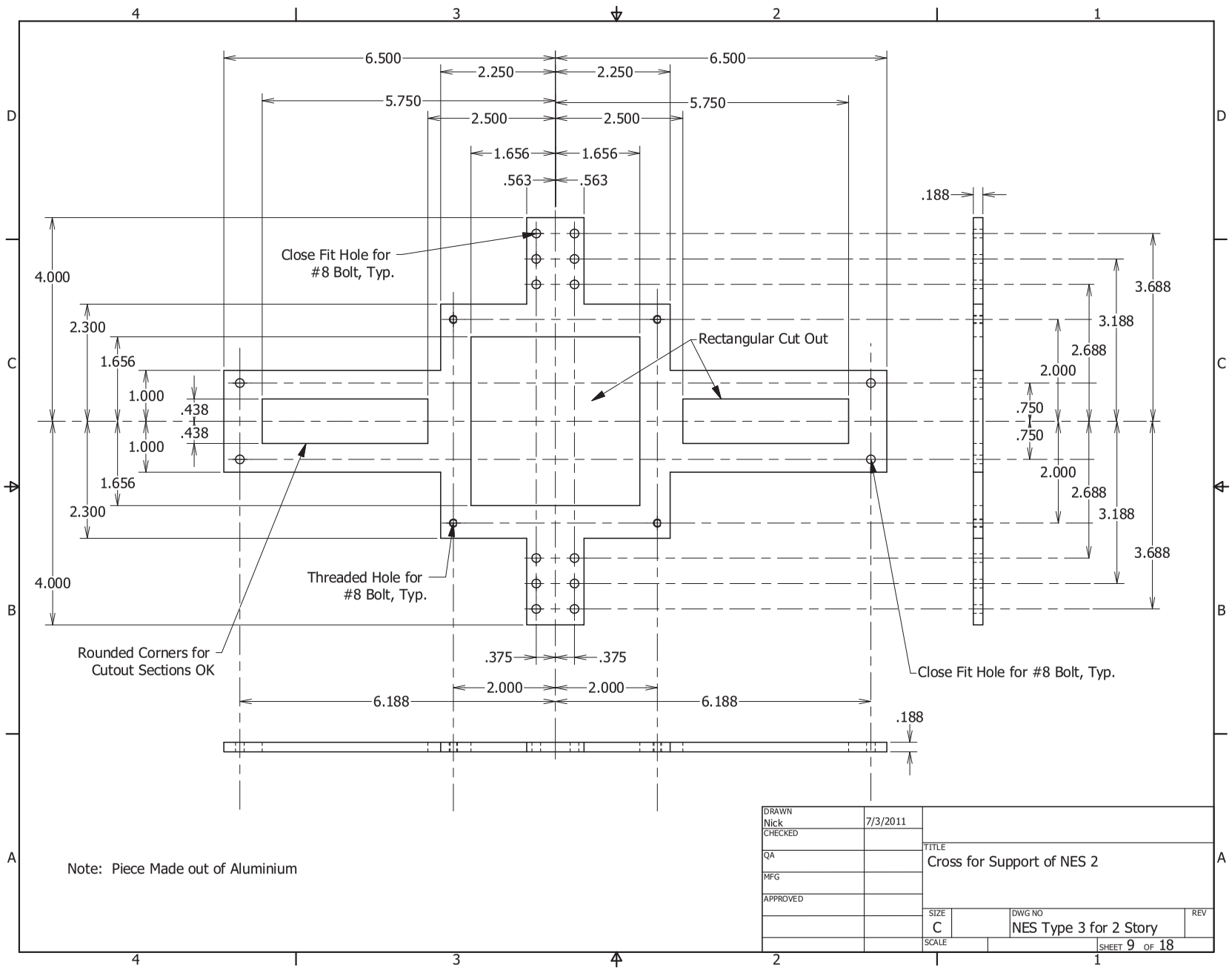
6.500
2.250
2.250
6.500
5.750
5.750
2.500
2.500
1.656
1.656
.563
.563
.188
Close Fit Hole for
#8 Bolt, Typ.
4.000
2.300
1.656
1.000
.438
.438
1.000
1.656
2.300
4.000
Rectangular Cut Out
3.688
3.188
2.688
2.000
.750
.750
2.000
2.688
3.188
3.688
Threaded Hole for
#8 Bolt, Typ.
Rounded Corners for
Cutout Sections OK
.375
.375
2.000
2.000
6.188
6.188
.188
Close Fit Hole for #8 Bolt, Typ.
Note: Piece Made out of Aluminium
DRAWN
Nick
7/3/2011
CHECKED
QA
MFG
APPROVED
TITLE
Cross for Support of NES 2
SIZE
C
DWG NO
NES Type 3 for 2 Story
REV
SCALE
SHEET 9 OF 18

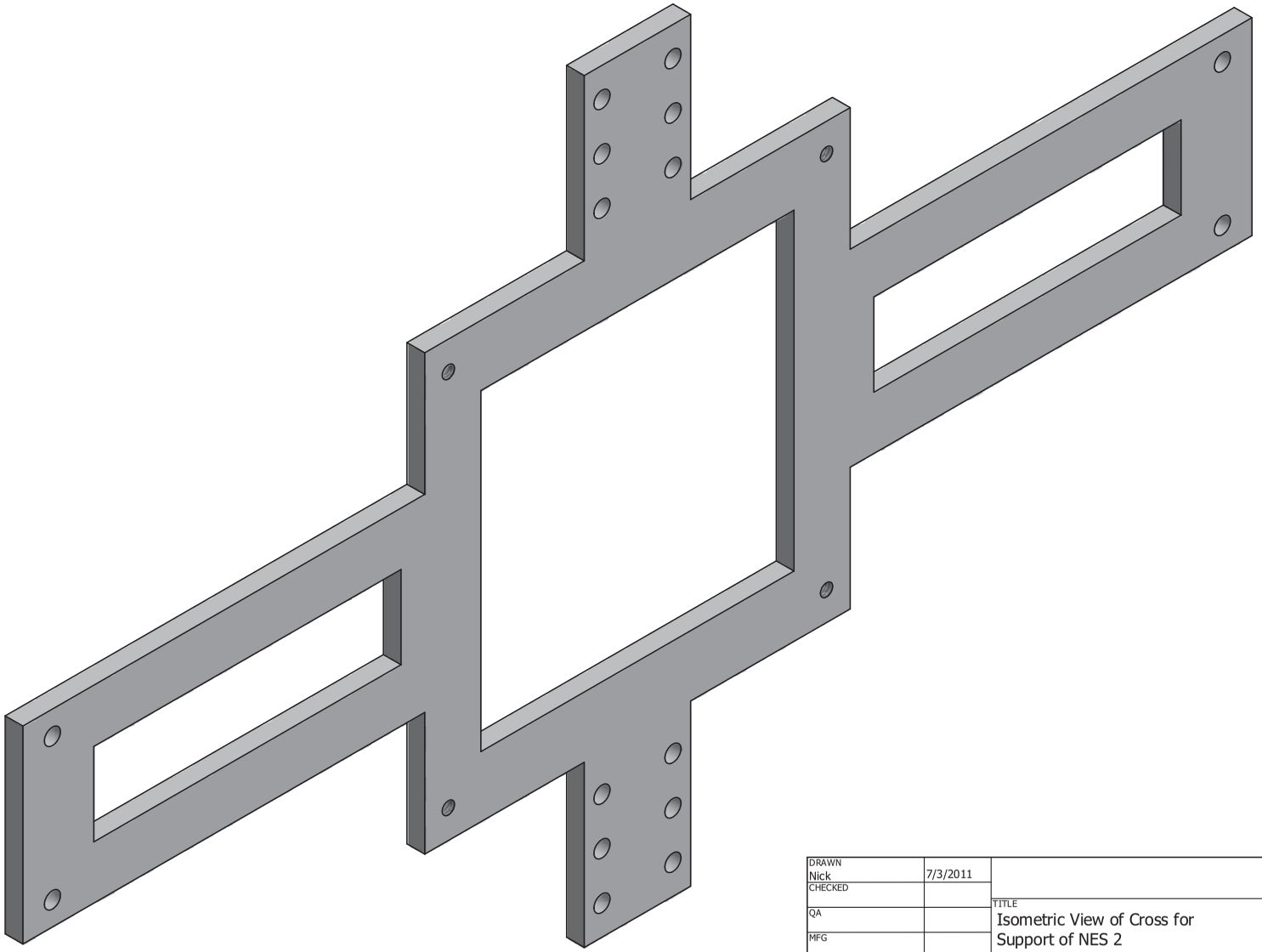

DRAWN Nick	7/3/2011	
CHECKED		
QA		TITLE Isometric View of Cross for Support of NES 2
MFG		
APPROVED		
		SIZE C / DWG NO NES Type 3 for 2 Story / REV
		SCALE / SHEET 10 OF 18

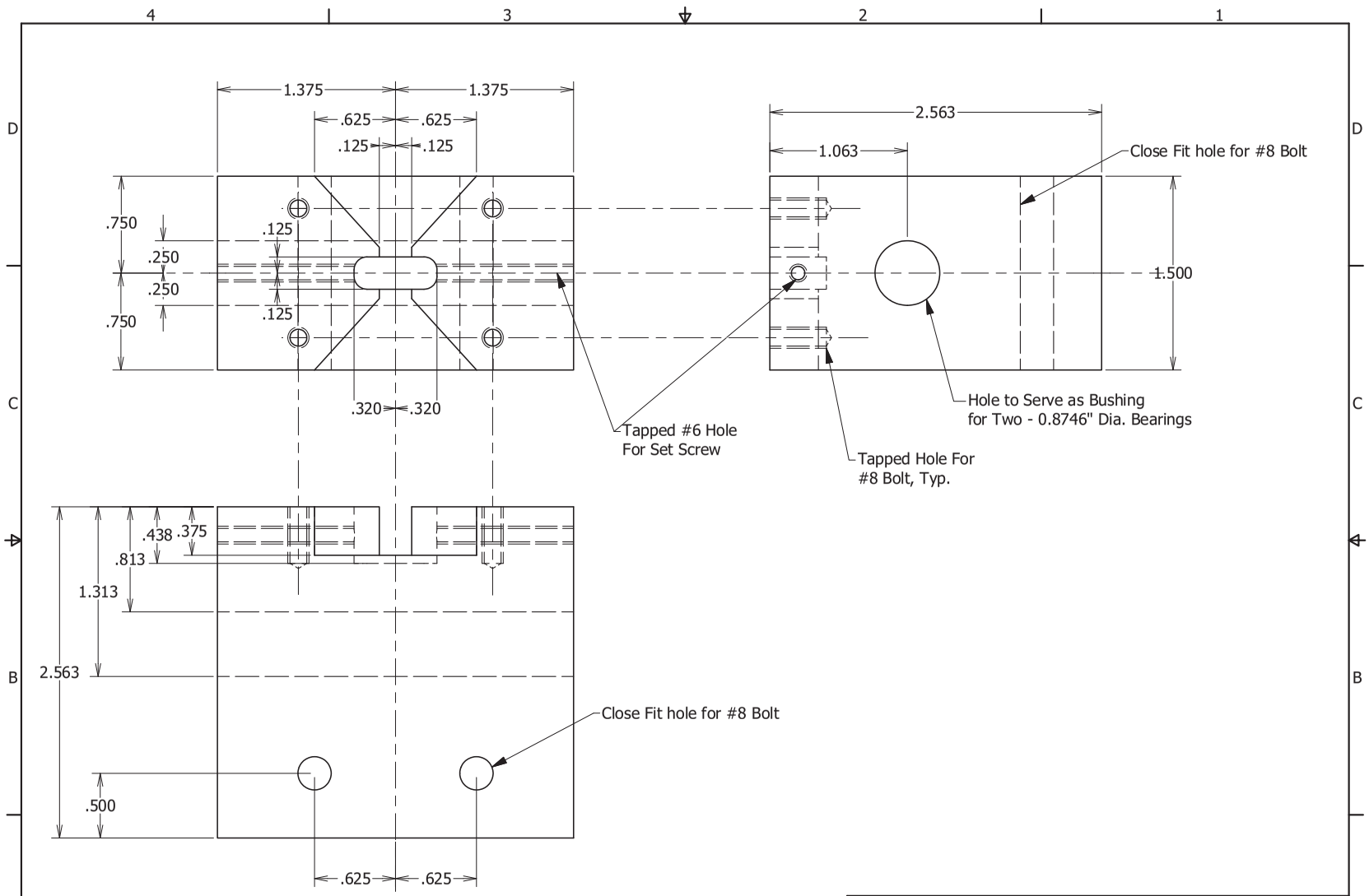
1.375
1.375
.625
.625
.125
.125
.750
.250
.250
.750
.125
.125
.320
.320
2.563
1.063
Close Fit hole for #8 Bolt
1.500
Hole to Serve as Bushing
for Two - 0.8746" Dia. Bearings
Tapped #6 Hole
For Set Screw
Tapped Hole For
#8 Bolt, Typ.
.438
.375
.813
1.313
2.563
Close Fit hole for #8 Bolt
.500
.625
.625
Note: Piece Made out of Aluminium
DRAWN
Nick
7/3/2011
CHECKED
QA
MFG
APPROVED
TITLE
NES 2 - Main Mass
SIZE
C
DWG NO
NES Type 3 for 2 Story
REV
SCALE
SHEET 11 OF 18

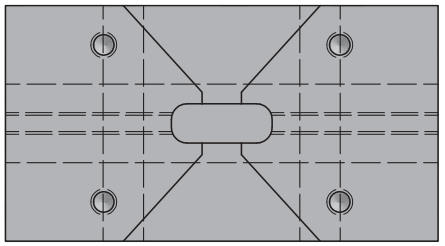

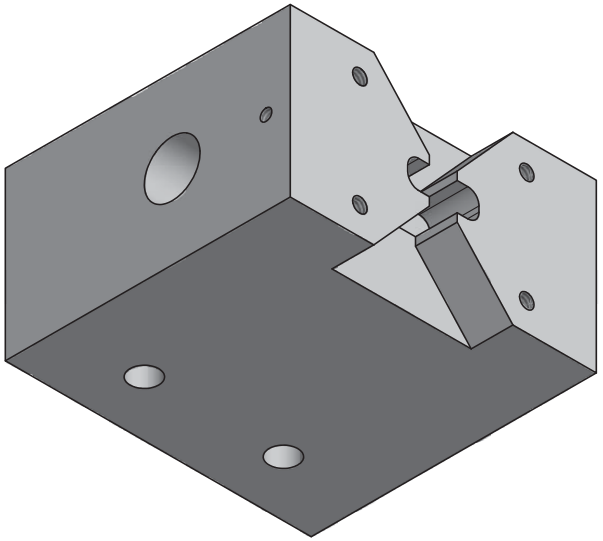

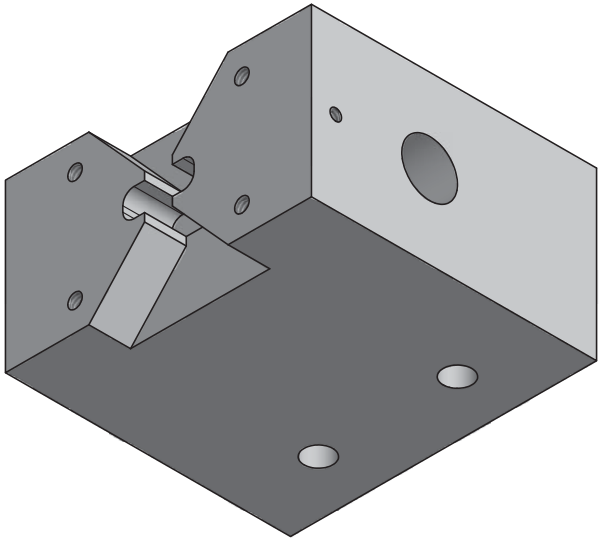

DRAWN Nick	7/3/2011		
CHECKED		TITLE Isometric View NES 2 - Main Mass	
QA			
MFG			
APPROVED			
		SIZE C	DWG NO NES Type 3 for 2 Story
		SCALE	SHEET 12 OF 18

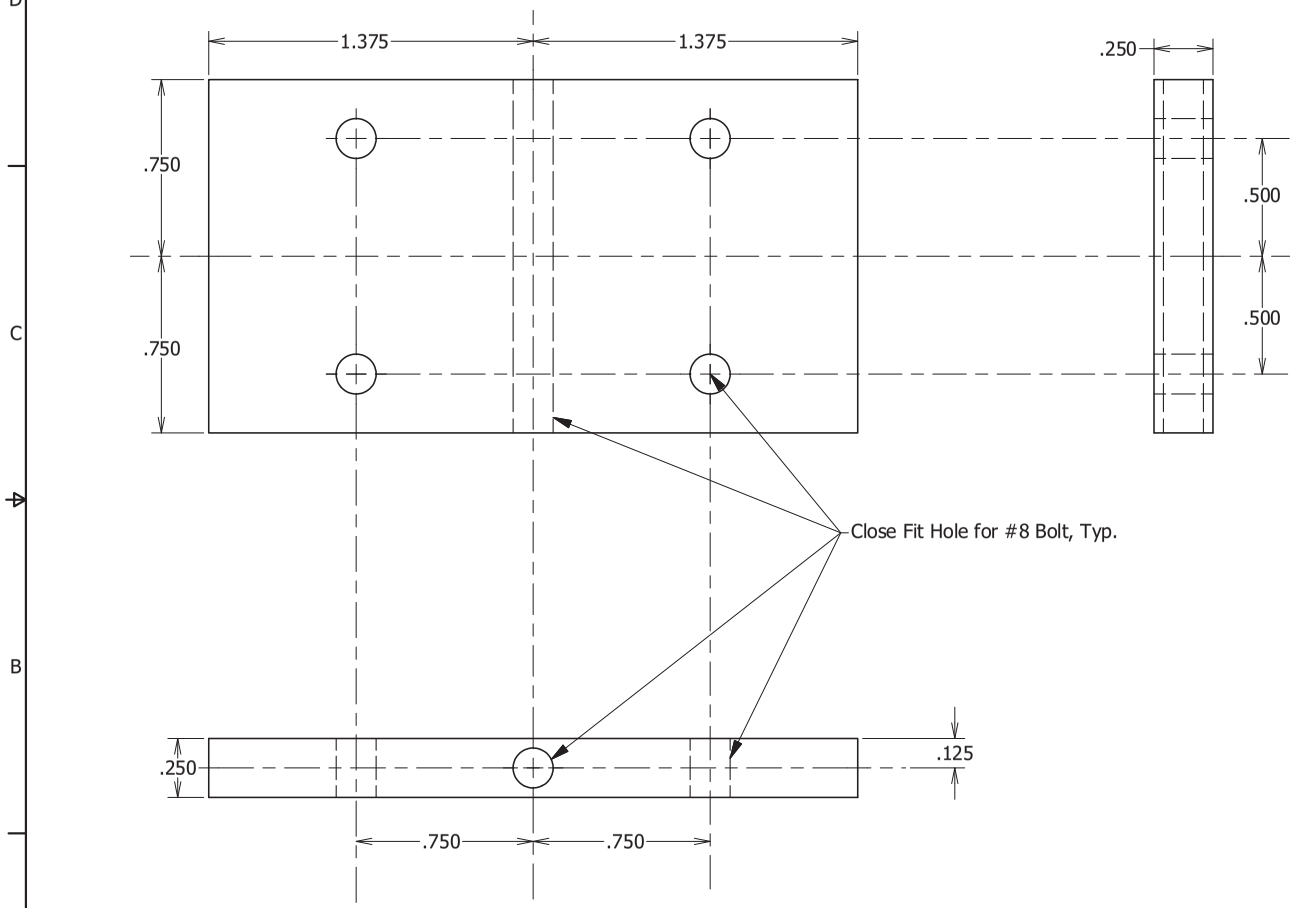

Note: Piece Made out of Aluminium

DRAWN Nick	7/3/2011	
CHECKED		TITLE: NES 2 - Main Mass Top
QA		
MFG		
APPROVED		SIZE: C; DWG NO: NES Type 3 for 2 Story; REV:
		SCALE: ; SHEET 13 OF 18

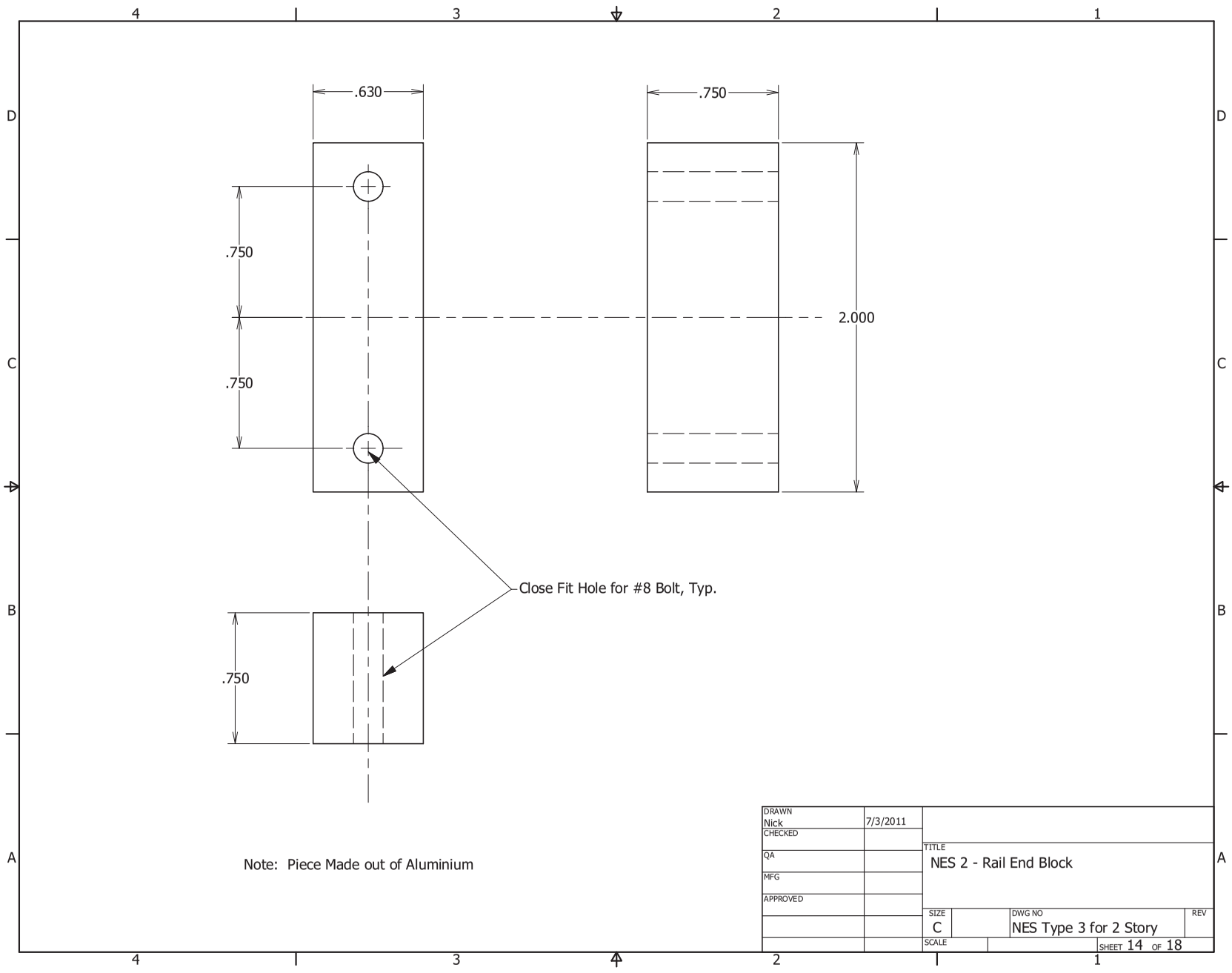
.630
.750
.750
.750
2.000
Close Fit Hole for #8 Bolt, Typ.
.750
Note: Piece Made out of Aluminium
DRAWN
Nick
7/3/2011
CHECKED
QA
MFG
APPROVED
TITLE
NES 2 - Rail End Block
SIZE
C
DWG NO
NES Type 3 for 2 Story
REV
SCALE
SHEET 14 OF 18

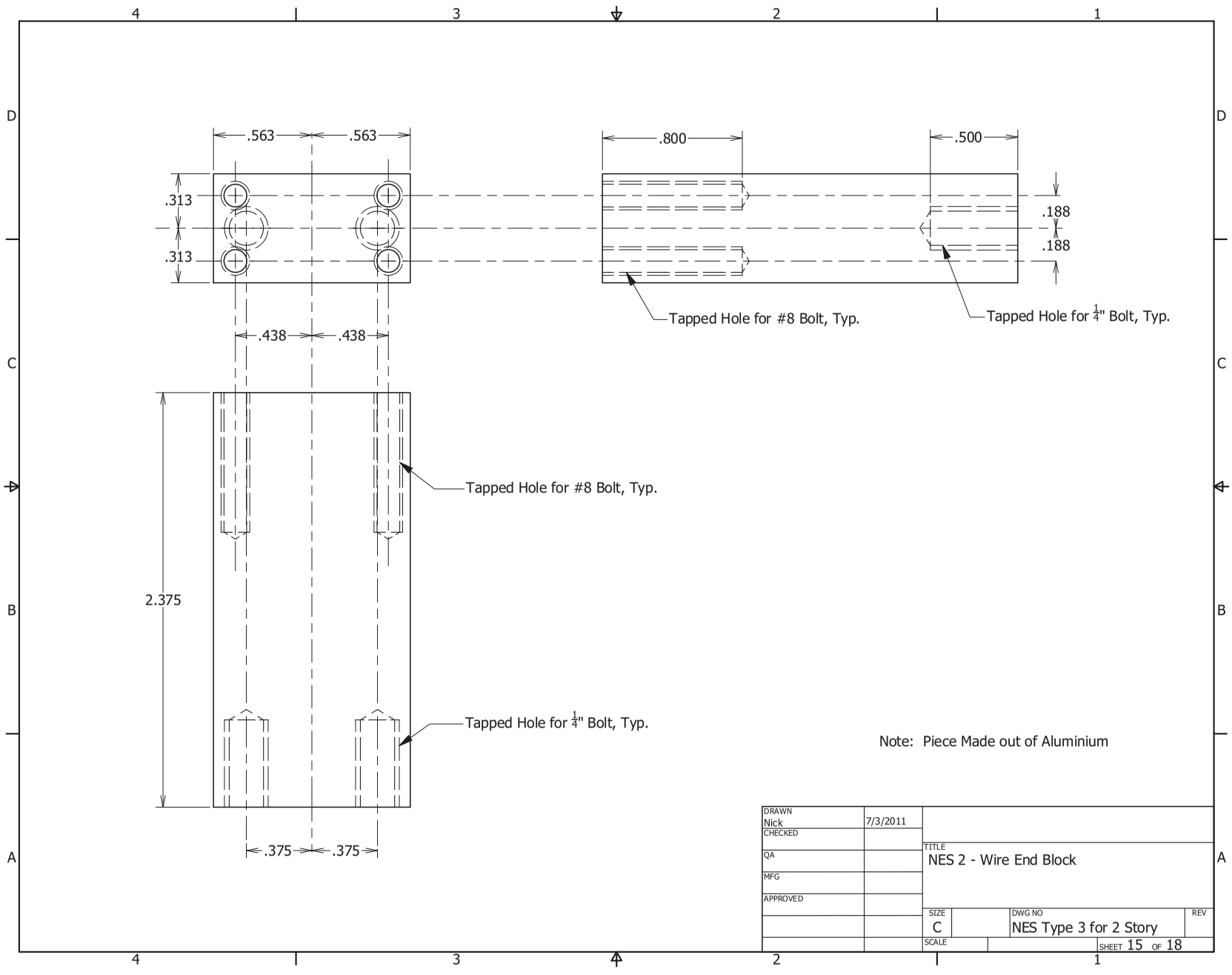
.563
.563
.800
.500
.313
.313
.188
.188
Tapped Hole for #8 Bolt, Typ.
Tapped Hole for 1/4" Bolt, Typ.
.438
.438
Tapped Hole for #8 Bolt, Typ.
2.375
Tapped Hole for 1/4" Bolt, Typ.
.375
.375
Note: Piece Made out of Aluminium
DRAWN
Nick
7/3/2011
CHECKED
QA
MFG
APPROVED
TITLE
NES 2 - Wire End Block
SIZE
C
DWG NO
NES Type 3 for 2 Story
REV
SCALE
SHEET 15 OF 18

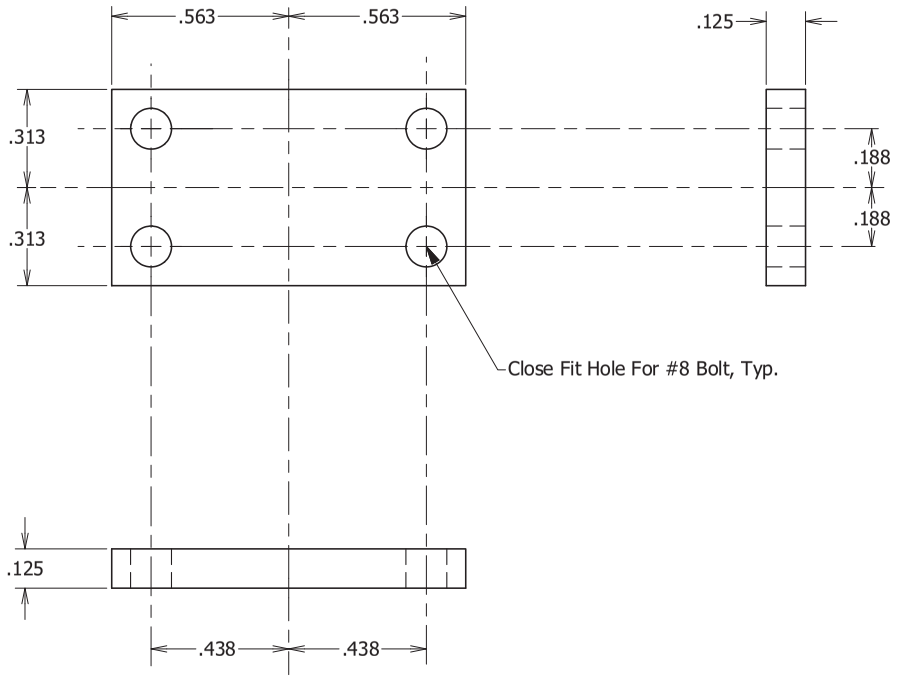

Note: Piece Made out of Steel

DRAWN Nick	7/3/2011	
CHECKED		TITLE: NES 2 - Wire End Block Top Pieces
QA		
MFG		
APPROVED		SIZE C | DWG NO NES Type 3 for 2 Story | REV
		SCALE | SHEET 16 OF 18

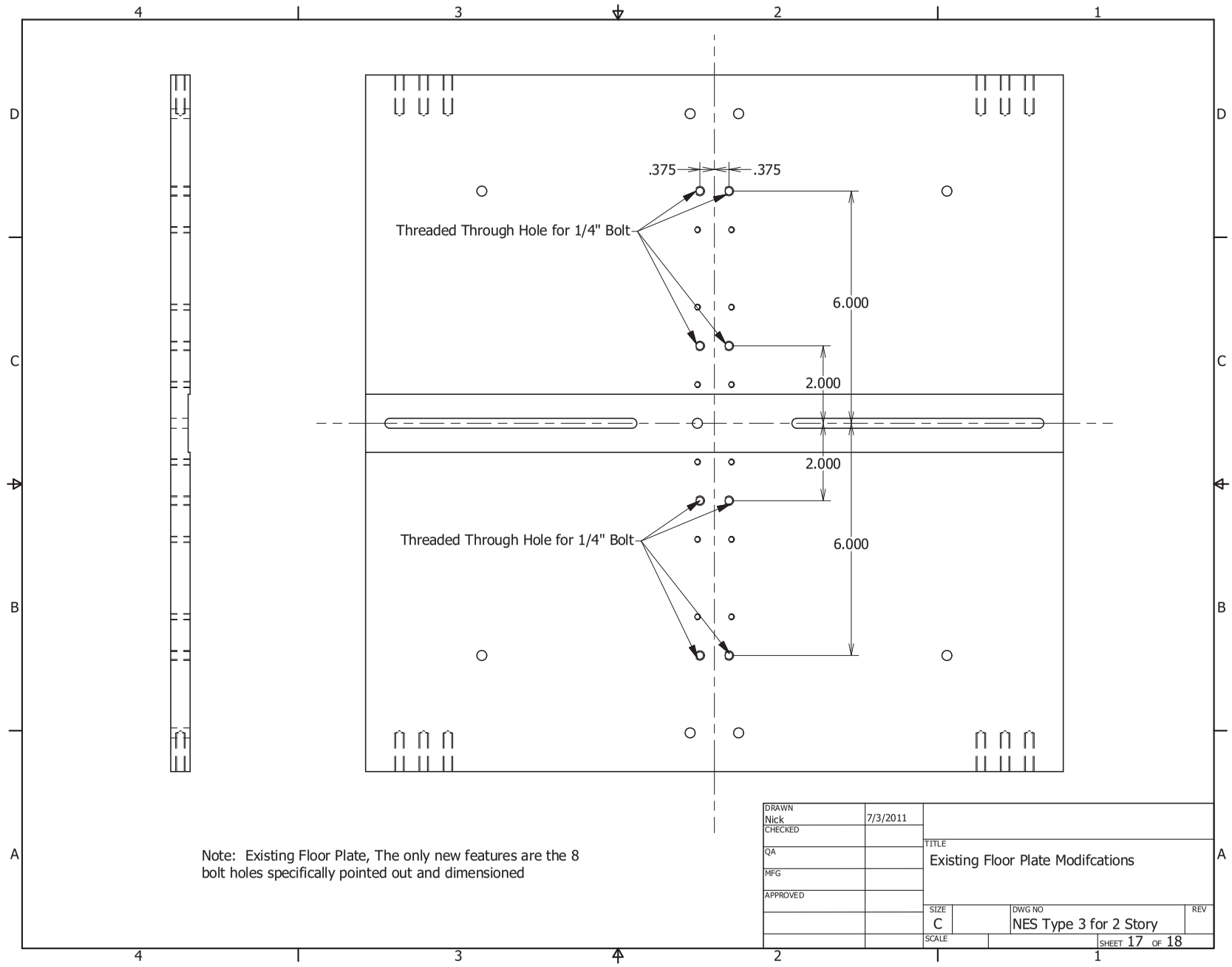

Note: Existing Floor Plate, The only new features are the 8 bolt holes specifically pointed out and dimensioned

DRAWN Nick	7/3/2011	
CHECKED		TITLE: Existing Floor Plate Modifcations
QA		
MFG		
APPROVED		SIZE C | DWG NO NES Type 3 for 2 Story | REV
		SCALE | SHEET 17 OF 18

Component Quantity / Material List		
Part	Material	Quantity
NES 1 - Wire Capture Block	Aluminium	1
NES 1 - Wire End Block	Steel	2
NES 1 - Wire End Block Top	Steel	2
Cross for Support of NES 2	Aluminium (Grade 6061- 35000 psi or Higher Strength)	1
NES 2 - Main Mass	Aluminum	1
NES 2 - Main Mass Top	Aluminum	1
NES 2 - Rail End Block	Aluminum	2
NES 2 - Wire End Block	Aluminum	2
NES 2 - Wire End Block Top Pieces	Steel	4
Existing Floor Plate Modifcations	Existing	1

DRAWN Nick	7/3/2011		
CHECKED		TITLE	
QA			
MFG			
APPROVED		SIZE C	DWG NO NES Type 3 for 2 Story
		SCALE	SHEET 18 OF 18

A.3 Medium-scale Base Structure

ILLINOIS, UNIVERSITY OF ILLINOIS AT URBANA-CHAMPAIGN		project: BUILDING TEST	
units: IN.	drawn by: TAM	scale: NTS	sheet: 1 of 6

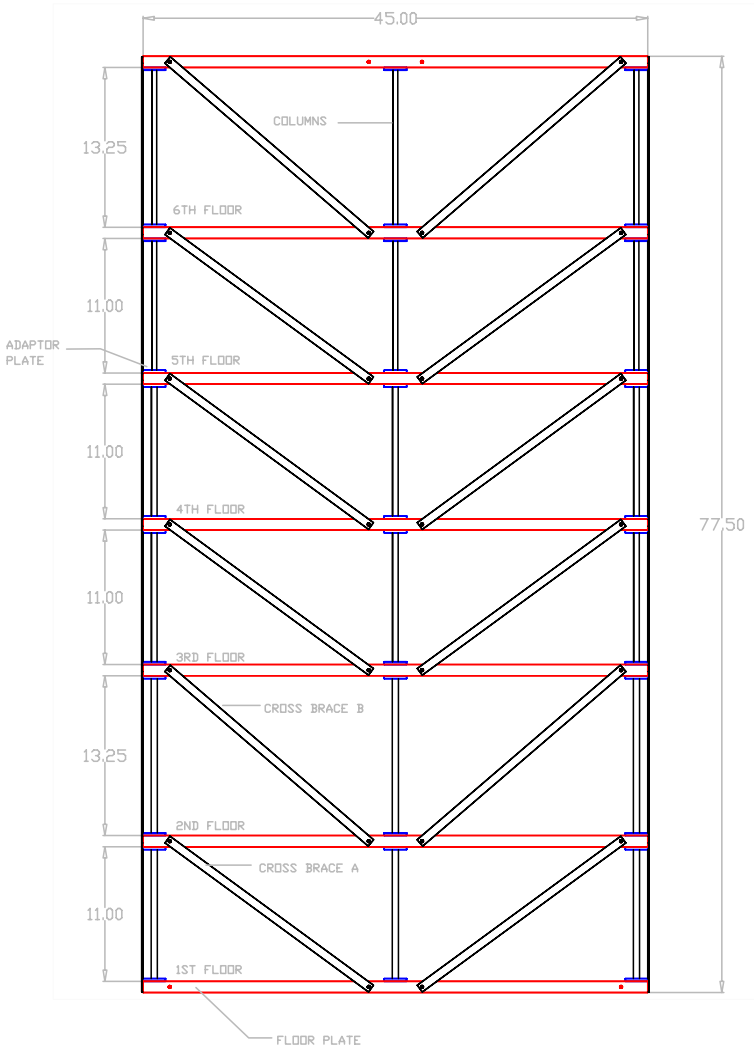

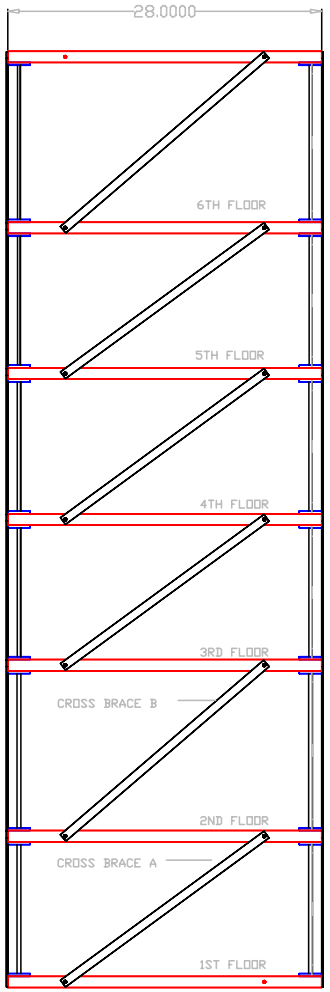

ITEM	QTY
TYPICAL FLOOR PLATE	6
BASE FLOOR PLATE	1
COLUMNS	--
CROSS BRACE A	24
CROSS BRACE B	12
ADAPTOR PLATE	72
ACTUATOR CONNECTION PIECE A	3
ACTUATOR CONNECTION PIECE B	1
ACUTATOR CONNECTION PIECE C	2

NOTE: ALL CONNECTIONS ARE BOLTED WITH #1/4" - 16 THREADED ROD, UNLESS OTHERWISE NOTED.

ILLINOIS
UNIVERSITY OF ILLINOIS AT URBANA-CHAMPAIGN

project: BUILDING TEST

drawing: MODEL BUILDING

units:	drawn by:	scale:	sheet:
IN.	TAM	NTS	2 of 6

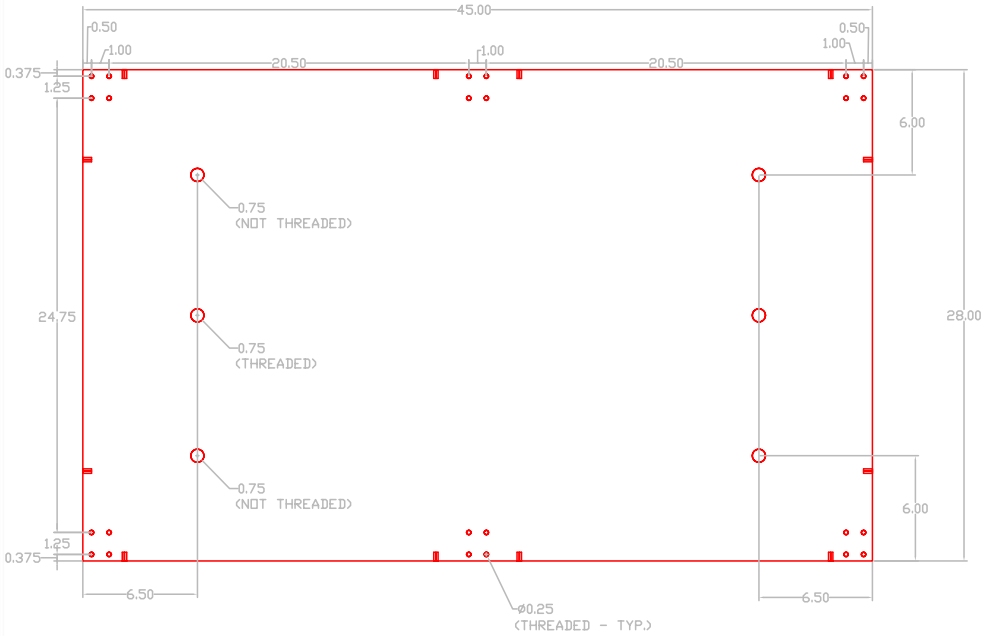

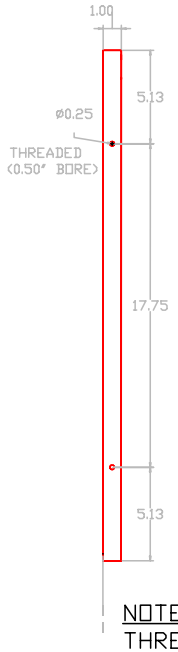

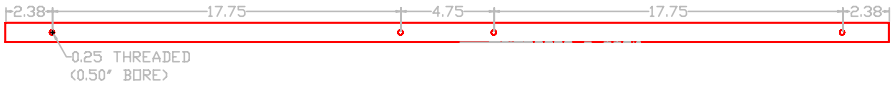

NOTE: ALL HOLES ARE TO BE THREADED FOR #1/4" - 16 THREADED ROD, UNLESS OTHERWISE NOTED.
NORMAL GRADE STEEL TO BE USED FOR FLOOR PLATES

ILLINOIS
UNIVERSITY OF ILLINOIS AT URBANA-CHAMPAIGN

project:	
BUILDING TEST	
drawing:	
TYPICAL FLOOR PLATE	

units:	drawn by:	scale:	sheet:
IN.	TAM	NTS	3 of 6

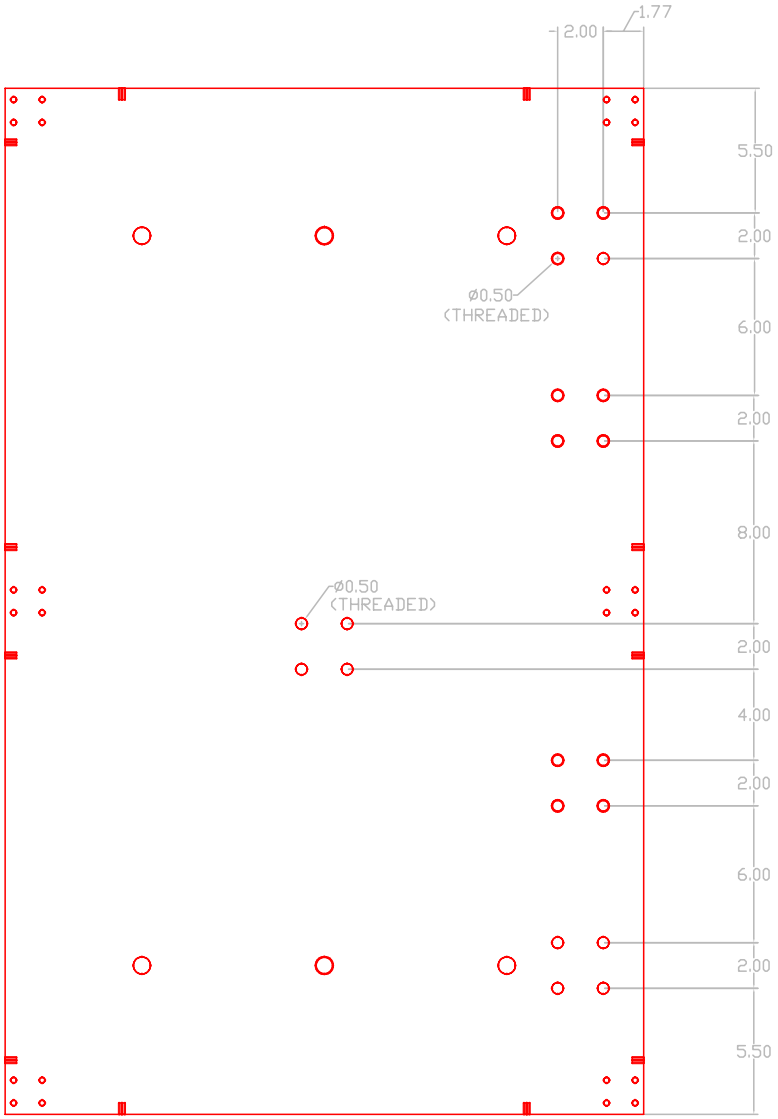

NOTE:
ONLY THE ADDITIONAL HOLES THAT ARE NOT INCLUDED ON THE NORMAL FLOOR PLATES ARE LABELED AND DIMENSIONED. FOR THE REMAINING DIMENSIONS, SEE PAGE 2.

ILLINOIS
UNIVERSITY OF ILLINOIS AT URBANA-CHAMPAIGN

project: BUILDING TEST			
drawing: BASE FLOOR PLATE			
units: IN.	drawn by: TAM	scale: NTS	sheet: 4 of 6

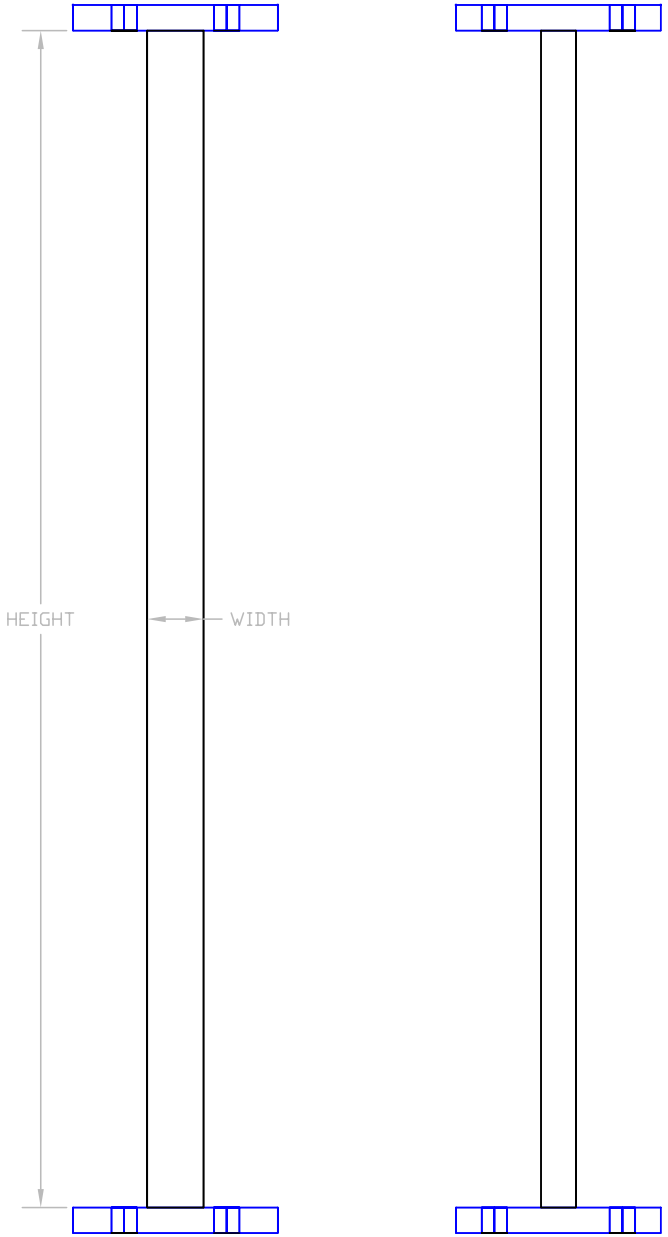

FLOOR	QTY.	HEIGHT	WIDTH	THICKNESS
1	6	10.25″	0.55″	0.3125″
2	6	12.5″	0.55″	0.3125″
3 & 4	12	10.25″	0.50″	0.3125″
5	6	10.25″	0.40″	0.3125″
6	6	12.5″	0.40″	0.3125″

NOTE: 100 KSI YIELD STRENGTH STEEL TO BE USED.

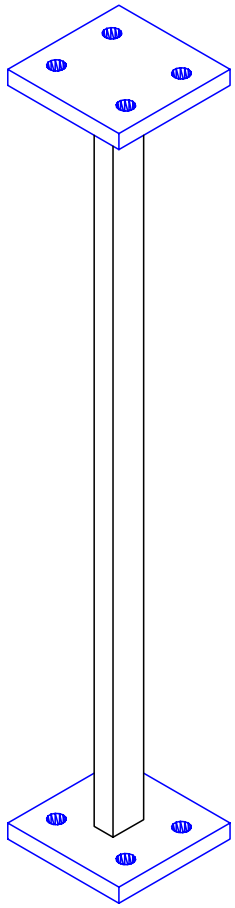

ILLINOIS
UNIVERSITY OF ILLINOIS AT URBANA-CHAMPAIGN

project: BUILDING TEST

drawing: TYPICAL COLUMN

units:	drawn by:	scale:	sheet:
IN.	TAM	NTS	5 of 6

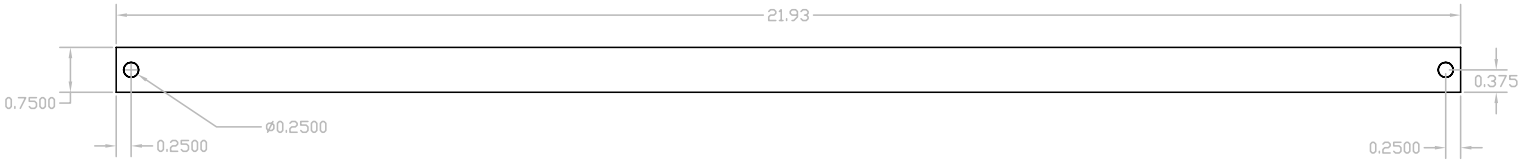

CROSS-BRACE A
REQUIRED FOR THE 1ST,
3RD, 4TH, AND 5TH FLOORS
(24 TOTAL)

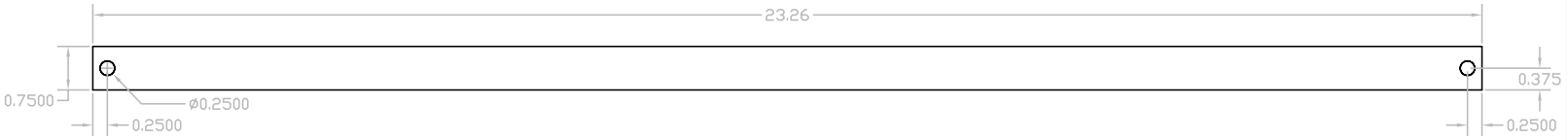

CROSS-BRACE B
REQUIRED FOR THE 2ND
AND 6TH FLOORS
(12 TOTAL)

NOTE:
(1) THE BRACES ARE 0.25" THICK
(2) ALL HOLES ARE TO BE THREADED
FOR #1/4" - 16 THREAD. ROD

ILLINOIS
UNIVERSITY OF ILLINOIS AT URBANA-CHAMPAIGN

project: BUILDING TEST			
drawing: CROSS BRACE			
units: IN.	drawn by: TAM	scale: NTS	sheet: 6 of 6

A.4 Large-scale Base Structure and System of NESs

Design Drawings

Completion Date: June 1st, 2012

Contact Information:

B.F. Spencer, Jr., PhD, PE
Nathan M. and Anne M. Newmark Endowed Chair in Civil Engineering
and Director, Newmark Structural Engineering Laboratory
Department of Civil and Environmental Engineering
University of Illinois at Urbana-Champaign
2213 Newmark Civil Engineering Laboratory, MC-250
205 North Mathews Ave
Urbana, IL 61801
Ph: (217) 333-8630, Mobile: (217) 419-4780
E-mail: bfs@illinois.edu, WWW: http://sstl.cee.illinois.edu/

Nicholas E. Wierschem
Ph.D. Candidate
Department of Civil and Environmental Engineering
Newmark Civil Engineering Laboratory, MC-250
University of Illinois at Urbana-Champaign
205 North Mathews Ave.
Urbana, IL 61801
Ph: (520) 245-3837
Email: nwiersc2@illinois.edu

Tim Prunkard
Machine Shop Supervisor
Department of Civil and Environmental Engineering
Newmark Civil Engineering Laboratory, MC-250
University of Illinois at Urbana-Champaign
205 North Mathews Ave.
Urbana, IL 61801
Ph: (217) 333-6913
Email: prunkard@illinois.edu

DRAWN Nick	5/4/2012		
CHECKED		TITLE Title Page	
QA			
MFG			
APPROVED		SIZE C	DWG NO CostEstimationDrawing REV
		SCALE	SHEET 1 OF 37

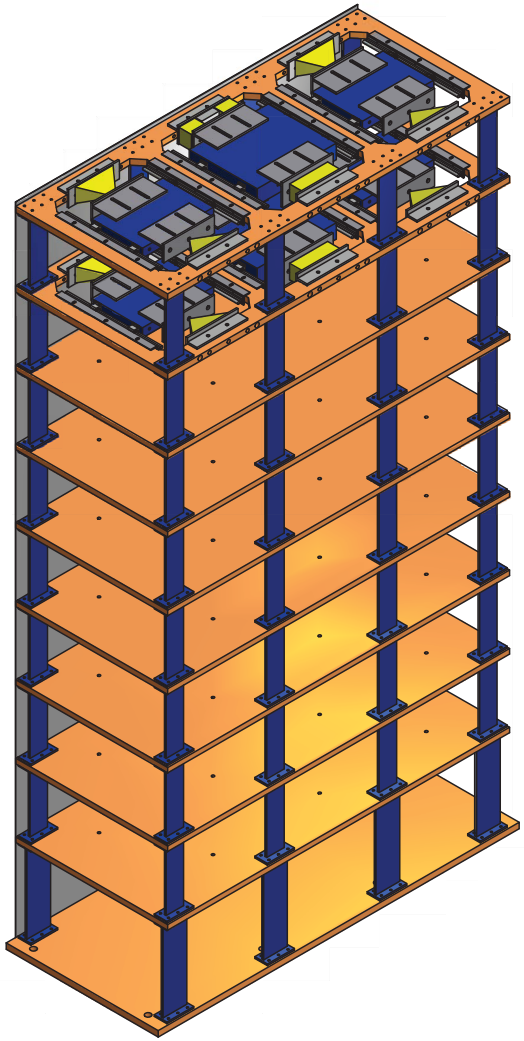

DRAWN Nick	5/4/2012	
CHECKED		TITLE Complete Structure Overiew
QA		
MFG		
APPROVED		SIZE C | DWG NO CostEstimationDrawing | REV
		SCALE | SHEET 2 OF 37

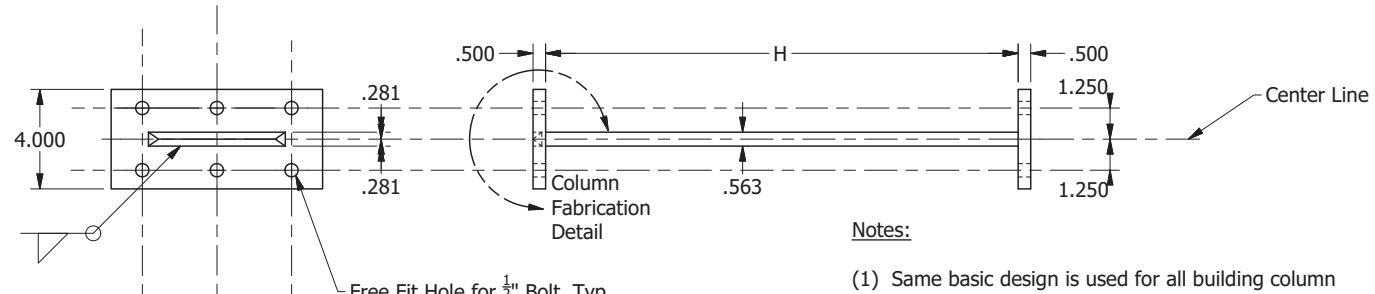

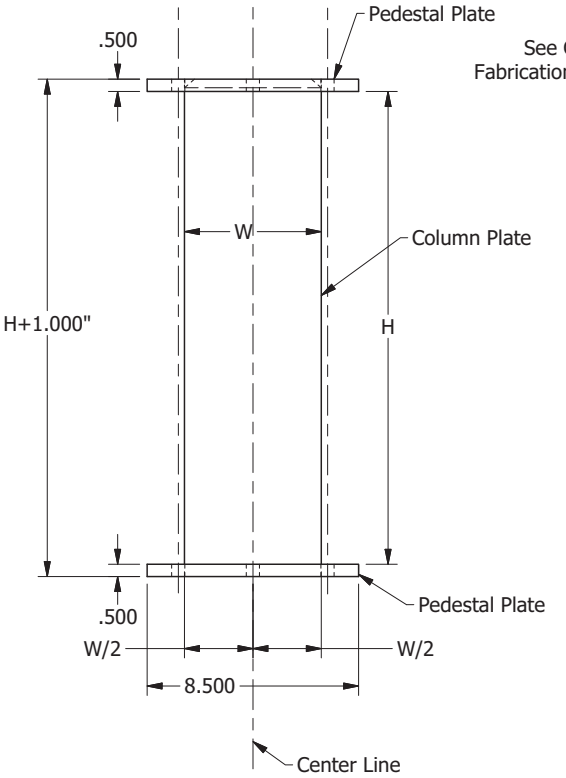

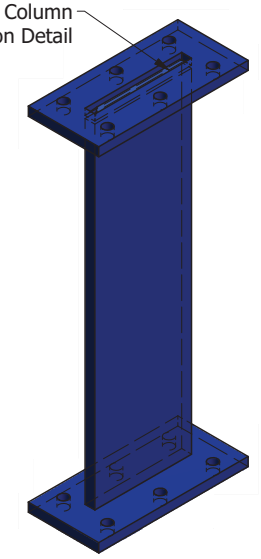

Notes:

(1) Same basic design is used for all building column assemblies. The difference that exists are the height and width of the central portion of the column assembly. These difference, and the quantity of each column needed, are shown in the below table.
(2) Material is high strength steel (>= 100 ksi)
(3) See Coumn Fabrication Detail for fabrication instructions.
(4) Columns are to be painted "Illini Blue" (RGB [0,60,125] or CMYK = [100,86,24,9])

(5) Column is connected to Base plate with 2.75" long ½" UNC bolts and corresponing washers and lock washers

(6) Other column connections are with 4.5" long ½" UNC bolts, and corresponing washers, lock washers, and nuts
(7) Connecting bolts and washers shall be Grade 5 or higher

Column Dimensions			
Stories	H (in)	W (in)	Quantity
1	25	7.5	8
2-9	19	5.5	64

DRAWN Nick	5/4/2012		
CHECKED		TITLE Columns	
QA			
MFG			
APPROVED		SIZE C	DWG NO CostEstimationDrawing REV
		SCALE	SHEET 3 OF 37

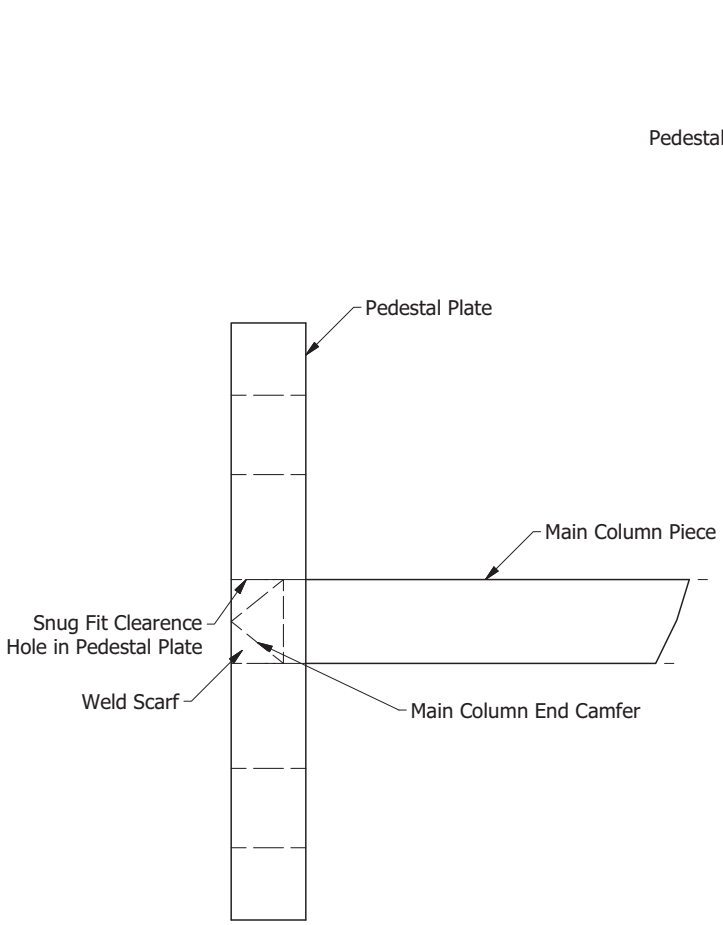

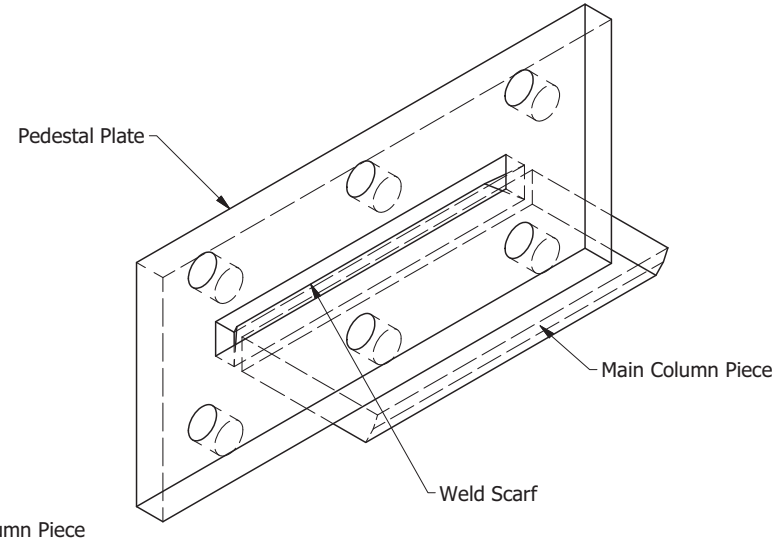

Notes:

(1) Pedestal plates are to be frabricated with snug fit clearance hole is to accomodate main column piece
(2) Ends of main column pieces are to be chamfered on all sides.
(3) To assemble, main column pieces are to fit through holes in pedestal plates. Combination of clearance hole and chamfer will form weld scarf.
(4) Using this weld scarf, main column pieces and pedestal plates are to be welded together with full penetration weld all around
(5) Once welded, surface of pedestal plates is to be finished to provide smooth surface for connecting the column assembly to the floor plates.

DRAWN Nick	5/4/2012	TITLE Column Fabrication Detail	
CHECKED			
QA			
MFG			
APPROVED			
		SIZE C	DWG NO CostEstimationDrawing REV
		SCALE	SHEET 4 OF 37

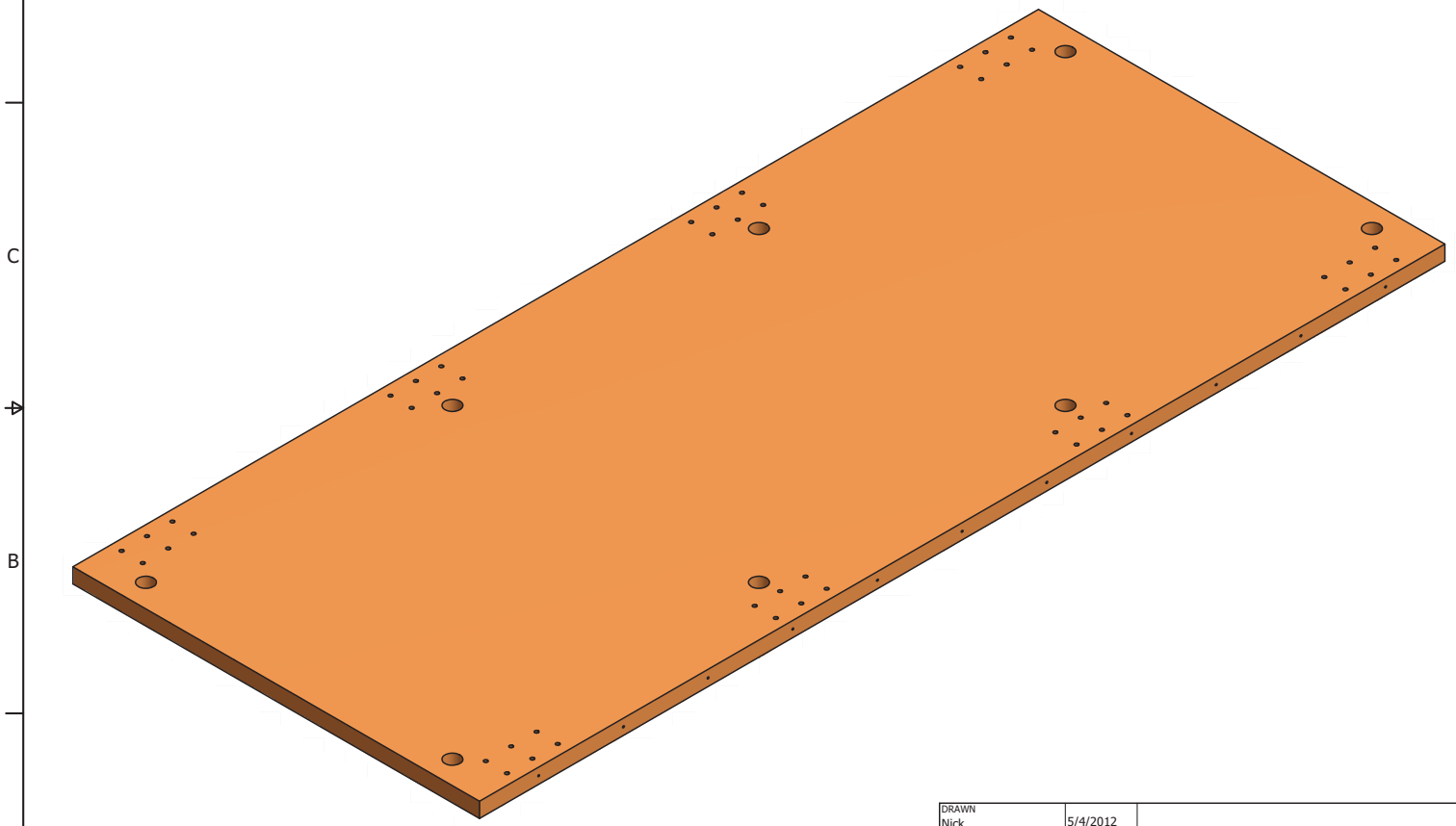

DRAWN	Nick	5/4/2012
CHECKED		
QA		
MFG		
APPROVED		

TITLE: Base Plate - Isometric View

SIZE: C | DWG NO: CostEstimationDrawing | REV:

SCALE: | SHEET 5 OF 37

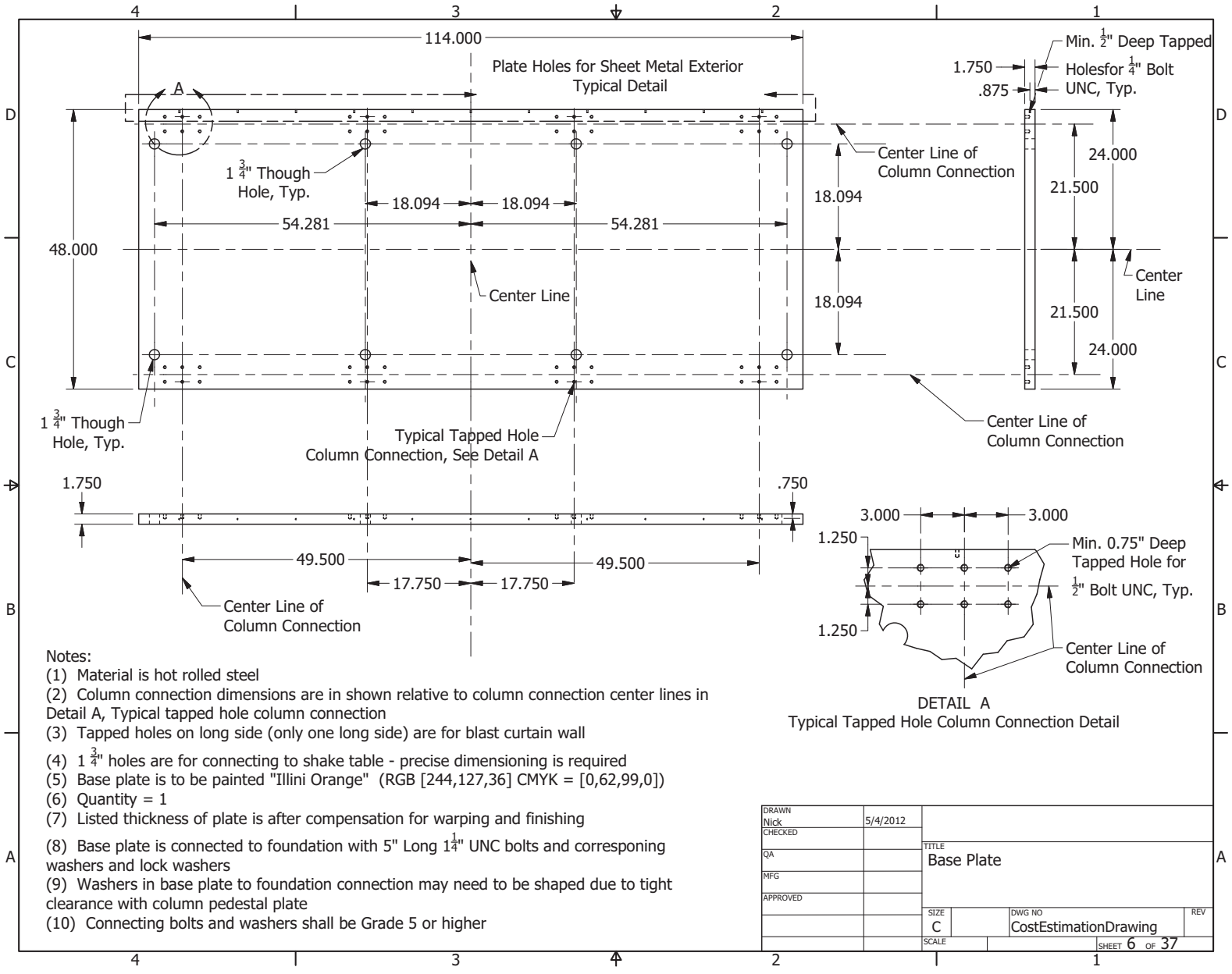

DETAIL A
Typical Tapped Hole Column Connection Detail

Notes:
(1) Material is hot rolled steel
(2) Column connection dimensions are in shown relative to column connection center lines in Detail A, Typical tapped hole column connection
(3) Tapped holes on long side (only one long side) are for blast curtain wall
(4) 1 3/4" holes are for connecting to shake table - precise dimensioning is required
(5) Base plate is to be painted "Illini Orange" (RGB [244,127,36] CMYK = [0,62,99,0])
(6) Quantity = 1
(7) Listed thickness of plate is after compensation for warping and finishing
(8) Base plate is connected to foundation with 5" Long 1 1/4" UNC bolts and corresponing washers and lock washers
(9) Washers in base plate to foundation connection may need to be shaped due to tight clearance with column pedestal plate
(10) Connecting bolts and washers shall be Grade 5 or higher

DRAWN Nick	5/4/2012	
CHECKED		TITLE Base Plate
QA		
MFG		
APPROVED		SIZE C / DWG NO CostEstimationDrawing / REV
		SCALE / SHEET 6 OF 37

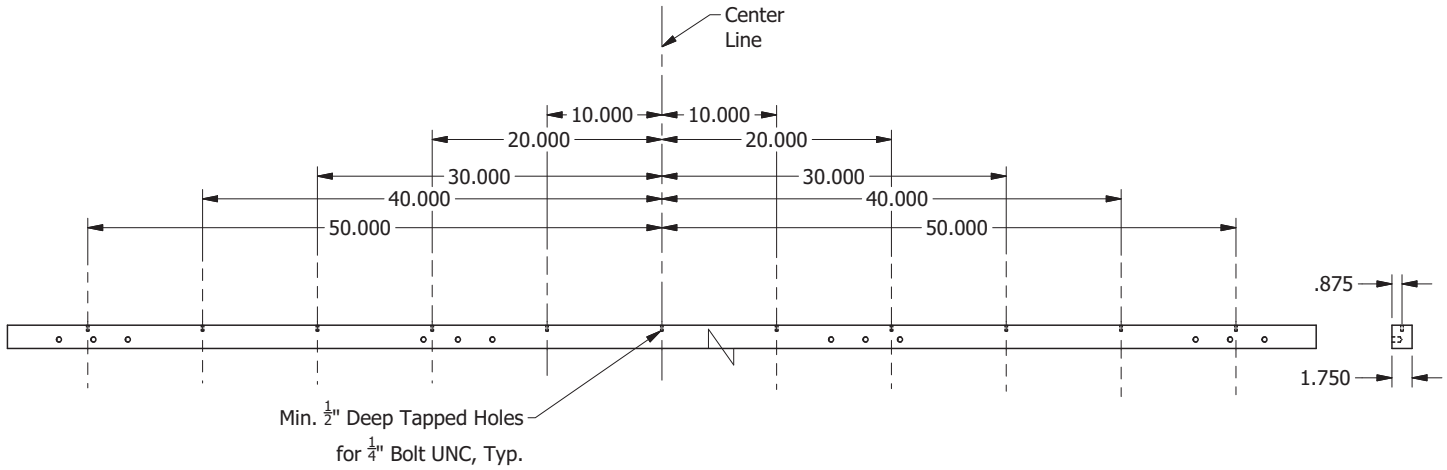

Plate Holes for Sheet Metal Exterior
Typical Detail

Notes:
(1) Holes only on one side of building, as denoted in drawings
(2) Typical detail of holes for sheet metal exterior for every floor

DRAWN Nick	5/4/2012	
CHECKED		TITLE
QA		
MFG		
APPROVED		
		SIZE C / DWG NO CostEstimationDrawing / REV
		SCALE / SHEET 7 OF 37

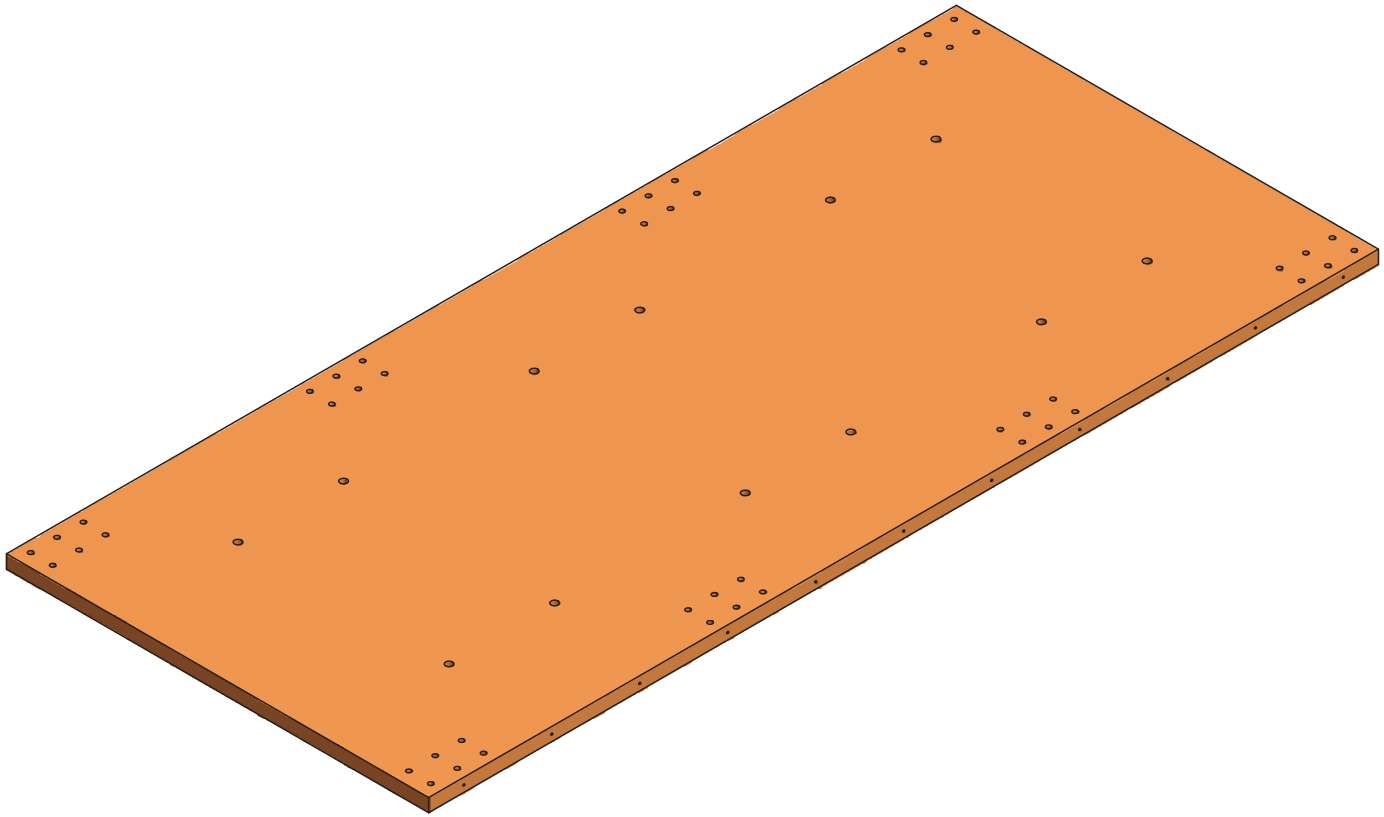

DRAWN	Nick	5/4/2012
CHECKED		
QA		
MFG		
APPROVED		

TITLE: Floor Plate - Isometric View

SIZE: C | DWG NO: CostEstimationDrawing | REV:

SCALE: | SHEET 8 OF 37

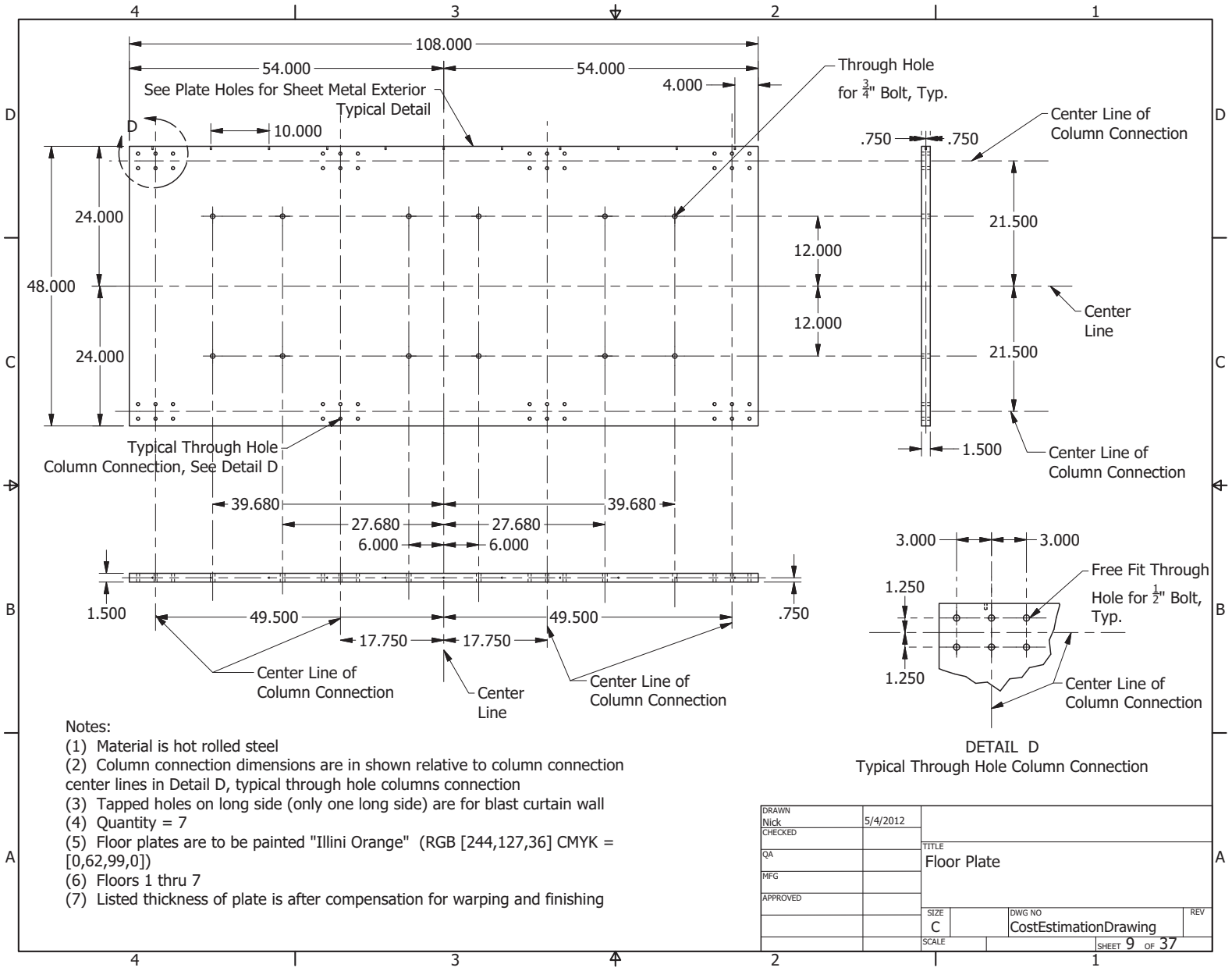

DETAIL D
Typical Through Hole Column Connection

Notes:
(1) Material is hot rolled steel
(2) Column connection dimensions are in shown relative to column connection center lines in Detail D, typical through hole columns connection
(3) Tapped holes on long side (only one long side) are for blast curtain wall
(4) Quantity = 7
(5) Floor plates are to be painted "Illini Orange" (RGB [244,127,36] CMYK = [0,62,99,0])
(6) Floors 1 thru 7
(7) Listed thickness of plate is after compensation for warping and finishing

DRAWN Nick	5/4/2012	
CHECKED		TITLE Floor Plate
QA		
MFG		
APPROVED		SIZE C / DWG NO CostEstimationDrawing / REV
		SCALE / SHEET 9 OF 37

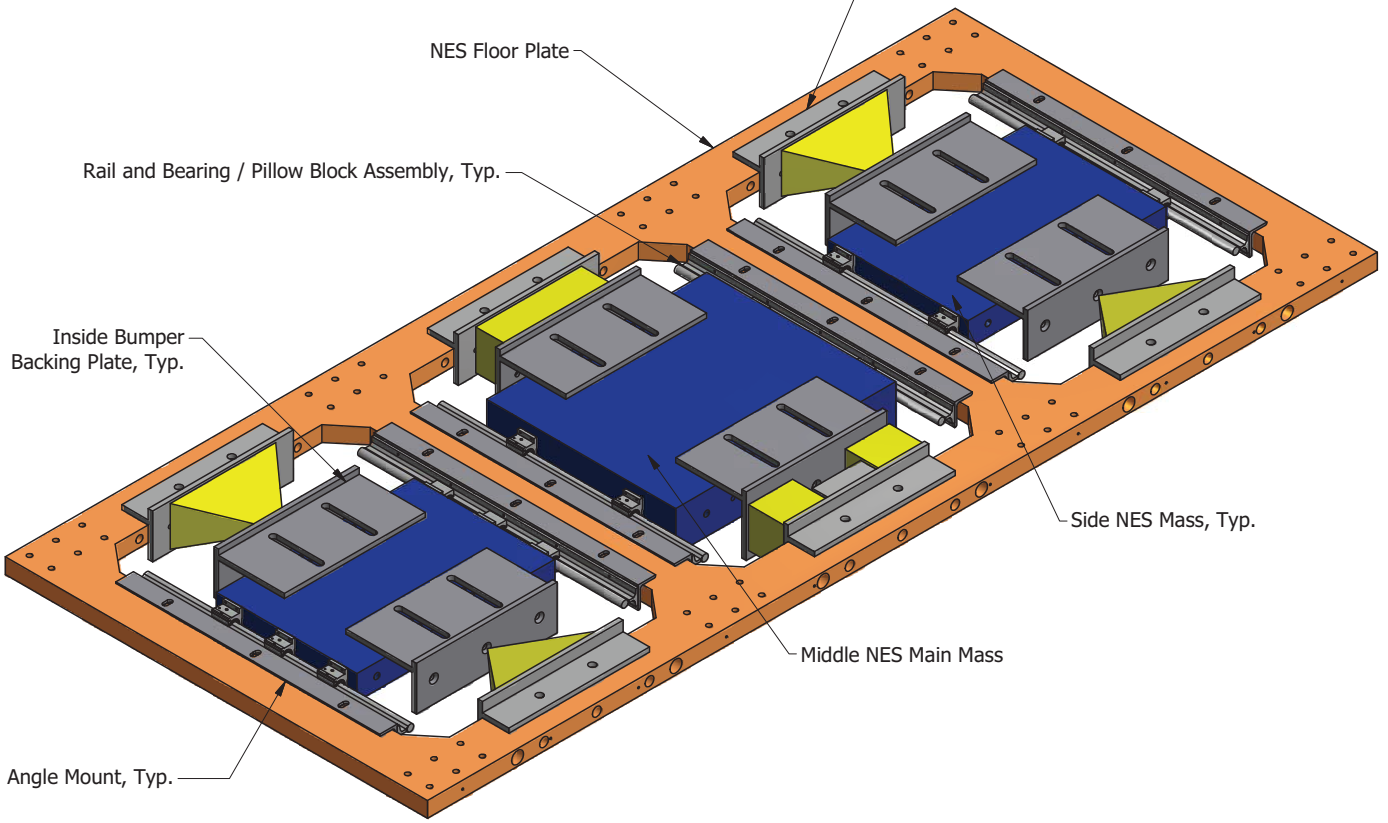

Notes:
(1) See additional drawings for component details
(2) Elastomeric bumpers provide by University of Illinois team

DRAWN Nick	5/4/2012	
CHECKED		TITLE: Overview of Complete NES Floor
QA		
MFG		
APPROVED		SIZE C | DWG NO CostEstimationDrawing | REV
		SCALE | SHEET 10 OF 37

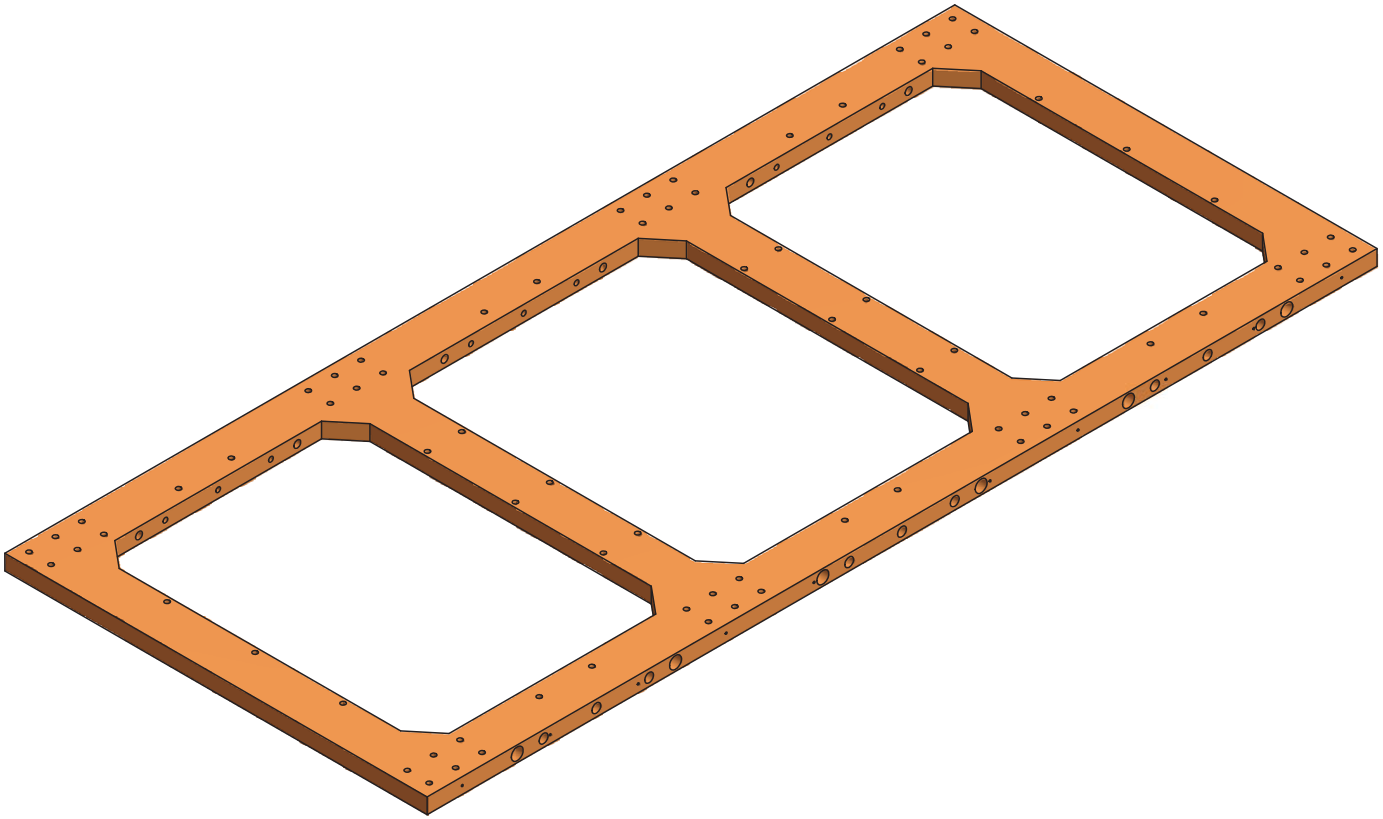

DRAWN Nick	5/4/2012	
CHECKED		TITLE NES Floor Plate - Isometric View
QA		
MFG		
APPROVED		SIZE C / DWG NO CostEstimationDrawing / REV
		SCALE / SHEET 11 OF 37

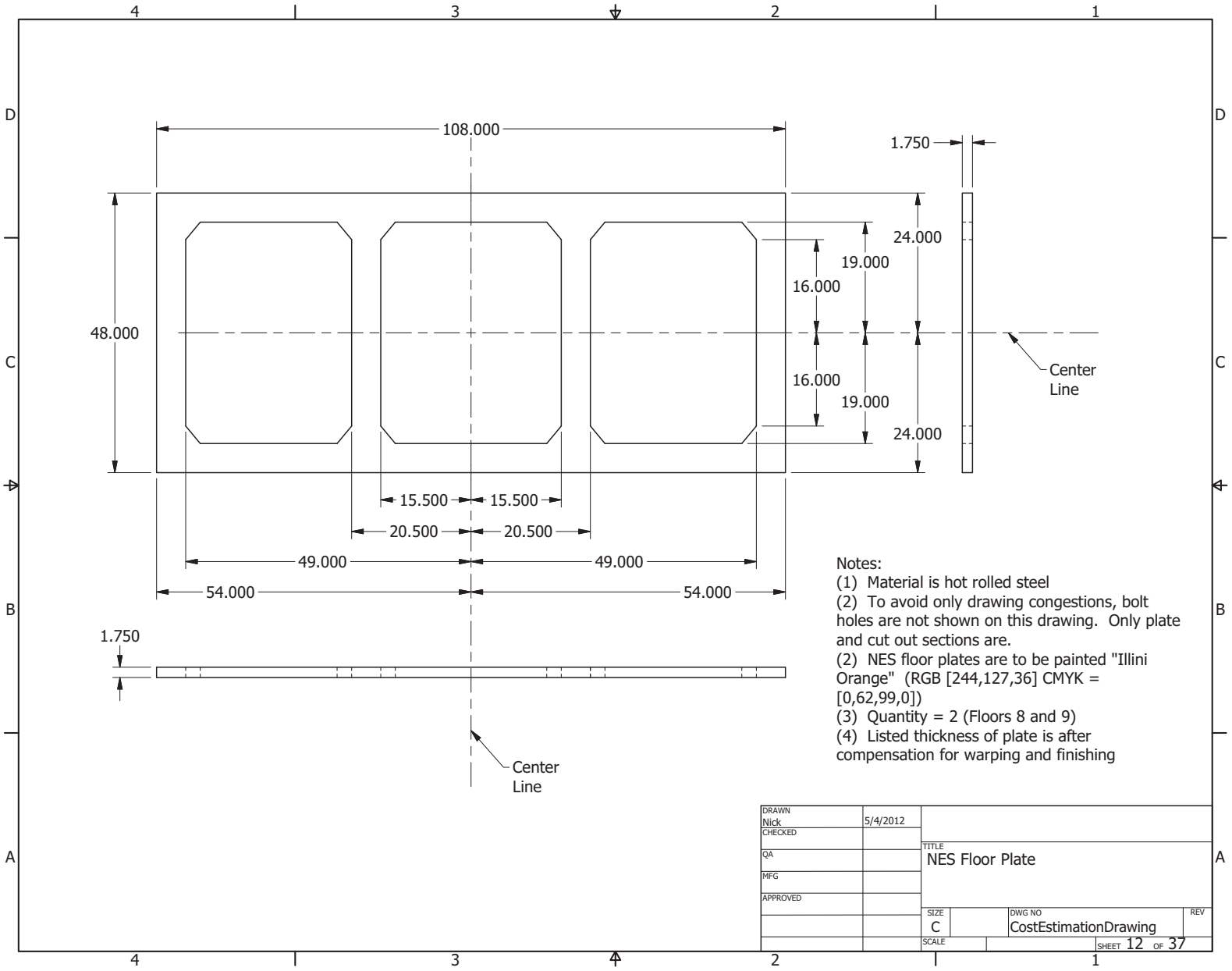
108.000
1.750
24.000
19.000
16.000
48.000
16.000
19.000
24.000
Center
Line
15.500
15.500
20.500
20.500
49.000
49.000
54.000
54.000
1.750
Center
Line
Notes:
(1) Material is hot rolled steel
(2) To avoid only drawing congestions, bolt holes are not shown on this drawing. Only plate and cut out sections are.
(2) NES floor plates are to be painted "Illini Orange" (RGB [244,127,36] CMYK = [0,62,99,0])
(3) Quantity = 2 (Floors 8 and 9)
(4) Listed thickness of plate is after compensation for warping and finishing
DRAWN
Nick
5/4/2012
CHECKED
QA
MFG
APPROVED
TITLE
NES Floor Plate
SIZE
C
DWG NO
CostEstimationDrawing
REV
SCALE
SHEET 12 OF 37

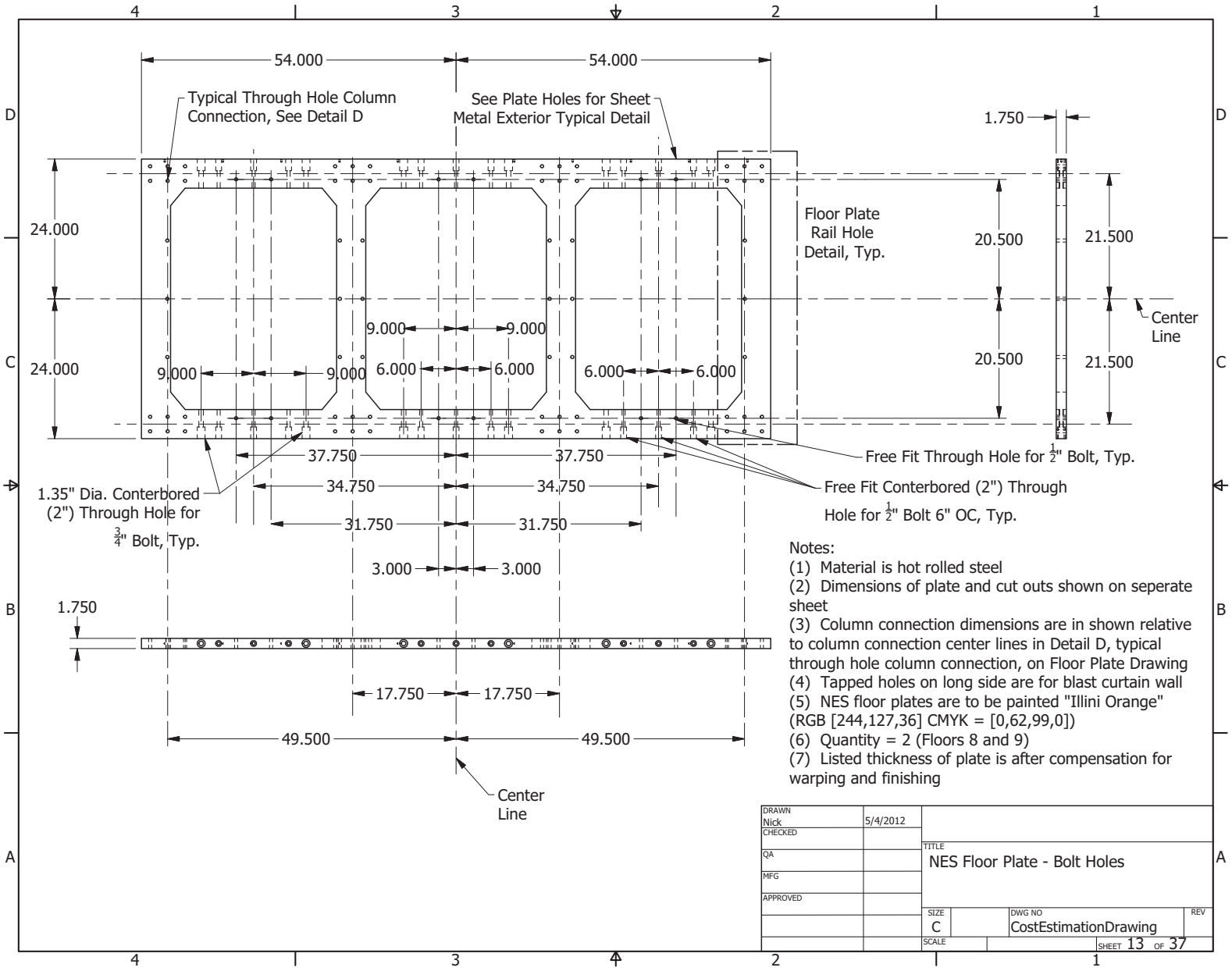

Notes:
(1) Material is hot rolled steel
(2) Dimensions of plate and cut outs shown on seperate sheet
(3) Column connection dimensions are in shown relative to column connection center lines in Detail D, typical through hole column connection, on Floor Plate Drawing
(4) Tapped holes on long side are for blast curtain wall
(5) NES floor plates are to be painted "Illini Orange" (RGB [244,127,36] CMYK = [0,62,99,0])
(6) Quantity = 2 (Floors 8 and 9)
(7) Listed thickness of plate is after compensation for warping and finishing

DRAWN Nick	5/4/2012	
CHECKED		TITLE: NES Floor Plate - Bolt Holes
QA		
MFG		
APPROVED		SIZE C | DWG NO CostEstimationDrawing | REV
		SCALE | SHEET 13 OF 37

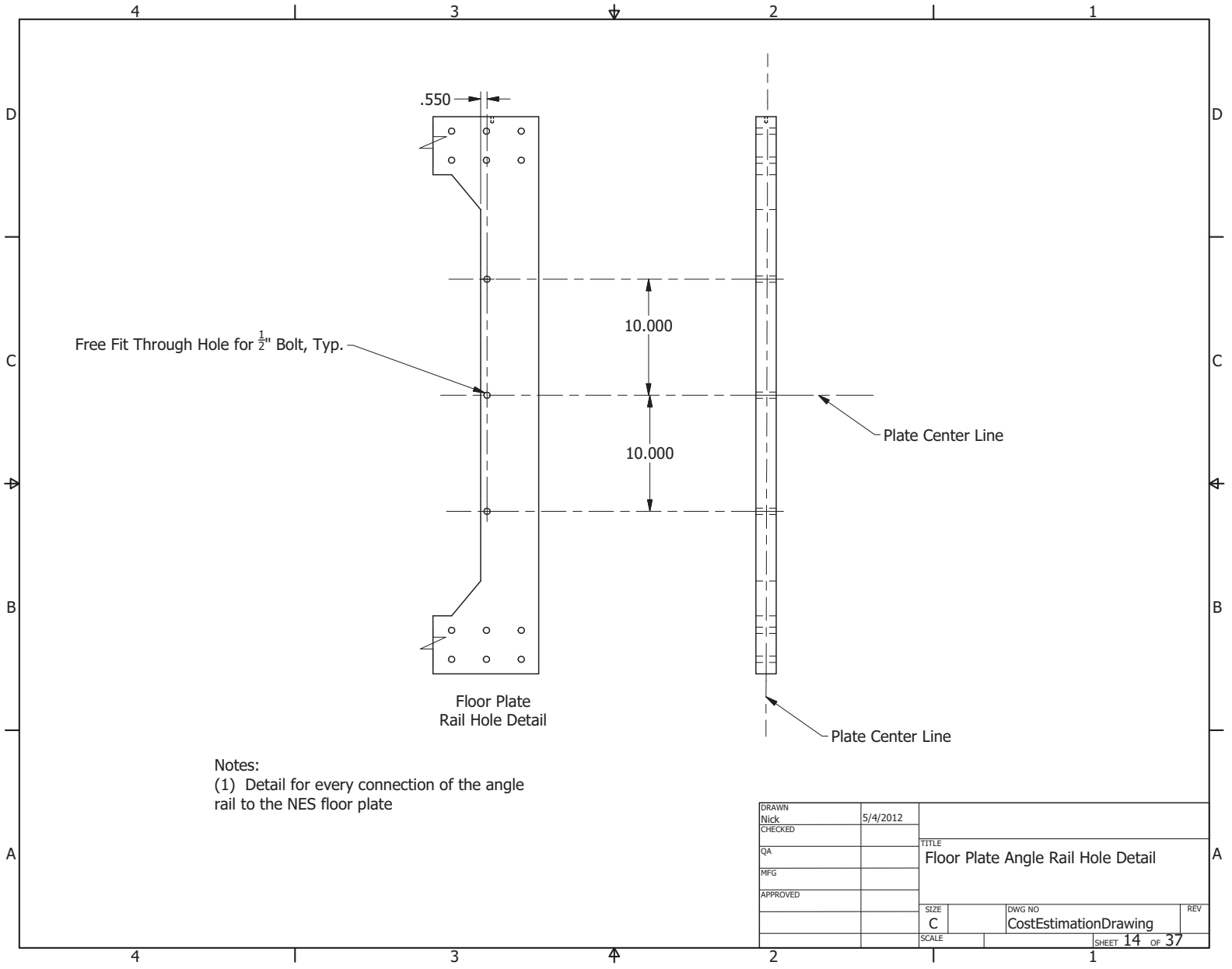
.550
Free Fit Through Hole for 1/2" Bolt, Typ.
10.000
10.000
Plate Center Line
Plate Center Line
Floor Plate
Rail Hole Detail
Notes:
(1) Detail for every connection of the angle rail to the NES floor plate
DRAWN
Nick
5/4/2012
CHECKED
QA
MFG
APPROVED
TITLE
Floor Plate Angle Rail Hole Detail
SIZE
C
DWG NO
CostEstimationDrawing
REV
SCALE
SHEET 14 OF 37

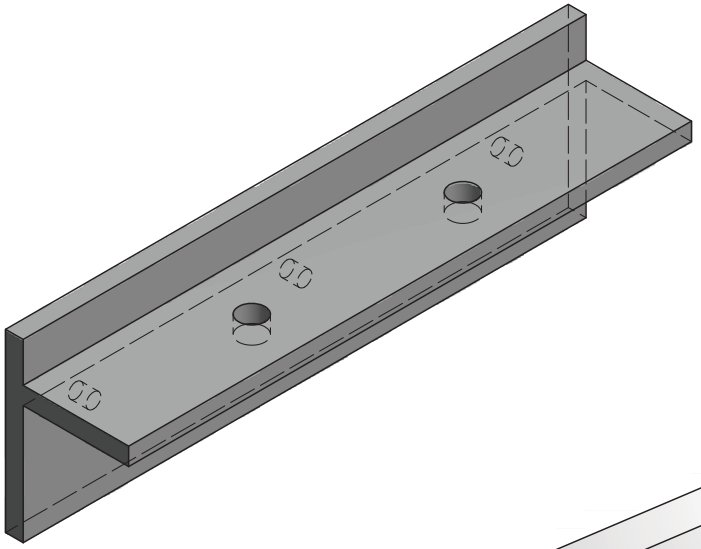

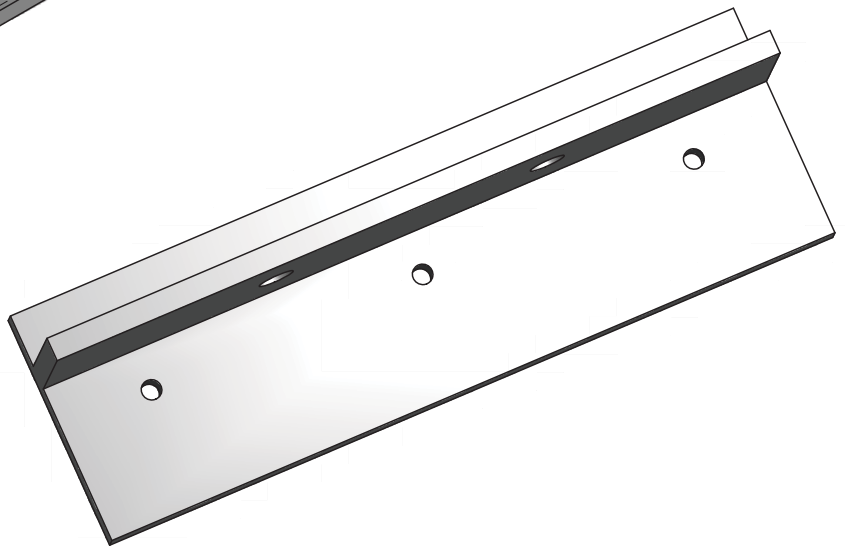

DRAWN Nick	5/4/2012	TITLE Bumper Backer Plate - Isometric View	
CHECKED			
QA			
MFG			
APPROVED			
		SIZE C	DWG NO CostEstimationDrawing REV
		SCALE	SHEET 15 OF 37

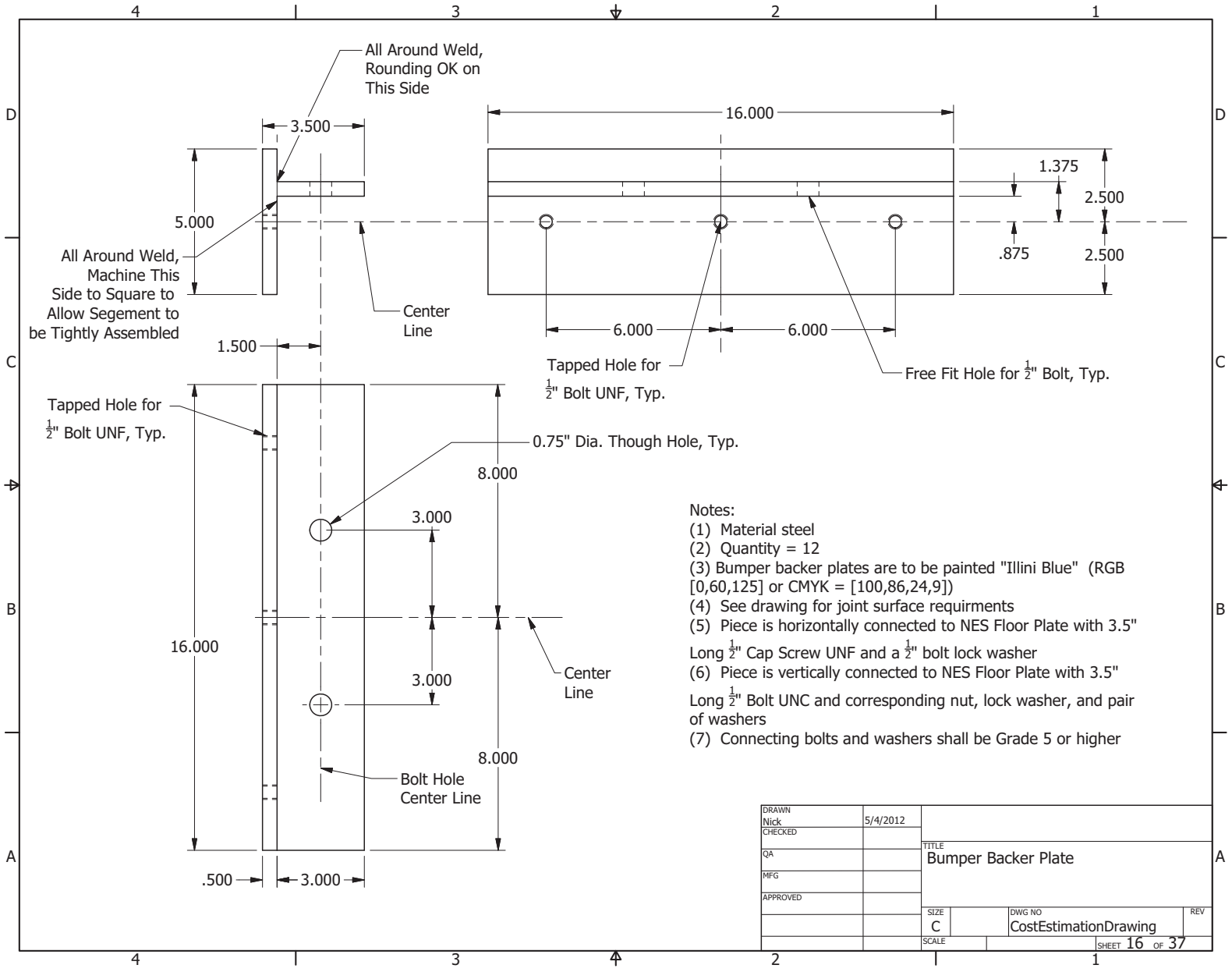

Notes:
(1) Material steel
(2) Quantity = 12
(3) Bumper backer plates are to be painted "Illini Blue" (RGB [0,60,125] or CMYK = [100,86,24,9])
(4) See drawing for joint surface requirments
(5) Piece is horizontally connected to NES Floor Plate with 3.5" Long ½" Cap Screw UNF and a ½" bolt lock washer
(6) Piece is vertically connected to NES Floor Plate with 3.5" Long ½" Bolt UNC and corresponding nut, lock washer, and pair of washers
(7) Connecting bolts and washers shall be Grade 5 or higher

DRAWN Nick	5/4/2012	TITLE: Bumper Backer Plate
CHECKED		
QA		
MFG		
APPROVED		
SIZE C	DWG NO CostEstimationDrawing	REV
SCALE	SHEET 16 OF 37	

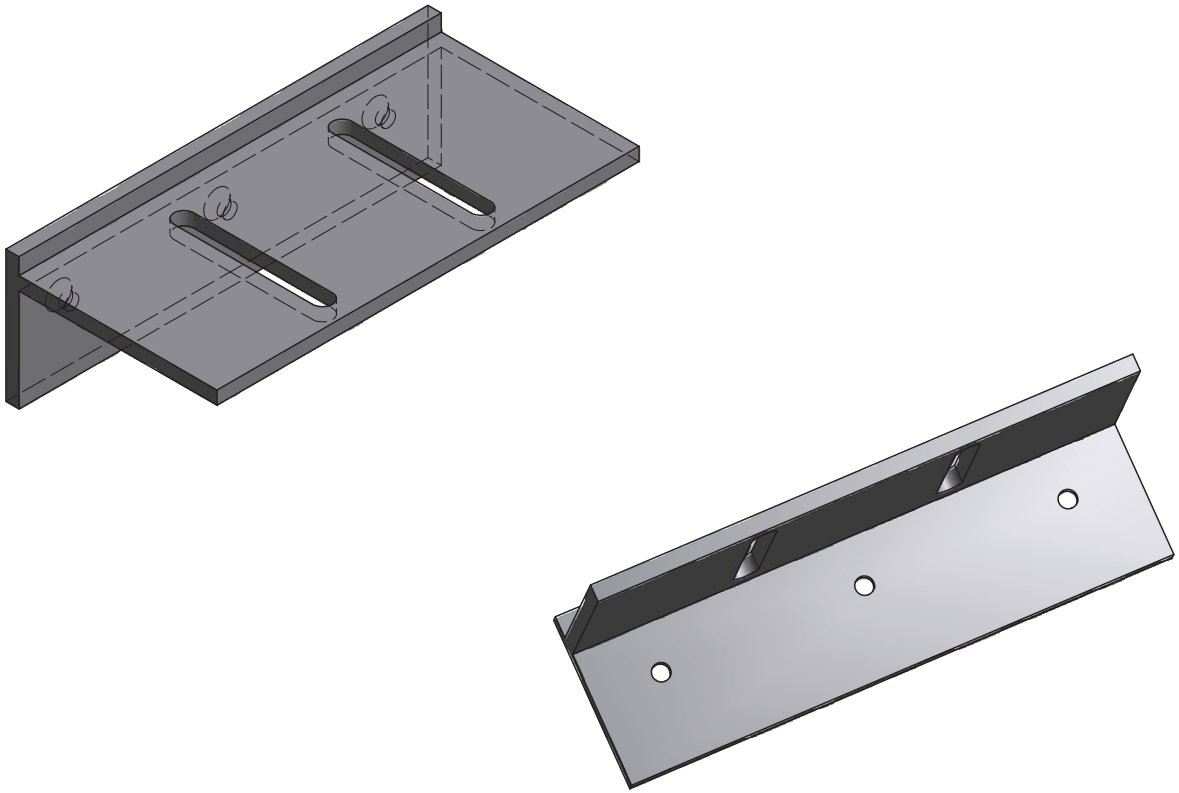

DRAWN Nick	5/4/2012	
CHECKED		TITLE: Inside Bumper Backer Plate - Isometric View
QA		
MFG		
APPROVED		
		SIZE C / DWG NO CostEstimationDrawing / REV
		SCALE / SHEET 17 OF 37

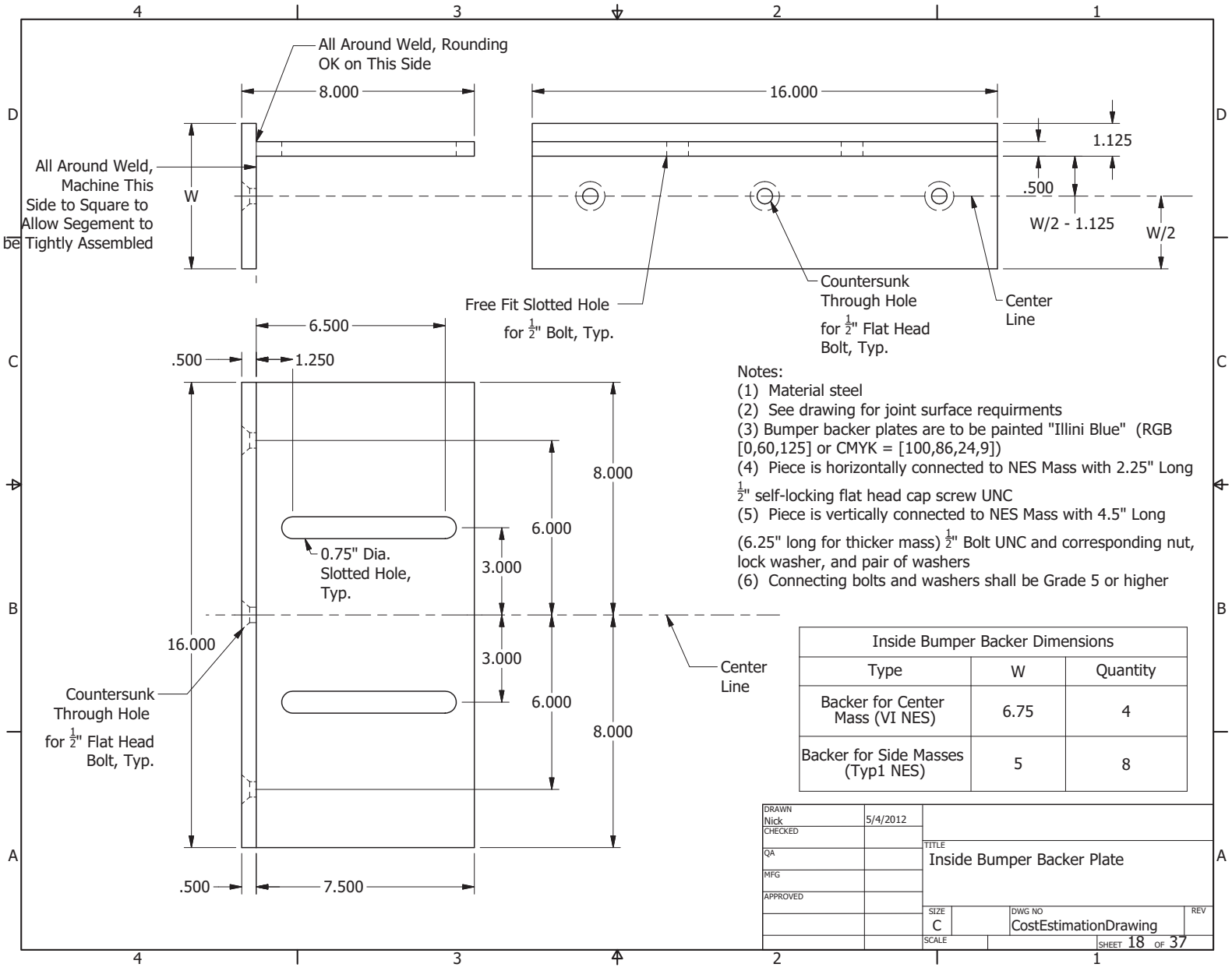

Notes:
(1) Material steel
(2) See drawing for joint surface requirments
(3) Bumper backer plates are to be painted "Illini Blue" (RGB [0,60,125] or CMYK = [100,86,24,9])
(4) Piece is horizontally connected to NES Mass with 2.25" Long $\frac{1}{2}$" self-locking flat head cap screw UNC
(5) Piece is vertically connected to NES Mass with 4.5" Long (6.25" long for thicker mass) $\frac{1}{2}$" Bolt UNC and corresponding nut, lock washer, and pair of washers
(6) Connecting bolts and washers shall be Grade 5 or higher

Inside Bumper Backer Dimensions		
Type	W	Quantity
Backer for Center Mass (VI NES)	6.75	4
Backer for Side Masses (Typ1 NES)	5	8

DRAWN Nick	5/4/2012	
CHECKED		TITLE: Inside Bumper Backer Plate
QA		
MFG		
APPROVED		SIZE C / DWG NO CostEstimationDrawing / REV
		SCALE / SHEET 18 OF 37

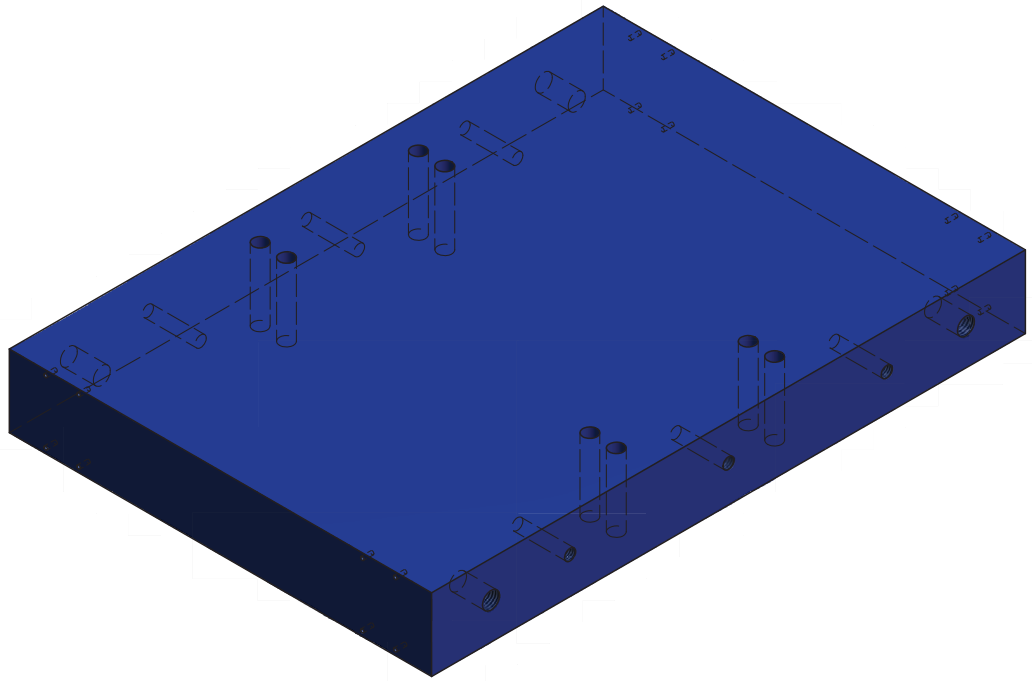

DRAWN Nick	5/4/2012		
CHECKED		TITLE NES Mass - Isometric View	
QA			
MFG			
APPROVED		SIZE C	DWG NO CostEstimationDrawing REV
		SCALE	SHEET 19 OF 37

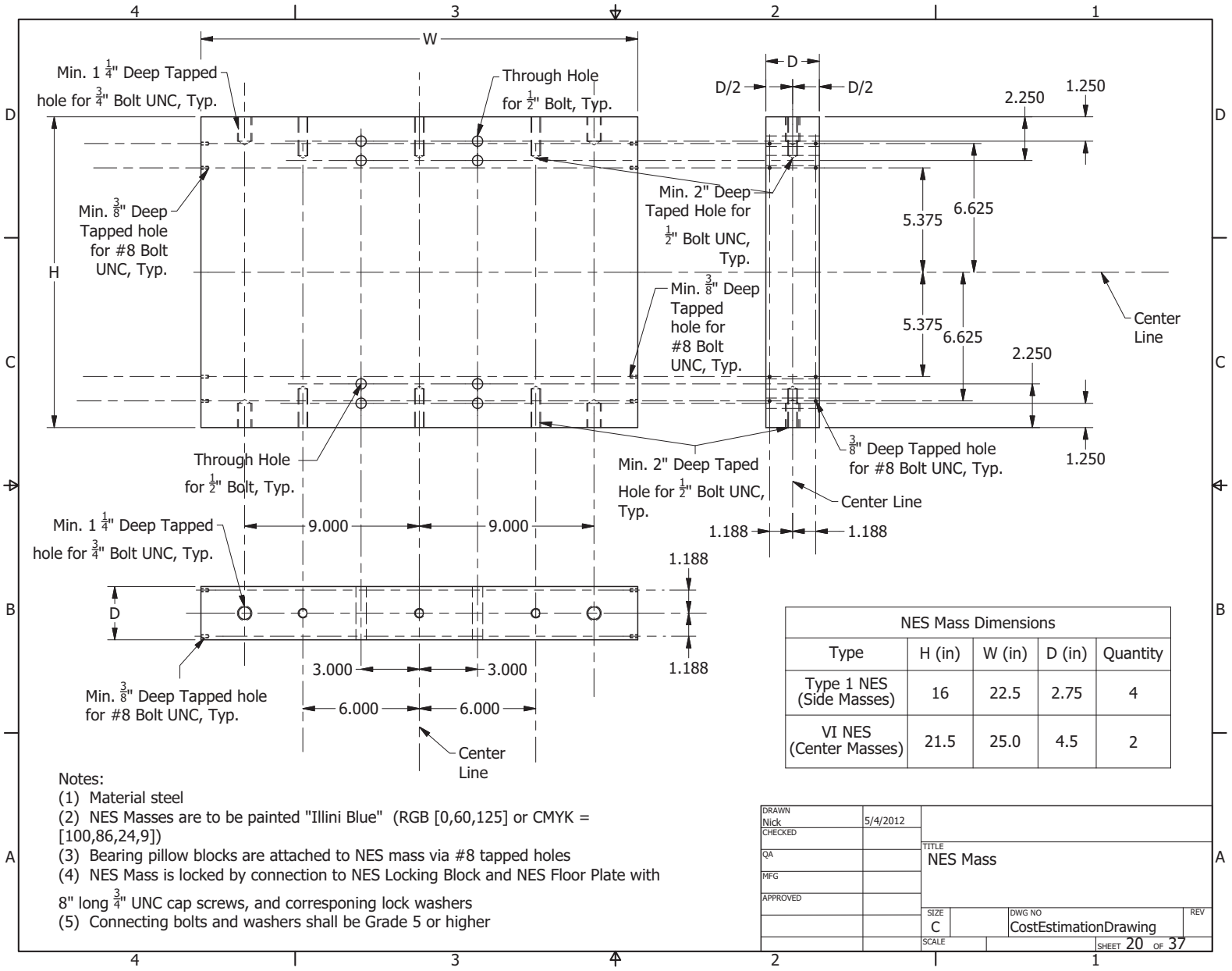

NES Mass Dimensions				
Type	H (in)	W (in)	D (in)	Quantity
Type 1 NES (Side Masses)	16	22.5	2.75	4
VI NES (Center Masses)	21.5	25.0	4.5	2

Notes:
(1) Material steel
(2) NES Masses are to be painted "Illini Blue" (RGB [0,60,125] or CMYK = [100,86,24,9])
(3) Bearing pillow blocks are attached to NES mass via #8 tapped holes
(4) NES Mass is locked by connection to NES Locking Block and NES Floor Plate with 8" long 3/4" UNC cap screws, and corresponing lock washers
(5) Connecting bolts and washers shall be Grade 5 or higher

DRAWN Nick	5/4/2012	TITLE: NES Mass
CHECKED		
QA		
MFG		
APPROVED		
SIZE C	DWG NO CostEstimationDrawing	REV
SCALE	SHEET 20 OF 37	

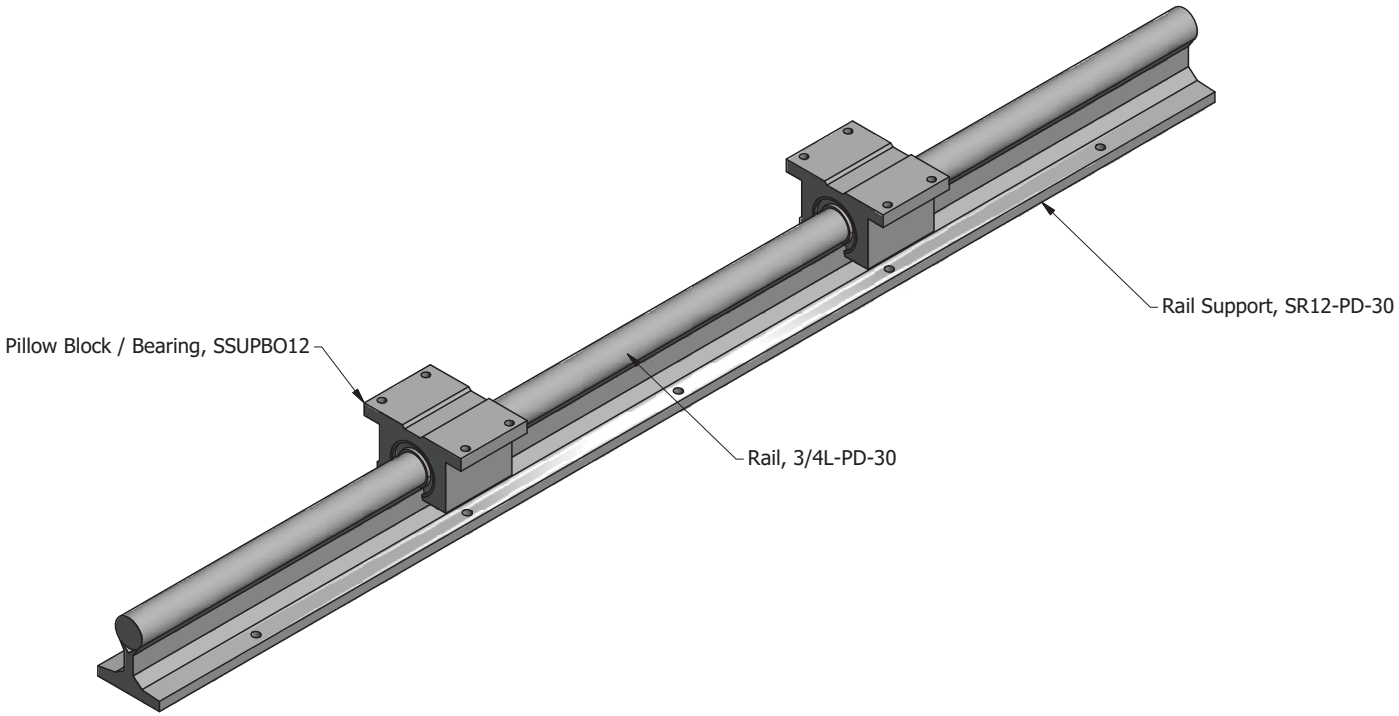

Notes:
(1) Rail, Rail Support, and Bearing/Pillow Block are stock parts from Thomson Bearing
(2) Rail is connected to NES floor plate and pillow blocks are connected to NES mass
(3) Bolt spacing on NES mass requires pillow blocks to be spaced at 12" OC
(4) Rail length = 30"
(5) Quantity 12
(6) Rail support is connected to angle piece with $\frac{3}{4}$" Long #10 UNC cap screws and corresponing lock washers
(7) Pillow block is connected to NES Mass with $\frac{5}{8}$" Long #8 UNC cap screws and corresponing lock washers
(8) Connecting bolts and washers shall be Grade 5 or higher

DRAWN Nick	5/4/2012	
CHECKED		TITLE: Rail and Bearing / Pillow Block Assembly
QA		
MFG		
APPROVED		
		SIZE C | DWG NO CostEstimationDrawing | REV
		SCALE | SHEET 21 OF 37

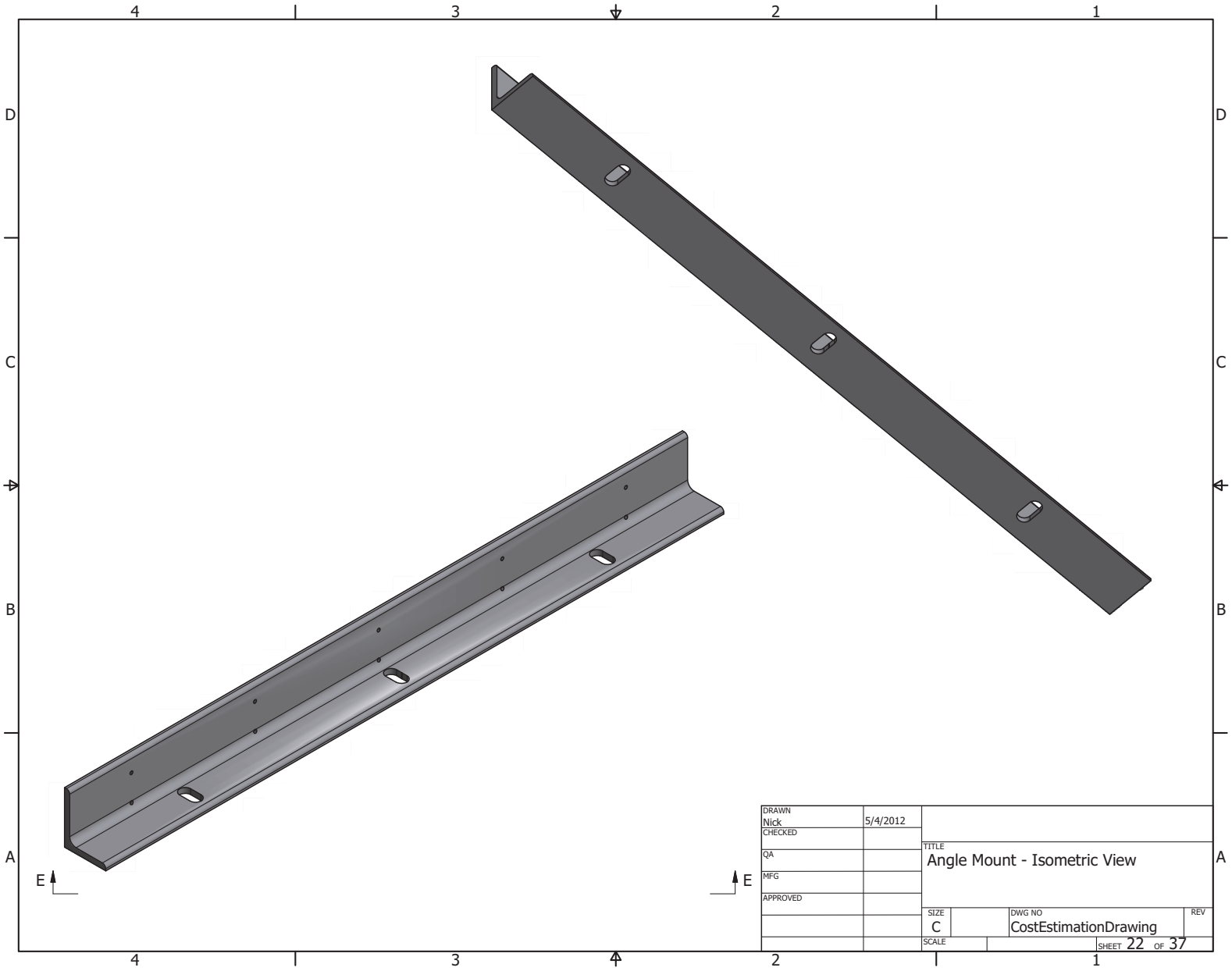
4
3
2
1
D
C
B
A
E
E
DRAWN
Nick
5/4/2012
CHECKED
QA
MFG
APPROVED
TITLE
Angle Mount - Isometric View
SIZE
C
DWG NO
CostEstimationDrawing
REV
SCALE
SHEET 22 OF 37

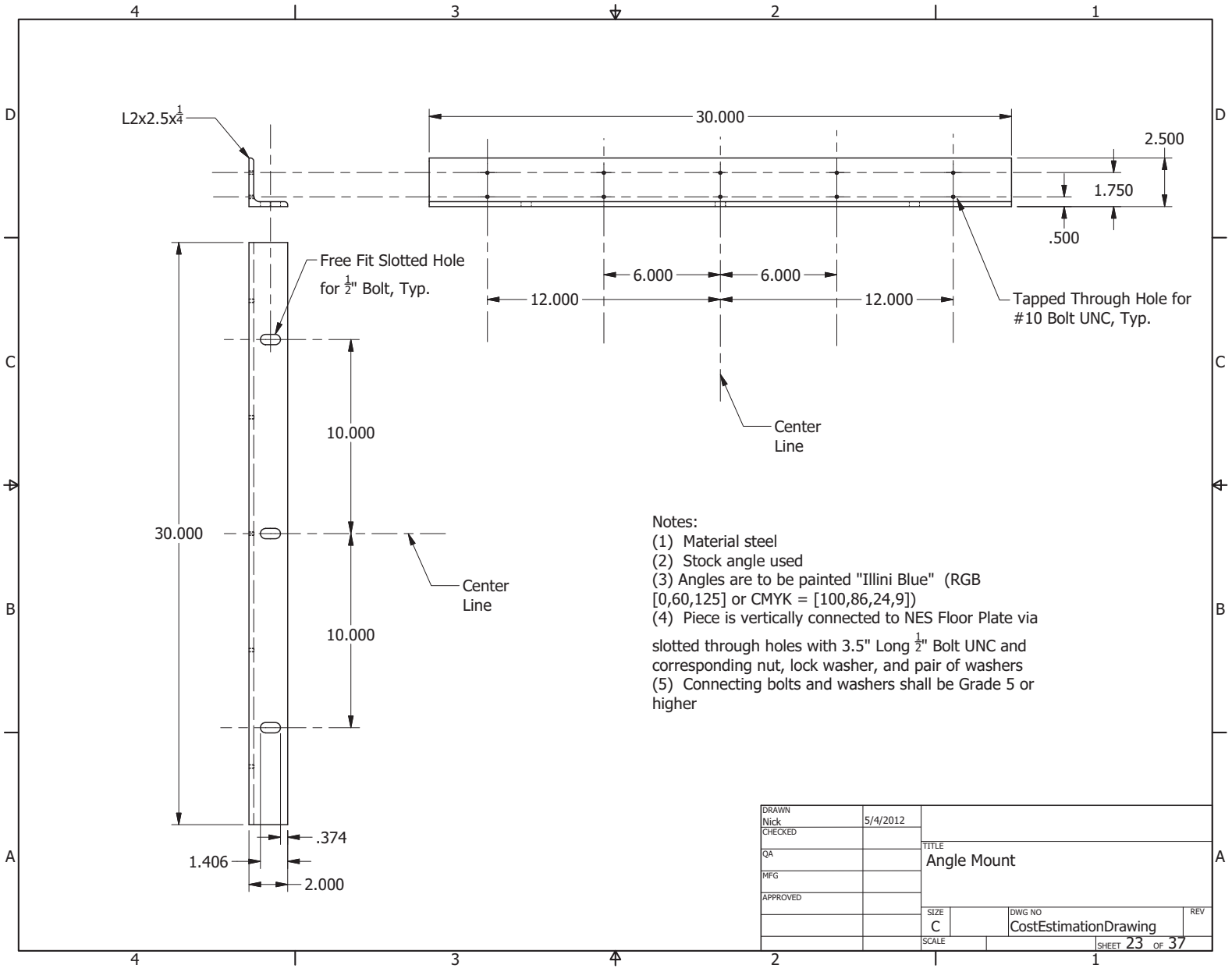
L2x2.5x1/4
30.000
2.500
1.750
.500
Free Fit Slotted Hole
for 1/2" Bolt, Typ.
6.000
6.000
12.000
12.000
Tapped Through Hole for
#10 Bolt UNC, Typ.
Center
Line
10.000
30.000
Center
Line
10.000
.374
1.406
2.000
Notes:
(1) Material steel
(2) Stock angle used
(3) Angles are to be painted "Illini Blue" (RGB [0,60,125] or CMYK = [100,86,24,9])
(4) Piece is vertically connected to NES Floor Plate via slotted through holes with 3.5" Long 1/2" Bolt UNC and corresponding nut, lock washer, and pair of washers
(5) Connecting bolts and washers shall be Grade 5 or higher
DRAWN
Nick
5/4/2012
CHECKED
QA
MFG
APPROVED
TITLE
Angle Mount
SIZE
C
DWG NO
CostEstimationDrawing
REV
SCALE
SHEET 23 OF 37

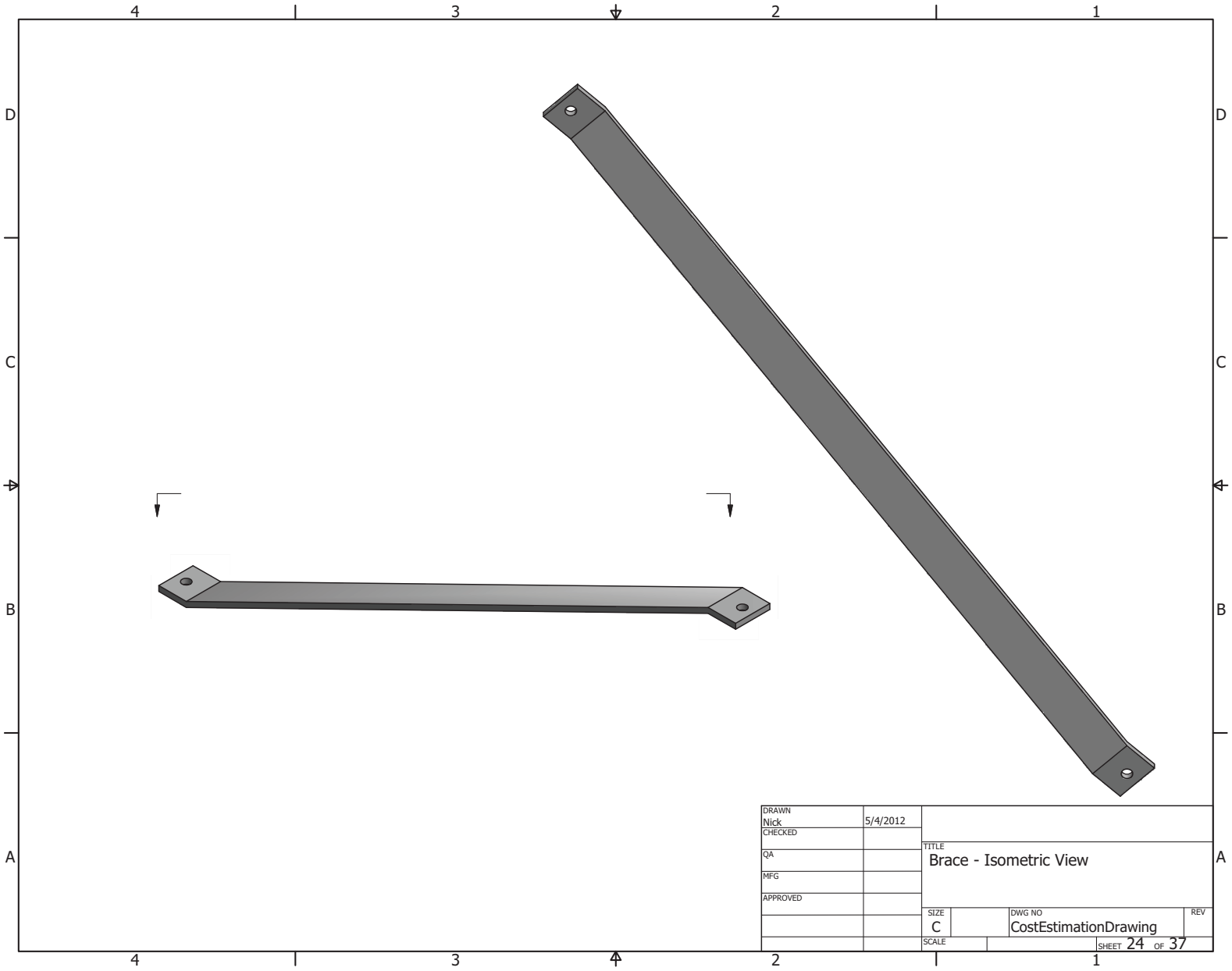
4
3
2
1
D
C
B
A
DRAWN
Nick
5/4/2012
CHECKED
QA
MFG
APPROVED
TITLE
Brace - Isometric View
SIZE
C
DWG NO
CostEstimationDrawing
REV
SCALE
SHEET 24 OF 37

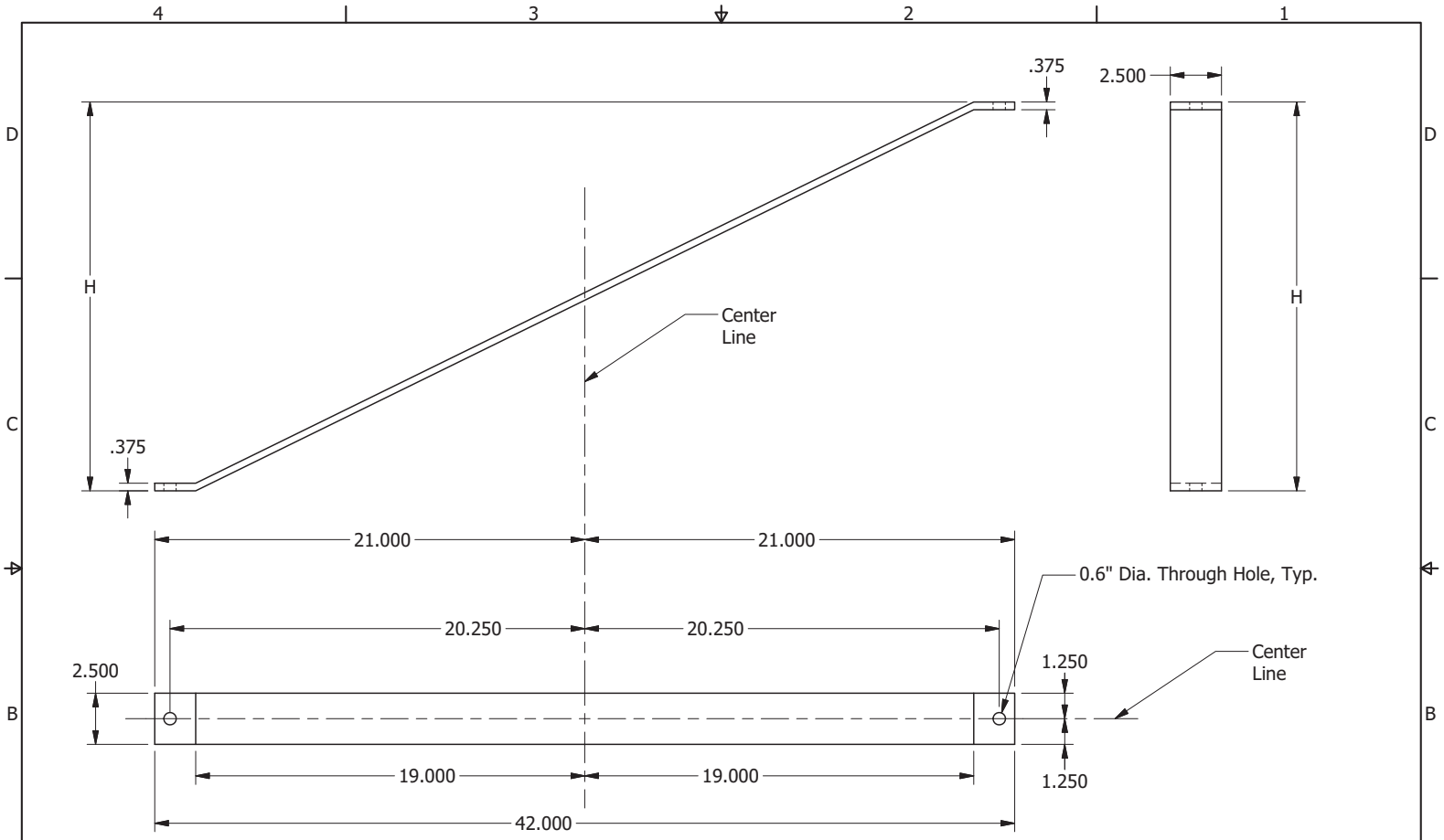

Notes:
(1) Material: Steel
(2) Braces Columns are to be painted "Illini Blue" (RGB [0,60,125] or CMYK = [100,86,24,9])
(3) Braces are to be fabricated by bending bar stock
(4) When connected to the structure, the braces run in the short direction of the building and are positioned on the exterior column lines. Braces use shared bolts and bolt holes also used by building columns to connect to the structure and rest between the column pedestal plates.

Brace Dimensions		
Stories	H (in)	Quantity
1	19	2
2-9	25	16

DRAWN Nick	5/4/2012	
CHECKED		TITLE
QA		
MFG		
APPROVED		
SIZE C	DWG NO CostEstimationDrawing	REV
SCALE	SHEET 25 OF 37	

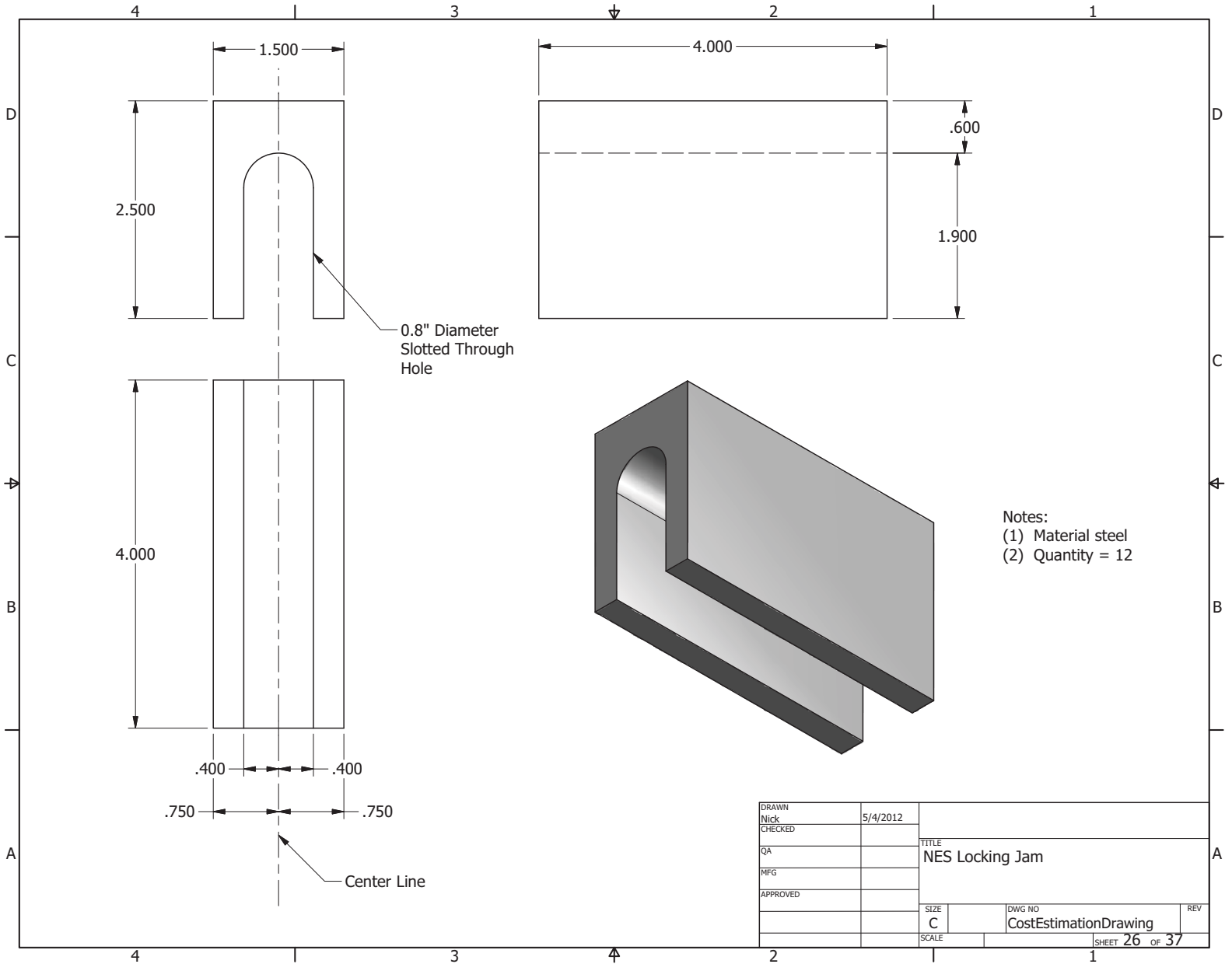
1.500
4.000
.600
2.500
1.900
0.8" Diameter
Slotted Through
Hole
4.000
.400
.400
.750
.750
Center Line
Notes:
(1) Material steel
(2) Quantity = 12
DRAWN
Nick
5/4/2012
CHECKED
QA
MFG
APPROVED
TITLE
NES Locking Jam
SIZE
C
DWG NO
CostEstimationDrawing
REV
SCALE
SHEET 26 OF 37

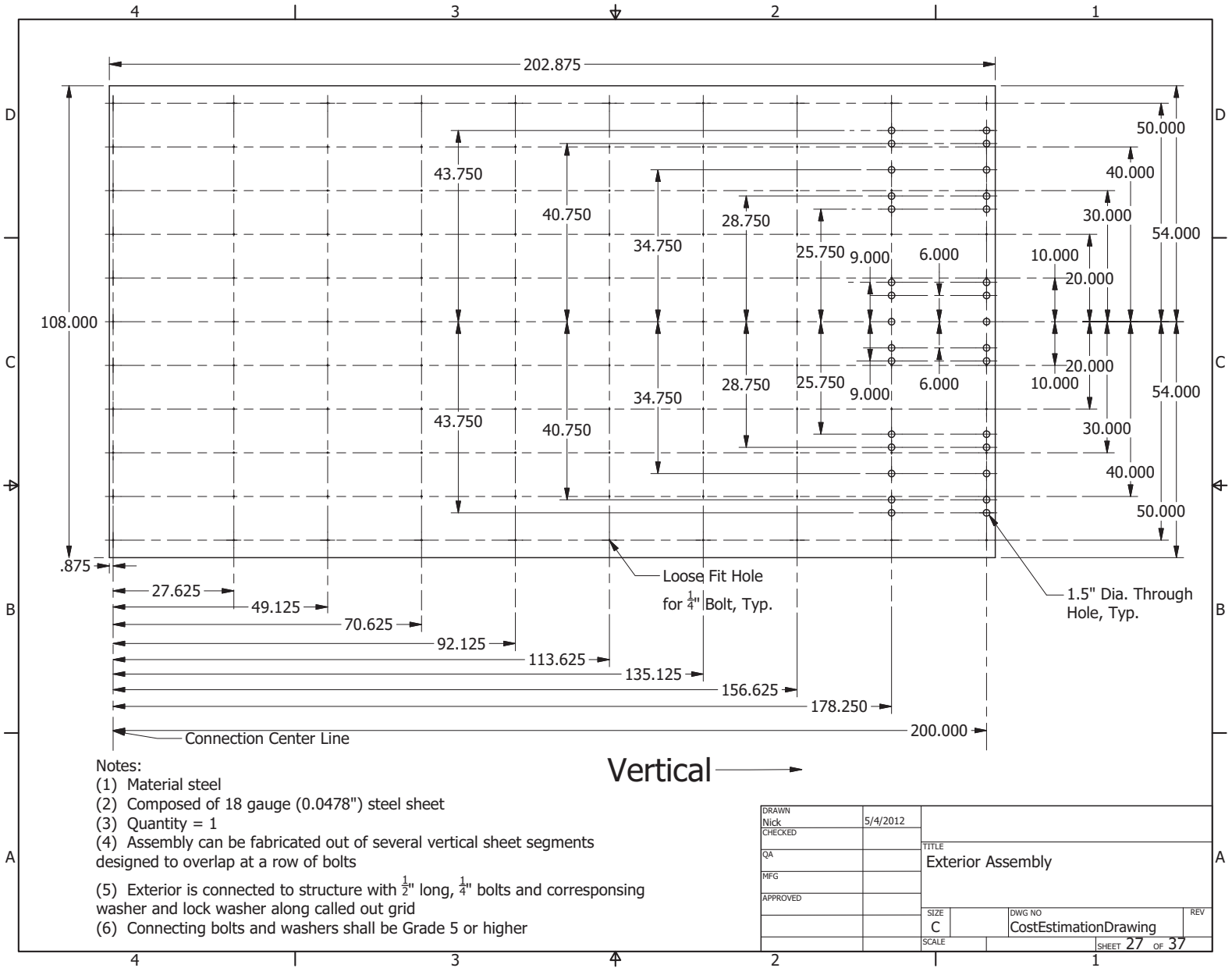

Notes:
(1) Material steel
(2) Composed of 18 gauge (0.0478") steel sheet
(3) Quantity = 1
(4) Assembly can be fabricated out of several vertical sheet segments designed to overlap at a row of bolts

(5) Exterior is connected to structure with $\frac{1}{2}$" long, $\frac{1}{4}$" bolts and corresponsing washer and lock washer along called out grid
(6) Connecting bolts and washers shall be Grade 5 or higher

DRAWN Nick	5/4/2012	
CHECKED		TITLE Exterior Assembly
QA		
MFG		
APPROVED		SIZE C | DWG NO CostEstimationDrawing | REV
		SCALE | SHEET 27 OF 37

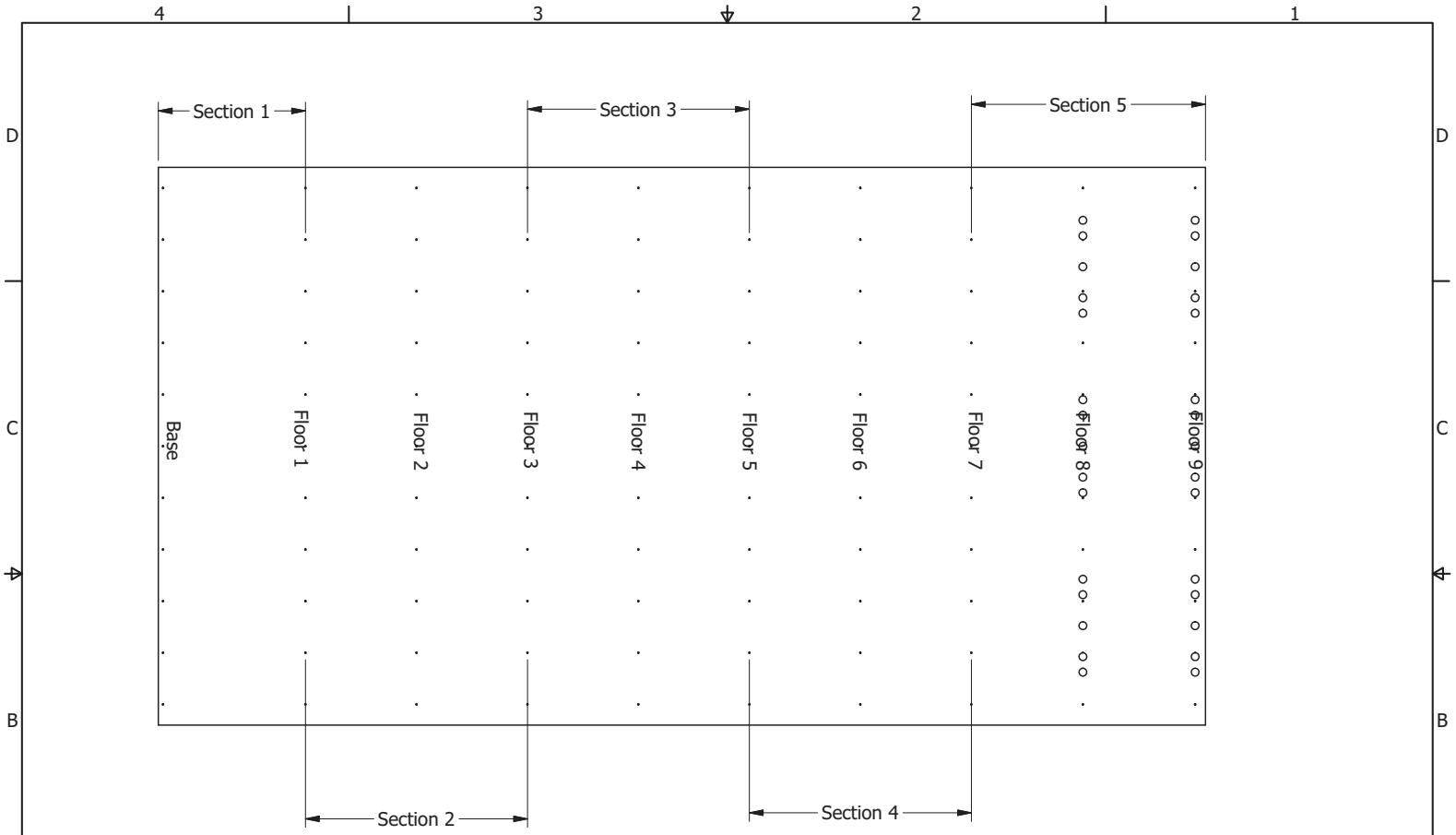

Notes:
(1) Proposed sections for exterior assembly shown above
(2) Sections overlap at the floor level
(3) Sections are limited to 48" maximum height

DRAWN Nick	5/4/2012	
CHECKED		TITLE Exterior Assembly - Sections
QA		
MFG		
APPROVED		SIZE C / DWG NO CostEstimationDrawing / REV
		SCALE / SHEET 28 OF 37

Parts List	
Part	Quantity
Column*	72
Base Plate	1
Floor Plate	7
NES Floor Plate	2
NES Mass*	6
Bumper Backer Plate	12
Inside Bumper Backer Plate*	12
Real, Bearings, and Pillow Blocks Assembly	12
Angle Mount	12
Brace*	18
NES Locking Jam	12
Exterior Assembly	1

* Parts vary, see specific sheet for details

Connecting bolts and washers shall be Grade 5 or higher

Nuts and Washer List	
Part	Quantity
1/4" - Washer	130
1/2" - Washer	1100
1 1/4" - Washer	20
#8 - Lock Washer	110
#10 - Lock Washer	140
1/4" - Lock Washer	130
1/2" - Lock Washer	850
3/4" - Lock Washer	16
1 1/4" - Washer	12
1/2" - Nut	550

Bolts List	
Part	Quantity
#8 - 5/8" Cap Screw	110
#10 - 3/4" Cap Screw	140
1/4" - 1/2"	130
1/2" - 3.5" UNF Cap Screw	25
1/2" - 3.5"	60
1/2" - 1.5"	60
1/2" - 4.5"	500
1/2" - 6.75"	12
1/2" - 2.25" Cap Screw	25
3/4" - 8" Cap Screw	16
1 1/4" - 5"	12

DRAWN Nick	5/4/2012	TITLE: Parts List
CHECKED		
QA		
MFG		
APPROVED		
SIZE C	DWG NO CostEstimationDrawing	REV
SCALE	SHEET 29 OF 37	

Assembly of NES Floors

Contact Information:

Nicholas E. Wierschem
Ph.D. Candidate
Department of Civil and Environmental Engineering
Newmark Civil Engineering Laboratory, MC-250
University of Illinois at Urbana-Champaign
205 North Mathews Ave.
Urbana, IL 61801
Ph: (520) 245-3837
Email: nwiersc2@illinois.edu

DRAWN Nick	5/4/2012		
CHECKED		TITLE Assembly of NES Floors - Title Page	
QA			
MFG			
APPROVED			
		SIZE C	DWG NO CostEstimationDrawing REV
		SCALE	SHEET 30 OF 37

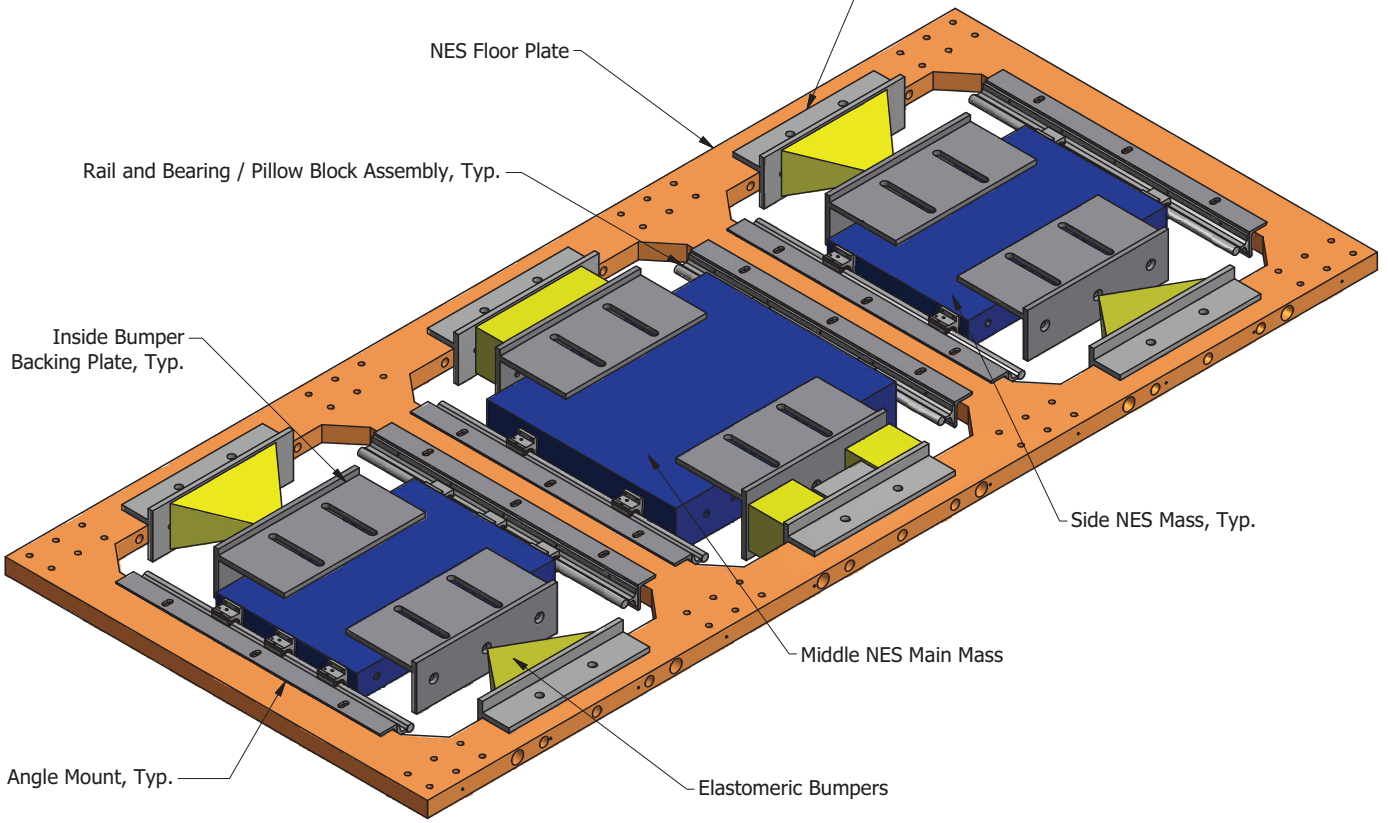

Notes:
(1) See additional drawings for component details
(2) Elastomeric bumpers (shown in yellow) provide by University of Illinois team after NES floor assembled
(3) Both NES floors are identical
(4) Bumper backer plates and rail angle mount are shown not painted so that the separate pieces can be more easily distinguished in these drawings. As indicated in the notes on the design drawings, these pieces are to be painted "Illini blue"

DRAWN Nick	5/4/2012	
CHECKED		TITLE: Overview of Complete NES Floor
QA		
MFG		
APPROVED		SIZE C | DWG NO CostEstimationDrawing | REV
		SCALE | SHEET 31 OF 37

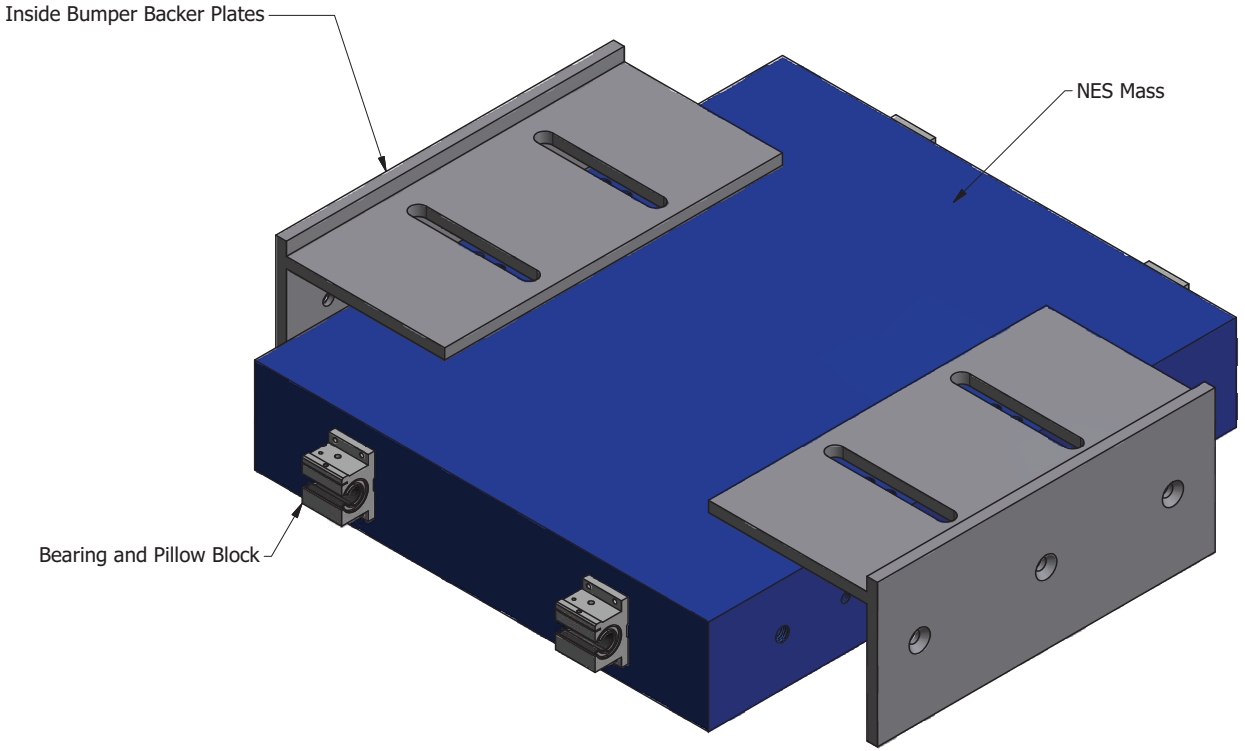

Assembly Instructions:
(1) Attach inside bumper backer plates to NES mass vertically via through bolt holes on the top of NES mass with 4.5" Long (6.25" long for thicker mass) 1/2" Bolt UNC and corresponding nut, lock washer, and pair of washers. These plates are designed with slotted holes so they can be positioned with a variable gap between the font plate and the NES mass; no precise gap is required during initial construction.
(2) Attach pillow blocks containing bearings to the sides of the NES mass with 5/8" Long #8 UNC socket cap screws and corresponding lock washers.

Notes:
(1) Similar assembly for each NES mass, the only difference is the bigger inside bumper backer plates are attached to the bigger NES masses.

DRAWN	Nick	5/4/2012
CHECKED		
QA		
MFG		
APPROVED		

TITLE: NES Floor Assembly Step 1
Install Inside Bumper Backer Plates and Bearing Pillow Blocks onto NES Mass

SIZE	DWG NO	REV
C	CostEstimationDrawing	

SCALE

SHEET 32 OF 37

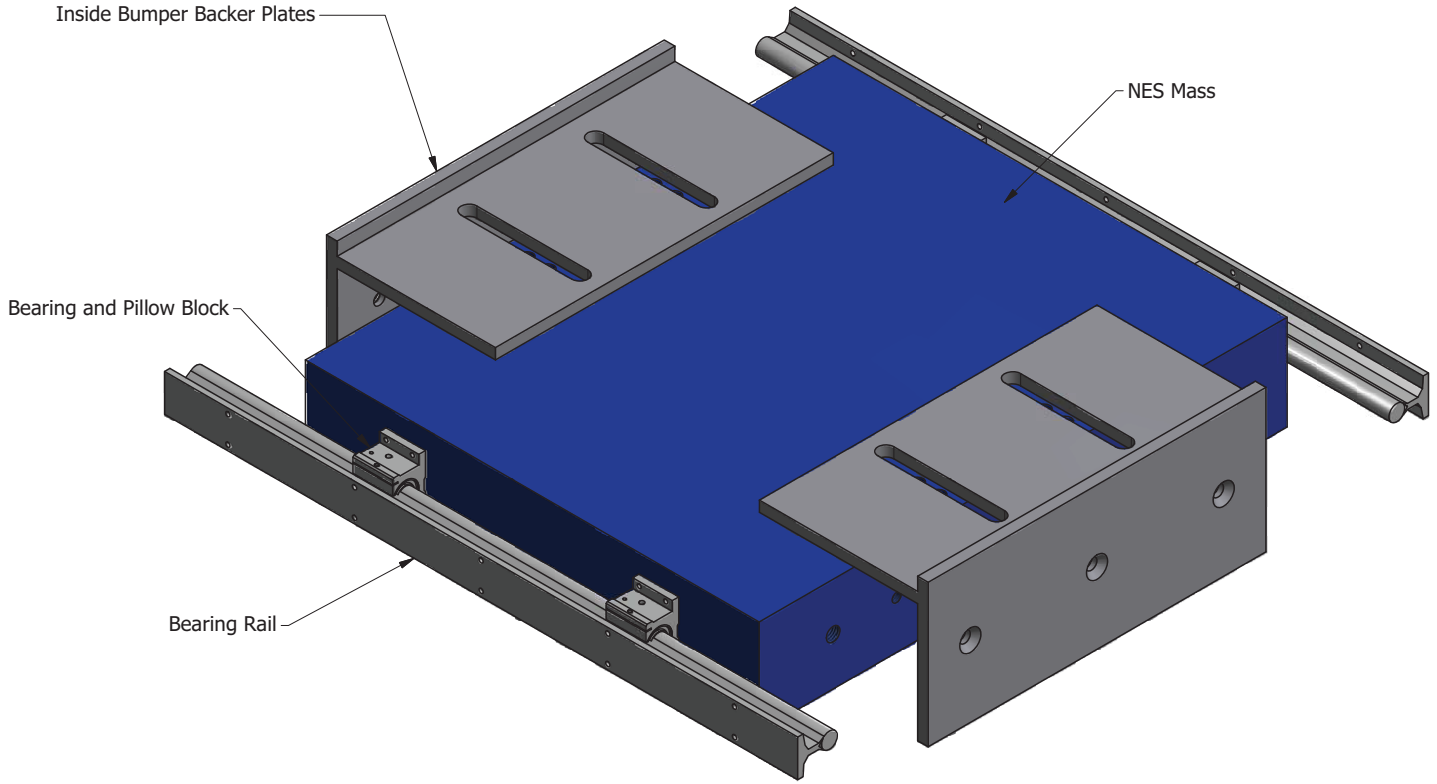

Assembly Instructions:
(1) Slide rail into bearings.

Notes:
(1) Be careful when sliding in rails as a misalignment may cause balls in the bearing to be removed

DRAWN Nick	5/4/2012	TITLE	NES Floor Assembly Step 2 Connect Rail and Bearings
CHECKED			
QA			
MFG			
APPROVED			
		SIZE C	DWG NO CostEstimationDrawing REV
		SCALE	SHEET 33 OF 37

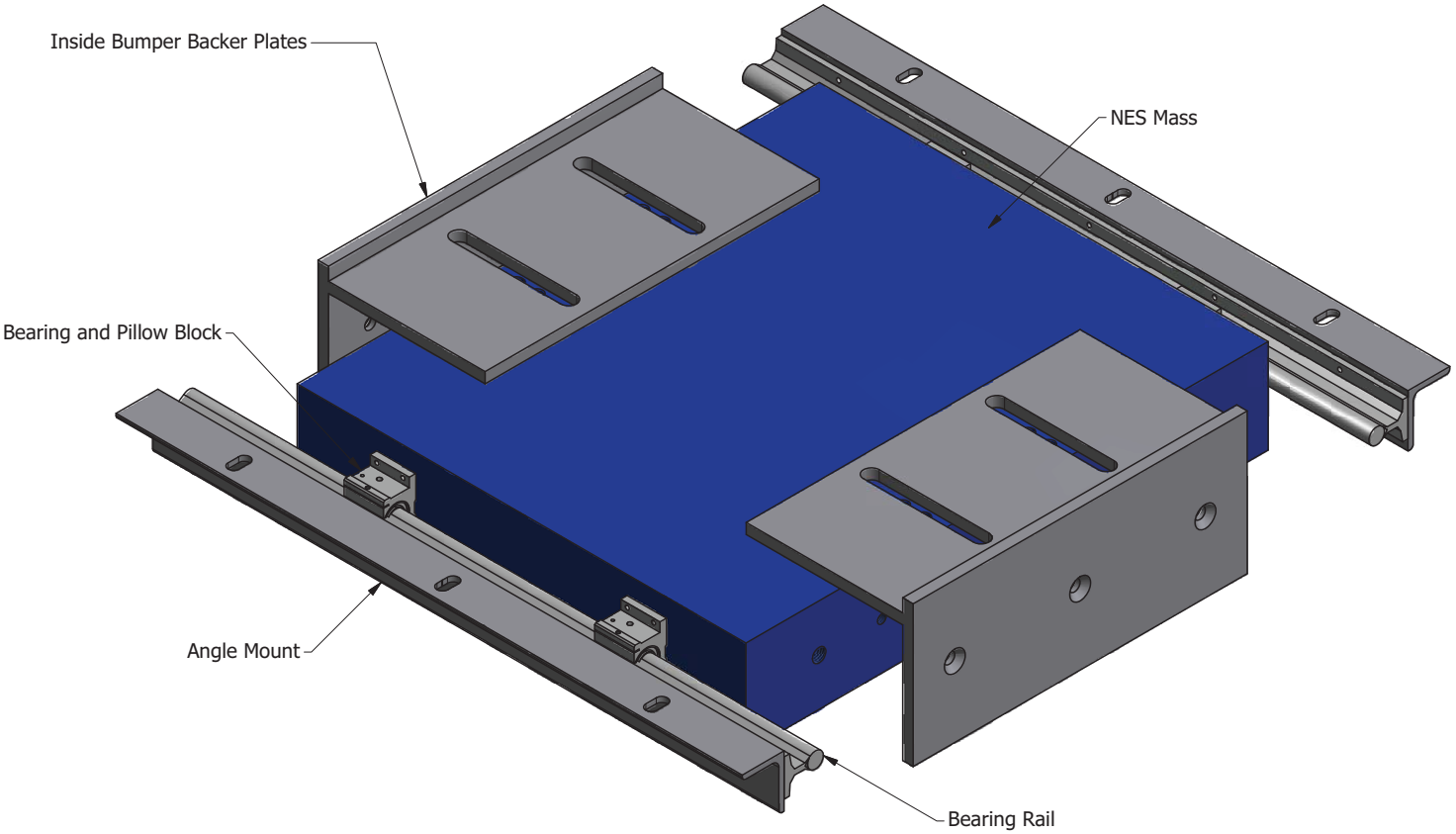

Assembly Instructions:
(1) Bolt rail to angle mount with 3/4" Long #10 UNC socket cap screws and corresponding lock washers. Bolts should be orientated such that socket cap is on the side of the connection with the rail.

DRAWN Nick	5/4/2012	
CHECKED		TITLE: NES Floor Assembly Step 3 Connect Angle Mounts to Rail
QA		
MFG		
APPROVED		
		SIZE C | DWG NO CostEstimationDrawing | REV
		SCALE | SHEET 34 OF 37

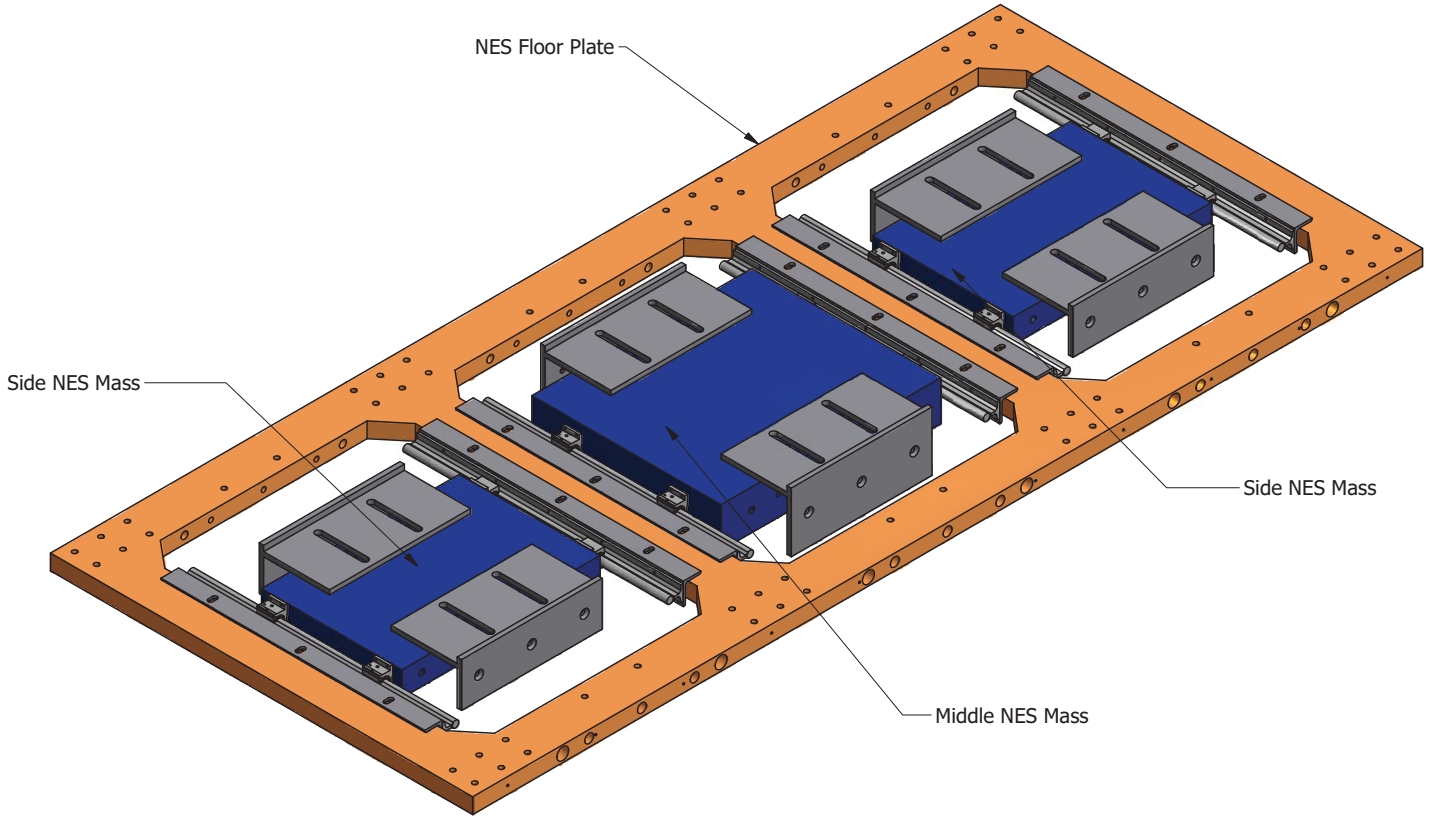

Assembly Instructions:
(1) Install NES masses into NES floor by using the slotted holes in the mounting angle to bolt it to the NES floor plate with 3.5" long $\frac{1}{2}$" bolt UNC and corresponding nut, lock washer, and pair of washers.

Notes:
(1) Place larger NES masses in the middle of the floor and smaller NES masses on the sides of the floor.
(2) Take care when installing NES mass into floor plate as the rails will slide off the bearings unless temporarily restrained during lift.
(3) Slotted holes in the angle mount allow for connection of NES masses to NES floor plate without compromising alignment of bearings.

DRAWN Nick	5/4/2012	
CHECKED		TITLE: NES Floor Assembly Step 4 Install NES Masses into NES Floor
QA		
MFG		
APPROVED		
		SIZE C | DWG NO CostEstimationDrawing | REV
		SCALE | SHEET 35 OF 37

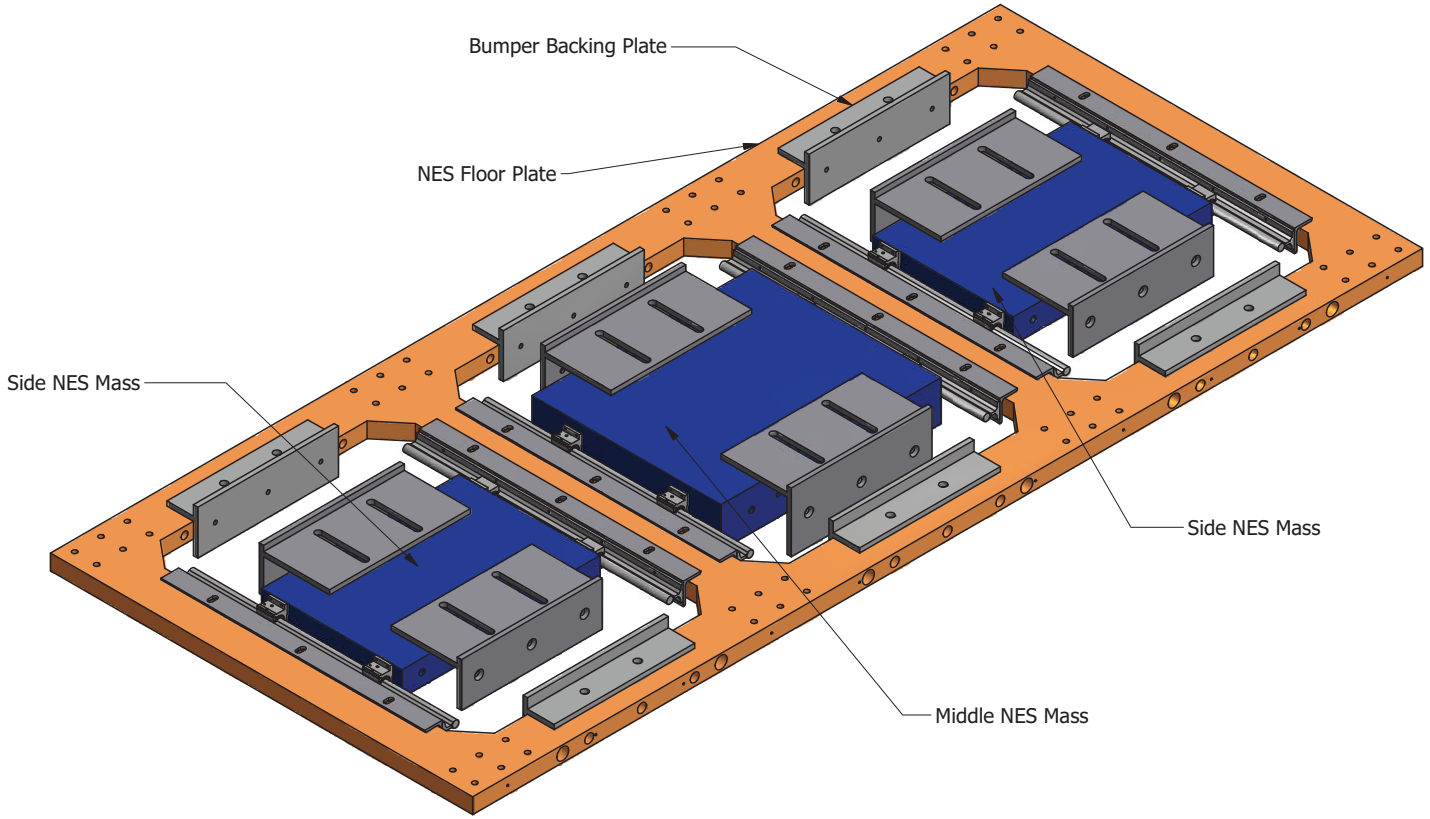

Assembly Instructions:
(1) Install bumper backer plates by horizontally bolting on to NES floor plate with 3.5" long 1/2" socket cap screw UNF and a 1/2" bolt lock washer
(2) Additionally, vertically connect bumper backer plates to NES floor plate with 3.5" long 1/2" bolt UNC and corresponding nut, lock washer, and pair of washers.

Notes:
(1) All 6 bumper backer plates attached to NES floor plate are identical

DRAWN Nick	5/4/2012	
CHECKED		TITLE: NES Floor Assembly Step 5 Install Bumper Backer Plates
QA		
MFG		
APPROVED		
		SIZE C | DWG NO CostEstimationDrawing | REV
		SCALE | SHEET 36 OF 37

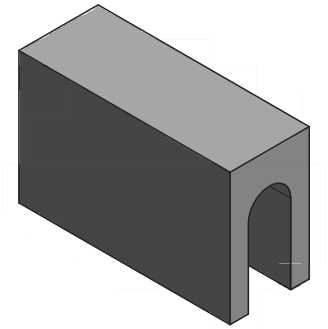

NES Locking Jam

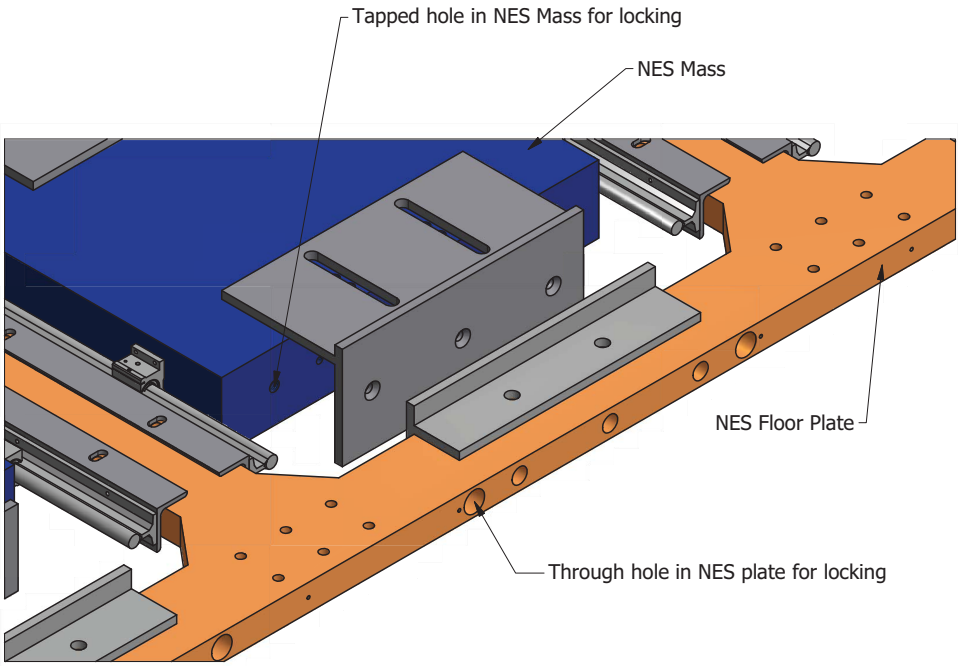

Assembly Instructions:
(1) To prevent NES movement, lock NES mass using NES locking jam. To do this loosely connecting a 8" long 3/4" UNC socket cap screws and corresponding lock washers (not shown in drawing) from the through hole on the NES floor plate called out in the drawing to the tapped hole in the NES mass called out on the drawing. Once bolt is loosely attached, place locking jam over bolt and tighten until locking jam has secured NES.

Notes:
(1) Connection detail the same for all NES masses.
(2) Bolt holes in NES mass and in NES floor plate are available to make locking connection at any of the 4 corners of the NES masses

DRAWN Nick	5/4/2012	TITLE: NES Floor Assembly Step 6 Lock NES Masses
CHECKED		
QA		
MFG		
APPROVED		
SIZE C	DWG NO CostEstimationDrawing	REV
SCALE	SHEET 37 OF 37	

APPENDIX B: ADDITIONAL EXPERIMENTAL RESPONSES OF THE SMALL-SCALE TYPE I NES AND BASE STRUCTURE

In this appendix, additional plots of the experimental response of the small-scale test structure and Type I NES are presented. The experimental setup and Type I NES utilized in these experiments were introduced in Chapter 5. The shake-table-produced ground motions used for the experiments presented in this section are scaled versions of the impulse-like ground motion considered in the experiments presented in Chapter 5. The response of the system with the NES unlocked and locked is shown for fourteen different scaling levels of this ground motion (denoted by load level 1 through load level 14). The responses of the system plotted in this appendix include the shake-table-produced ground acceleration, second floor acceleration, second floor acceleration wavelet spectrum, estimated second floor displacement, modal accelerations, NES acceleration, and NES acceleration wavelet spectrum.

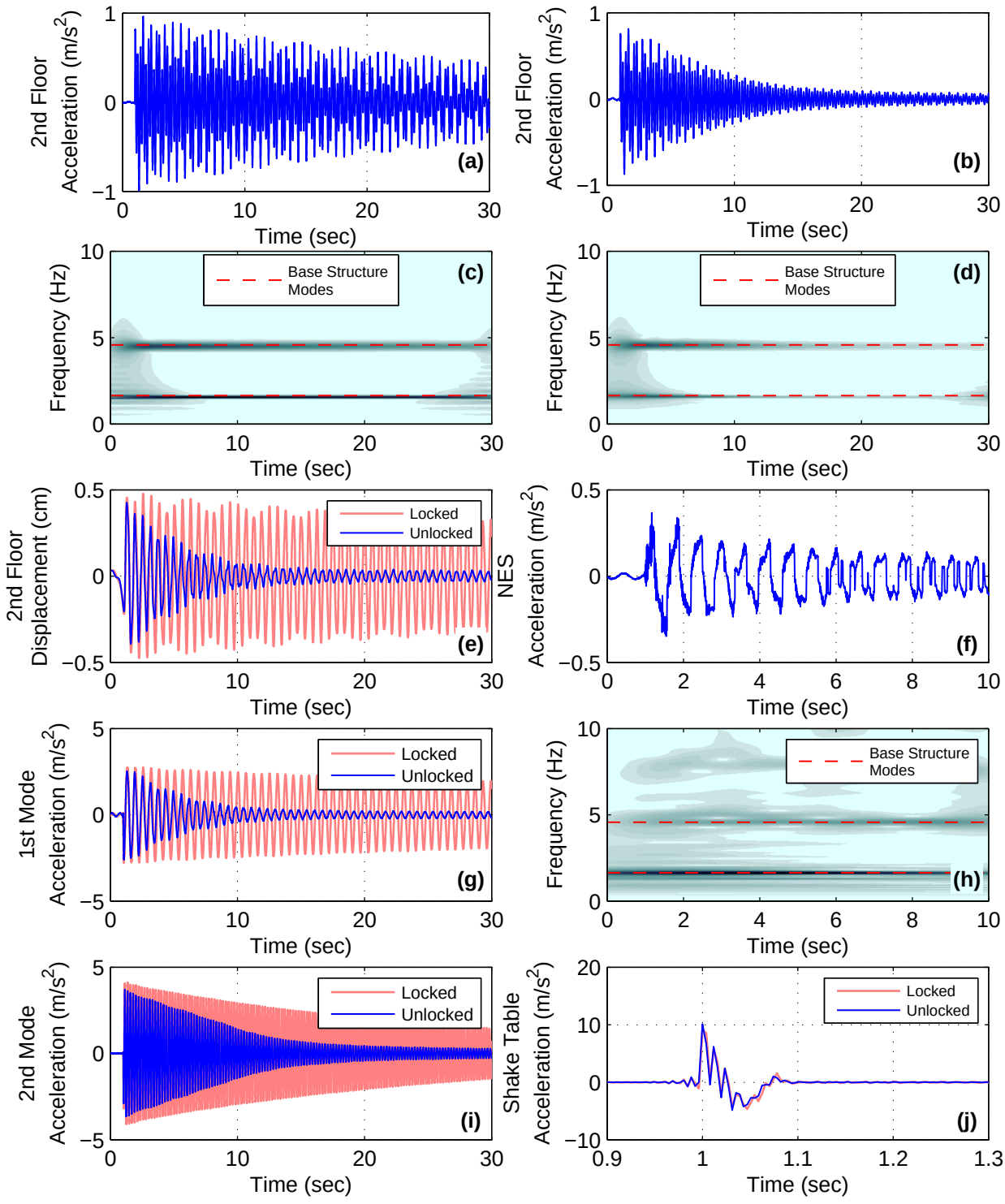

Figure B-1. Response of system with Type I NES to ground motion level 1 (a) second floor accel. NES locked, (b) second floor accel. NES unlocked, (c) wavelet of second floor accel. NES locked, (d) wavelet of second floor accel. NES unlocked, (e) second floor displacement, (f) NES accel., (g) mode one accel., (h) wavelet of NES accel., (i) mode two accel., (j) ground accel.

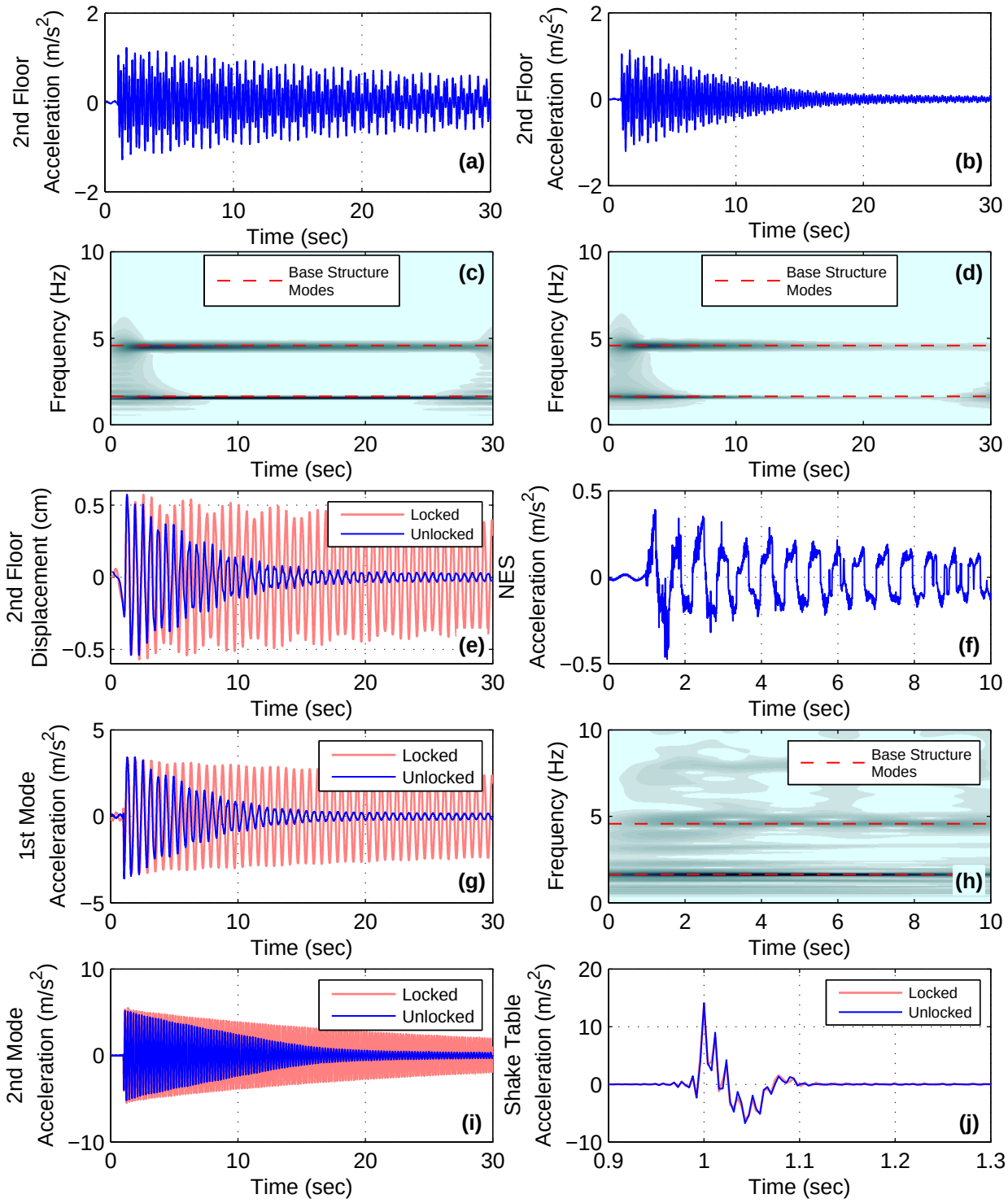

Figure B-2. Response of system with Type I NES to ground motion level 2 (a) second floor accel. NES locked, (b) second floor accel. NES unlocked, (c) wavelet of second floor accel. NES locked, (d) wavelet of second floor accel. NES unlocked, (e) second floor displacement, (f) NES accel., (g) mode one accel., (h) wavelet of NES accel., (i) mode two accel., (j) ground accel.

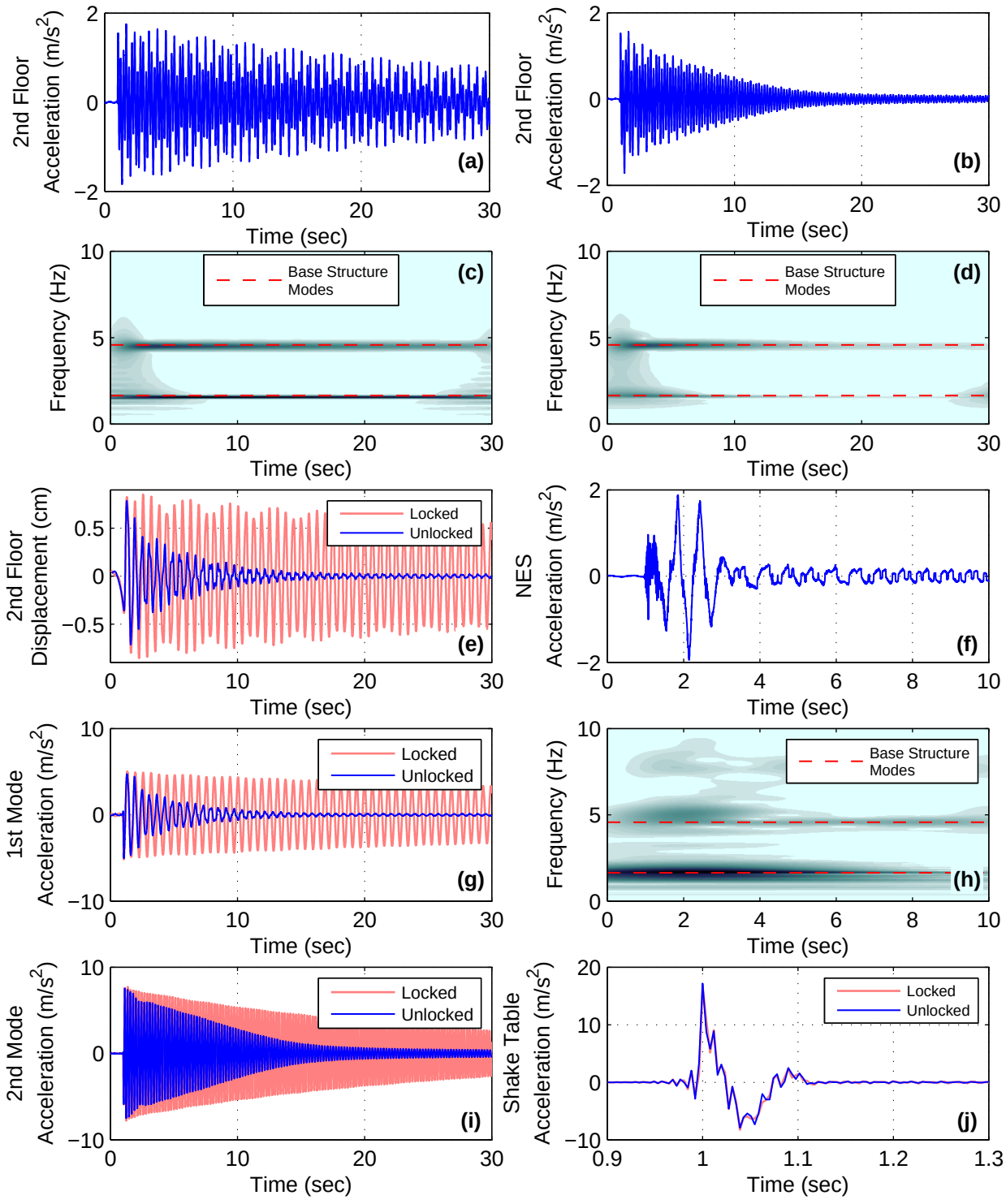

Figure B-3. Response of system with Type I NES to ground motion level 3 (a) second floor accel. NES locked, (b) second floor accel. NES unlocked, (c) wavelet of second floor accel. NES locked, (d) wavelet of second floor accel. NES unlocked, (e) second floor displacement, (f) NES accel., (g) mode one accel., (h) wavelet of NES accel., (i) mode two accel., (j) ground accel.

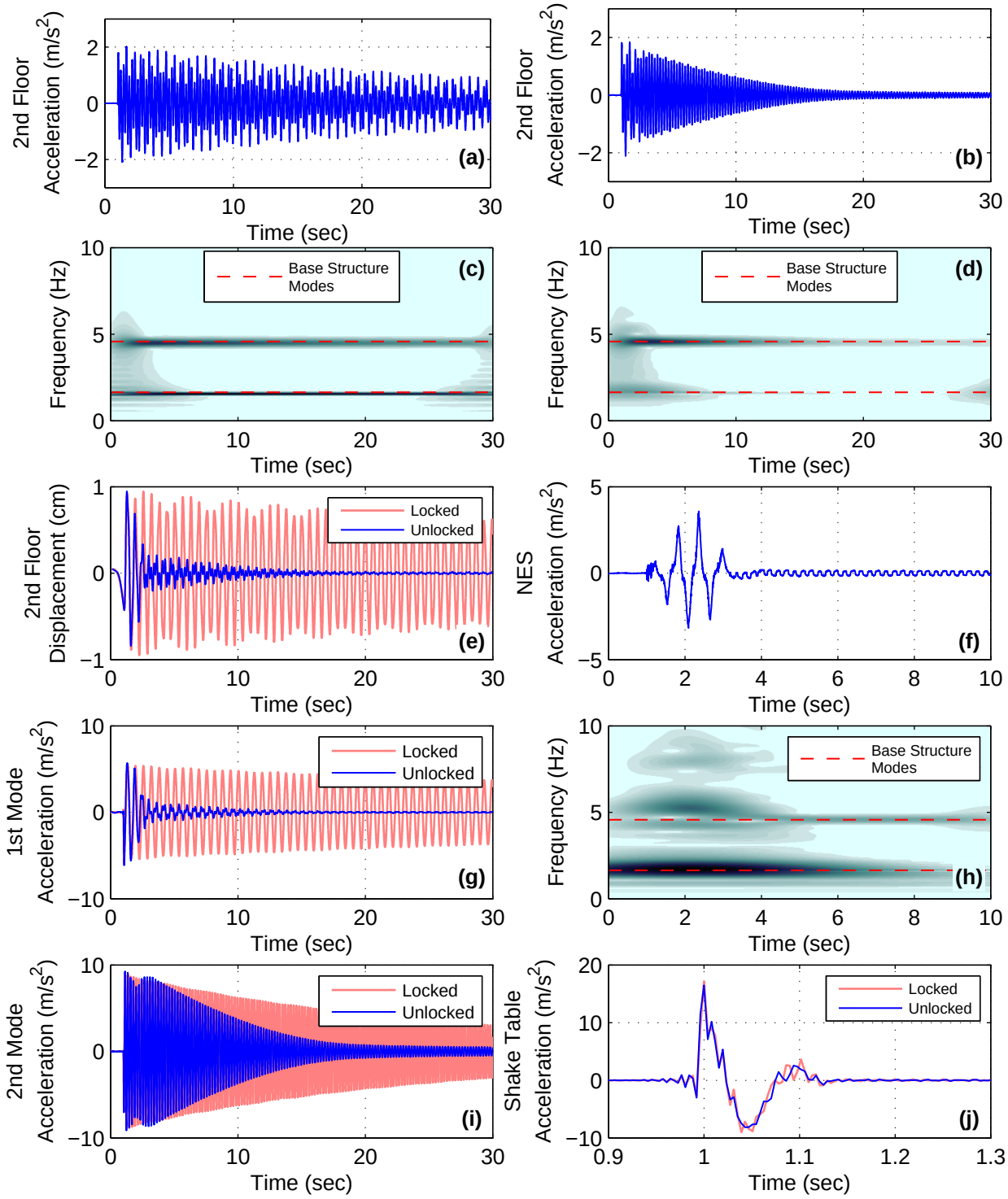

Figure B-4. Response of system with Type I NES to ground motion level 4 (a) second floor accel. NES locked, (b) second floor accel. NES unlocked, (c) wavelet of second floor accel. NES locked, (d) wavelet of second floor accel. NES unlocked, (e) second floor displacement, (f) NES accel., (g) mode one accel., (h) wavelet of NES accel., (i) mode two accel., (j) ground accel.

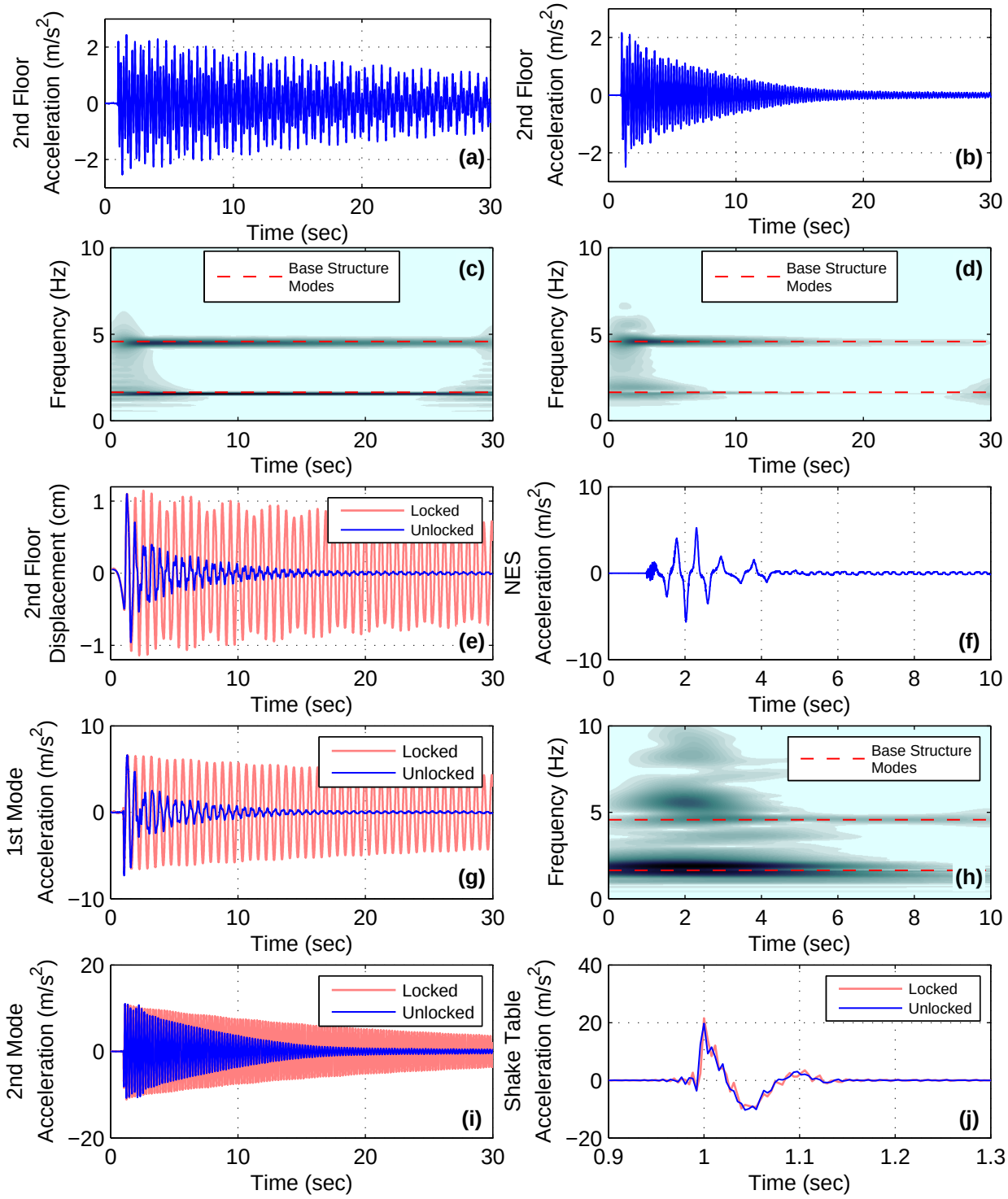

Figure B-5. Response of system with Type I NES to ground motion level 5 (a) second floor accel. NES locked, (b) second floor accel. NES unlocked, (c) wavelet of second floor accel. NES locked, (d) wavelet of second floor accel. NES unlocked, (e) second floor displacement, (f) NES accel., (g) mode one accel., (h) wavelet of NES accel., (i) mode two accel., (j) ground accel.

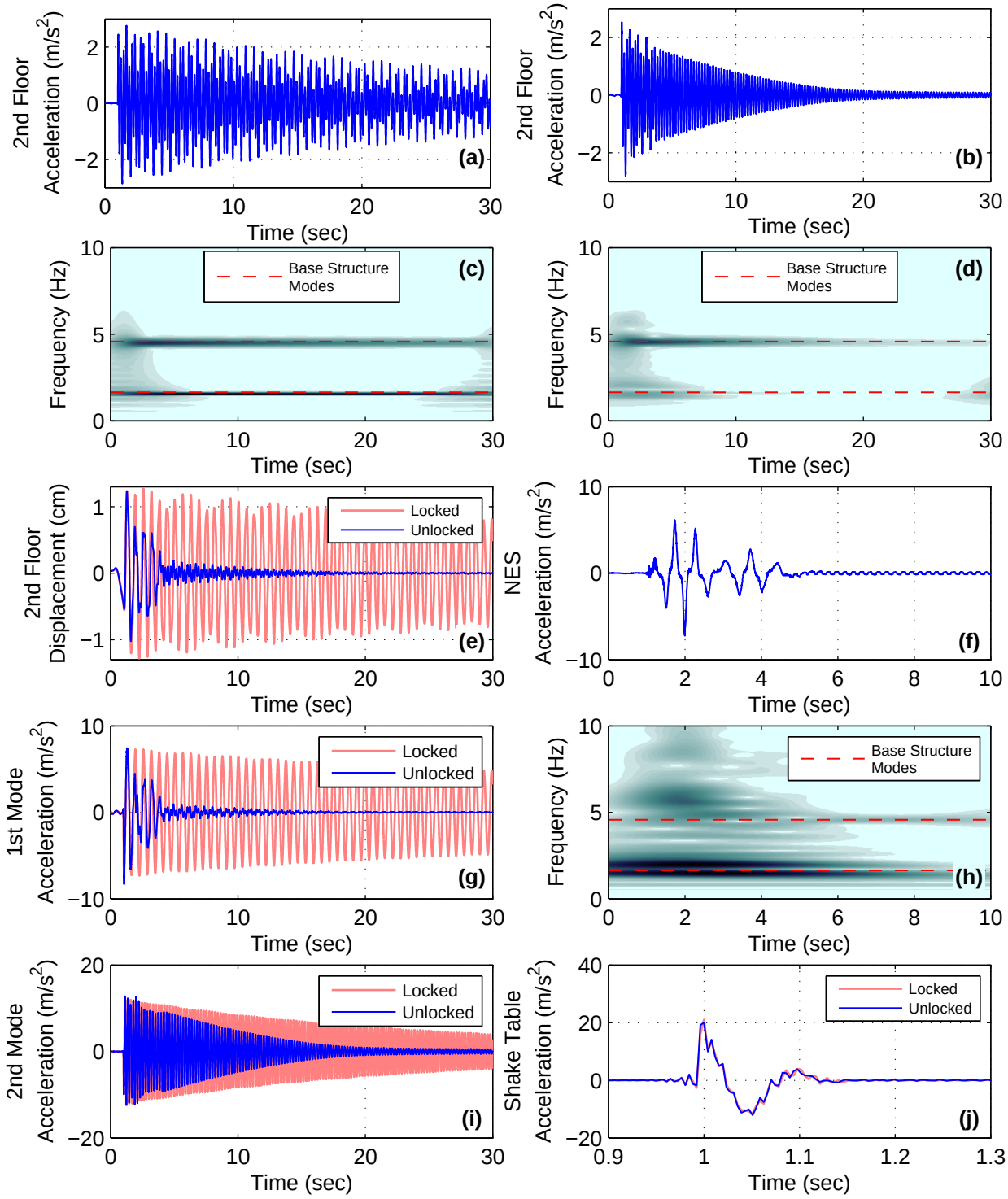

Figure B-6. Response of system with Type I NES to ground motion level 6 (a) second floor accel. NES locked, (b) second floor accel. NES unlocked, (c) wavelet of second floor accel. NES locked, (d) wavelet of second floor accel. NES unlocked, (e) second floor displacement, (f) NES accel., (g) mode one accel., (h) wavelet of NES accel., (i) mode two accel., (j) ground accel.

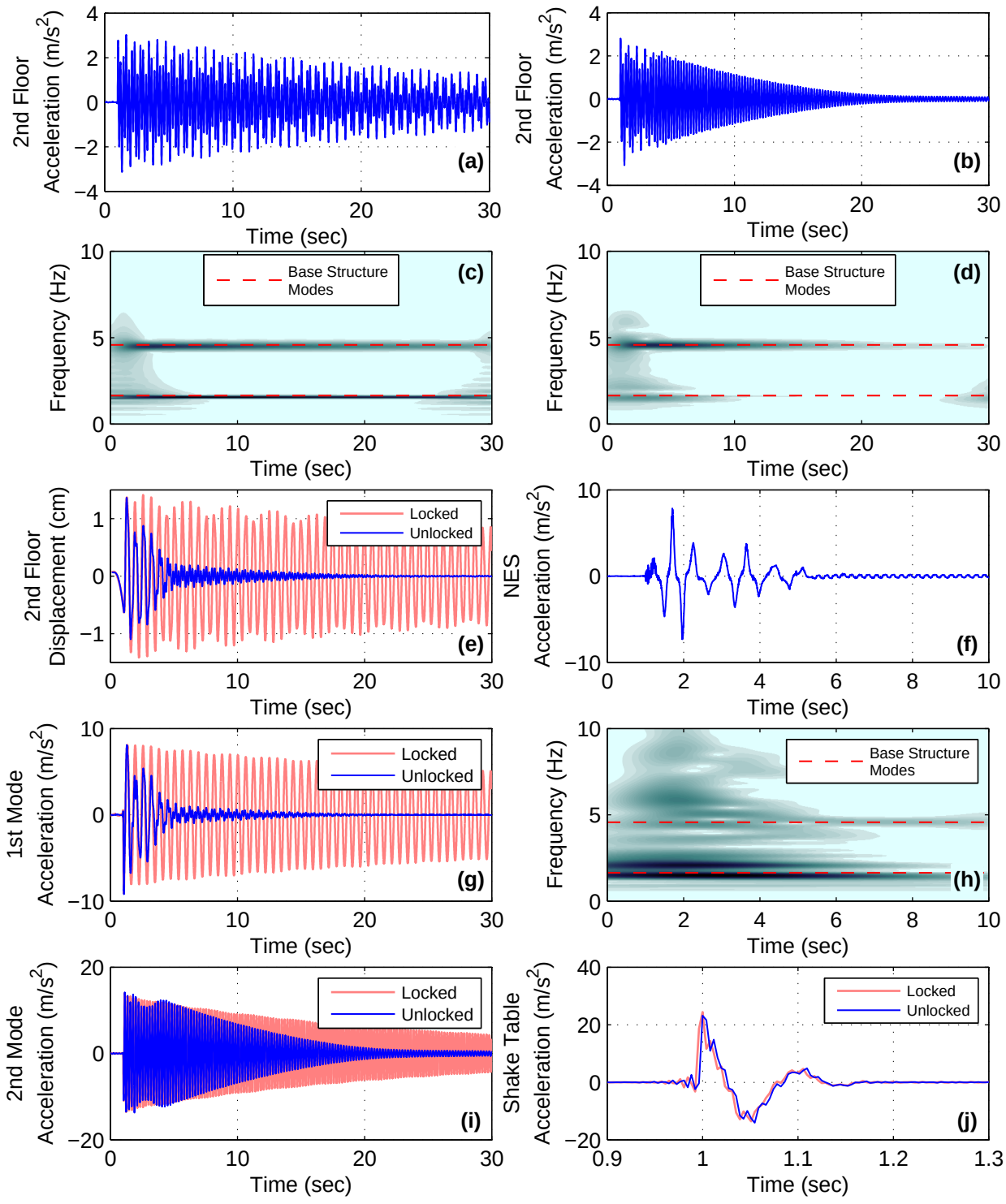

Figure B-7. Response of system with Type I NES to ground motion level 7 (a) second floor accel. NES locked, (b) second floor accel. NES unlocked, (c) wavelet of second floor accel. NES locked, (d) wavelet of second floor accel. NES unlocked, (e) second floor displacement, (f) NES accel., (g) mode one accel., (h) wavelet of NES accel., (i) mode two accel., (j) ground accel.

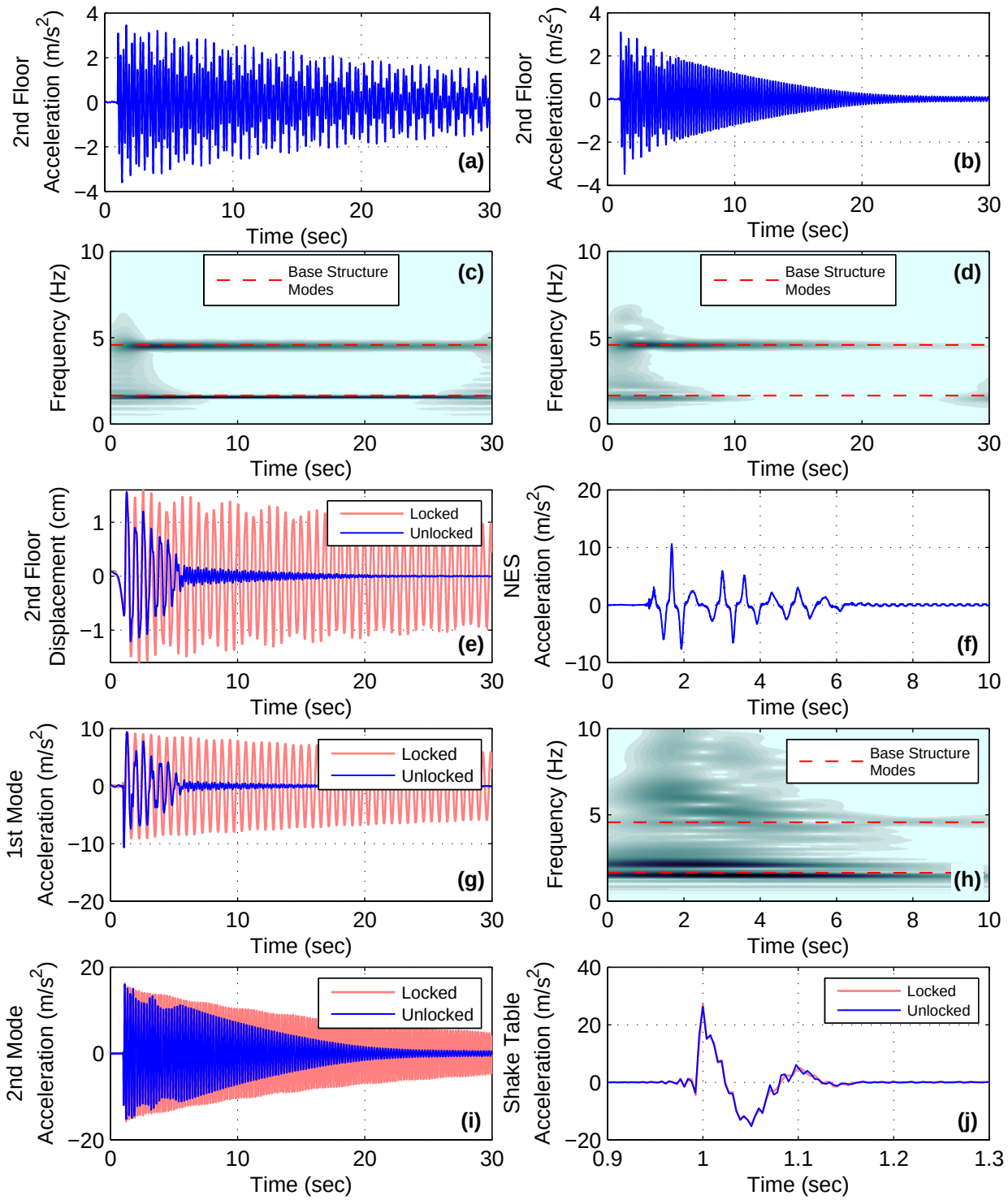

Figure B-8. Response of system with Type I NES to ground motion level 8 (a) second floor accel. NES locked, (b) second floor accel. NES unlocked, (c) wavelet of second floor accel. NES locked, (d) wavelet of second floor accel. NES unlocked, (e) second floor displacement, (f) NES accel., (g) mode one accel., (h) wavelet of NES accel., (i) mode two accel., (j) ground accel.

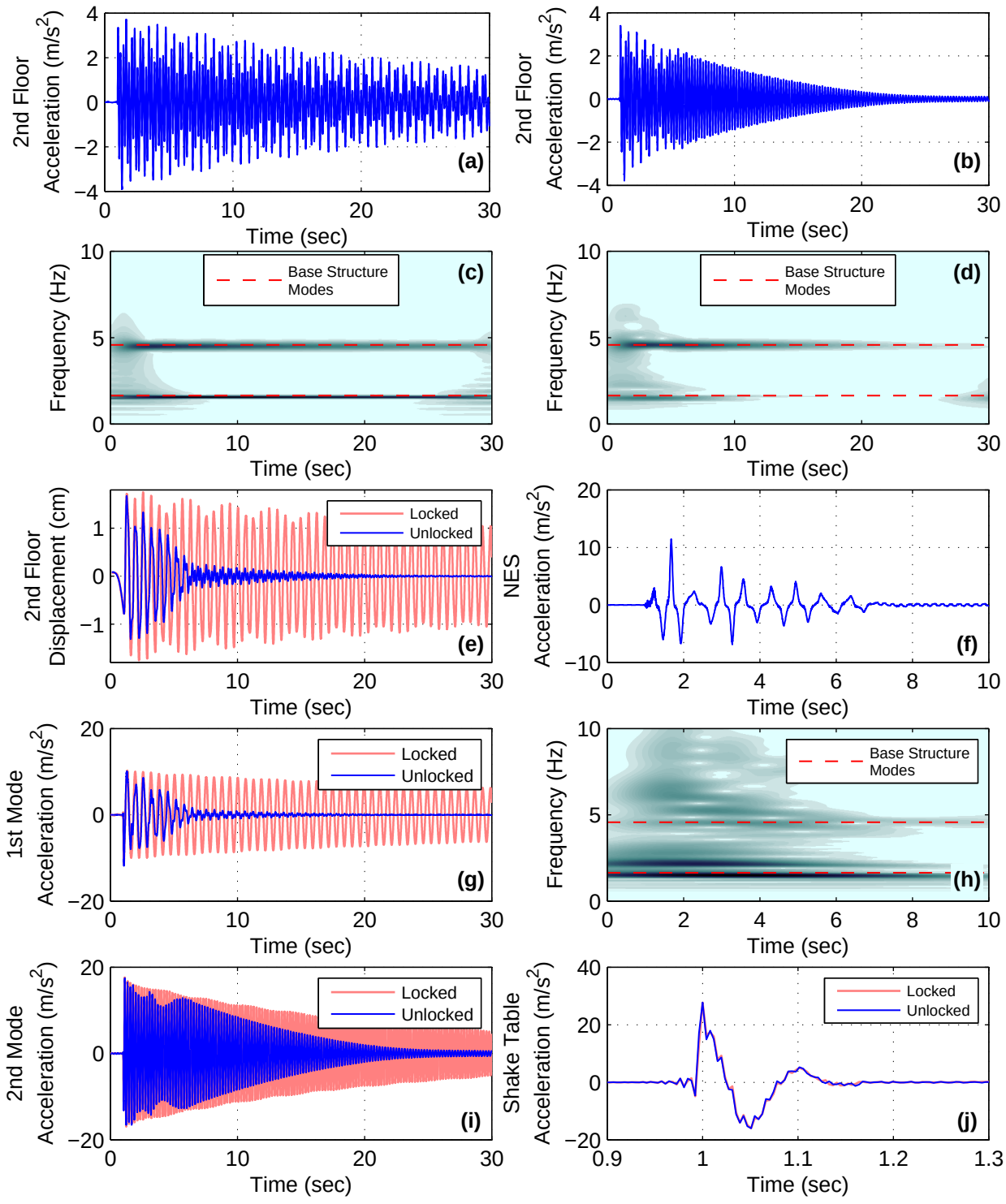

Figure B-9. Response of system with Type I NES to ground motion level 9 (a) second floor accel. NES locked, (b) second floor accel. NES unlocked, (c) wavelet of second floor accel. NES locked, (d) wavelet of second floor accel. NES unlocked, (e) second floor displacement, (f) NES accel., (g) mode one accel., (h) wavelet of NES accel., (i) mode two accel., (j) ground accel.

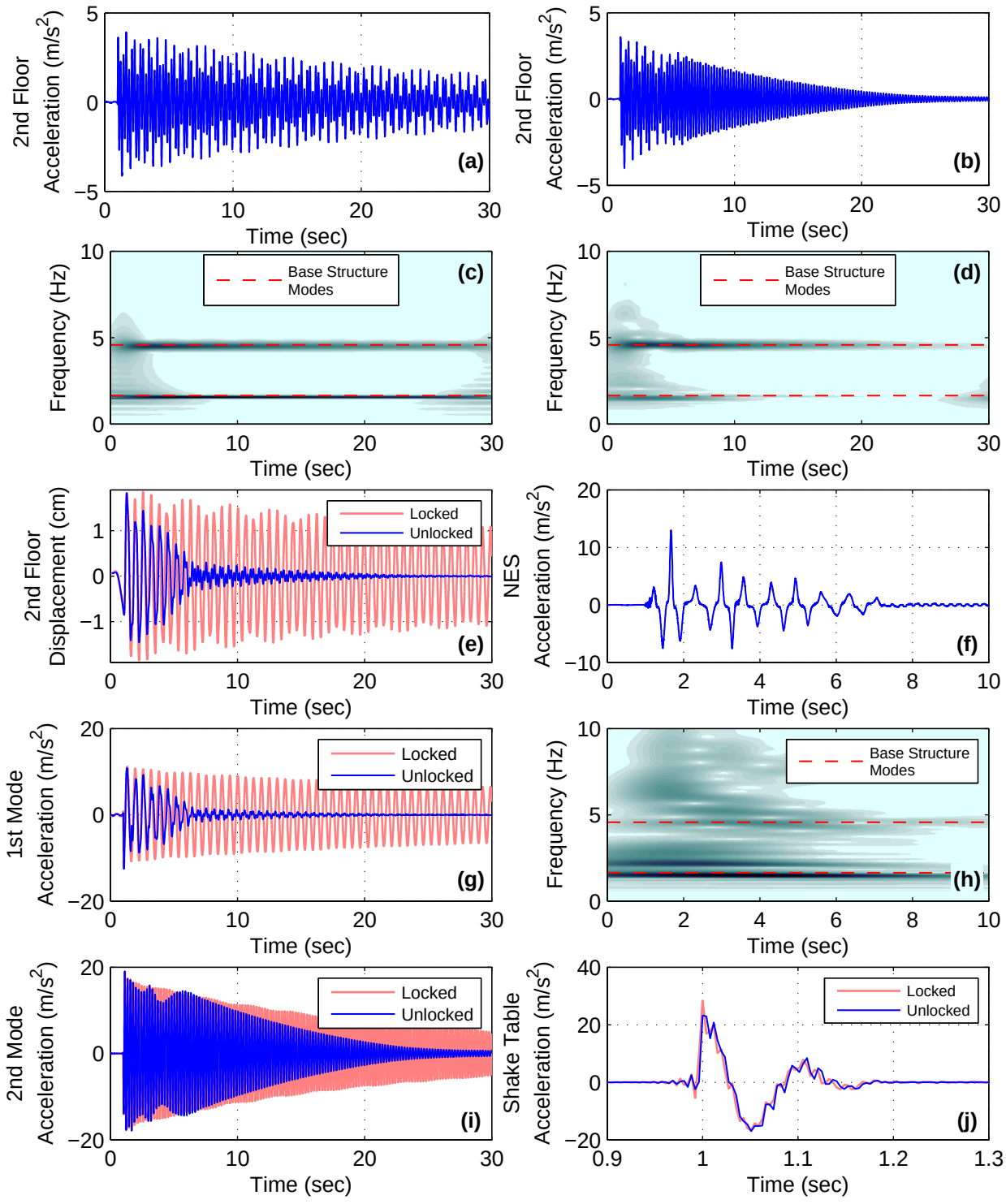

Figure B-10. Response of system with Type I NES to ground motion level 10 (a) second floor accel. NES locked, (b) second floor accel. NES unlocked, (c) wavelet of second floor accel. NES locked, (d) wavelet of second floor accel. NES unlocked, (e) second floor displacement, (f) NES accel., (g) mode one accel., (h) wavelet of NES accel., (i) mode two accel., (j) ground accel.

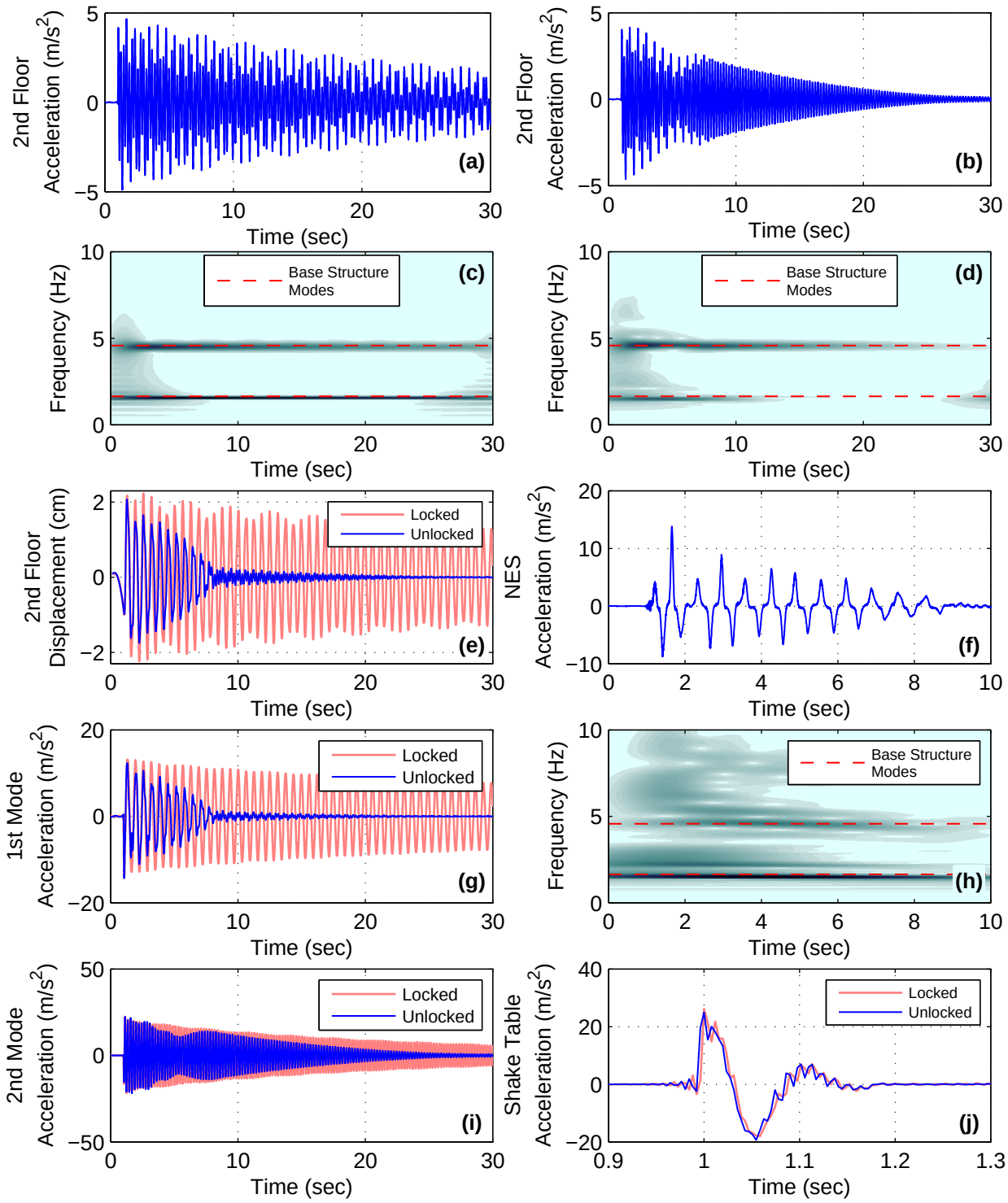

Figure B-11. Response of system with Type I NES to ground motion level 11 (a) second floor accel. NES locked, (b) second floor accel. NES unlocked, (c) wavelet of second floor accel. NES locked, (d) wavelet of second floor accel. NES unlocked, (e) second floor displacement, (f) NES accel., (g) mode one accel., (h) wavelet of NES accel., (i) mode two accel., (j) ground accel.

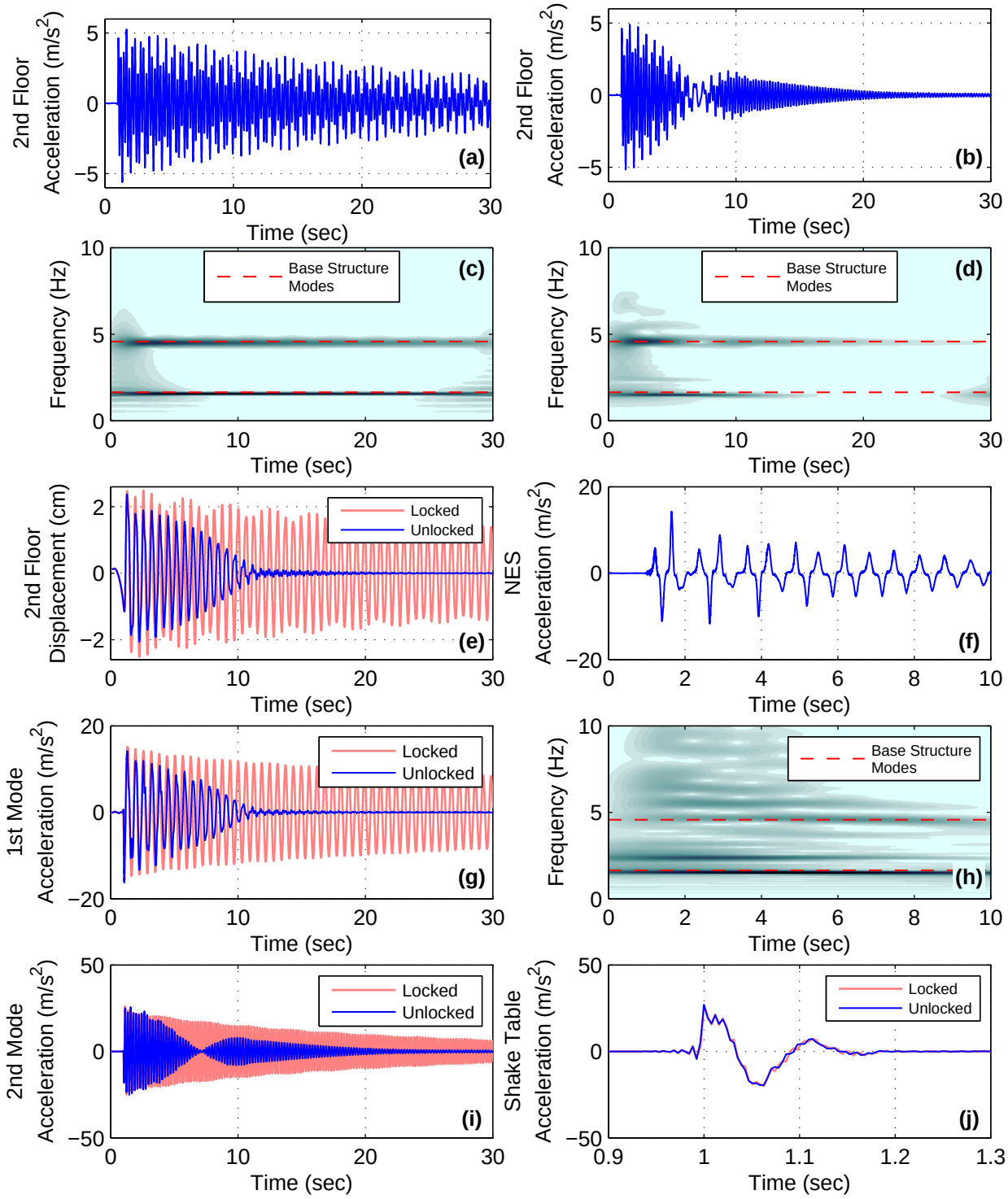

Figure B-12. Response of system with Type I NES to ground motion level 12 (a) second floor accel. NES locked, (b) second floor accel. NES unlocked, (c) wavelet of second floor accel. NES locked, (d) wavelet of second floor accel. NES unlocked, (e) second floor displacement, (f) NES accel., (g) mode one accel., (h) wavelet of NES accel., (i) mode two accel., (j) ground accel.

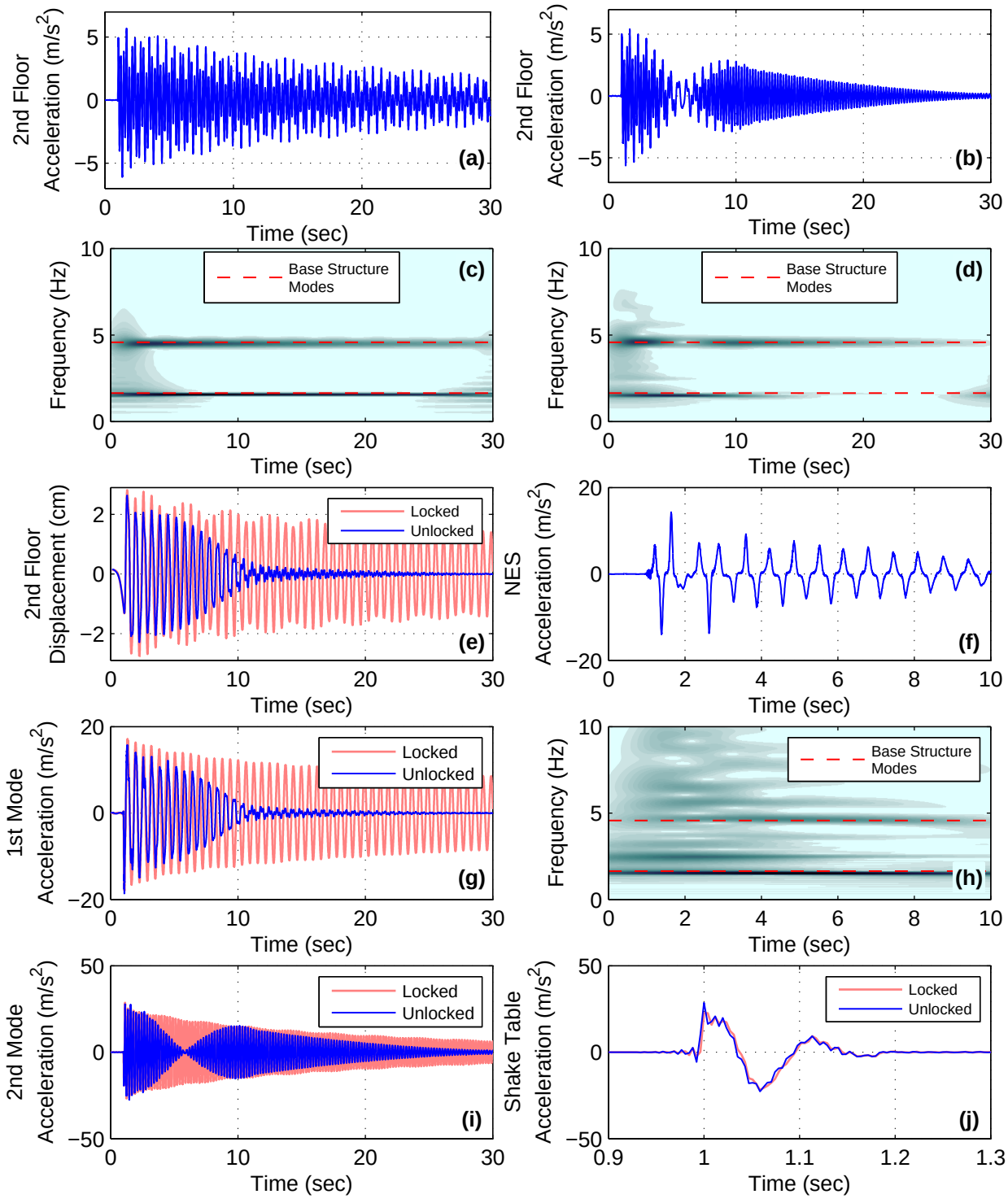

Figure B-13. Response of system with Type I NES to ground motion level 13 (a) second floor accel. NES locked, (b) second floor accel. NES unlocked, (c) wavelet of second floor accel. NES locked, (d) wavelet of second floor accel. NES unlocked, (e) second floor displacement, (f) NES accel., (g) mode one accel., (h) wavelet of NES accel., (i) mode two accel., (j) ground accel.

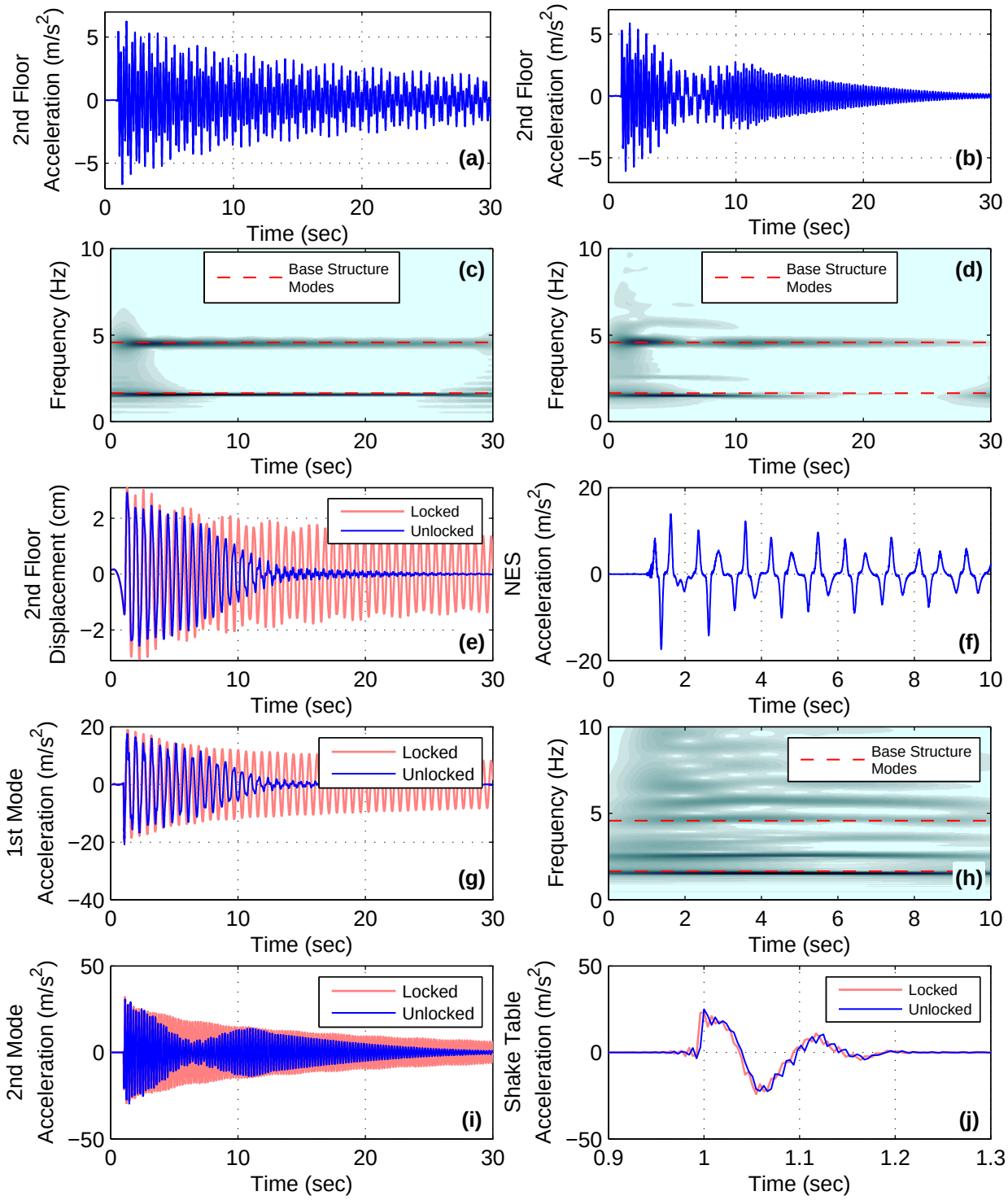

Figure B-14. Response of system with Type I NES to ground motion level 14 (a) second floor accel. NES locked, (b) second floor accel. NES unlocked, (c) wavelet of second floor accel. NES locked, (d) wavelet of second floor accel. NES unlocked, (e) second floor displacement, (f) NES accel., (g) mode one accel., (h) wavelet of NES accel., (i) mode two accel., (j) ground accel.

APPENDIX C: ADDITIONAL EXPERIMENTAL RESPONSES OF THE SMALL-SCALE TYPE III NES AND BASE STRUCTURE

In this appendix, additional plots of the experimental response of the small-scale test structure and Type III NES are presented. The experimental setup and Type III NES utilized in these experiments were introduced in Chapter 5. The shake-table-produced ground motions used for the experiments presented in this section are scaled versions of the impulse-like ground motion considered in the experiments presented in Chapter 5. The response of the system with the NES unlocked is shown for twenty-four different scaling levels of this ground motion (denoted by load level 1 through load level 24). Only a limited number of load levels were tested with the Type III NES locked (load level 2, 14, and 22). To supplement this data, in this appendix, the previously measured response of the system with the small-scale Type I NES locked is used for comparison at load levels 3, 5, 7, 10, 12, 16, 18, 20, 21, 23, and 24. For load levels with no corresponding data with the NES locked (load levels 1, 4, 6, 8, 9, 11, 13, 15, 17, and 19), only the response of the system with the NES unlocked is show. The responses of the system plotted in this appendix include the shake-table-produced ground acceleration, second floor acceleration, second floor acceleration wavelet spectrum, estimated second floor displacement, modal accelerations, NES accelerations, and NES acceleration wavelet spectra.

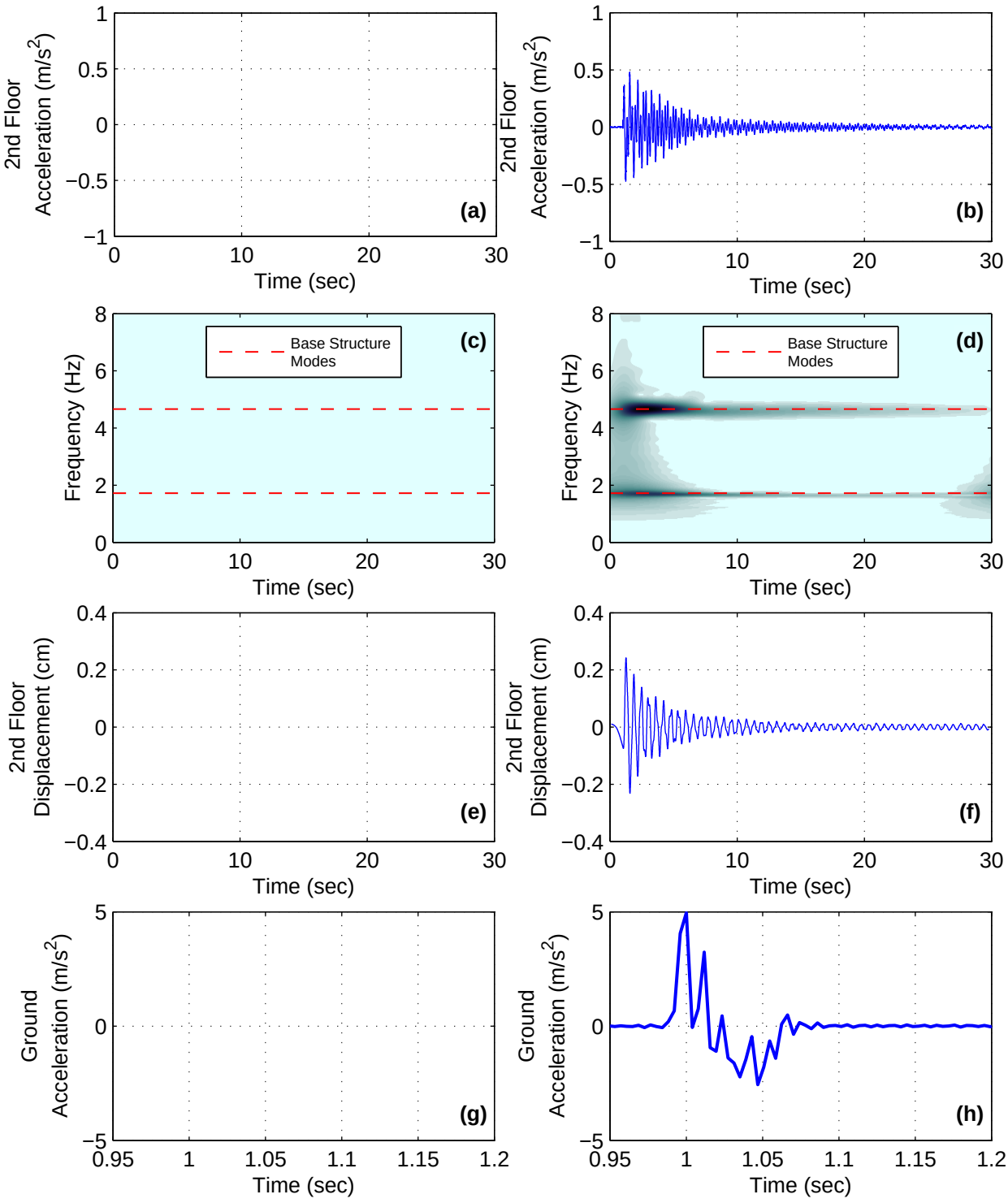

Figure C-1. Response of system with small-scale Type III NES to ground motion level 1 (a) second floor accel., NES locked, (b) second floor accel., NES unlocked, (c) wavelet of second floor accel., NES locked, (d) wavelet of second floor accel., NES unlocked, (e) second floor disp., NES locked (f) second floor disp., NES unlocked, (g) ground accel., NES locked, and (h) ground accel., NES unlocked

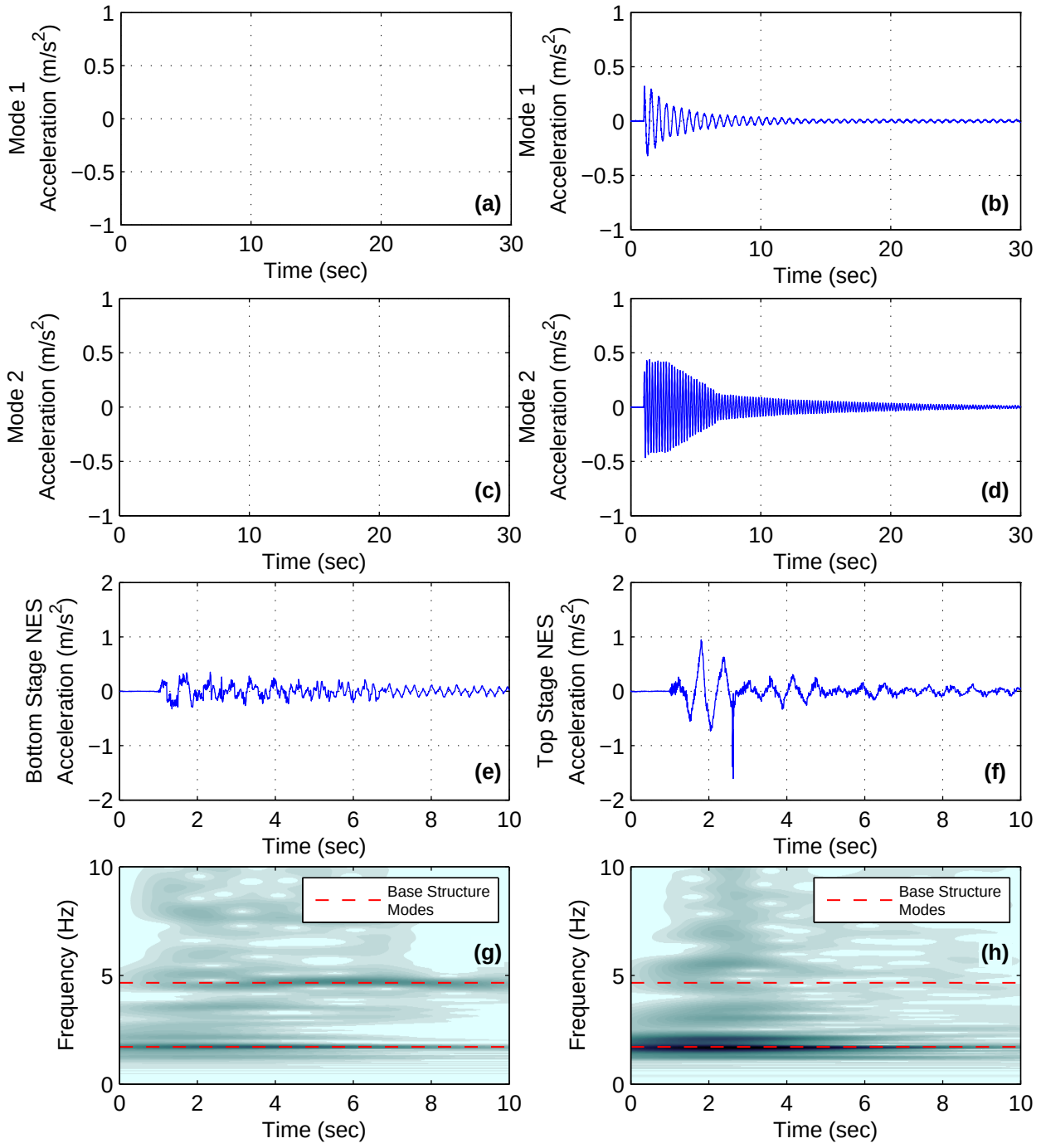

Figure C-2. Response of system with small-scale Type III NES to ground motion level 1 (a) mode 1 accel., NES locked, (b) mode 1 accel., NES unlocked, (c) mode 2 accel., NES locked, (d) mode 2 accel., NES unlocked, (e) bottom stage NES accel., NES unlocked (f) top stage NES accel., NES unlocked, (g) wavelet of bottom stage NES accel., NES unlocked, and (f) wavelet of top stage NES accel., NES unlocked

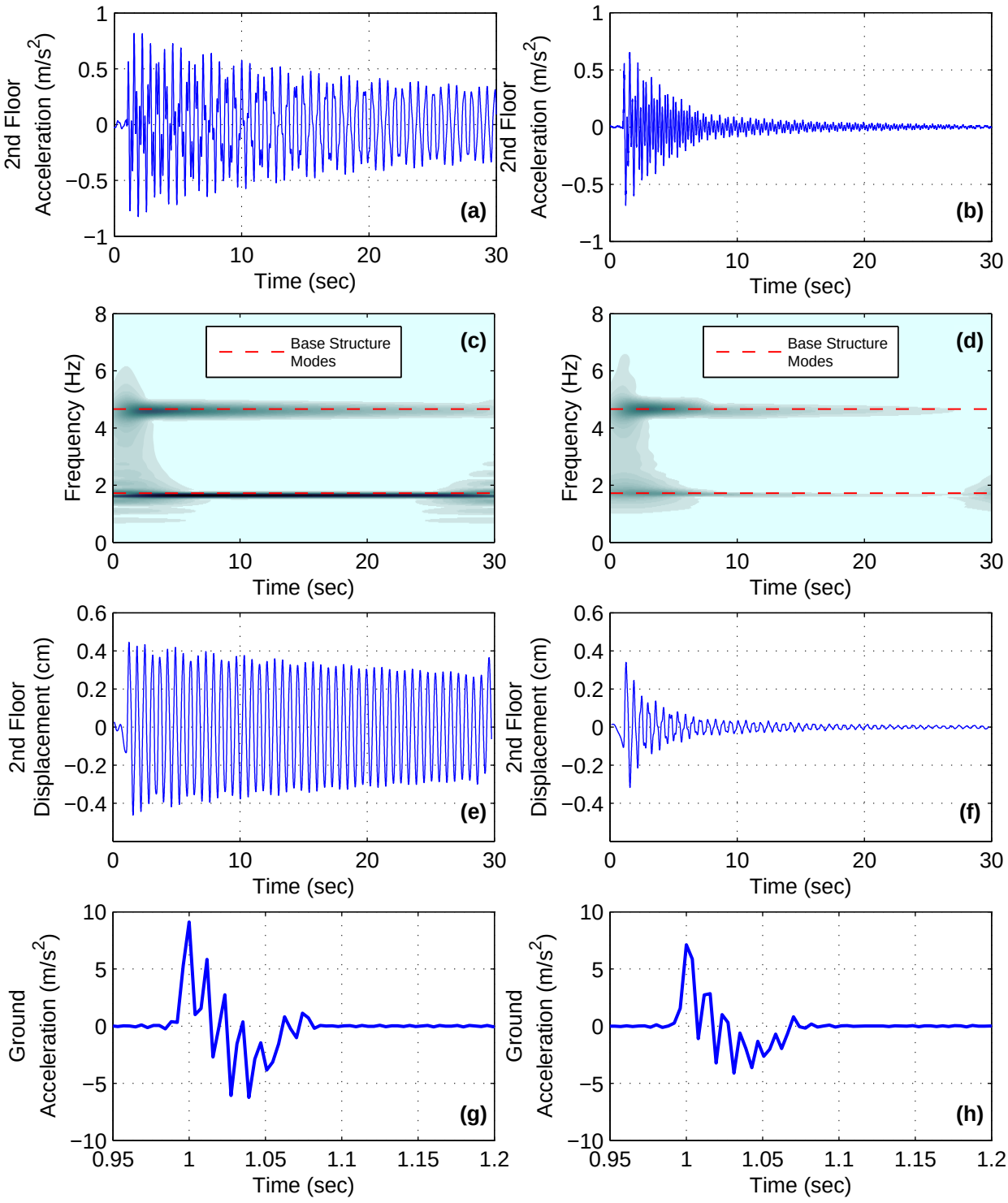

Figure C-3. Response of system with small-scale Type III NES to ground motion level 2 (a) second floor accel., NES locked, (b) second floor accel., NES unlocked, (c) wavelet of second floor accel., NES locked, (d) wavelet of second floor accel., NES unlocked, (e) second floor disp., NES locked (f) second floor disp., NES unlocked, (g) ground accel., NES locked, and (h) ground accel., NES unlocked

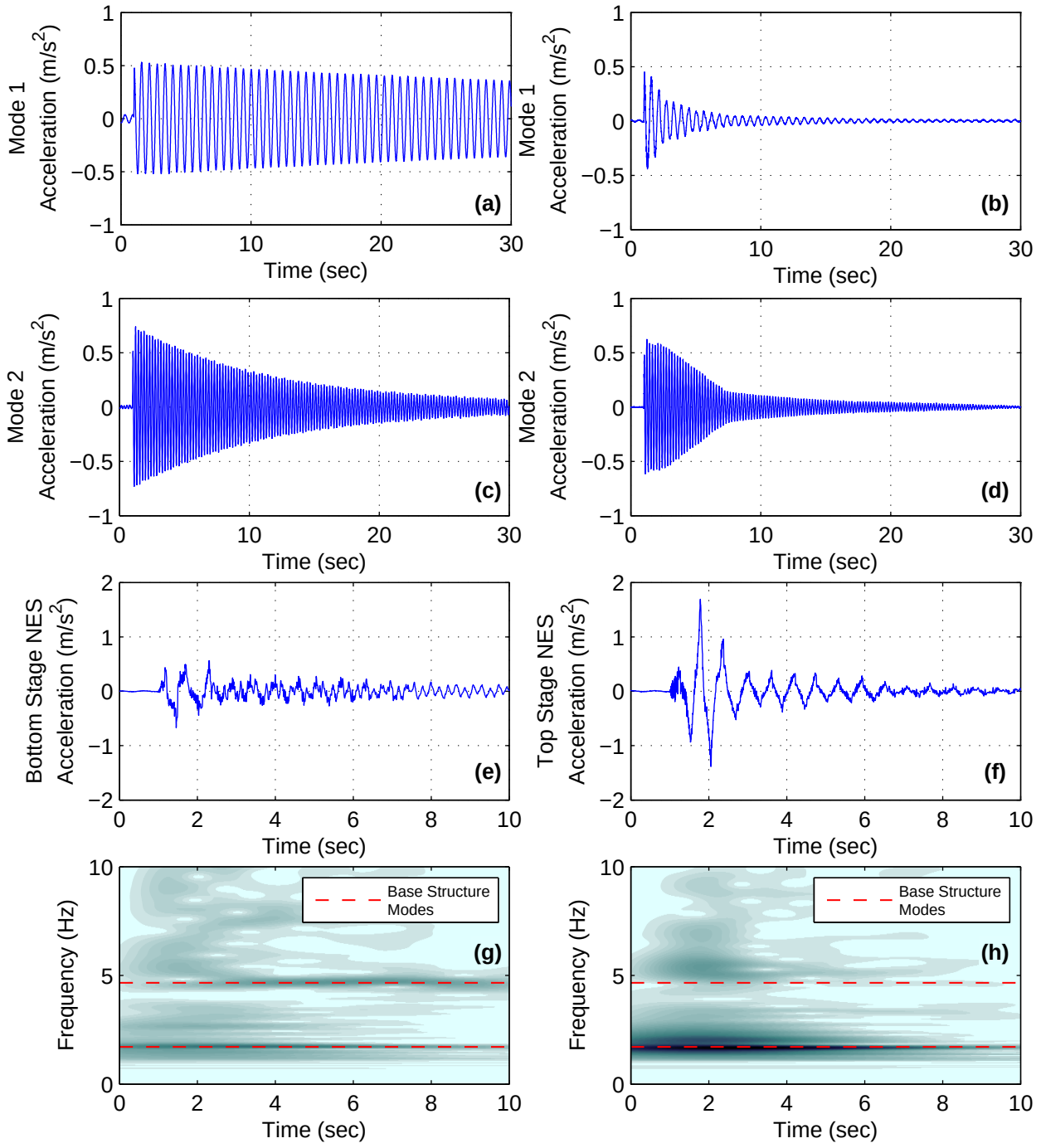

Figure C-4. Response of system with small-scale Type III NES to ground motion level 2 (a) mode 1 accel., NES locked, (b) mode 1 accel., NES unlocked, (c) mode 2 accel., NES locked, (d) mode 2 accel., NES unlocked, (e) bottom stage NES accel., NES unlocked (f) top stage NES accel., NES unlocked, (g) wavelet of bottom stage NES accel., NES unlocked, and (f) wavelet of top stage NES accel., NES unlocked

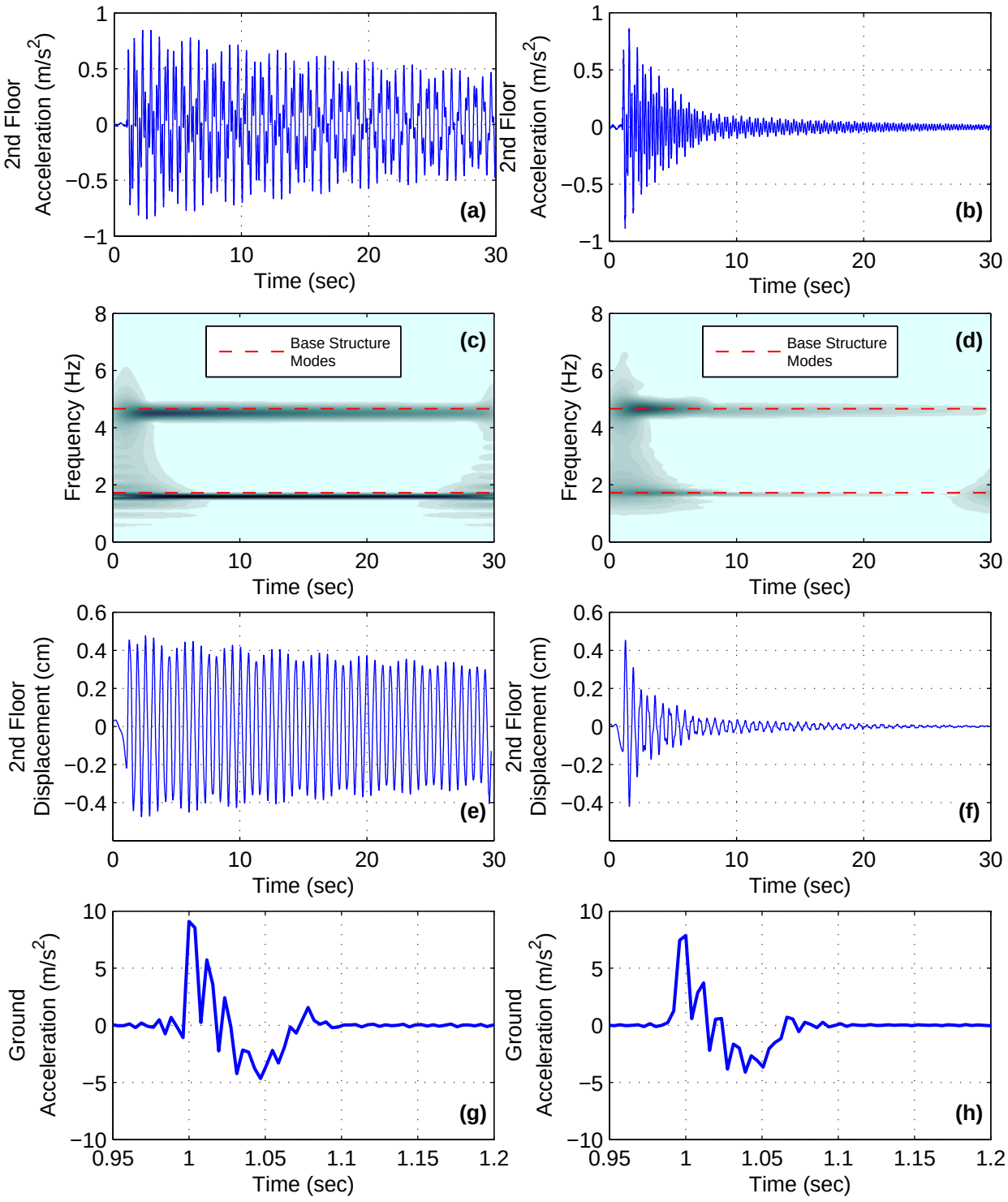

Figure C-5. Response of system with small-scale Type III NES to ground motion level 3 (a) second floor accel., NES locked, (b) second floor accel., NES unlocked, (c) wavelet of second floor accel., NES locked, (d) wavelet of second floor accel., NES unlocked, (e) second floor disp., NES locked (f) second floor disp., NES unlocked, (g) ground accel., NES locked, and (h) ground accel., NES unlocked

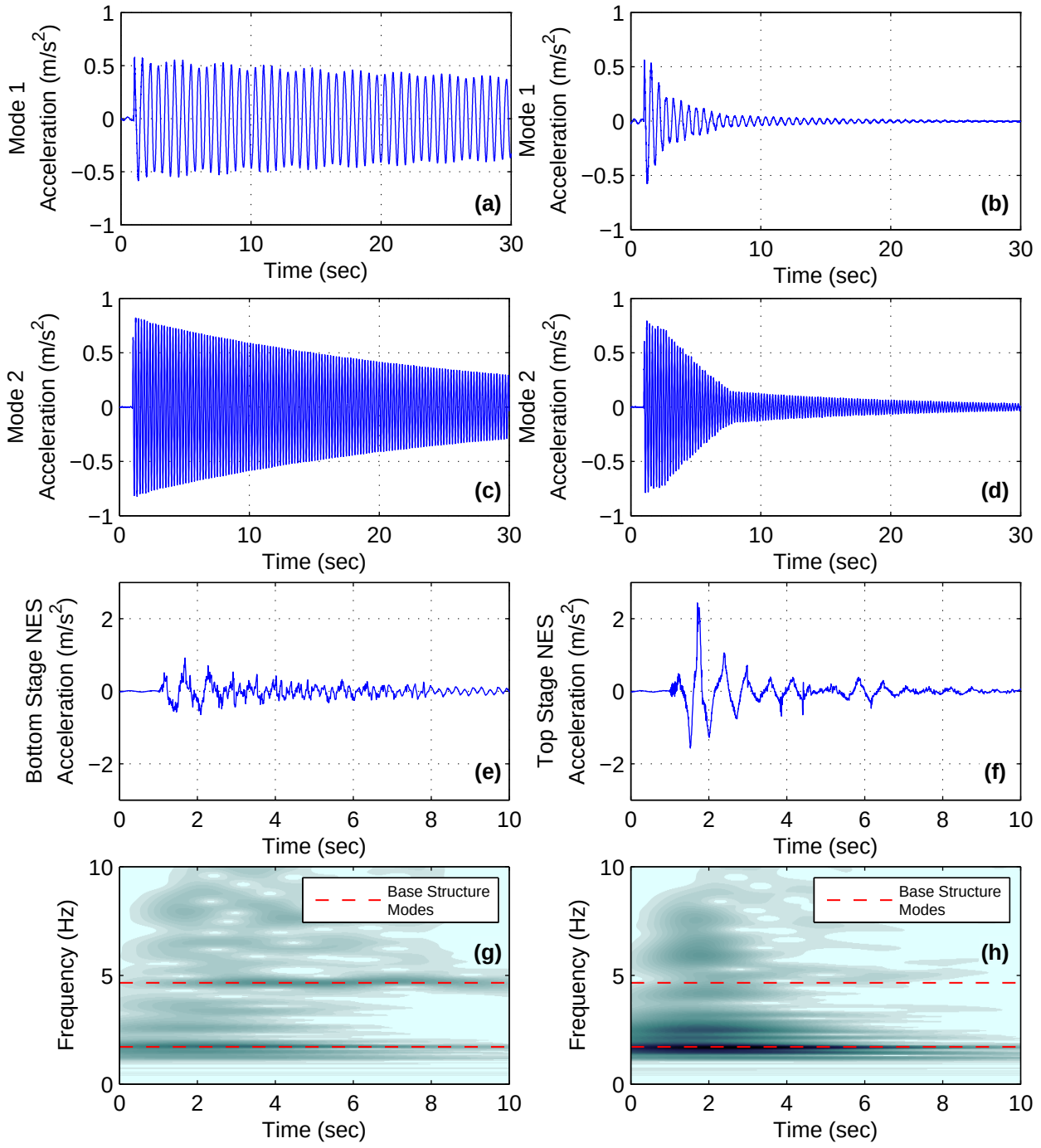

Figure C-6. Response of system with small-scale Type III NES to ground motion level 3 (a) mode 1 accel., NES locked, (b) mode 1 accel., NES unlocked, (c) mode 2 accel., NES locked, (d) mode 2 accel., NES unlocked, (e) bottom stage NES accel., NES unlocked (f) top stage NES accel., NES unlocked, (g) wavelet of bottom stage NES accel., NES unlocked, and (f) wavelet of top stage NES accel., NES unlocked

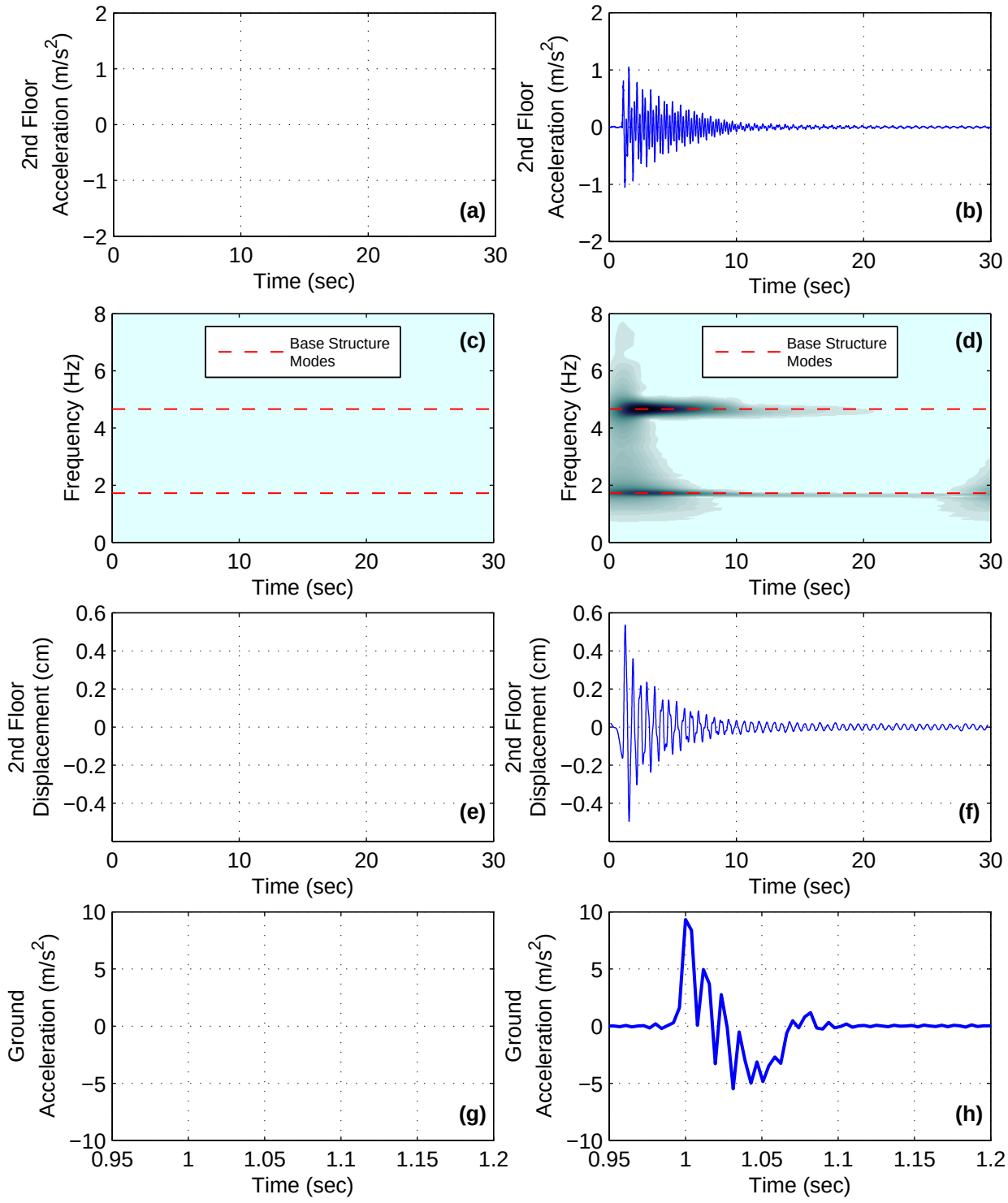

Figure C-7. Response of system with small-scale Type III NES to ground motion level 4 (a) second floor accel., NES locked, (b) second floor accel., NES unlocked, (c) wavelet of second floor accel., NES locked, (d) wavelet of second floor accel., NES unlocked, (e) second floor disp., NES locked (f) second floor disp., NES unlocked, (g) ground accel., NES locked, and (h) ground accel., NES unlocked

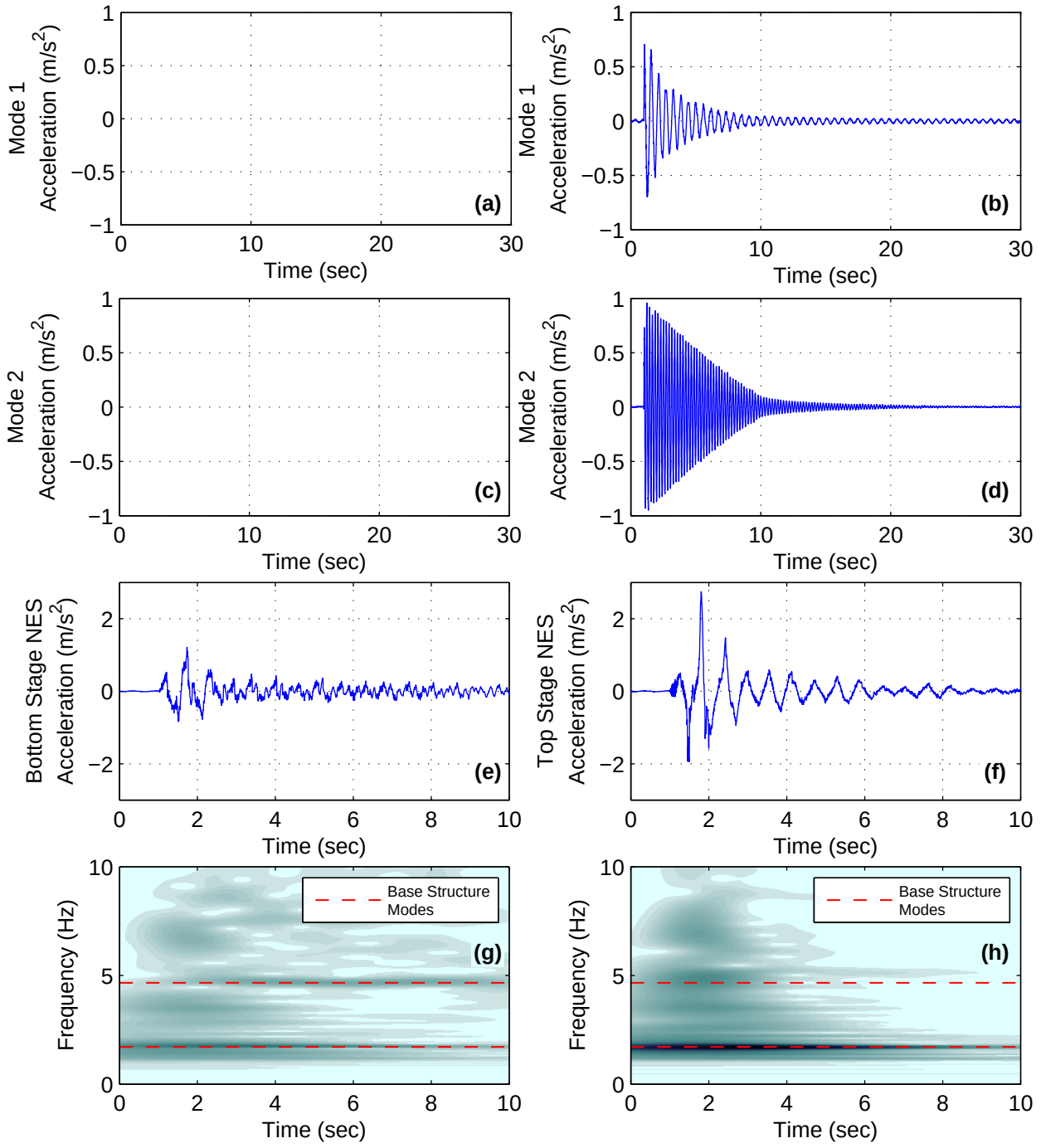

Figure C-8. Response of system with small-scale Type III NES to ground motion level 4 (a) mode 1 accel., NES locked, (b) mode 1 accel., NES unlocked, (c) mode 2 accel., NES locked, (d) mode 2 accel., NES unlocked, (e) bottom stage NES accel., NES unlocked (f) top stage NES accel., NES unlocked, (g) wavelet of bottom stage NES accel., NES unlocked, and (f) wavelet of top stage NES accel., NES unlocked

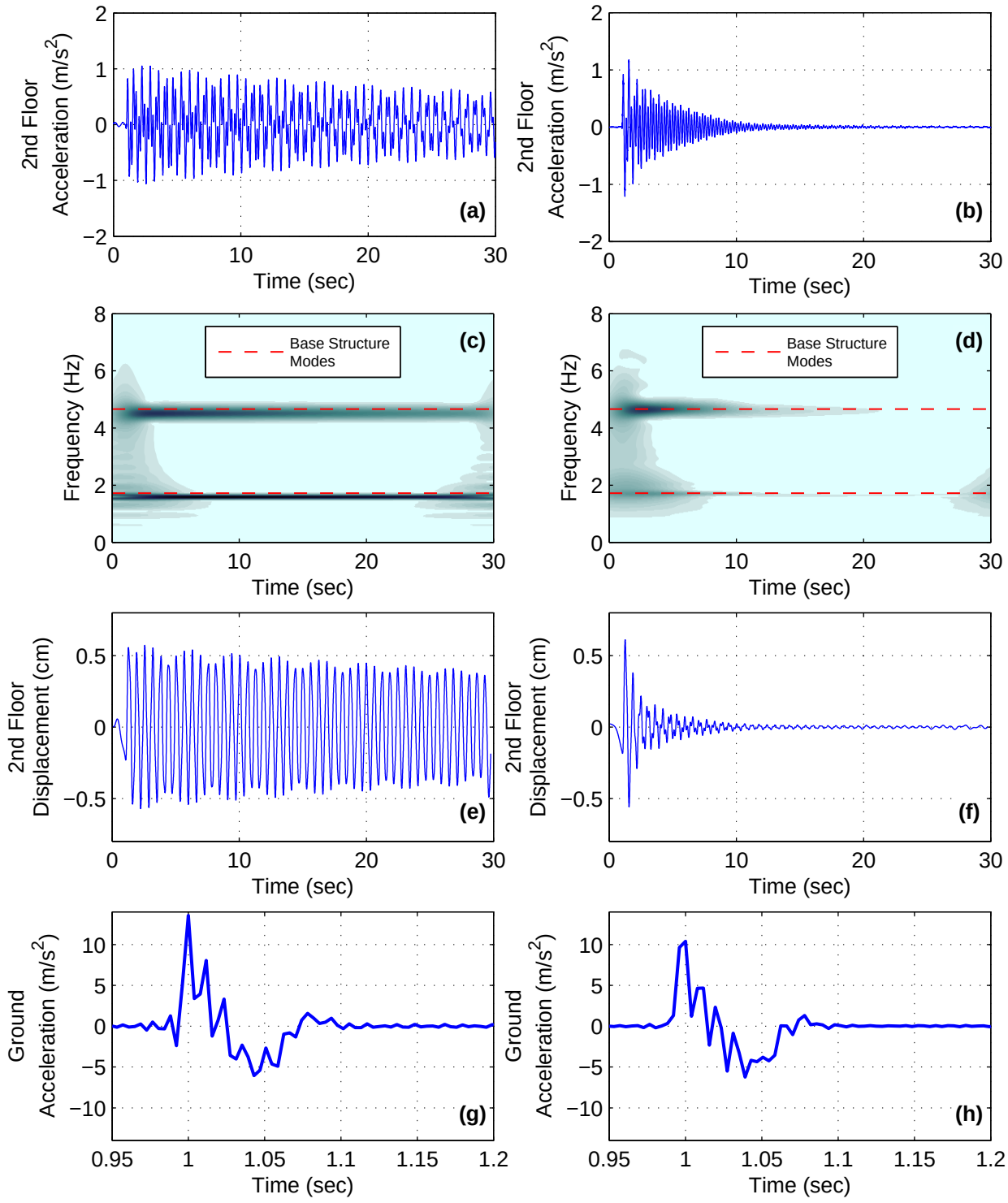

Figure C-9. Response of system with small-scale Type III NES to ground motion level 5 (a) second floor accel., NES locked, (b) second floor accel., NES unlocked, (c) wavelet of second floor accel., NES locked, (d) wavelet of second floor accel., NES unlocked, (e) second floor disp., NES locked (f) second floor disp., NES unlocked, (g) ground accel., NES locked, and (h) ground accel., NES unlocked

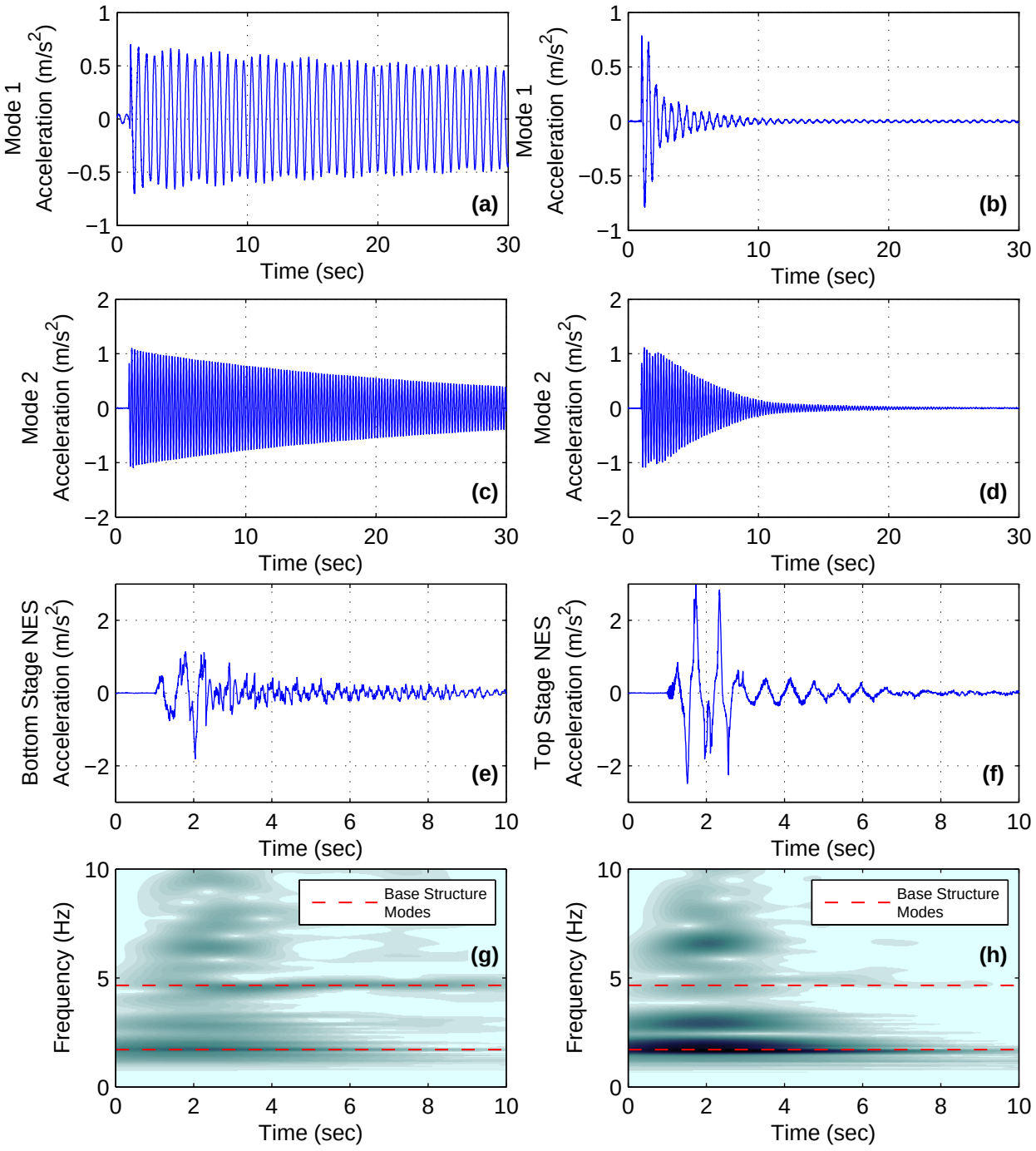

Figure C-10. Response of system with small-scale Type III NES to ground motion level 5 (a) mode 1 accel., NES locked, (b) mode 1 accel., NES unlocked, (c) mode 2 accel., NES locked, (d) mode 2 accel., NES unlocked, (e) bottom stage NES accel., NES unlocked (f) top stage NES accel., NES unlocked, (g) wavelet of bottom stage NES accel., NES unlocked, and (f) wavelet of top stage NES accel., NES unlocked

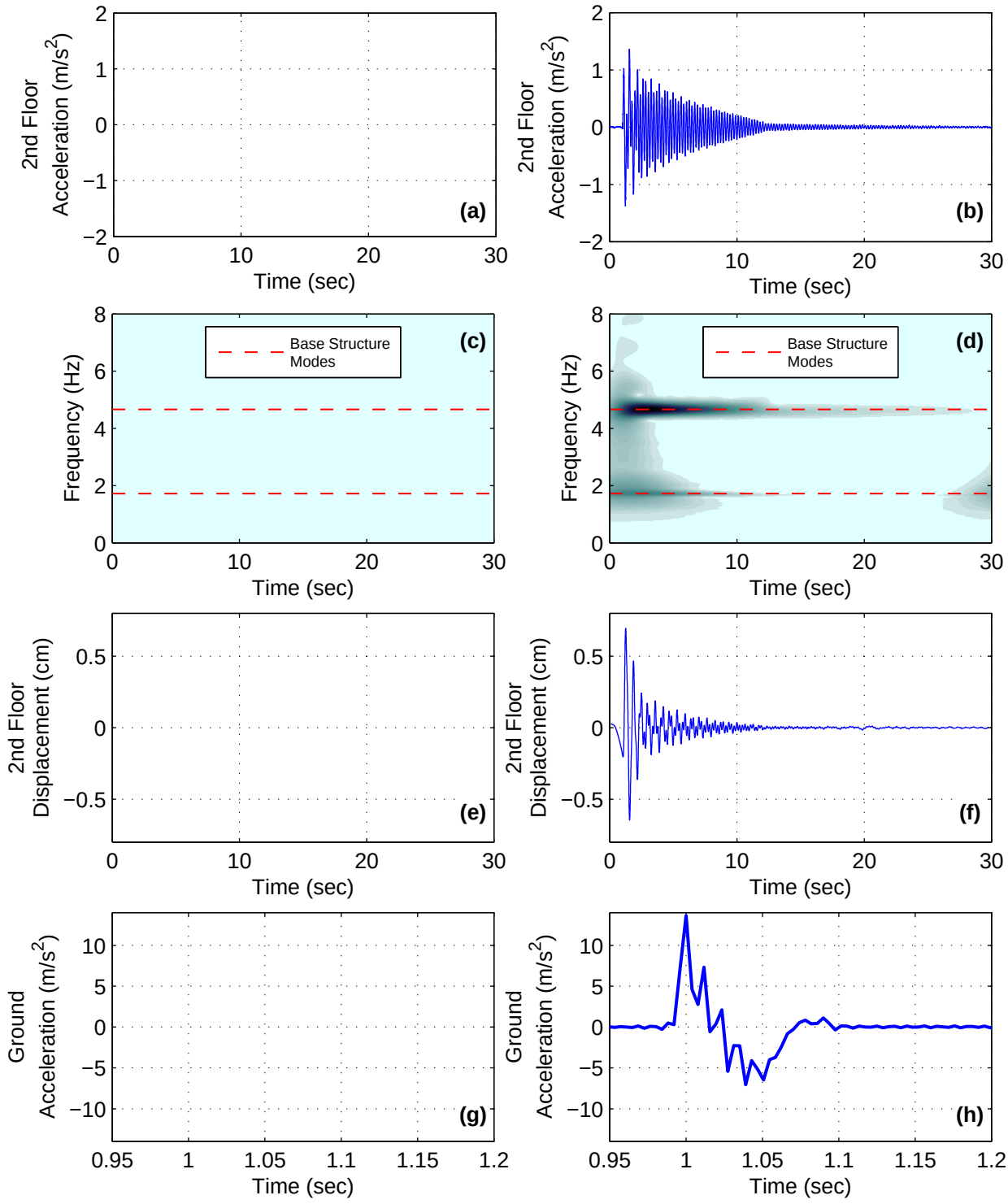

Figure C-11. Response of system with small-scale Type III NES to ground motion level 6 (a) second floor accel., NES locked, (b) second floor accel., NES unlocked, (c) wavelet of second floor accel., NES locked, (d) wavelet of second floor accel., NES unlocked, (e) second floor disp., NES locked (f) second floor disp., NES unlocked, (g) ground accel., NES locked, and (h) ground accel., NES unlocked

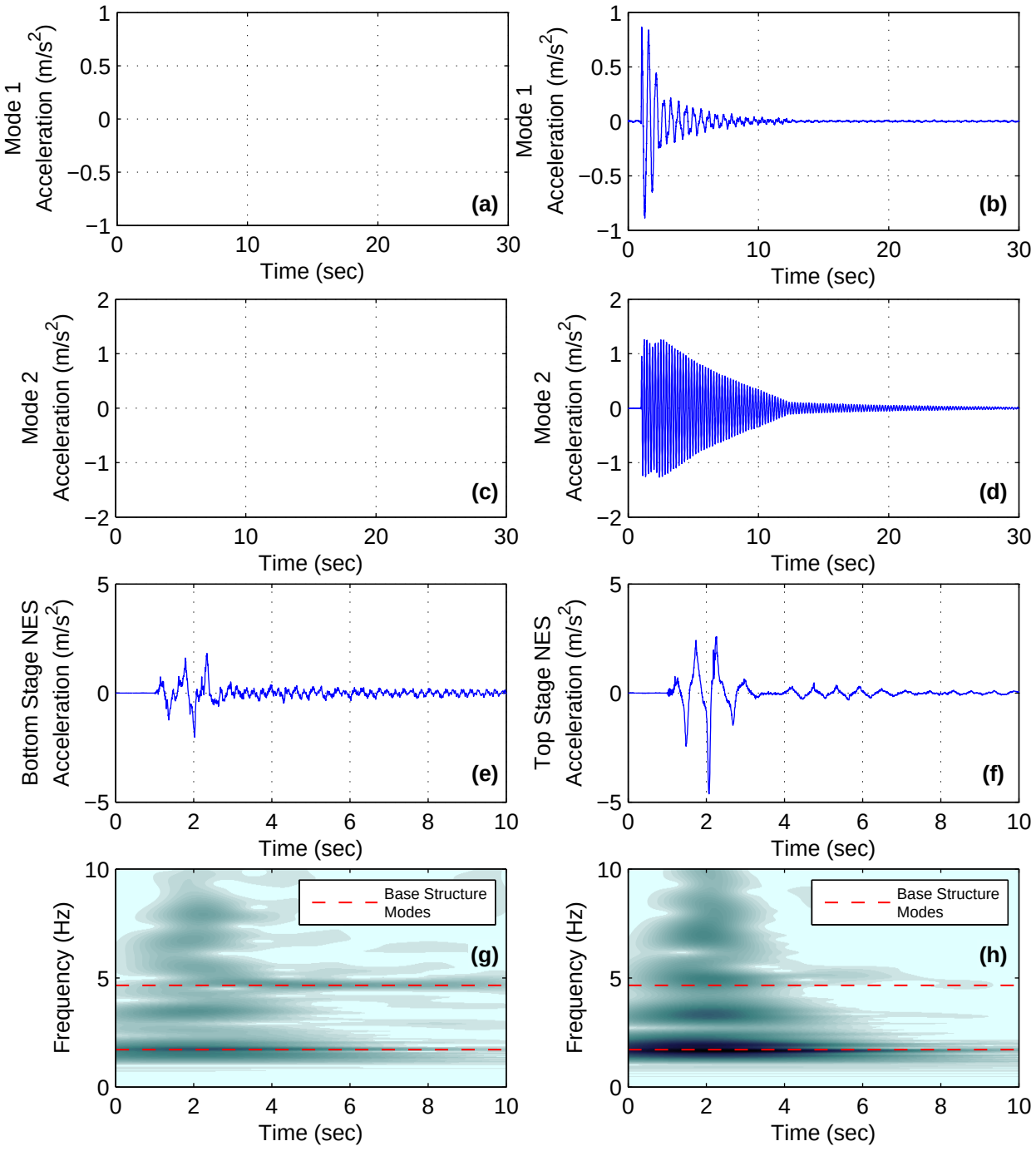

Figure C-12. Response of system with small-scale Type III NES to ground motion level 6 (a) mode 1 accel., NES locked, (b) mode 1 accel., NES unlocked, (c) mode 2 accel., NES locked, (d) mode 2 accel., NES unlocked, (e) bottom stage NES accel., NES unlocked (f) top stage NES accel., NES unlocked, (g) wavelet of bottom stage NES accel., NES unlocked, and (f) wavelet of top stage NES accel., NES unlocked

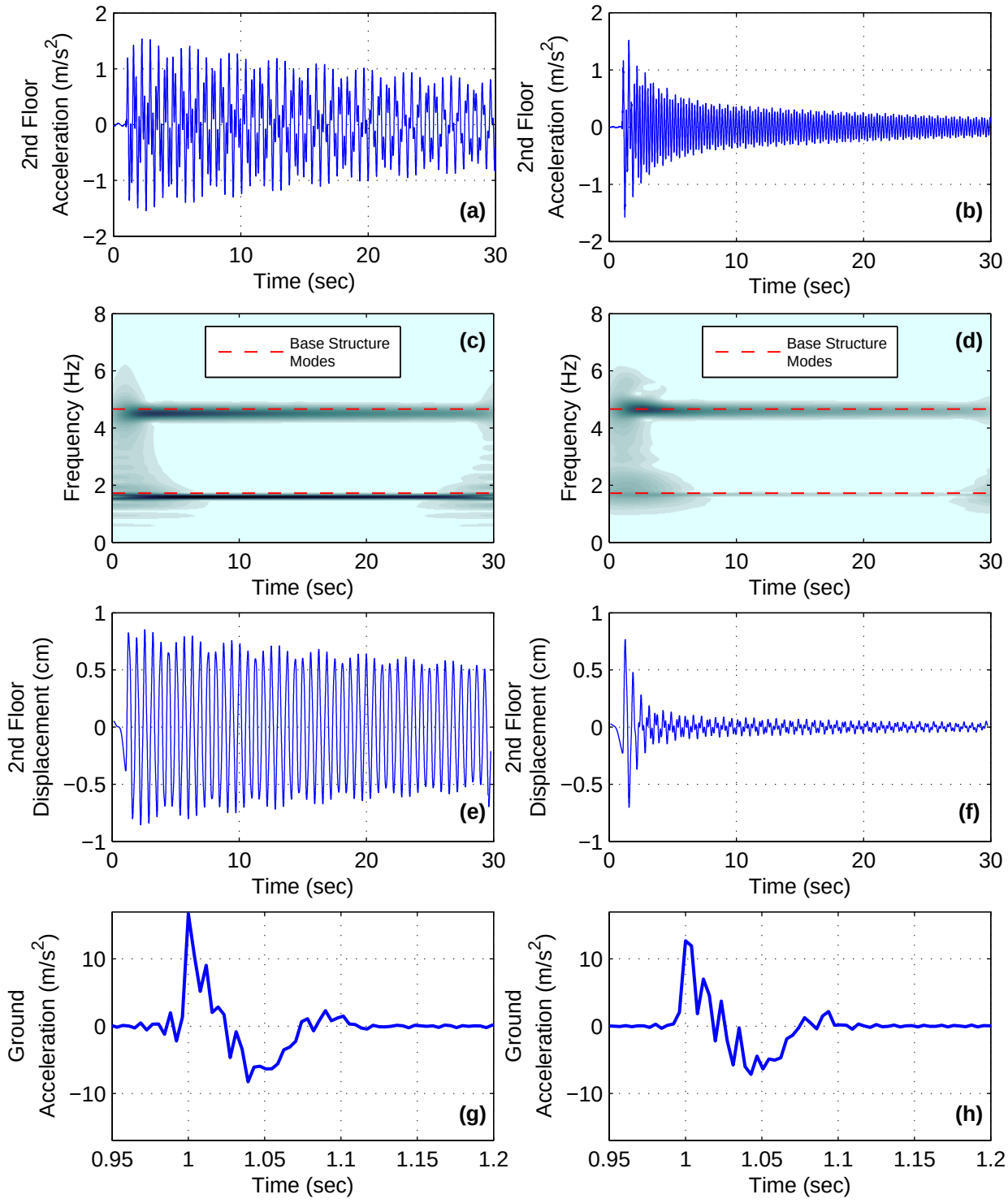

Figure C-13. Response of system with small-scale Type III NES to ground motion level 7 (a) second floor accel., NES locked, (b) second floor accel., NES unlocked, (c) wavelet of second floor accel., NES locked, (d) wavelet of second floor accel., NES unlocked, (e) second floor disp., NES locked (f) second floor disp., NES unlocked, (g) ground accel., NES locked, and (h) ground accel., NES unlocked

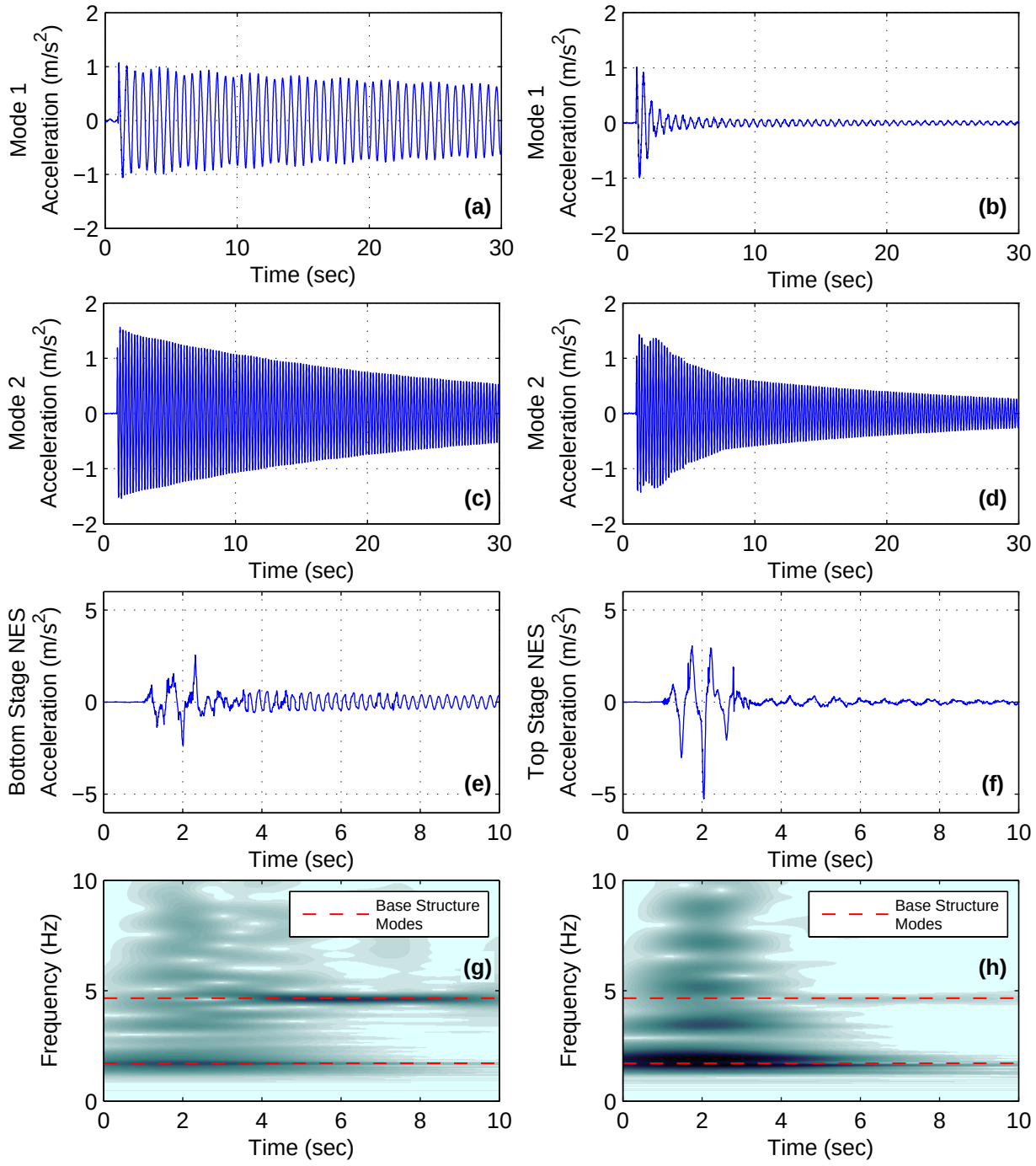

Figure C-14. Response of system with small-scale Type III NES to ground motion level 7 (a) mode 1 accel., NES locked, (b) mode 1 accel., NES unlocked, (c) mode 2 accel., NES locked, (d) mode 2 accel., NES unlocked, (e) bottom stage NES accel., NES unlocked (f) top stage NES accel., NES unlocked, (g) wavelet of bottom stage NES accel., NES unlocked, and (f) wavelet of top stage NES accel., NES unlocked

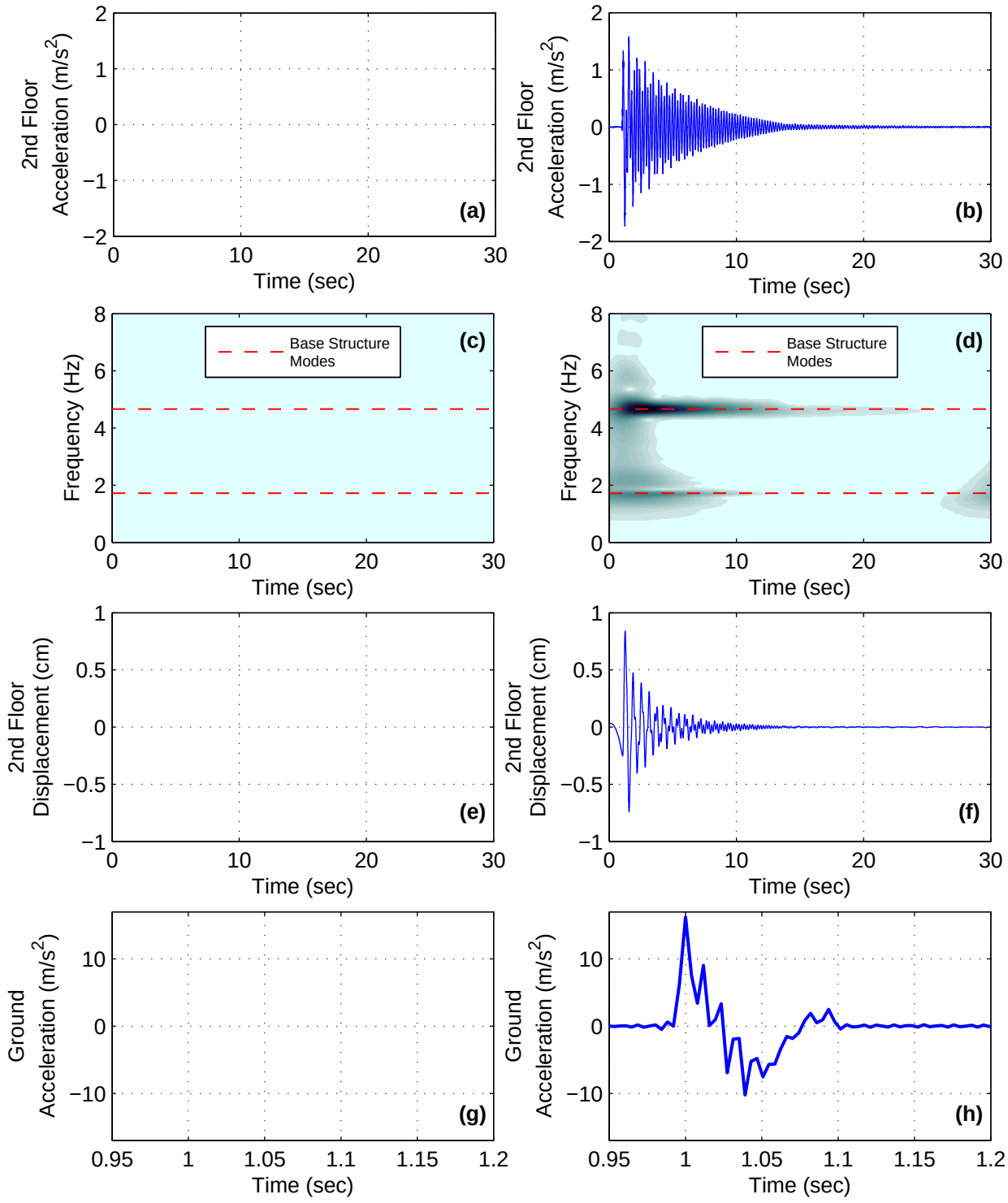

Figure C-15. Response of system with small-scale Type III NES to ground motion level 8 (a) second floor accel., NES locked, (b) second floor accel., NES unlocked, (c) wavelet of second floor accel., NES locked, (d) wavelet of second floor accel., NES unlocked, (e) second floor disp., NES locked (f) second floor disp., NES unlocked, (g) ground accel., NES locked, and (h) ground accel., NES unlocked

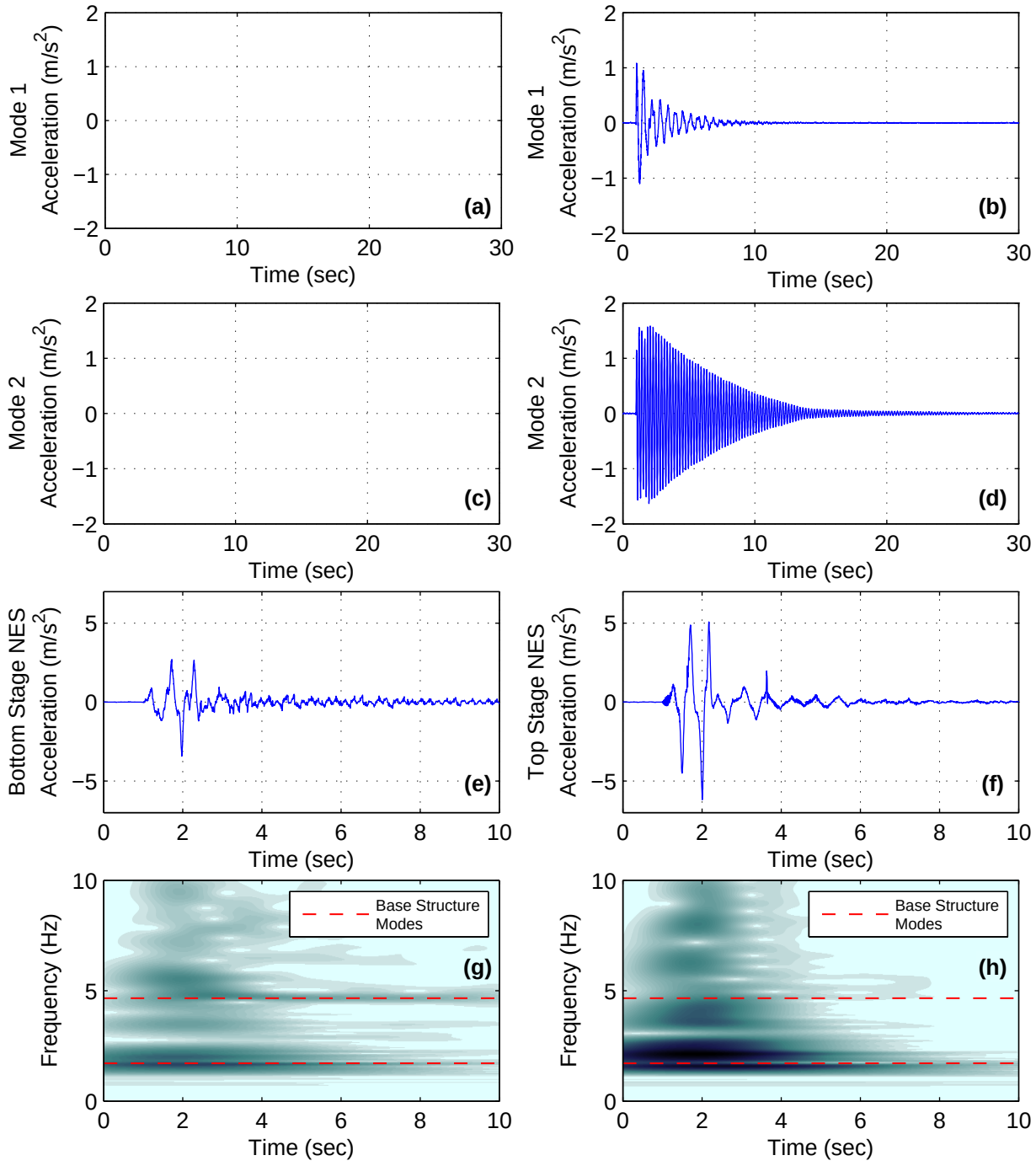

Figure C-16. Response of system with small-scale Type III NES to ground motion level 8 (a) mode 1 accel., NES locked, (b) mode 1 accel., NES unlocked, (c) mode 2 accel., NES locked, (d) mode 2 accel., NES unlocked, (e) bottom stage NES accel., NES unlocked (f) top stage NES accel., NES unlocked, (g) wavelet of bottom stage NES accel., NES unlocked, and (f) wavelet of top stage NES accel., NES unlocked

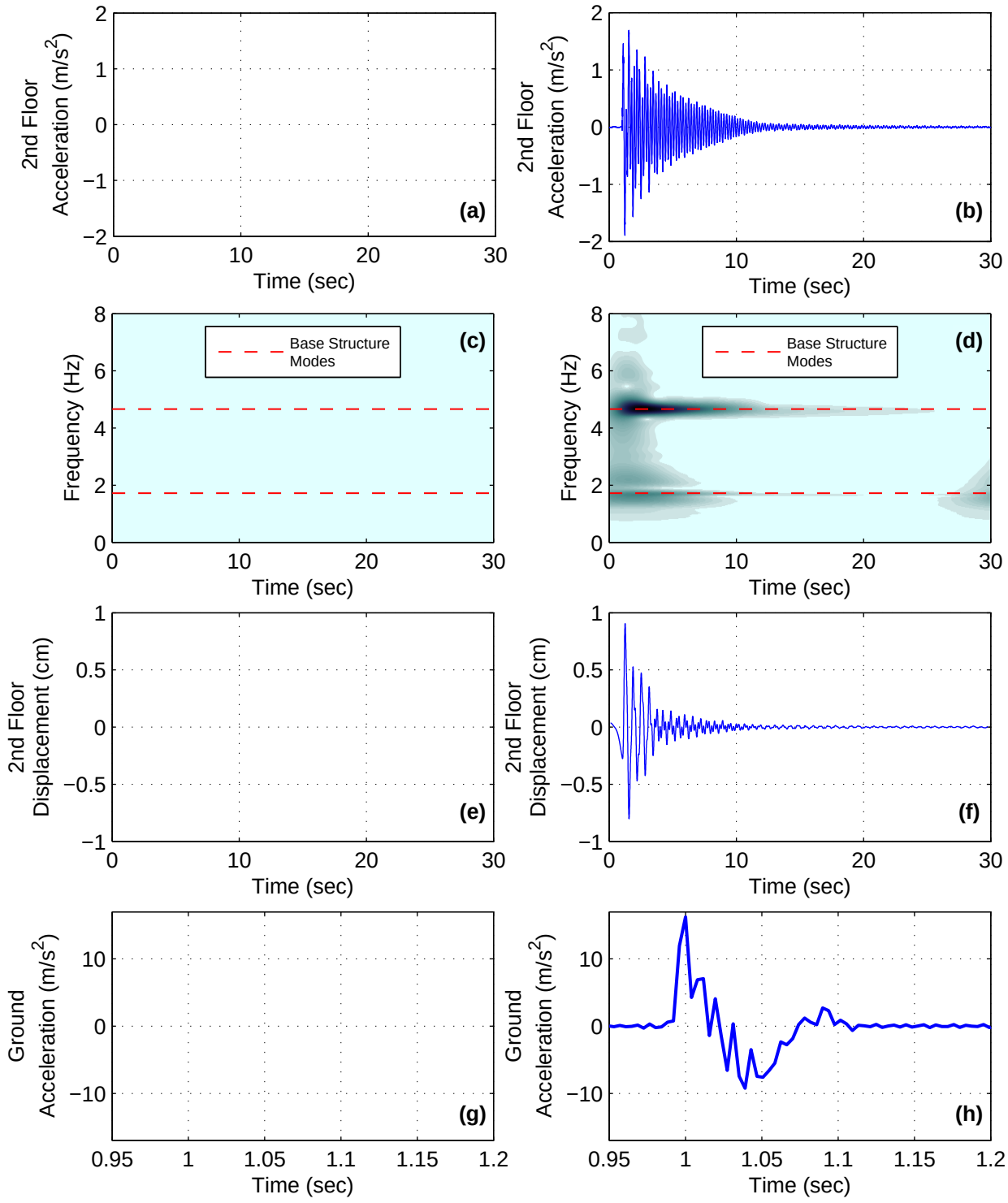

Figure C-17. Response of system with small-scale Type III NES to ground motion level 9 (a) second floor accel., NES locked, (b) second floor accel., NES unlocked, (c) wavelet of second floor accel., NES locked, (d) wavelet of second floor accel., NES unlocked, (e) second floor disp., NES locked (f) second floor disp., NES unlocked, (g) ground accel., NES locked, and (h) ground accel., NES unlocked

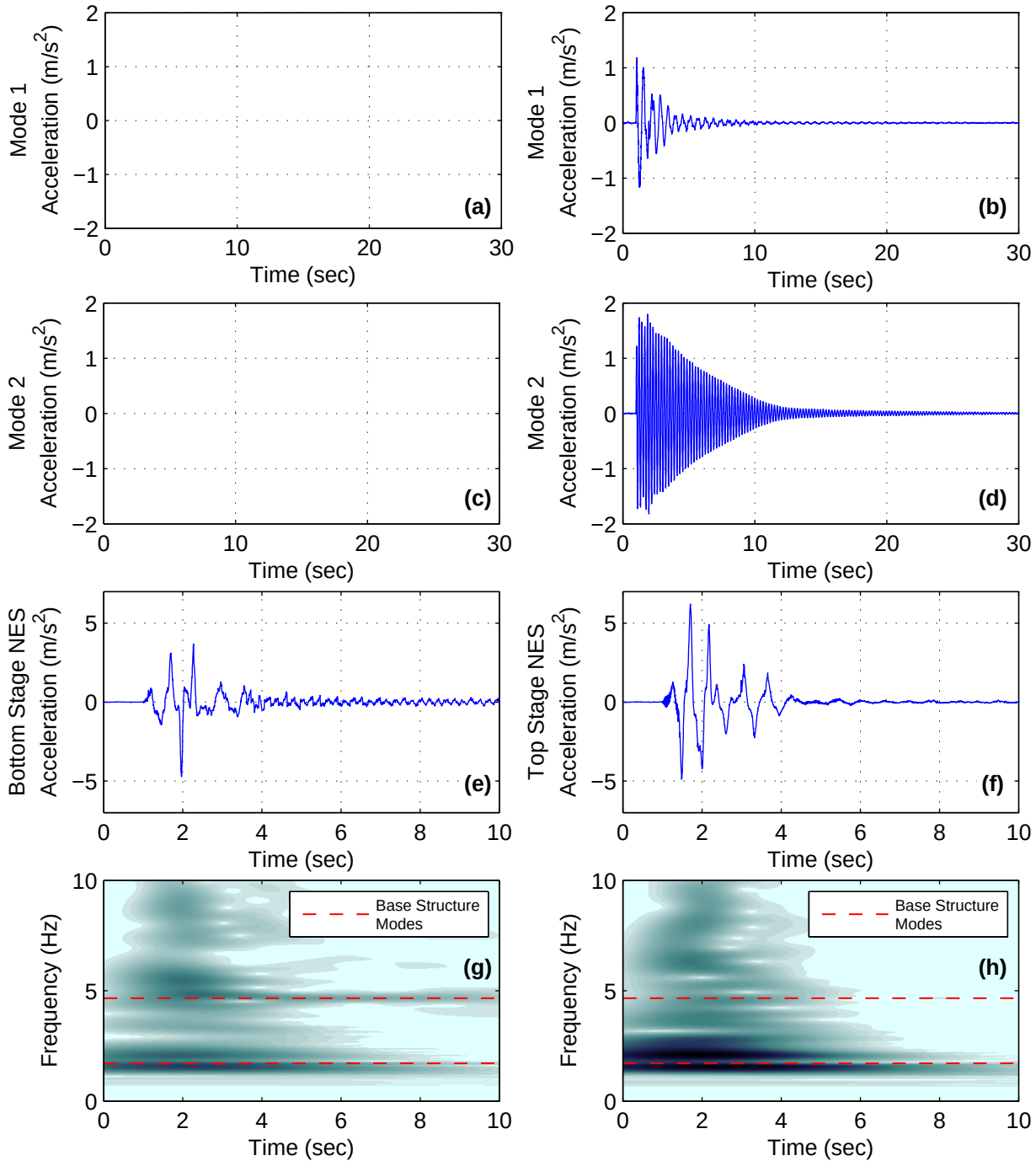

Figure C-18. Response of system with small-scale Type III NES to ground motion level 9 (a) mode 1 accel., NES locked, (b) mode 1 accel., NES unlocked, (c) mode 2 accel., NES locked, (d) mode 2 accel., NES unlocked, (e) bottom stage NES accel., NES unlocked (f) top stage NES accel., NES unlocked, (g) wavelet of bottom stage NES accel., NES unlocked, and (f) wavelet of top stage NES accel., NES unlocked

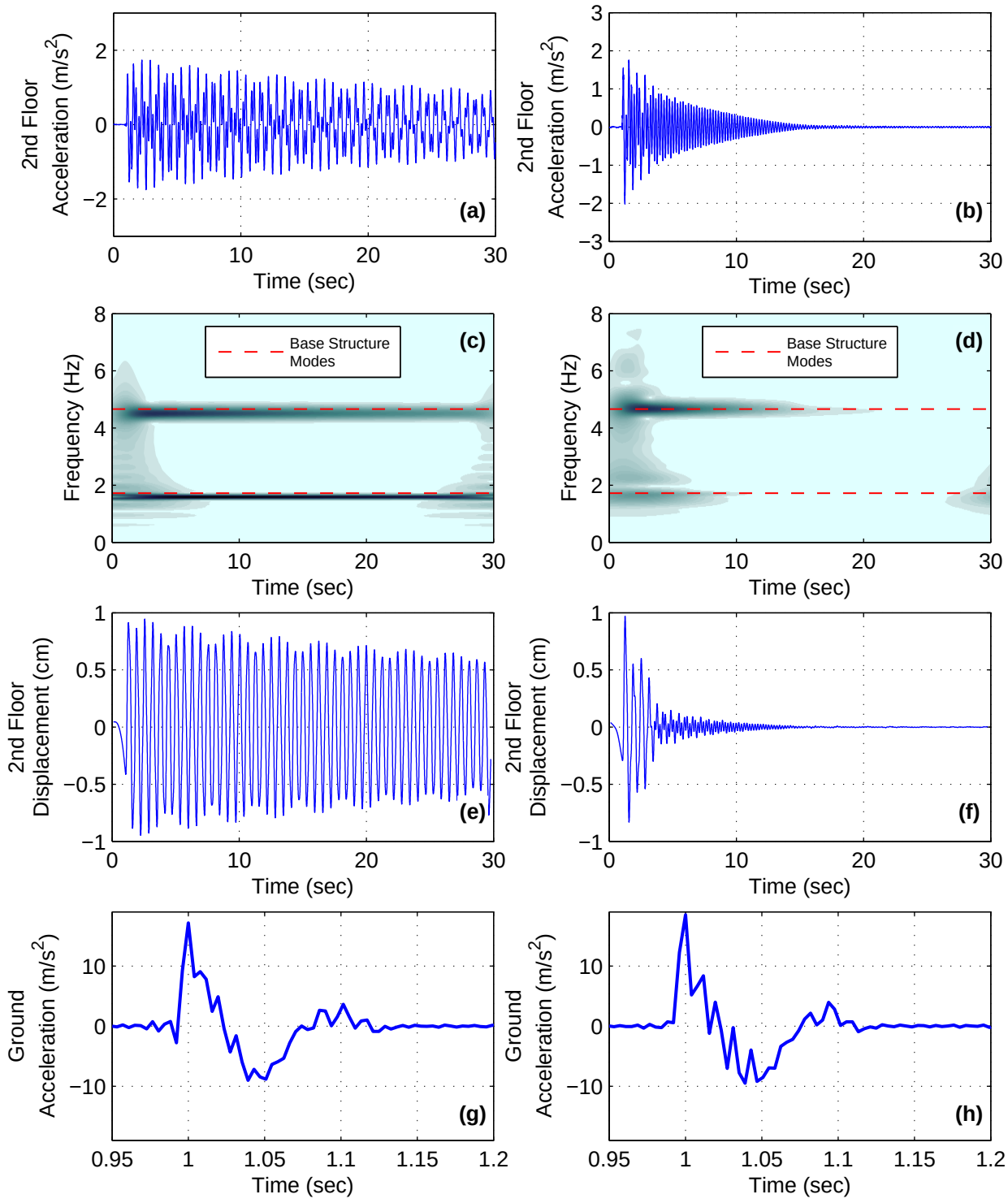

Figure C-19. Response of system with small-scale Type III NES to ground motion level 10 (a) second floor accel., NES locked, (b) second floor accel., NES unlocked, (c) wavelet of second floor accel., NES locked, (d) wavelet of second floor accel., NES unlocked, (e) second floor disp., NES locked (f) second floor disp., NES unlocked, (g) ground accel., NES locked, and (h) ground accel., NES unlocked

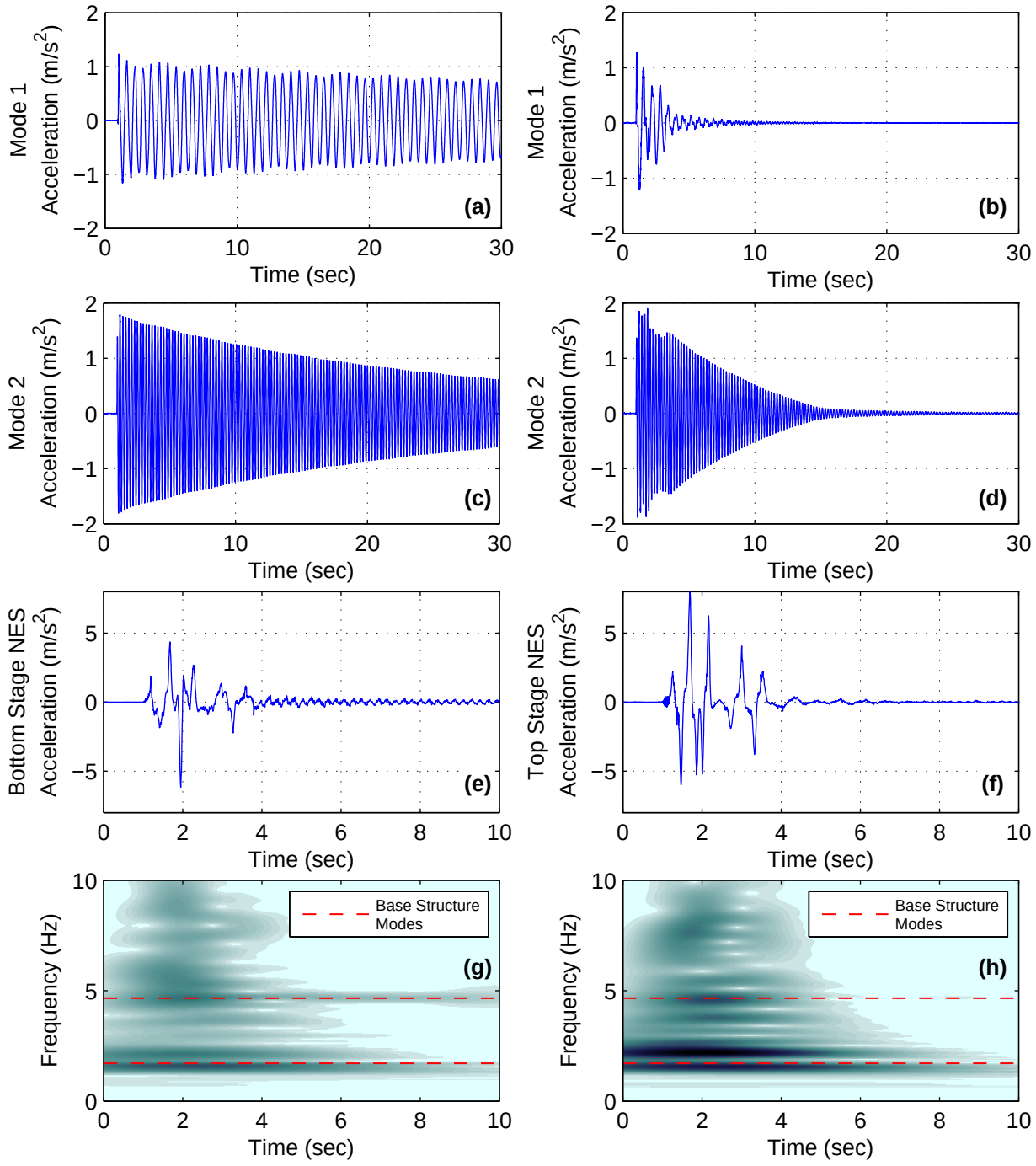

Figure C-20. Response of system with small-scale Type III NES to ground motion level 10 (a) mode 1 accel., NES locked, (b) mode 1 accel., NES unlocked, (c) mode 2 accel., NES locked, (d) mode 2 accel., NES unlocked, (e) bottom stage NES accel., NES unlocked (f) top stage NES accel., NES unlocked, (g) wavelet of bottom stage NES accel., NES unlocked, and (f) wavelet of top stage NES accel., NES unlocked

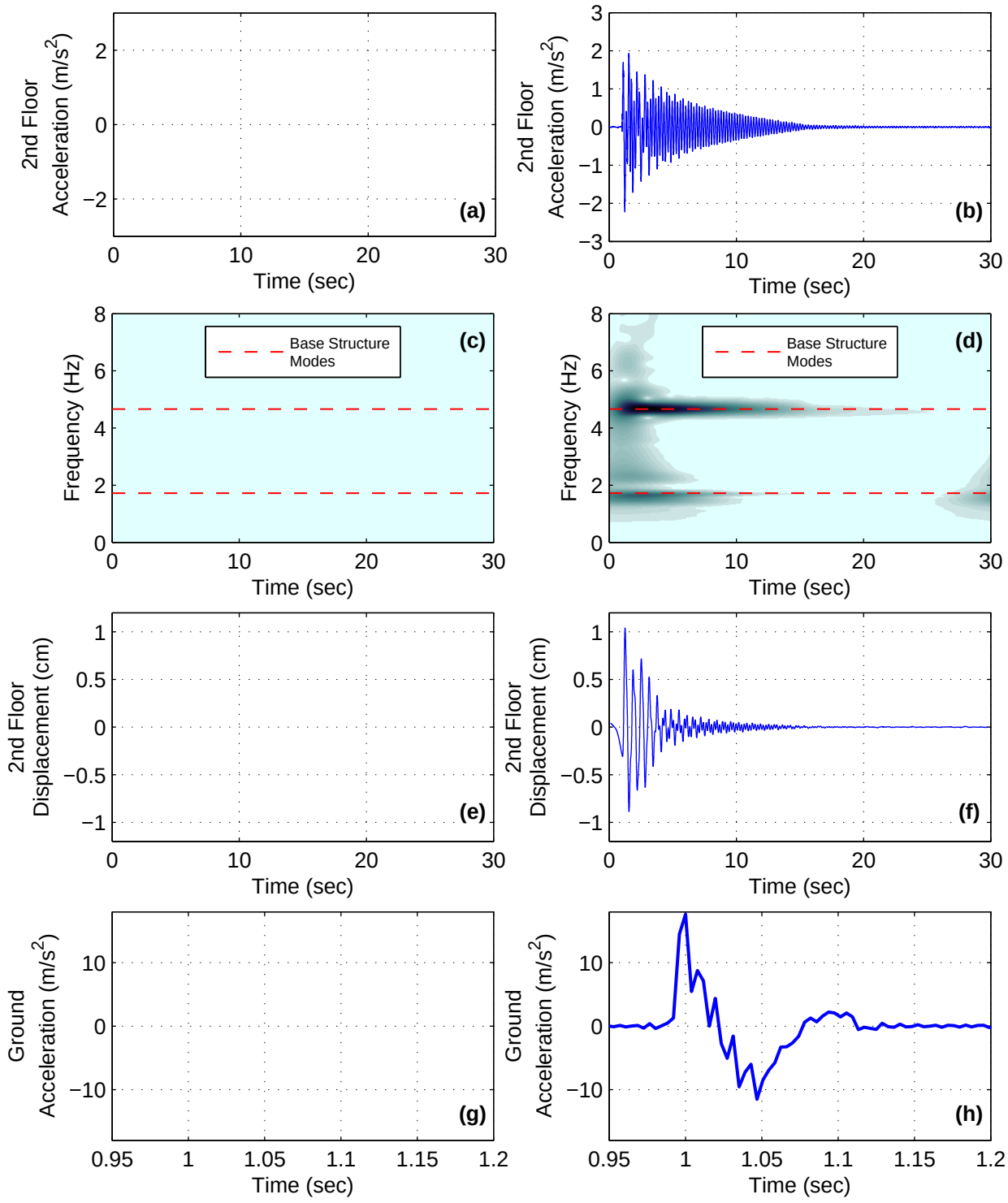

Figure C-21. Response of system with small-scale Type III NES to ground motion level 11 (a) second floor accel., NES locked, (b) second floor accel., NES unlocked, (c) wavelet of second floor accel., NES locked, (d) wavelet of second floor accel., NES unlocked, (e) second floor disp., NES locked (f) second floor disp., NES unlocked, (g) ground accel., NES locked, and (h) ground accel., NES unlocked

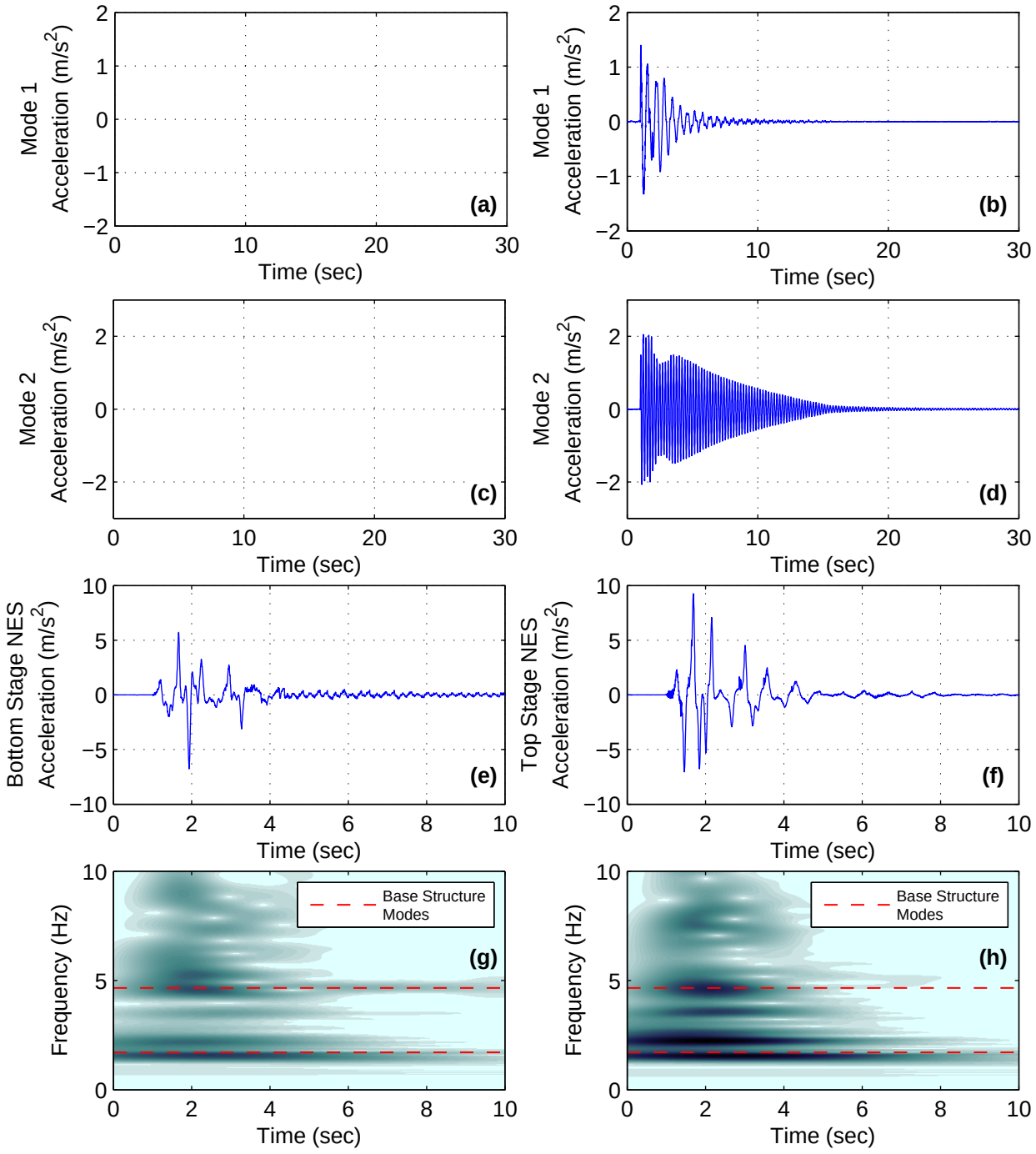

Figure C-22. Response of system with small-scale Type III NES to ground motion level 11 (a) mode 1 accel., NES locked, (b) mode 1 accel., NES unlocked, (c) mode 2 accel., NES locked, (d) mode 2 accel., NES unlocked, (e) bottom stage NES accel., NES unlocked (f) top stage NES accel., NES unlocked, (g) wavelet of bottom stage NES accel., NES unlocked, and (f) wavelet of top stage NES accel., NES unlocked

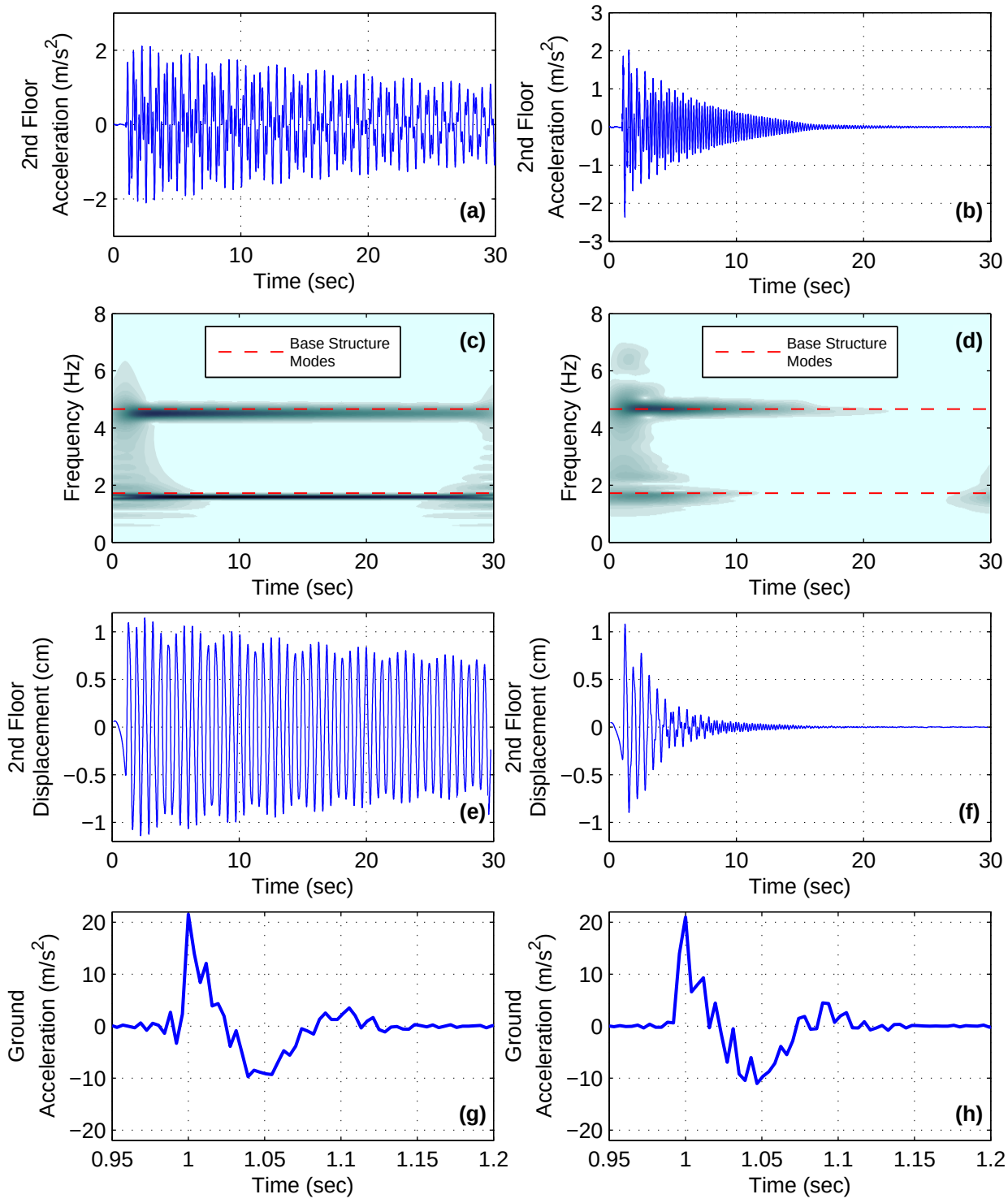

Figure C-23. Response of system with small-scale Type III NES to ground motion level 12 (a) second floor accel., NES locked, (b) second floor accel., NES unlocked, (c) wavelet of second floor accel., NES locked, (d) wavelet of second floor accel., NES unlocked, (e) second floor disp., NES locked (f) second floor disp., NES unlocked, (g) ground accel., NES locked, and (h) ground accel., NES unlocked

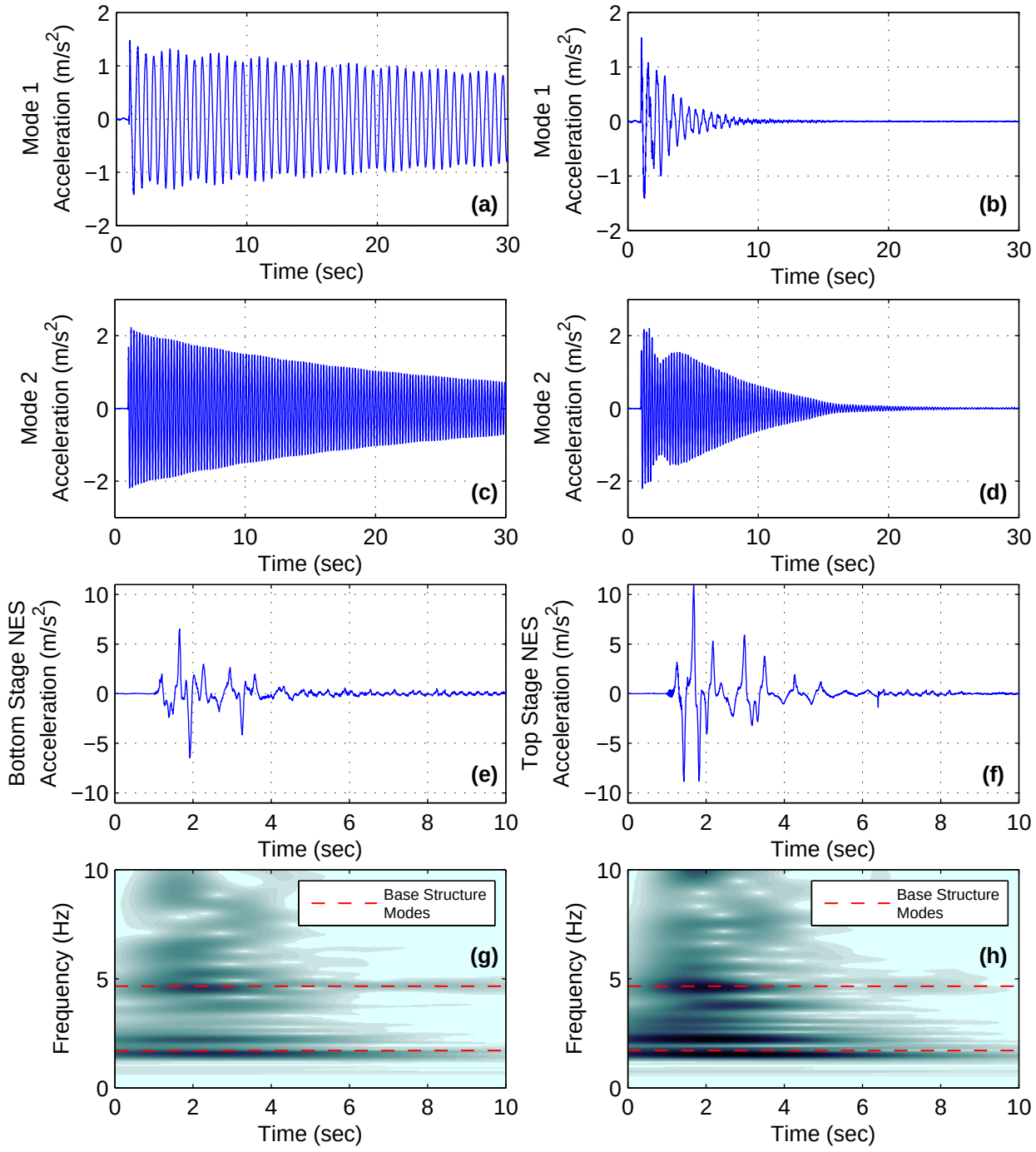

Figure C-24. Response of system with small-scale Type III NES to ground motion level 12 (a) mode 1 accel., NES locked, (b) mode 1 accel., NES unlocked, (c) mode 2 accel., NES locked, (d) mode 2 accel., NES unlocked, (e) bottom stage NES accel., NES unlocked (f) top stage NES accel., NES unlocked, (g) wavelet of bottom stage NES accel., NES unlocked, and (f) wavelet of top stage NES accel., NES unlocked

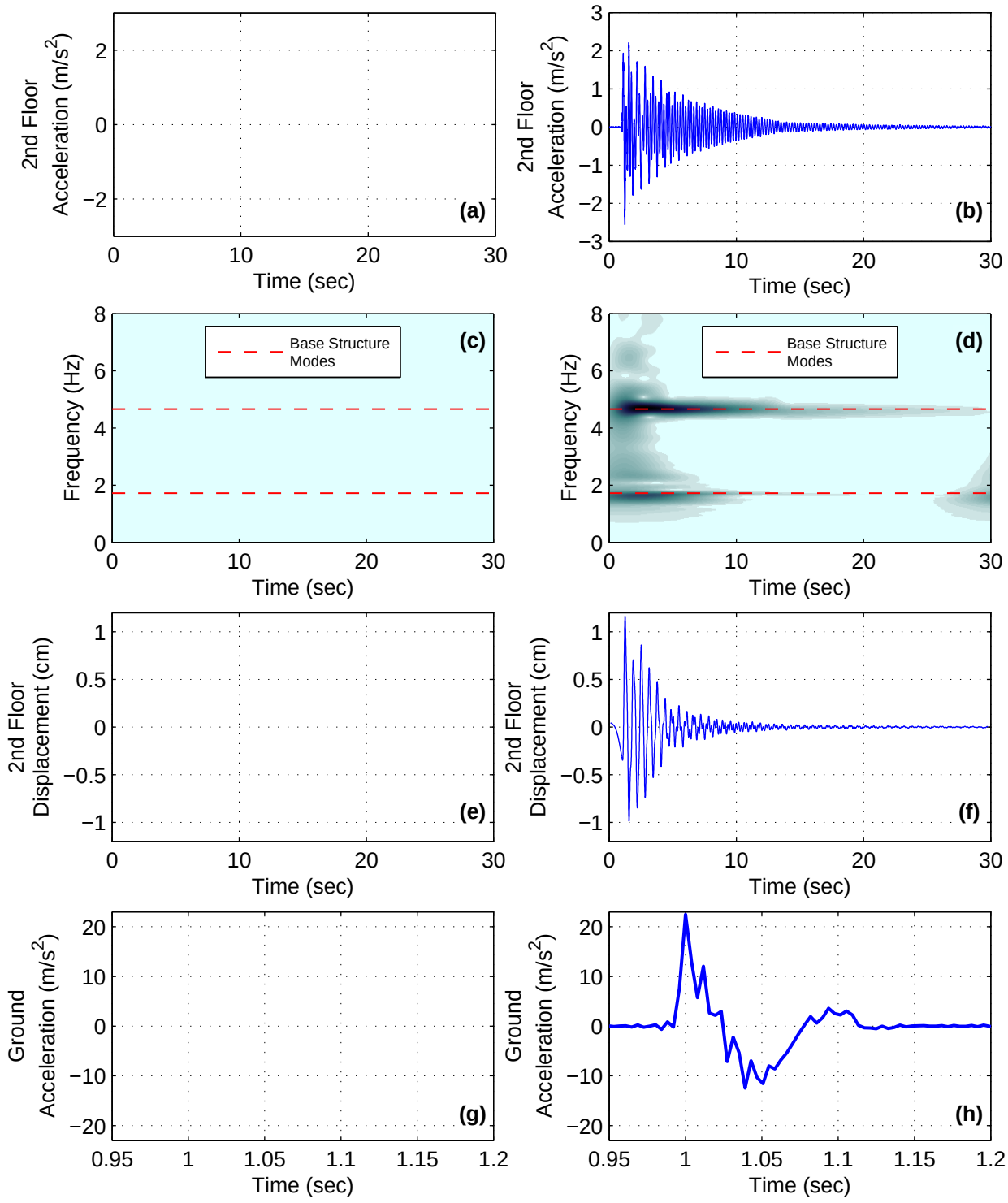

Figure C-25. Response of system with small-scale Type III NES to ground motion level 13 (a) second floor accel., NES locked, (b) second floor accel., NES unlocked, (c) wavelet of second floor accel., NES locked, (d) wavelet of second floor accel., NES unlocked, (e) second floor disp., NES locked (f) second floor disp., NES unlocked, (g) ground accel., NES locked, and (h) ground accel., NES unlocked

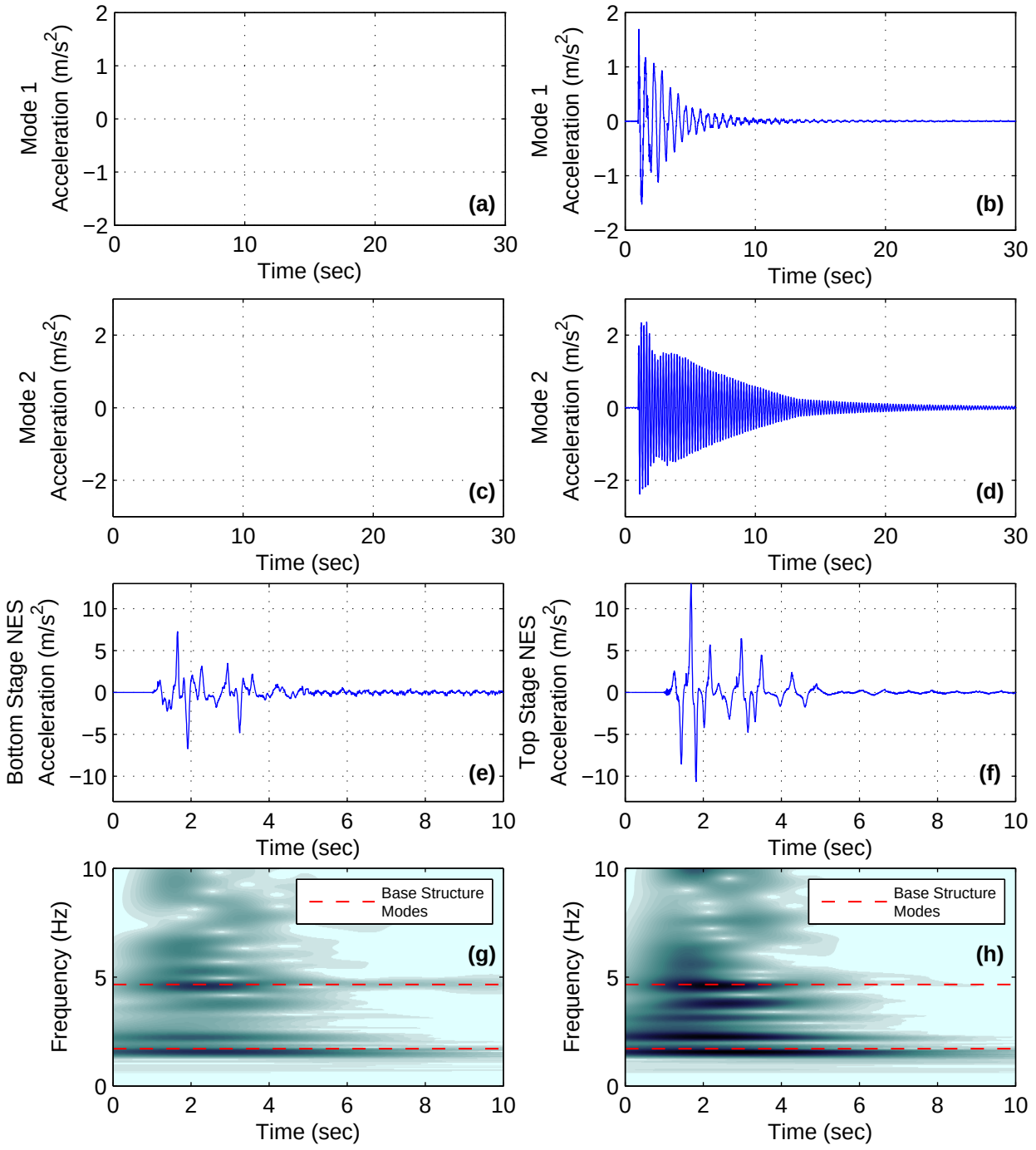

Figure C-26. Response of system with small-scale Type III NES to ground motion level 13 (a) mode 1 accel., NES locked, (b) mode 1 accel., NES unlocked, (c) mode 2 accel., NES locked, (d) mode 2 accel., NES unlocked, (e) bottom stage NES accel., NES unlocked (f) top stage NES accel., NES unlocked, (g) wavelet of bottom stage NES accel., NES unlocked, and (f) wavelet of top stage NES accel., NES unlocked

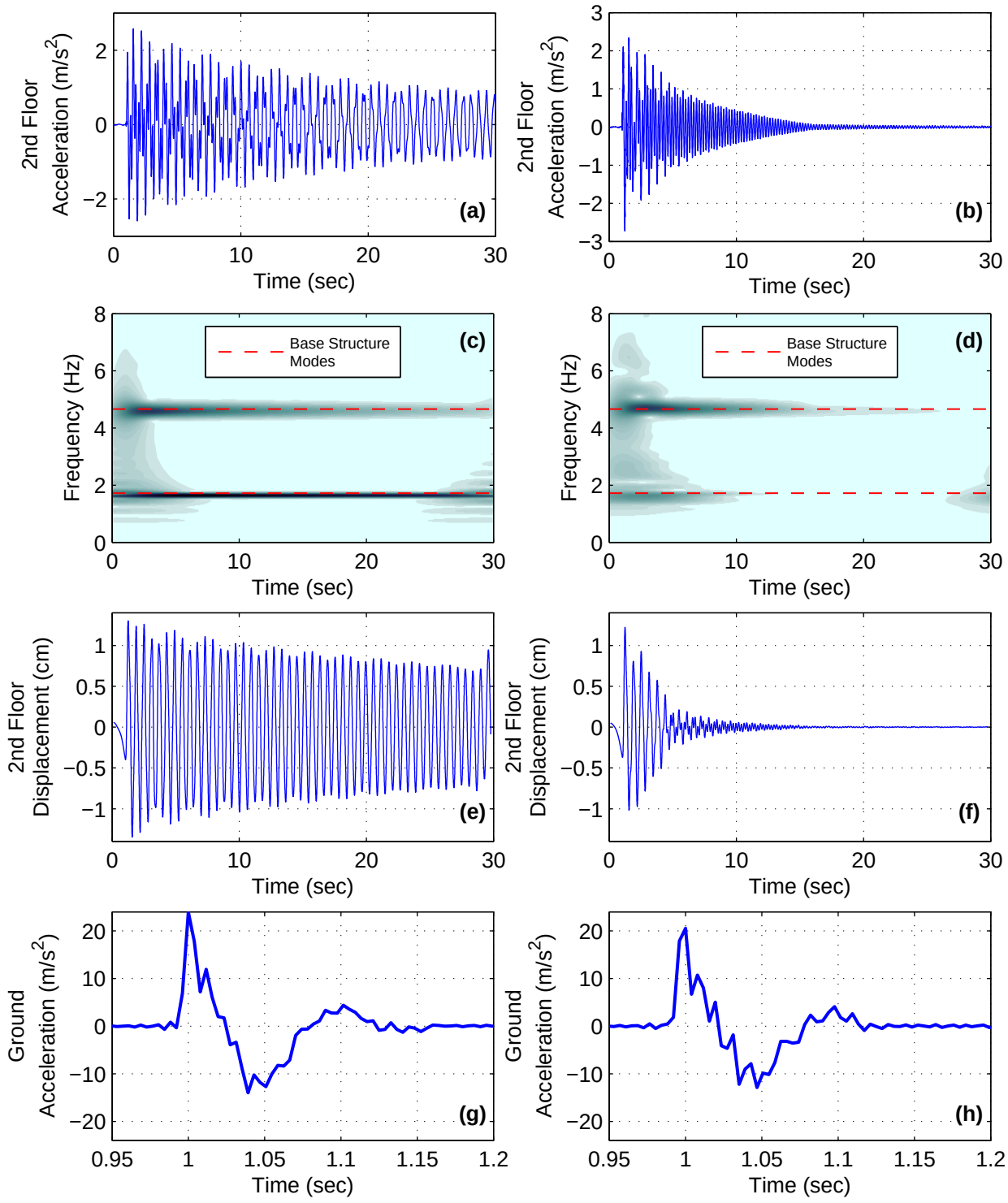

Figure C-27. Response of system with small-scale Type III NES to ground motion level 14 (a) second floor accel., NES locked, (b) second floor accel., NES unlocked, (c) wavelet of second floor accel., NES locked, (d) wavelet of second floor accel., NES unlocked, (e) second floor disp., NES locked (f) second floor disp., NES unlocked, (g) ground accel., NES locked, and (h) ground accel., NES unlocked

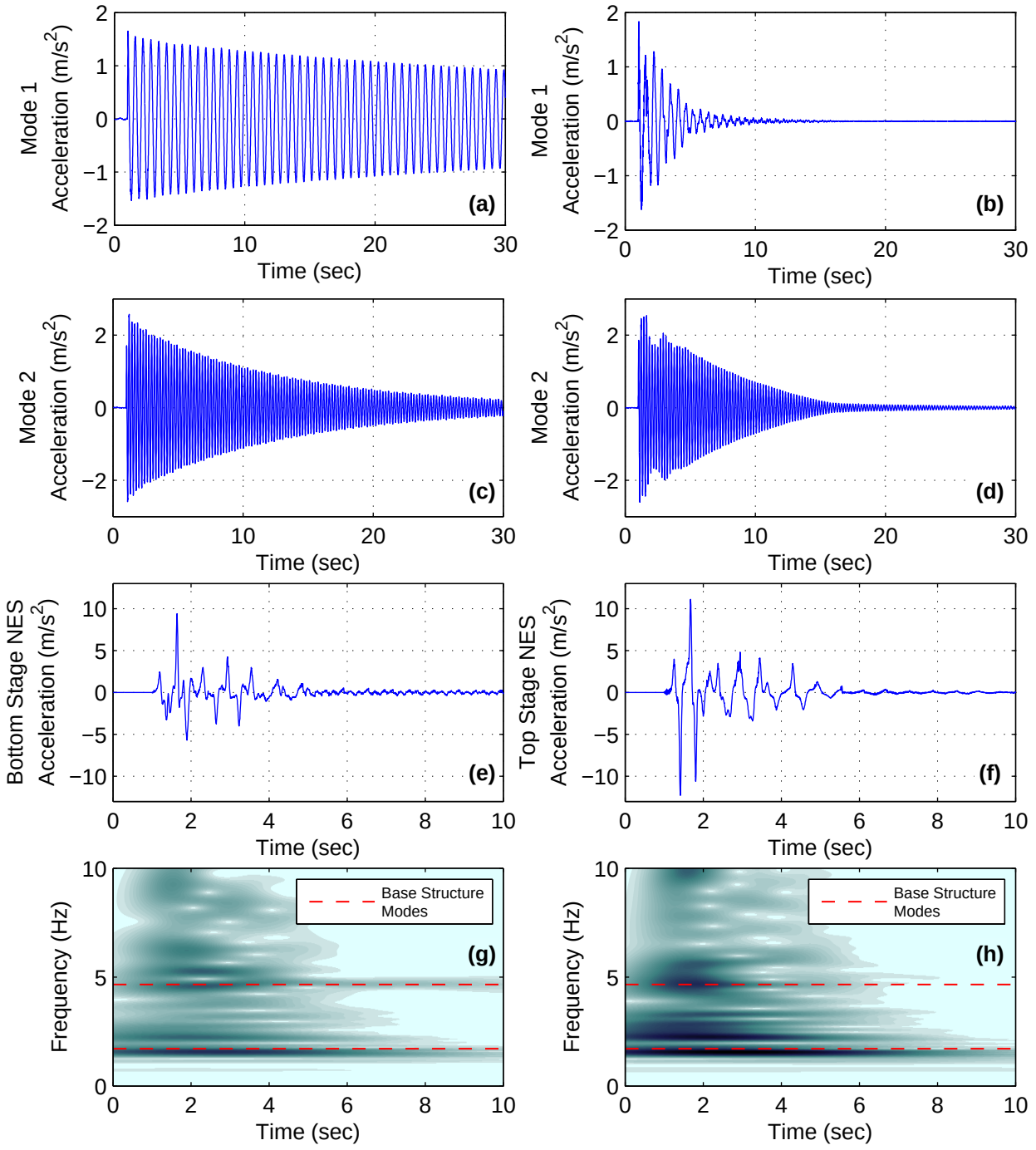

Figure C-28. Response of system with small-scale Type III NES to ground motion level 14 (a) mode 1 accel., NES locked, (b) mode 1 accel., NES unlocked, (c) mode 2 accel., NES locked, (d) mode 2 accel., NES unlocked, (e) bottom stage NES accel., NES unlocked (f) top stage NES accel., NES unlocked, (g) wavelet of bottom stage NES accel., NES unlocked, and (f) wavelet of top stage NES accel., NES unlocked

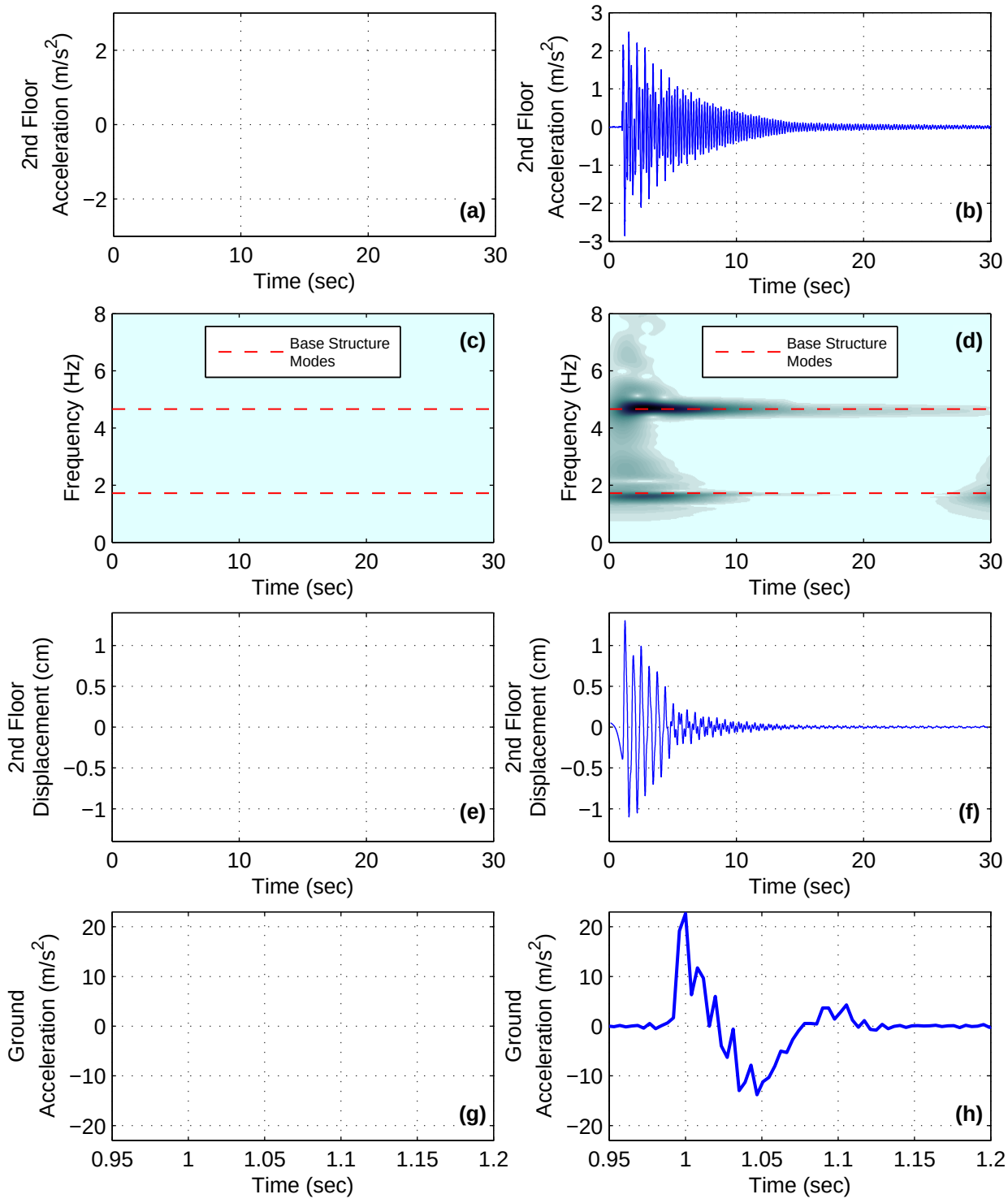

Figure C-29. Response of system with small-scale Type III NES to ground motion level 15 (a) second floor accel., NES locked, (b) second floor accel., NES unlocked, (c) wavelet of second floor accel., NES locked, (d) wavelet of second floor accel., NES unlocked, (e) second floor disp., NES locked (f) second floor disp., NES unlocked, (g) ground accel., NES locked, and (h) ground accel., NES unlocked

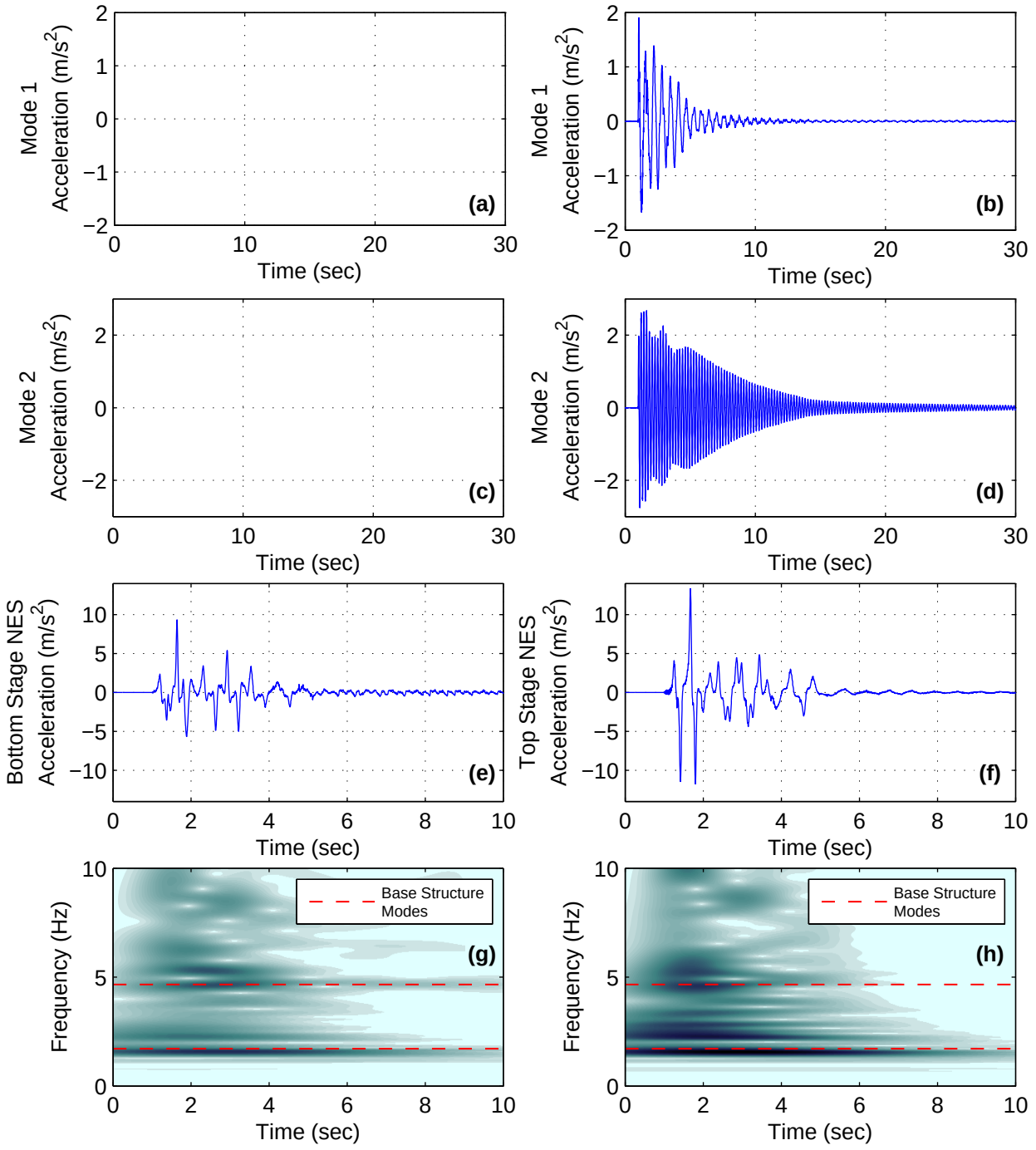

Figure C-30. Response of system with small-scale Type III NES to ground motion level 15 (a) mode 1 accel., NES locked, (b) mode 1 accel., NES unlocked, (c) mode 2 accel., NES locked, (d) mode 2 accel., NES unlocked, (e) bottom stage NES accel., NES unlocked (f) top stage NES accel., NES unlocked, (g) wavelet of bottom stage NES accel., NES unlocked, and (f) wavelet of top stage NES accel., NES unlocked

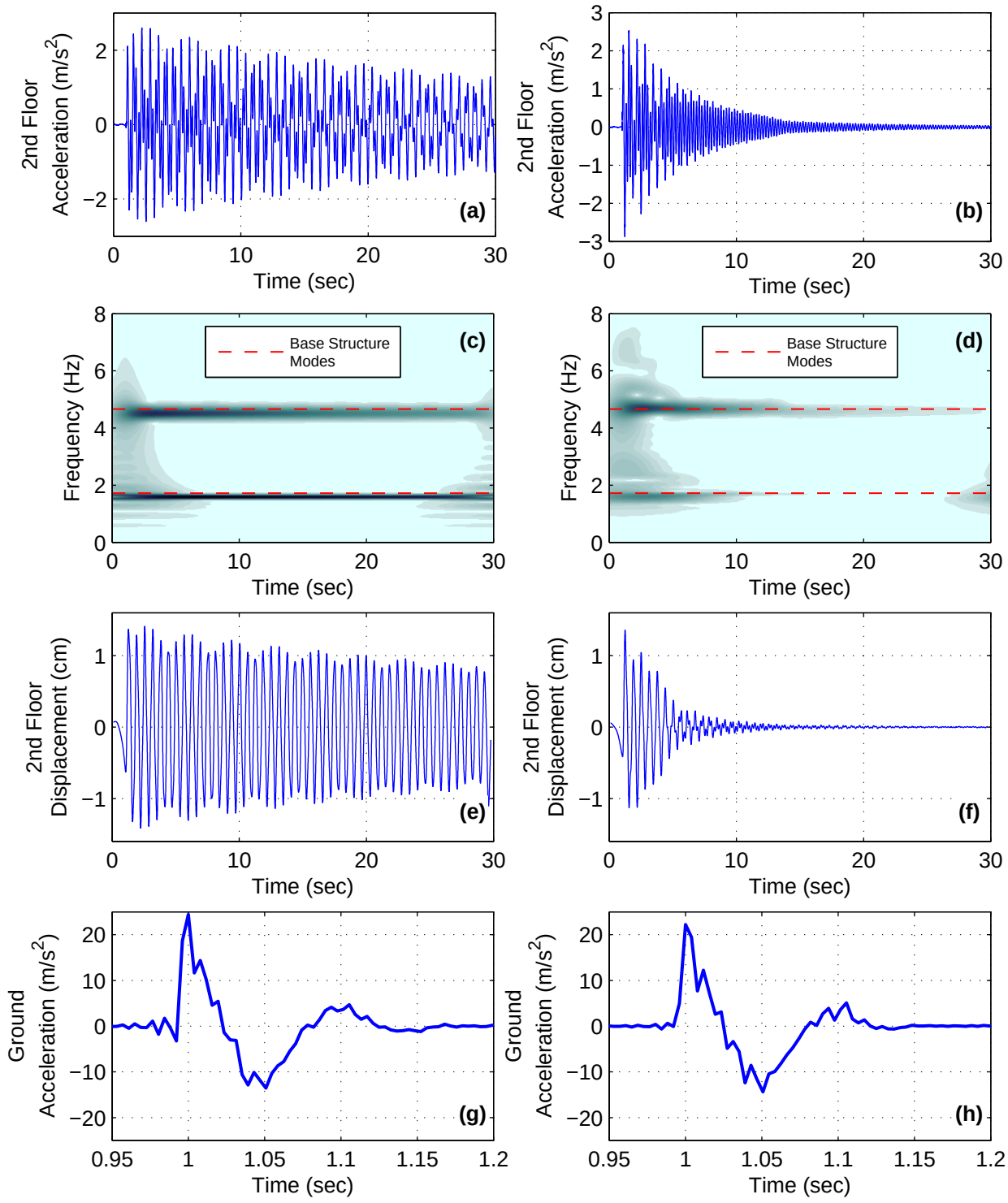

Figure C-31. Response of system with small-scale Type III NES to ground motion level 16 (a) second floor accel., NES locked, (b) second floor accel., NES unlocked, (c) wavelet of second floor accel., NES locked, (d) wavelet of second floor accel., NES unlocked, (e) second floor disp., NES locked (f) second floor disp., NES unlocked, (g) ground accel., NES locked, and (h) ground accel., NES unlocked

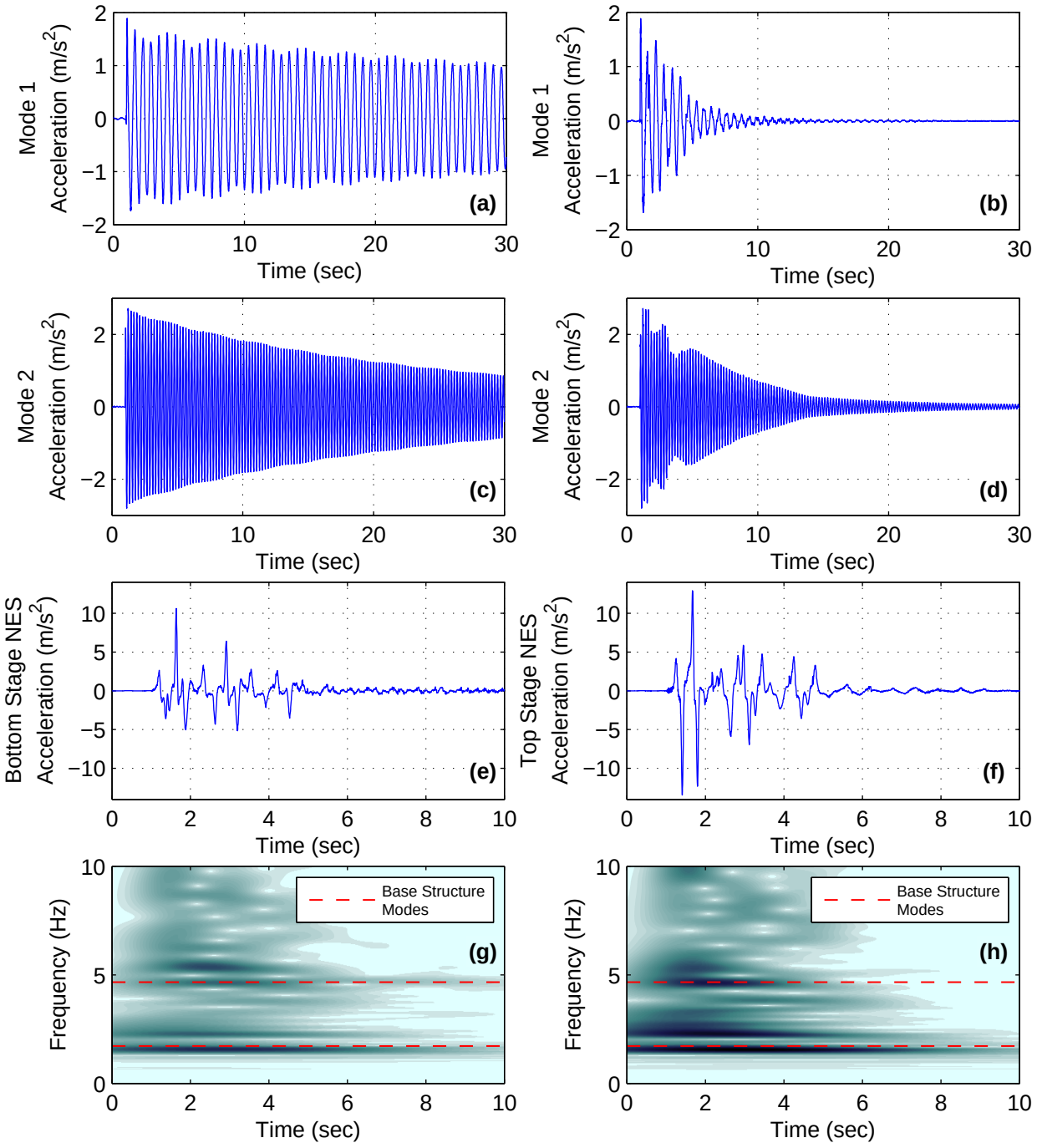

Figure C-32. Response of system with small-scale Type III NES to ground motion level 16 (a) mode 1 accel., NES locked, (b) mode 1 accel., NES unlocked, (c) mode 2 accel., NES locked, (d) mode 2 accel., NES unlocked, (e) bottom stage NES accel., NES unlocked (f) top stage NES accel., NES unlocked, (g) wavelet of bottom stage NES accel., NES unlocked, and (f) wavelet of top stage NES accel., NES unlocked

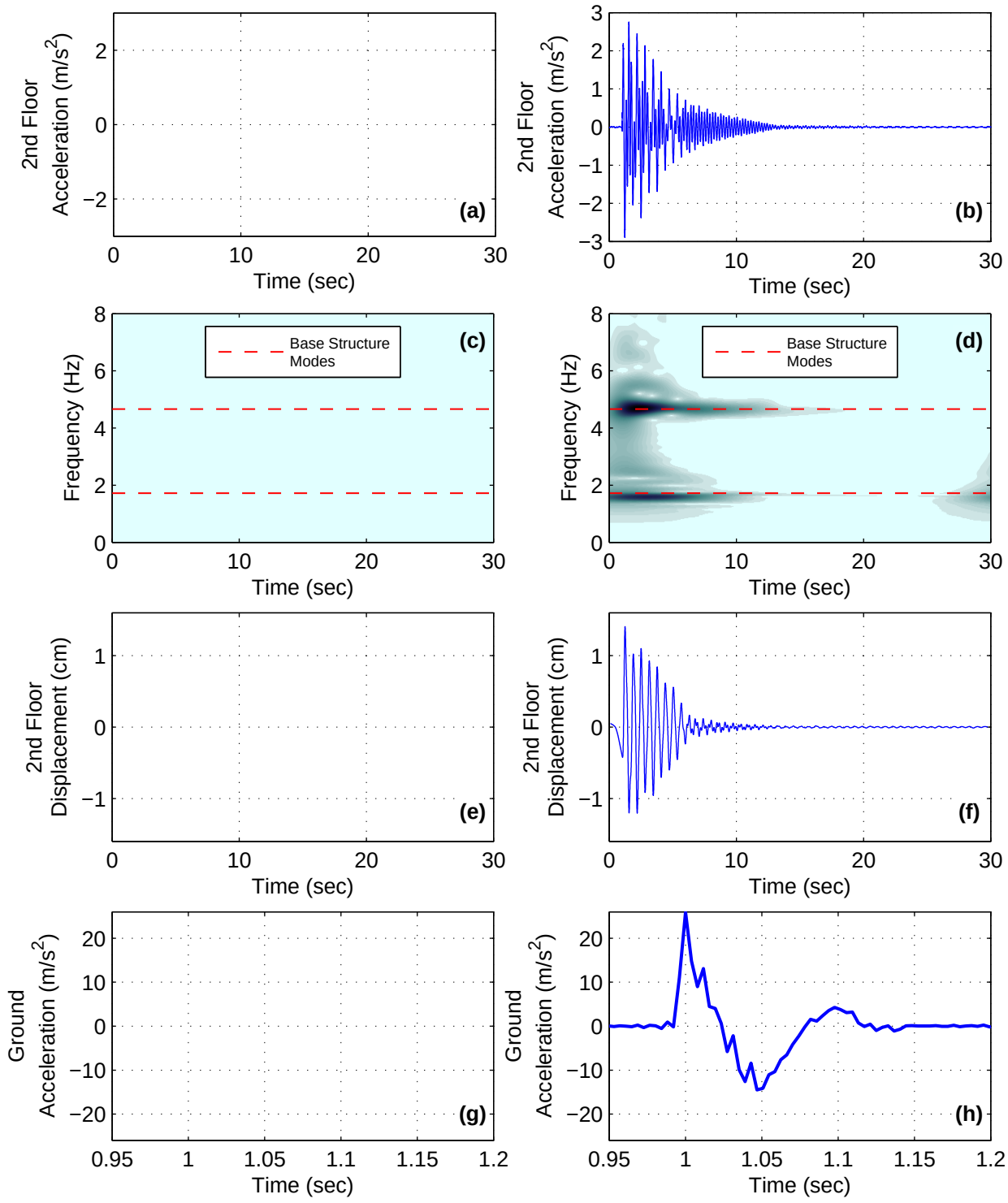

Figure C-33. Response of system with small-scale Type III NES to ground motion level 17 (a) second floor accel., NES locked, (b) second floor accel., NES unlocked, (c) wavelet of second floor accel., NES locked, (d) wavelet of second floor accel., NES unlocked, (e) second floor disp., NES locked (f) second floor disp., NES unlocked, (g) ground accel., NES locked, and (h) ground accel., NES unlocked

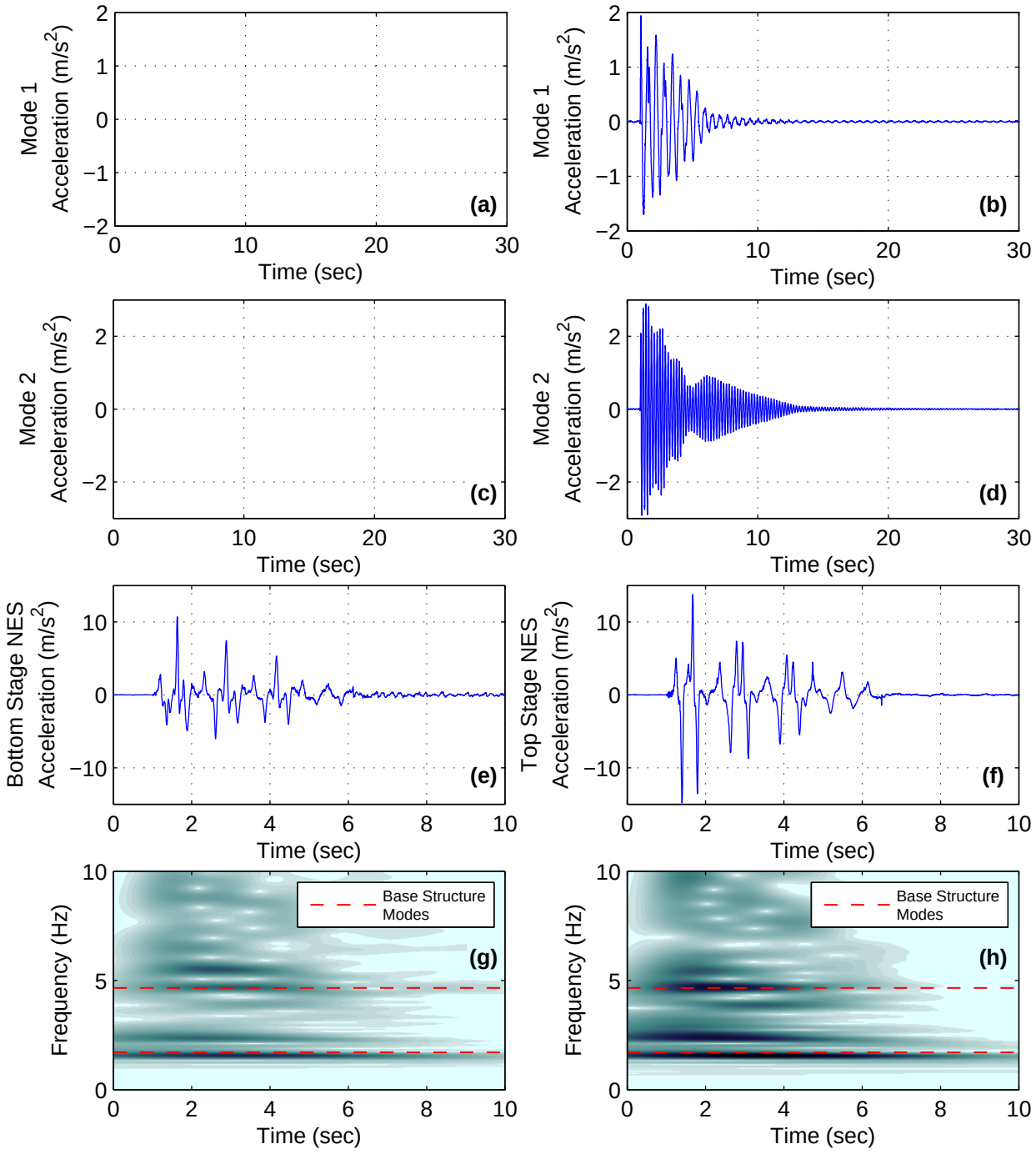

Figure C-34. Response of system with small-scale Type III NES to ground motion level 17 (a) mode 1 accel., NES locked, (b) mode 1 accel., NES unlocked, (c) mode 2 accel., NES locked, (d) mode 2 accel., NES unlocked, (e) bottom stage NES accel., NES unlocked (f) top stage NES accel., NES unlocked, (g) wavelet of bottom stage NES accel., NES unlocked, and (f) wavelet of top stage NES accel., NES unlocked

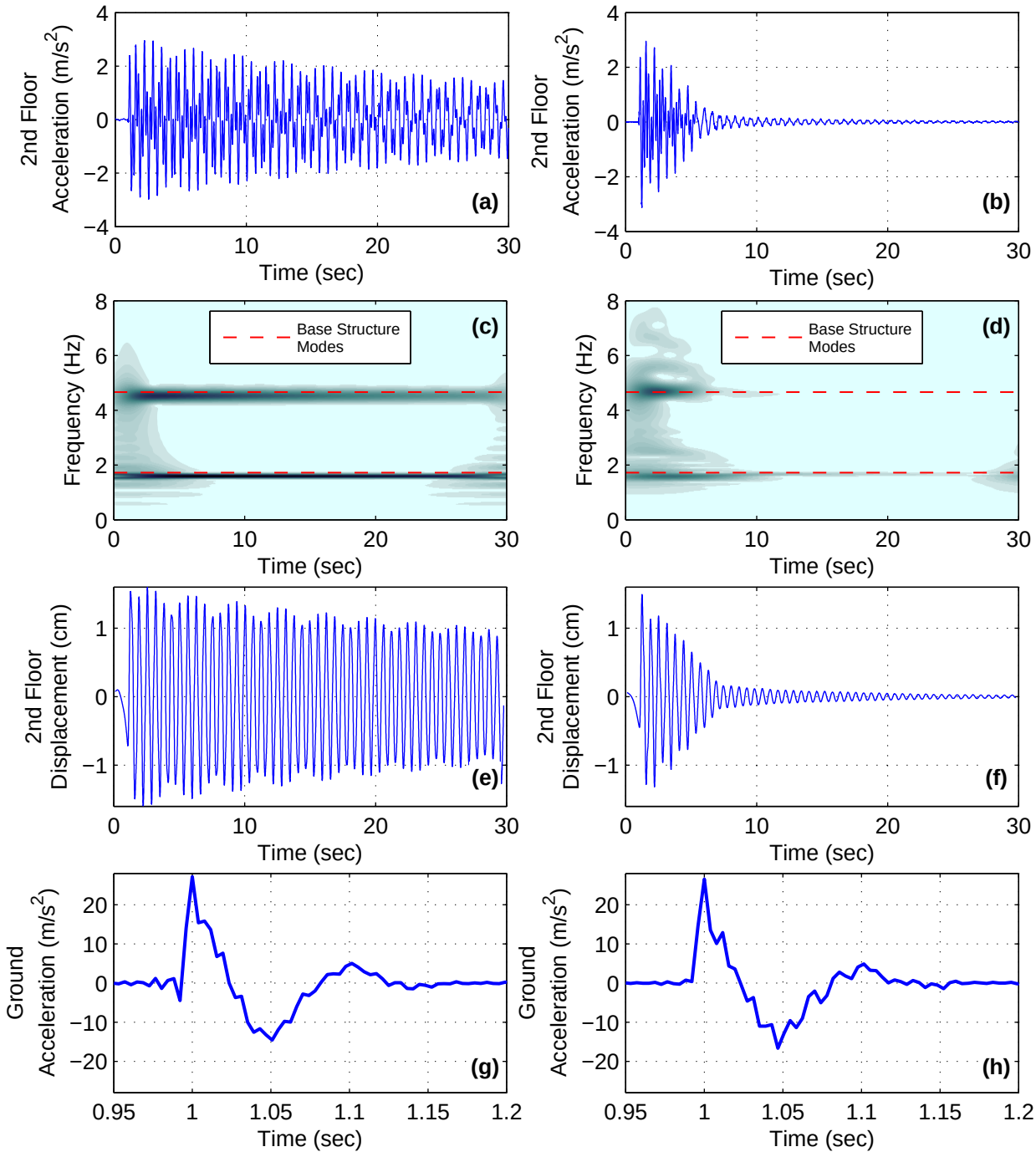

Figure C-35. Response of system with small-scale Type III NES to ground motion level 18 (a) second floor accel., NES locked, (b) second floor accel., NES unlocked, (c) wavelet of second floor accel., NES locked, (d) wavelet of second floor accel., NES unlocked, (e) second floor disp., NES locked (f) second floor disp., NES unlocked, (g) ground accel., NES locked, and (h) ground accel., NES unlocked

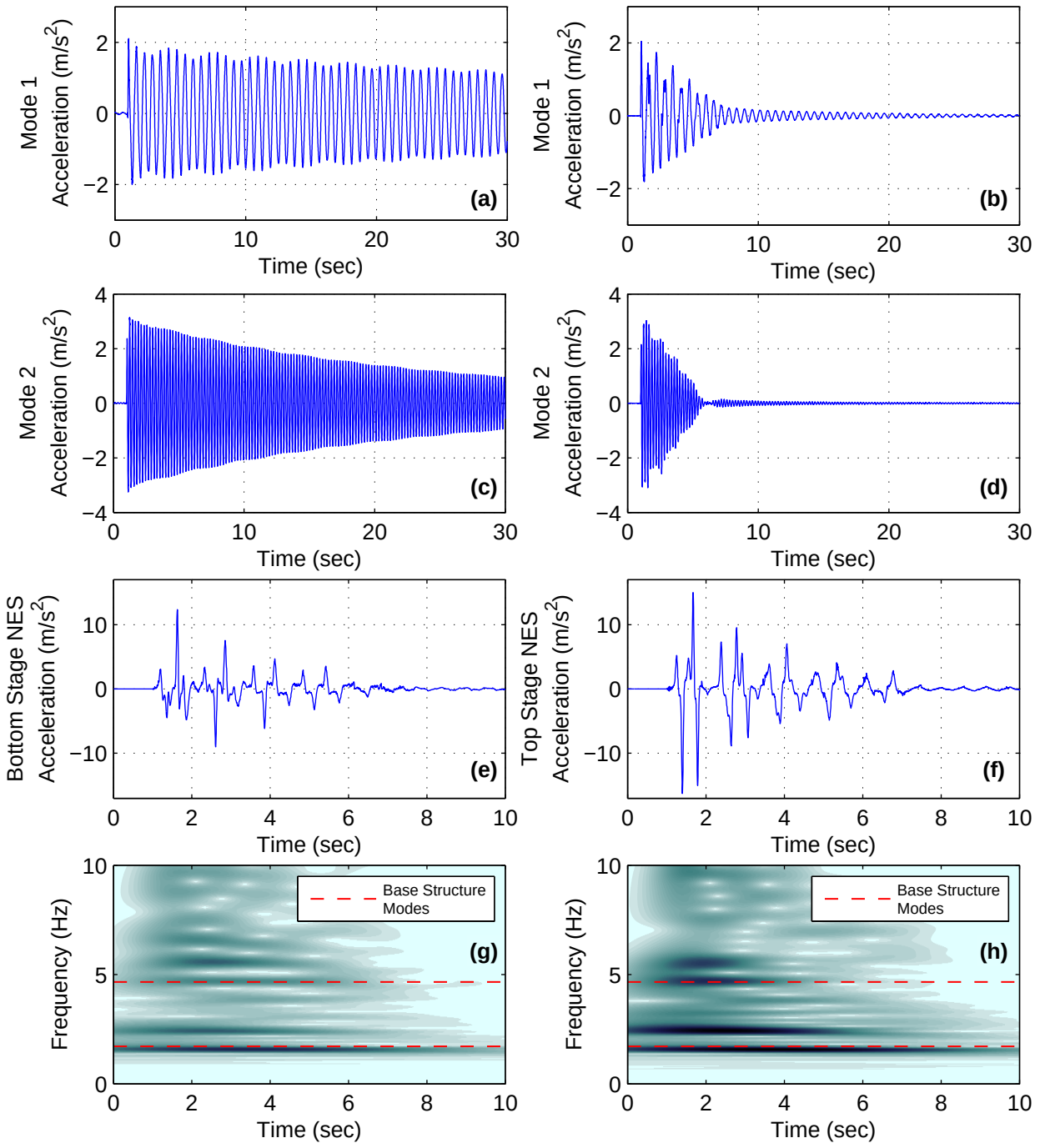

Figure C-36. Response of system with small-scale Type III NES to ground motion level 18 (a) mode 1 accel., NES locked, (b) mode 1 accel., NES unlocked, (c) mode 2 accel., NES locked, (d) mode 2 accel., NES unlocked, (e) bottom stage NES accel., NES unlocked (f) top stage NES accel., NES unlocked, (g) wavelet of bottom stage NES accel., NES unlocked, and (f) wavelet of top stage NES accel., NES unlocked

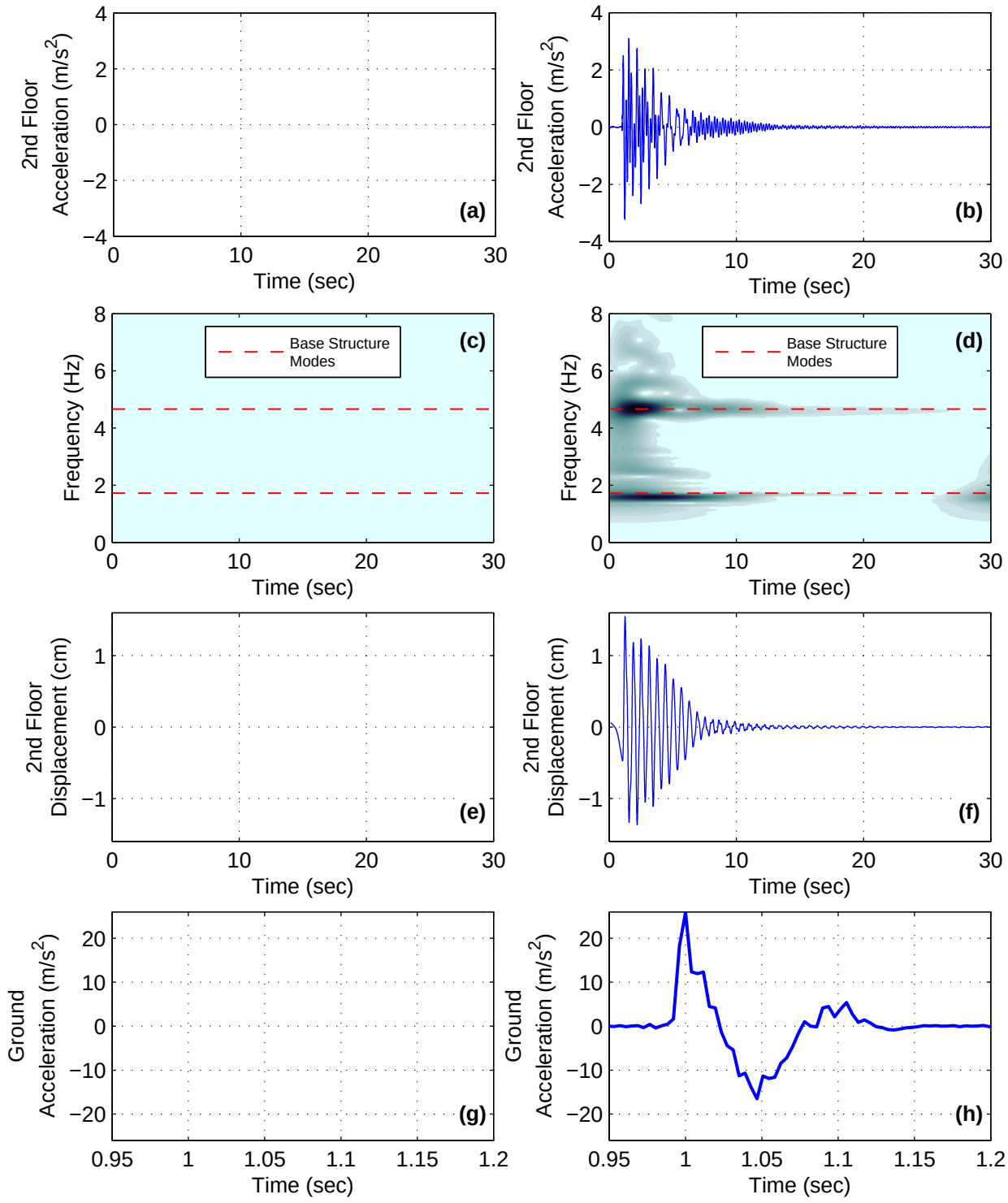

Figure C-37. Response of system with small-scale Type III NES to ground motion level 19 (a) second floor accel., NES locked, (b) second floor accel., NES unlocked, (c) wavelet of second floor accel., NES locked, (d) wavelet of second floor accel., NES unlocked, (e) second floor disp., NES locked (f) second floor disp., NES unlocked, (g) ground accel., NES locked, and (h) ground accel., NES unlocked

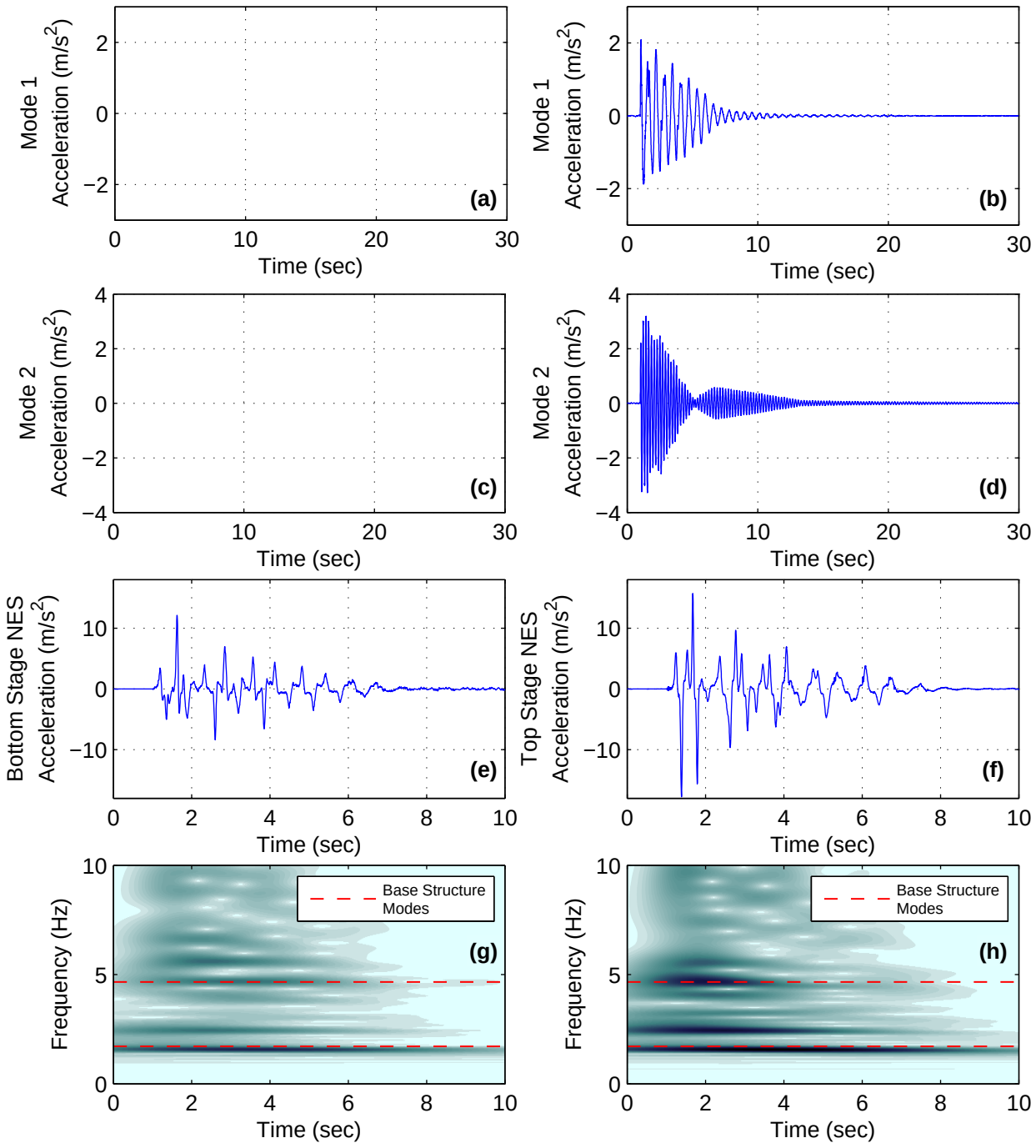

Figure C-38. Response of system with small-scale Type III NES to ground motion level 19 (a) mode 1 accel., NES locked, (b) mode 1 accel., NES unlocked, (c) mode 2 accel., NES locked, (d) mode 2 accel., NES unlocked, (e) bottom stage NES accel., NES unlocked (f) top stage NES accel., NES unlocked, (g) wavelet of bottom stage NES accel., NES unlocked, and (f) wavelet of top stage NES accel., NES unlocked

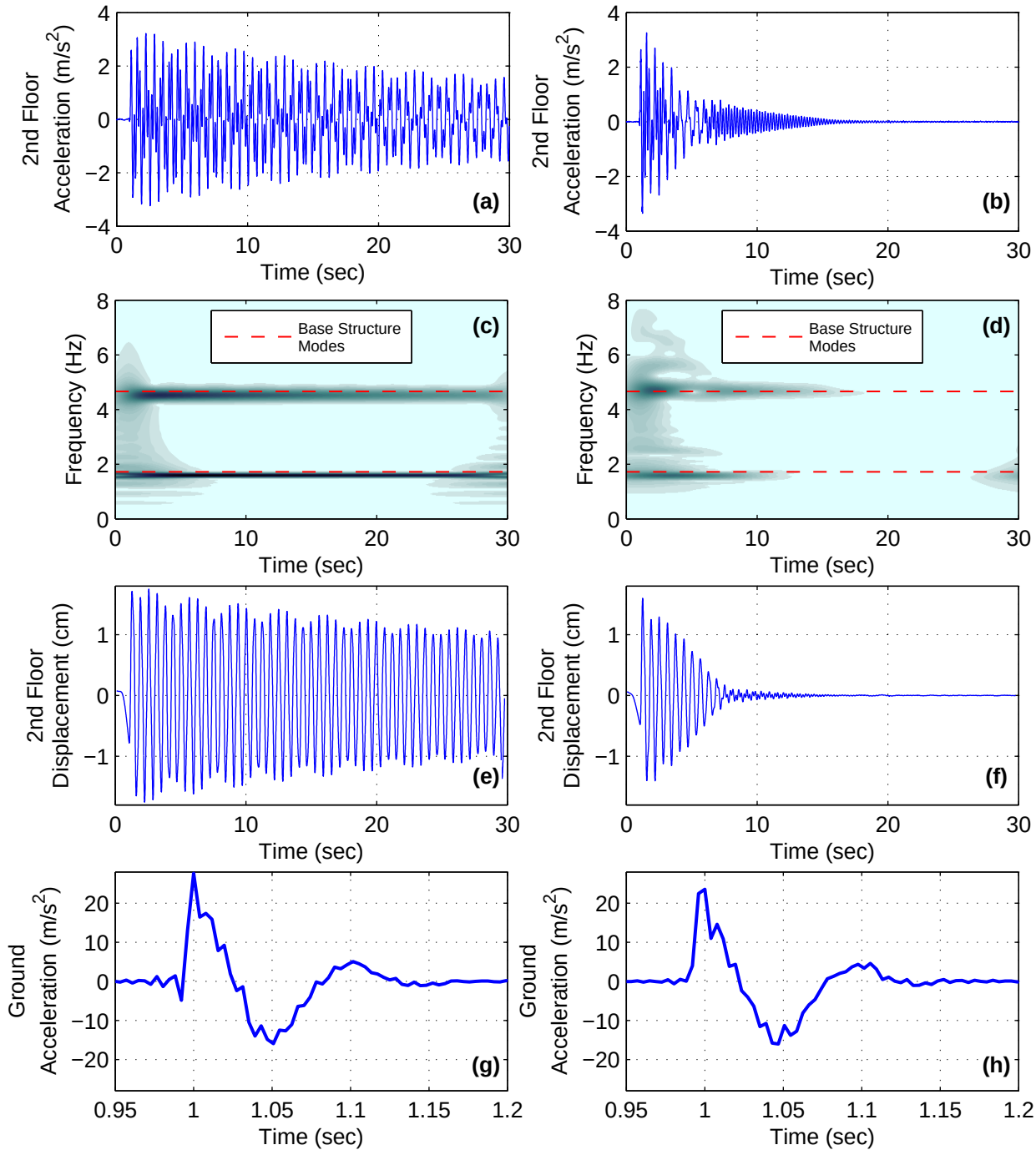

Figure C-39. Response of system with small-scale Type III NES to ground motion level 20 (a) second floor accel., NES locked, (b) second floor accel., NES unlocked, (c) wavelet of second floor accel., NES locked, (d) wavelet of second floor accel., NES unlocked, (e) second floor disp., NES locked (f) second floor disp., NES unlocked, (g) ground accel., NES locked, and (h) ground accel., NES unlocked

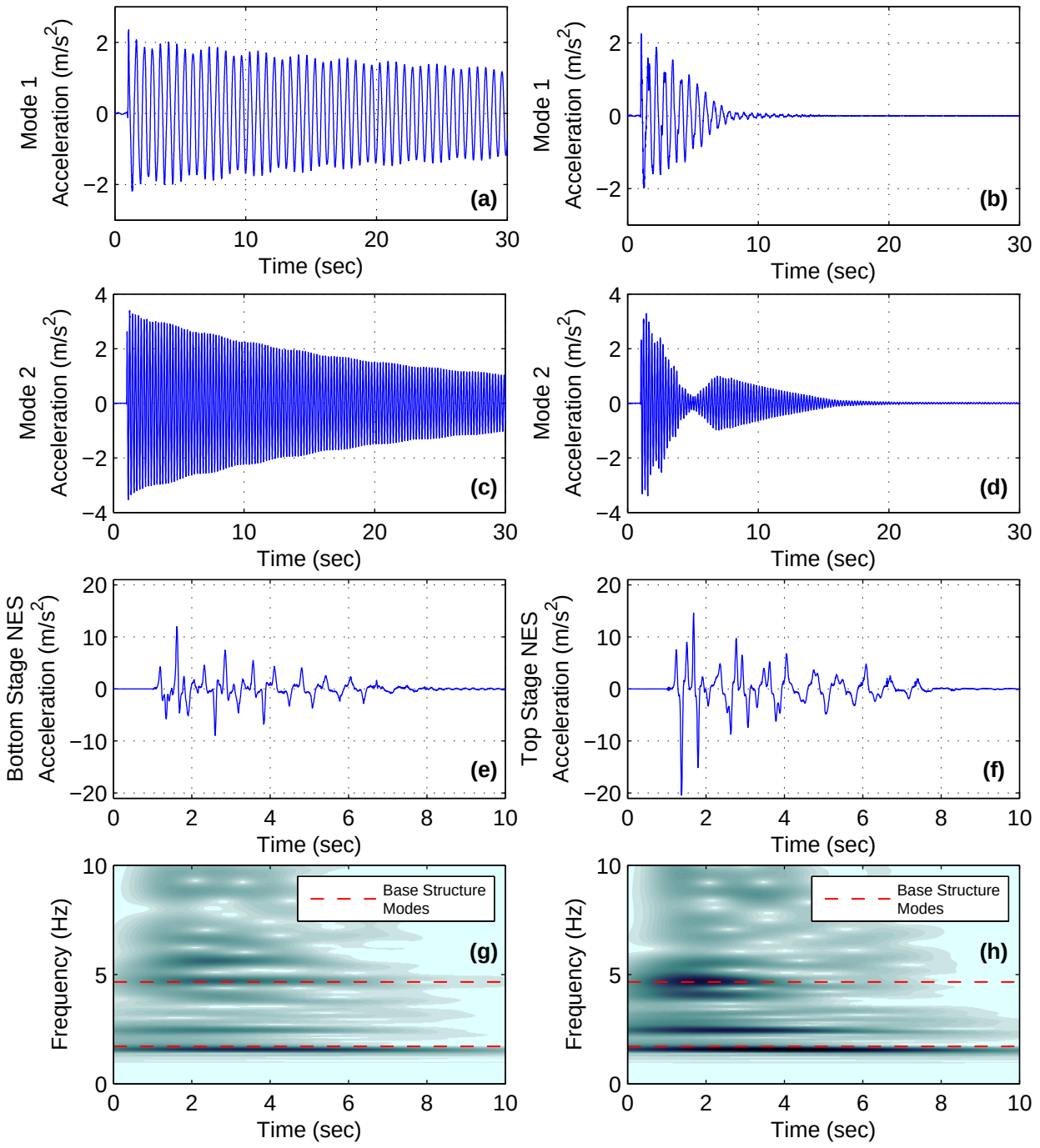

Figure C-40. Response of system with small-scale Type III NES to ground motion level 20 (a) mode 1 accel., NES locked, (b) mode 1 accel., NES unlocked, (c) mode 2 accel., NES locked, (d) mode 2 accel., NES unlocked, (e) bottom stage NES accel., NES unlocked (f) top stage NES accel., NES unlocked, (g) wavelet of bottom stage NES accel., NES unlocked, and (f) wavelet of top stage NES accel., NES unlocked

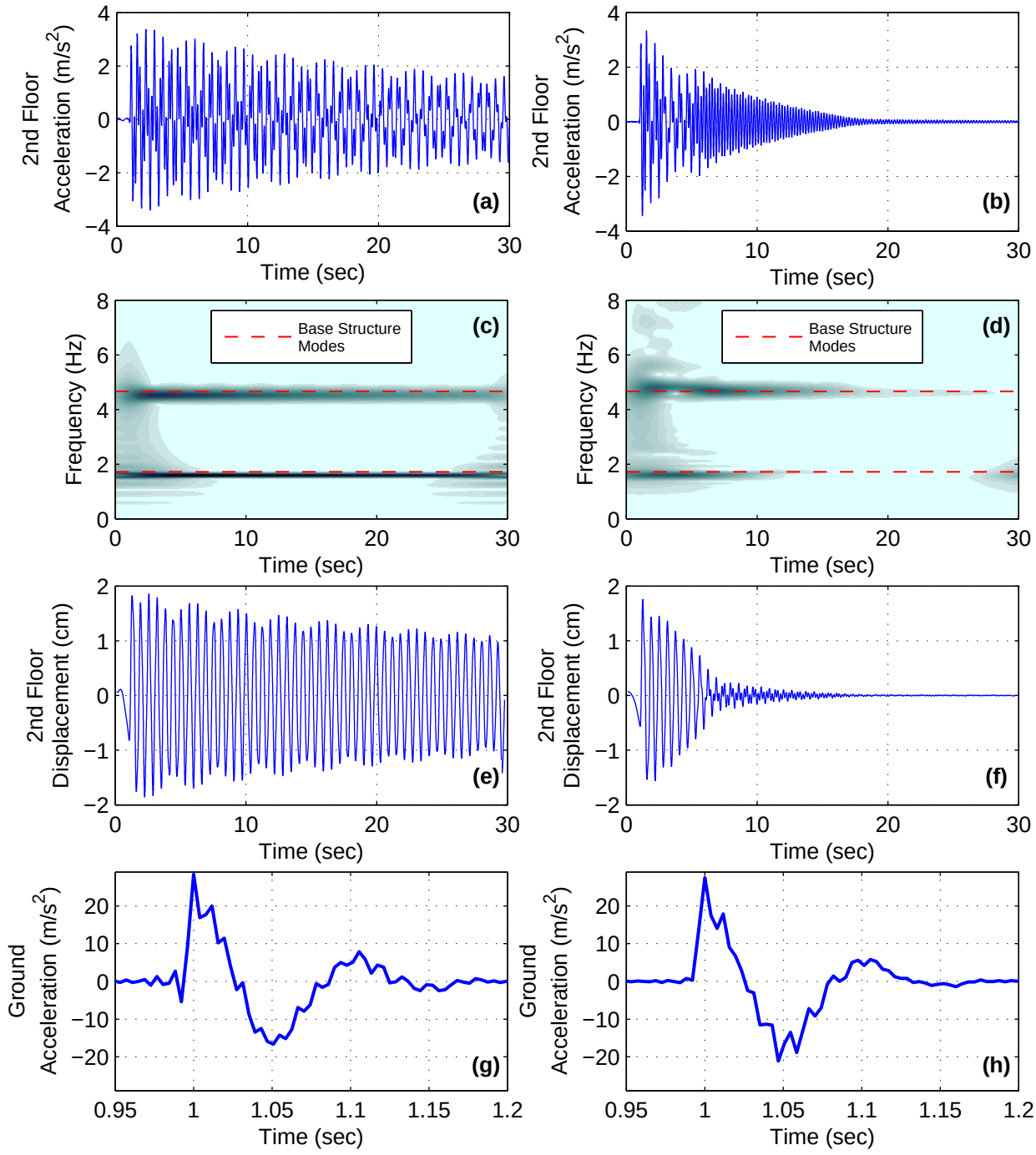

Figure C-41. Response of system with small-scale Type III NES to ground motion level 21 (a) second floor accel., NES locked, (b) second floor accel., NES unlocked, (c) wavelet of second floor accel., NES locked, (d) wavelet of second floor accel., NES unlocked, (e) second floor disp., NES locked (f) second floor disp., NES unlocked, (g) ground accel., NES locked, and (h) ground accel., NES unlocked

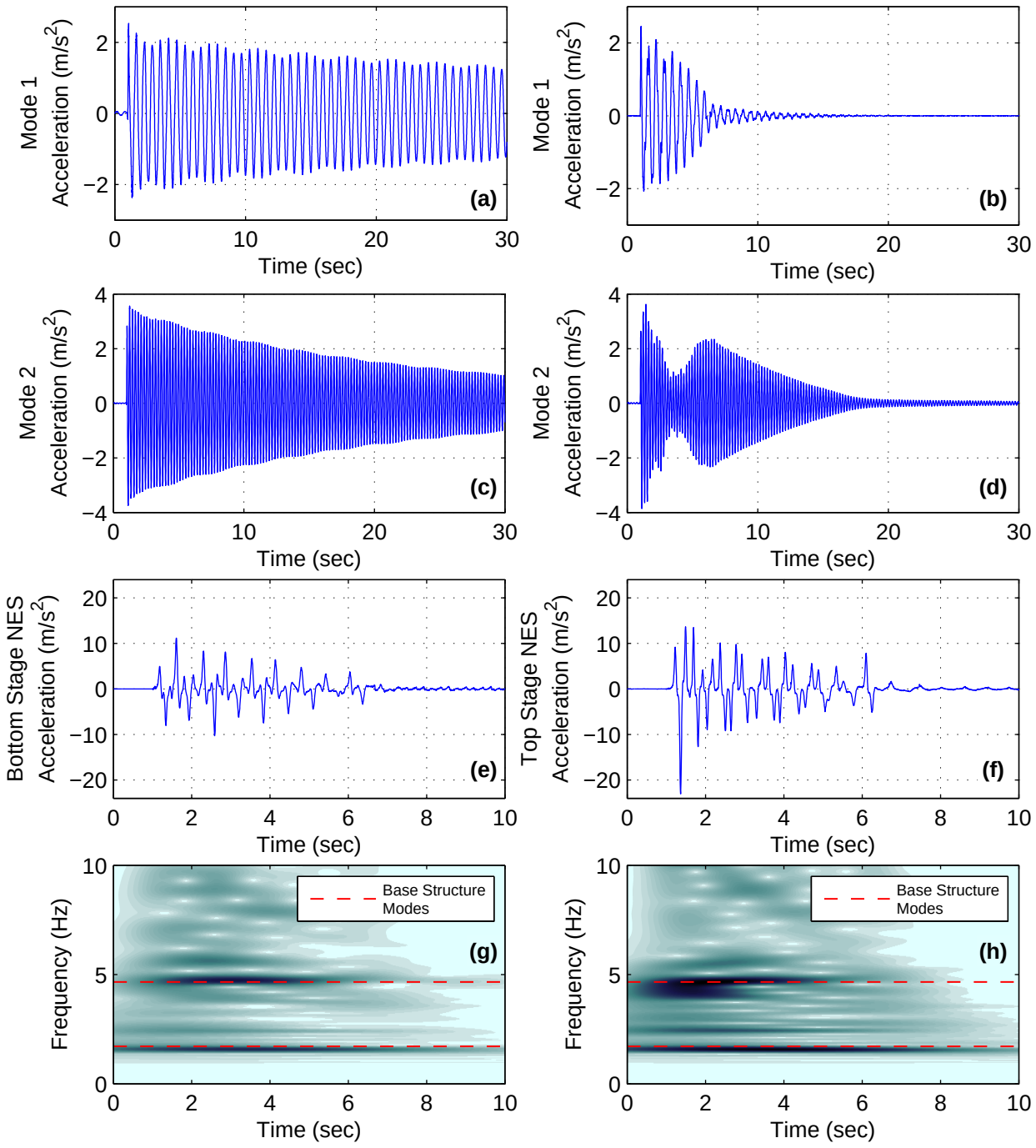

Figure C-42. Response of system with small-scale Type III NES to ground motion level 21 (a) mode 1 accel., NES locked, (b) mode 1 accel., NES unlocked, (c) mode 2 accel., NES locked, (d) mode 2 accel., NES unlocked, (e) bottom stage NES accel., NES unlocked (f) top stage NES accel., NES unlocked, (g) wavelet of bottom stage NES accel., NES unlocked, and (f) wavelet of top stage NES accel., NES unlocked

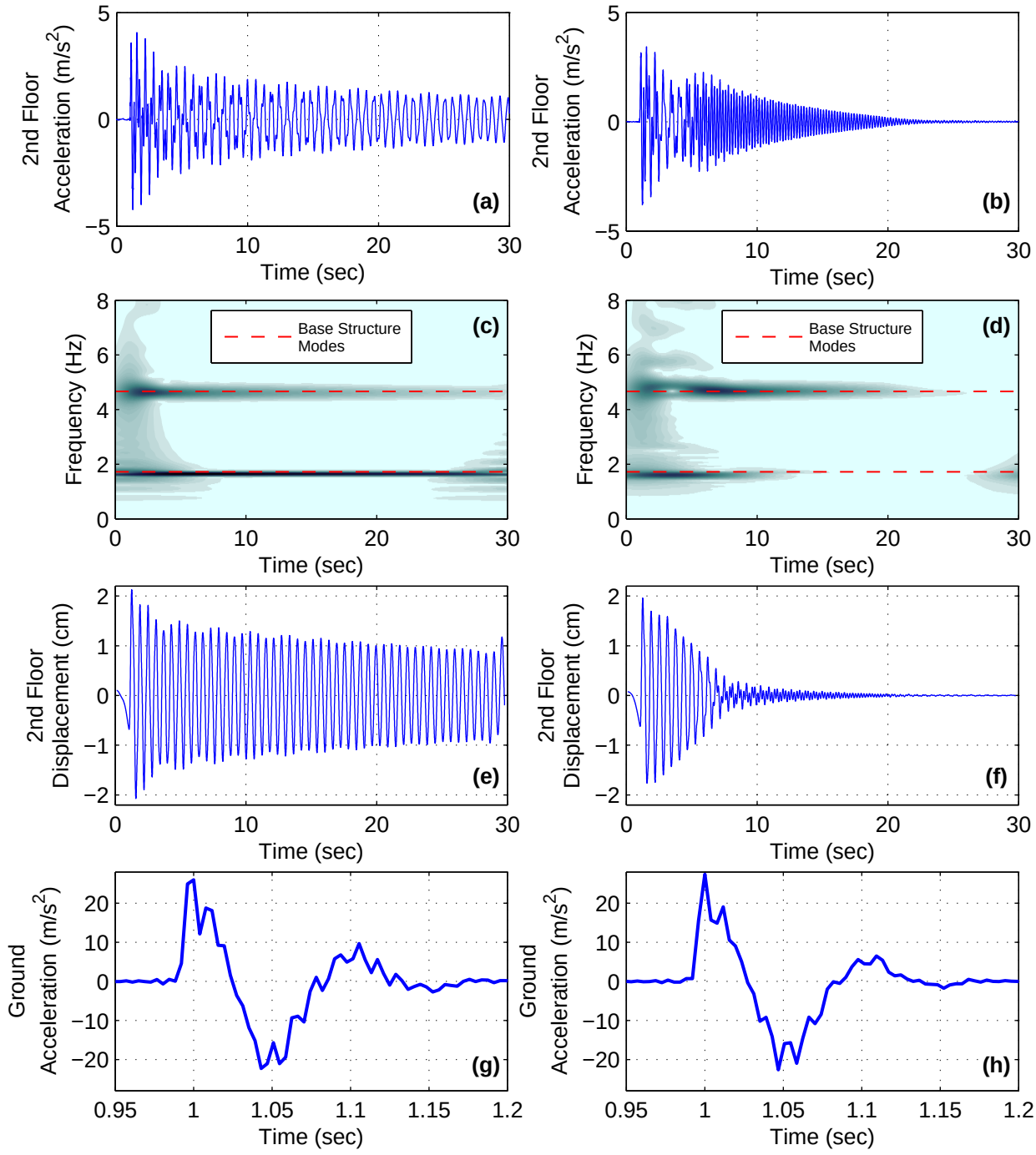

Figure C-43. Response of system with small-scale Type III NES to ground motion level 22 (a) second floor accel., NES locked, (b) second floor accel., NES unlocked, (c) wavelet of second floor accel., NES locked, (d) wavelet of second floor accel., NES unlocked, (e) second floor disp., NES locked (f) second floor disp., NES unlocked, (g) ground accel., NES locked, and (h) ground accel., NES unlocked

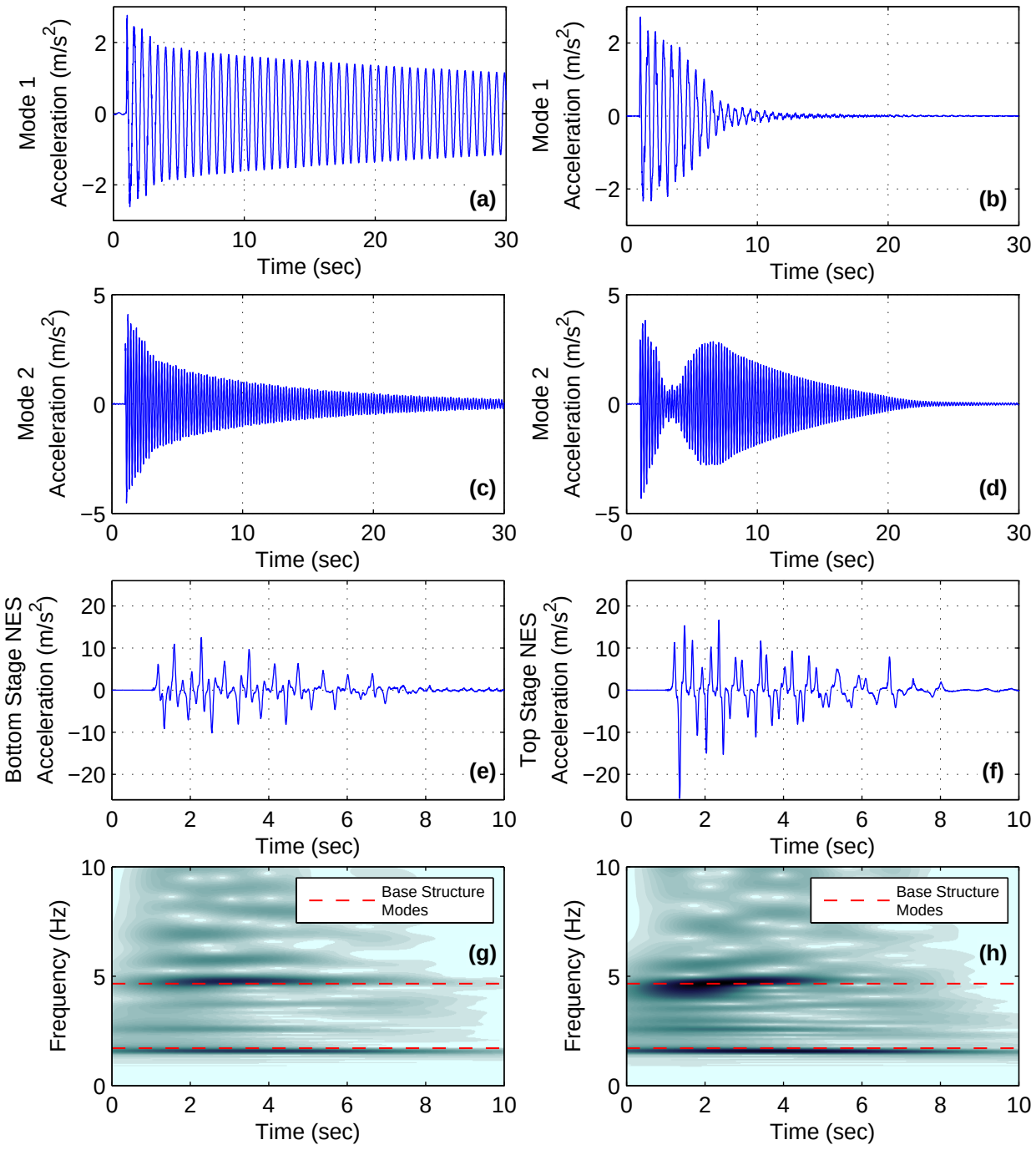

Figure C-44. Response of system with small-scale Type III NES to ground motion level 22 (a) mode 1 accel., NES locked, (b) mode 1 accel., NES unlocked, (c) mode 2 accel., NES locked, (d) mode 2 accel., NES unlocked, (e) bottom stage NES accel., NES unlocked (f) top stage NES accel., NES unlocked, (g) wavelet of bottom stage NES accel., NES unlocked, and (f) wavelet of top stage NES accel., NES unlocked

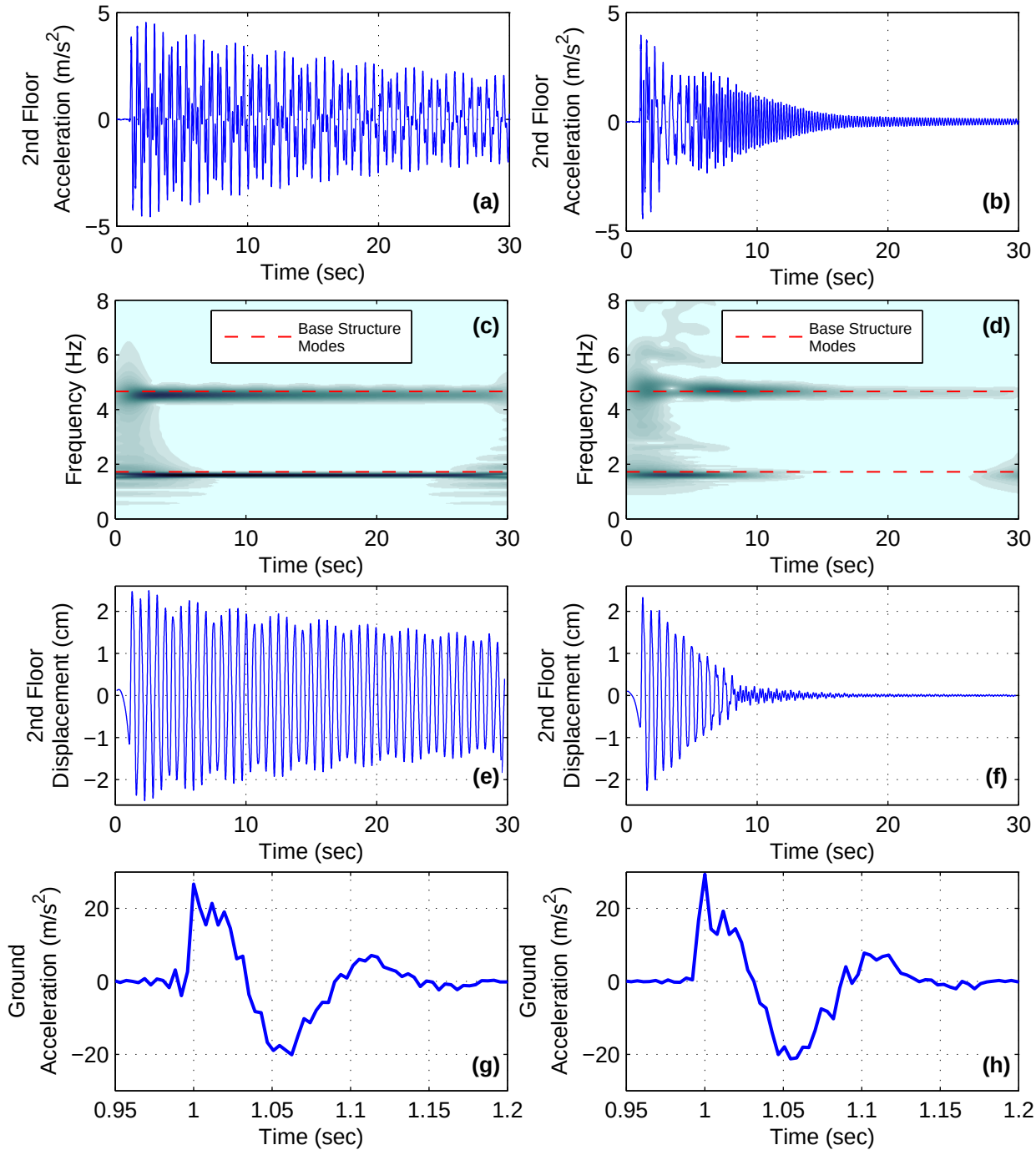

Figure C-45. Response of system with small-scale Type III NES to ground motion level 23 (a) second floor accel., NES locked, (b) second floor accel., NES unlocked, (c) wavelet of second floor accel., NES locked, (d) wavelet of second floor accel., NES unlocked, (e) second floor disp., NES locked (f) second floor disp., NES unlocked, (g) ground accel., NES locked, and (h) ground accel., NES unlocked

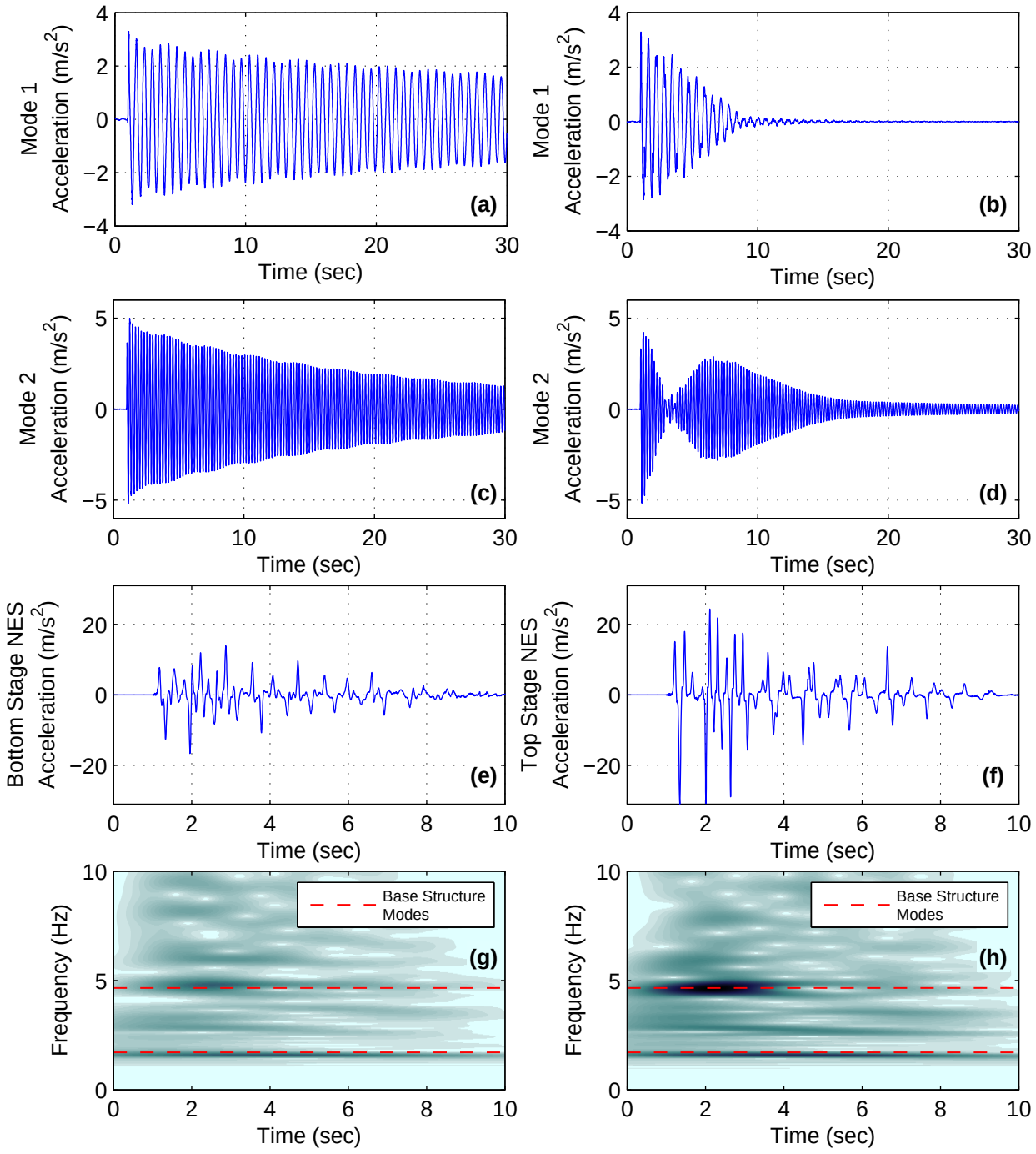

Figure C-46. Response of system with small-scale Type III NES to ground motion level 23 (a) mode 1 accel., NES locked, (b) mode 1 accel., NES unlocked, (c) mode 2 accel., NES locked, (d) mode 2 accel., NES unlocked, (e) bottom stage NES accel., NES unlocked (f) top stage NES accel., NES unlocked, (g) wavelet of bottom stage NES accel., NES unlocked, and (f) wavelet of top stage NES accel., NES unlocked

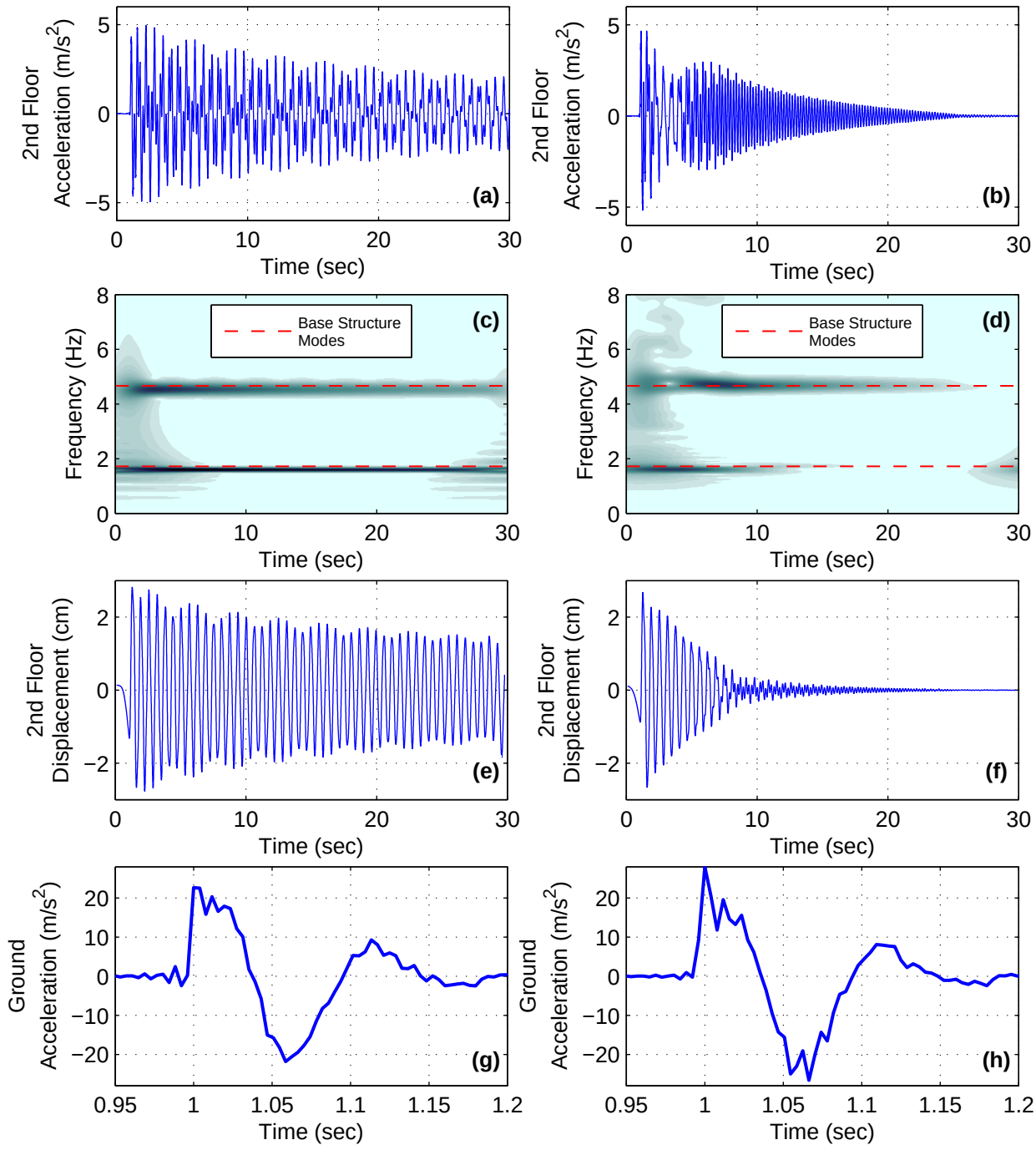

Figure C-47. Response of system with small-scale Type III NES to ground motion level 24 (a) second floor accel., NES locked, (b) second floor accel., NES unlocked, (c) wavelet of second floor accel., NES locked, (d) wavelet of second floor accel., NES unlocked, (e) second floor disp., NES locked (f) second floor disp., NES unlocked, (g) ground accel., NES locked, and (h) ground accel., NES unlocked

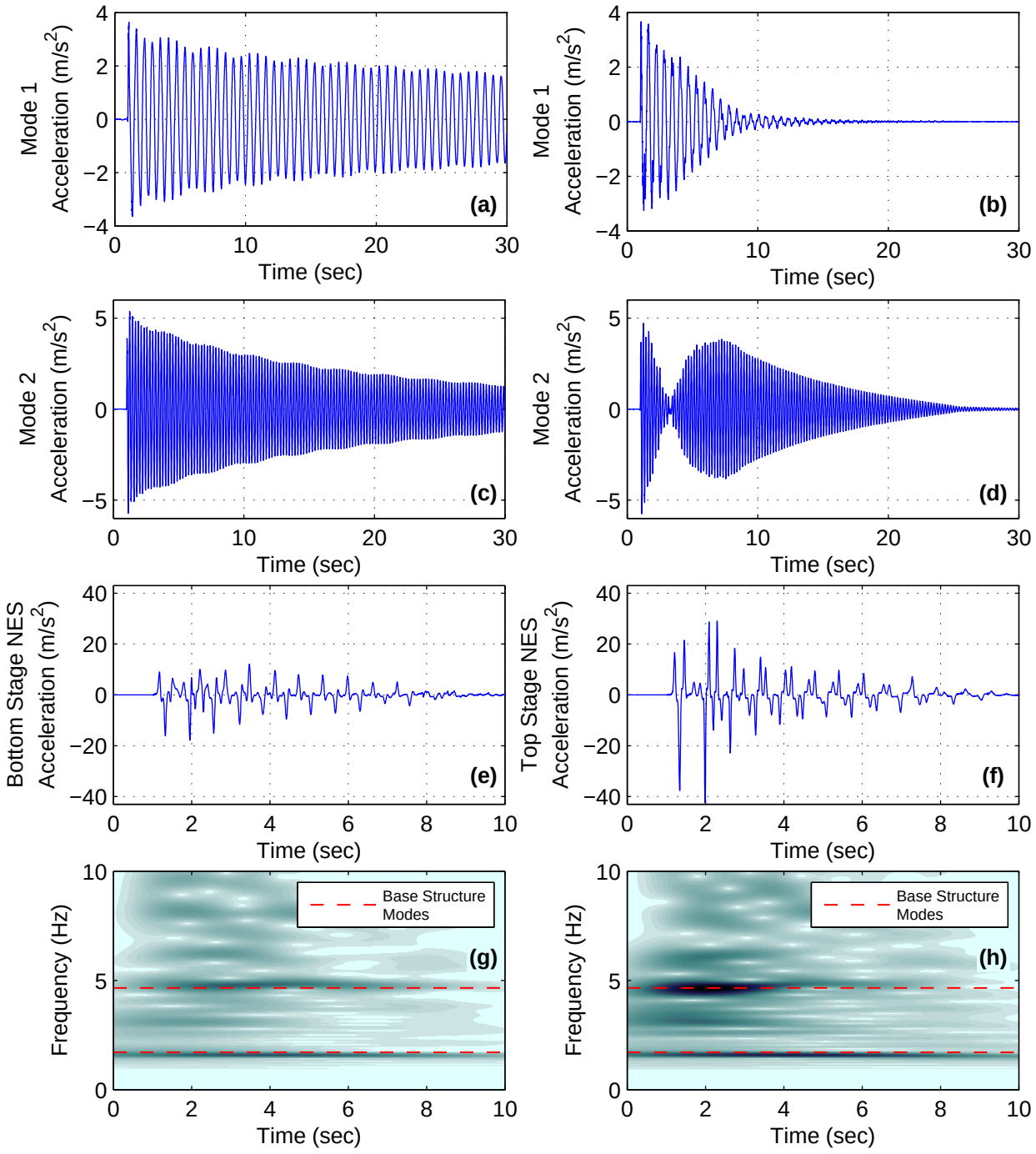

Figure C-48. Response of system with small-scale Type III NES to ground motion level 24 (a) mode 1 accel., NES locked, (b) mode 1 accel., NES unlocked, (c) mode 2 accel., NES locked, (d) mode 2 accel., NES unlocked, (e) bottom stage NES accel., NES unlocked (f) top stage NES accel., NES unlocked, (g) wavelet of bottom stage NES accel., NES unlocked, and (f) wavelet of top stage NES accel., NES unlocked

APPENDIX D: ADDITIONAL EXPERIMENTAL RESPONSES FOR THE LARGE-SCALE TEST STRUCTURE AND SYSTEM OF NESs

In this appendix, additional plots of the experimental response of the large-scale test structure and system of NESs to the shake-table-produced simulated blast loading are presented. The ground motion used for the tests presented here are the 50%, 100%, 150%, and 200% scaling levels of the of the prototype blast simulation ground motion presented in Chapter 7. In addition to various loading levels, the response of the structure with the four configurations of the system of NESs (all NESs locked, Type I NESs unlocked, SSVI NESs unlocked, and all NESs unlocked) is examined. The responses of the structure plotted in this appendix include shake-table-produced ground acceleration, floor accelerations, floor acceleration wavelet spectra, estimated floor displacement, first floor column strain, modal accelerations, NES accelerations, and NES acceleration wavelet spectra. The locations on the structure where the measurements plotted in this appendix were obtained are shown in Figure D-1.

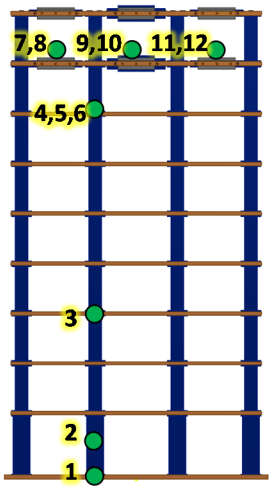

1) Table Acceleration
2) 1st Floor Column Strain
3) 3rd Floor Acceleration
4) 7th Floor Acceleration
5) 7th Floor Acceleration Wavelet Spectra
6) 7th Floor Displacement
7) 9th Floor Left Type I NES Acceleration
8) 9th Floor Left Type I NES Acceleration Wavelet Spectra
9) 9th Floor SSVI NES Acceleration
10) 9th Floor SSVI NES Acceleration Wavelet Spectra
11) 9th Floor Right Type I NES Acceleration
12) 9th Floor Right Type I NES Acceleration Wavelet Spectra

Not Pictured
13) 1st Mode Acceleration
14) 2nd Mode Acceleration

Figure D-1. Location on structure of measurements plotted in this appendix

D.1 Response to 50% Prototype Blast Simulation Ground Motion

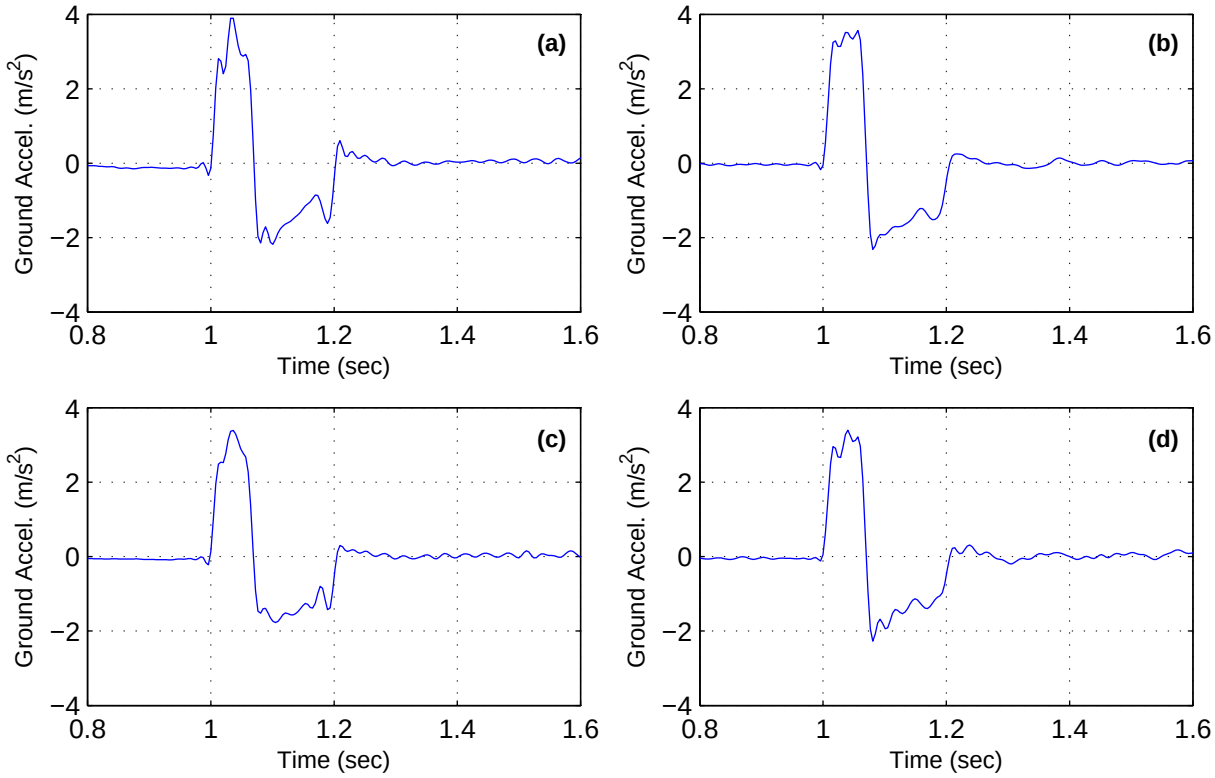

Figure D-2. Measured table acceleration response to 50% blast simulation GM (a) all NESs locked, (b) Type I NESs unlocked, (c) SSVI NESs unlocked, and (d) all NESs unlocked

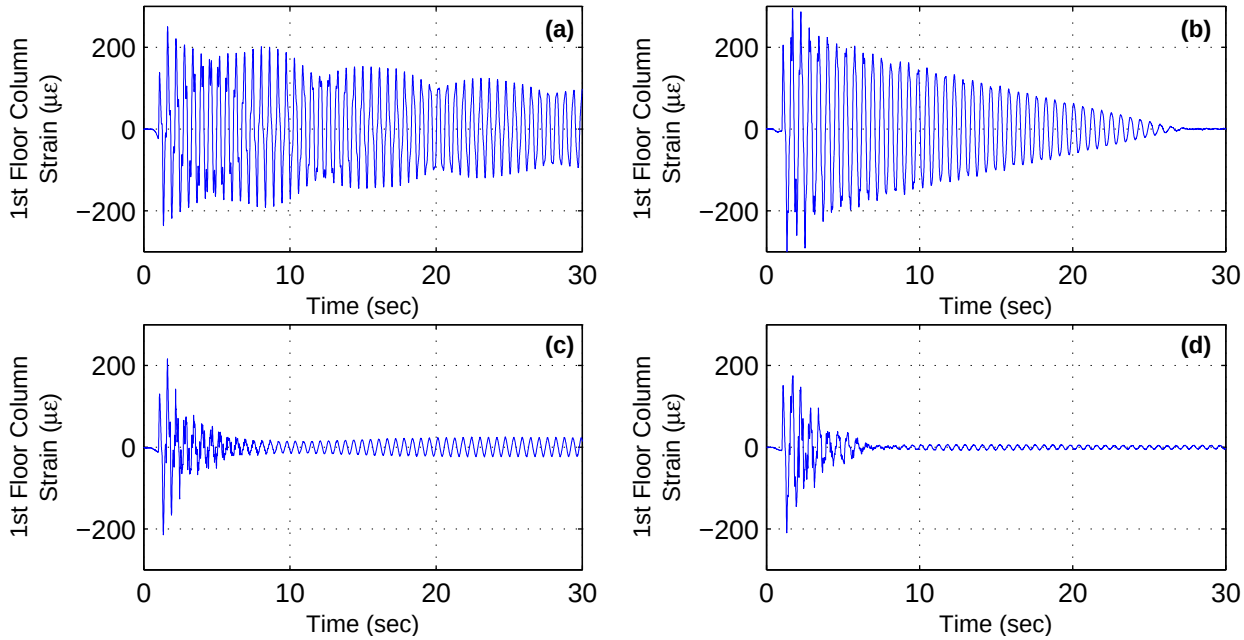

Figure D-3. First floor column strain response to 50% blast simulation GM (a) all NESs locked, (b) Type I NESs unlocked, (c) SSVI NESs unlocked, and (d) all NESs unlocked

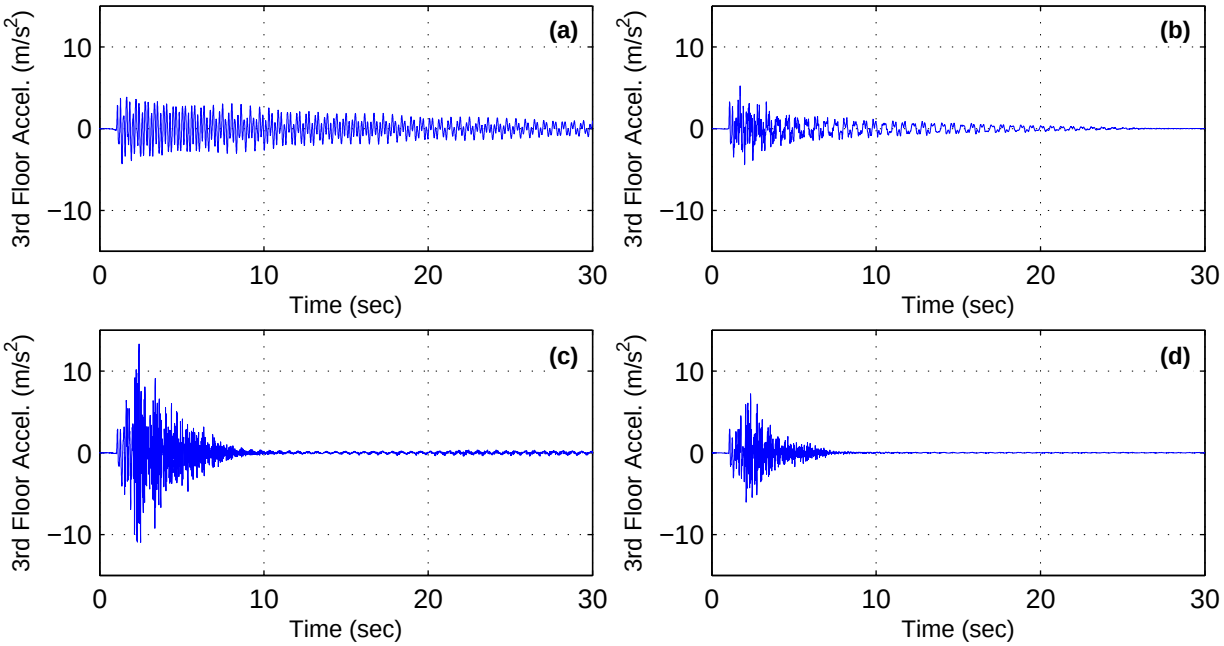

Figure D-4. Third floor acceleration response to 50% blast simulation GM (a) all NESs locked, (b) Type I NESs unlocked, (c) SSVI NESs unlocked, and (d) all NESs unlocked

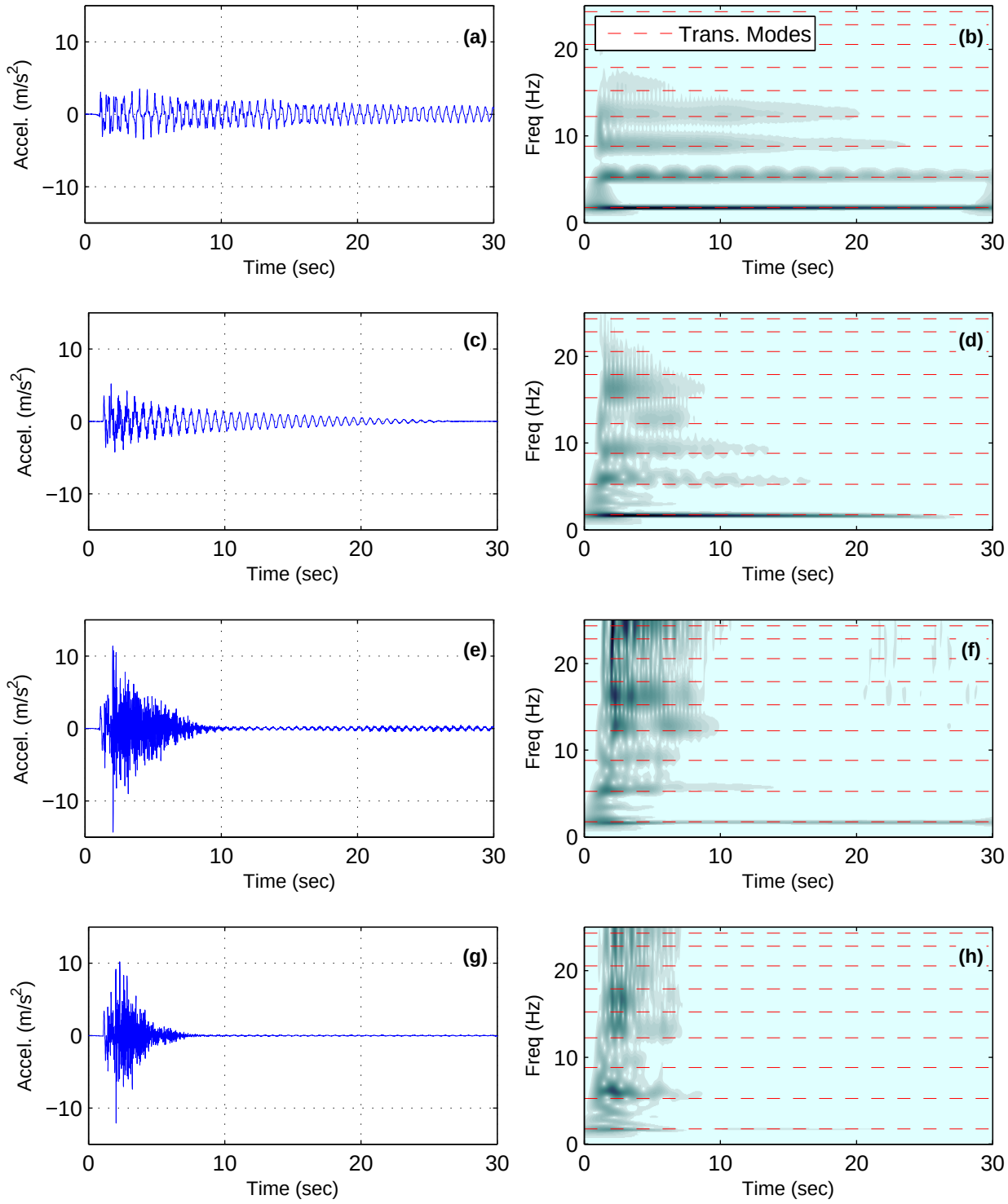

Figure D-5. Time history of seventh floor acceleration and seventh floor acceleration wavelet spectrum response to 50% blast simulation GM for (a, b) all locked configuration, (c, d) Type I NESs unlocked configuration, (e, f) SSVI NESs unlocked configuration, and (g, h) all unlocked configuration

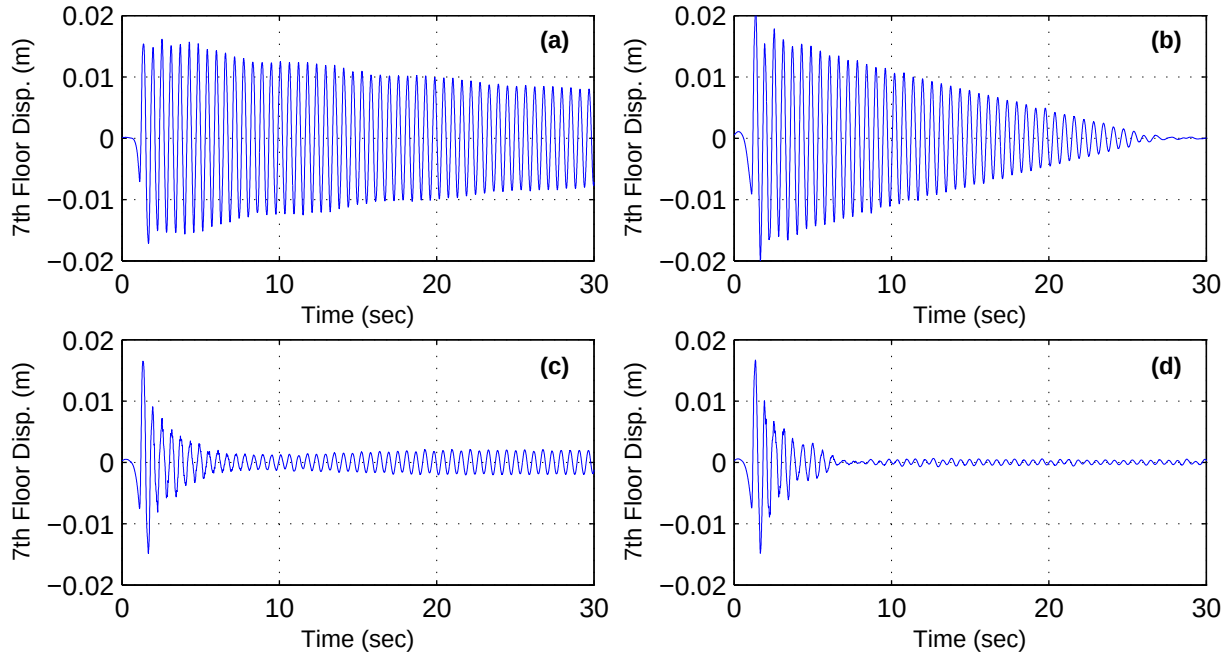

Figure D-6. Seventh floor displacement response to 50% blast simulation GM (a) all NESs locked, (b) Type I NESs unlocked, (c) SSVI NESs unlocked, and (d) all NESs unlocked

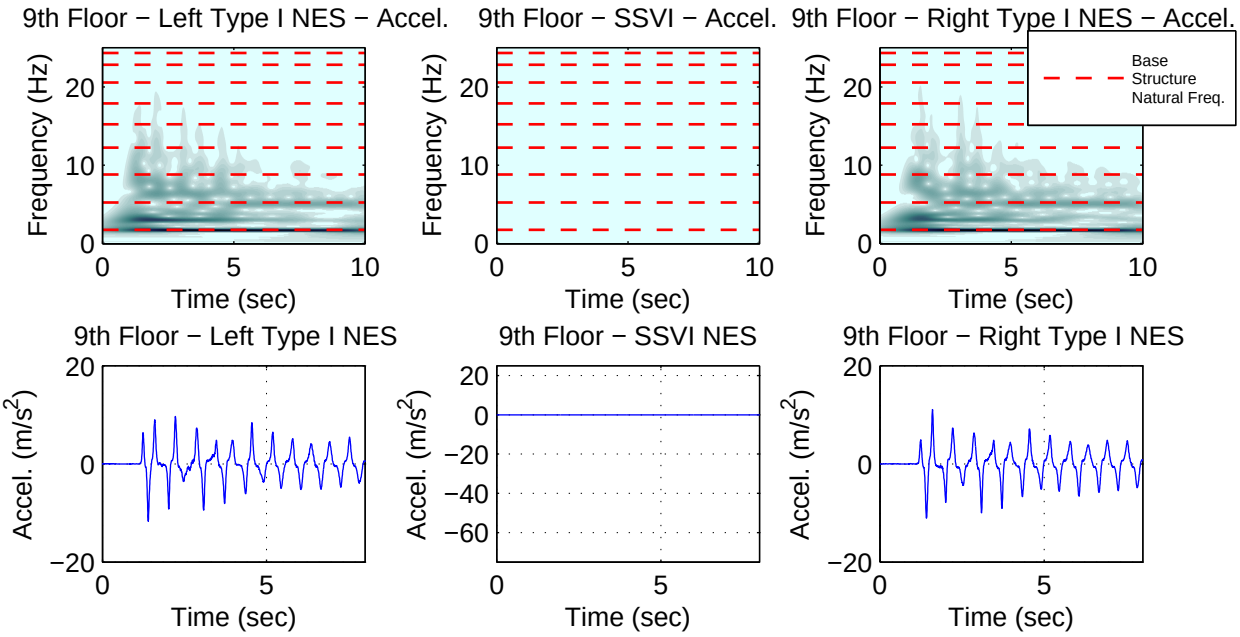

Figure D-7. Ninth floor NESs acceleration response to 50% blast simulation GM with Type I NESs unlocked

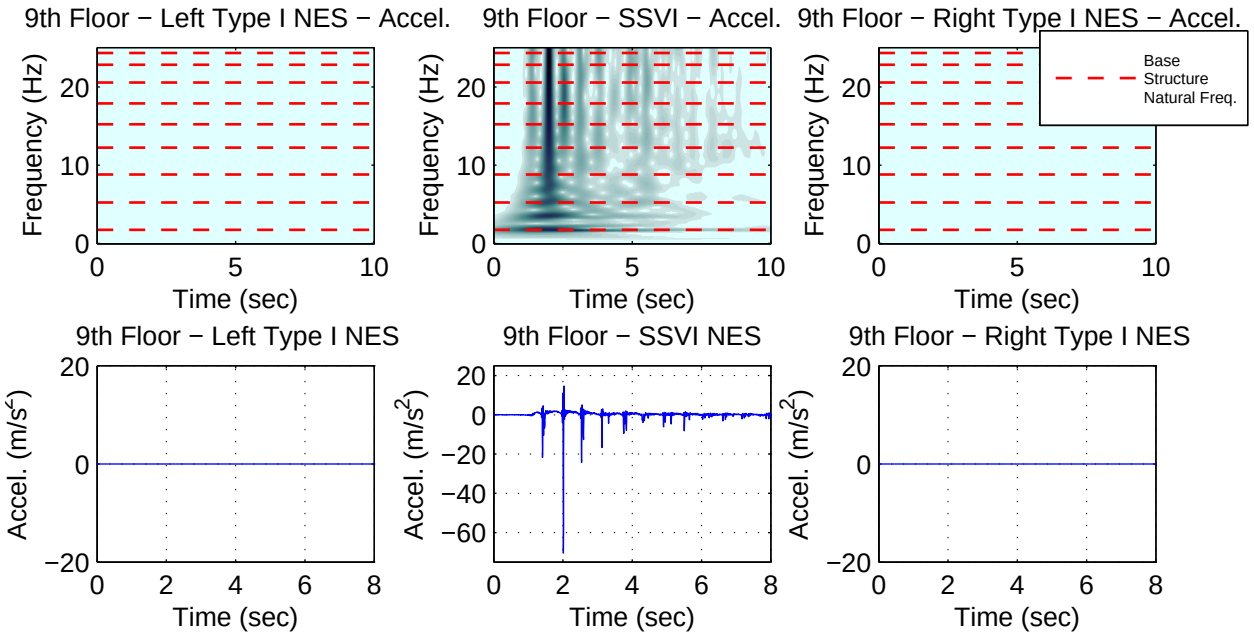

Figure D-8. Ninth floor NESs acceleration response to 50% blast simulation GM with SSVI NESs unlocked

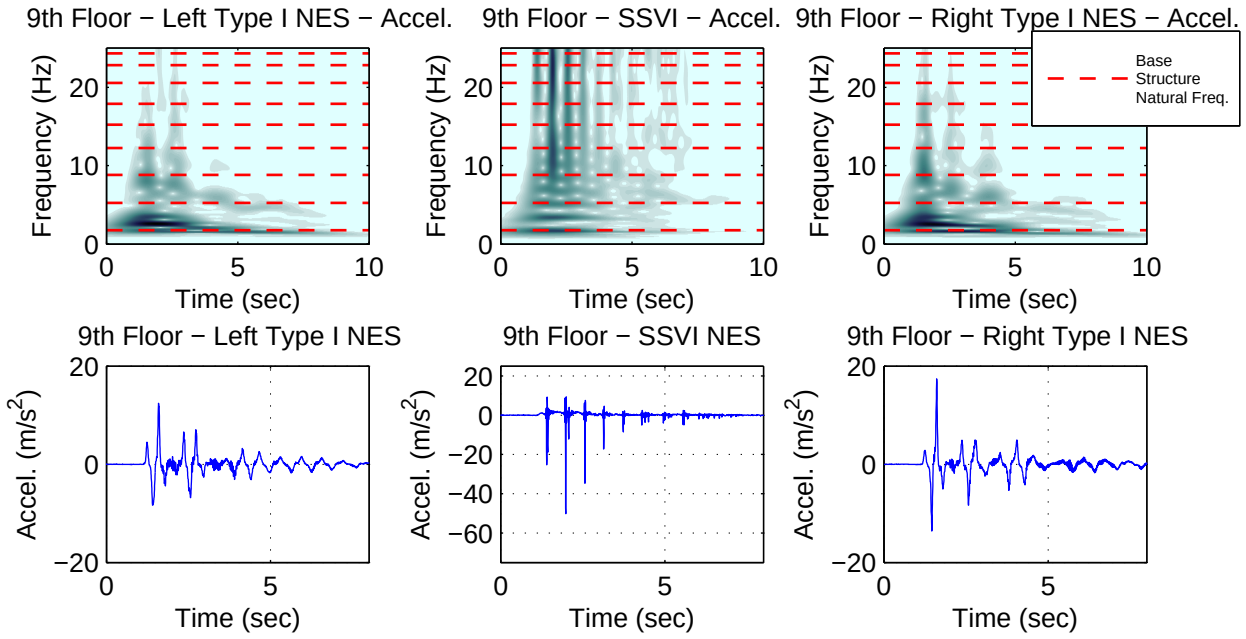

Figure D-9. Ninth floor NESs acceleration response to 50% blast simulation with all NESs unlocked

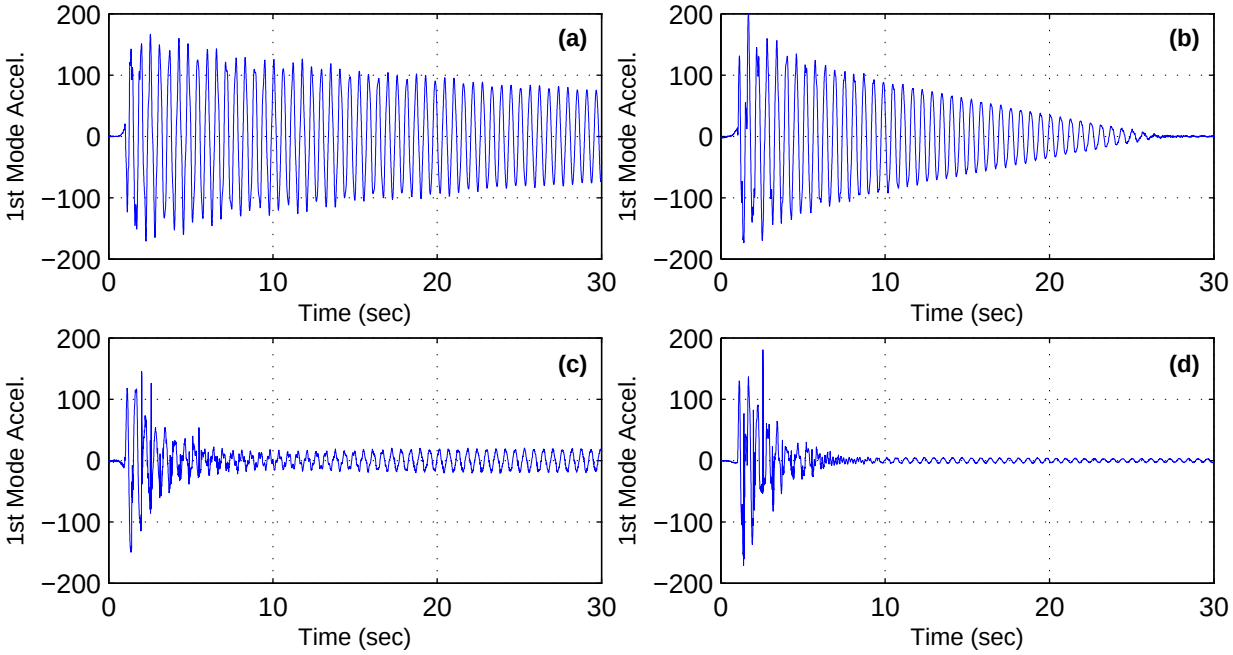

Figure D-10. First mode acceleration response to 50% blast simulation GM (a) all NESs locked, (b) Type I NESs unlocked, (c) SSVI NESs unlocked, and (d) all NESs unlocked

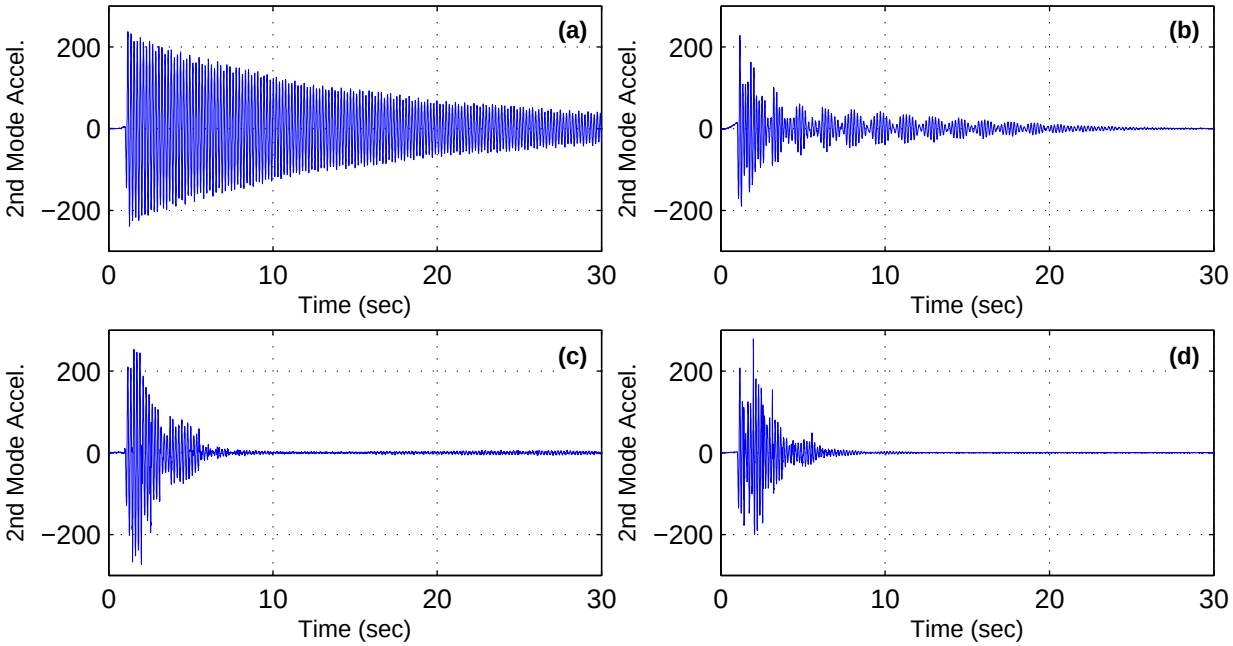

Figure D-11. Second mode acceleration response to 50% blast simulation GM (a) all NESs locked, (b) Type I NESs unlocked, (c) SSVI NESs unlocked, and (d) all NESs unlocked

D.2 Response to 100% Prototype Blast Simulation Ground Motion

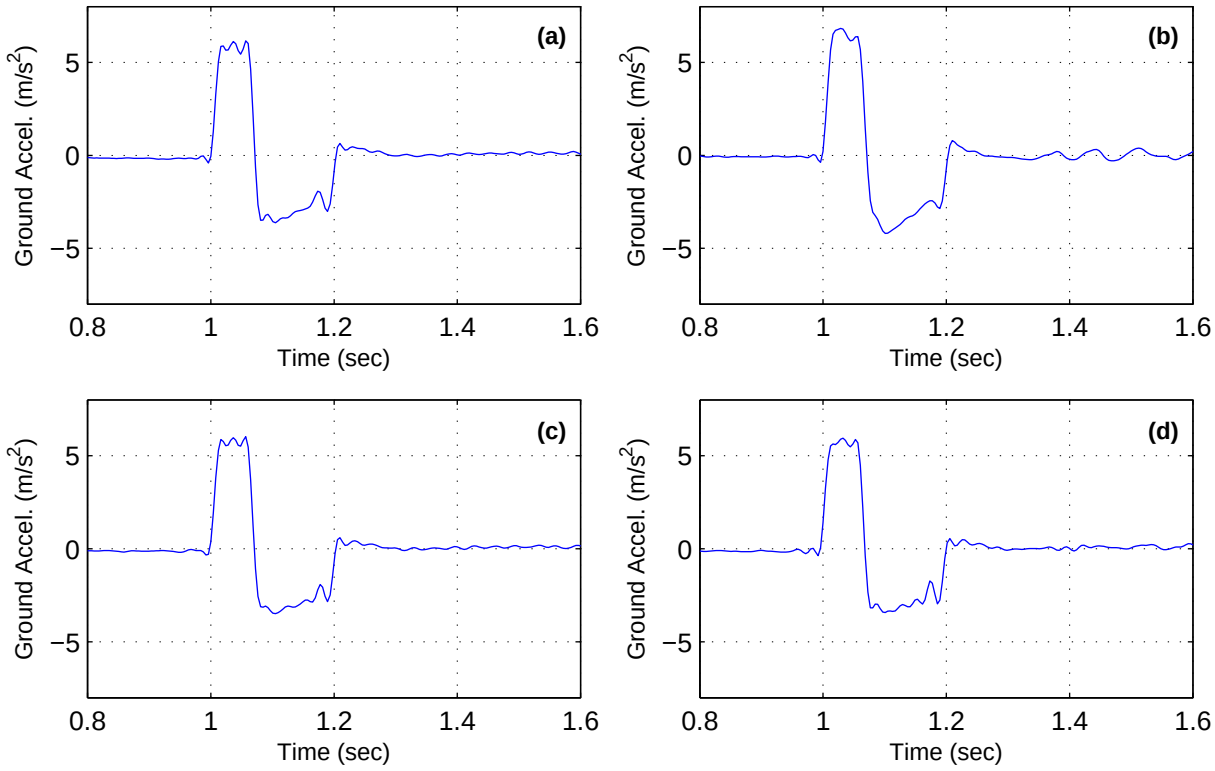

Figure D-12. Measured table acceleration response to 100% blast simulation GM (a) all NESs locked, (b) Type I NESs unlocked, (c) SSVI NESs unlocked, and (d) all NESs unlocked

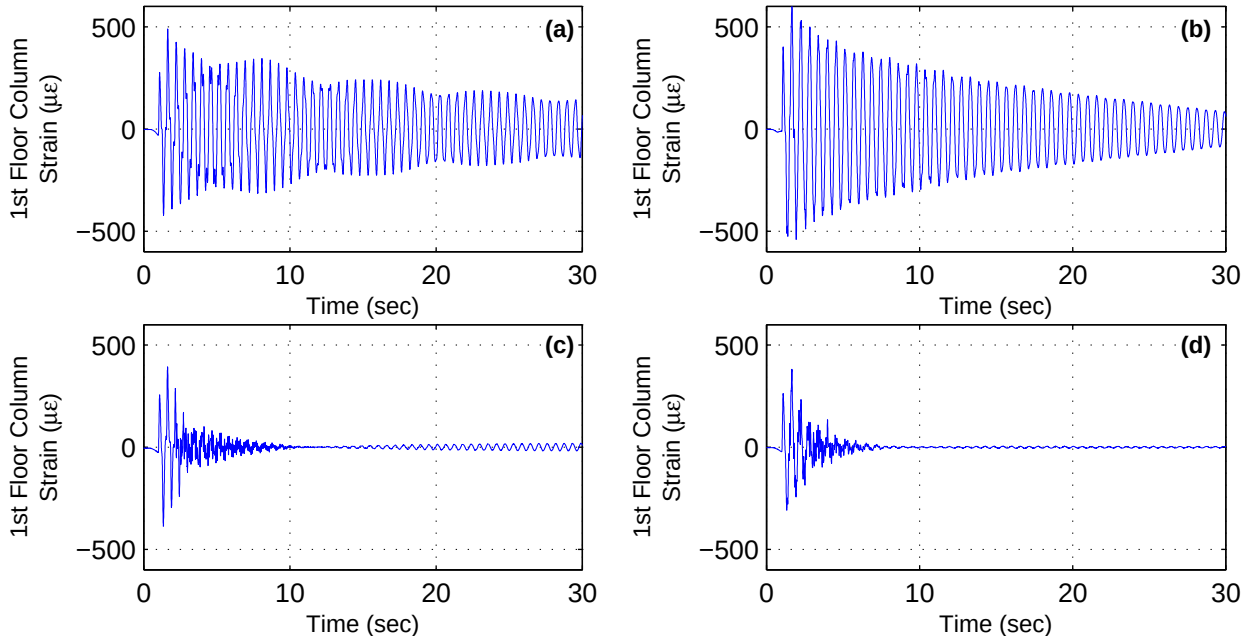

Figure D-13. First floor column strain response to 100% blast simulation GM (a) all NESs locked, (b) Type I NESs unlocked, (c) SSVI NESs unlocked, and (d) all NESs unlocked

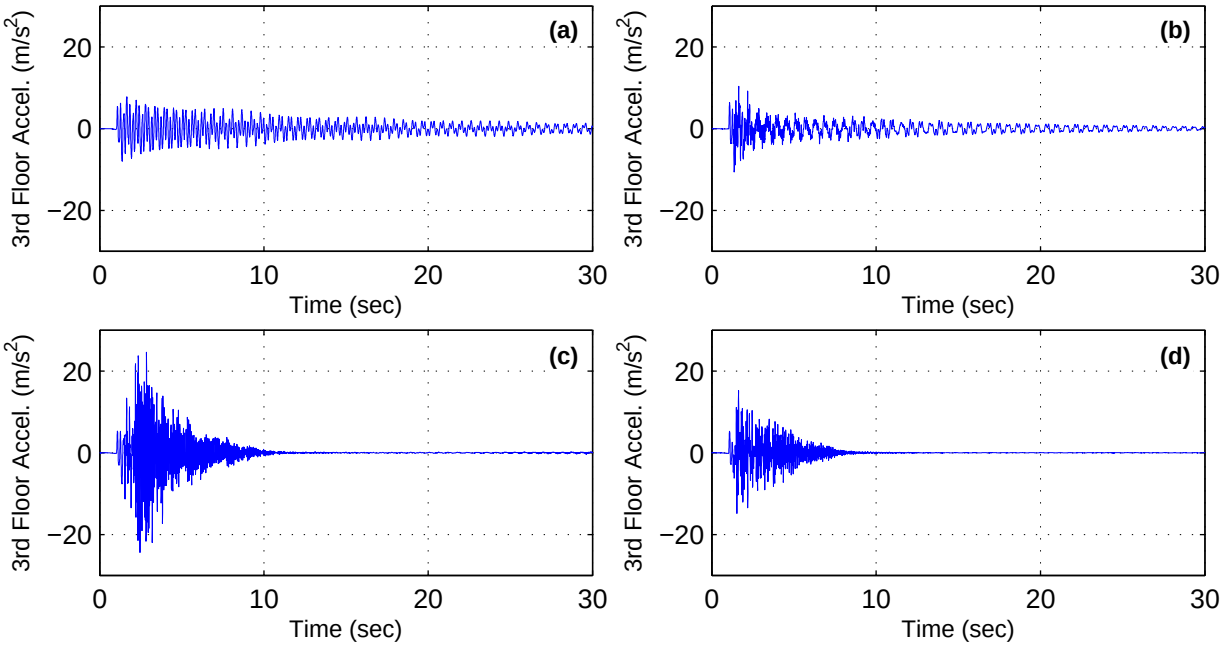

Figure D-14. Third floor acceleration response to 100% blast simulation GM (a) all NESs locked, (b) Type I NESs unlocked, (c) SSVI NESs unlocked, and (d) all NESs unlocked

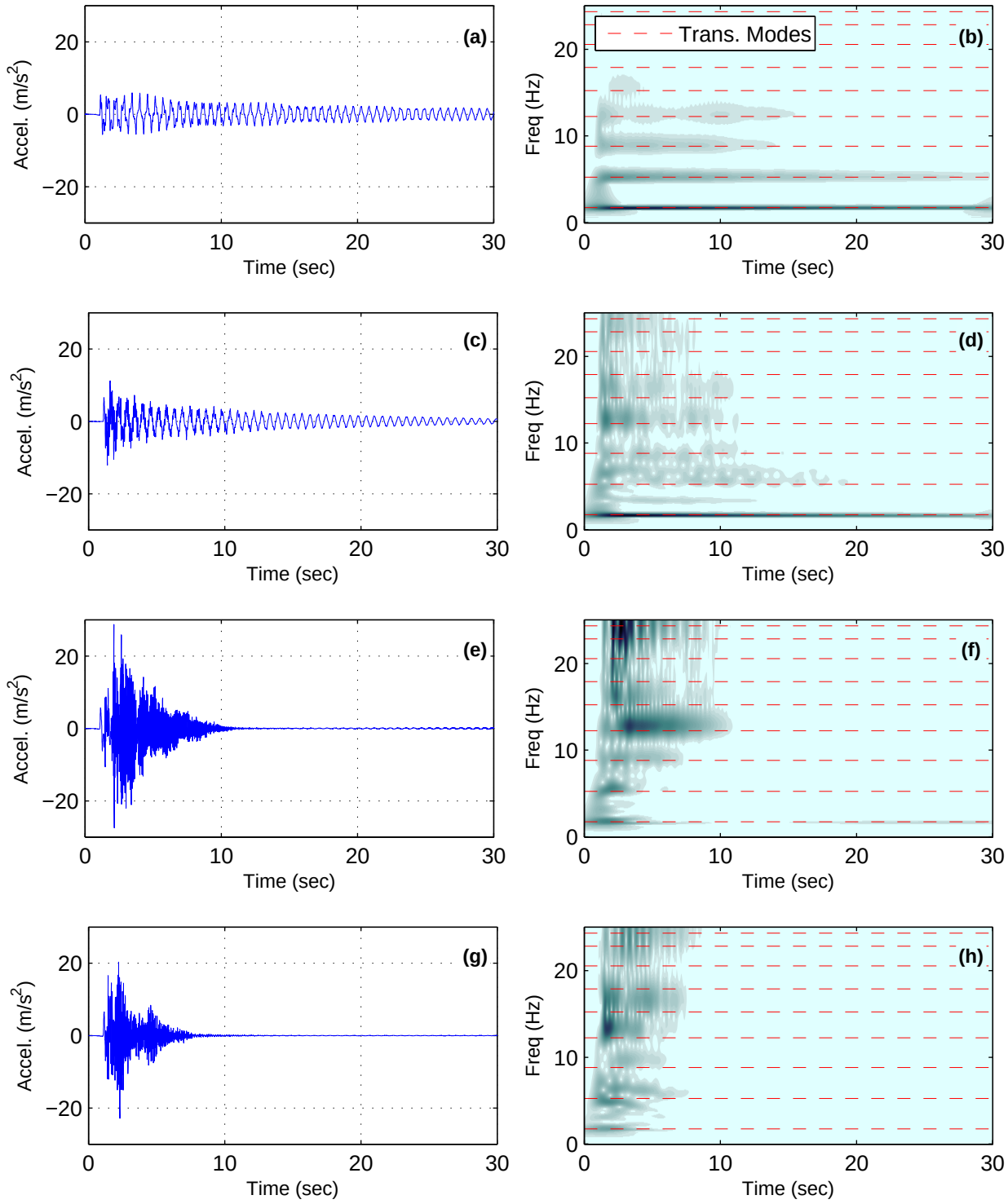

Figure D-15. Time history of seventh floor acceleration and seventh floor acceleration wavelet spectrum response to 100% blast simulation GM for (a, b) all locked configuration, (c, d) Type I NESs unlocked configuration, (e, f) SSVI NESs unlocked configuration, and (g, h) all unlocked configuration

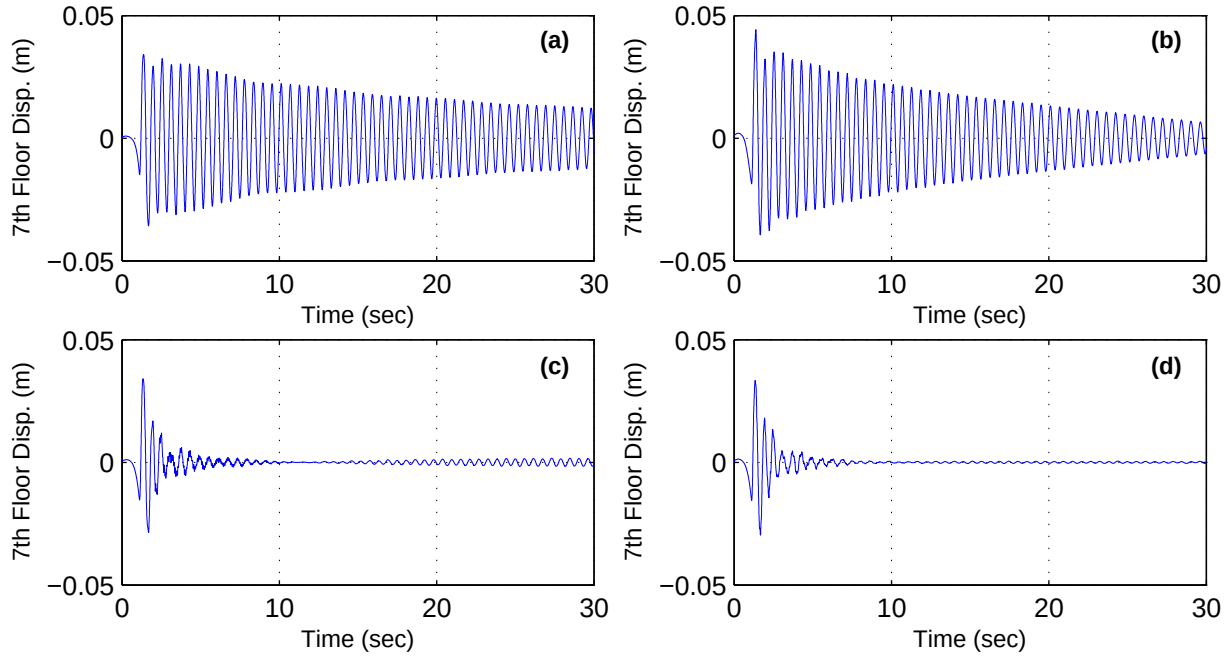

Figure D-16. Seventh floor displacement response to 100% blast simulation GM (a) all NESs locked, (b) Type I NESs unlocked, (c) SSVI NESs unlocked, and (d) all NESs unlocked

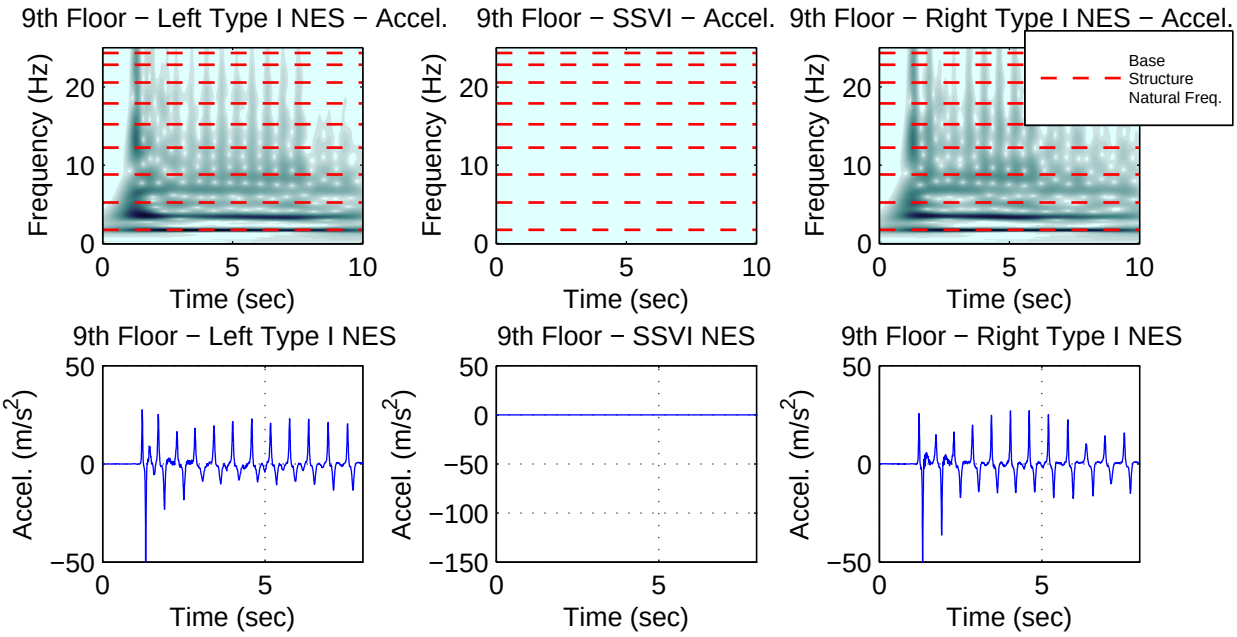

Figure D-17. Ninth floor NESs acceleration response to 100% blast simulation GM with Type I NESs unlocked

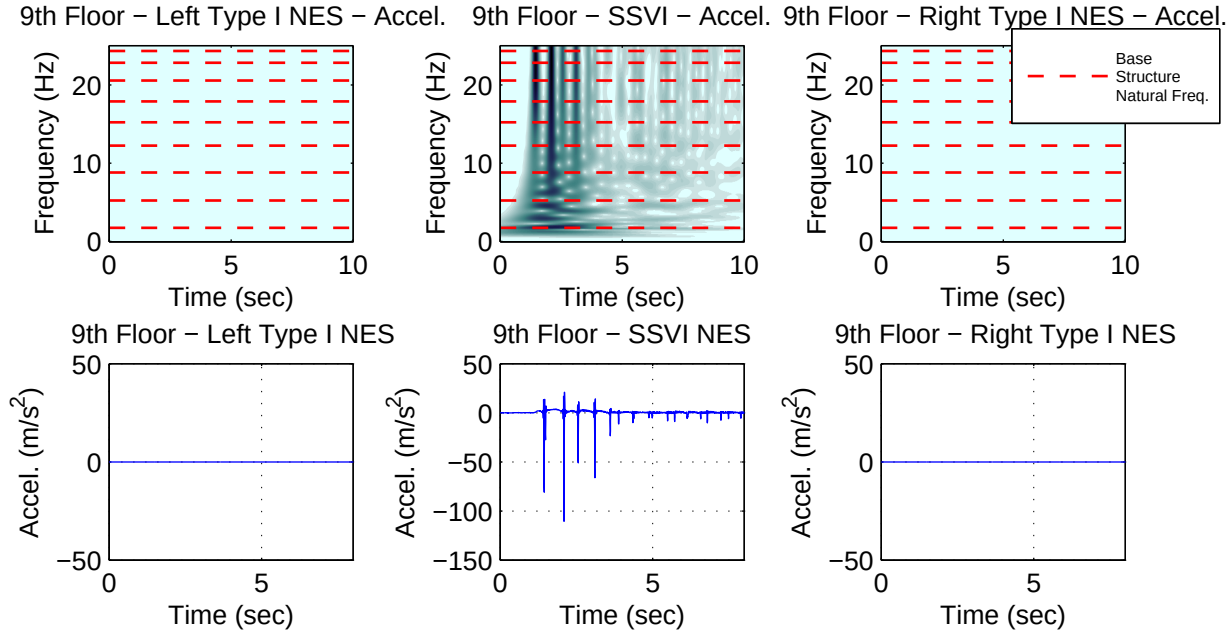

Figure D-18. Ninth floor NESs acceleration response to 100% blast simulation GM with SSVI NESs unlocked

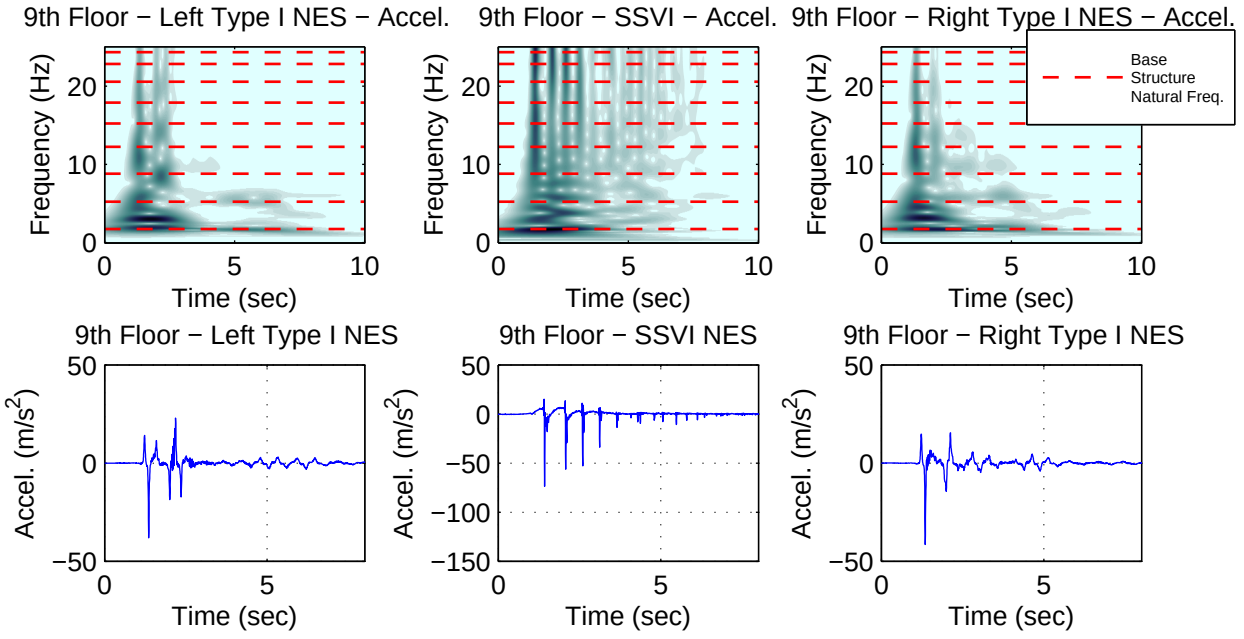

Figure D-19. Ninth floor NESs acceleration response to 100% blast simulation with all NESs unlocked

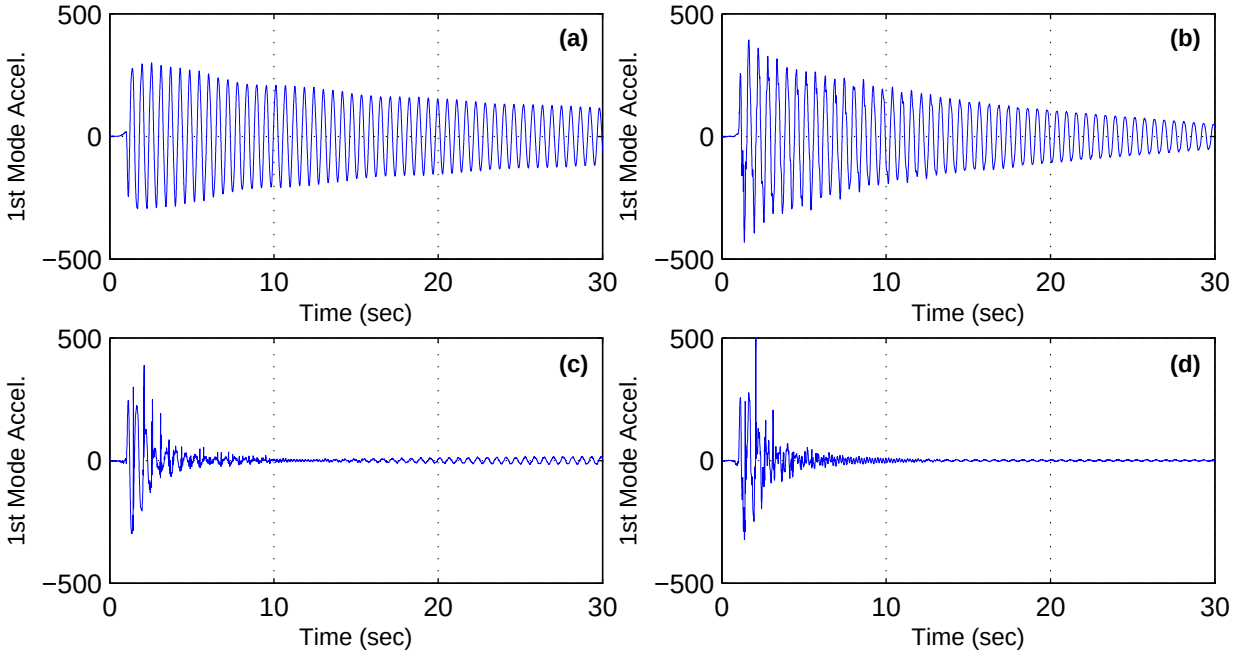

Figure D-20. First mode acceleration response to 100% blast simulation GM (a) all NESs locked, (b) Type I NESs unlocked, (c) SSVI NESs unlocked, and (d) all NESs unlocked

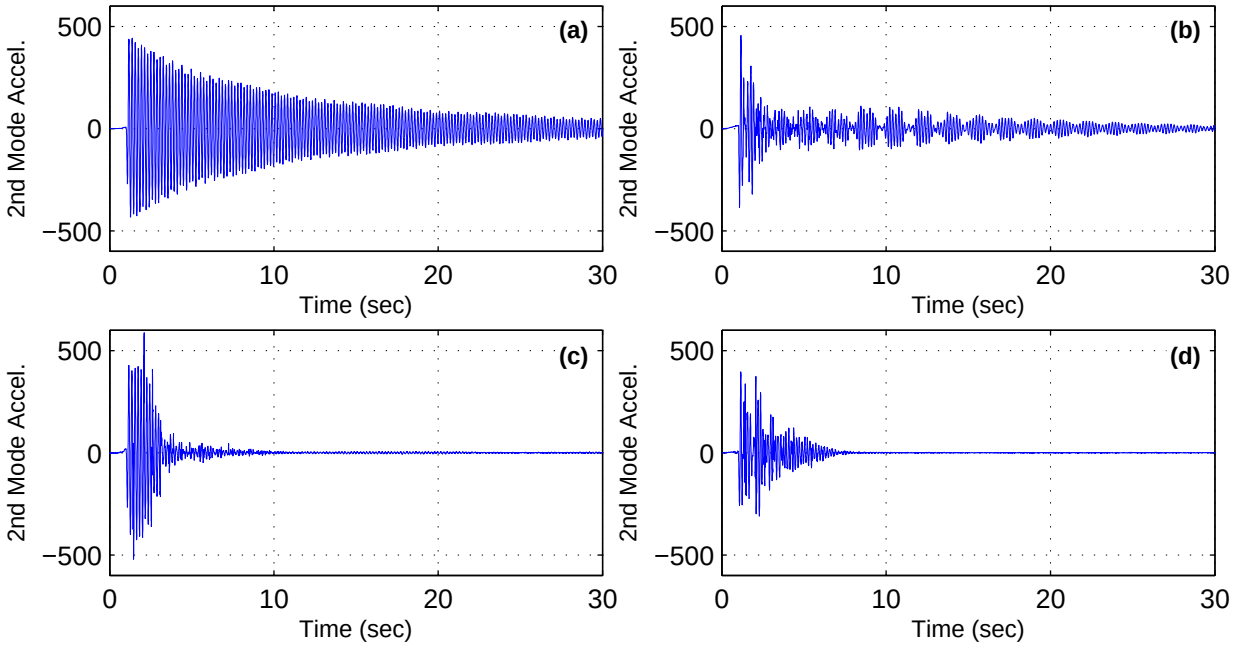

Figure D-21. Second mode acceleration response to 100% blast simulation GM (a) all NESs locked, (b) Type I NESs unlocked, (c) SSVI NESs unlocked, and (d) all NESs unlocked

D.3 Response to 150% Prototype Blast Simulation Ground Motion

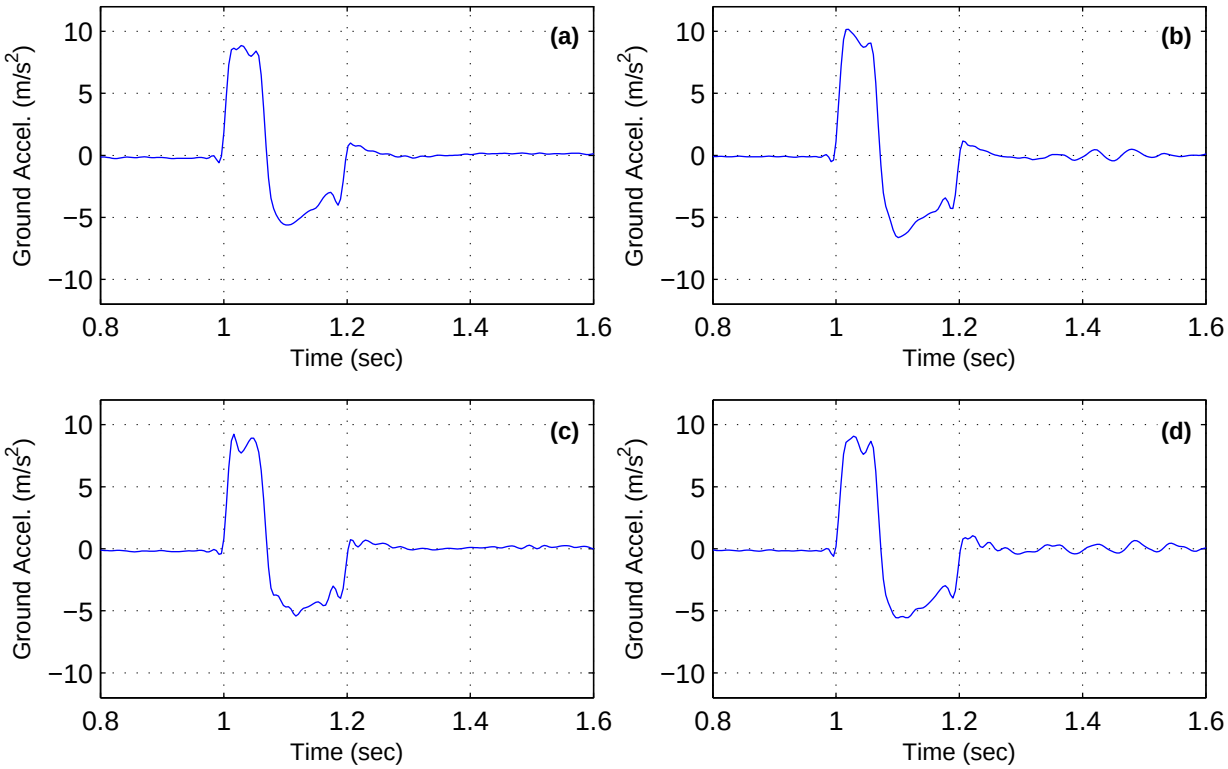

Figure D-22. Measured table acceleration response to 150% blast simulation GM (a) all NESs locked, (b) Type I NESs unlocked, (c) SSVI NESs unlocked, and (d) all NESs unlocked

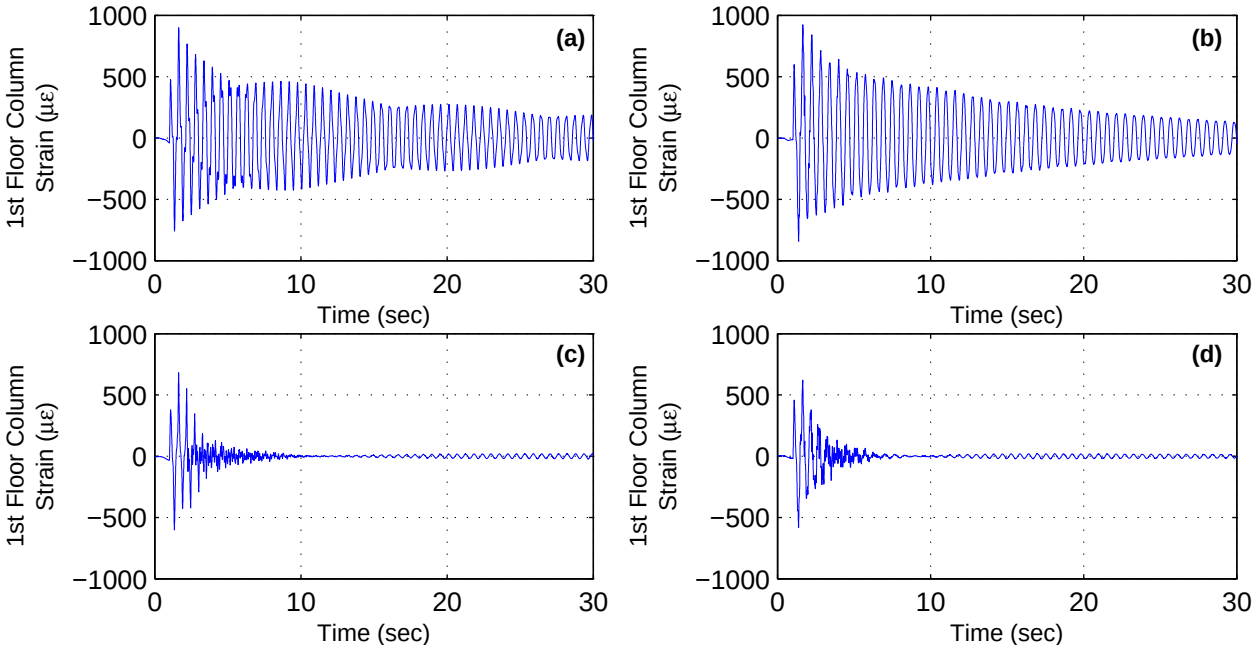

Figure D-23. First floor column strain response to 150% blast simulation GM (a) all NESs locked, (b) Type I NESs unlocked, (c) SSVI NESs unlocked, and (d) all NESs unlocked

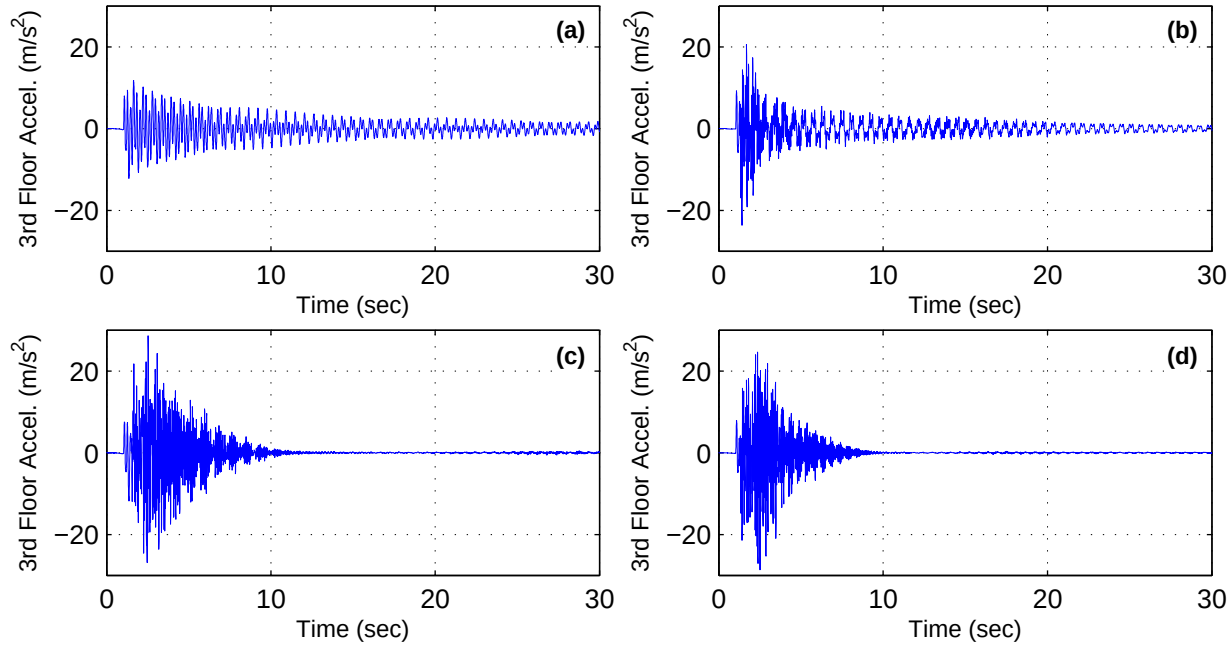

Figure D-24. Third floor acceleration response to 150% blast simulation GM (a) all NESs locked, (b) Type I NESs unlocked, (c) SSVI NESs unlocked, and (d) all NESs unlocked

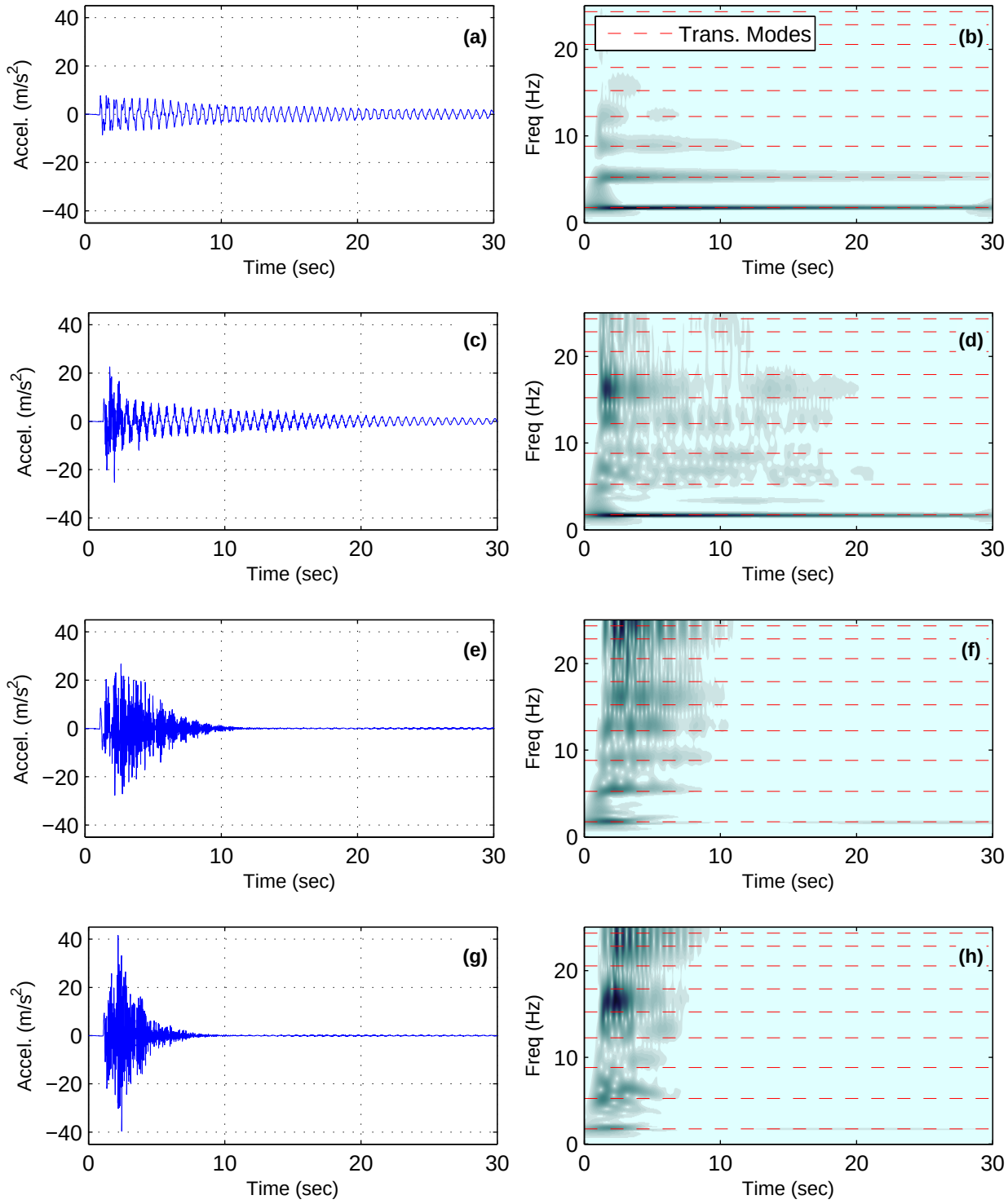

Figure D-25. Time history of seventh floor acceleration and seventh floor acceleration wavelet spectrum response to 150% blast simulation GM for (a, b) all locked configuration, (c, d) Type I NESs unlocked configuration, (e, f) SSVI NESs unlocked configuration, and (g, h) all unlocked configuration

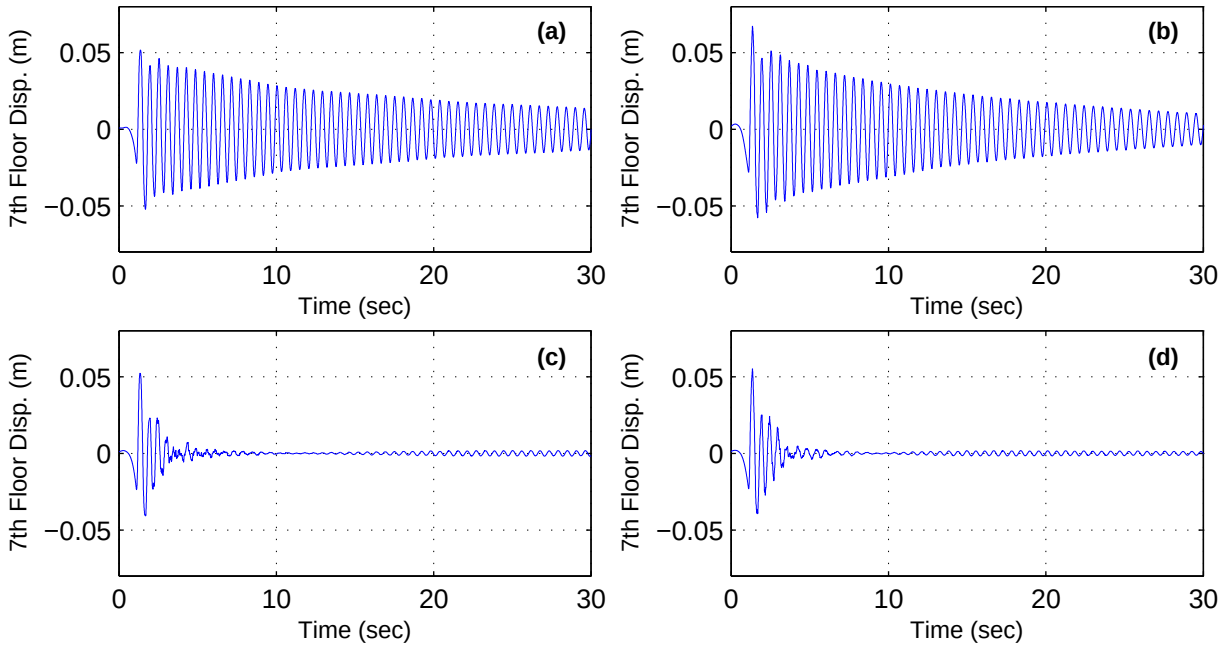

Figure D-26. Seventh floor displacement response to 150% blast simulation GM (a) all NESs locked, (b) Type I NESs unlocked, (c) SSVI NESs unlocked, and (d) all NESs unlocked

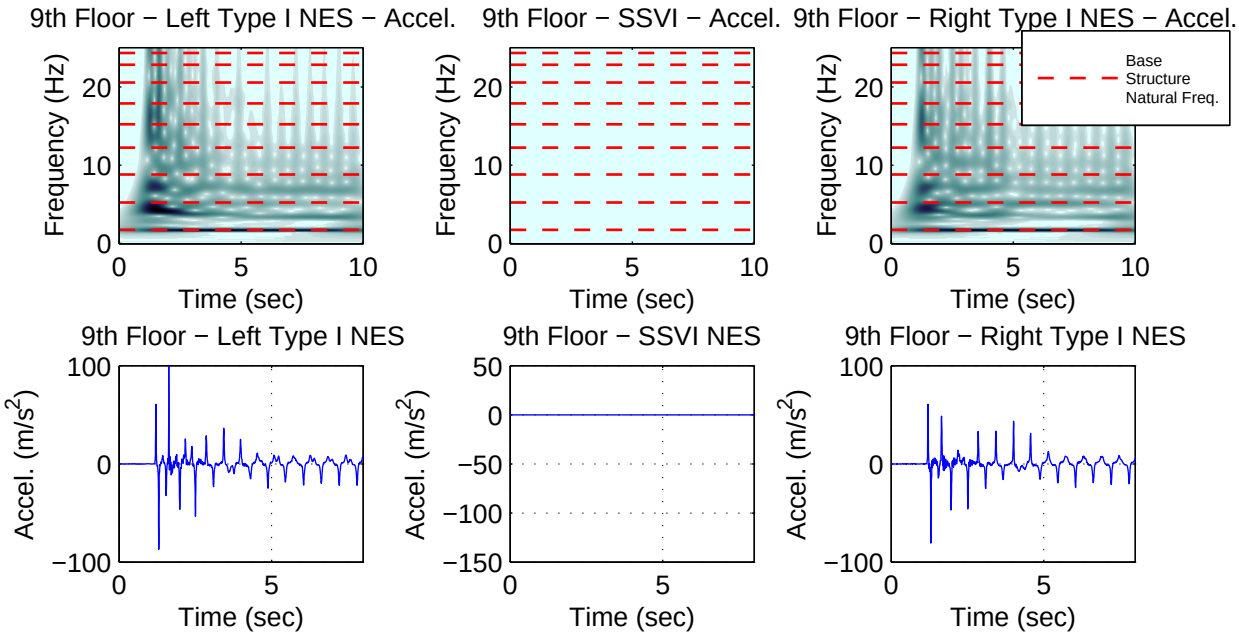

Figure D-27. Ninth floor NESs acceleration response to 150% blast simulation GM with Type I NESs unlocked

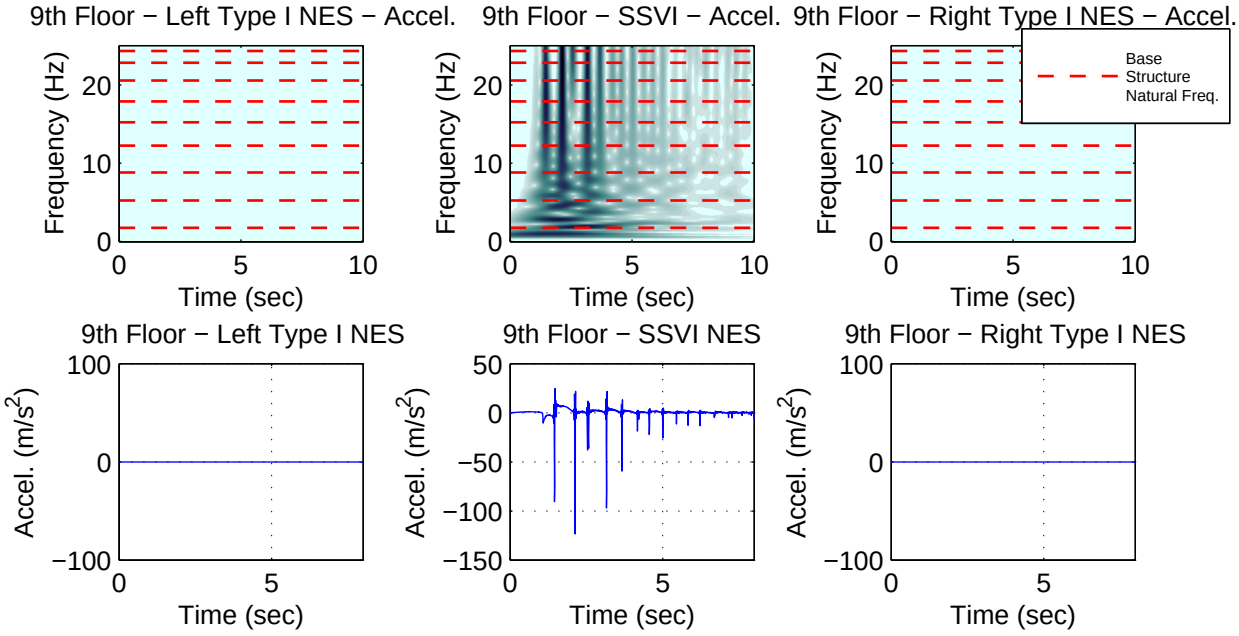

Figure D-28. Ninth floor NESs acceleration response to 150% blast simulation GM with SSVI NESs unlocked

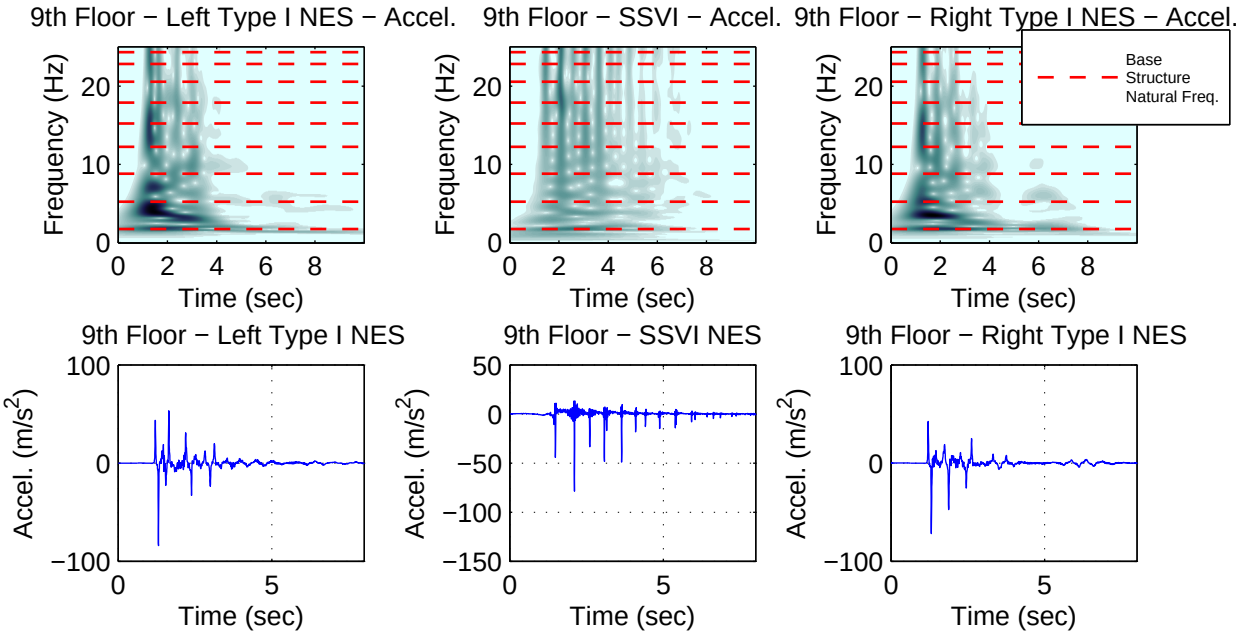

Figure D-29. Ninth floor NESs acceleration response to 150% blast simulation with all NESs unlocked

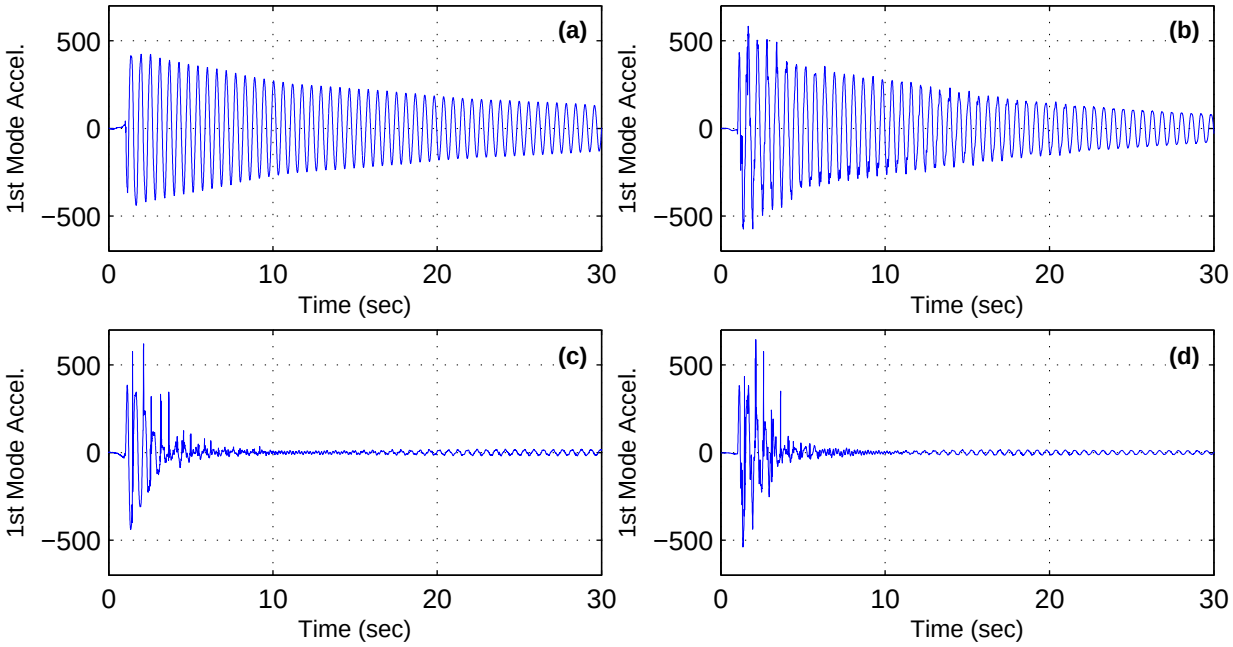

Figure D-30. First mode acceleration response to 150% blast simulation GM (a) all NESs locked, (b) Type I NESs unlocked, (c) SSVI NESs unlocked, and (d) all NESs unlocked

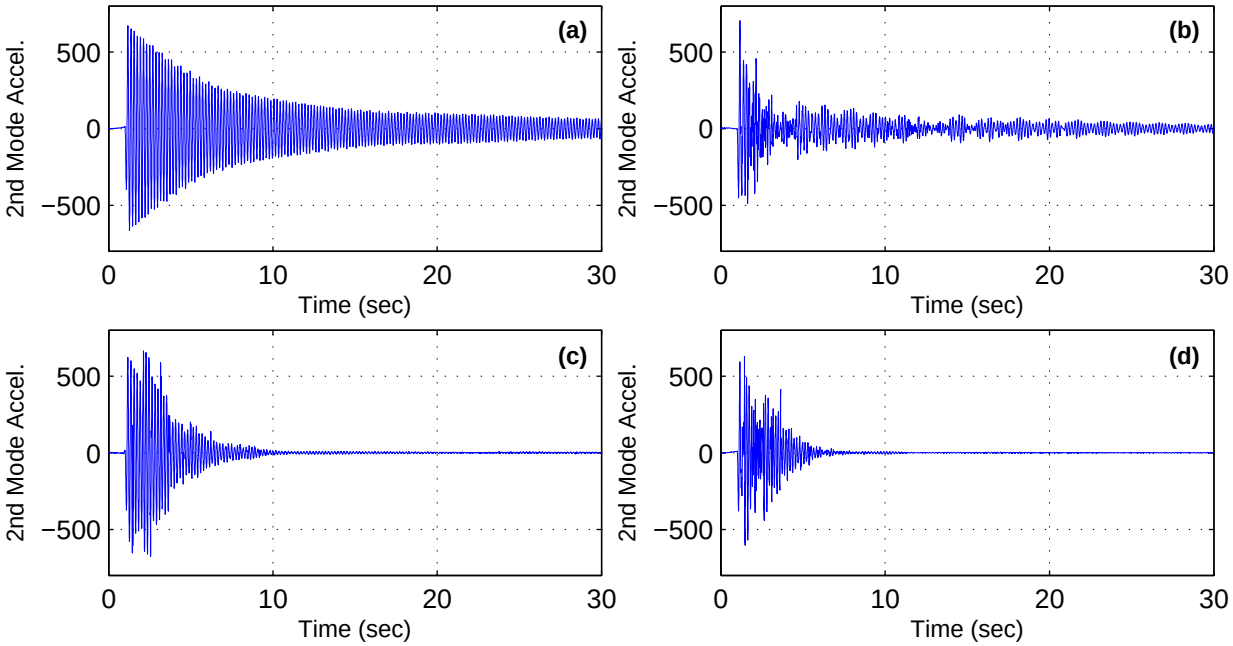

Figure D-31. Second mode acceleration response to 150% blast simulation GM (a) all NESs locked, (b) Type I NESs unlocked, (c) SSVI NESs unlocked, and (d) all NESs unlocked

D.4 Response to 200% Prototype Blast Simulation Ground Motion

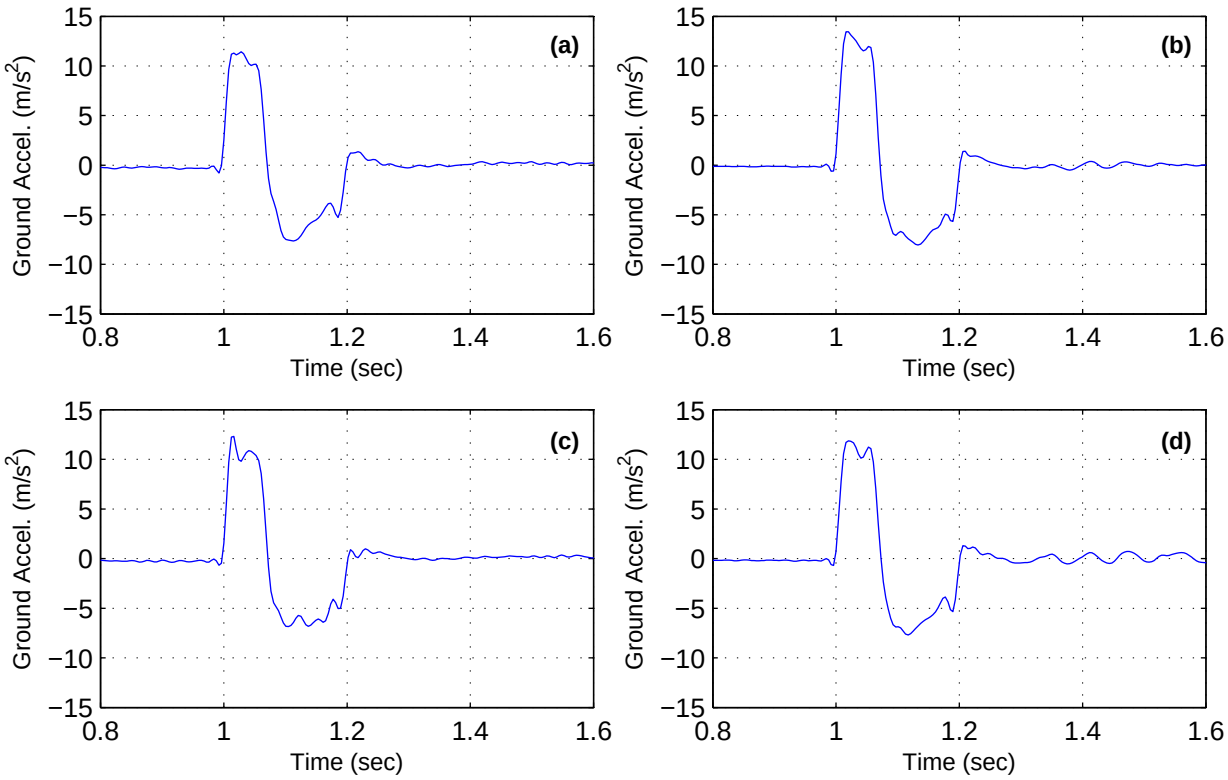

Figure D-32. Measured table acceleration response to 200% blast simulation GM (a) all NESs locked, (b) Type I NESs unlocked, (c) SSVI NESs unlocked, and (d) all NESs unlocked

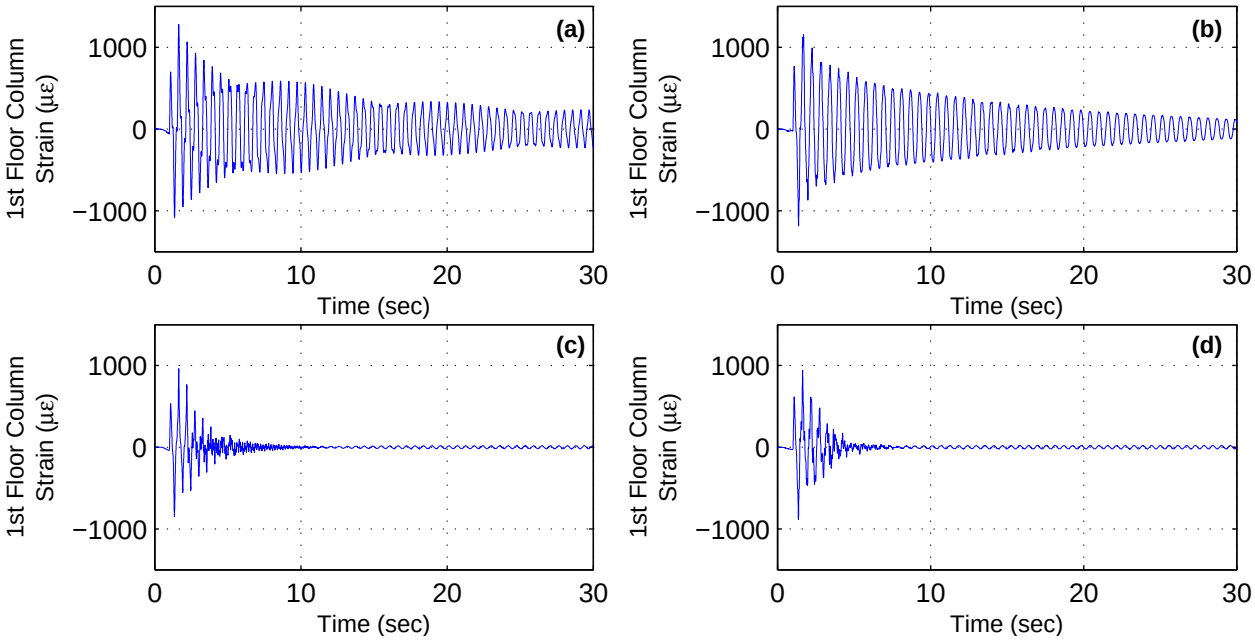

Figure D-33. First floor column strain response to 200% blast simulation GM (a) all NESs locked, (b) Type I NESs unlocked, (c) SSVI NESs unlocked, and (d) all NESs unlocked

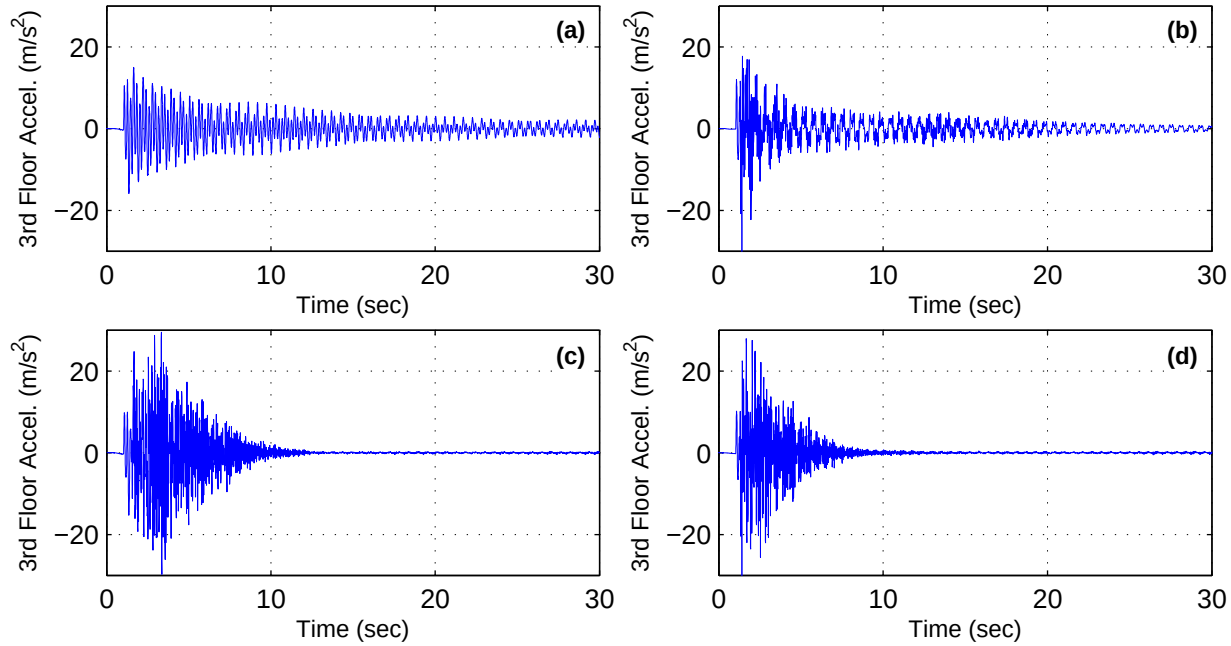

Figure D-34. Third floor acceleration response to 200% blast simulation GM (a) all NESs locked, (b) Type I NESs unlocked, (c) SSVI NESs unlocked, and (d) all NESs unlocked

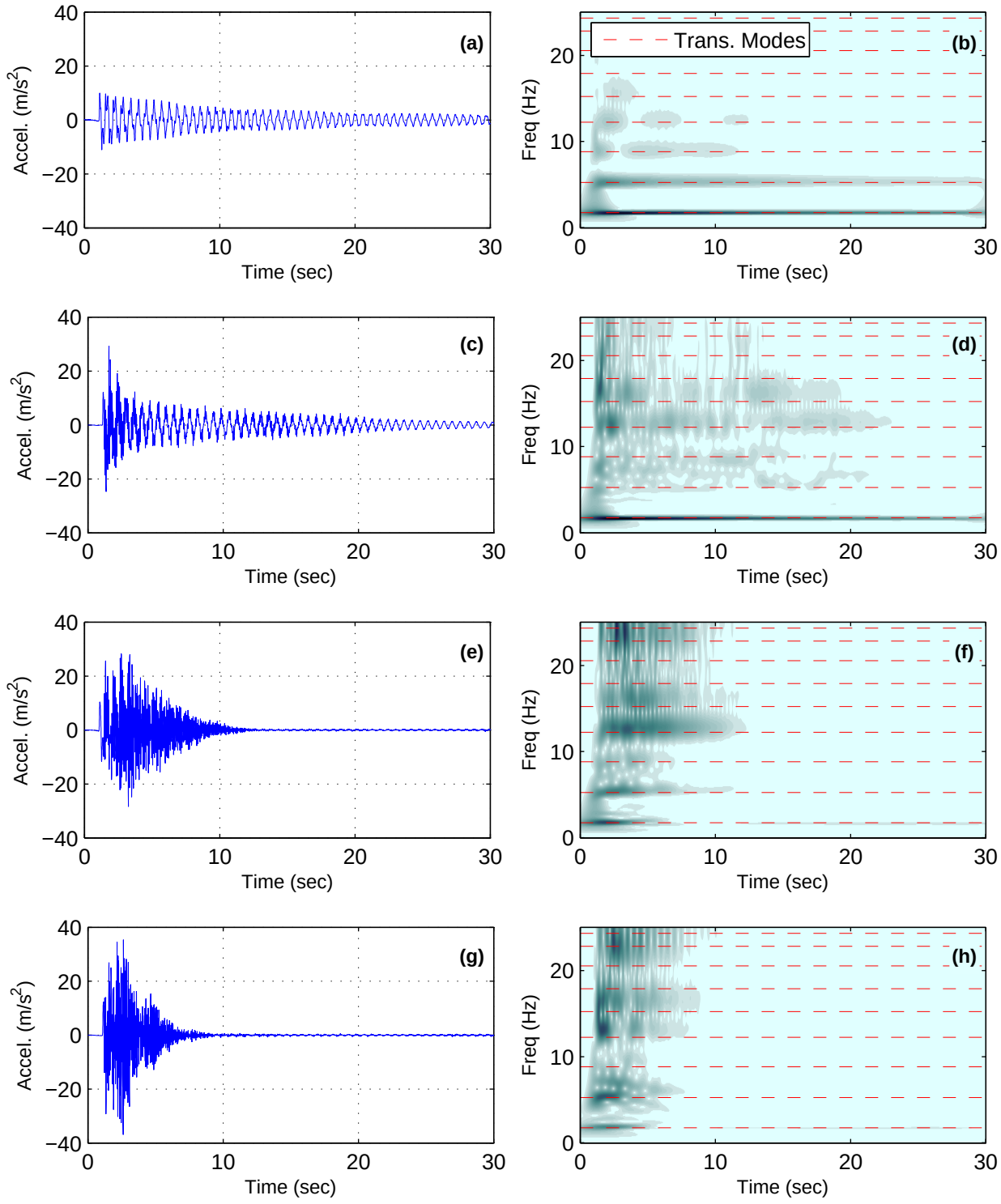

Figure D-35. Time history of seventh floor acceleration and seventh floor acceleration wavelet spectrum response to 200% blast simulation GM for (a, b) all locked configuration, (c, d) Type I NESs unlocked configuration, (e, f) SSVI NESs unlocked configuration, and (g, h) all unlocked configuration

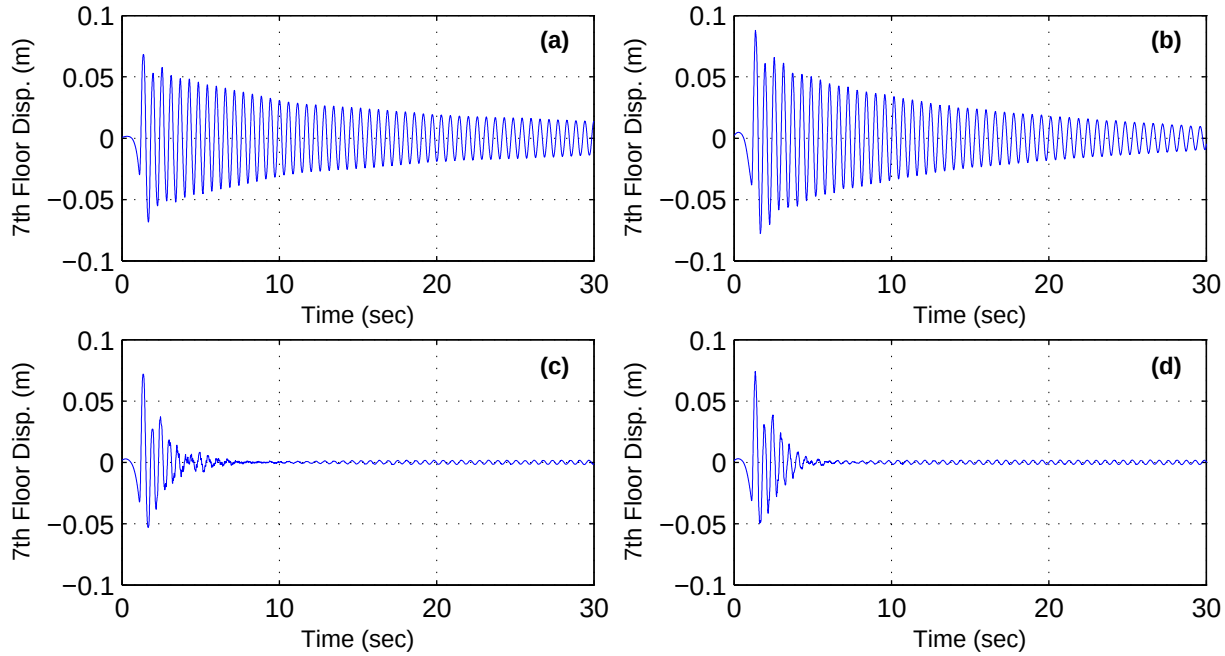

Figure D-36. Seventh floor displacement response to 200% blast simulation GM (a) all NESs locked, (b) Type I NESs unlocked, (c) SSVI NESs unlocked, and (d) all NESs unlocked

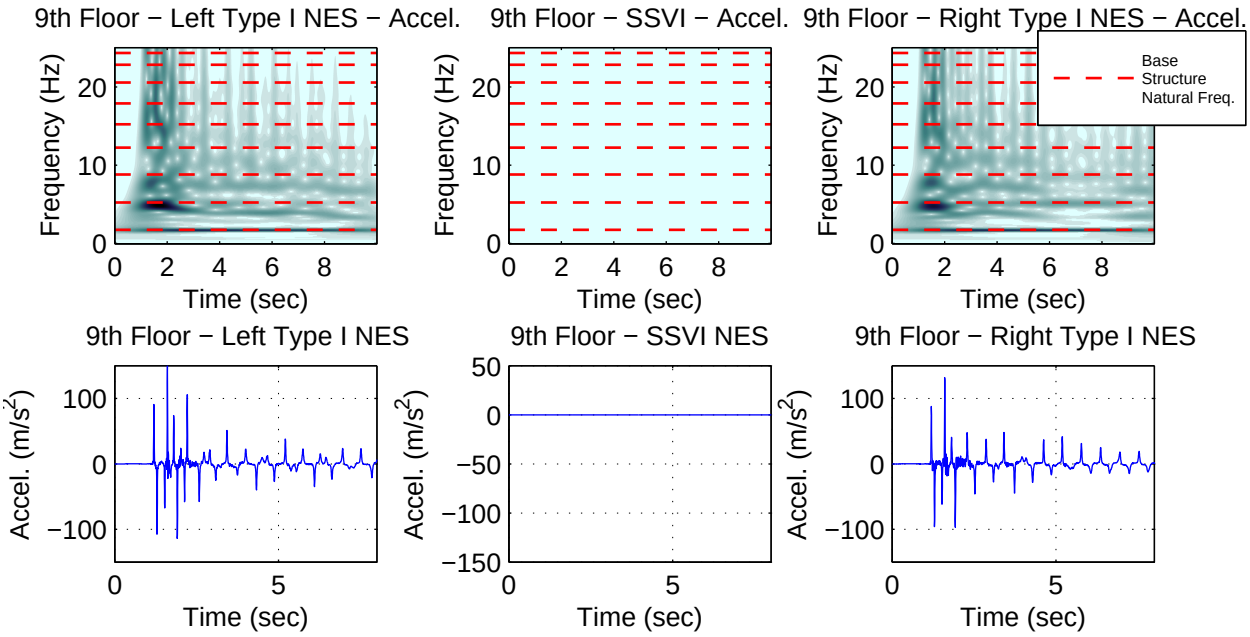

Figure D-37. Ninth floor NESs acceleration response to 200% blast simulation GM with Type I NESs unlocked

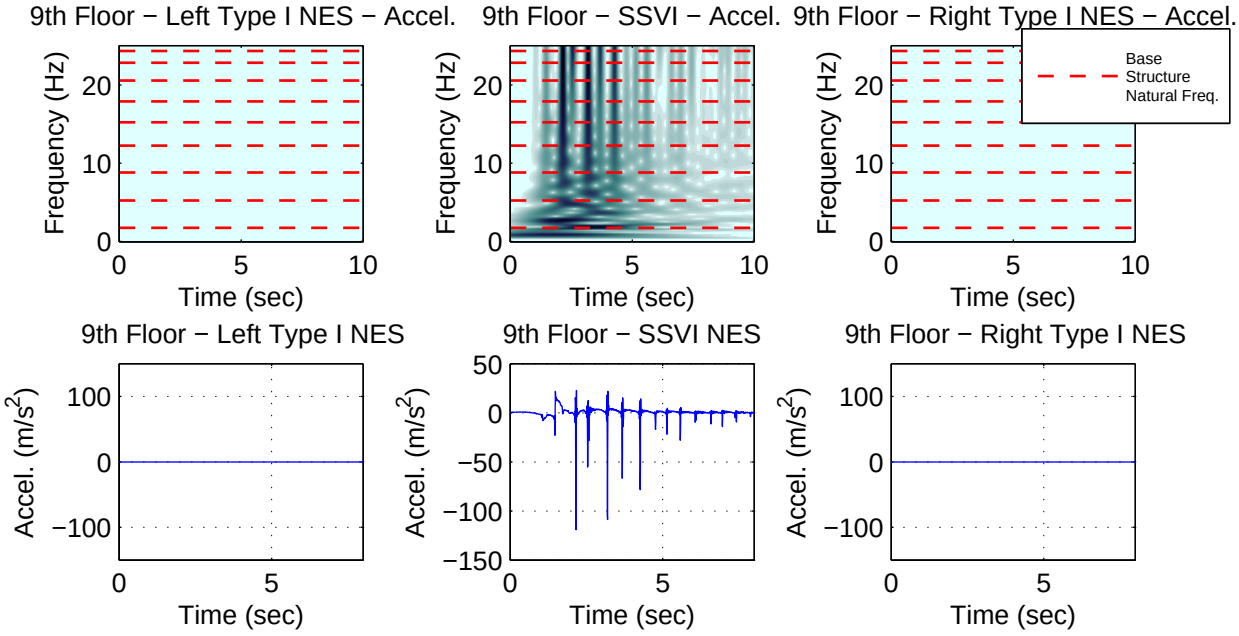

Figure D-38. Ninth floor NESs acceleration response to 200% blast simulation GM with SSVI NESs unlocked

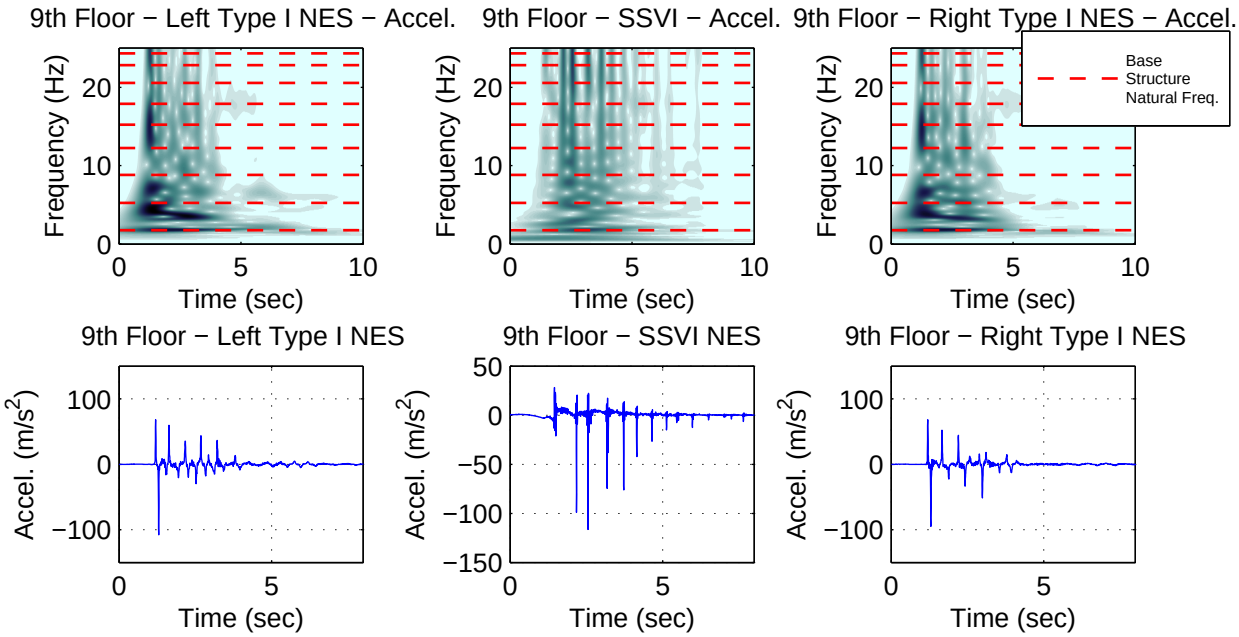

Figure D-39. Ninth floor NESs acceleration response to 200% blast simulation with all NESs unlocked

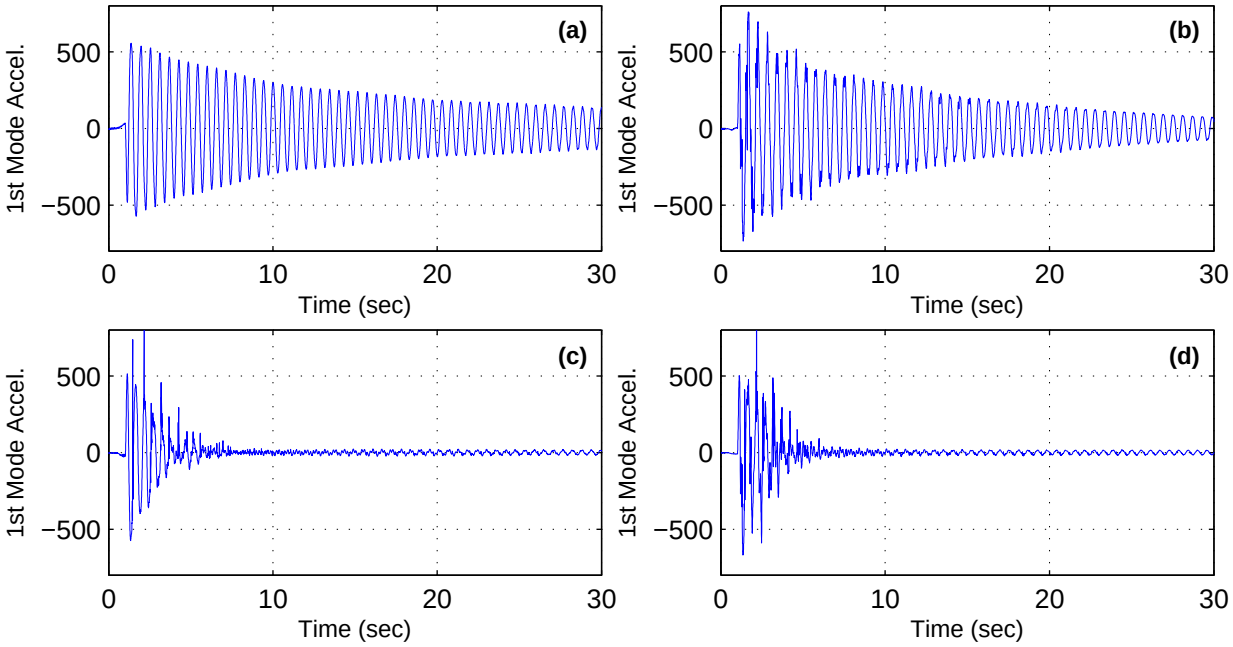

Figure D-40. First mode acceleration response to 200% blast simulation GM (a) all NESs locked, (b) Type I NESs unlocked, (c) SSVI NESs unlocked, and (d) all NESs unlocked

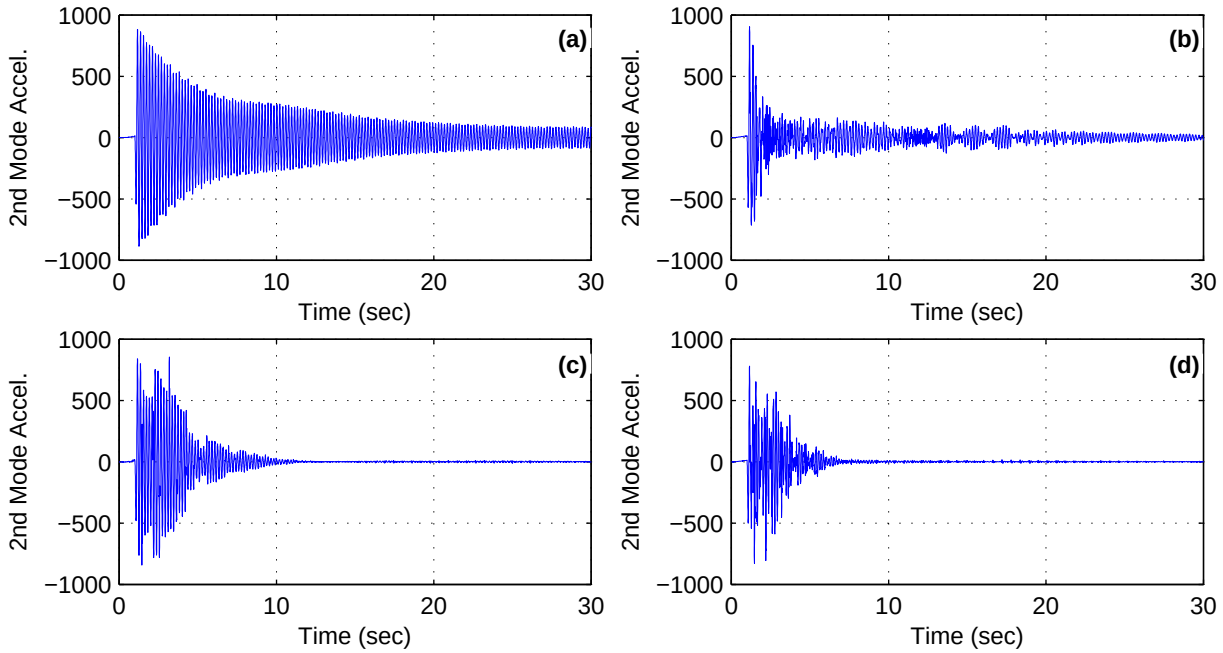

Figure D-41. Second mode acceleration response to 200% blast simulation GM (a) all NESs locked, (b) Type I NESs unlocked, (c) SSVI NESs unlocked, and (d) all NESs unlocked

List of Recent NSEL Reports

No.	*Authors*	*Title*	*Date*
029	Linderman, L.E., Mechitov, K.A., and Spencer, B.F.	Real-Time Wireless Data Acquisition for Structural Health Monitoring and Control	June 2011
030	Chang, C.-M. and Spencer, B.F.	Multi-axial Active Isolation for Seismic Protection of Buildings	May 2012
031	Phillips, B.M. and Spencer, B.F.	Model-Based Framework for Real-Time Dynamic Structural Performance Evaluation	August 2012
032	Moreu, F. and LaFave, J.M.	Current Research Topics: Railroad Bridges and Structural Engineering	October 2012
033	Linderman, L.E., Spencer, B.F.	Smart Wireless Control of Civil Structures	January 2014
034	Denavit, M.D. and Hajjar, J.F.	Characterization of Behavior of Steel-Concrete Composite Members and Frames with Applications for Design	July 2014
035	Jang, S. and Spencer, B.F.	Structural Health Monitoring for Bridge Structures using Wireless Smart Sensors	May 2015
036	Jo, H. and Spencer, B.F.	Multi-scale Structural Health Monitoring using Wireless Smart Sensors	May 2015
037	Li, J. and Spencer, B.F.	Monitoring, Modeling, and Hybrid Simulation: An Integrated Bayesian-based Approach to High-fidelity Fragility Analysis	May 2015
038	Sim, S-H. and Spencer, B.F.	Decentralized Identification and Multimetric Monitoring of Civil Infrastructure using Smart Sensors	June 2015
039	Giles, R.K. and Spencer, B.F.	Development of a Long-term, Multimetric Structural Health Monitoring System for a Historic Steel Truss Swing Bridge	June 2015
040	Spencer, B.F., Moreu, F. and Kim, R.E.	Campaign Monitoring of Railroad Bridges in High-Speed Rail Shared Corridors using Wireless Smart Sensors	June 2015
041	Moreu, F. and Spencer, B.F.	Framework for Consequence-based Management and Safety of Railroad Bridge Infrastructure Using Wireless Smart Sensors (WSS)	June 2015
042	Spencer, B.F. and Gardoni, P. (Eds.)	Innovations and Advances in Structural Engineering: Honoring the Career of Yozo Fujino	August 2015
043	Asai, T. and Spencer, B.F.	Structural Control Strategies for Earthquake Response Reduction of Buildings	August 2015
044	Kim, R. and Spencer, B.F.	Modeling and Monitoring of the Dynamic Response of Railroad Bridges using Wireless Smart Sensors	September 2015
045	Wierschem, N. and Spencer, B.F.	Targeted Energy Transfer using Nonlinear Energy Sinks for the Attenuation of Transient Loads on Building Structures	September 2015